This work was performed for the Jet Propulsion Laboratory, California Institute of Technology, sponsored by the National Aeronautics and Space Administration under Contract NAS7-100.

N68-18658

Surveyor Spacecraft System

SURVEYOR I FLIGHT PERFORMANCE

FINAL REPORT

Volume II of III

JPL Contract 950056 / October 1966

SSD 68222R

J.D. CLOUD
Manager
System Engineering and Analysis Laboratory

K.C. BEALL
Director
Surveyor I Post Flight Evaluation

R.H. LEUSCHNER
Head
Post Flight Analysis Section

HUGHES
HUGHES AIRCRAFT COMPANY
SPACE SYSTEMS DIVISION

PRECEDING PAGE BLANK NOT FILMED.

CONTENTS

			Page
5.0	PERFORMANCE ANALYSIS (CONTINUED)		
	5.3	ELECTRICAL POWER SUBSYSTEM	
		5.3.1 Introduction	5.3-1
		5.3.2 Major Transit Events and Times	5.3-1
		5.3.3 Summary of Results	5.3-2
		5.3.4 Anomaly Description	5.3-21
		5.3.5 Conclusions and Recommendations	5.3-22
		5.3.6 Analysis	5.3-22
		5.3.7 References	5.3-47
		5.3.8 Acknowledgments	5.3-47
	5.4	RF DATA LINK SUBSYSTEM	
		5.4.1 Introduction	5.4-1
		5.4.2 Items Constituting Analysis	5.4-3
		5.4.3 Mode, Bit Rate, and Subsystem Configuration Summary	5.4-3
		5.4.4 Summary of Results	5.4-3
		5.4.5 Anomaly Description	5.4-8
		5.4.6 Conclusions and Recommendations	5.4-15
		5.4.7 Subsystem Performance Analysis	5.4-17
		5.4.8 References	5.4-76
		5.4.9 Acknowledgments	5.4-76
	5.5	SIGNAL PROCESSING	
		5.5.1 Introduction	5.5-1
		5.5.2 Major Signal Processing Subsystem Events During Transit	5.5-1
		5.5.3 Performance Summary	5.5-1
		5.5.4 Anomaly Summary	5.5-2
		5.5.5 Conclusions and Recommendations	5.5-2
		5.5.6 Subsystem Performance Analysis	5.5-3
		5.5.7 References	5.5-35
		5.5.8 Acknowledgments	5.5-35

5.6 FLIGHT CONTROL

5.6.1	Introduction	5.6-1
5.6.2	Analysis Items	5.6-3
5.6.3	Major Events	5.6-6
5.6.4	Flight Control Results Summary	5.6-6
5.6.5	Control System Anomalies	5.6-6
5.6.6	Conclusions and Recommendations	5.6-15
5.6.7	Flight Control System Analyses	5.6-15
5.6.8	References	5.6-217
5.6.9	Acknowledgments	5.6-219

ILLUSTRATIONS

		Page
5.3-1	Electrical Power Schematic	5.3-3
5.3-2	Battery Energy Remaining	5.3-3
5.3-3	Power Consumed and Loads	5.3-6
5.3-4	Shunt Unbalance Current	5.3-10
5.3-5	Battery Charge Regulator Efficiency	5.3-14
5.3-6	Boost Regulator Efficiency	5.3-15
5.3-7	22-Volt Unregulated Bus	5.3-25
5.3-8	Unregulated Output Current	5.3-26
5.3-9	Boost Regulator Difference Current	5.3-27
5.3-10	Battery Discharge Current	5.3-28
5.3-11	Solar Cell Array Voltage	5.3-29
5.3-12	Solar Cell Array Current	5.3-30
5.3-13	Regulated Output Current	5.3-31
5.3-14	Auxiliary Battery Voltage	5.3-32
5.3-15	Auxiliary Battery Temperature	5.3-33
5.3-16	Unregulated Output Current	5.3-38
5.3-17	Coast Phase II	5.3-39
5.3-18	Altitude Marking Radar Electronic Temperature	5.3-40
5.3-19	Vernier Line Temperatures	5.3-42
5.3-20	Radar and Squib Current During Terminal Descent	5.3-45
5.4-1	Communications Subsystem Block Diagram	5.4-2
5.4-2	Receiver AGE	5.4-18
5.4-3	Transmitter Frequency Versus Time From Launch	5.4-21
5.4-4	NBVXO Frequency History After High Power Turnon	5.4-23
5.4-5	Signal Levels at Initial Acquisition	5.4-26
5.4-6	Gain Coverage Curve for Omnidirectional Antenna B During Initial Acquisition	5.4-27
5.4-7	Earth Vector Path Relative to Omnidirectional Antenna Gain Contours	5.4-29
5.4-8	DSIF Received Signal Levels	5.4-32
5.4-9	Receiver A and B Automatic Gain Control Versus Time	5.4-32
5.4-10	Bit Error Rate Versus Time	5.4-36
5.4-11	Number of Parity Errors Versus Commutator Word Position	5.4-38
5.4-12	DSIF Receiver Automatic Gain Control During Canopus Acquisition	5.4-41

		Page
5.4-13	Receiver B Automatic Gain Control During Canopus Acquisition	5.4-44
5.4-14	Receiver A Automatic Gain Control During Canopus Acquisition	5.4-44
5.4-15	Receiver A Automatic Gain Control During Canopus Acquisition	5.4-45
5.4-16	Omnidirectional Antenna B Transmitter Power	5.4-46
5.4-17	DSIF Received Signal Strength During Reverse Midcourse Maneuvers	5.4-51
5.4-18	Signal Strength During Reverse Midcourse Maneuvers	5.4-53
5.4-19	DSIF Received Signal Strength During Preterminal Maneuvers	5.4-57
5.4-20	DSIF Received Signal Strength During Terminal Descent	5.4-59
5.4-21	Omnidirectional Antenna B Transmitter Power	5.4-61
5.4-22	Transmitter A Traveling-Wave Tube Temperature Versus Time	5.4-63
5.4-23	Receiver Signal Level Variations During A/SPP Positioning	5.4-65
5.4-24	Receiver A Automatic Gain Control Versus Time	5.4-68
5.4-25	Receiver B Automatic Gain Control Versus Time	5.4-68
5.4-26	Receiver A Automatic Frequency Control Versus Time	5.4-69
5.4-27	Static Phase Error B Versus Time	5.4-69
5.4-28	Static Phase Error A Versus Time	5.4-70
5.4-29	Receiver B Automatic Frequency Control Versus Time	5.4-71
5.4-30	Compartment A Tray Top Temperature Versus Time	5.4-72
5.4-31	Compartment A Tray Bottom Temperature Versus Time	5.4-73
5.4-32	Transmitter A Temperature Versus Time	5.4-74
5.4-33	Transmitter B Temperature Versus Time	5.4-75
5.5-1	ESP Commutator Unbalance Current	5.5-5
5.5-2	AESP Commutator Unbalance Current	5.5-6
5.5-3	Reference Voltage	5.5-22
5.5-4	Potentiometer Reference Return	5.5-23
5.6-1	Pitch Gyro Error, FC-16	5.6-19
5.6-2	Low Gyro Error, FC-17	5.6-20
5.6-3	Roll Gyro Response at Beginning of Sun Acquisition Phase	5.6-24
5.6-4	Roll Gyro Response to a Negative Rate Command at Midcourse	5.6-25
5.6-5	Roll Gyro Response During Sun Acquisition Phase	5.6-26
5.6-6	Roll Gyro Response to a Positive Rate Command	5.6-27
5.6-7	Star Map	5.6-31
5.6-8	Star Intensity Profile During First Canopus	5.6-33
5.6-9	Star Intensity Profile During Postmidcourse Roll	5.6-34
5.6-10	Star Intensity Profile During Ratio Maneuver (Roll 1)	5.6-35
5.6-11	Canopus Error Signal Profile During First Midcourse Roll	5.6-36
5.6-12	Canopus Error Signal (Star Map)	5.6-40

		Page
5.6-13	Star Intensity Signal (Star Map)	5.6-41
5.6-14	Roll Gyro Response at Beginning of Star Acquisition	5.6-42
5.6-15	Primary Sun Sensor Pitch Error	5.6-43
5.6-16	Primary Sun Sensor Yaw Error	5.6-44
5.6-17	Primary Sun Sensor Yaw Error	5.6-45
5.6-18	Primary Sun Sensor Pitch Error	5.6-46
5.6-19	215-Minute Sample of Optical Limit Cycle	5.6-53
5.6-20	140-Minute Sample of Inertial Limit Cycle	5.6-55
5.6-21	Gyro Drift Test	5.6-63
5.6-22	Time History of Gyro (Non-g) Drift	5.6-65
5.6-23	Roll Gyro Response for Premidcourse Roll Maneuver	5.6-68
5.6-24	Roll Gyro Response Profile for Premidcourse Roll Maneuver	5.6-69
5.6-25	Yaw Gyro Response Profile for Premidcourse Yaw Maneuver	5.6-70
5.6-26	Pitch Sun Sensor Error Signal	5.6-73
5.6-27	Yaw Sun Sensor Error Signal	5.6-73
5.6-28	Canopus Error Signal	5.6-73
5.6-29	Premidcourse Maneuver Errors	5.6-79
5.6-30	Yaw Gyro Response Profile for Postmidcourse Yaw Maneuver	5.6-79
5.6-31	Roll Gyro Response Profile for Postmidcourse Roll Maneuver	5.6-80
5.6-32	Star Intensity, FC-14, During Premidcourse Roll Maneuver	5.6-80
5.6-33	Canopus Error, FC-12, During Premidcourse Roll Maneuver	5.6-81
5.6-34	Star Intensity, FC-14, During Postmidcourse Roll Maneuver	5.6-81
5.6-35	Canopus Error, FC-12, During Postmidcourse Roll Maneuver	5.6-82
5.6-36	Commanded Angle to Roll Actuator From SC-1 Telemetry of FC-43 at Midcourse	5.6-89
5.6-37	Roll Precession Command From SC-1 Telemetry of FC-49 at Midcourse	5.6-91
5.6-38	Roll Precession Command and Commanded Angle to Roll Actuator from SC-1 Telemetry of FC-49 and FC-43 at Midcourse	5.6-93
5.6-39	Acceleration Error Signal Profile at Midcourse	5.6-95
5.6-40	Acceleration Error Signal	5.6-97
5.6-41	Midcourse Thrust-Time Profile From Flight Control Telemetry	5.6-101
5.6-42	Midcourse Total Thrust-Time Profile	5.6-103
5.6-43	Orientation of Vernier Engines in Spacecraft Coordinates	5.6-108
5.6-44	Moments About Spacecraft X-Y Axes Due to Vernier Engine Thrusts Using Corrected SC-1 Thrust Command Telemetry for FC-25, FC-26, and FC-27	5.6-109

		Page
5.6-45	Pitch Gyro Error Signal at Midcourse	5.6-111
5.6-46	Yaw Gyro Error Signal at Midcourse	5.6-113
5.6-47	Roll Inertial, Long Duration Attitude Maneuver	5.6-117
5.6-48	Yaw Inertial, Long Duration Attitude Maneuver	5.6-118
5.6-49	Roll Precession Command (First Roll)	5.6-119
5.6-50	Pitch Gyro Error (First Roll)	5.6-120
5.6-51	Yaw Gyro Error (First Roll)	5.6-121
5.6-52	Yaw Gyro Error (Yaw Maneuver)	5.6-122
5.6-53	Pitch Gyro Error (Yaw Maneuver)	5.6-123
5.6-54	Roll Precession Command (Second Roll)	5.6-124
5.6-55	Pitch Gyro Error (Second Roll)	5.6-125
5.6-56	Yaw Gyro Error (Second Roll)	5.6-126
5.6-57	Main Retro Phase Vernier Engine Thrust-Time Profile From Flight Control Telemetry for FC-25, FC-26, and FC-27	5.6-139
5.6-58	Main Retro Phase Total Commanded Vernier Engine Thrust From Telemetry for FC-25, FC-26, and FC-27	5.6-145
5.6-59	Moments About Spacecraft X-Y Axes Due to Vernier Engine Thrusts Using SC-1 Corrected Thrust Command Telemetry for FC-25, FC-26, and FC-27	5.6-147
5.6-60	Moments About Predicted Spacecraft Center of Gravity Due to Vernier Engine Thrusts Using Corrected SC-1 Thrust Command Telemetry for FC-25, FC-26, and FC-27	5.6-149
5.6-61	Pitch Gyro Error, FC-16	5.6-155
5.6-62	Yaw Gyro Error, FC-17	5.6-156
5.6-63	Roll Actuator Signal, FC-43	5.6-157
5.6-64	Retro Accelerometer, FC-32	5.6-158
5.6-65	Thrust Command to Engine 1	5.6-159
5.6-66	Thrust Command to Engine 2	5.6-160
5.6-67	Thrust Command to Engine 3	5.6-161
5.6-68	Vernier Descent Trajectory	5.6-162
5.6-69	Vernier Descent Trajectory, Range > 1000 Feet	5.6-163
5.6-70	Pitch Gyro Error Signal	5.6-167
5.6-71	Yaw Gyro Error Signal	5.6-168
5.6-72	True V_x	5.6-169
5.6-73	True V_y	5.6-170
5.6-74	True V_z	5.6-171
5.6-75	True Slant Range	5.6-172
5.6-76	Thrust Command, Engine 1	5.6-173
5.6-77	Thrust Command, Engine 2	5.6-174
5.6-78	Thrust Command, Engine 3	5.6-175
5.6-79	Spacecraft Attitude With Respect to Selenographic Coordinate System	5.6-178
5.6-80	Geometry	5.6-178
5.6-81	Nitrogen Weight History	5.6-181
5.6-82	Nitrogen Weight Curve	5.6-183

		Page
5.6-83	Nitrogen Pressure Telemetry Calibration Curve	5.6-184
5.6-84	Acceleration Time History	5.6-190
5.6-85	Pitch and Yaw Gyro Signals During Retro Phase	5.6-191
5.6-86	Offset Voltage Due to Unbalanced Commutator Current	5.6-193
5.6-87	Flight Control Variables for Terminal Descent	5.6-195
5.6-88	V_z Noise Amplitude	5.6-197
5.6-89	Slant Range Noise Amplitude	5.6-198
5.6-90	V_x or V_y Noise Amplitude	5.6-199
5.6-91	Roll Gyro Error and Canopus Sensor Signals	5.6-204
5.6-92	Spacecraft Seen Along Pitch Axis in Positive Direction	5.6-206
5.6-93	Spacecraft Seen Along Roll Axis in Positive Direction	5.6-207
5.6-94	Particle Trajectory	5.6-208
5.6-95	Roll Actuator (FC-43) SC-1 Telemetry and Preflight Prediction	5.6-211
5.6-96	Roll Precession Command and Commanded Angle to Roll Actuator From SC-1 Telemetry of FC-49 and FC-43	5.6-213
5.6-97	Acceleration Loop Parameters (Near Cutoff)	5.6-215
5.6-98	Analyses of Precutoff Glitch Anomaly	5.6-216

PRECEDING PAGE BLANK NOT FILMED.

TABLES

		Page
5. 3-1	Events and Times, Electrical Power	5. 3-2
5. 3-2	Summary of Results, Electrical Power	5. 3-4
5. 3-3	Battery Energy Used	5. 3-5
5. 3-4	Optimum Charge Regulator Efficiency	5. 3-16
5. 3-5	Boost Regulator Efficiency	5. 3-17
5. 3-6	Boost Regulator Efficiency Versus EP-30 and Regulated Power	5. 3-18
5. 3-7	Selected Equipment Loads	5. 3-21
5. 3-8	Tabulation of EP Values Versus Event	5. 3-34
5. 3-9	Main Battery Efficiency	5. 3-34
5. 3-10	Solar Panel Output Energy	5. 3-35
5. 3-11	Index of Mission Plots	5. 3-48
5. 4-1	Listing of Up-Link and Down-Link Parameters From FAT, STV, and CDC Tests	5. 4-4
5. 4-2	Telemetry Mode Summary	5. 4-9
5. 4-3	Spacecraft Configuration Sheet	5. 4-11
5. 4-4	Performance Parameter Summary	5. 4-12
5. 4-5	Acquisition Events	5. 4-25
5. 4-6	Comparison of Parity Error Rate for "Good" and "Bad" Tapes	5. 4-37
5. 4-7	Change of BCD Magnitude in Bad Parity Words	5. 4-40
5. 4-8	Parity Errors Versus Bit Position in a Word	5. 4-43
5. 4-9	Midcourse Maneuver Summary Table	5. 4-50
5. 4-10	Terminal Maneuver Summary	5. 4-55
5. 4-11	Teletype Data During Receiver Threshold Test	5. 4-64
5. 5-1	Summary of Signal Processing Performance Parameters	5. 5-2
5. 5-2	Data Channel Output Impedances	5. 5-7
5. 5-3	Offset Voltage Corrections Compared to Total Error for 6 μa Unbalanced Current	5. 5-19
5. 5-4	Offset Voltage Corrections Compared to Total Error for 12 μa Unbalanced Current	5. 5-20
5. 5-5	Comparison of Mechanism Signals in ESP and AESP Commutators	5. 5-24
5. 5-6	Average Value of Current Calibration Signals	5. 5-25
5. 5-7	Temperature Measurements Influenced by Preceding Temperature Measurement at 4400 bits/sec	5. 5-27

		Page
5. 5-8	Temperature Measurements That Will Have Significant Positive Errors at 4400 bits/sec	5. 5-30
5. 5-9	Limits of True Values in BCD and Approximate Temperature Error for Those Measurements Listed in Table 5. 5-8	5. 5-31
5. 5-10	Commutator Table for Change From Mode 2 to Mode 3	5. 5-33
5. 6-1	Time and Events Log	5. 6-7
5. 6-2	Flight Control Results	5. 6-8
5. 6-3	Control System Anomalies	5. 6-14
5. 6-4	Gyro Temperatures, °F	5. 6-16
5. 6-5	Events Between Launch and Centaur Separation	5. 6-17
5. 6-6	Centaur Separation Phase	5. 6-18
5. 6-7	Calibration Coefficients for Rate Mode Calculations	5. 6-22
5. 6-8	Nitrogen Gas Consumption	5. 6-22
5. 6-9	Canopus Lockon Signal	5. 6-37
5. 6-10	Major Events and Times	5. 6-48
5. 6-11	Summary of Results	5. 6-49
5. 6-12	SC-1 Performance Detail	5. 6-71
5. 6-13	Direction Cosine Matrices	5. 6-76
5. 6-14	Midcourse Ignition Transient Control Summary	5. 6-83
5. 6-15	Midcourse Shutdown Summary	5. 6-85
5. 6-16	SC-1 Performance Detail	5. 6-96
5. 6-17	Major Events and Times (Day 153), Preretro Maneuvers	5. 6-115
5. 6-18	Time and Events Log	5. 6-136
5. 6-19	Terminal Descent Phase Impulse Dispersions	5. 6-137
5. 6-20	Retro Phase Attitude Control Summary	5. 6-138
5. 6-21	Calculation of SC-1 Center of Gravity at Retro Ignition	5. 6-153
5. 6-22	Time and Events Log	5. 6-164
5. 6-23	Nitrogen Gas Consumption	5. 6-185
5. 6-24	Gyro Nulls	5. 6-187
5. 6-25	Estimated Levels for Different Mission Times	5. 6-194
5. 6-26	Summary of Significant Roll System Parameters at Different Mission Times	5. 6-209

5. 3 ELECTRICAL POWER SUBSYSTEM

5. 3. 1 INTRODUCTION

The electrical power (EP) subsystem involves the storage, expenditure, and allocation of electrical energy. There are two sources for this energy: 1) storage batteries, and 2) radiant energy converted directly to electrical energy used for system loads or battery charging. During transit the primary source of power is via the solar panels.

The performance of the EP subsystem during the SC-1 mission was nominal as compared with flight acceptance test (FAT) data and simulation analyses predictions. Specific comparisons will follow within the body of this subsection.

The subsystem may conveniently be considered with the following equipment groupings (Figure 5. 3-1):

1) Solar panel

2) Battery charge regulator

3) Main and auxiliary batteries

4) Boost regulation of the basic unregulated voltage

An evaluation of the EP subsystem related to the total system involves power management. The first considerations are efficiencies of the regulators, total energy generated via the solar panels, and energy dissipated during the transit period of flight. Analysis of specific loads, comparison to prediction, and explanation of discrepancies will follow.

5. 3. 2 MAJOR TRANSIT EVENTS AND TIMES

In Table 5. 3-1, major events during transit are presented with 1) time from launch for easy reference to mission plots (subsection 5. 3. 6. 3) and, 2) time in GMT for reference to various list information, i. e. , commands and Engineering Data Reduction System (EDRS) processed data. In general, the major events correspond to the mission (transit) phases; however, there may be differences in time when compared to similar mission subdivisions in other

TABLE 5. 3-1. EVENTS AND TIMES, ELECTRICAL POWER

Total Flight Time = 63. 60 Hours

Event	Time, GMT (day:hour:min:sec)		Time From Launch, hours			Comment
	From	To	From	To	Increment	
0	150 14 41 00	150 14 53 27	0	0.21	0.21	Launch to Centaur separation
1	150 14 53 27	150 15 20 44	0.21	0.66	0.45	Transmitter high power on
2	150 15 20 44	150 18 44 24	0.66	4.05	3.39	Coast I
3	150 18 44 24	150 19 21 04	4.05	4.68	0.63	Transmitter high power on
4	150 19 21 04	151 06 08 25	4.68	15.40	10.72	Coast I
5	151 06 08 25	151 07 12 44	15.40	16.53	1.13	Transmitter high power on
6	151 07 12 44	152 11 46 34	16.53	45.09	28.56	Coast II
7	152 11 46 34	153 01 16 42	45.09	58.59	13.50	Auxiliary battery on
8	153 01 16 42	153 05 20 18	58.59	62.66	4.07	Coast II
9	153 05 20 18	153 06 16 02	62.66	63.60	0.94	Transmitter high power on for terminal descent sequence

Note: Total solar panel suntime was 63.60 - 0.8 = 62.8 hours.

subsections. Basically, the transit region is divided into times corresponding to significant changes in electrical loads. Such increases in load are best illustrated in the transit mission plot of the battery discharge current (EP-9).

5. 3. 3 SUMMARY OF RESULTS

5. 3. 3. 1 Tables and Figures

Table 5. 3-2 presents a summary of the comparison of flight data to predicted or FAT data for the electrical power subsystem.

Figure 5. 3-2 presents the battery energy remaining as a function of time. Predicted total energy used during transit (63. 6 hours) was obtained from a run of the Power Management Program using SC-1 transit commands. Battery efficiency was assumed to be approximately the same as the predict run since the total energy used from flight data and the predicted loads are approximately identical. Table 5. 3-3 gives the battery energy used in each mission phase.

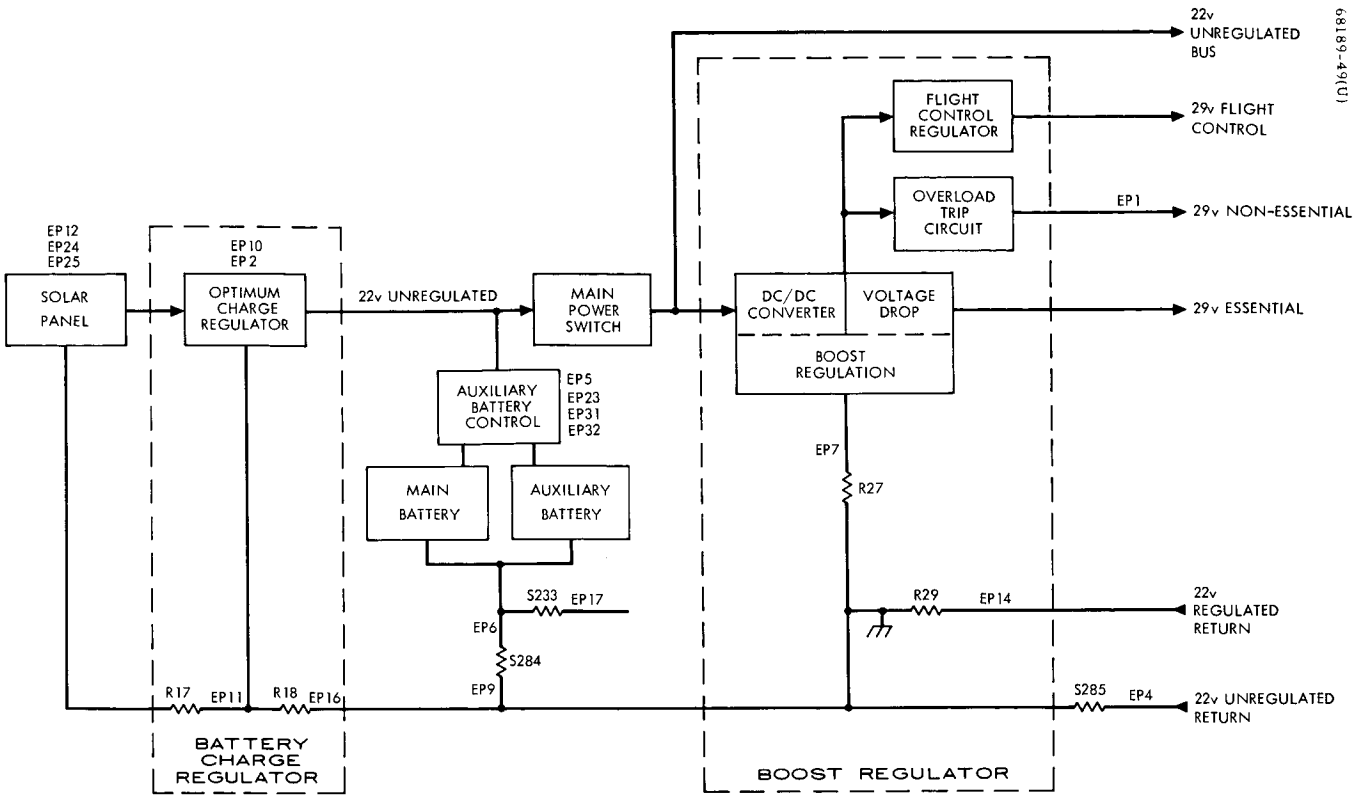


Figure 5.3-1. Electrical Power Schematic

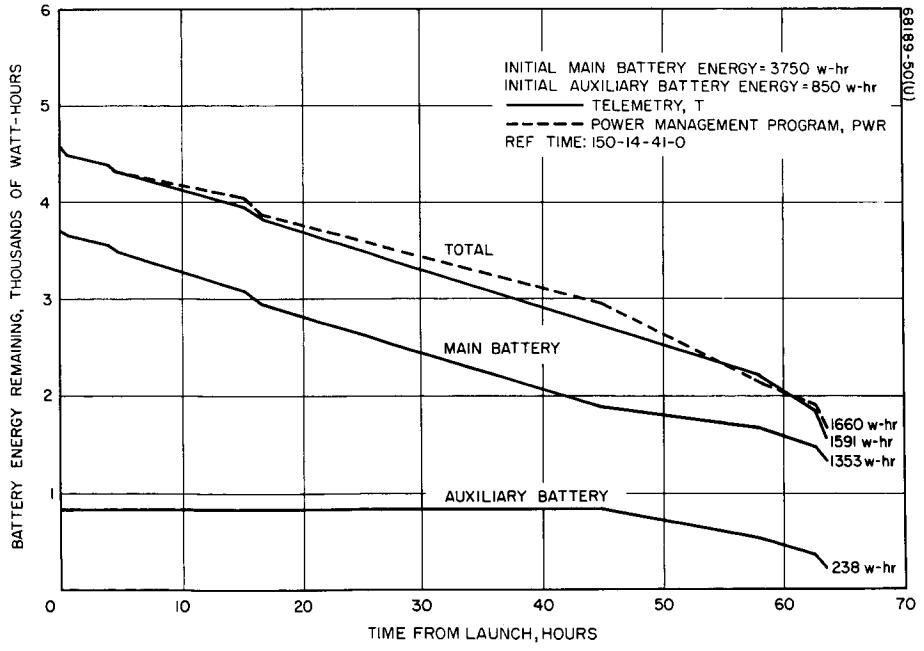


Figure 5.3-2. Battery Energy Remaining

TABLE 5.3-2. SUMMARY OF RESULTS, ELECTRICAL POWER

	From Flight Data	Predicted Specification or FAT
Boost regulator efficiency	78.76 percent	75 percent
OCR efficiency	80.34 percent	>78 percent
Battery efficiency	–	94 percent**
Solar panel output energy	5262 ± 242 watt-hr	5168 watt-hr
OCR output energy	4225 ± 194 watt-hr	4038 watt-hr
Battery energy used‡	3008 ± 418 watt-hr	–
Total energy used	7233 ± 460 watt-hr	7112 ± 345 watt-hr
Selected Loads		
XMTR B high voltage	1782 ± 160 milliamperes (B)*	
	2043 ± 204 milliamperes (E)*	2159 milliamperes reg
Vernier ignition reg	338 ± 210 milliamperes	119 milliamperes
unreg	2780 ± 179 milliamperes	3000 milliamperes
Thrust phase power on reg	1452 ± 535 milliamperes	1160 milliamperes
unreg	470 ± 497 milliamperes	470 milliamperes
Electronic temperature control survey camera	1802 ± 638 milliamperes	1830 milliamperes unreg
AMR and vernier line heaters	320 milliamperes	290 milliamperes
Gyro heaters	540 milliamperes	577 milliamperes

*Values near beginning (B) and end (E) of flight.

**See Table 5.3-9.

‡Main battery energy at start = 3750 watt-hr (Reference 2: 3700 ± 200 watt-hr).

TABLE 5. 3-3. BATTERY ENERGY USED

Total Watt-Hours = 3008. 92 ± 418

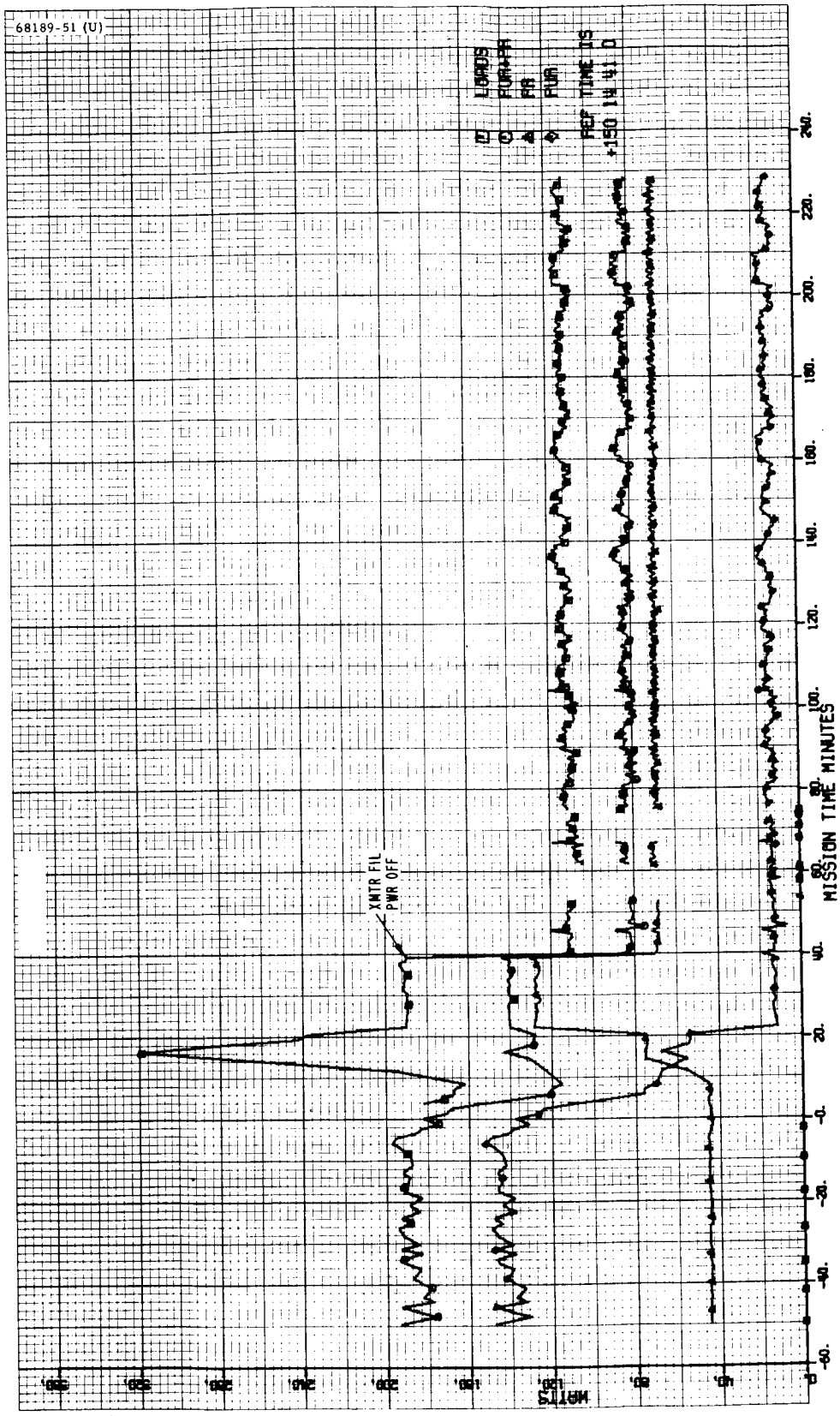
Event	Energy From Batteries				
	EP-9	EP-2	Power, watts (= EP-9 * EP-2)	Delta Time, hours	Energy, watt-hr. (= Power * Delta Time)
0	(8. 95)	(22. 2 ± 0. 2)	(198. 7 ± 1. 72)	(0. 21)	41. 73 ± 0. 36
1	(5. 0 ± 0. 3)	(22. 2 ± 0. 2)	(111. 0 ± 6. 82)	(0. 45)	49. 95 ± 3. 06
2	(1. 4 ± 0. 2)	(23. 0 ± 0. 2)	(32. 2 ± 4. 92)	(3. 39)	109. 16 ± 16. 67
3	(5. 0 ± 0. 3)	(21. 68 ± 0. 04)	(108. 4 ± 6. 71)	(0. 63)	68. 29 ± 4. 22
4	(1. 6 ± 0. 3)	(21. 92 ± 0. 04)	(35.07 ± 6. 64)	(10. 72)	375. 95 ± 71. 18
5	(5. 6 ± 0. 4)	(21. 6 ± 0. 04)	(120. 96 ± 8. 87)	(1. 13)	136. 68 ± 11. 02
6	(1. 73 ± 0. 3)	(21. 89 ± 0. 04)	(37. 86 ± 6. 63)	(28. 56)	1081. 28 ± 189. 35
7	(1. 85 ± 0. 3)	(21. 89 ± 0. 04)	(40. 50 ± 6. 59)	(13. 50)	546. 75 ± 88. 96
8	(3. 7 ± 0. 3)	(21. 89 ± 0. 04)	(80. 99 ± 6. 67)	(4. 07)	329. 63 ± 33. 41
9	(13. 2)	(21. 72 ± 0. 04)	(286. 70 ± 0. 53)	(0. 94)	269. 50

Figure 5. 3-3 shows total power consumed as well as the sum of the regulated and unregulated loads for launch, midcourse, preterminal descent, and a period of postlanding. During midcourse (Figure 5. 3-3b), occurrence of vernier ignition and thrust phase power off can be noted in the unregulated power. Also, the turnoff of the high voltage of the transmitter shows a drop of about 58 watts in the regulated power. The preterminal descent (Figure 5. 3-3c) shows the turnon of the temperature control in the survey camera. There is an approximate 40-watt increase in the unregulated load, whereas the regulated load is relatively constant. During postlanding (Figure 5. 3-3d), the small unregulated (heater) load and the first TV sequence are noted.

Figure 5. 3-4 shows the shunt unbalance current for launch, midcourse, preterminal descent, and postlanding. The current is generally biased at about 0. 44 amp during transit. In Figure 5. 3-4d, it follows the regulated loads during high voltage on, but increases when high voltage is turned off.

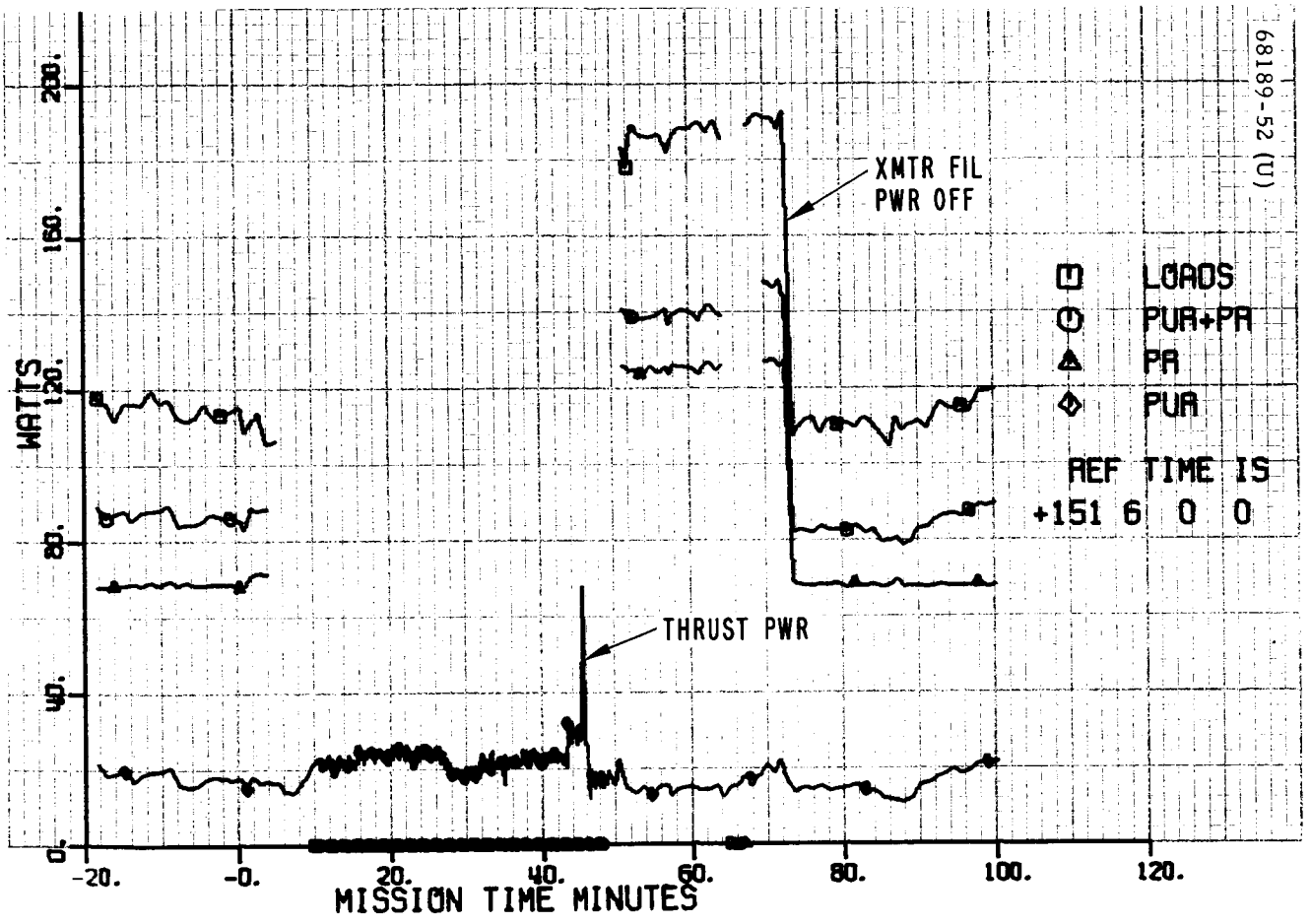
Figure 5. 3-5 is a mission plot of optimum charge regulator (OCR) efficiency. The figure shows an approximate value of 80 percent; Table 5. 3-4 shows a time-weighted average efficiency of 80. 34 percent.

Figure 5. 3-6 is a mission plot of boost regulator efficiency which is relatively constant at 78. 5 percent. Likewise, Table 5. 3-5 gives a time-weight average efficiency of 78. 76 percent. In Table 5. 3-6, boost regulator efficiency (BREFF) is tabulated for a short time period versus boost regulated preregulated voltage (EP-30) and regulated power (PR).



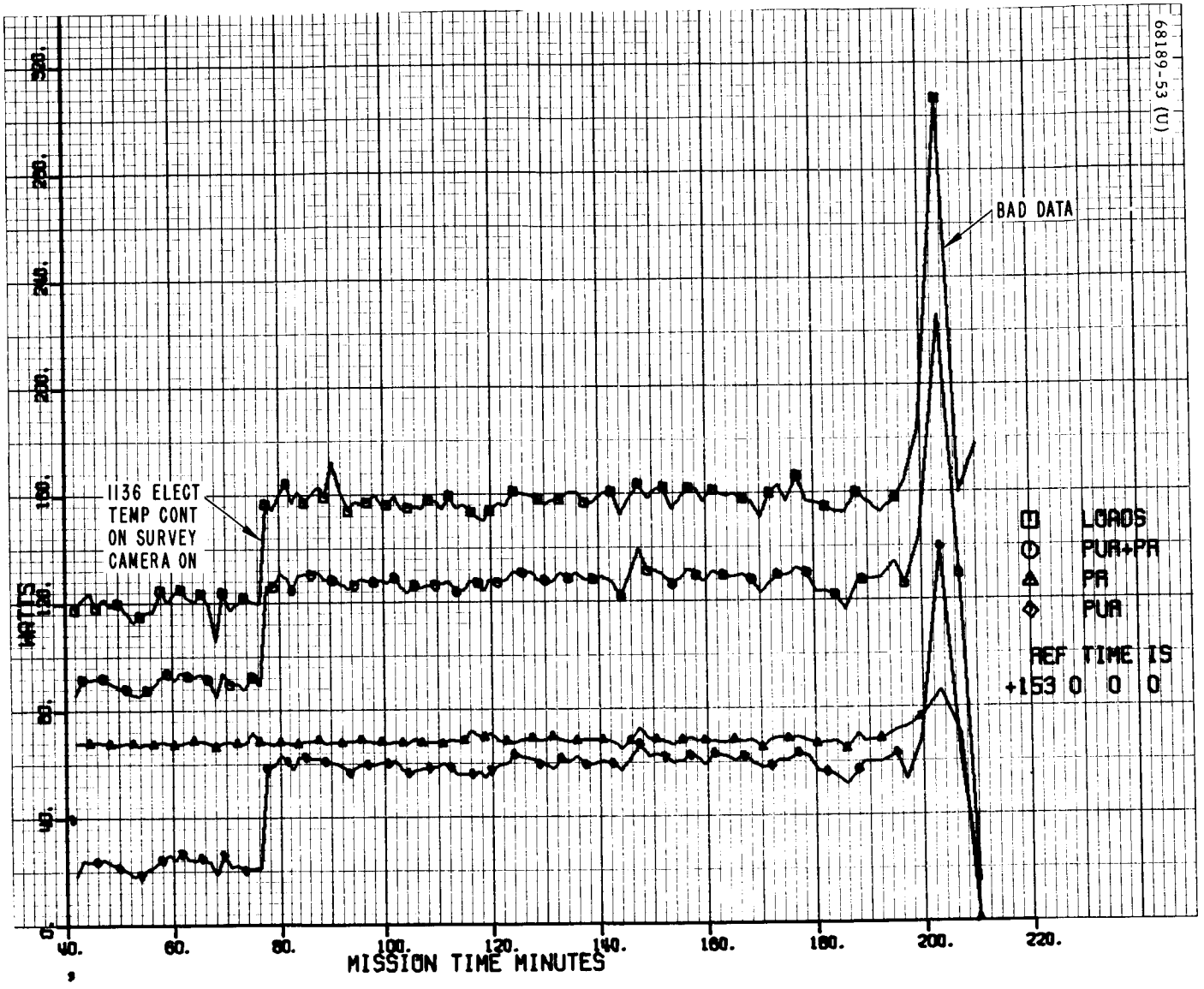
a) Launch

Figure 5.3-3. Power Consumed and Loads



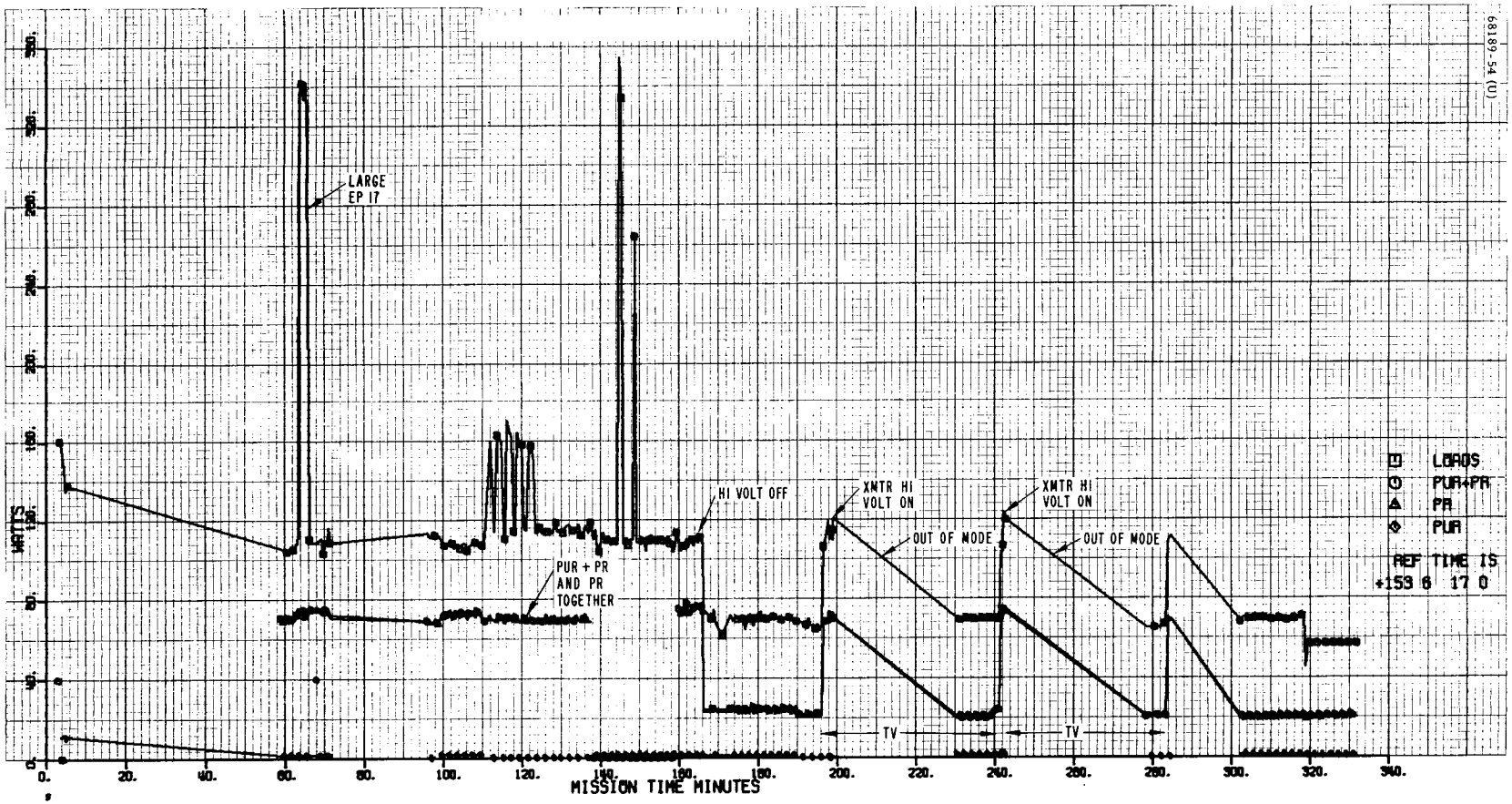
b) Midcourse

Figure 5.3-3 (continued). Power Consumed and Loads



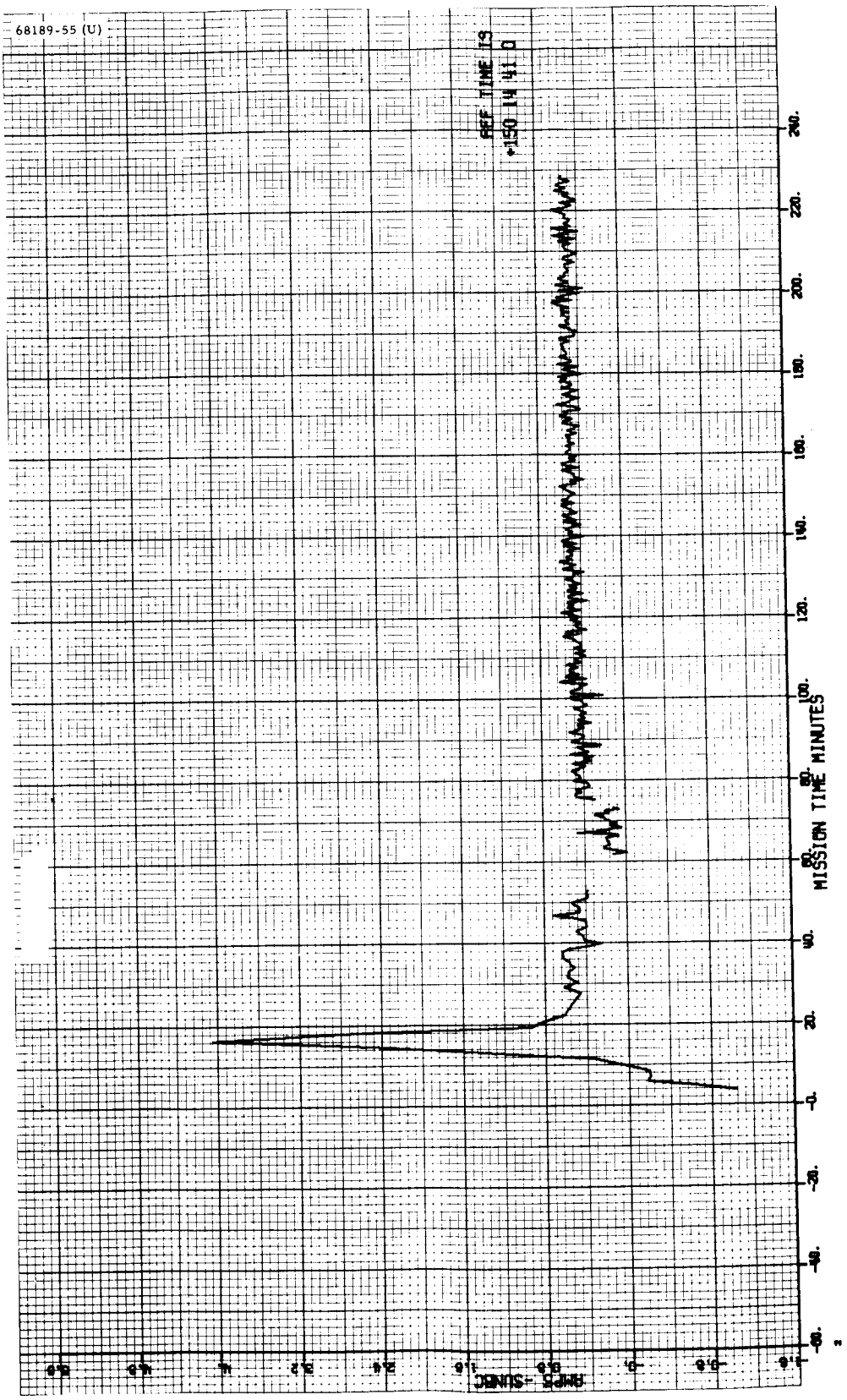
c) Preterminal Descent

Figure 5.3-3 (continued). Power Consumed and Loads



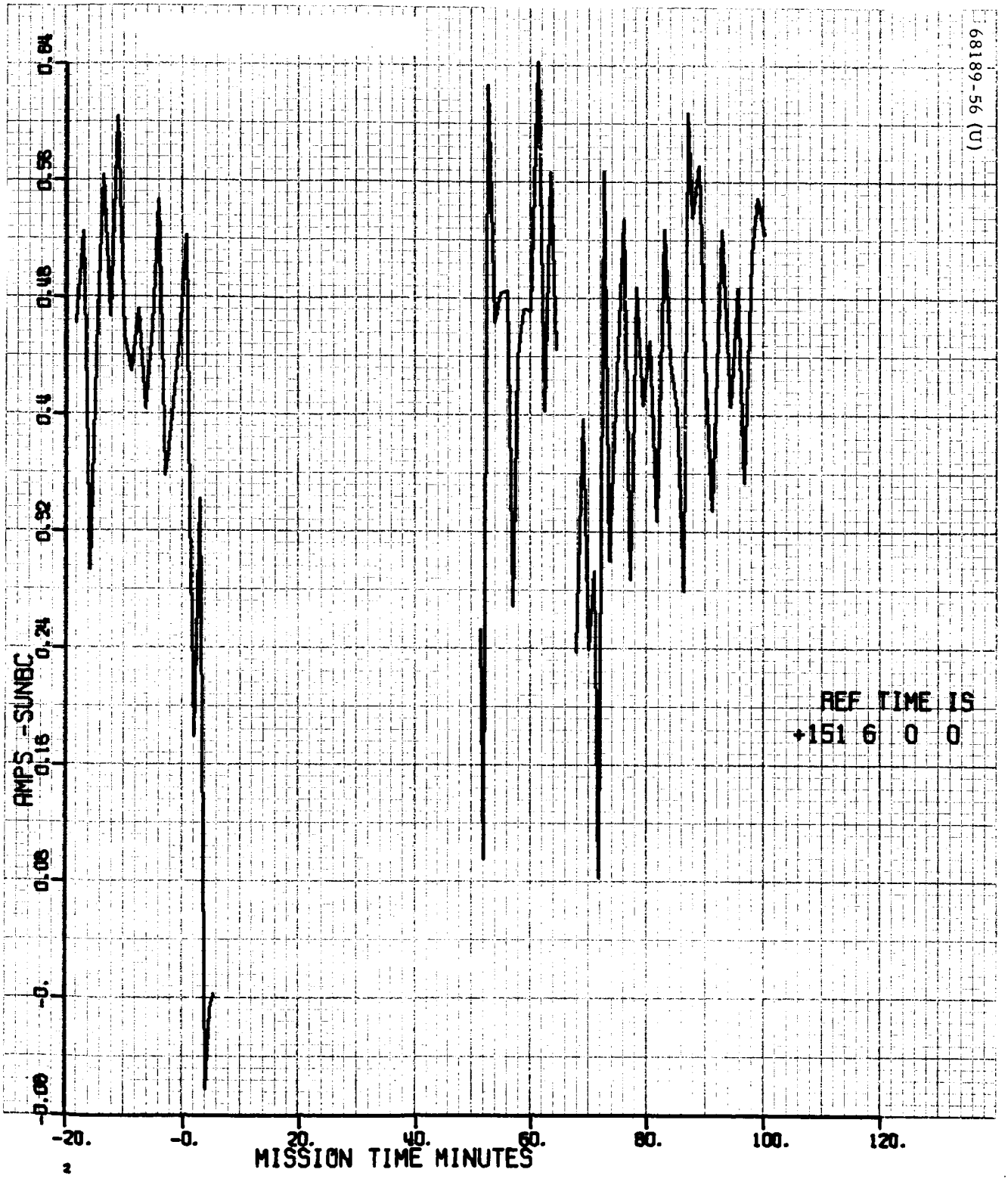
d) Postlanding

Figure 5.3-3 (continued). Power Consumed and Loads



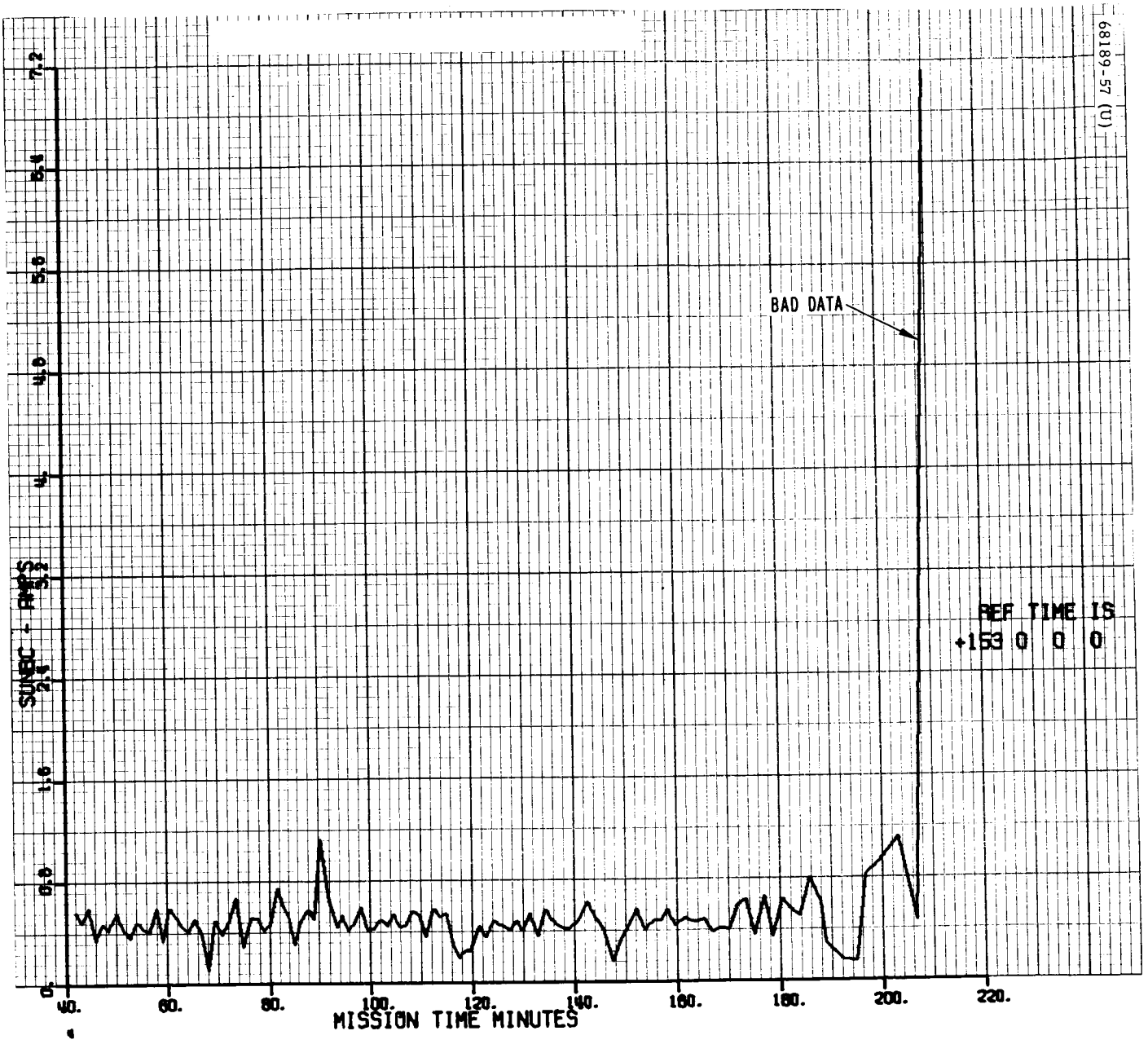
a) Launch

Figure 5.3-4. Shunt Unbalance Current



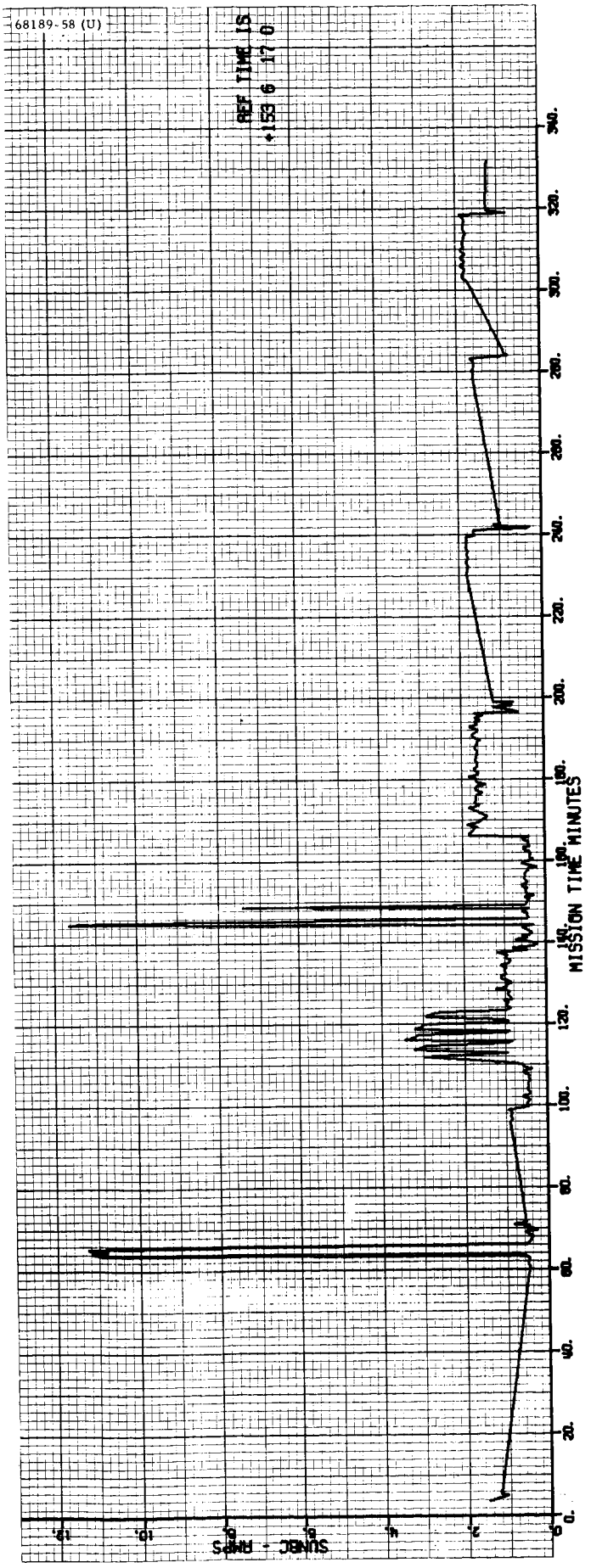
b) Midcourse

Figure 5.3-4 (continued). Shunt Unbalance Current



c) Preterminal Descent

Figure 5.3-4 (continued). Shunt Unbalance Current



d) Postlanding

Figure 5.3-4 (continued). Shunt Unbalance Current

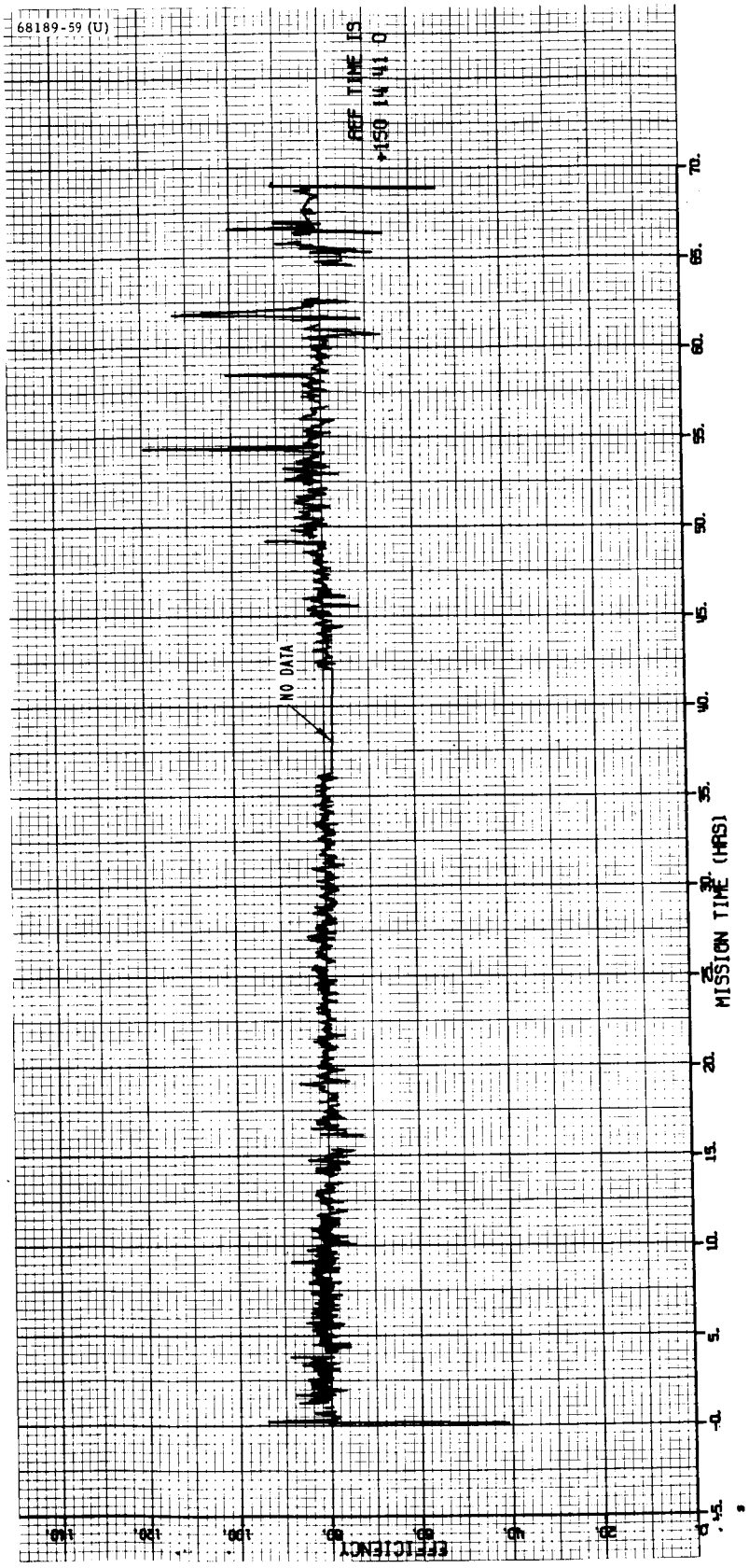


Figure 5.3-5. Battery Charge Regulator Efficiency

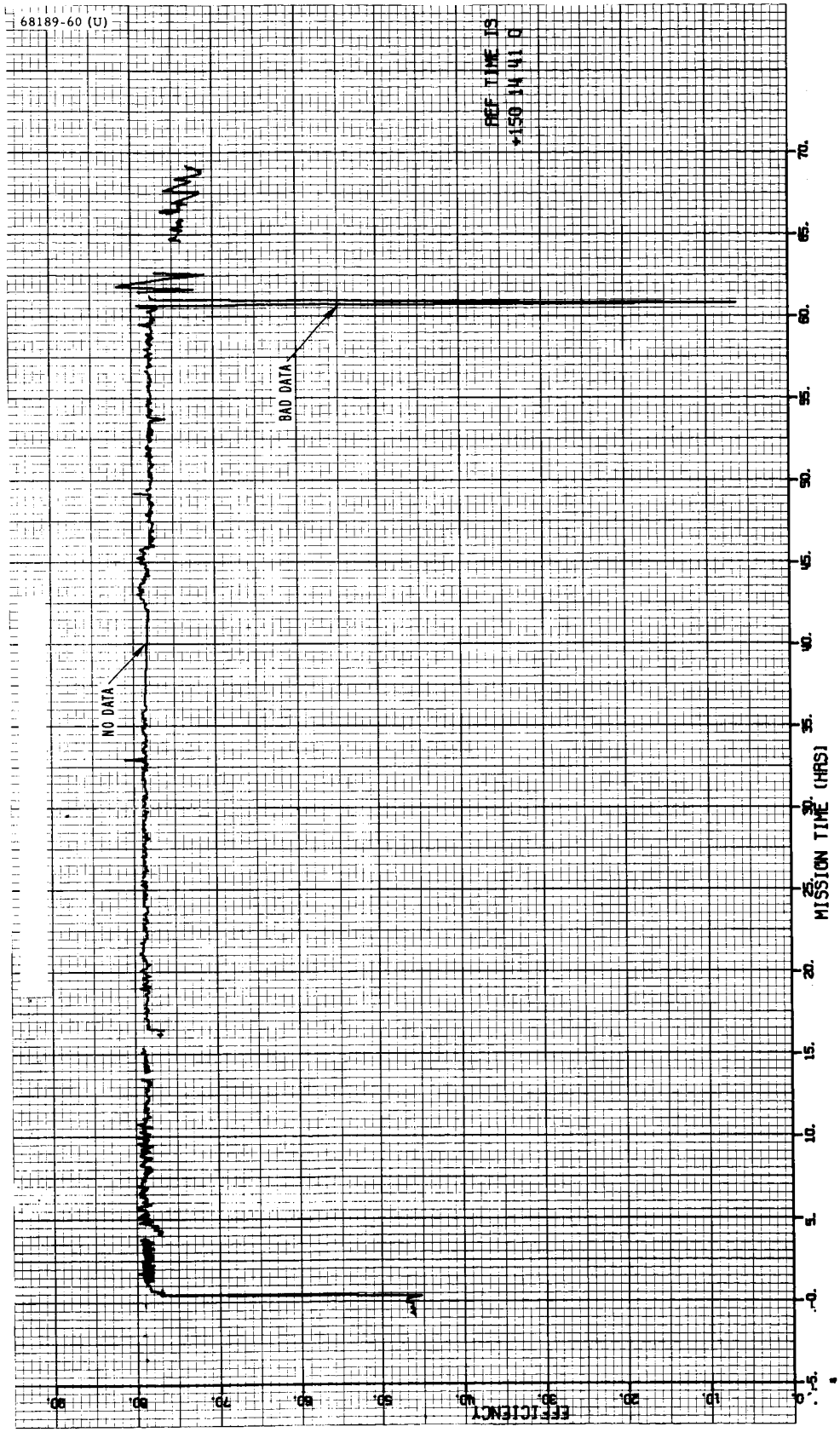


Figure 5.3-6. Boost Regulator Efficiency

TABLE 5.3-4. OPTIMUM CHARGE REGULATOR EFFICIENCY

Time-Weighted Average Efficiency = 80.34 percent

Event	Input Power (IP) (EP-10) (EP-11)	Output Power (OP) (EP-2) (EP-16)	Efficiency (OP/IP) 100
1	(48.2 ± 1.4) (1.77 ± 0.08) = 85.3 ± 6.44	(22.2 ± 0.2) (3.24 ± 0.04) = 71.92 ± 1.55	84.30
2	(48.2 ± 1.4) (1.77 ± 0.08) = 85.3 ± 6.44	(23 ± 0.2) (3.24 ± 0.04) = 74.52 ± 1.58	87.35
3	(48.2 ± 1.4) (1.77 ± 0.08) = 85.3 ± 6.44	(21.68 ± 0.1) (3.24 ± 0.04) = 70.24 ± 1.19	82.33
4	(48.2 ± 1.4) (1.77 ± 0.08) = 85.3 ± 6.44	(21.68 ± 0.1) (3.17 ± 0.06) = 68.72 ± 1.62	80.55
5	(48.2 ± 1.4) (1.77 ± 0.08) = 85.3 ± 6.44	(21.6 ± 0.1) (3.32 ± 0.08) = 71.71 ± 2.06	84.05
6 7 8	(48.8 ± 1.2) (1.78 ± 0.02) = 86.86 ± 3.12	(21.89 ± 0.04) (3.16 ± 0.03) = 69.17 ± 0.78	79.63
9	(48.5 ± 0.8) (1.77 ± 0.06) = 85.08 ± 4.36	(21.72) (3.17 ± 0.05) = 68.85 ± 1.08	80.23

5.3.3.2 Comments on Individual Items

Load Sharing

Estimates of load sharing of the auxiliary battery and the main battery were based upon engineering design and tests prior to the SC-1 mission. During high current mode on conditions, the load sharing was assumed to be 1:1 without the diode. During auxiliary battery mode on, where the diode was between the main battery and the unregulated bus, the load sharing was assumed to be 3:2 (auxiliary to main).

The load sharing assumptions were optimistic and conditionally based upon differences in auxiliary and main battery states of charge and temperatures. The auxiliary battery operated mainly in high current mode during auxiliary battery mode on in transit. The temperatures of both batteries were more nearly the same (main battery = 115°F and auxiliary battery = 75°F) at

TABLE 5. 3-5. BOOST REGULATOR EFFICIENCY

Time-Weighted Average Efficiency = 78. 76 percent

Event	Input Power (IP) (EP-14 + EP-7) (EP-2)	Output Power (OP) (EP-14) (EP-1)	Efficiency (OP/IP) 100
1	(4. 36 ± 0. 02 + 3. 00 ± 0. 02) (22. 2 ± 0. 2) = 1630. 39	(4. 36 ± 0. 02) (29. 08) = 126. 78	77. 59
2	(2. 32 ± 0. 04 + 1. 32 ± 0. 02) (23 ± 0. 2) = 83. 72	(2. 32 ± 0. 04) (29. 08) = 67. 46	80. 57
3	(4. 33 ± 0. 08 + 3. 18 ± 0. 02) (21. 68 ± 0. 1) = 162. 81	(4. 33 ± 0. 08) (29. 08) = 125. 91	77. 33
4	(2. 32 ± 0. 06 + 1. 60 ± 0. 04) (21. 92 ± 0. 1) = 85. 92	(2. 32 ± 0. 06) (29. 24) = 67. 83	78. 94
5	(4. 40 ± 0. 08 + 3. 24 ± 0. 04) (21. 6 ± 0. 1) = 165. 02	(4. 40 ± 0. 08) (29. 24) = 128. 65	77. 96
6 7 8	(2. 32 ± 0. 04 + 1. 62 ± 0. 01) (21. 89 ± 0. 1) = 86. 24	(2. 32 ± 0. 04) (29. 24) = 67. 83	78. 65
9	(2. 34 ± 0. 04 + 1. 68 ± 0. 01) (21. 72 ± 0. 1) = 87. 31	(2. 34 ± 0. 04) (29. 24) = 68. 92	78. 36

touchdown. In addition, both were assumed to be operating on their respective lower (voltage versus state of charge) plateaus. It was on this temperature and lower plateau basis that the above sharing ratios were determined.

Energy Bookkeeping

In the Quick Look Report (Reference 1), total battery energy remaining at touchdown was predicted from telemetry as 72 ± 17 amp-hr. The variability was 47 percent of the mean predicted value. Similar results have already been presented in Table 5. 3-2, based upon telemetry. In addition, results from computer runs using the Power Management Program indicate large standard deviations in predicting battery energy remaining. In one case, the variability is due to the accumulated uncertainties in the telemetry signal values and, in the other, the variability is due to the predicted inaccuracies of the model simulating the usage of energy.

TABLE 5.3-6. BOOST REGULATOR EFFICIENCY VERSUS EP-30 AND REGULATED POWER

Time, day:hr:min:sec	BREFF	EP-30	PR
150 16 41 2	0.7890	30.3961	69.0862
	0.7838	30.3925	68.3875
	0.7880	30.3990	68.5515
	0.7901	30.3860	69.1733
	0.7822	30.4006	67.3658
	0.7908	30.3974	69.5750
	0.7777	30.3982	66.4503
	0.7894	30.3990	69.1842
	0.7869	30.3925	68.3594
	0.7879	30.3999	68.6038
	0.7939	30.3974	70.0497
	0.7821	30.4055	67.6855
	0.7894	30.4023	69.5620
	0.7822	30.4120	67.7642
	0.7866	30.4023	68.8948
	0.7823	30.3909	68.6051
	0.7846	30.4066	67.9976
	0.7943	30.3958	69.9911
	0.7824	30.4088	67.9274
	0.7877	30.4104	69.3959
	0.7832	30.4006	67.6395
	0.7877	30.4120	68.7248
	0.7950	30.3925	70.1960
	0.7793	30.4137	67.2900
	0.7906	30.3958	69.6814
	0.7823	30.4104	67.7354
	0.7862	30.4023	68.8924
	0.7865	30.3941	69.2305
	0.7847	30.4055	67.9241
	0.7937	30.4023	69.9457
	0.7816	30.4072	67.2713
	0.7885	30.3974	68.8935
	0.7873	30.3927	68.3486
	0.7857	30.4120	68.4414
	0.7898	30.3958	69.7588
	0.7848	30.4055	67.9019
	0.7911	30.4072	69.1139
	0.7853	30.3974	68.0603
	0.7838	30.4055	68.6956
	0.7909	30.3958	69.7498
	0.7828	30.4104	67.7378
	0.7926	30.4006	69.7798
	0.7823	30.4055	67.8249
	0.7901	30.4023	69.2322
	0.7867	30.4104	68.3570

Table 5.3-6 (continued)

Time, day:hr:min:sec	BREFF	EP-30	PR
150 16 41 2	0.7917	30.3990	69.8693
	0.7811	30.4023	67.4110
	0.7903	30..4023	69.2942
	0.7850	30.3990	67.7360
	0.7882	30.3990	68.5355

At some time in the mission (after touchdown), such a prediction (from telemetry or simulation) may become meaningless because of growth in variance – specifically, when cycles of charge and discharge occur in its usage during operations on the lunar surface. The actual accounting of battery energy remaining from simulation and telemetry is close (Figure 5.3-2) at touchdown.

Since the computation of energy remaining diverges in time from actual energy in the batteries, whether computed from a simulation or from actual data, what is needed is a new set of initial battery conditions. Updating of initial conditions would give more credence to the energy accounting system.

Initial conditions for the battery are open circuit voltage, temperature, pressure, and state of charge. Voltage, pressure, and temperature are available from telemetry. There is, however, no direct method of computing state of charge either during transit, when only discharge conditions prevail, or during lunar operations where charge/discharge cycles occur.

Possible methods of estimating state of charge would depend upon knowing the rate of charge as a function of battery charge efficiency and battery charge efficiency as a function of state of charge. These methods are therefore temperature and state of charge dependent.

Part of the difficulty in measuring the battery's state of charge is that a chemical (transport) phenomenon is being accounted from external electrical measurements. No information of the electrolytic state of the battery is measured except for pressure which is only indirect evidence. The charge/discharge cycle, when viewed as battery voltage versus state of charge, shows hysteresis effects and wide variation of the voltage/charge rate of change as a function of the state of charge. The hysteresis effects, not easily modeled, are at least functions of rate of charge/discharge, temperature, present state of charge, and cell structure.

The important function of internal transport is implied in rate of charge, hysteresis effect, and present state of charge. Present telemetry will not give the state of charge directly, and perhaps only indirectly if functions of the electrochemical nature of the battery are available or measured. A measurement of solution concentration might directly relate to battery state of charge.

Then the question is: If accounting of the energy in the battery becomes uncertain, can the battery model be readjusted? If this cannot be accomplished, then a method is needed to arrive at a new set of initial conditions for the battery model. Then the accounting procedure can be properly restarted from the inception of new initial conditions.

Uncertainty could be reduced if a battery underwent a prolonged charge period during which battery charge current, open circuit voltage, and pressure were monitored and a conservative battery charging efficiency assumed. At a time determined from engineering measurements, a 100 percent state of charge and thus battery initial conditions could be assumed and accounting started anew. Another method to remove uncertainty in the state of charge would be to use the auxiliary battery with the main battery in independent charge/discharge cycles.

For example, during the first lunar day, charge and discharge cycles of the main battery can be monitored on EP-6 and EP-9, respectively. Teletype data indicates that for most of the lunar day the battery was in a charge condition. Since the battery charge regulator was operating in the optimum charge regulator bypass mode, an estimate of the battery voltage is available from the unregulated bus voltage (EP-2) when the battery is discharging.

Teletype data at approximately 1.3 hours before sunset (165:15:41) indicates that EP-2 is about 25 volts and the battery is discharging at about 1.2 amperes. By observing a function of battery voltage versus battery energy remaining in the battery, it can be estimated that there was approximately 3200 ± 100 watt/hr remaining in the battery 1.3 hours before sunset. Teletype data indicates no further battery charge before lunar night.

Auxiliary Battery Temperature

During launch, midcourse, and part of the second coast phase, the temperature decreased continuously, reaching a minimum value of 34° F. Figure 5.3-15 illustrates the auxiliary battery temperature during the transit portion of the mission and shows a staircase decrease in temperature. This decrease is representative of a change in the least significant bit in the analog to digital conversion of the signal in the central signal processor.

At approximately launch plus 45 hours, the auxiliary battery was turned on in order to raise its temperature for later use. Most of the operation was in high current mode throughout the remainder of transit. At this point, a staircase rise in the battery temperature occurred, reaching 67° F at the start of terminal descent.

5.3.4 ANOMALY DESCRIPTION

Owing to the nominal nature of the mission, there was little of an anomalous nature in the electrical power system during flight. The load incurred by the unregulated current because of the transmitter B high voltage on slowly converged during transit time to near the FAT value (Table 5.3-7).

In addition, there were certain glitches, dropouts, and misrepresentations in some of the mission plots which have been specially annotated. In particular, EP-4, EP-9, and EP-14 showed large current drains during a time of ESP current calibration dropout (launch plus 62.6 to 64.5 hours). These excessive values were ignored. All glitches noted as "bad data" on the mission plots have been shown to be due to ground data processing and not to the raw data from the spacecraft.

TABLE 5.3-7. SELECTED EQUIPMENT LOADS

Command	Time, GMT	EDRS Telemetry, milliamperes	FAT, milliamperes	Current
0106 XMTR B high voltage on	150 18 44 2	1782 ± 160	2159	Regulated
0106	151 06 08 25	1881 ± 180	2159	Regulated
0110 (0106 off)	151 07 12 43	2019 ± 84	2159	Regulated
0106	153 05 20 18	2043 ± 204	2159	Regulated
0721 vernier ignition*	151 06 45 03	338 ± 210	119	Regulated
		2780 ± 179	3000	Unregulated
0727 thrust phase power on	151 06 43 05	1452 ± 535	1160	Regulated
		470 ± 497	470	Unregulated
1136 electronic temperature control survey camera on	153 01 16 42	1802 ± 638	1830	Unregulated

*0721 was on for approximately 22 seconds.

5.3.5 CONCLUSION AND RECOMMENDATIONS

The operation of the electrical power subsystem was nominal throughout the transit portion of the flight.

It may be better to correct telemetry data only when the current calibrations exceed an operating bandwidth rather than always updating for any error. Also, continued investigation of battery parameters should be pursued, leading to a better understanding of battery charge as determined from telemetry.

Energy remaining in the batteries during transit is shown in Figure 5.3-2. Agreement between telemetry and simulation (power management program) is excellent. The largest difference is approximately 7.3 percent at L + 45 hours, and it becomes smaller as touchdown approaches. The power management program is already a powerful predictive tool that can be enhanced by further knowledge of battery initial conditions, thermal environment, and battery modelling.

5.3.6 ANALYSIS

The analysis is divided into three areas: techniques, development of data, and mission plots.

5.3.6.1 Techniques

1) Boost regulator efficiency (η_{BR})

$$\eta_{BR} = \frac{(\text{output power})_{BR}}{(\text{input power})_{BR}} = \frac{EP\text{-}14 * EP\text{-}1}{(EP\text{-}14 + EP\text{-}7) * EP\text{-}2} * 100$$

(Reference 3)

2) Optimum charge regulator efficiency (η_{OCR})

$$\eta_{OCR} = \frac{(\text{output power})_{OCR}}{(\text{output power})_{SP}} = \frac{EP\text{-}2 * EP\text{-}16}{EP\text{-}11 * EP\text{-}10} * 100$$

(Reference 3)

3) Battery efficiency (η_{MB})

$$\eta_{MB} = \frac{\text{energy (loads) - energy (losses)}}{\text{energy used (loads)}} * 100$$

(Reference 4)

4) Solar panel output energy (E_{SP})

$$E_{SP} = \text{EP-10} * \text{EP-11} * \text{time (hours)}$$

(Reference 3)

5) OCR output energy (E_{OCR})

Flight data:

$$E_{OCR} = \frac{\eta_{OCR}}{100} * E_{SP}$$

FAT data:

$$E_{OCR} = \left[V_{SP} \times I_{SP} - \text{OCR losses}\right] * S_{SP}$$

where

V_{SP} = solar panel voltage (temperature sensitive) (Reference 2: Figure 3.1)

I_{SP} = EP-11

S_{SP} = solar panel suntime during transit

OCR losses are computed as in Reference 2: Figures 3.2 and 3.3

6) Battery energy used (E_{BU})

$$E_{BU} = \text{EP-9} * \text{EP-2} * \text{time (hours)}$$

where

EP-9 = battery discharge current

EP-2 = 22 volts unregulated bus voltage

7) Loads are estimated from graphs and are compared to FAT data in References 2 and 5.

8) Data summaries from telemetry

Total loads are computed from sources of power

Loads = (EP-9 + EP-16 + EP-17) * EP-2

Power regulated (PR) and power unregulated (PUR)

PR = EP-14 * EP-1

PUR = EP-4 * EP-2

PR + PUR = power – losses

Unbalanced shunt current (SUNBC)

SUNBC = (EP-9 + EP-16) – (EP-4 + EP-14 + EP-7)

9) OCR hunting losses (estimate)

The standard deviations from the means of a fairly large sample of solar panel voltage (EP-10) and current (EP-11) data are used to estimate the OCR hunting losses at the solar panel maximum power point. A quiet time during Coast Mode II where no commands are issued is monitored and a normal distribution is assumed with system noise governing the selection of the confidence limits associated with the means of the data samples.

5.3.6.2 Development of Data

Tabular Information

Table 5.3-8 is a summary of values to be used in the analysis. The data in this table was obtained from the mission plots (Figures 5.3-7 through 5.3-15).

Tables 5.3-4 and 5.3-5 are summaries of the calculations of optimum charge regulator and boost regulator efficiencies, respectively. In each table a time-weighted average of the efficiency was computed to obtain a representative number for transit operation. Table 5.3-9 summarizes main battery efficiency up to launch plus 45.09 hours.

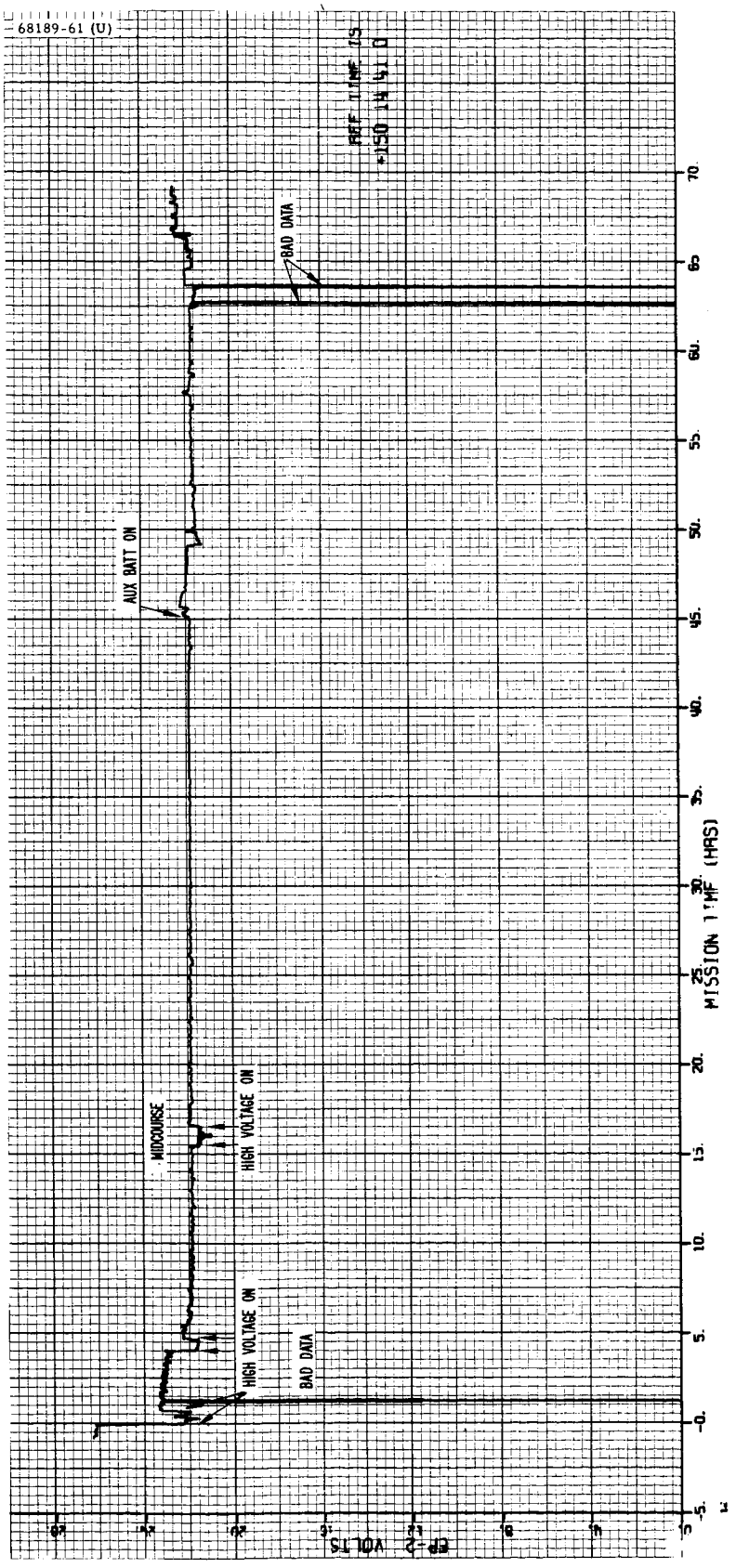


Figure 5.3-7. 22-Volt Unregulated Bus

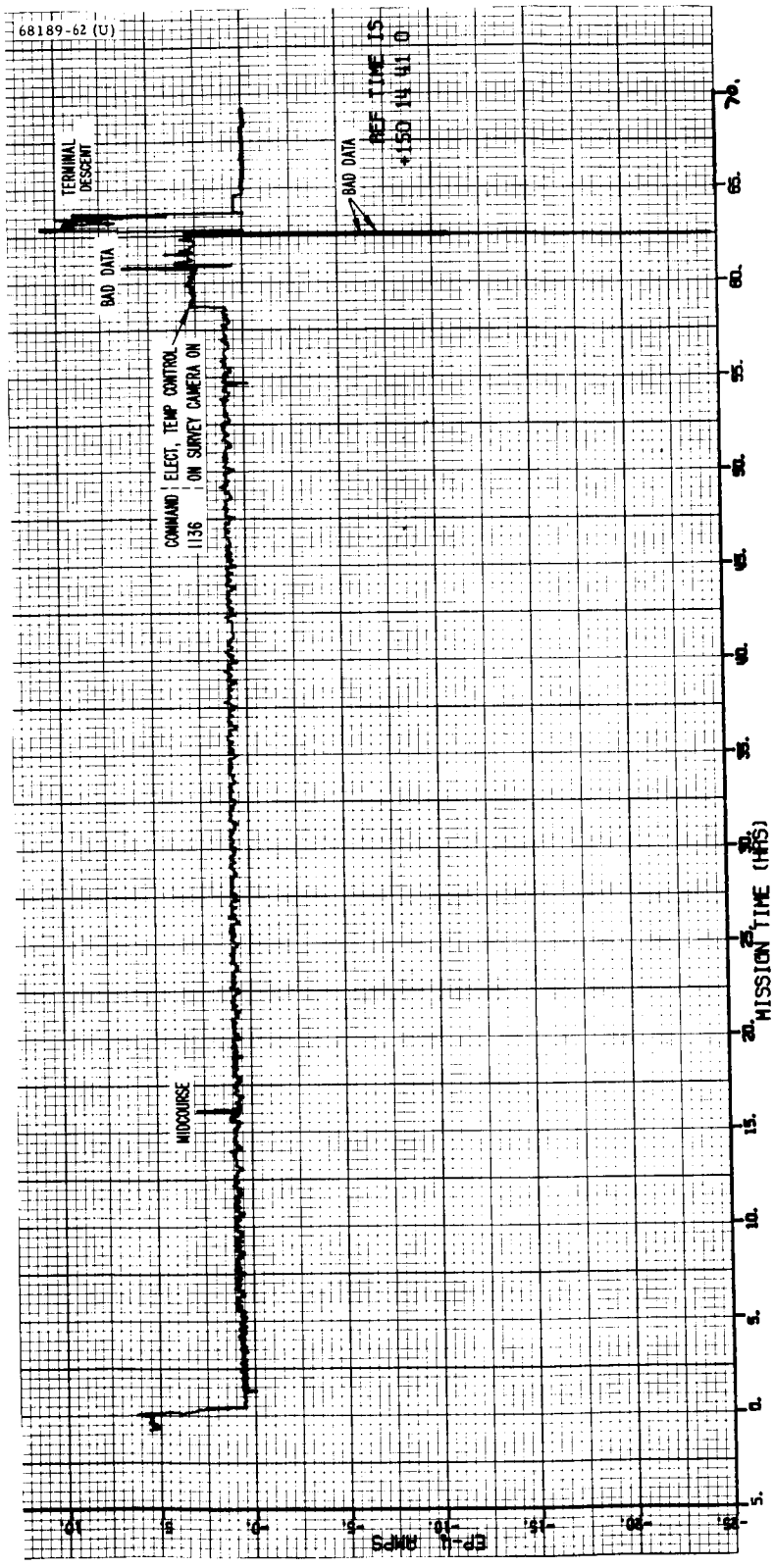


Figure 5.3-8. Unregulated Output Current

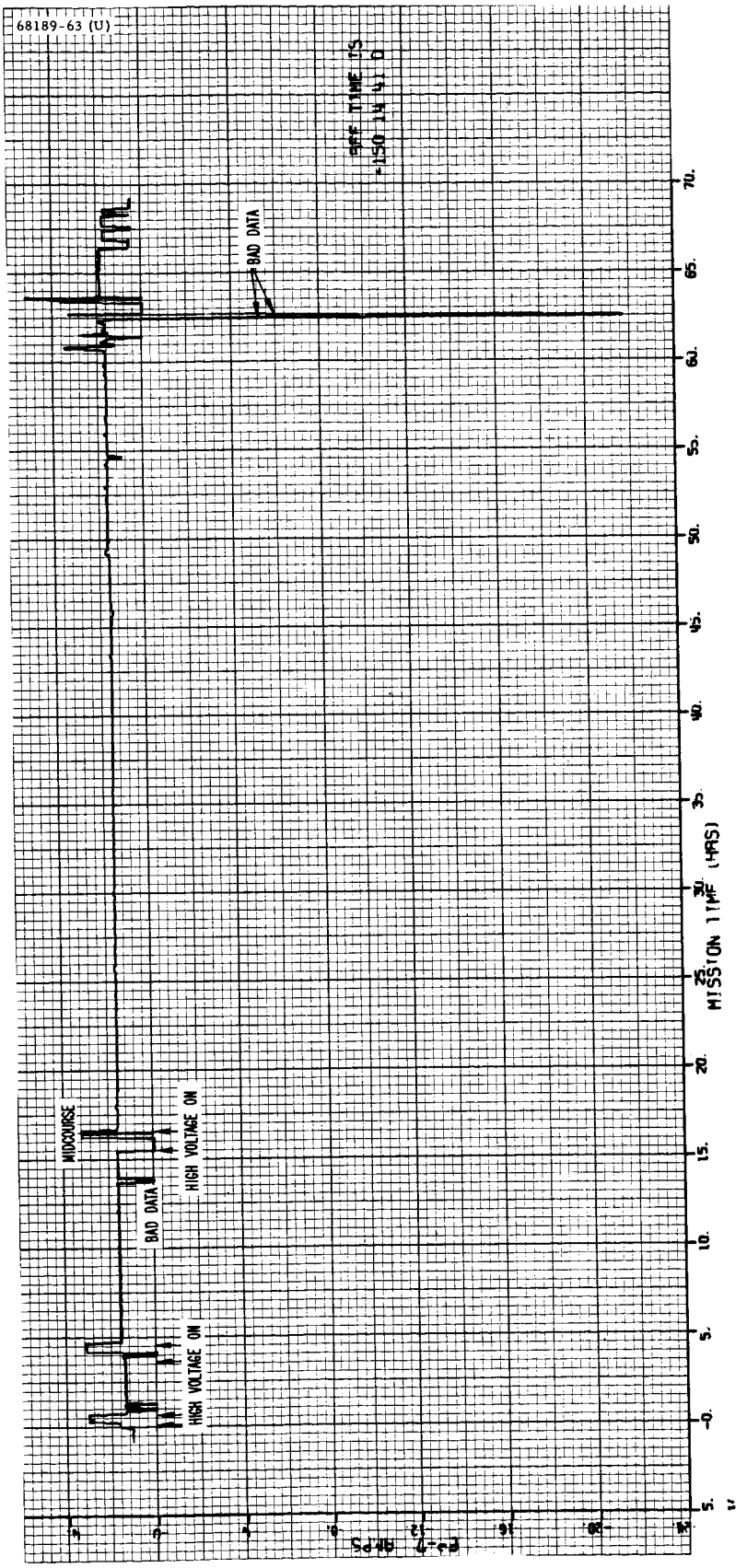


Figure 5.3-9. Boost Regulator Difference Current

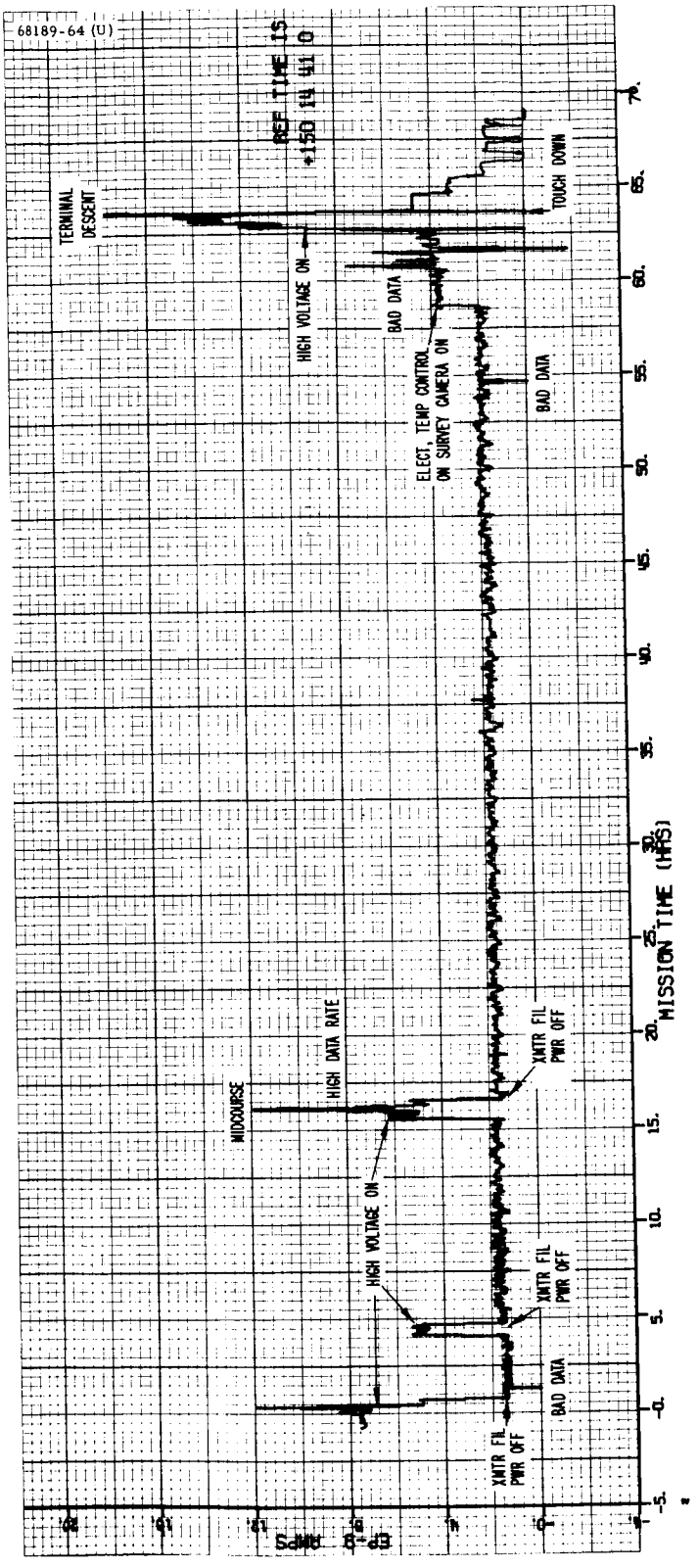


Figure 5.3-10. Battery Discharge Current

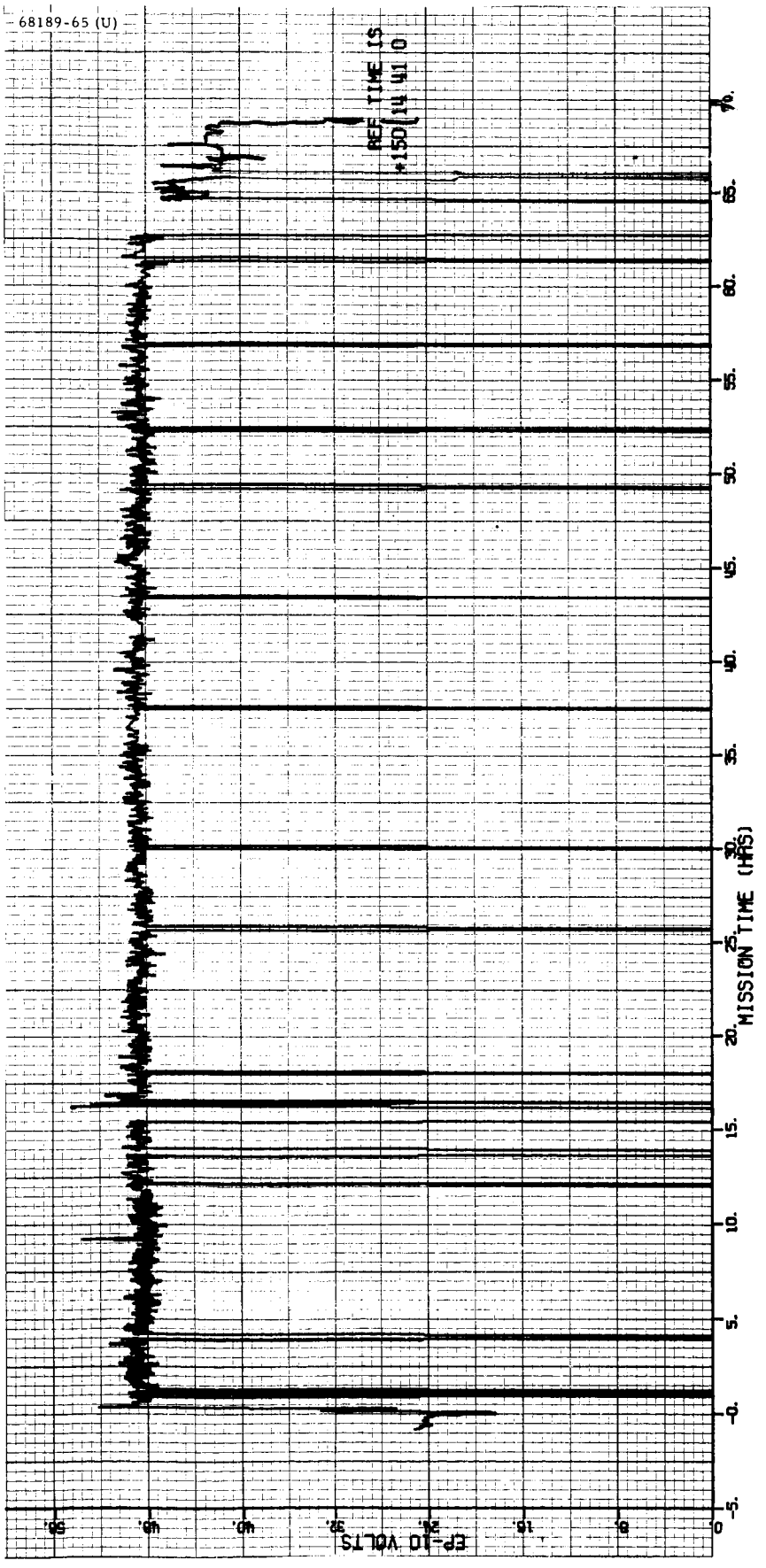


Figure 5.3-11. Solar Cell Array Voltage

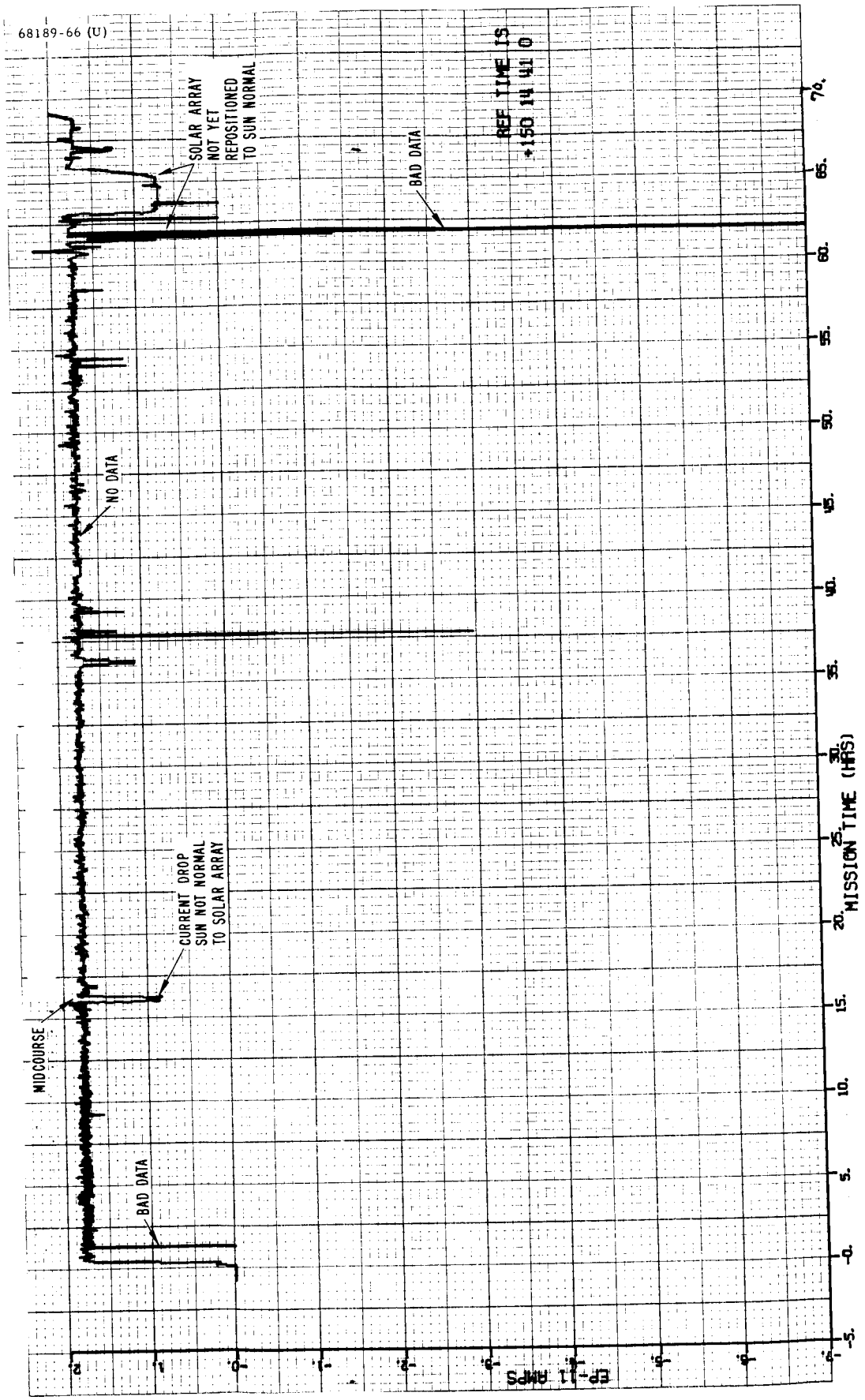


Figure 5.3-12. Solar Cell Array Current

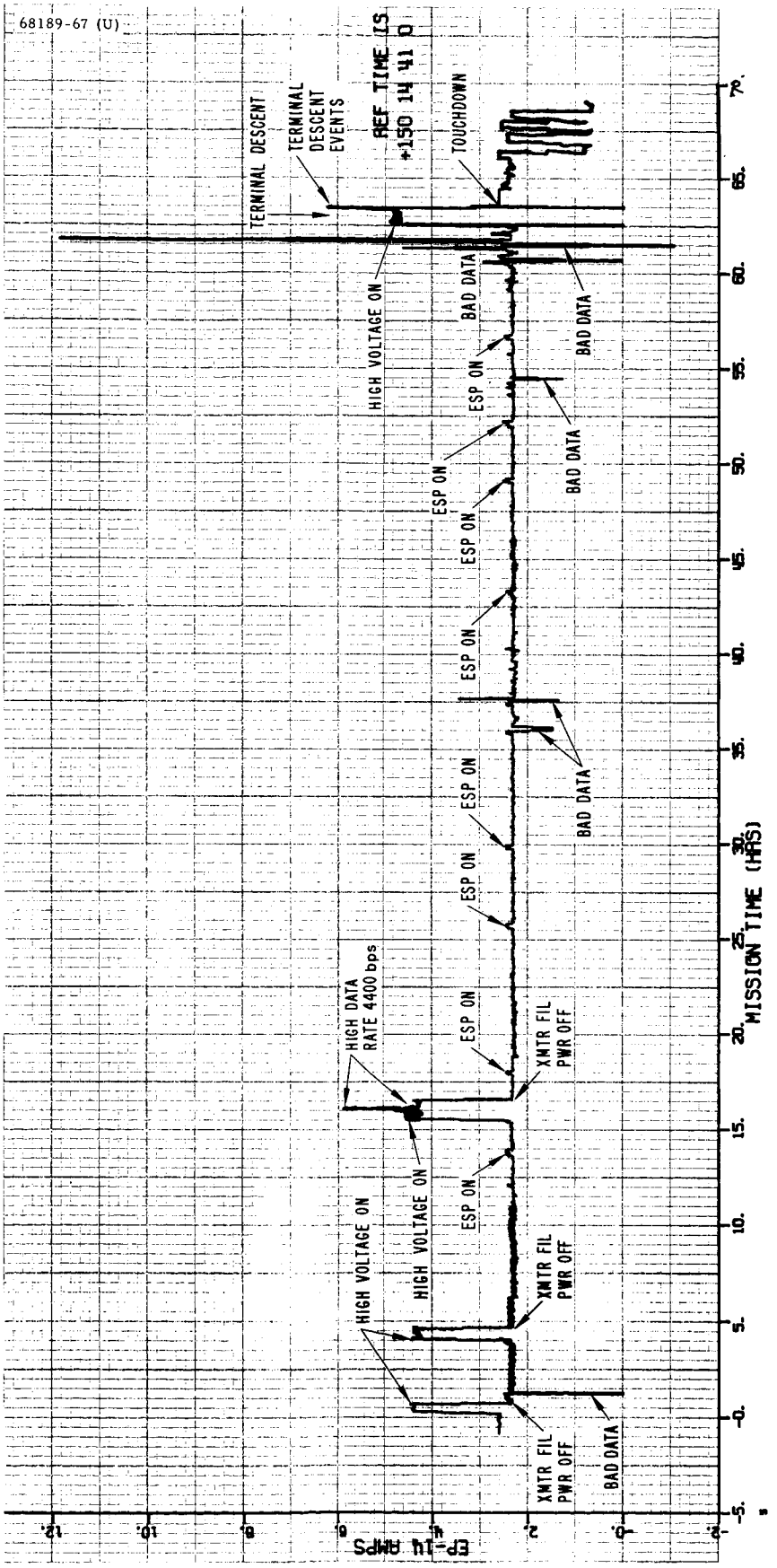


Figure 5.3-13. Regulated Output Current

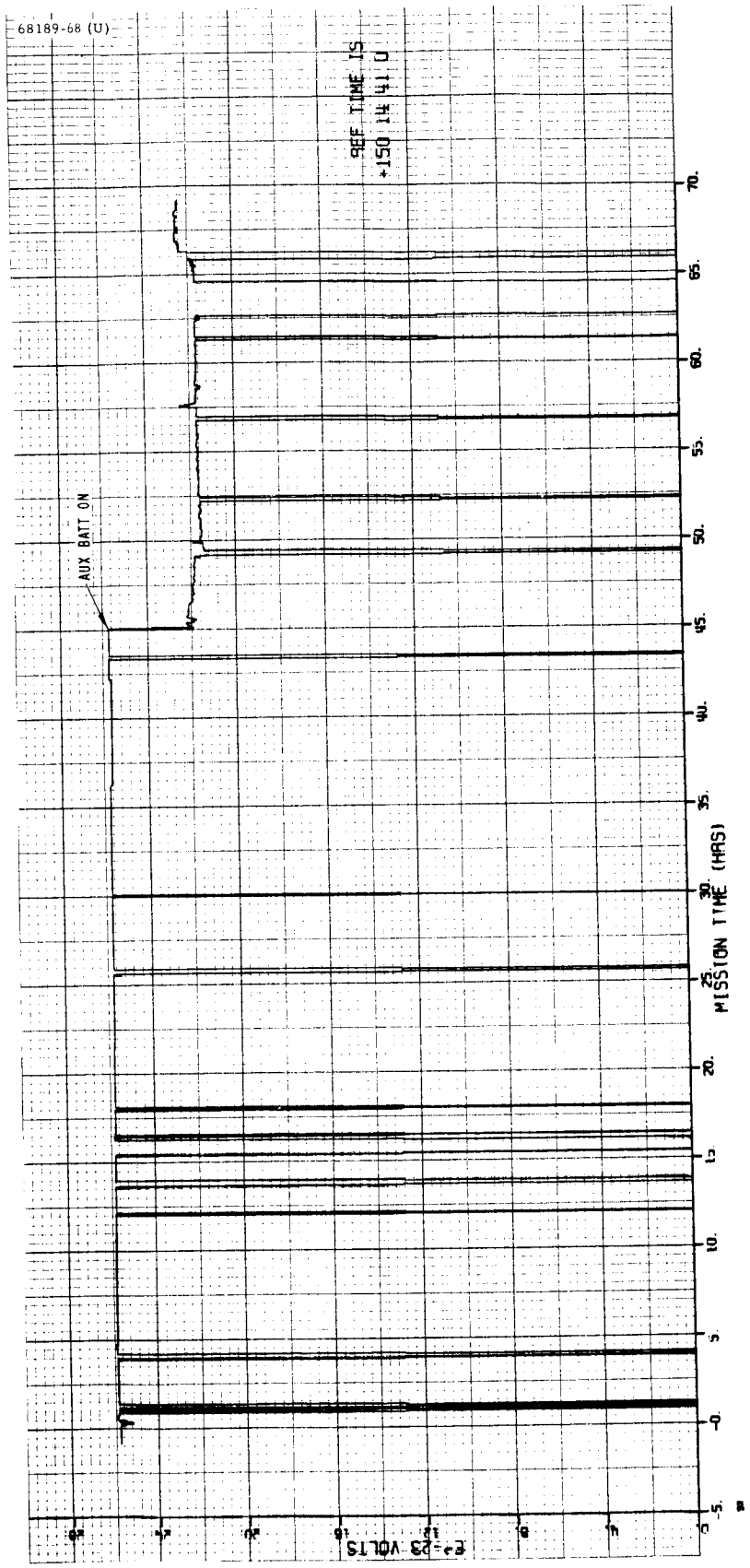


Figure 5.3-14. Auxiliary Battery Voltage

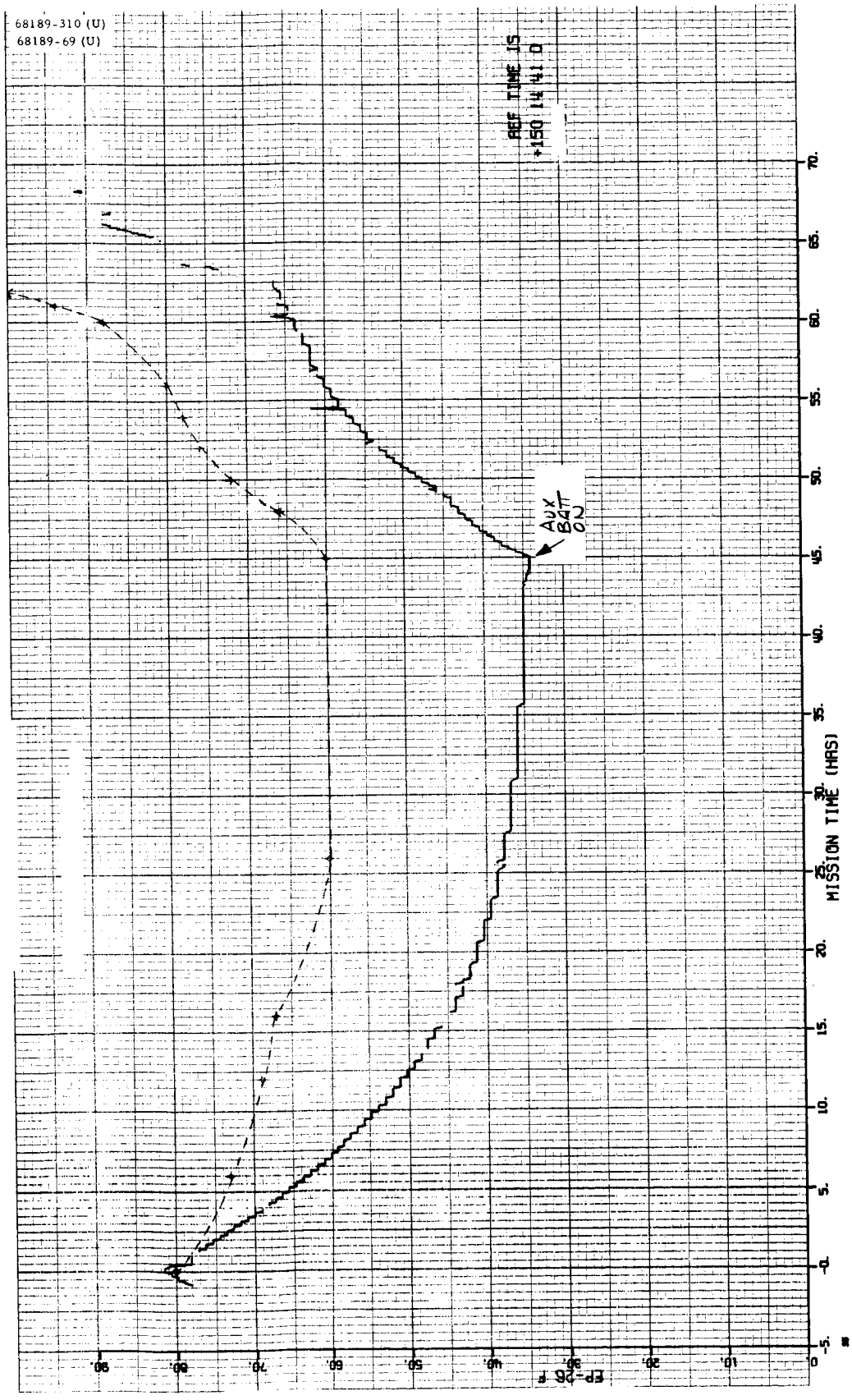


Figure 5.3-15. Auxiliary Battery Temperature

TABLE 5.3-8. TABULATION OF EP VALUES * VERSUS EVENT

Event	EP-14	EP-7	EP-2	EP-1	EP-10	EP-11	EP-16	EP-9	EP-4
0	2.6 ± 0.02	2.00 ± 1.00	22.2 ± 0.2	29.08				8.95	4.25 ± 1.25
1	4.36 ± 0.02	3.00 ± 0.02	22.2 ± 0.2	29.08	48.2 ± 1.4	1.77 ± 0.08	3.24 ± 0.04	5.0 ± 0.3	1.75 ± 1.25
2	2.32 ± 0.04	1.32 ± 0.02	23. ± 0.2	29.08	48.2 ± 1.4	1.77 ± 0.08	3.24 ± 0.04	1.4 ± 0.2	0.64 ± 0.16
3	4.33 ± 0.08	3.18 ± 0.02	21.68 ± 0.1	29.08	48.2 ± 1.4	1.77 ± 0.08	3.24 ± 0.04	5.0 ± 0.3	0.64 ± 0.16
4	2.32 ± 0.06	1.60 ± 0.04	21.92 ± 0.1	29.24	48.2 ± 1.4	1.77 ± 0.08	3.17 ± 0.06	1.6 ± 0.3	0.84 ± 0.22
5	4.40 ± 0.08	3.24 ± 0.04	21.6 ± 0.1	29.24	48.2 ± 1.4	1.77 ± 0.08	3.32 ± 0.08	5.6 ± 0.4	1.2 ± 0.16
6	2.32 ± 0.04	1.62 ± 0.01	21.89 ± 0.1	29.24	48.8 ± 1.2	1.78 ± 0.02	3.16 ± 0.03	1.73 ± 0.3	0.88 ± 0.16
7	2.32 ± 0.04	1.62 ± 0.01	21.89 ± 0.1	29.24	48.8 ± 1.2	1.78 ± 0.02	3.16 ± 0.03	1.85 ± 0.3	0.96 ± 0.2
8	2.32 ± 0.04	1.62 ± 0.01	21.89 ± 0.1	29.24	48.8 ± 1.2	1.78 ± 0.02	3.16 ± 0.03	3.7 ± 0.3	2.8 ± 0.2
9	2.34 ± 0.04	1.68 ± 0.01	21.72 ± 0.1	29.24	48.5 ± 1.2	1.77 ± 0.06	3.17 ± 0.05	3.7 ± 0.3	2.8 ± 0.2

*Data is taken from mission plots.

TABLE 5.3.9. MAIN BATTERY EFFICIENCY

Average efficiency = 94 percent

Event	E_{MB}	Loss	E_{MB} − Loss	$\frac{E_{MB} - \text{Loss}}{E_{MB}}$, percent
0-1	76.98	9.03	67.95	88.26
1-2	115.21	13.37	101.84	88.39
2-3	73.80	9.11	64.69	87.65
3-4	361.14	37.70	323.44	89.56
4-5	161.44	7.95	153.49	95.07
5-6	931.37	24.75	906.62	97.34

Output energy of the solar panel computed from flight data is presented in Table 5.3-10. The solar panel time in sunlight is approximately 62.8 hours. The output energy of the OCR is computed to be

$$E_{OCR} = E_{SP} * \frac{\eta_{OCR}}{100}$$

$$E_{OCR} = (5262 \pm 292 \text{ watt-hr}) * (0.8034)$$

$$E_{OCR} = 4225 \pm 194 \text{ watt-hr}$$

In contrast, the E_{OCR} can be computed from FAT data found in Reference 2.

From flight data

T_{SP} (average) = 108°F = 42.2°C

From Reference 2: Figure 3-1

OCR input voltage = 46.5 volts

From Table 5.3-7

OCR input current (EP-11) = 1.77 amps

Solar panel suntime equals 62.8 hours

Total OCR input energy = (46.5) * (1.77) * (62.8)

= 5168.44 watt-hr

TABLE 5.3.10. SOLAR PANEL OUTPUT ENERGY

Total Watt-Hour = 6262.40 ± 242.40

	Power		Energy			
Event	(EP-10)	(EP-11)	Power		Time	
1-5	(42.2 ± 1.4)	(1.77 ± 0.08) =	(74.69 ± 5.95)	(15.73) =	1174.87 ±	93.69
6-8	(48.8 ± 1.2)	(1.78 ± 0.02) =	(86.86 ± 3.12)	(46.13) =	4006.85 ±	143.92
9	(48.5 ± 1.2)	(1.77 ± 0.06) =	(85.84 ± 5.10)	(0.94) =	80.68 ±	4.79

From Reference 2: Figures 3-2 and 3-3, the OCR losses (battery voltage equals 22 volts) are

$$\text{OCR losses} = 13.9 + (0.05)(82.3) = 18 \text{ watts}$$

Then,

$$\text{Total OCR output energy} = [(46.5)(1.77)-18](62.8)$$

$$= 4038 \text{ watt-hr}$$

And so

$$\eta_{OCR}\,(\text{FAT}) = \frac{4038}{5168} * 100 = 78.1 \text{ percent}$$

Now consider the following comparison of flight and FAT solar panel energy

$$\Delta\eta_{OCR} = \eta_{OCR}\,(\text{flight}) - \eta_{OCR}\,(\text{FAT}) = 80.3 - 78.1$$

$$= 2.2 \text{ percent}$$

From Table 5.3-9,

$$E_{SP} = 5262 \text{ watt-hr}$$

$$(E_{SP} * \Delta\eta_{OCR}) = 5262 * 0.022 = 115 \text{ watt-hr}$$

$$\text{Let } \Delta E_{SP} = E_{SP} * \Delta\eta_{OCR}$$

$$\text{Call } E'_{SP} = E_{SP} - \Delta E_{SP}$$

$$E'_{SP} = 5262 - 115$$

$$E'_{SP} = 5147 \text{ watt-hr}$$

E'_{SP} is the total solar panel energy adjusted for the difference in flight and FAT efficiencies. E'_{SP} compares very favorably to E_{SP} (FAT) = 5168 watt-hr.

Comparison of Loads: Telemetry and FAT

The comparison of telemetry-measured and FAT-measured loads (Reference 2) will be made for selected units, various heaters, and large current drains.

Selected Equipment Loads. The determination of the regulated (EP-14) or unregulated (EP-4) currents used by a selected equipment is obscured by the general variability of frame-by-frame data on either side of the point of turnon or turnoff. Data smoothing provided by the EDRS processing was helpful, but the standard deviations of EP-4 and EP-14 within an averaging interval were often the same order of magnitude as many of the equipment load changes. For example, during Coast I the average standard deviation for EP-14 was approximately 60 milliamperes; the same in terminal descent was 100 to 200 milliamperes. EP-4 showed a standard deviation of approximately 300 milliamperes owing to cycling loads. Consequently, only changes in loads which caused significant changes in EP-4 or EP-14 could be considered.

The results of selected equipment loads are presented in Table 5.3-7. Data for command 0106, XMTR HI VOLT ON, is given at various times during transit, and the current change is seen to approach the FAT value although initially it was low (~200 milliamperes during Coast I). Command 0721 was a little high for unregulated current, but its standard deviation was of the same order of magnitude. Thrust power turnon showed a reasonable comparison with FAT data. Finally, the turnon of the survey camera electronics temperature control agreed well with the FAT value.

In general, the large standard deviations associated with unregulated current loads were due to superimposed cyclic heater loads. The unregulated load values from EDRS in Table 5.3-7 agree reasonably well with FAT data even though large standard deviations were associated with the presented values. Cyclic loads in EP-4 will be considered separately.

Selected Cyclic Loads

AMR and Vernier Line Heaters

The unregulated current (EP-4), was observed to be cyclic during transit (Figure 5.3-16). In a plot of EP-4 at 4 hr/in., a gross correlation of the cycling with the AMR and vernier line heaters operation was apparent (Figures 5.3-18 and 5.3-19).

If launch plus 20 hours to launch plus 36 hours was considered, a mean unregulated current (I_{UR}) of 880 milliamperes ± 160 milliamperes could be measured (Figure 5.3-16). The AMR and vernier line heaters did not have the same duty cycles nor did these loads turn on or off at the same time, since each was thermostatically controlled. Superposition of these heater loads resulting in a somewhat aperiodic plot which can be ovserved in EP-4 (Figure 5.3-16).

Total variation = 320 milliamperes (Figure 5.3-16)

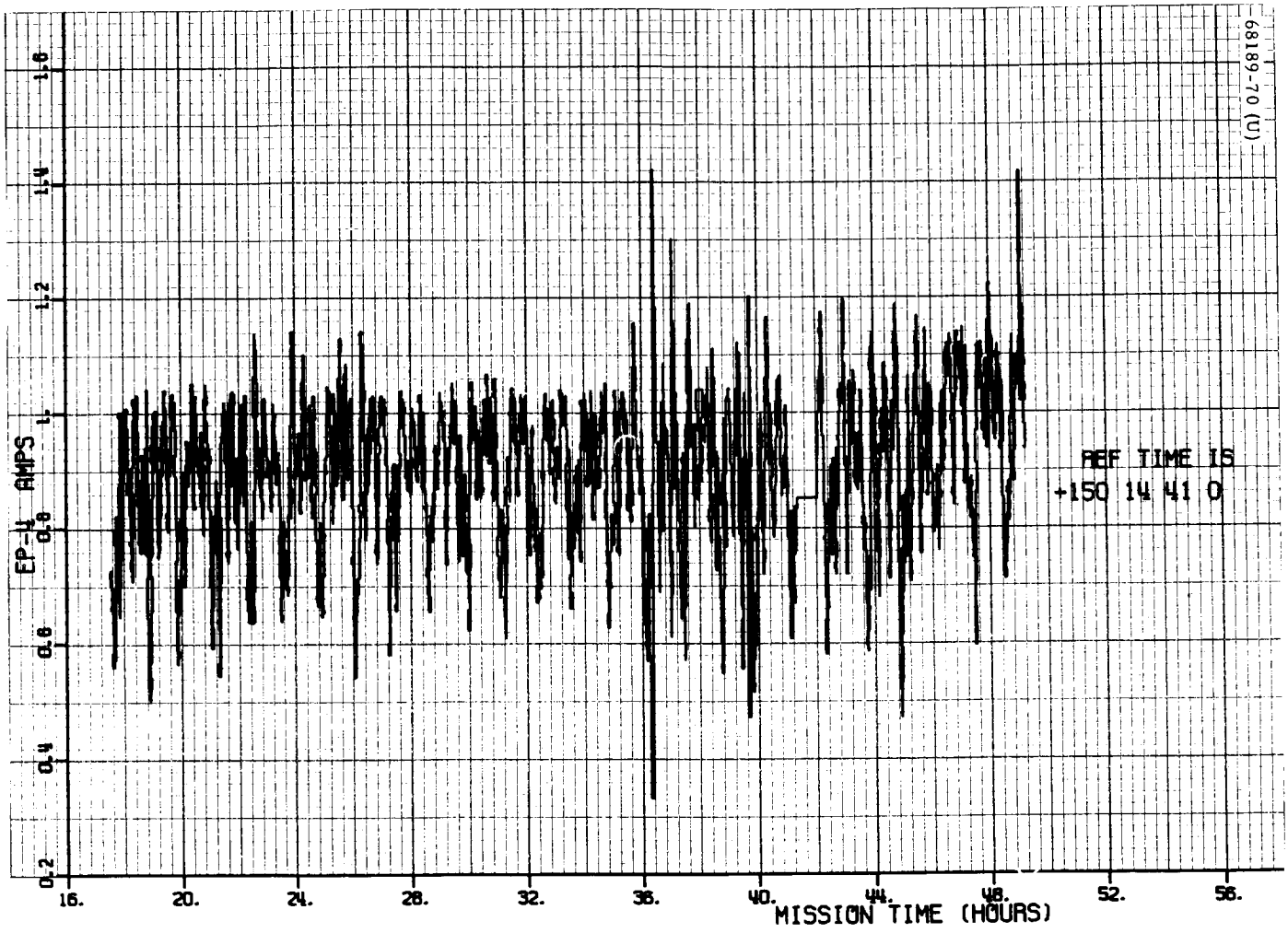


Figure 5.3-16. Unregulated Output Current

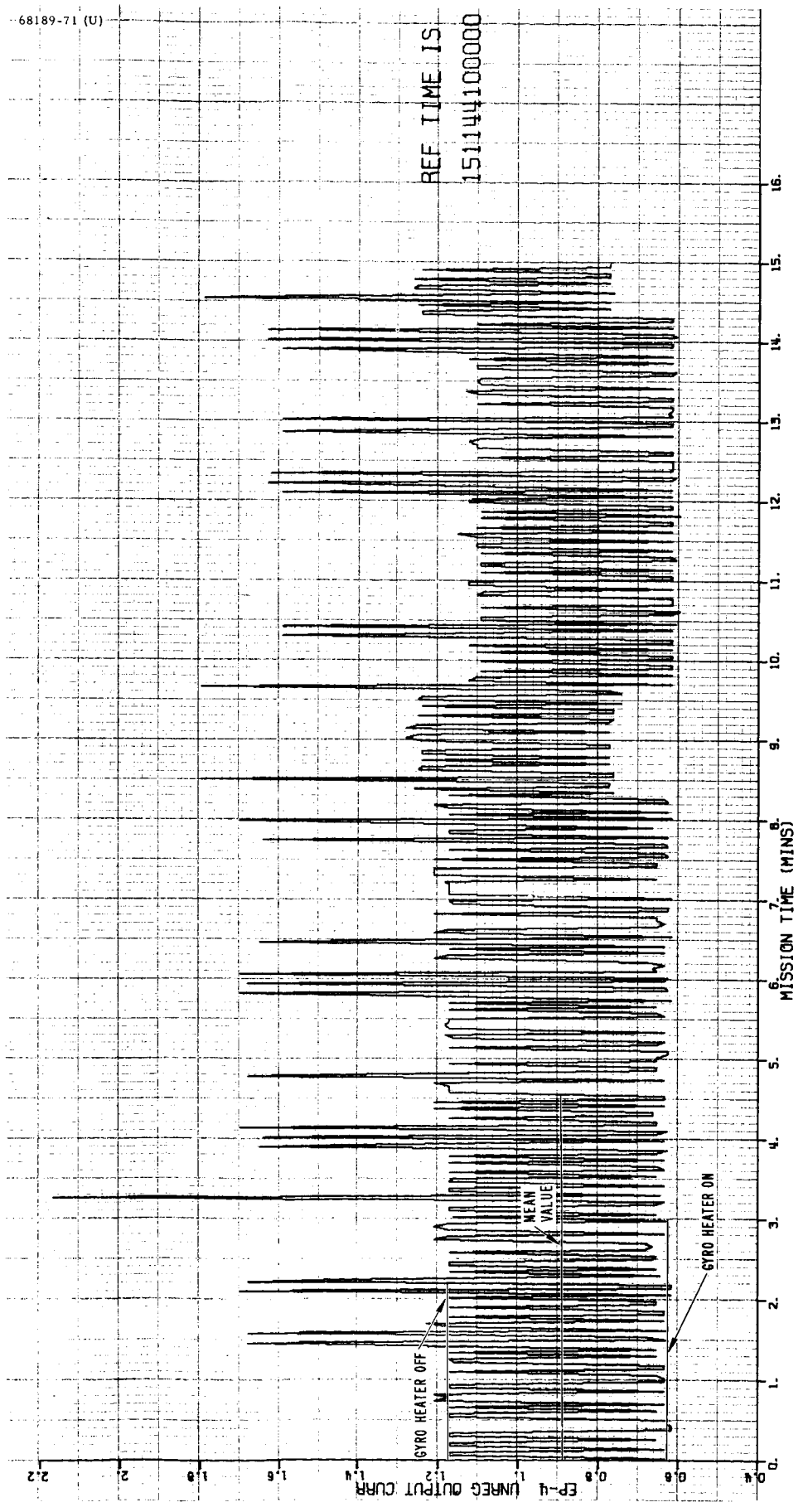


Figure 5.3-17. Coast Phase II

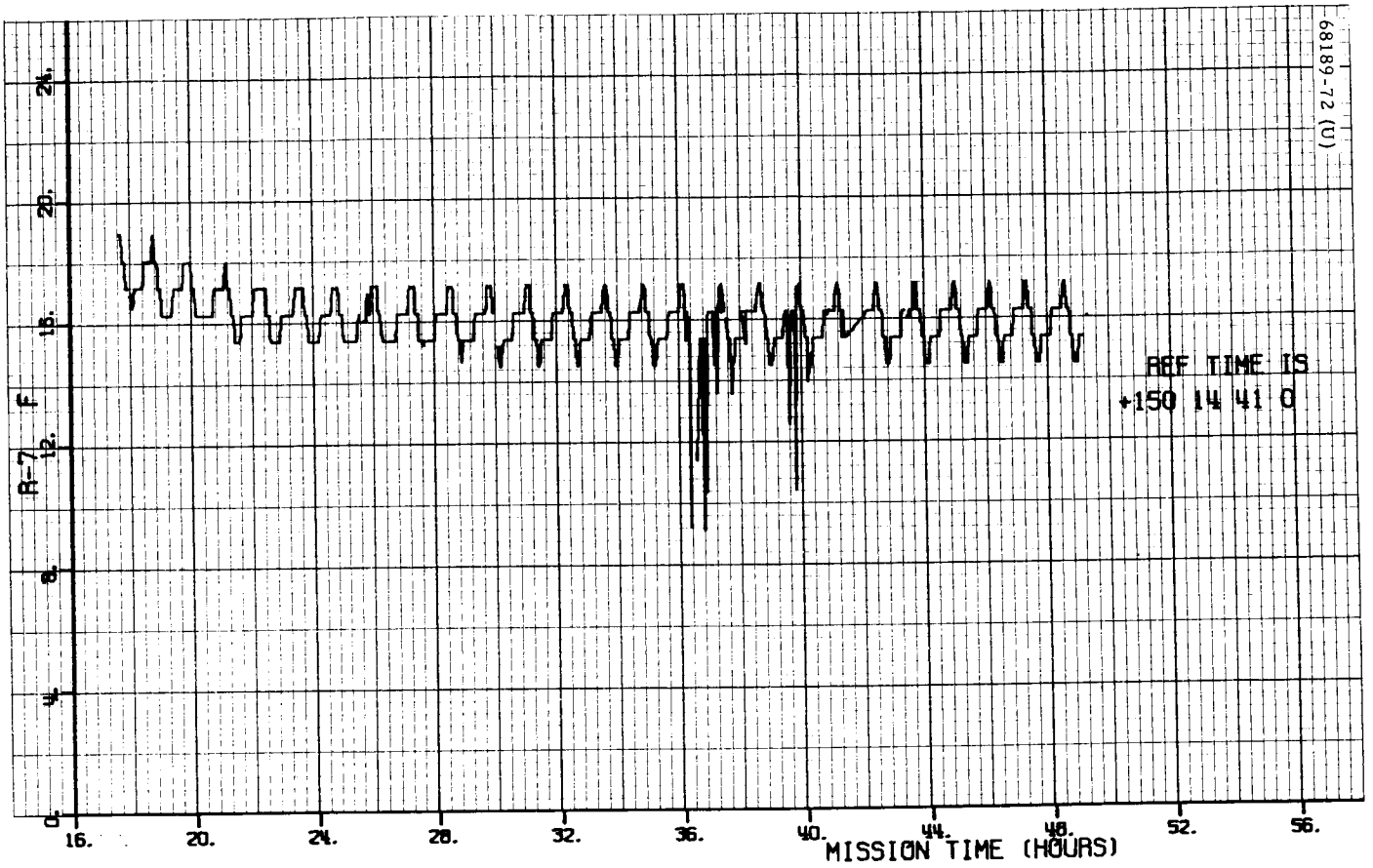


Figure 5.3-18. Altitude Marking Radar Electronic Temperature

Sum of heater loads = 290 milliamperes (FAT data found in Reference 3)

These values compare favorably since there are other unregulated loads that could affect this variation over the long time interval considered.

Gyro Heater

In addition to the long cycles of loading owing to the AMR and vernier line heaters, a further periodic loading occurred in EP-4 resulting from the gyro heaters. The load has a short on-off cycle when compared to the AMR and vernier line heaters. In a 15-minute graph of frame-by-frame telemetry data (Figure 5.3-19) plotted at 1 min/in., the unregulated current is seen to oscillate 7 or 8 times per minute. This oscillation is not seen in Figure 5.3-16 since EDRS data is averaged, and thus the oscillation due to gyro heaters appears only as an increase in the standard deviation of EP-4 for each EDRS data point.

The variation in I_{UR} (one-half period in Figure 5.3-19) represents the current drawn to operate the IRU heaters and gyro thermal control amplifiers.

Total variation = 540 milliamperes (Figure 5.3-17) (one unit)

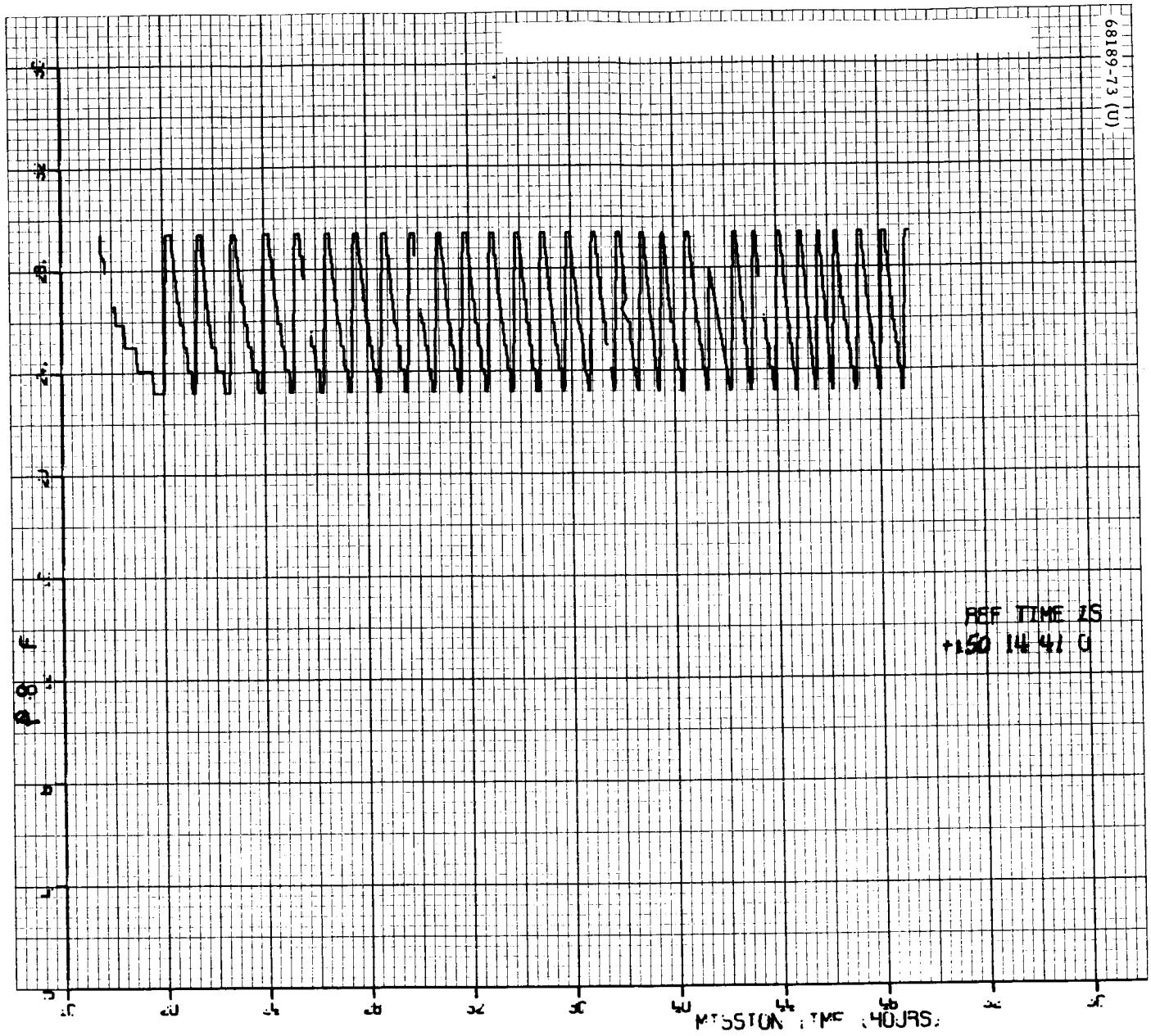
IRU heaters and gyro control amplifier = 577 milliamperes (FAT data found in Reference 5)

This constitutes favorable agreement. Furthermore, gross considerations of Figure 5.3-15 indicate a duty cycle of approximately 25 percent (FAT value: 26 percent, Reference 5).

RADVS. During the final portion of terminal descent, the RADVS draws current. The unregulated current drain is observed as EP-17. In EDRS data at 153:06:15:50 GMT, the RADVS and squib current were recorded at 27.4 ± 1.2 amps. This is close to the expected value of 29 amps. Figure 5.3-20 is a 360-second plot of EP-17 starting at 153:06:10 GMT. AMR power is on at the start of this plot, drawing approximately 1.9 amps. The EP-17 signal is noisy, but changes owing to load differences are apparent. At about 177 seconds, the AMR is enabled, increasing the current by 1.8 amps. Finally, RADVS power is completely on at about 310 seconds, drawing about a 27-amps average.

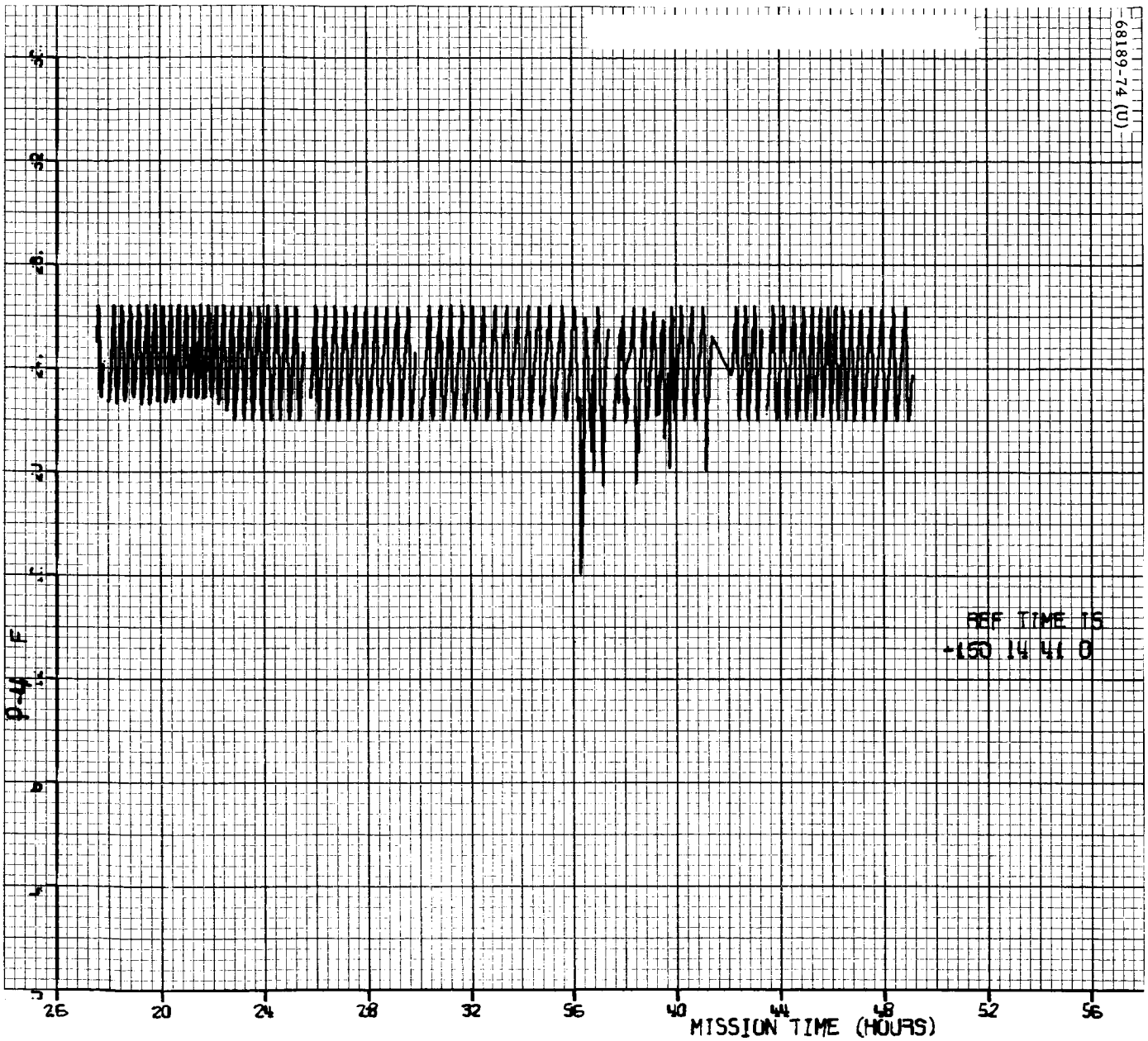
Current Calibration

Observation of mission plots of engineering signal processor (ESP) and auxiliary engineering signal processor (AESP) current calibration signals indicates variation throughout the transit portion of the mission. Further examination of frame-by-frame data and graphs during the coast phases shows a maximum of a 3 bcd (or 300 milliamperes) noise variation in the zero scale current calibration (EP-29) of the AESP. The midscale current calibration (EP-28) is more slowly varying around 200 milliamperes, and the full scale current calibration is essentially constant.



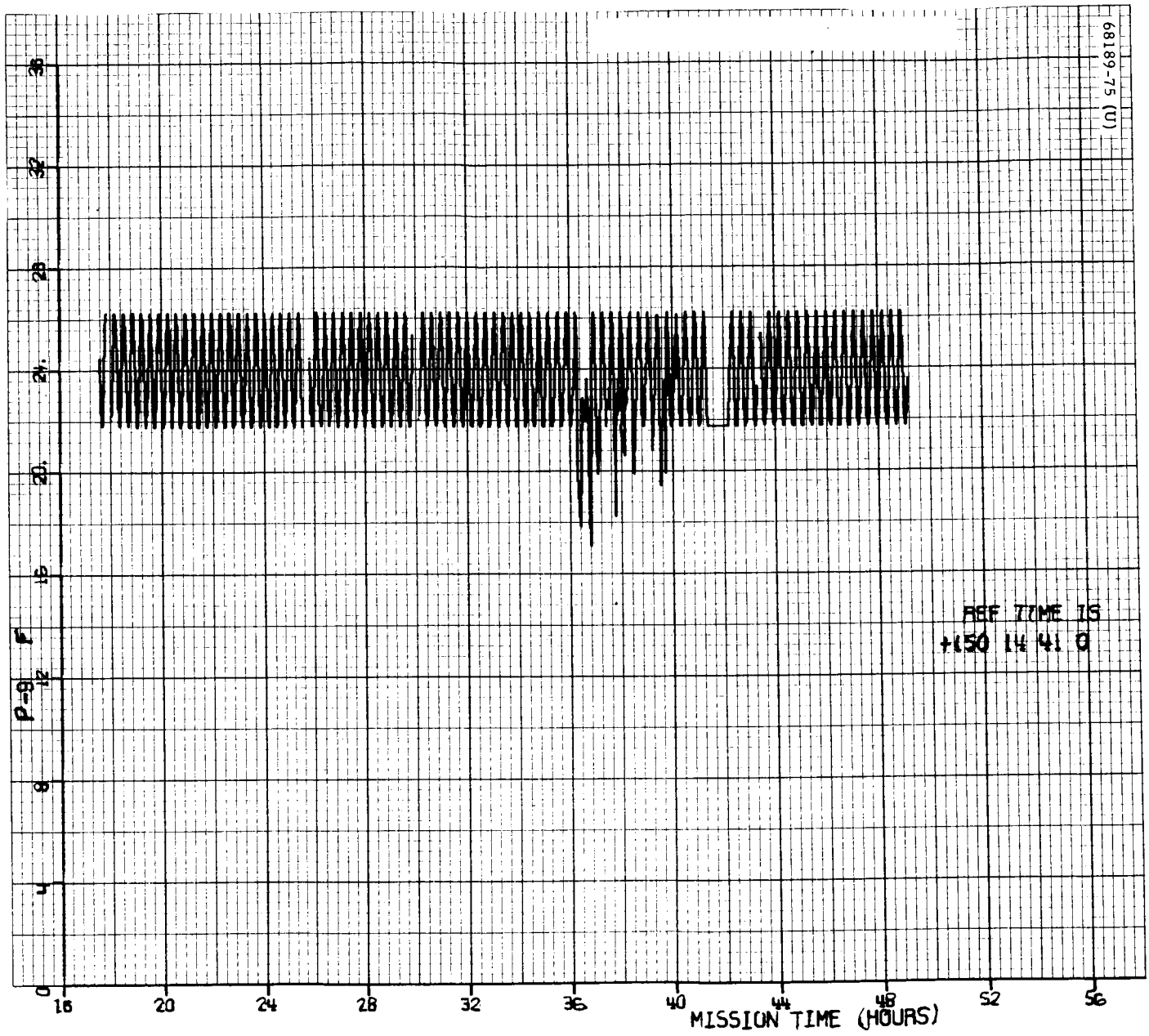
a) Line 1

Figure 5.3-19. Vernier Line Temperatures



b) Line 2

Figure 5.3-19 (continued). Vernier Line Temperatures



c) Line 3

Figure 5.3-19 (continued). Vernier Line Temperatures

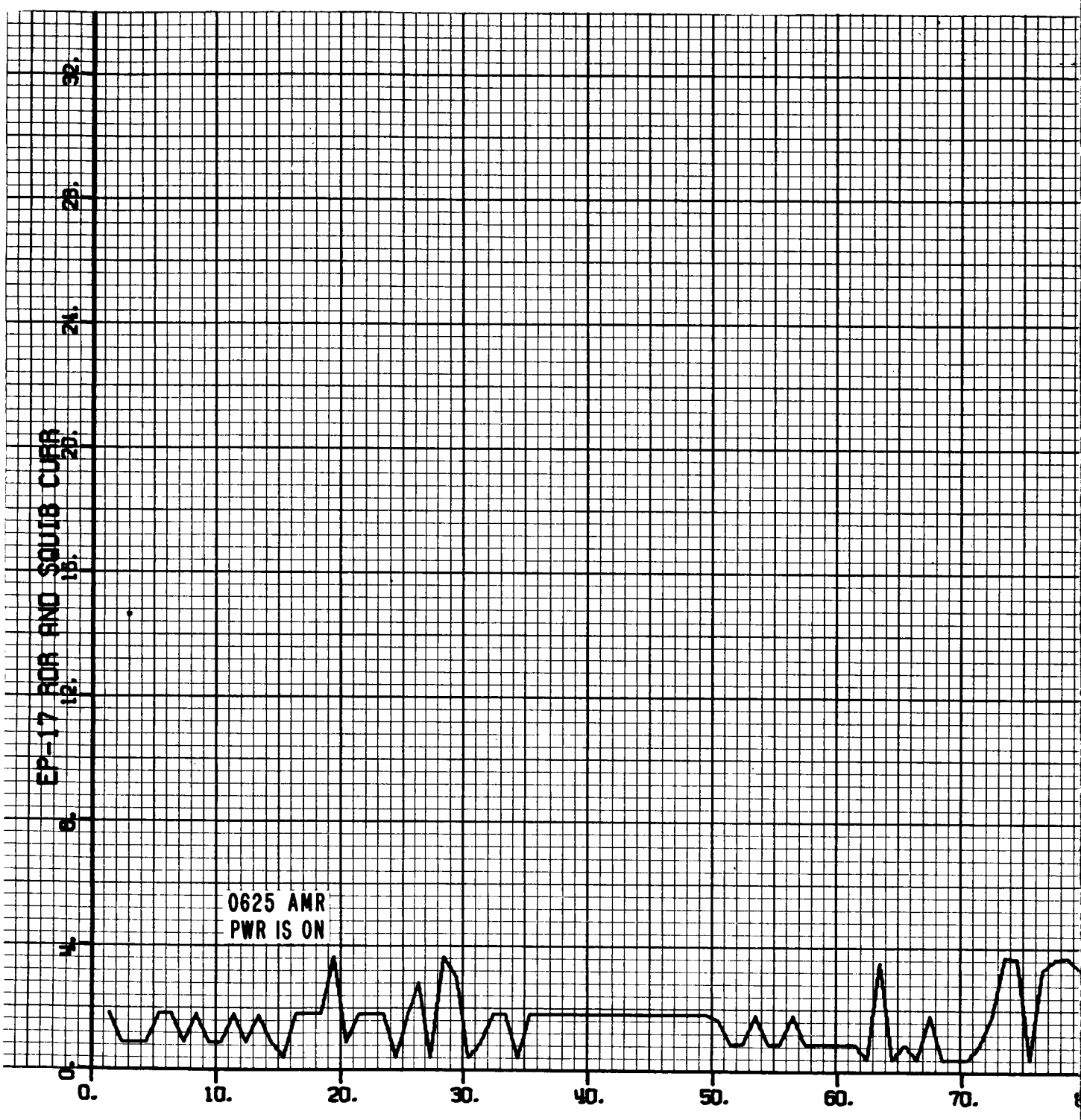
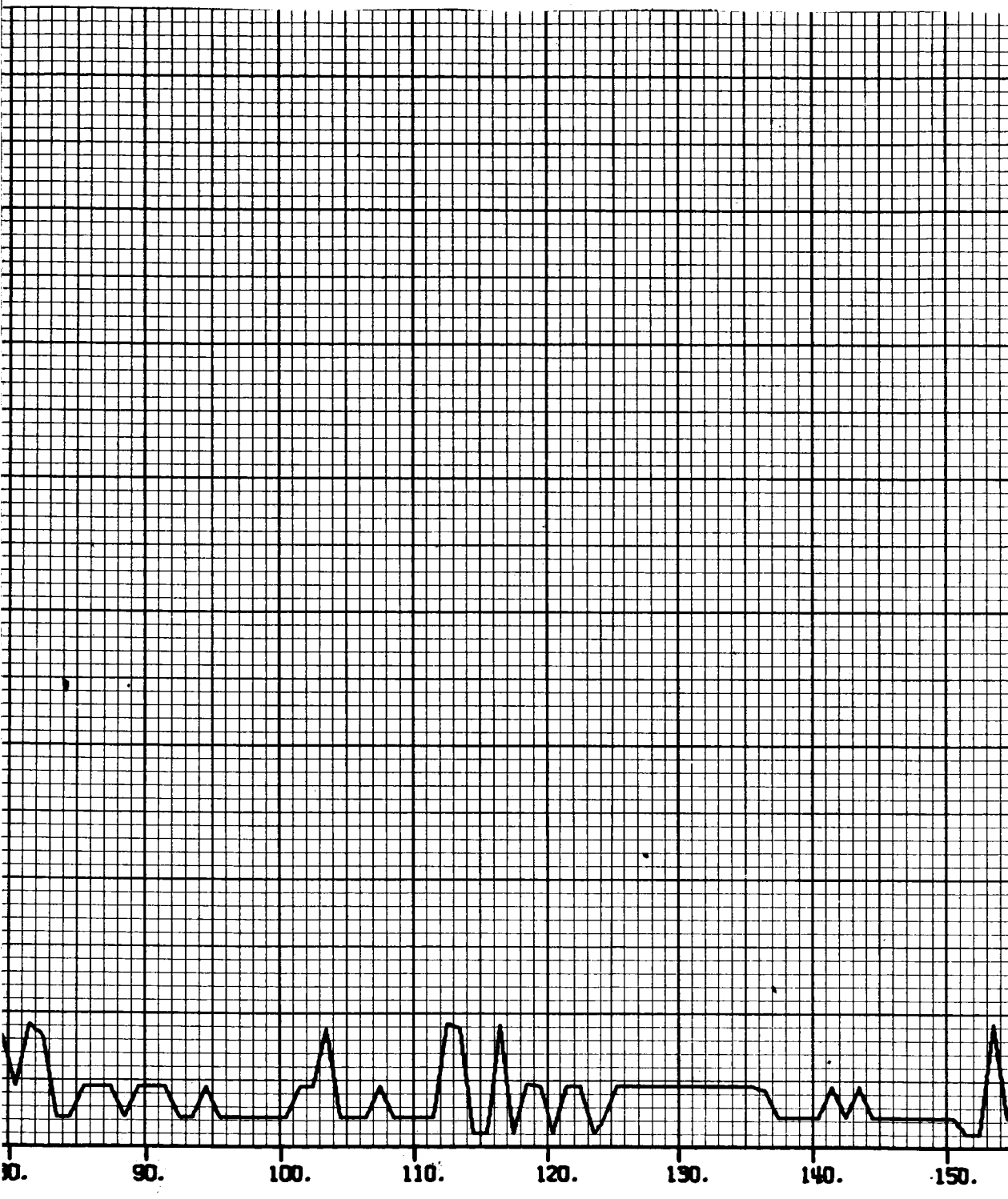


Figure 5.3-20. Radar and Squib Current During Terminal Descent

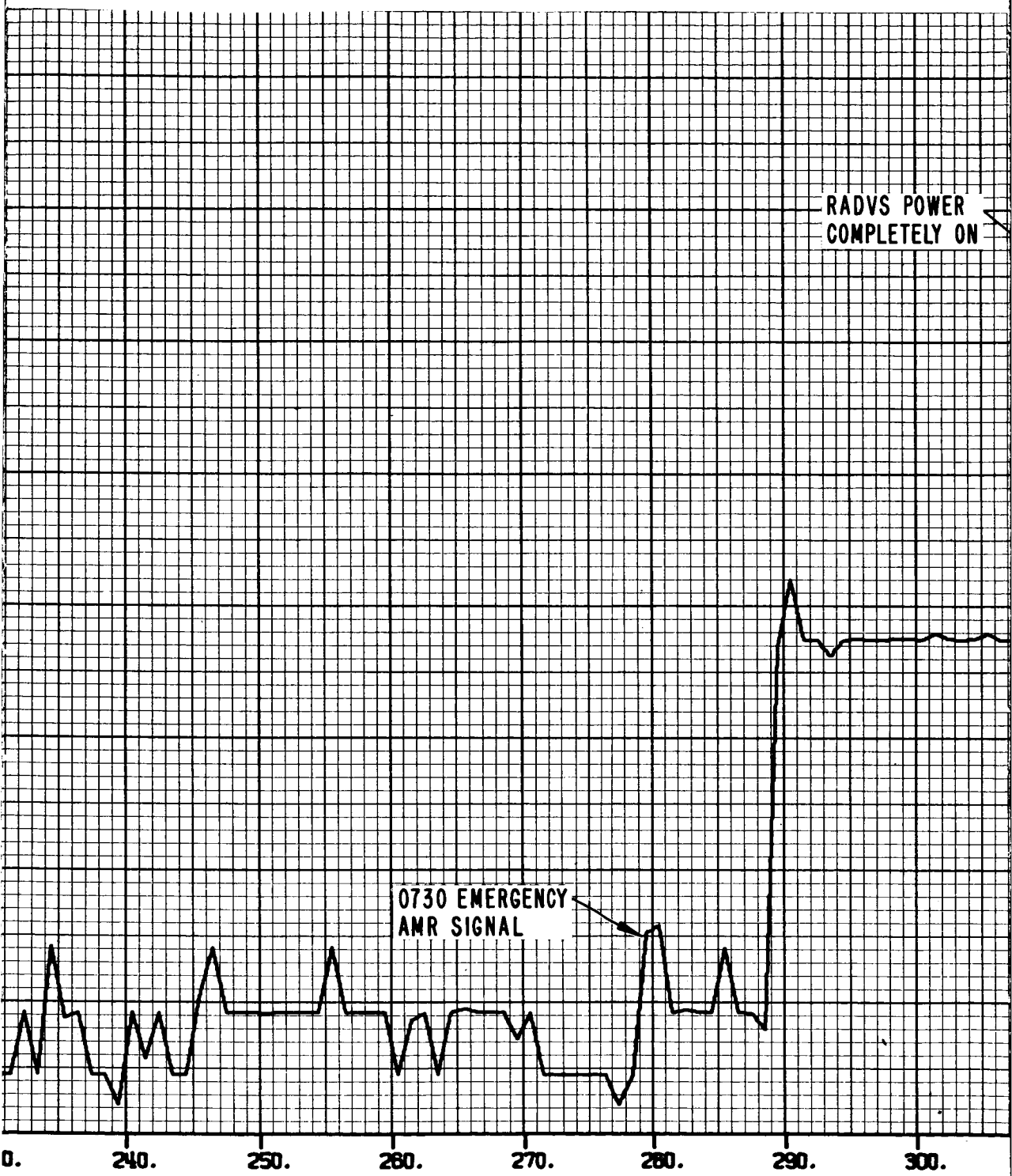


FOLDOUT FRAME

5-3-45-2

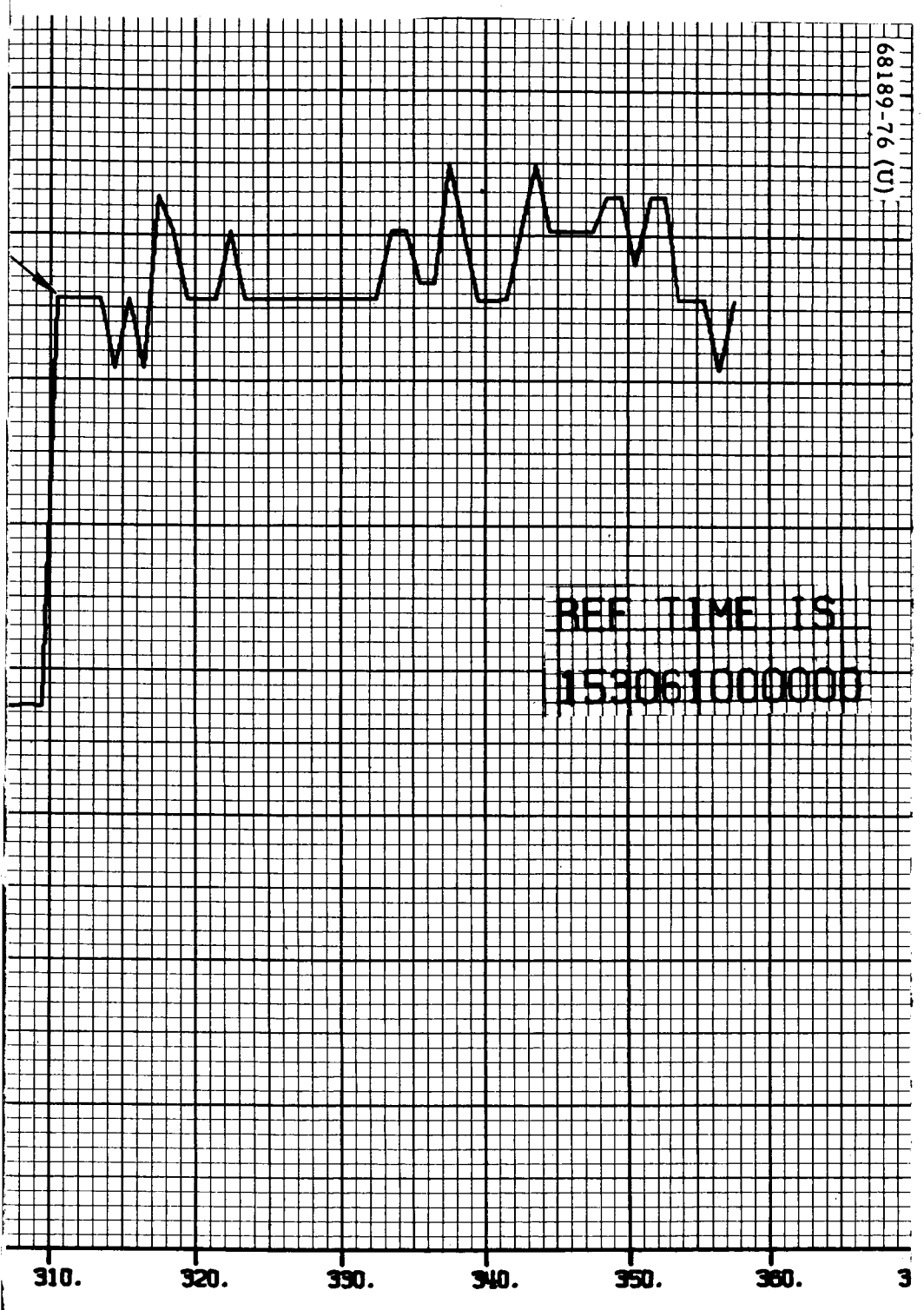


FOLDOUT FRAME



FOLDOUT FRAME

5-3-46-1



FOLDOUT FRAME

S-E-C-R-E-T

A brief examination of the ESP current calibration signals (EP-18, -19, and -20) also shows a noise variation of approximately 3 bcd counts (or 300 milliamperes).

This variation can probably be attributed to system noise. Since these current calibration signals are essentially constant over the mission, the need for continual updating of telemetry signal values frame-by-frame, based upon changes in the calibration signals, may not be warranted. It would be better to change the telemetry current corrections only when the current calibration signals exceed a specific operating bandwidth, say 4 to 8 bcd counts.

5.3.6.3 Summary of EP Mission Plots

Plots of selected electrical power subsystem signals for the entire flight phase of the mission are included in Figures 5.3-7 through 5.3-15. Table 5.3-11 is an index to these plots.

5.3.7 REFERENCES

1. "Surveyor I Flight Performance Quick Look Report," Hughes Aircraft Company, 17 June 1966.

2. J. Mundy, "System Specification Power Management Data Summary SC-1 Spacecraft 291000," 19 April 1965.

3. J.C. Jensen, "Power Data Sheets," IDC 2255.1/1664, 18 May 1966.

4. Power Management Program, Hughes Aircraft Company.

5. J. Mundy, "System Specification, Power and Thermal Dissipations by Functional Event For Engineering Payload 239523," Revision C, 1 July 1965.

5.5.8 ACKNOWLEDGMENTS

Appreciation is expressed to W. McIntyre for technical coordination, S.A. Volansky and J. Berger for special processing, and J.R. Oelschlaeger for power management program data. Advice is acknowledged from R. Virzi of JPL. Thanks are given to R.H. Leuschner and K.C. Beall for review and criticism.

TABLE 5.3-11. INDEX OF MISSION PLOTS

Name	EP Number	Value	Graph	Comments
29 volts nonessential	1	(See Table 5.3-8)		Within specification
22 volts unregulated	2	(See Table 5.3-8)	Yes	Within specification
Main battery man. pressure	3			Within specification
Unregulated output current	4	(See Table 5.3-8)	Yes	
Main battery voltage	5			~ 23.2/22.8 volts first 4 hours, then essentially constant. Within specification.(Reference 4: minimum 17.4 volts)
Battery charge current	6			Charge intervals after touch-down were hours 65 to 70.
Boost regulator differential current	7	(See Table 5.3-8)	Yes	
Main battery temperature	8	88 to 109°F in transit		Within specification (Reference 4: 70 to 125°F)
Battery discharge current	9	(See Table 5.3-8)	Yes	
Solar array voltage	10	(See Table 5.3-8)	Yes	
Solar array current	11	(See Table 5.3-8)	Yes	
Solar array temperature	12	108 to 110°F in transit		Reference 4: specification +122°F ± 10°F
Boost regulator temperature	13			
Regulator output current	14	(See Table 5.3-8)	Yes	
OCR output current	16	(See Table 5.3-8)		
Radar and squibb current	17	26.32 amps at 63.6 hours		See 5.3.6.2,"RADVS"
ESP	18			See 5.3.7.2,"Current Calibration"
Current	19			
Calibration	20			
Compartment A heater current	21	< 80 milliamperes		
Compartment B heater current	22	< 80 milliamperes		
Auxiliary battery voltage	23		Yes	Within specifications
SC-S4-current	24			
SC-S6-current	25			
Auxiliary battery temperature	26		Yes	See 5.3.3.2,"Auxiliary Battery Temperature"
AESP	27			See 5.3.6.2,"Current Calibration"
Current	28	0 to 3 BCD change during coast		
Calibration	29			
Boost pre-regulator voltage	30	Approximately 30.4 volts		Within specifications
Battery charge regulator temperature	34	109 to 128°F		

5.4 RF DATA LINK SUBSYSTEM

5.4.1 INTRODUCTION

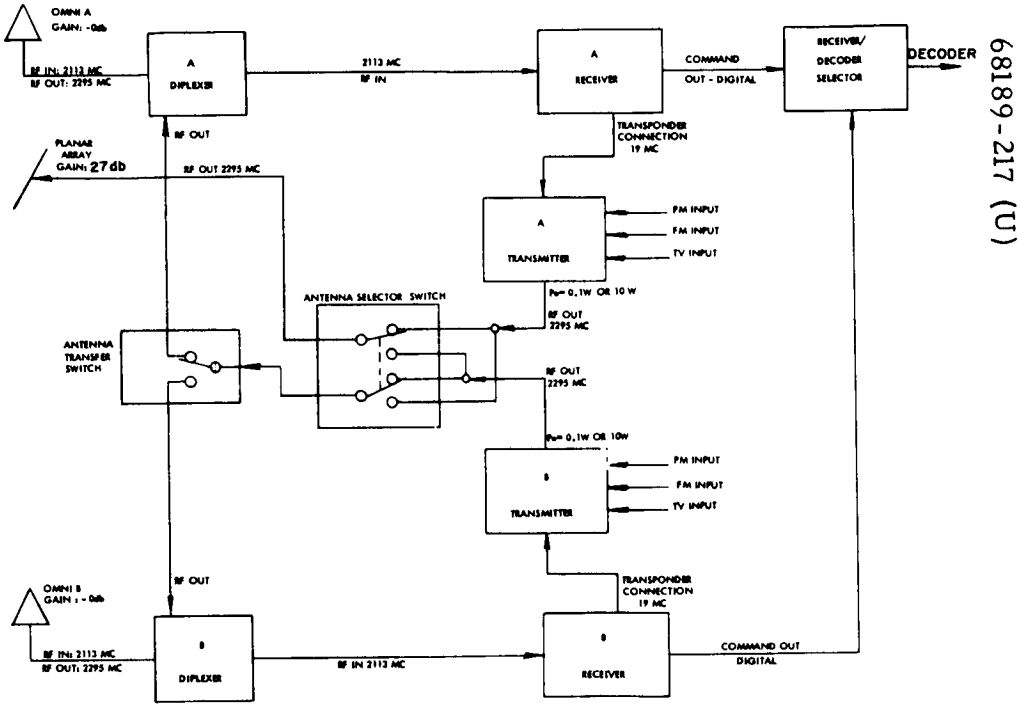
This section contains a summary and analysis of the performance of the data link subsystem during Surveyor Mission A.

The data link subsystem consists of the transmitters, transponders, receivers, command decoders, and antennas. It is the function of this subsystem: 1) to provide engineering data transmission from the spacecraft at bit rates compatible with specific mission phases, 2) to provide analog data, such as television and strain gages, at signal levels high enough for proper discrimination, 3) to provide phase coherent two-way doppler for tracking and orbit determination, and 4) to provide command reception capability throughout the mission to allow for complete control of the spacecraft from the ground. A simplified block diagram of the communications subsystem is shown in Figure 5.4-1.

The pertinent subsystem units that were on the spacecraft during the mission are as follows:

Unit	Part Number	Serial Number
Receiver A	231900-3	13
Receiver B	231900-3	14
Transmitter A	263220-4	14
Transmitter B	263220-4	20
Command decoder unit	232000-3	5

Unlike most subsystems, individual data link subsystem parameters such as losses, threshold sensitivity, modulation index, etc., are not measured or individually determined from mission data. The composite effect of the performance of these parameters is measured as received signal power at the spacecraft and the tracking station (DSIF) and as telemetry and command error rates. Consequently, it is impossible to compare individual link



68189-217 (U)

Figure 5. 4-1. Communications Subsystem Block Diagram

parameters to specified performance criterion. The best that can be done is to compare measured signal levels to predicted levels, and telemetry quality and command capability to predicted capabilities. To further cloud the analysis, omnidirectional antenna gain is a major contributor to the uncertainty in received signal levels. Accurate omni-gain measurements are difficult to achieve and, in most cases, deviations from predictions can most likely be attributed to antenna gain uncertainty. Because of the probelms outlined above, analysis of the data link subsystem performance will, in general, be a qualitative analysis of the performance of the entire subsystem versus a quantitative assessment of the performance of the individual subsystem parameters. Equally as important as subsystem performance evaluation in this analysis is the qualitative assessment of the premission and real-time prediction techniques used during Mission A since future missions must rely on these techniques as guidelines during the real time operation.

The data link parameters used in the performance predictions are tabulated in Table 5.4-1. This data is measured data taken from FAT, STV, and CDC tests, as well as specified parameters where measured data was not available.

Except for the failure of omnidirectional antenna A to properly deploy at separation, the data link subsystem performed exactly as expected. The performance was very close to nominal, and all subsystem requirements and objectives were satisfied.

5.4.2 ITEMS CONSTITUTING ANALYSIS

The data contained in this report consists of spacecraft telemetered, DSIF, and mission event time data. Where meaningful, the data is correlated to and compared with equipment specifications, previous test data, preflight predictions, and in-flight analysis predictions.

5.4.3 MODE, BIT RATE, AND SUBSYSTEM CONFIGURATION SUMMARY

The telemetry modes, bit rates and subsystem configuration are tabulated as functions of time from launch to touchdown in Tables 5.4-2 and 5.4-3, respectively. Also, the various telemetry signals and the modes in which they appear are tabulated in Table 2.2-1 in Section 2.2. (The times shown in the these tables are accurate only to ±1.0 minute.) These tables do not contain lunar data because of the large number of times that the modes and configuration were changed due to lunar TV and assessment operations.

5.4.4 SUMMARY OF RESULTS

As discussed in the introduction, a quantitative assessment of the individual subsystem parameters is not possible in most cases. However, the parameters that can be related either to predictions or requirements or both are summarized in Table 5.4-4.

TABLE 5.4-1. LISTING OF UP-LINK AND DOWN-LINK PARAMETERS FROM FAT, STV, AND CDC TESTS

Description	Value
Transmitting system (DSIF)	
RF power	70.0 dbm 0.5 dbm -0.0 dbm
Antenna gain	
SAA	20.0 db ± 2.0 db
SCM	51.0 db, ±1.0 db, -0.5 db
Circuit loss	
SAA	-0.5 db ± 0.0 db
SCM	-0.4 db ± 0.1 db
Receiving system (SC-1)	
Circuit loss	
Receiver A	-3.2 db ± 1.3 db
Receiver B	-3.7 db ± 0.3 db
Up-link carrier tracking loop	
Equivalent noise	
Bandwidth	-240 Hz + 10 percent
Threshold, SNR	12 db
Up-link channel	
Threshold, SNR	9 db
System noise	
Temperature	2700°K
Equivalent noise	
Bandwidth (predetection)	13430 Hz
SCO center frequency	2.3 kHz
Data/subcarrier	
Modulator indices	7.2

Table 5.4-1 (continued)

Description	Value
Modulator indices	1.6 ± 10 percent
Transmitting system (SC-1)	
RF power	
Transmitter A	
(low power)	20.7 dbm, +1.05 dbm, -1.8 dbm
Transmitter B	
(low power)	20.8 dbm, +0.5 dbm, -1.6 dbm
Transmitter A	
(high power)	40.5 dbm, +0.1 dbm, -0.5 dbm
Transmitter B	
(high power)	40.15 dbm, +0.35 dbm, -0.15 dbm
Planar array gain	27.0 dbm, ±0.5 db
Circuit loss	
Omnidirectional antenna A	-3.6 db ± 0.6 db
Omnidirectional antenna B	-3.8 db ± 0.6 db
Planar array	2.7 db ± 0.3 db
Carrier frequency	2295 MHz
Receiving system (DSIF)	
Antenna gain	
SAA	21.0 db, ± 1.0 db
SCM	53.0 db, ± 1.0 db, -0.5 db
Circuit loss	
SAA	-0.5 db ± 0.0 db
SCM	-0.18 db ± 0.05 db

Table 5.4-1 (continued)

Description	Value
Effective noise Temperature	
Maser	55°K ± 10°K
Parametric Amplifier	270°K ± 50°K
Lunar temperature	110°K ± 25°K
Carrier channel	
Equivalent noise bandwidth for maneuvers (at threshold)	152 Hz
Equivalent noise bandwidth for coast mode (at threshold)	12 Hz
Threshold, SNR	
Acquisition	3.0 db ± 1.0 db
Maneuvers	14.0 db ± 1.0 db
Coast mode	6 db
SCO descriptions	
Equivalent noise bandwidth (predetection)	
4400 bits/sec	4770 Hz ± 10 percent
1100 bits/sec	1190 Hz ± 10 percent
550 bits/sec	644 Hz ± 10 percent
137.5 bits/sec	158.5 Hz ± 10 percent
17.2 bits/sec	25.1 Hz ± 10 percent
Strain gage 1	281.0 Hz ± 10 percent
Strain gage 2	524.0 Hz ± 10 percent
Strain gage 3	464.0 Hz ± 10 percent
Reject/enable	377.0 Hz ± 10 percent
Gyro speed check	874.0 Hz ± 10 percent

Table 5.4-1 (continued)

Description	Value
SCO center frequency	
4400 bits/sec	33.0 kHz
1100 bits/sec	7.35 kHz
550 bits/sec	3.90 kHz
137.5 bits/sec	0.96 kHz
17.2 bits/sec	0.56 kHz
Strain gage 1	1.70 kHz
Strain gage 2	3.00 kHz
Strain gage 3	5.40 kHz
Reject/enable	2.3 kHz
Gyro speed check	5.4 kHz
SCO modulator indices	
4400 bits/sec	1.6 ± 10 percent
1100 bits/sec	0.935 ± 10 percent
550 bits/sec (acquisition)	0.3 ± 10 percent
550 bits/sec	1.15 ± 10 percent
137.5 bits/sec	1.45 ± 10 percent
17.2 bits/sec	1.45 ± 10 percent
Strain gage 1	0.615 ± 10 percent
Strain gage 2	0.615 ± 10 percent
Strain gage 3	0.61 ± 10 percent
Reject/enable	0.655 ± 10 percent
Gyro speed check	1.600 ± 10 percent
Carrier noise bandwidth for television modes	
600 line	3.3 MHz ± 10 percent
200 line	11.4 kHz ± 10 percent
Threshold, SNR, for television modes	
600 line	10.5 db ± 1.0 db
200 line	4.5 db ± 1.0 db

Table 5.4-1 (continued)

Description	Value
Television mode modulation index parameters	
600 line, maximum frequency deviation	2.5 MHz
200 line, maximum frequency deviation	10 kHz
Polarization and pointing loss	0
Atmosphere Absorption	0 db, +0 db -0.2 db

5.4.5 ANOMALY DESCRIPTION

5.4.5.1 Omnidirectional Antenna A Nonextension During Transit (TFR 18233)

The major subsystem anomaly observed during the mission was the apparent failure of omnidirectional antenna A to deploy just prior to spacecraft separation from the Centaur. Any mechanical problems and any conclusions relative to these problems will not be discussed in detail in this section but will be treated in Section 5.12, "Mechanisms." Only the RF data relating to the anomaly will be treated here.

Without drawing any conclusions as to the actual failure mechanism, it is necessary to present a brief history of the problem and some possible causes in order to relate the observed RF data to the anomaly. Real-time data was not available at the SFOF during deployment. Postmission telemetry through Centaur shows normal simultaneous leg extension, followed about 9 seconds later by the omnidirectional antenna B deployed signal. Once the signal went to the "on" condition, it did not return to "off." Further, the omnidirectional antenna A deployed signal did not, at any time during transit, indicate "on."

It was learned sometime after the mission that omnidirectional antenna A was slightly misaligned with the clamp that held it in the stowed position. It is therefore possible that one of the following events resulted in the observed anomaly:

1) Omnidirectional antenna A extended, but did not actuate the microswitch from which the omnidirectional antenna extend signal is derived.

TABLE 5.4-2. TELEMETRY MODE SUMMARY

	Time	Mission Phase	Mode	Bit Rate	DSIF Automatic Gain Control	Comment
150	14 41 01	Launch	5	550		Low modulation index
	15 10 16		5	550	-88.0	Initial acquisition – station 51
	15 34 22		1	550		
	15 39 28		4	1100		Normal bit rate
	15 42 35		4	1100		
	15 48 20		2	1100		
	15 54 36		3	1100		
	15 56 03		5	1100	-120.0	
	18 31 53		4	1100		
	18 34 31		2	1100		
	18 39 08		1	1100		
	18 44 00		1	1100	-129.2	Low power } Pre-Canopus
	18 44 50		1	1100	-109.0	High power }
	18 49 33		5	1100		
	19 14 25		5	1100	-108.0	High power } Star lock
	19 21 42		5	1100	-128.5	Low power }
151	01 38 18		5	550	-134.8	Bit rate reduction
	02 22 54		5	550	-136.5	Station 11 in two-way
	02 24 07		4	550		
	02 44 52		2	550		
	02 47 07		5	550		
	04 14 11		4	550		
	04 17 09		2	550		
	04 20 02		1	550		
	04 26 03		Gyro	550		Gyro speed check
	04 30 16		1	550		
	04 33 57		5	550		
	06 01 20		4	550		
	06 04 07		2	550		
	06 05 25		1	550		
	06 07 54		1	550	-136.9	Low power } Premidcourse
	06 08 55		1	550	-117.0	High power }
	06 10 21		1	4400	-121.0	Increase bit rate for midcourse
	06 49 26		5	550		(Special reverse midcourse data)
	07 04 30		4	550		
	07 07 –		2	550		
	07 09 –		1	550		

Table 5.4-2 (continued)

	Time	Mission Phase	Mode	Bit Rate	DSIF Automatic Gain Control	Comment
151	07 11 53		5	550	-117.2	High power } Postmidcourse
	07 13 30		5	550	-137.98	Low power }
	08 32 09		4	550		
	08 36 49		2	550		
	08 41 27		5	550		
	16 13 27		4	550	-138.9	
	16 18 06		2	550		
	16 27 27		5	550		
	20 32 42		4	550		
	20 36 –		2	550		
152	04 06 03		4	550		
	04 08 22		2	550		
	04 11 52		5	550	-143.6	DSIF 11 having transmitter trouble
	09 58 52		4	550		
	10 02 44		2	550		
	10 07 20		5	550		
	15 48 18		4	550	-142.7	
	15 53 48		2	550		
	16 02 20		5	550		
	18 44 16		4	550		
	18 54 05		2	550		
	19 01 20		5	550	-143.0	
	23 19 53		4	550		
	23 25 –		2	550		
153	01 55 23		4	550		
	02 00 22		5	550		
	02 47 00		5	550	-146.0	DSIF 11 tracking
	03 13 17		4	550		
	03 16 52		5	550		
	03 55 33		4	550		
	03 58 54		2	550		
	04 01 06		1	550		
	04 05 52		5	550		
	05 18 13		4	550	-146.0	Low power } Preterminal
	05 21 26		4	1100	-124.0	High power }
	05 22 10		3	1100		
	05 23 00		1	1100		
	06 00 33		2	1100		
	06 16 01		3	1100		Pretouchdown data on touchdown
	06 17 37		3	1100		Touchdown

TABLE 5.4-3. SPACECRAFT CONFIGURATION SHEET

Day	Time	Mission Phase	Transmitter A/B	Transmitter Power H/L	Transmitter Omni A/B	A/D Converter 1/2	Receiver A φL/AFC	Receiver A Xpond	Receiver B φL/AFC	Receiver B Xpond	Command Decoder A/B	Comments
150	14 41 01	Launch	B	L	B	1	AFC		φL		B	Launch configuration
	14 53 26			H								Centaur command on high power
	15 21 00	Post-acquisition		L						ON		
	16 26 00										A	Modulation interrupt
	18 44 24	Star		H								Star acquisition phase
	19 21 04			L								
151	02 16 20										B	Decoder index at station transfer (DSIF 51 to 11)
	02 35 00										A	
	04 26 03					Gyro						Gyro speed measurement
	04 30 16					1						
	06 08 25			H								Midcourse phase
	07 12 43			L								
	08 53 –										B	Decoder index at station transfer (DSIF 11 to 42)
	09 29 –										A	
	15 16 –										B	Decoder index at station transfer
	17 00 –										A	Decoder index at station transfer
152	04 27 –									OFF	B	DSIF 11 transmitter OFF
	06 22 –									ON		DSIF 11 transmitter ON
	06 25 –										A	Select decoder A/receiver B
	06 54 –										B	Decoder index at station transfer
	08 50 –										A	Select decoder A/receiver B
	17 04 –										B	Decoder index at station transfer
	19 26 –										A	Select decoder A/receiver B
153	02 45 11										B	Decoder index at station transfer
	04 05 –								AFC	OFF		NBVCXO check
	04 12 –								φL	ON		
	05 04 –										A	Select decoder A/receiver B
	05 20 18			H								Terminal phase
	05 29 47								AFC	OFF		NBVCXO mode ON
	06 17 37											Touchdown

2) Omnidirectional antenna A did not get free of the clamp that held it in the stowed position due to the resulting friction force developed by the misalignment of the omnidirectional antenna in the clamp.

Throughout the entire coast phase, the omnidirectional antenna A extend signal never indicated that the omnidirectional antenna had extended even though the omnidirectional antenna extend command was transmitted during two separate periods, the first attempt being made at L+ 1H 40M and the second attempt being made at L+ 39H 50M. Finally, after touchdown, when the telemetry modes were interrogated, it was noted that the omnidirectional antenna A extend signal indicated that omnidirectional antenna A was extended.

Antenna pattern data is of primary importance in determining which of the above possible failure mechanisms was the true failure. This data can be determined from RF subsystem data by observing receiver A signal levels throughout the mission and attempting to relate the observed levels with extended or stowed omnidirectional antenna pattern data. Unfortunately, as discussed

TABLE 5.4-4. PERFORMANCE PARAMETER SUMMARY

Parameter	Predicted Value	Requirement	Actual Performance
Transmitter frequency at acquisition	2294.994627	2295 mc ± 23 kc	***
Receiver B frequency at acquisition	2113.312224	2113.31 mc ± 21 kc	***
Receiver A* signal levels during coast phases	Time variable predictions. Predicts are some nominal value ± ≃8 db	> -114 dbm	Level between 0 and 12 db above nominal and > -95 dbm
Receiver A* signal levels during maneuvers	Time variable predictions. Predicts are some nominal value ± ≃8 db	> -114 dbm	Level between 4.0 and -20.0 db about nominal and > -104 dbm
Receiver B signal levels during coast phases	Time variable predictions. Predicts are some nominal value ± ≃6 db	> -114 dbm	Level between ±4.0 db about nominal and > -100 dbm
Receiver B signal levels during maneuvers	Time variable predictions. Predicts are some nominal value ± ≃7.0 db	> -114 dbm	Level between 6 and -7 db about nominal and > -100 dbm
DSIF signal levels during coast phases	Time variable predictions. Predicts are some nominal value ± ≃8.0 db	> -159.3 dbm (carrier power)(17.2 bits/sec threshold)	Level between ±3.0 db of nominal and > -146 dbm
DSIF signal levels during maneuvers	Time variable predictions. Predicts are some nominal value ± ≃7.0 db	> -135.5 dbm (carrier power) (1100 bits/sec – high power)	Level between +7 and -3 db of nominal and > -129 dbm
Transmitter A high power output	$40.5\ ^{+0.1}_{-0.5}$ dbm	> 39.6 dbm	Output between 40.5 and 39.7 dbm
Transmitter A low power output	$20.7\ ^{+1.05}_{-1.8}$ dbm	> 19.1 dbm	No data
Transmitter B high power output	$40.15\ ^{+0.35}_{-0.15}$ dbm	> 39.6 dbm	Output between 40.6 and 39.9 dbm
Transmitter B low power output	$20.8\ ^{+0.5}_{-1.6}$ dbm	> 19.1 dbm	Output between 20.5 and 19.6 dbm
Phase jitter 12 cps bandwidth	< 36 degrees	< 36 degrees (3σ)	***
Phase jitter 152 cps bandwidth (thrust phase)	< 22 degrees	< 22 degrees (3σ)	***
Phase jitter 152 cps bandwidth (touchdown)	< 30 degrees	< 30 degrees (3σ)	***
Command reject rate	< 1/2000	≤ 1/2000 at signal level > 114 dbm	No rejected commands in ≃ 100,000 at signal levels > -104 dbm
Telemetry** bit error rate	< 3/1000	≤ 3/1000 at input SNR ≥ 11 db	< 3/1000 at input SNR ≃ 9 ± 1 db

*Predictions are based on gains relative to an extended omnidirectional antenna.

**BER was allowed to increase above requirement, but this occurred at input SNRs below specification value of 11 db.

***DSIF data not available for this report

earlier, any single parameter value is difficult to access especially antenna gain.

Accurate omnidirectional antenna gain measurements are difficult to make. The omnidirectional antenna data used during the mission and throughout this report is derived from five complete sets of antenna patterns and represents the composite gain determined by noting the bounds on the maximum and minimum gain exhibited by all five patterns for all points on the sphere. In addition to the actual measurement deviations from pattern to pattern, other error sources must be included. Range reflections and spacecraft-to-model differences can cause errors up to $\simeq \pm 5$ db in measured gain values. Null positions and depths are very susceptible to the above error sources. Because of these problems, no particular measurement can be used to confirm the position of omnidirectional antenna A during transit. However, by observing the data for the entire mission, it is possible to conclude that omnidirectional antenna A was not fully deployed and, in fact, was probably closer to the stowed position than to the deployed position.

Examination of a scale model of the spacecraft indicated that a stowed or nearly stowed omnidirectional antenna position would result in relatively high gain during most of the transit phase when the attitude was determined by the sun and Canopus. In addition, the pre-Canopus spacecraft attitude and the selected maneuvers could result in severe nulls due to a direct interception of the line of sight from the stowed omnidirectional antenna to earth by either the solar panel or planar array or both.

Plots of automatic gain control (AGC) data contained in subsection 5.4.7 tend to confirm the stowed or nearly stowed omnidirectional antenna A position hypothesis. Prior to listing the appropriate figures and drawing any conclusions from the data, it should be noted that the downlink omnidirectional antenna B data and the uplink omnidirectional antenna B data was observed to agree with measured data to within the expected measurement errors. In no case did either up- or downlink omnidirectional antenna B data go below the worst-case predicted data. Omnidirectional antenna A data did not agree well with measured data and did go outside the worst-case predicted gain. The following is a list of pertinent graphs of telemetry data and conclusions drawn from this data:

1) Receiver A and B AGC during transit (Figure 5.4-9) – This data indicates that receiver A experienced large variations in signal levels prior to Canopus acquisition. A 20-db null can be observed between L+1.5 and L+2.0 hours. A null of this depth is not predicted from extended omnidirectional antenna A pattern data. After Canopus acquisition, the antenna gain exhibited by omnidirectional antenna A was apparently high since input signal levels were as much as 12 db above predictions.

2) Receiver A AGC during Canopus acquisition compared to extended omnidirectional antenna A data (Figure 5.4-14) – This data shows receiver A signal level during the roll maneuver instigated to

acquire Canopus. The extended omnidirectional antenna A pattern data is also shown, including the worst-case expected gain level. As can be noted, deep nulls were experienced which were not predicted. Nulls 12 db below worst-case expected levels were observed. Also, a predicted small null did not exist.

3) Receiver A AGC during Canopus acquisition compared to stowed omnidirectional antenna A data (Figure 5.4-15) – This data contains the same receiver AGC data as Figure 5.4-14 but is compared to stowed omnidirectional antenna A data. The stowed data shown was measured during the mission on the JPL range and represents a single measurement. Of primary interest is the fact that the stowed data indicates deep nulls in the same region as the observed receiver AGC data. Also of concern is the fact that worse nulls were measured in the region corresponding to the roll maneuver than were experienced. Relative positional differences of 0.5 to 1.0 inch, however, can cause major pattern changes at 2113 mc, and it is concluded that the observed data behaved more like the stowed pattern predictions than like the extended pattern predictions.

4) Receiver A AGC during the reverse midcourse maneuvers (Figure 5.4-18) – This data shows the receiver A AGC levels during the reverse midcourse maneuvers compared to predicted data relative to an extended omnidirectional antenna. Again, very little correlation can be noted. Also, the signal level went below the worst-case predicted level during both maneuvers.

The composite picture developed by observing the data outlined in this section seems to confirm that omnidirectional antenna A was stowed or near to the stowed position. A final bit of evidence occurred during the first roll maneuver during the terminal maneuvers. At 153:05:38:46, a receiver index occurred resulting from a deep null on either omnidirectional antenna A or B. Neither omnidirectional antenna pattern indicated that a deep null should exist during this roll maneuver. This leads to the conclusion that the null was due to a stowed omnidirectional antenna pattern null caused by interference by the planar array or solar panel. Receiver AGC data is not available during the terminal maneuvers to verify which omnidirectional antenna experienced the null. However, downlink omnidirectional antenna B data, which is similar to the uplink data, did not have a deep null as determined from DSIF signal levels.

Based on RF data, it is concluded that omnidirectional antenna A was not fully extended during transit. Furthermore, it is concluded that the omnidirectional antenna was near the solar panel and planar array similar to the actual stowed position. This conclusion being based on the correlation noted between the observed data and expected data determined by observing the spacecraft model, as well as the lack of correlation between the observed data and extended omnidirectional antenna data. It is not possible to conclude from this data whether omnidirectional antenna A remained in the clamp or if it started to extend. However, if omnidirectional antenna A were partially extended, it is concluded that its position was closer to the stowed than the extended position.

5.4.5.2 Spacecraft Receiver AGC Telemetry Calibration Anomaly (TFR 27628)

During lunar operations, a special spacecraft receiver threshold test was performed (see subsection "Special Receiver Threshold List") on 10 June 1966. This data indicated that the preflight calibration data, when applied to system performance using telemetered temperatures for the assumed unit temperatures, does not give adequate results. Data from this special test was then used to develop new calibration curves for use with the flight data. These new curves differed from the preflight curves by as much as 8 db for Receiver A and 2 db for Receiver B. This anomaly is discussed in detail in subsection "Spacecraft Receiver AGC Data."

5.4.6 CONCLUSIONS AND RECOMMENDATIONS

Based on data contained in this section of the report, the following conclusions can be made:

1) The RF subsystem performed as expected with the exception of omnidirectional antenna A. In most cases, close to nominal performance was experienced in both the up- and downlinks.

2) Antenna pattern data for omnidirectional antenna B (up- and downlink) was relatively accurate. In most cases, actual performance indicated better than or equal to predicted gain data, and in no case was the actual data worse than the worst-case predicted data.

3) The RF subsystem premission predictions and real-time analysis techniques used during Mission A were accurate and in most cases were conservative.

4) Omnidirectional antenna did not properly deploy until sometime between retro firing and touchdown. The actual antenna position was either a stowed or nearly stowed position (see subsection 5.4.5 for details).

As a result of the data contained in this section, including in many cases the problems encountered in reducing this data, the following recommendations are made:

1) Spacecraft receiver AGC data should be telemetered in every mode. This fact is emphasized by the lack of data during the terminal maneuver relative to the observed receiver index, and the required deviation from normal procedures in order to get this data during the star and reverse midcourse maneuvers.

2) Spacecraft receiver AGC data temperature sensitivity should either be lessened or procedures instigated to better calibrate out the temperature effect. Relatively large errors in absolute signal level exist in this report due to the lack of knowledge about the AGC temperature interaction. Considering that the hardware is

built for most spacecraft, a possible solution would be to calibrate the receiver AGC signals relative to compartment A tray temperatures during the STV tests. This data would be invaluable during the mission and during postmission analysis since the STV data on SC-1 was at least similar to the actual mission data. (The unit temperature/AGC calibration data is nearly useless since the unit temperature data does not correlate well with any telemetered temperatures and is calibrated at temperatures that are not experienced during transit.)

3) Temperature transducers should be placed on the transmitter and receiver modules that contain the respective VCXOs. As in the case of the AGC signals, it is very difficult, if not impossible, to correlate unit temperature data to any single presently telemetered temperature. The ability to check prelaunch frequency reports and to update DSIF tracking predictions is severely lessened because of this lack of correlation between frequencies and telemetered temperature data.

4) Receiver frequency/temperature data should be provided for the receivers in both the phase lock and AFC modes. Present data applies only to the phase lock mode. AFC and static phase errors observed during lunar operations indicated deviations that were not explainable from available data.

5) DSIF data, specifically AGC and dynamic phase error signals, must be made available in a timely manner after a mission. No valid DSIF data was received for this report; consequently, DSIF AGC data is very inaccurate since it is made up from verbal reports, station hourly reports, and, in the case of Goldstone data, from the real-time analog recorder data provided during the mission. No dynamic phase error analysis is included in this report even though it is felt to be of considerable interest.

6) DSIF station reports should include the zero to peak or peak-to-peak phase jitter observed. The data should include a measurement every hour and specific measurements during midcourse thrusting, retro burn, and touchdown phases.

7) DSIF receiver AGC levels should be reported just prior to and after going from high to low or low to high power. This data is necessary to compute the spacecraft transmitter low power output before and after going to high power. Since this data was not always available, the low power output during Mission A is not as well known as it might be.

8) The allowable telemetry bit error rate or word error rate should be allowed to go above the present specification value of 3 bits in 1000 or ≈1 word in 30. During coast phases, the limit should be determined by the data users in real time provided the postmission data reduction requirements are not jeopardized.

5.4.7 SUBSYSTEM PERFORMANCE ANALYSIS

This subsection contains plots and analysis of the mission data. The data is discussed in subsections 5.4.7.2 through 5.4.7.7 in relation to specific mission phases and is discussed in subsection 5.4.7.8 in relation to mission plots of the subsystem parameters.

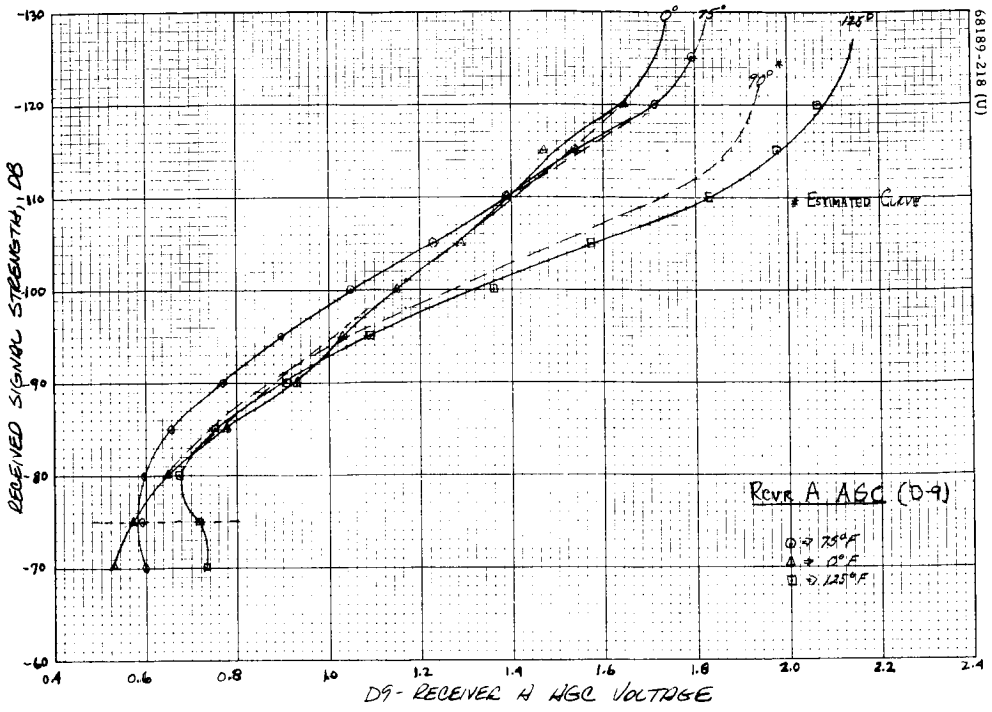
Received signal levels for both the up- and downlinks constitute a significant portion of the analysis contained in this report. The absolute levels at the spacecraft receivers were established by using considerable engineering judgment. An attempt was made to reduce the errors due to temperature sensitivity of the AGC signals. Likewise, the absolute levels at the DSIF were established primarily by attempting to interpret the low resolution analog recording of the Goldstone AGC data received in the SPAC operations area. The absolute value of both the uplink and downlink AGC signals may be somewhat in error; consequently, a brief discussion of the data accuracy will be included prior to the actual data discussions.

5.4.7.1 Data Accuracy

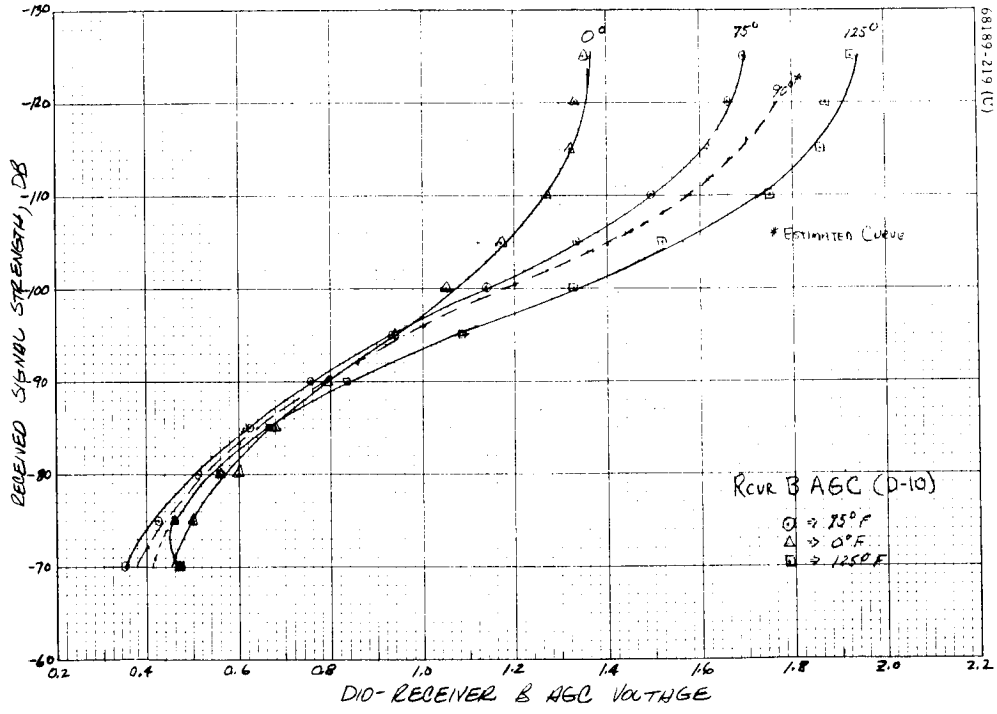
Spacecraft Receiver Automatic Gain Control Data

Figure 5.4.2 shows the receiver A and receiver B AGC calibration data as a function of temperature for temperatures of 0, 75, and 125°F. This data is in agreement with system data taken at the Cape just prior to the mission and is considered to be the most accurate data available. The dotted 90-degree curve represents the curve used in the analysis and was derived primarily from the special receiver threshold test run on SC-1 during the first lunar day.

As can be noted, receiver A AGC can vary between 5 and 12 db, and receiver B AGC can vary between 2 and 9 db in absolute signal level over the range of interest depending on the temperature of the unit (considering only the 75 and 125°F curves). The tray bottom temperature in compartment A was between 90 and 100°F throughout the majority of the mission, leading to the conclusion that the unit temperature was somewhere between the two calibration curves. For the mission real-time analysis, a linear relationship was considered to exist between the curves, and signal levels were reported on this basis. However, a threshold test was run on 10 June 1966 in which the DSIF output signal level was carefully reduced 26 db in steps, and the receiver AGC voltages were recorded. The tray bottom temperature during this test was 91°F, and the tray top temperature was 81°F. Although not exact, the tray temperatures during this test were similar to the transit temperature. (The actual data from this test is contained in subsection "Special Receiver Threshold Test.") By using the linear relationship between the 75 and 125°F curves, both the receiver A and receiver B AGC levels were obviously in error (Reference TFR 27628). Receiver A indicated a total change of 33 db and receiver B a total change of 32 db, and the final signal value at the observed point of receiver/decoder indexing was -134 db for receiver A and -124 db for receiver B. Previous test data taken at the Cape indicated that receiver/decoder indexing would occur at -122 ±1 db for receiver A and -116 ±1 db for receiver B.



a) Receiver A



b) Receiver B

Figure 5.4-2. Receiver AGC

Based on the above data, it was decided to establish a 90°F curve by setting the signal levels at the observed point of indexing to -122 db for receiver A and -116 db for receiver B and work back in increments exactly equivalent to the change in transmitted power. The obvious error in this technique is that it is not known which receiver caused the indexing. The new curve, however, does represent an upper limit on the data and, in the case of receiver A, makes a considerable change in the absolute value from the linear relationship used previously. New coefficients were thus generated from the 90°F curve, and all receiver AGC voltages were converted to engineering units from the new coefficients. This new AGC data is estimated to be accurate to $\simeq \pm 2.0$ db in absolute value.

DSIF Receiver AGC Data

DSIF AGC data was not made available by the time of this report due to problems encountered in postmission data reduction (see Section 5.1). Consequently, the data contained in this report was derived from other available sources. The data from all stations except Goldstone is primarily voice report and station report data. It is considered to be quite accurate, but the time intervals between data points do not allow for transient of "glitch" evaluation relative to unexpected level changes. A good example of this is the DSIF data during star acquisition. Fortunately, good verbal reporting took place during this phase of the mission and the plot contained in this report is relatively good. Variations may have occurred, however, that are not shown. But it is impossible to determine this from the available data.

The Goldstone data plotted during the midcourse and terminal maneuvers is derived from the analog recorder data discussed earlier. Initial calibration errors of the recorder, as well as basic resolution, are obvious error sources. In addition, the exact time correlation of the maneuvers with the data is difficult since no time code exists on the recorder. An effort was made to establish time correlation by noting signal level changes corresponding to known commands such as bit rate change, etc., but this was difficult. The estimated error in this data is $\simeq \pm 2$ db.

5.4.7.2 Subsystem Mission Performance

This subsection contains data and analysis pertinent to specific mission phases. Only those parameters directly related to the mission phase under discussion will be treated here. (All subsystem telemetry for the entire mission is discussed in detail in subsection 5.4.7.8.)

Prelaunch Phase Performance

During the prelaunch phase, the subsystem performance is assessed during the launch pad systems readiness test (SRT) and prelaunch countdown test. Next to assuring normal system performance prior to launch, the most important subsystem data taken during this phase is transmitter and receiver frequency data. This frequency data is used to predict the frequencies at initial acquisition and is transmitted from the Cape prior to launch. The DSIF, in turn, uses this data to tune the DSIF receiver for one-way lock and the DSIF transmitter for eventual two-way lock.

Figure 5.4-3 represents the receiver and transmitter frequency predictions based on frequency reports received prior to launch. The receiver data shown is converted to the equivalent DSIF voltage-controlled oscillator (VCO) frequency by the expression

$$f_{\text{DSIF VCO}} = \left[\frac{f_1 + f_2}{2}\right]\left[\frac{16}{96}\right]$$

where

f_1 = upper pull in frequency in frequency report

f_2 = lower pull in frequency in frequency report

The transmitter data shown is converted to S-band by the expression

$$f_{\text{transmitter}} = 16\, f_3 + 5\, f_4$$

where

f_3 = spacecraft transmitter frequency in frequency report

f_4 = 10 mc reference frequency

With the exception of the last receiver B frequency, the frequency data received during this phase agreed with earlier test data within the expected uncertainty caused by lack of one-to-one frequency telemetered temperature correlation. The drop in frequency at L-100 minutes was caused by an expected temperature increase of ≃5°F as indicated by telemetered tray temperature changes.

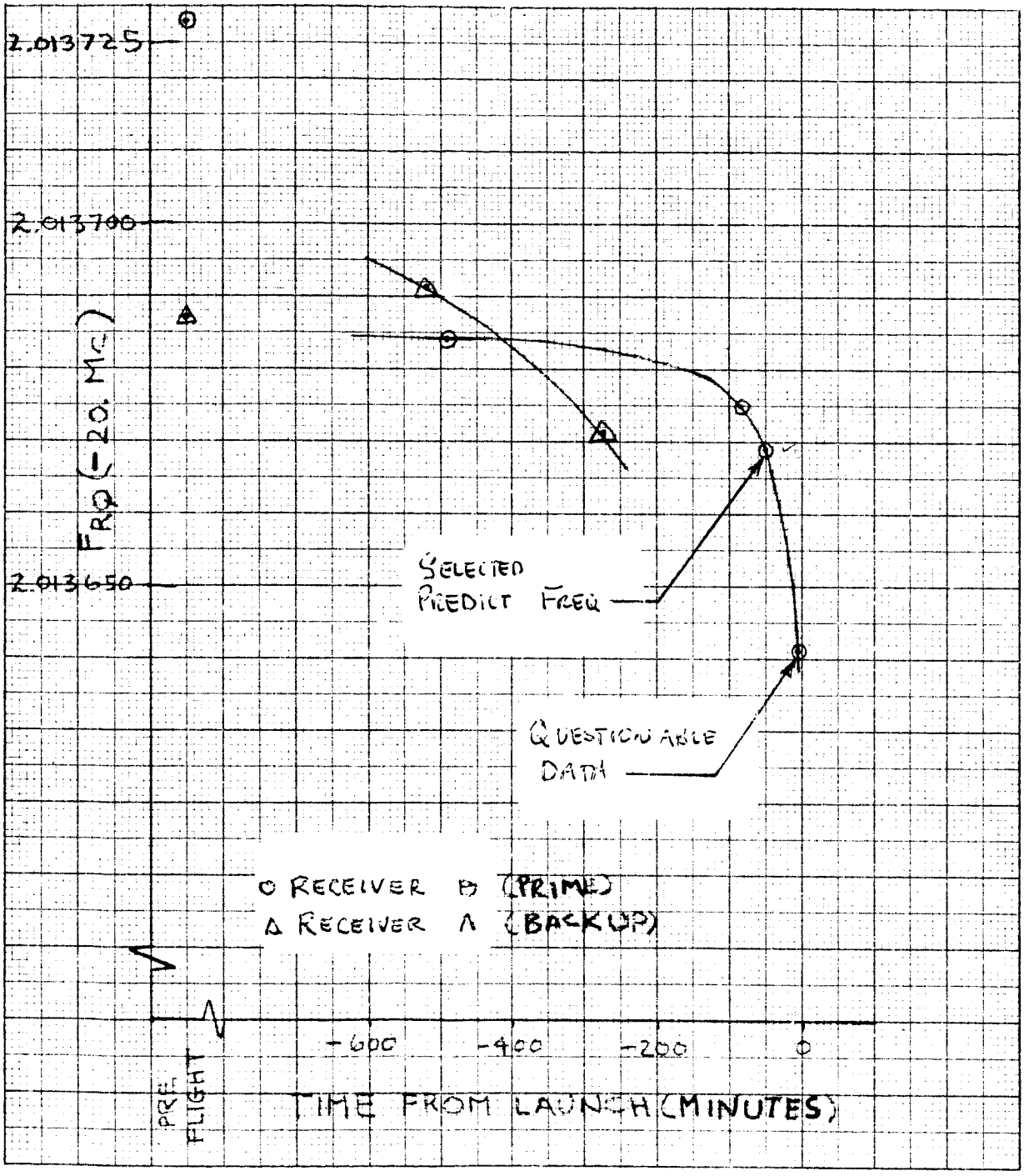
The actual predictions used by the DSIF were made on the indicated frequencies (L-50 minutes report) because the L-5 minutes frequency report contained a questionable receiver B frequency.

No attempt was made to adjust the reported frequencies for temperature changes resulting from going to transmitter high power at separation since earlier data taken during the DSIF compatibility tests indicated a considerable time lag existed between the high power on time and a resulting transmitter frequency shift. Figure 5.4-4 shows this data.

The predicted frequencies, less doppler shift corrections, were as follows:

Transmitter one-way frequency = 2294.994627 mc

Receiver best lock frequency = 2113.31224 mc or
22.013669 mc at DSIF VCO frequency

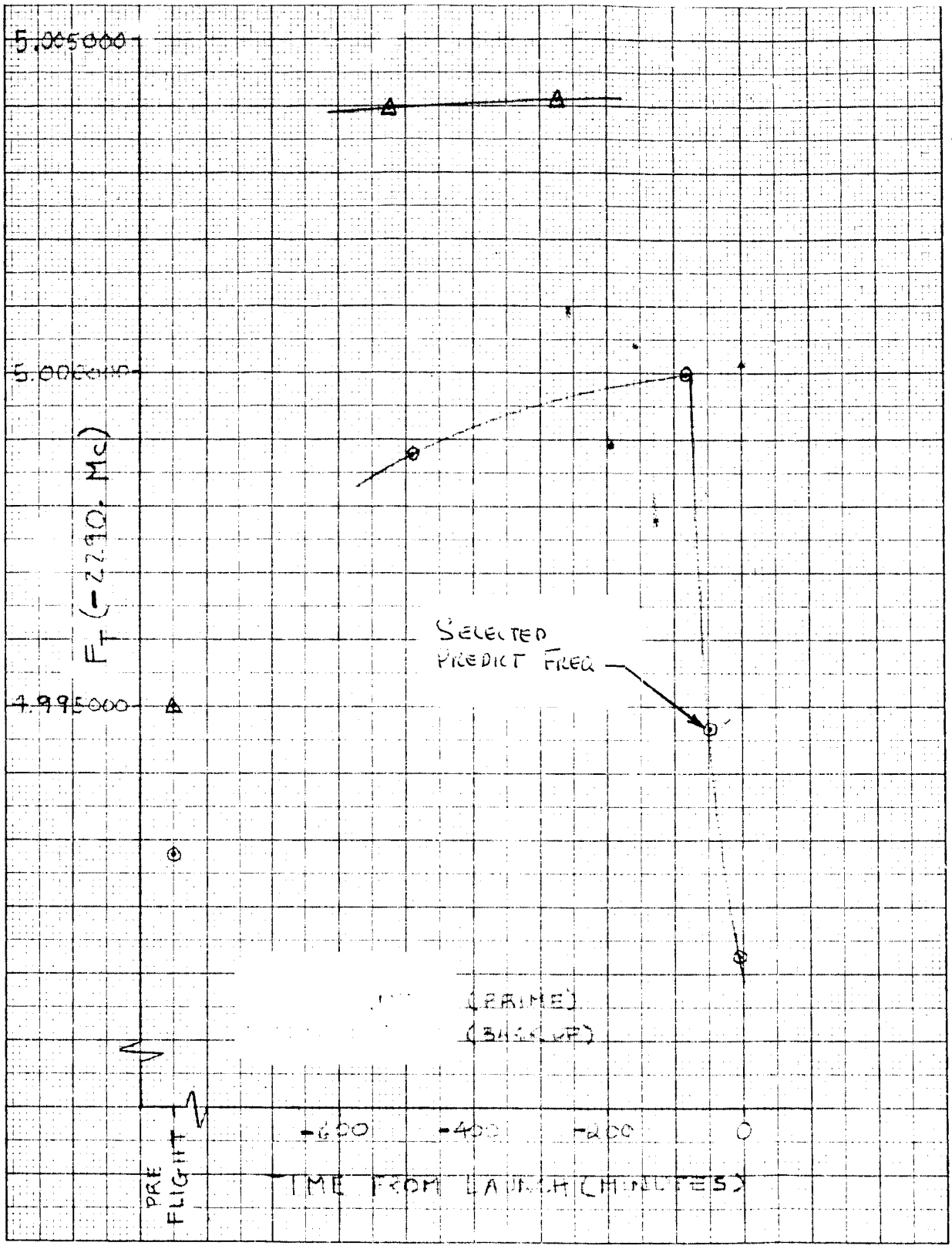


68189-220 (U)

a) Two-way

Ground VCO level

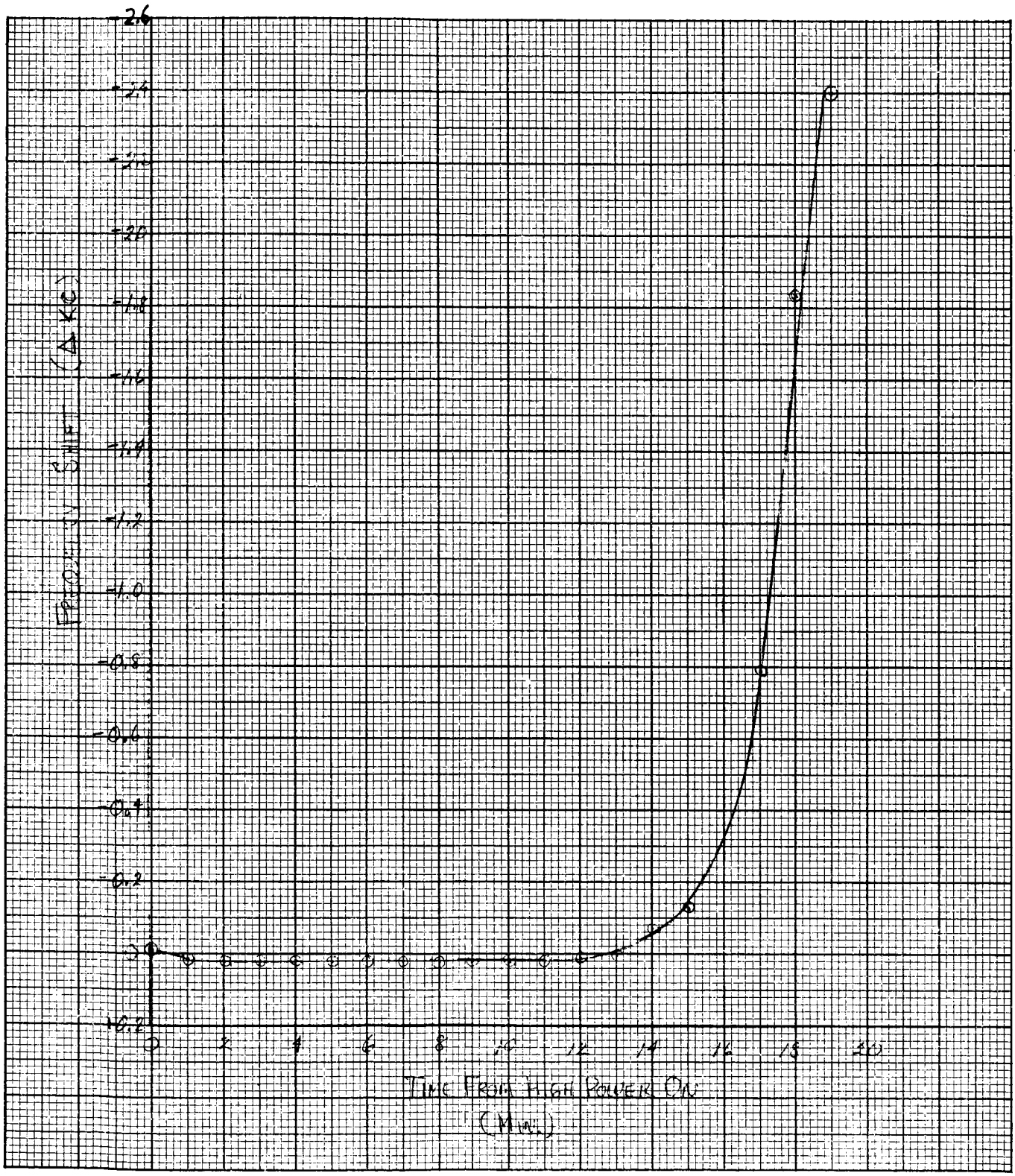
Figure 5. 4-3. Transmitter Frequency Versus Time From Launch



68189-221 (U)

b) One-way

Figure 5.4-3 (continued). Transmitter Frequency Versus Time From Launch



68189-222 (U)

Figure 5.4-4. NBVXO Frequency History After High Power Turn-On

The actual frequencies at initial acquisition, less doppler shift were as follows:

Transmitter one-way frequency = *

Receiver best lock frequency = *

In addition to the frequency data, the transmitter high power output was checked at ≃13:25 GMT or ≃1 hour and 15 minutes prior to launch. The output power was ≃40.4 dbm as determined from telemetry.

5.4.7.3 Spacecraft Initial Acquisition Phase Performance

Table 5.4-5 is a summary of the significant events during the spacecraft initial RF acquisition.

The signal levels at initial acquisition for both receivers are shown in Figure 5.4-5. Note the relatively slow increase in signal level at receiver B and the relatively fast increase in signal level at receiver A. The difference is due to the fact that receiver B was in the transponder mode and hence did not actually "lock" to the incoming signal until well after the receiver AGC had been peaked. Receiver A, however, was in the AFC mode and "captured" the signal almost as soon as it entered the bandpass.

The DSIF signal level at initial acquisition was ≃-120 dbm which was ≃25 db above carrier acquisition threshold. Upon going to the 85-foot antenna, the signal level increased to ≃-88 dbm. The omnidirectional B gain at the downlink frequency was between 0 and -2 db during this phase. Figure 5.4-6 is a curve representing the expected gain coverage for the downlink at initial acquisition. Based on this curve, somewhere between 50 and 70 percent of the gains available during this phase were below the actual gain achieved at acquisition.

The transmitter high power output during acquisition was ≃40.4 dbm. The transmitter low power output cannot be determined because DSIF AGC data at the time of high power turnoff is not available.

Low power output is not telemetered and is thus computed on the assumption that the change in received power at the DSIF at the time of high power off is identical to the difference between low and high power output. Since the high power output is telemetered, the low power output is simply given by the following:

$$P_{low} = P_{high} - P_{DSIF_H} + P_{DSIF_L} \text{ (dbm)}$$

*Data not provided by time of preparation of this report.

TABLE 5.4-5. ACQUISITION EVENTS

Event	Time, GMT	Comments
Transmitter B high power on	14:53:26	Spacecraft commanded to high power by the Centaur
DSIF acquires spacecraft in one-way mode	15:04:20	Acquisition ≃23 minutes and 20 seconds from launch and ≃11 seconds prior to predicted first visibility
DSIF switch from acquisition antenna (SAA) to 85-foot dish (SCM)	15:06:28	Signal level at ground receiver increased 32 db due to increased gain
DSIF transmitter turned on	15:06:50	
Phase lock receiver B	≃15:08:05	DSIF receiver dropped phase lock indicating phase lock on Receiver B
DSIF acquires spacecraft in two-way mode	15:08:17	DSIF reacquired downlink indicating a complete two-way acquisition in 27 minutes and 17 seconds from launch
DSIF confirms good two-way phase lock	15:08:41	
Transmitter B high power off	15:20:42	Spacecraft was in high power just 39 minutes 42 seconds for the complete acquisition phase. (A maximum time of 1 hour is allowed)

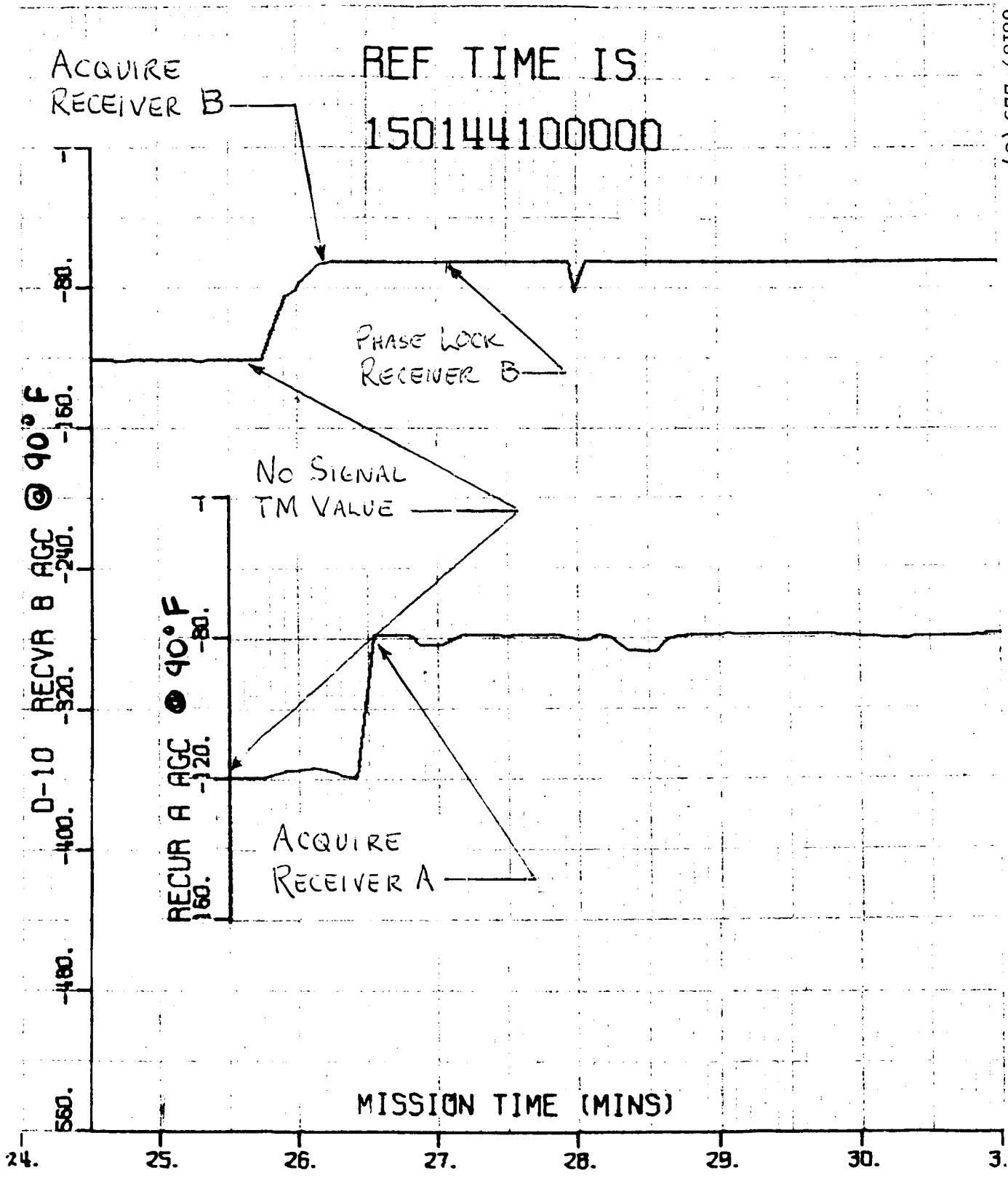
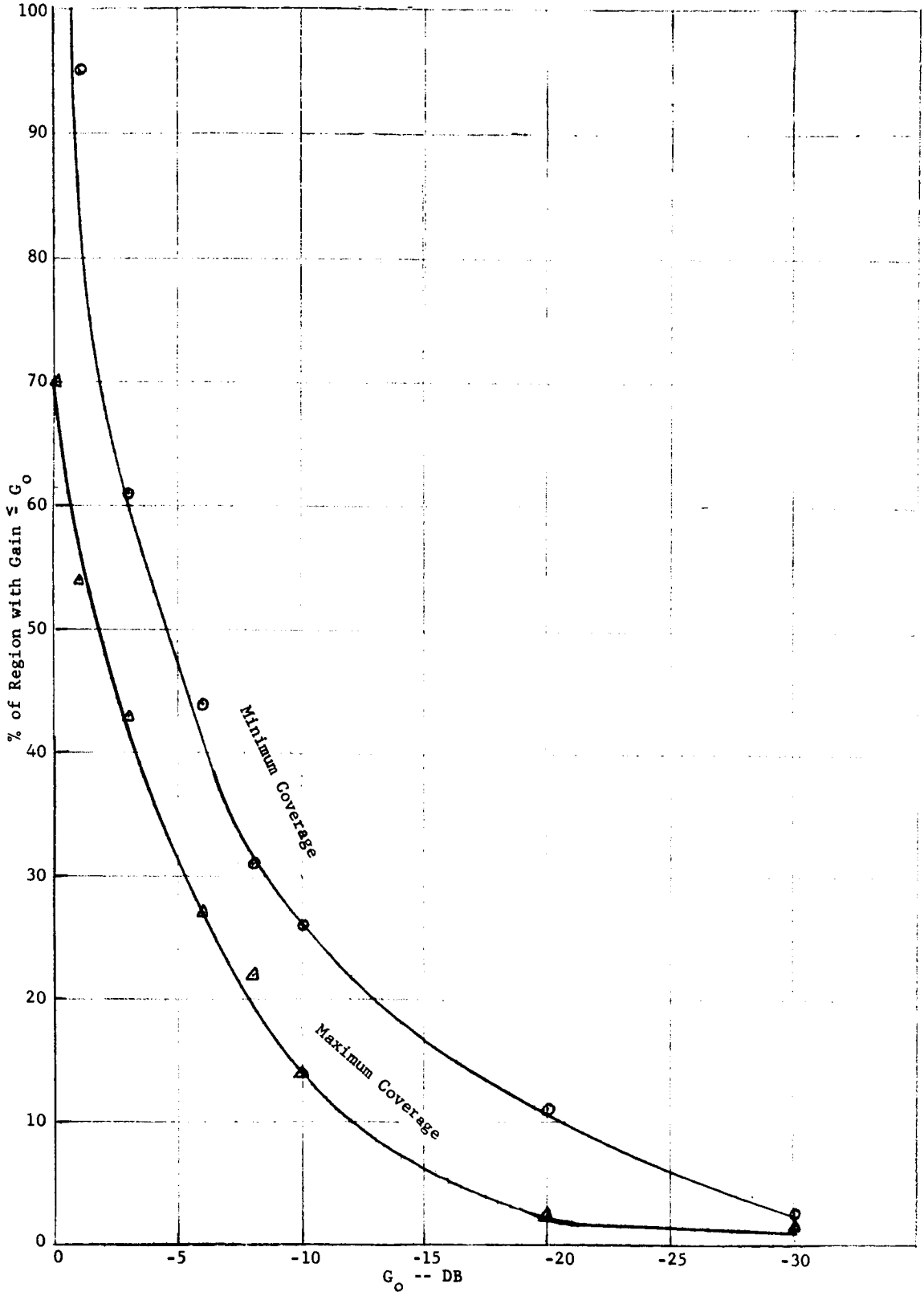


Figure 5.4-5. Signal Levels at Initial Acquisition



68189-224 (U)

Figure 5.4-6. Gain Coverage Curve for Omnidirectional Antenna B During Initial Acquisition

θ assumed to be between 146 and 45 degrees during acquisition period

where

P_{low} = transmitter low power output

P_{high} = telemetered transmitter high power output

P_{DSIF_H} = received signal level at high power

P_{DSIF_L} = received signal level at low power

5.4.7.4 Coast Phase Performance

The coast phases consist of three separate phases which are defined as follows:

1) Pre-Canopus acquisition phase – The period from initial spacecraft acquisition until Canopus acquisition during which time the spacecraft attitude is random in roll and the spacecraft -Z axis is pointed toward the sun.

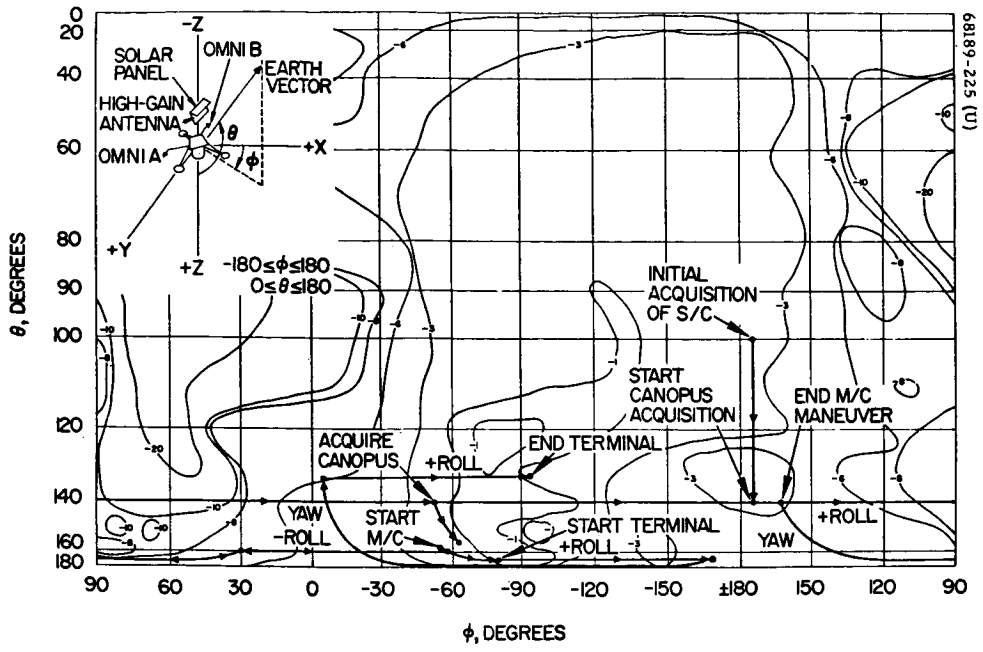
2) Premidcourse phase – The period from Canopus acquisition until the midcourse maneuvers.

3) Postmidcourse phase – The period from just after the midcourse maneuvers until the terminal maneuvers.

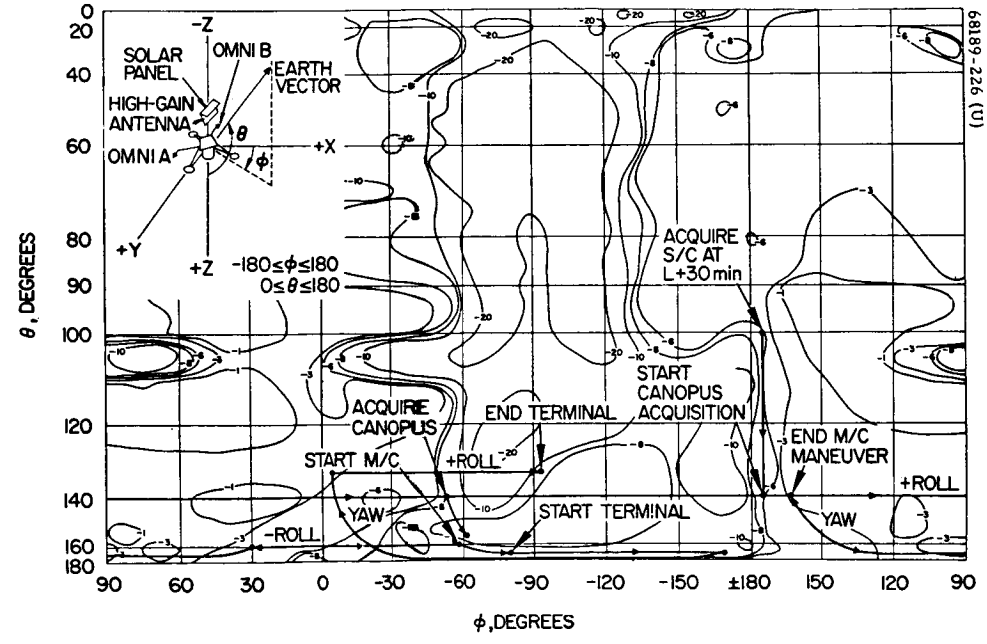
Figure 5.4-7 shows the path of the spacecraft-to-earth vector during the transit phase mapped on omnidirectional antenna B downlink, omnidirectional antenna A uplink, and omnidirectional antenna B uplink gain contour maps, respectively. The gain contour maps for each omnidirectional pattern show contours of equal gain and give a three-dimensional representation of the omnidirectional antenna pattern over the entire sphere. (Gain contours are analogous to elevation contours found on relief maps.) The gains can be related to the spacecraft geometry by the coordinate system shown in the upper corner of the figure. The earth vector path during the three coast phases can be identified on each figure by noting the various maneuver beginning and ending points.

Pre-Canopus Acquisition Phase

By knowing how far Canopus was from the point from which Canopus acquisition started, and also by noting that the roll gyro drift during transit drift tests was small, the path of the earth vector during the pre-Canopus acquisition phase was determined and is shown in these figures. Based on these figures, the omnidirectional antenna gains expected during this phase were as follows:

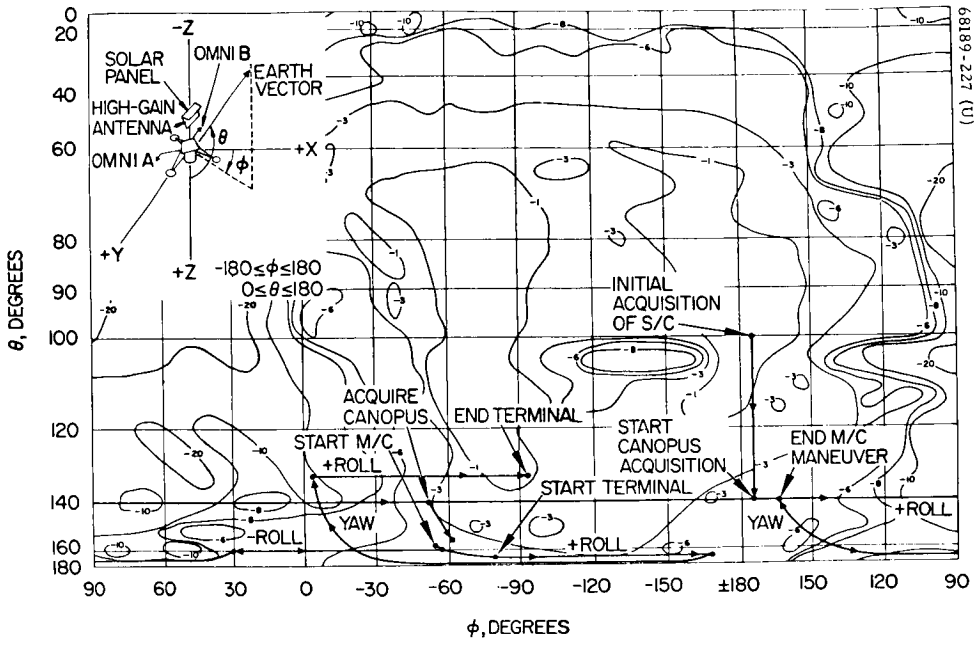


a) Antenna B Downlink



b) Antenna A Uplink

Figure 5. 4-7. Earth Vector Path Relative to Omnidirectional Antenna Gain Contours



c) Antenna B Uplink

Figure 5.4-7 (continued). Earth Vector Path Relative to Omnidirectional Antenna Gain Contours

$-2 < G < -3$ db for the downlink omnidirectional antenna B

$-1 < G < -3$ db for the uplink on omnidirectional antenna B

$-6 < G < -8$ db for the uplink on omnidirectional antenna A, if omnidirectional antenna A were extended

The omnidirectional antenna gains as determined from actual signal levels for each of the above cases were approximately as follows:

$-2 > G > -3$ db for the downlink (omnidirectional antenna B)

$0 > G > -3$ db for the uplink on omnidirectional antenna B

$-7 > G > -25$ db for the uplink on omnidirectional antenna A

With the exception of the omnidirectional antenna A uplink, very good agreement was noted between the expected and actual data. As discussed in detail in the anomaly section, the low gain experienced on the omnidirectional antenna A uplink is considered to be strong evidence that the omnidirectional antenna was stowed. It should be noted that if the omnidirectional antenna were stowed, the planar array would be interfering with the omnidirectional antenna during this phase since the omnidirectional antenna would be near the mast and behind the planar array. (Refer to the spacecraft picture and coordinate system shown in Figure 5.4-7.)

The actual downlink signal level throughout transit, as well as predicted signal levels, is shown in Figure 5.4-8, and the uplink signal levels, also with predicted levels, are shown in Figure 5.4-9. The pre-Canopus phase is represented in these figures as the period from 0 to approximately 4.5 hours. The deep null and somewhat erratic behavior on omnidirectional antenna A during this period is apparent in the receiver A AGC signal shown in Figure 5.4-9.

The transmitter low power output could not be determined for the start of this phase. However, upon going to high power for the Canopus acquisition phase, enough data was available to allow a low power output calculation. The low power output was thus determined to be $\simeq$20.4 dbm at the time of high power turnon.

Premidcourse Phase

Based on Figure 5.4-7, the expected omnidirectional antenna gains during this phase were as follows:

$-1 > G > -3$ db for the downlink (omnidirectional antenna B)

$-3 > G > -6$ db for the uplink on omnidirectional antenna B

$-6 > G > -10$ db for the uplink on omnidirectional antenna A

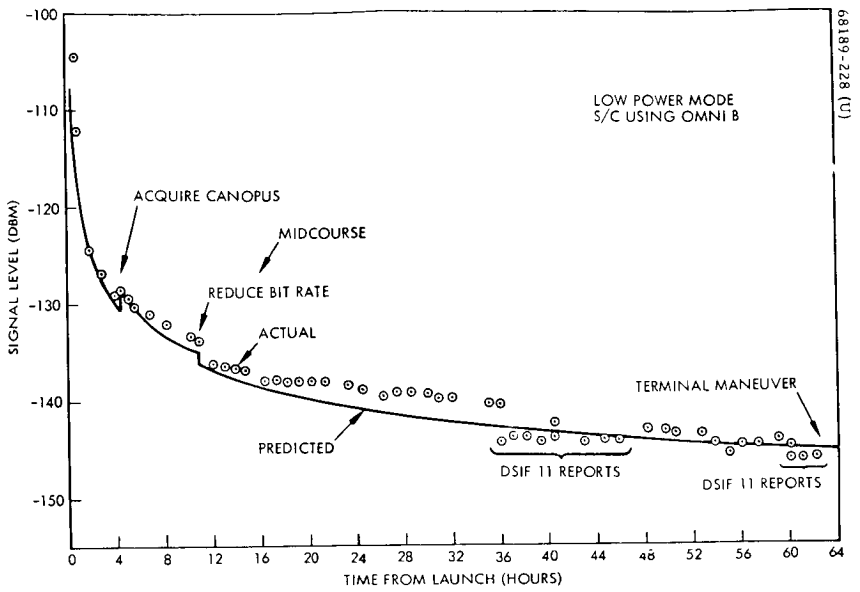


Figure 5. 4-8. DSIF Received Signal Levels

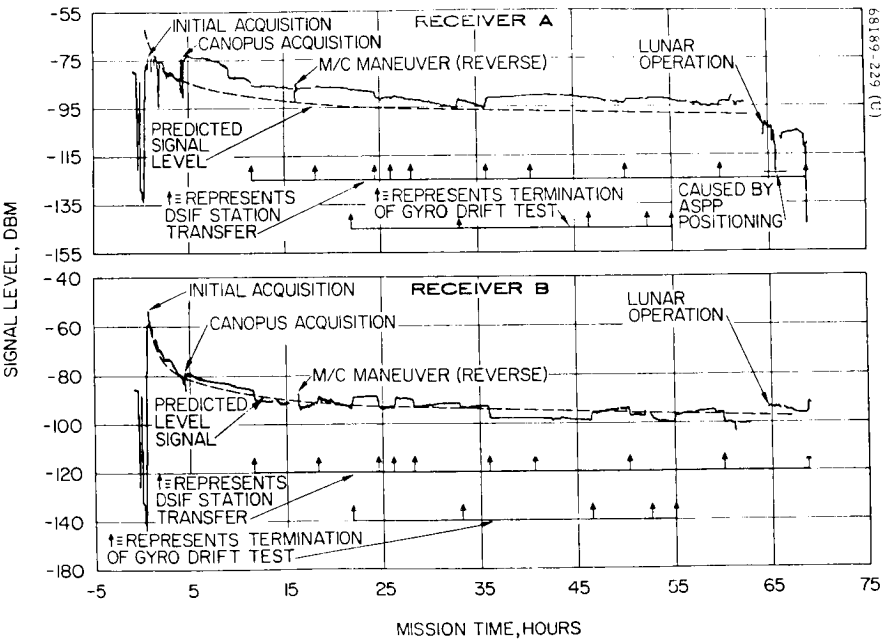


Figure 5. 4-9. Receiver A and B Automatic Gain Control Versus Time

The omnidirectional antenna gains as determined from measured signal levels were as follows:

$0 > G > -3$ db for the downlink (omnidirectional antenna B)

$0 > G > -6$ db for the uplink on omnidirectional antenna B

$6 > G > -2$ db for the uplink on omnidirectional antenna A

The actual signal levels are contained in Figures 5.4-8 and 5.4-9 with the phase being represented by the period from 4.5 hours to 16 hours.

Again, with the exception of omnidirectional antenna A, good agreement between predicted and measured data was observed. The exceptionally high gain noted on omnidirectional antenna A is somewhat consistant with the stowed omnidirectional antenna hypothesis since the earth vector during this phase moved across the head of the omnidirectional antenna with no apparent spacecraft structural obstructions. A positive gain of 6 db is not normally found on the primary omnidirectional antenna patterns but could be attributed to constructive interference resulting from radiated energy reflected from the solar panel or planar array. The sharp drop in signal level at 9.5 hours tends to support this theory. Also, the errors discussed earlier relative to absolute AGC level could contribute to an error in the estimated gain since the estimated gain is calculated from the following expression:

$$G_R = \frac{P_R}{P_T G_T \left(\frac{\lambda}{4\pi R}\right)^2 L}$$

where

G_R = received omnidirectional antenna gain (uplink gain)

P_R = received signal level (determined from spacecraft AGC)

P_T = DSIF nominal transmitter power

G_T = DSIF nominal antenna gain

λ = wavelength of uplink signal

R = slant range at time of computation

L = nominal spacecraft and DSIF losses

The step change in receiver input signal levels during this phase is attributed, as noted on Figure 5.4-9, to the station transfer from Johannesburg, South Africa (Station 51), to Goldstone, California. A pointing vector change of $\simeq$2 to 3 degrees occurs at station transfer.

The transmitter low power output at the beginning of this phase was ≃20.0 dbm, and just prior to going to high power at midcourse it was computed to be ≃20.5 dbm. The increase in output power was not unexpected since a dropoff in low power output after high power operation during star acquisition was predicted.

The telemetry bit rate was 1100 bits/sec at the beginning of this phase and was reduced to 550 bits/sec at ≃L + 11 hours. A bit rate reduction was requested at this time because Station 51 was having trouble with noise spikes on their maser. The computed SNR, based on reported signal levels, at the time of the change in bit rate was 14.0 ± 1 db.

Postmidcourse Phase

The earth vector during this phase moved only slightly relative to the spacecraft omnidirectional antenna patterns. Based on the previously discussed contour data, the expected omnidirectional antenna gains during this phase were as follows:

$-1 < G < -3$ db for the downlink (omnidirectional antenna B)

$-3 < G < -6$ db for the uplink on omnidirectional antenna B

$-8 < G < -10$ db for the uplink on omnidirectional antenna A

The omnidirectional antenna gains, as determined from received signal levels shown in Figures 5.4-8 and 5.4-9, were approximately:

$1 > G > -2$ db for the downlink (omnidirectional antenna B)

$-2 > G > -7$ db for the uplink on omnidirectional antenna B

$0 > G > -6$ db for the uplink on omnidirectional antenna A

As in the two previous coast phases, good agreement between predicted and observed data was noted for all but omnidirectional antenna A.

Step variations are noted throughout this final coast phase and are attributed either to station transfers or the termination of gyro drift tests which were being performed throughout the mission. In both cases, the variations are the result of pointing vector changes, relative to the omnidirectional antenna patterns, on the order of 1 to 3 degrees.

The downlink receiver signal level data also shows that Goldstone data (Station II) was consistently lower than the other stations during this phase. Calibration errors of 1 to 2 db are presently suspected as the cause of this discrepancy.

The transmitter low power output at the start of this phase was computed to be ≃19.6 dbm and was ≃19.7 dbm just prior to going to high power at the time of the terminal maneuver.

The telemetry bit rate during this entire phase was maintained at 550 bits/sec. The bit error rate during the later portion of this phase did go above the specified requirement of 3×10^{-3}, but this was done intentionally. A decision was made during the mission to stay at 550 bits/sec, even though the error rate was above the requirement based on the conclusion that a reduction in bit rate to 137.5 bits/sec would result in less "good data" per unit time than the 550 bits/sec data with errors.

Since this was the only time in the mission where the input SNR were close to threshold, this data is of considerable interest in evaluating telemetry threshold performance.

A study was thus made of various aspects of parity errors during this later portion of the mission (each 10-bit telemetry word has an associated parity bit set by the spacecraft to always have an odd number of "ones" in the entire 11-bit word). The time interval chosen for study was the last 5 hours before terminal descent high power on; here parity errors were more frequent than at any other time in the flight. While sampling techniques were used, rather than an exhaustive examination of the 10 million bits of data sent in this interval, it is felt that sufficient data was used to justify the conclusions reached in this discussion.

The first investigation made concerned the variation of the parity error rate with time. From this data the approximate bit error rate during this period was deduced. This was accomplished by counting the total number of parity errors in telemetry words in samples of at least 18,000 words taken at 1-hour intervals. The bit error rate is then assumed to be 1/11 of the parity error rate. While this method neglects double bit errors in the same word (since these are not directly detectable), the error introduced into the bit error rate is less than 8 percent since single bit errors should occur 12 times more often than double ones at the worst condition encountered. This data is shown in Figure 5.4-10.

An interesting point was discovered when computing this data. As noted on Figure 5.4-10, two points fell well above the otherwise smoothly increasing curve. This effect is assumed to be due to either poor recording or poor discrimination during playback for the magnetic tape containing data for this time.

As clearly demonstrated in Table 5.4-6, parity errors during the same intervals were 3.5 times higher on one tape as on the other "good" tape. This demonstrates the need to properly process the telemetry by assuring optimum discriminator and decommutator set up.

The telemetry input SNR at the subcarrier discriminator during the last 5 hours (corresponding to the bit error rate cure in Figure 5.4-10) was approximately 9.5 db at the beginning of the period and decreased to approximately 8.0 db at the end. The above SNRs are computed from the following expression:

$$SNR = \frac{MP_R}{K T_{eff} BW_{sc}}$$

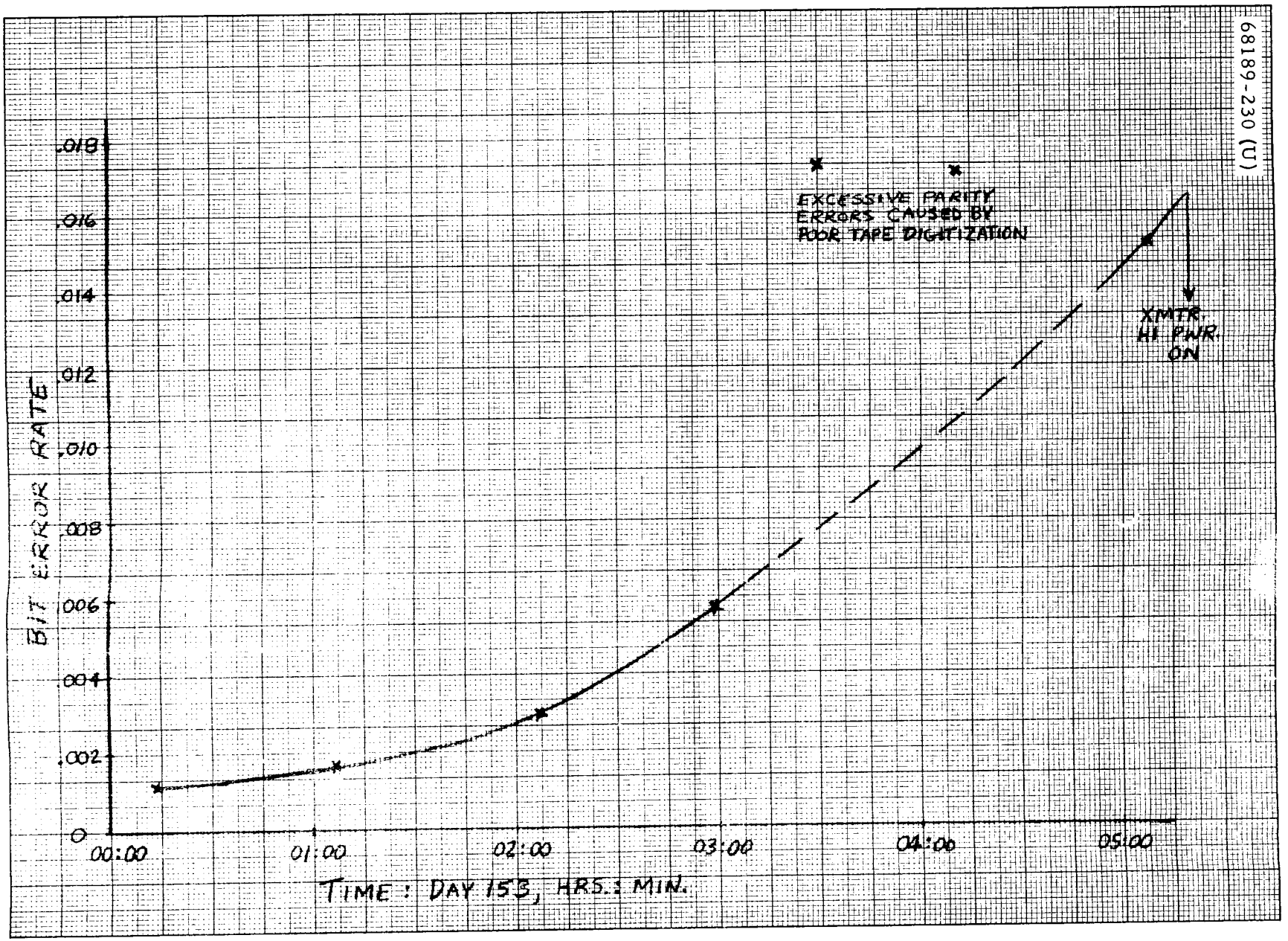


Figure 5.4-10. Bit Error Rate Versus Time

Coast mode data at 550 bits/sec preceding terminal descent

TABLE 5.4-6. COMPARISON OF PARITY ERROR RATE FOR "GOOD" AND "BAD" TAPES

"Good" Tape		"Bad" Tape	
Time	Number of Parity Errors in 3240 words	Time	Number of Parity Errors in 3240 words
02:54:39	180		
02:56:34	179	02:56:36	776
02:58:23	210		
03:00:14	209	03:01:12	777

where

M = Carrier to subcarrier modulation loss adjustment constant based on $\beta = 1.115$ (3.9 kc SCO)

P_R = Received carrier power reported by the DSIF

K = Boltzmann's constant

T_{eff} = DISF system temperature reported by the DSIF (T_{eff} reported as 45° K)

BW_{sc} = Nominal 3.9 kc SCO discriminator noise bandwidth (BW_{sc} = 664 cps)

The SNR computed from the above equation is estimated to be accurate to ±1.0 db. The above data agrees fairly closely with preflight test data taken during CDC tests. Also, it can be deduced from this data that the present requirement of maintaining a bit error rate (BER) less the 3×10^{-3} at input SNRS ≥ 11 db was met quite easily during this mission. The signal to noise ratio (SNR) at the time when the BER was 3×10^{-3} is estimated to be ≃9.0 ± 1.0 db.

In addition to BER-SNR relationships, a second check was made to see if parity errors were distributed evenly over the entire telemetry frame of 120 words (see Figure 5.4-11). There was no detectable pattern to the variations, and a frequency histogram of the good tape sample showed relatively normal distribution. The only point of note is that the maximum of both curves occurs at word 115, corresponding to FC-14, star intensity. There is no known reason why maximum bad parity should occur here; when the error rate is lower, this effect does not occur.

Finally, a check was made for the bit position of errors within a word. This requires a certain amount of interpretation, since a "true" value of each word must be known in order to decide which bit has changed if that

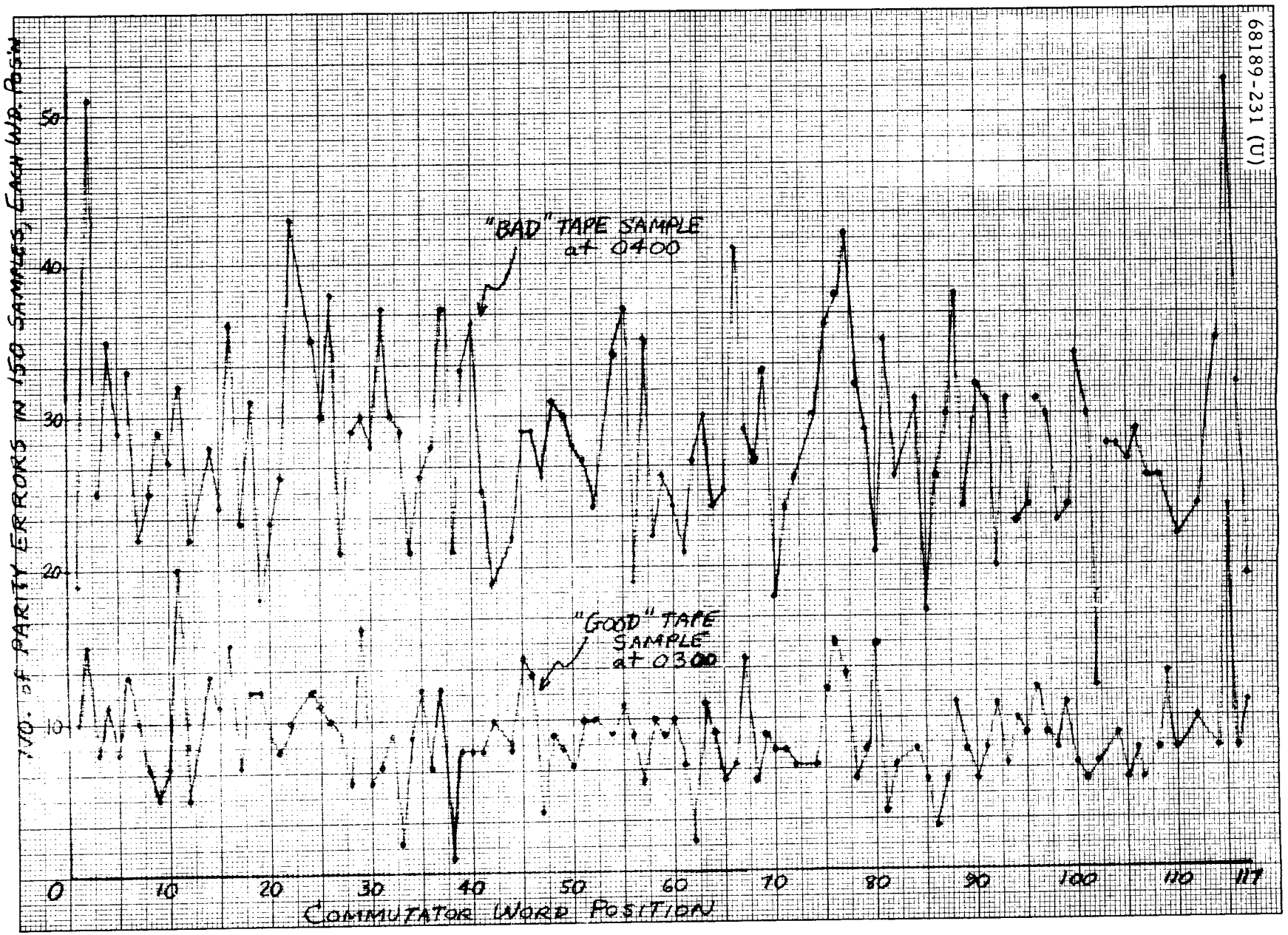


Figure 5.4-11. Number of Parity Errors Versus Commutator Word Position
Day 153; mode 5 at 550 bits/sec

word shows bad parity. Fortunately, there are 58 temperature signals in mode C that have extremely stable values, and thus Table 5.4-7 was prepared. A zero change in value for a bad parity word implies that the parity bit itself must have been changed. Table 5.4-8 summarizes the data and shows essentially a constant distribution of errors, both positive (0 bit changed to 1) and negative (1 changed to 0) over all bit positions of the word.

The conclusion drawn from the above is that the spacecraft's signal processing did not contribute to the telemetry bit error rate. All effects seen can be explained as being due to random errors resulting from noise, or else are introduced by subsequent ground processing of the data.

5.4.7.5 Maneuver Phases Performance

The following maneuvers were executed during the mission:

1) Canopus acquisition maneuver – The spacecraft was rolled to acquire Canopus.

2) Midcourse maneuver – The spacecraft was maneuvered such that the vernier engines could be turned on and the trajectory adjusted slightly.

3) Terminal maneuver – The spacecraft +Z axis was aligned with the spacecraft velocity vector and rolled to optimize omnidirectional antenna B gain for the retro firing to touchdown phase.

Canopus Acquisition

The Canopus acquisition phase was initiated earlier than normally planned in hopes of gathering enough data to confirm whether or not omnidirectional antenna A had deployed. The acquisition was initiated at 18:53:39, 4 hours and 12 minutes from launch instead of the nominal time of 6 hours and 9 minutes from launch.

The premaneuver analysis indicated that during the maneuver the omnidirectional B antenna gain for the downlink would not go below -15.0 db, and that the uplink gain would not go below -15 db for antenna A or antenna B. Based on the above gain information and an additional gain measurement uncertainty of ±5 db, the downlink telemetry margin was calculated to be ≃7.0 db for high power operation, and the uplink command margin was 17 db for both receivers. As a result of this analysis, it was recommended that the acquisition be accomplished using omnidirectional antenna B for transmitting at high power, and that the spacecraft could remain in the transponder mode.

Receiver signal levels for the downlink (DSIF) and both receivers during the roll maneuver are shown in Figure 5.4-12 through 5.4-14. Also shown on the figure is antenna data. The equivalent omnidirectional antenna gain is computed and antenna data plotted in an attempt to show actual performance relative to predicted performance. The bounds of five sets of antenna pattern data

TABLE 5.4-7. CHANGE OF BCD MAGNITUDE IN BAD PARITY WORDS

Bad Parity, Command Word Number	BCD Value	Assumed "True" Value	Difference	Bad Parity, Command Word Number	BCD Value	Assumed "True" Value	Difference
2	507	507	0	8	532	562	-30(-32)
13	16	0	16	17	69	68	1
15	0	0	0	19	426	295	131(128)
17	100	68	32	22	525	541	-16
27	521	525	-4	26	367	495	-128
40	621	620	1	43	1	0	1
49	6	7	-1	47	84	115	-31(-32)
53	0	0	0	57	772	768	4
56	784	528	256	69	683	748	-65(-64)
62	66	578	-512	83	300	296	4
64	364	380	-16	88	377	505	-128
68	690	674	16	89	530	786	-256
73	256	0	256	91	368	496	-128
77	230	484	-254(-256)	94	528	529	-1
82	515	531	-16	102	74	586	-512
83	40	296	-256	103	8	0	8
90	415	413	2	106	481	483	-2
96	680	552	128	111	329	331	-2
113	481	449	32	115	1019	1023	-4
115	1019	1023	4	1	590	526	64
116	358	486	-128	3	516	524	-8
1	519	526	-7(-8)	8	818	562	256
20	96	608	-512	11	15	528	-513(-512)
23	993	992	1	16	333	335	-2
24	495	510	-15(-16)	17	67	68	-1
43	2	0	2	18	430	494	-64
48	550	566	-16	26	367	495	-128
53	4	0	4	46	545	609	-64
78	583	591	-8	62	834	578	256
79	741	742	-1	83	424	296	128
105	87	600	-513(-512)	94	537	529	8
				95	105	105	0
				104	568	570	-2
				109	606	544	62(64)
				110	545	673	-128
				111	363	331	32
				113	449	449	0
				116	230	486	-256
				117	12	4	8

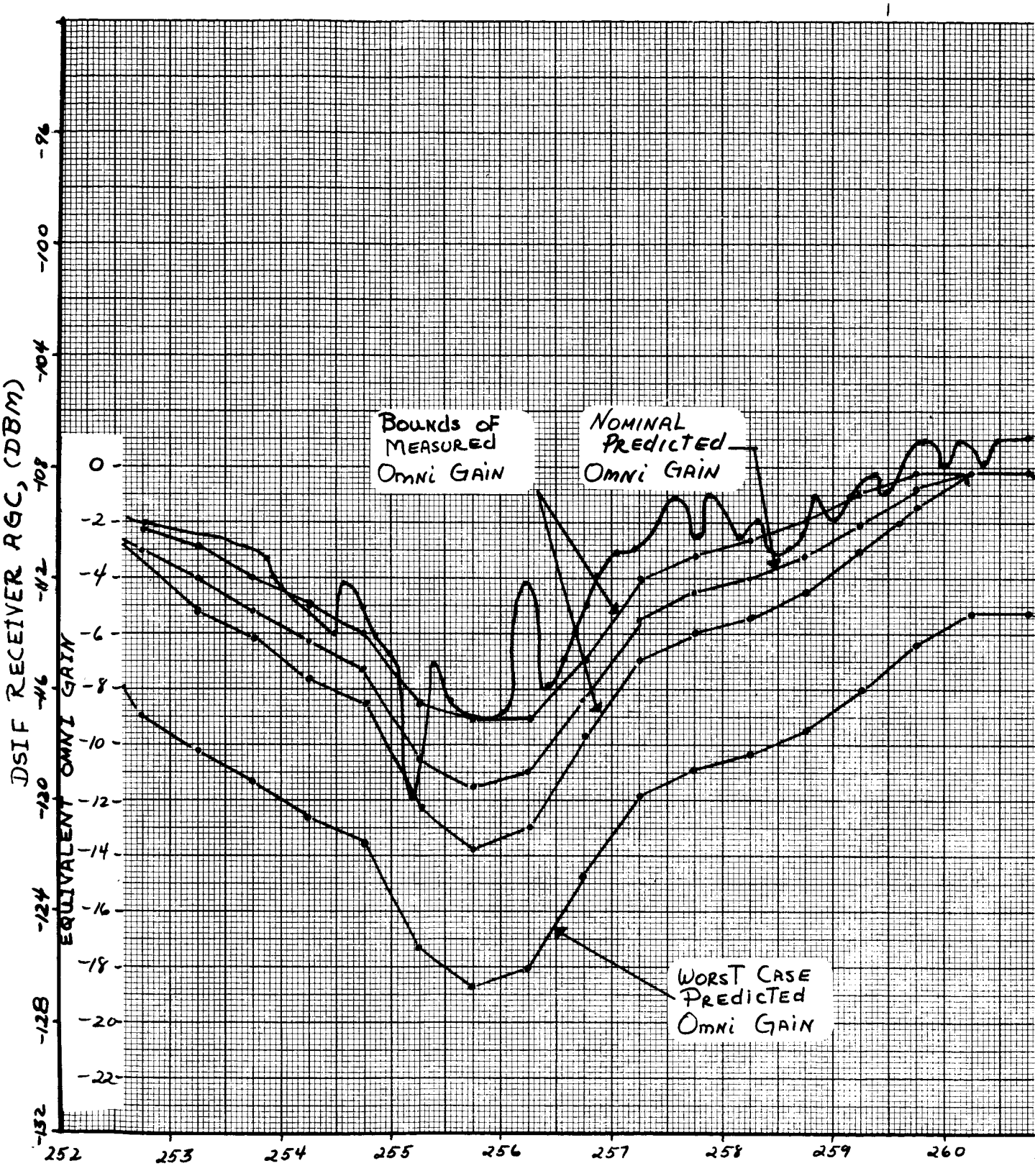
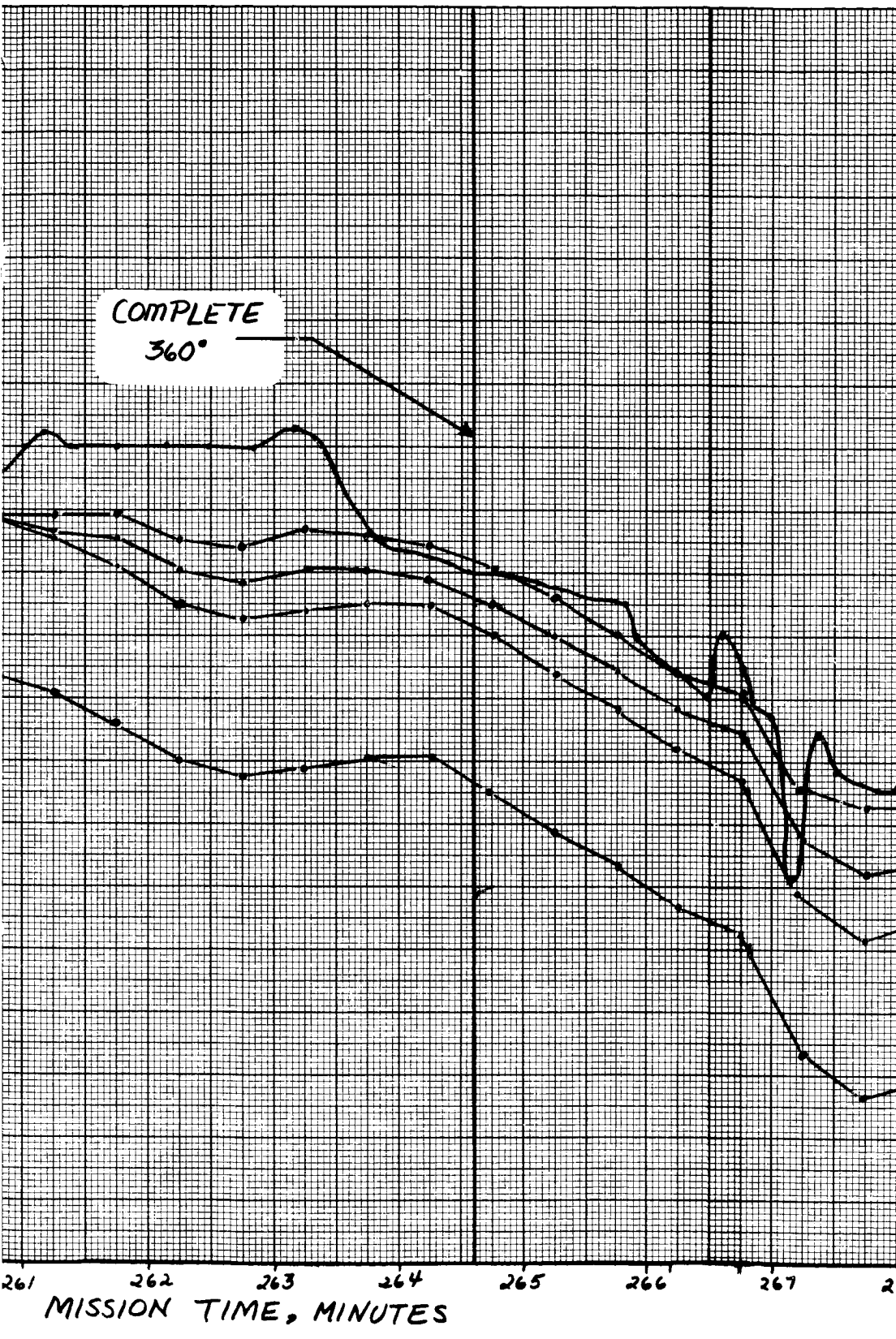


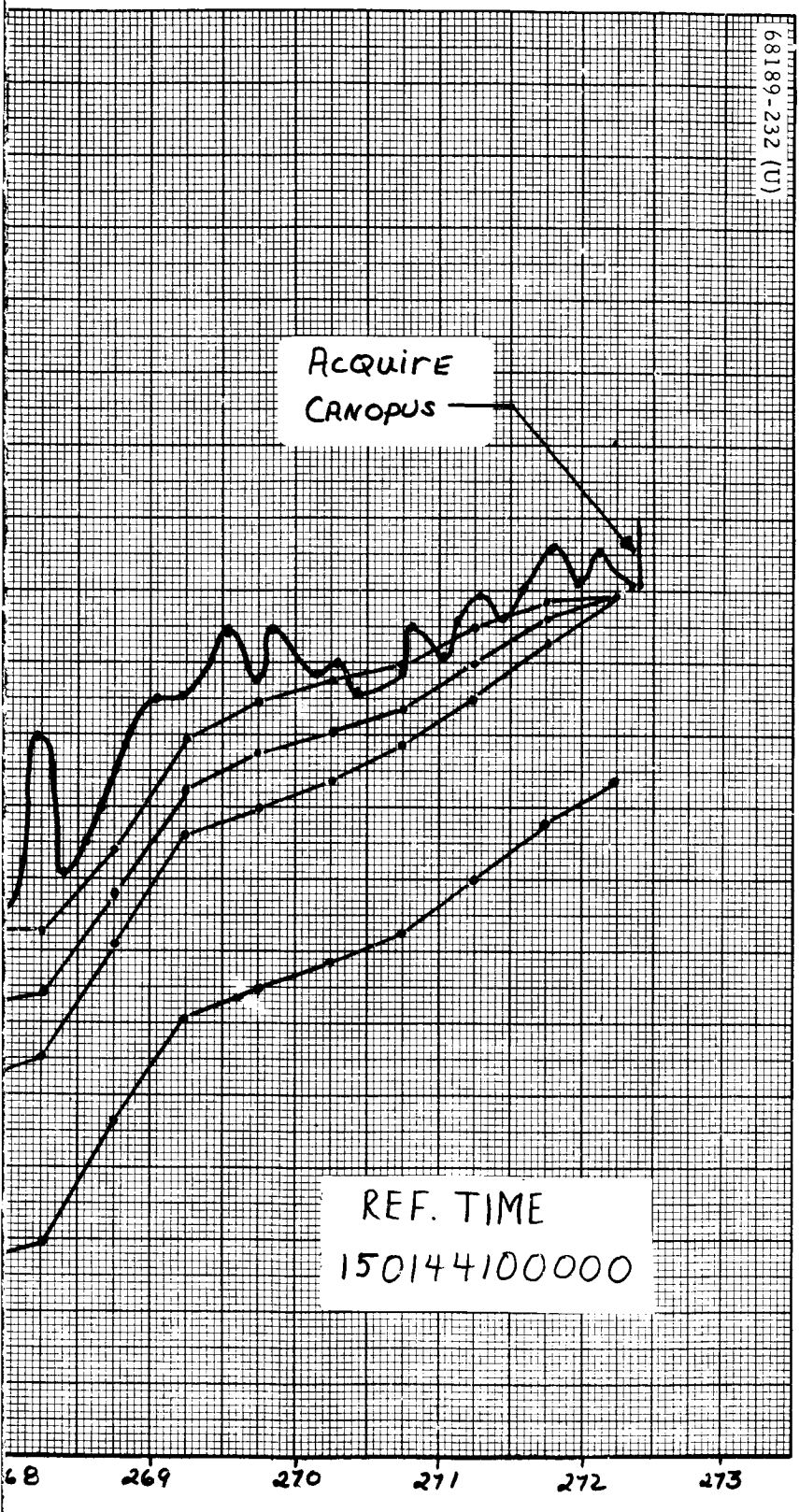
Figure 5.4-12. DSIF Receiver Automatic Gain Control During Canopus Acquisition

FOLDOUT FRAME



FOLDOUT FRAME

5-4-41-2



FOLDOUT FRAME

5.4-42

TABLE 5.4-8. PARITY ERRORS VERSUS BIT POSITION IN A WORD

Bit Position	1	2	4	8	16	32	64	128	256	512	Par.	Total
Number of positive errors	4	2	4	3	2	3	2	3	4	0	5	32
Number of negative errors	4	4	2	3	5	2	3	6	4	5	—	38
Total	8	6	6	6	7	5	5	9	8	5	5	70

and predicted nominal and worst-case gains are shown on each figure. The nominal gain is defined as the average of the bounded data, and the worst case is defined as being 5 db below the lower bound of the measured data. (The worst-case gain was used during all maneuver evaluations.)

As can be observed, fair correlation between measured and predicted levels was found for both the up- and downlink on omnidirectional antenna B. In both cases, the actual levels were slightly above the predicted data during most of the maneuver. In no case did the levels go below the worst-case predicted levels.

As discussed in detail in the anomaly portion of this report, omnidirectional antenna A data did not correlate with predictions based on extended omnidirectional antenna patterns. Figure 5.4-15 shows the same receiver AGC data compared with a single antenna pattern for a stowed omnidirectional antenna. This data is better correlated in the area of the observed deep antenna nulls, thus leading to the conclusion that omnidirectional antenna A was stowed during this maneuver.

The spacecraft transmitted power during this maneuver is shown in Figure 5.4-16. High power was actually turned on 5 minutes prior to the time where the data begins. The telemetry was not available until mode 5 was selected, resulting in no data at initial turnon. The plot shows output power in watts at the power monitor. This telemetry is converted to output power at the transmitter in dbm by the following equation:

$$P_{xmtr}(\text{dbm}) = 10 \log (P_{tm} \times 10^3) + L$$

where

P_{xmtr} = transmitter power (dbm)

P_{tm} = telemetered power output (watts)

L = loss from transmitter to power monitor $\simeq$ 1.8 db (value determined from pre-STV 6 hardline calibration data)

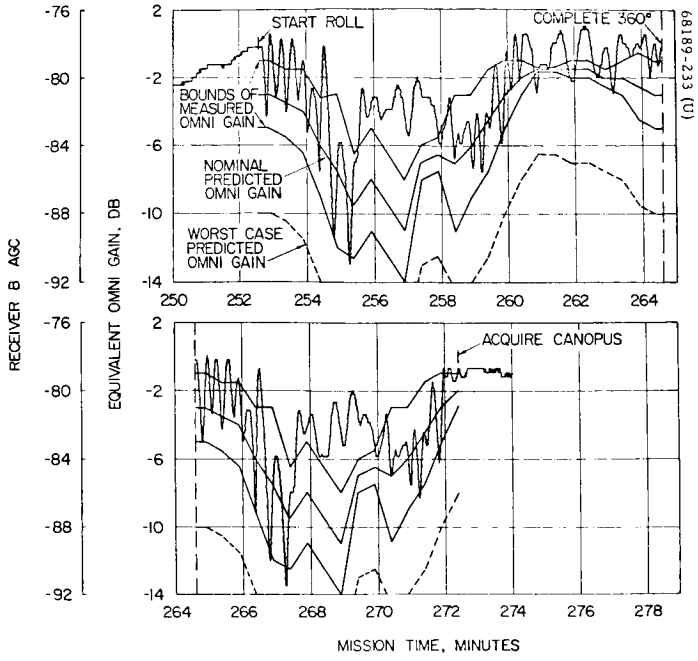


Figure 5.4-13. Receiver B Automatic Gain Control During Canopus Acquisition

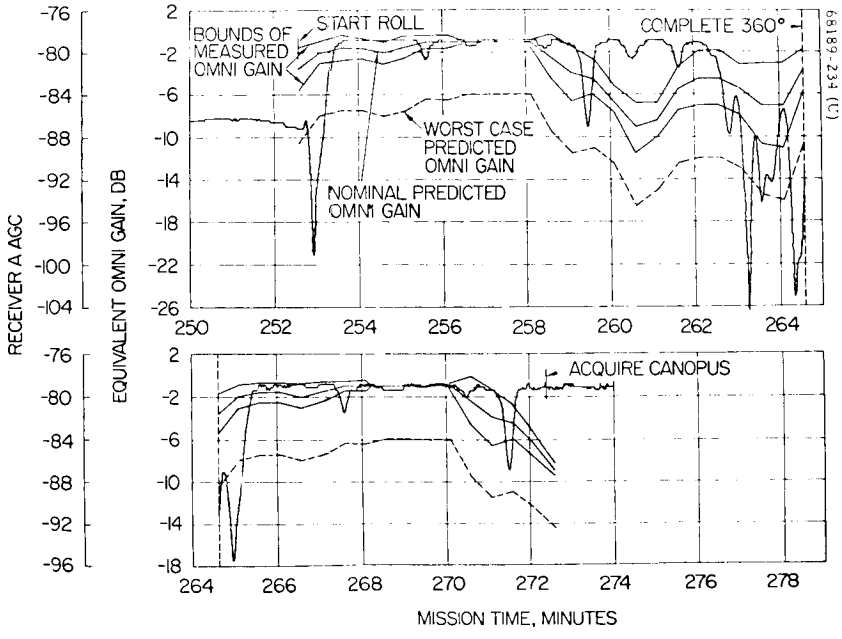


Figure 5.4-14. Receiver A Automatic Gain Control During Canopus Acquisition

Extended omnidirectional antenna data

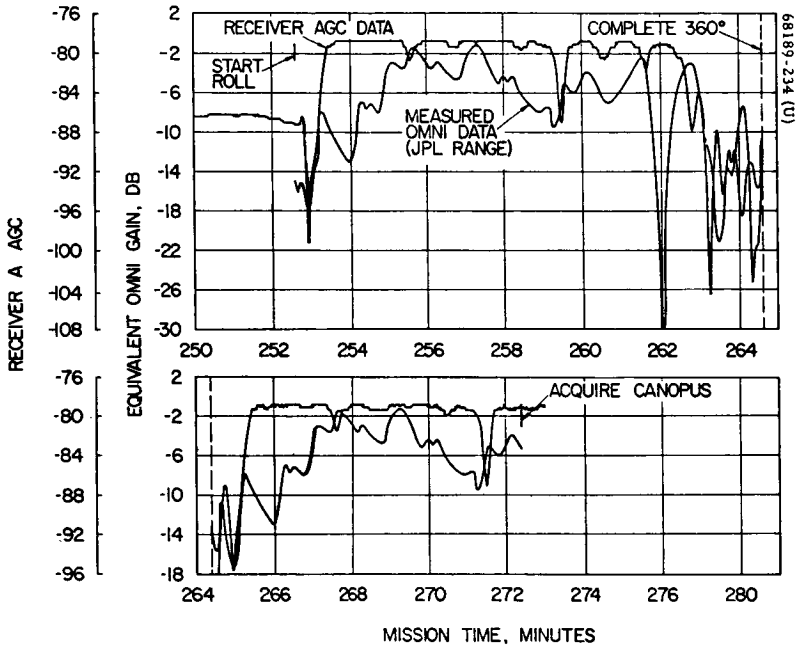
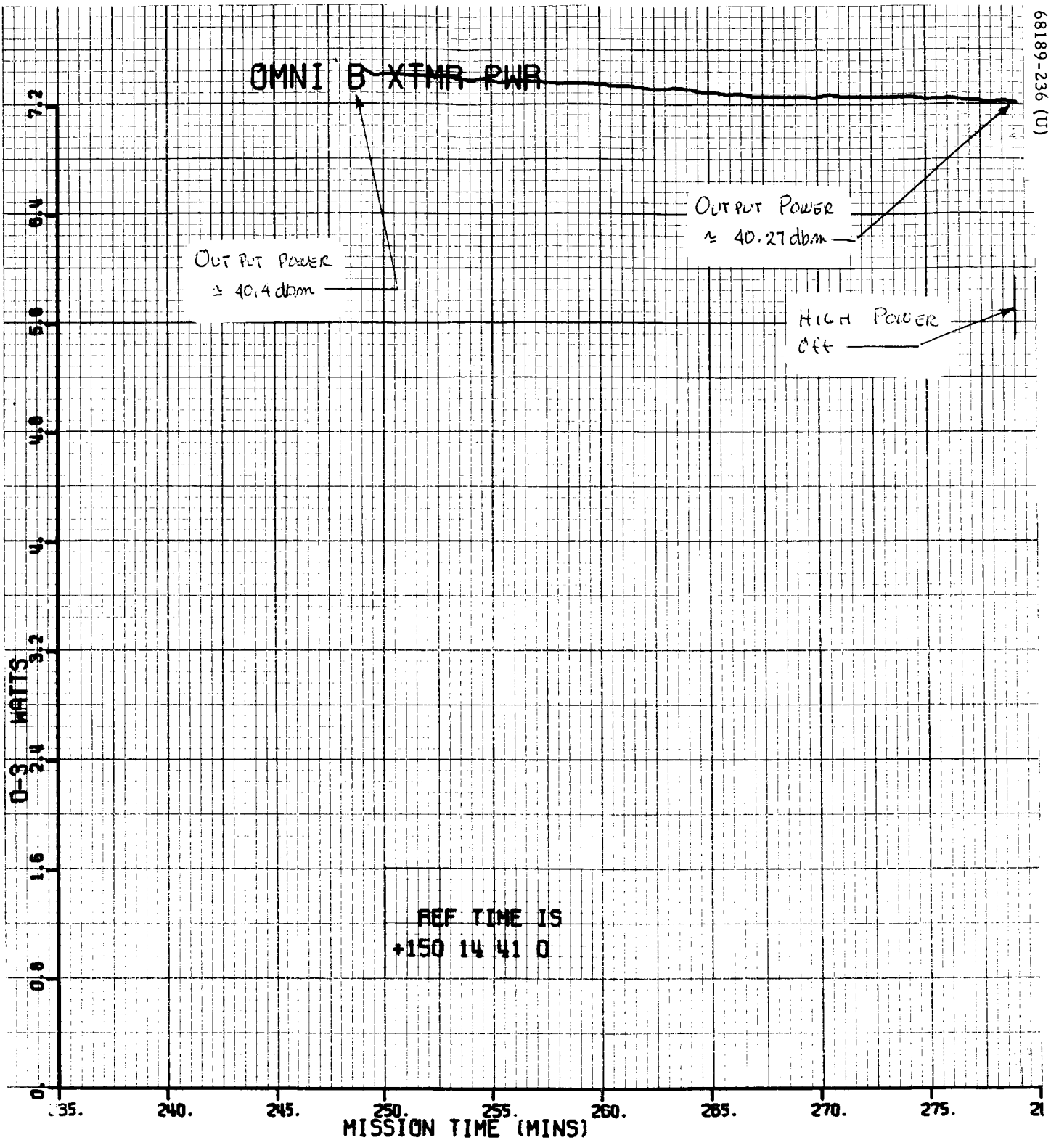


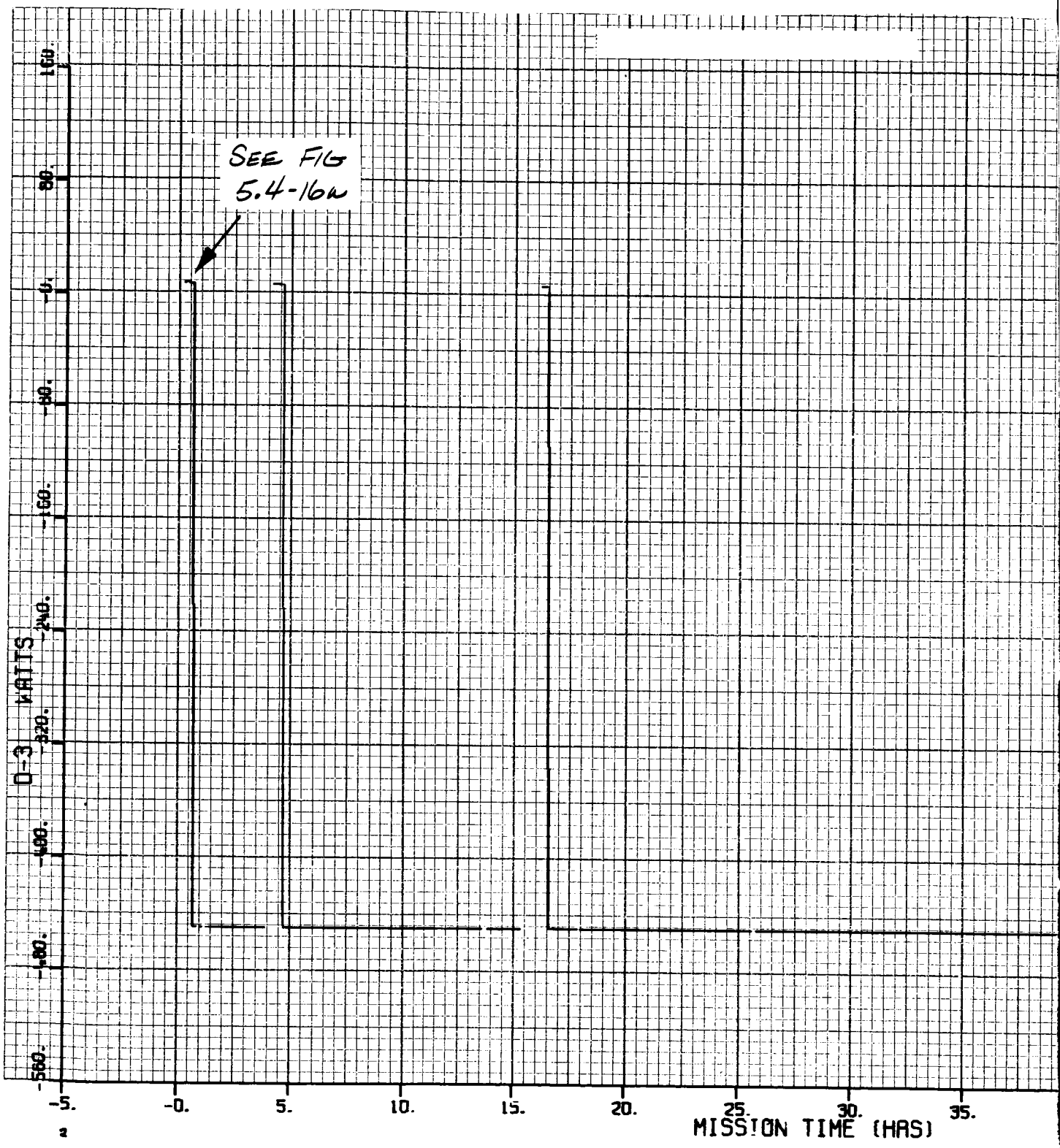
Figure 5.4-15. Receiver A Automatic Gain Control During Canopus Acquisition

Folded omnidirectional antenna data



a) Postlaunch High Power Interval

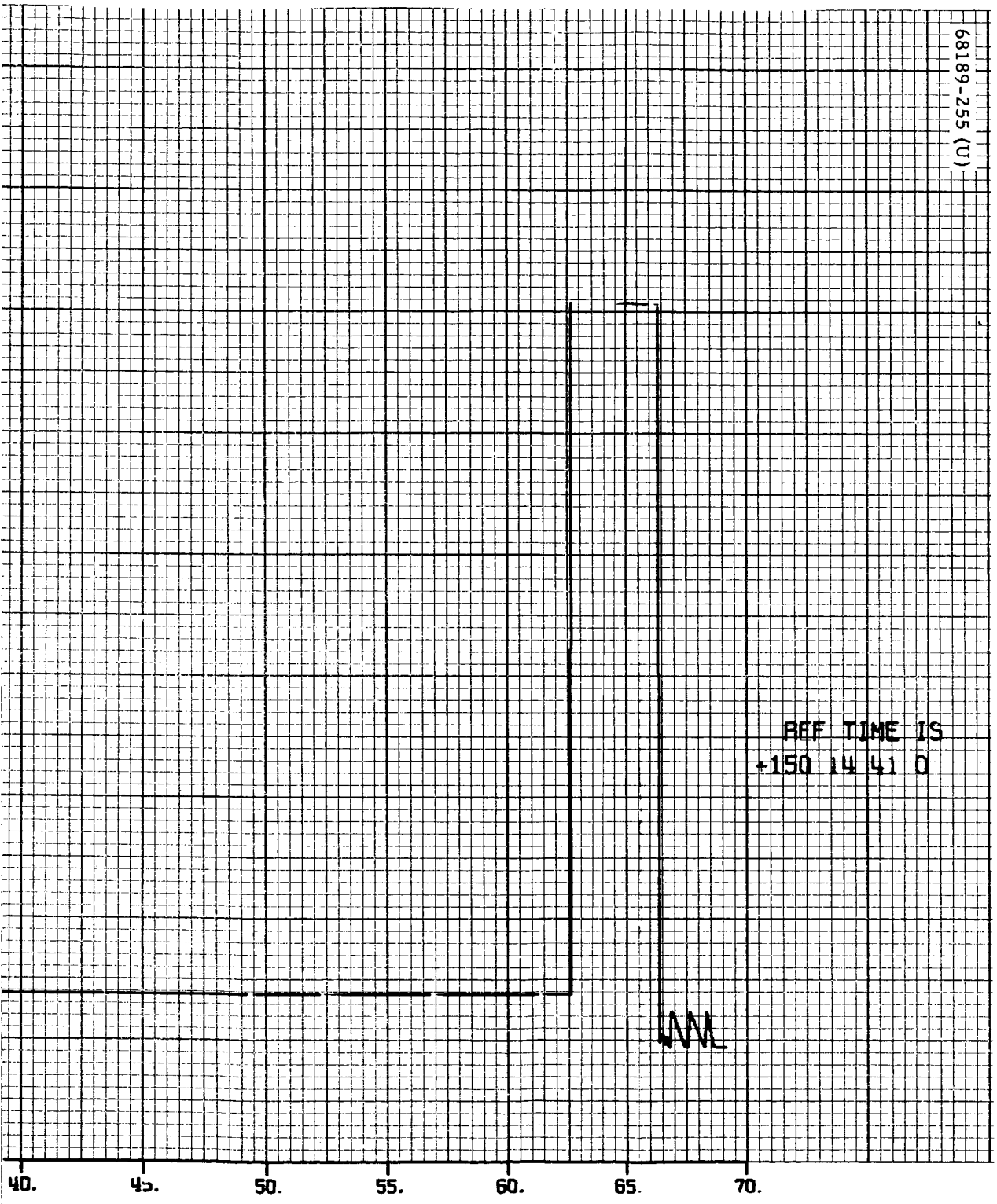
Figure 5.4-16. Omnidirectional Antenna B Transmitter Power



b) Complete Mission

Figure 5.4-16 (continued). Omnidirectional Antenna B Transmitter Power

FOLDOUT FRAME



FOLDOUT FRAME

As noted, the transmitter output power was between 40.4 and 40.27 dbm during the period of high power operation.

The star acquisition phase was completed at 19:13:20, taking 20 minutes. The spacecraft high power transmitter was on from 18:44:24 to 19:21:04, resulting in a total time in high power of ≃37 minutes.

Midcourse Maneuver

The midcourse maneuver was initiated at 151:06:20:20, ≃15 hours and 40 minutes from launch. The maneuver executed was a roll yaw maneuver with a 20 m/sec correction.

Eight possible maneuvers were analyzed from a telecommunications view point with the roll yaw for a 20 m/sec correction being recommended. Four maneuvers for a 1.0 m/sec correction, and four maneuvers for the 20.0 m/sec correction were analyzed. A summary of the analysis presented during the maneuver conferences is contained in Table 5.4-9. Because there were strong indications that omnidirectional antenna A had not deployed at this time, a maneuver on omnidirectional antenna B was highly desirable. As can be observed, the 1.0 m/sec correction maneuvers all indicated good margins on omnidirectional antenna B. However, terminal burnout velocity considerations favored the 20.0 m/sec correction maneuvers. Of the 20.0 m/sec maneuvers, only the roll yaw was acceptable on omnidirectional antenna B. This particular maneuver required that the spacecraft earth vector go through an area close to the deep null found at the back of the omnidirectional antennas. Evaluation of the margins indicated that the maneuver was feasible utilizing omnidirectional antenna B and was thus recommended. Based on up-link margins, it was also recommended that the maneuver be made in the transponder mode.

The earth vector path relative to the omnidirectional antenna patterns during the selected maneuver is shown in Figure 5.4-7. Signal levels at the DSIF station and at both receivers during the reverse maneuvers are shown in Figure 5.4-17 and 5.4-18. Data is not available during the forward maneuvers because the telemetry mode selected during the maneuvers did not contain AGC data.

As can be observed in Figures 5.4-17 and 5.4-18, omnidirectional antenna B data correlated relatively well with predicted data. During the yaw maneuver, received levels were below the worst-case measured gain at times, but were never below the worst-case predicted performance upon which the margins were computed. This is not surprising since this maneuver skirted the natural omnidirectional antenna null and some additional gain uncertainty was expected in this region.

Omnidirectional antenna A data again failed to correlate with extended omnidirectional antenna predictions and exceeded the worst case prediction during both the roll and yaw maneuvers. This again is considered to be further evidence that omnidirectional antenna A was stowed.

TABLE 5.4-9. MIDCOURSE MANEUVER SUMMARY TABLE

1 m/sec Correction Maneuvers						
Maneuvers Considered	Maneuver Duration		Spacecraft to Earth		Earth to Spacecraft	
	Angle, degrees	Time, seconds	Antenna B Gain,* db	Margin B, db	Antenna B Gain,* db	Margin B, db
1 Roll	-89.4	179	-7	2	-8	14
Pitch	35.6	71	-7	2	-8	14
2 Roll	0.6	0	-2	7	-4	18
Yaw	-35.6	71	-5	4	-4	18
3 Pitch	0.4	0	-2	7	-4	18
Yaw	-35.6	71	-5	4	-4	18
4 Yaw	-35.6	71	-5	4	-4	18
Pitch	-3.0	0	-5	4	-3	19

20 m/sec Correction Maneuvers										
Maneuvers Considered	Maneuver Duration		Spacecraft to Earth				Earth to Spacecraft			
	Angle, degrees	Time, seconds	Antenna A Gain,* db	Antenna B Gain,* db	Margin A	Margin B	Antenna A Gain,* db	Antenna B Gain,* db	Margin A	Margin B
1 Roll	2.4		-7	-2	2	7	-8	-4	14	18
Pitch	-58.5		-7	-15	2	-6	-15	-15	7	7
2 Roll**	-87.6		-7	-7	2	2	-15	-7	7	15
Yaw	-58.5		-1	-7	8	2	-5	-10	17	12
3 Pitch	-58.5		-7	-15	2	-6	-15	-15	7	7
Yaw	-5.1		-1	-15	8	-6	-2	-15	20	7
4 Yaw	-3.9		-7	-2	2	7	-8	-4	14	18
Pitch	-58.5		-7	-15	2	-6	-15	-15	7	7

*Antenna gains shown represent minimum measured gain, not worst-case expected gain.

**Selected maneuver.

The transmitter high power output telemetry during this phase was not available until ≃54 minutes after high power turnon due to the commutator mode selected. When the data was available, the output power was computed to be ≃40.3 dbm. The transmitter was in high power for ≃62 minutes during this mission phase.

Terminal Maneuver

Four terminal maneuvers were considered and analyzed during the mission. As in the case of the midcourse maneuver, a maneuver on omnidirectional antenna B was highly desirable. Three maneuvers using omnidirectional antenna B and one using omnidirectional antenna A were thus analyzed. The analysis summary of the maneuvers is continued in Table 5.4-10.

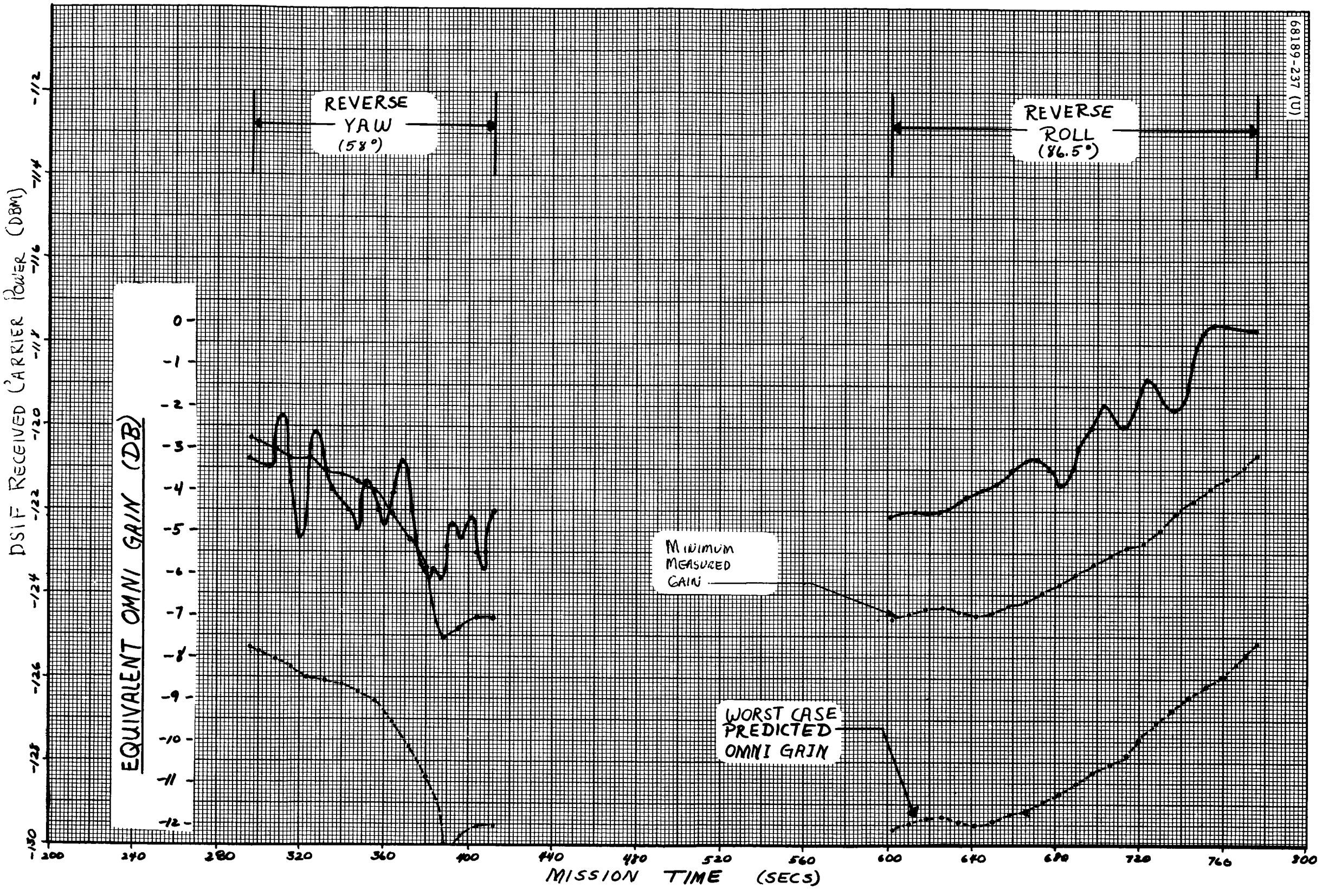
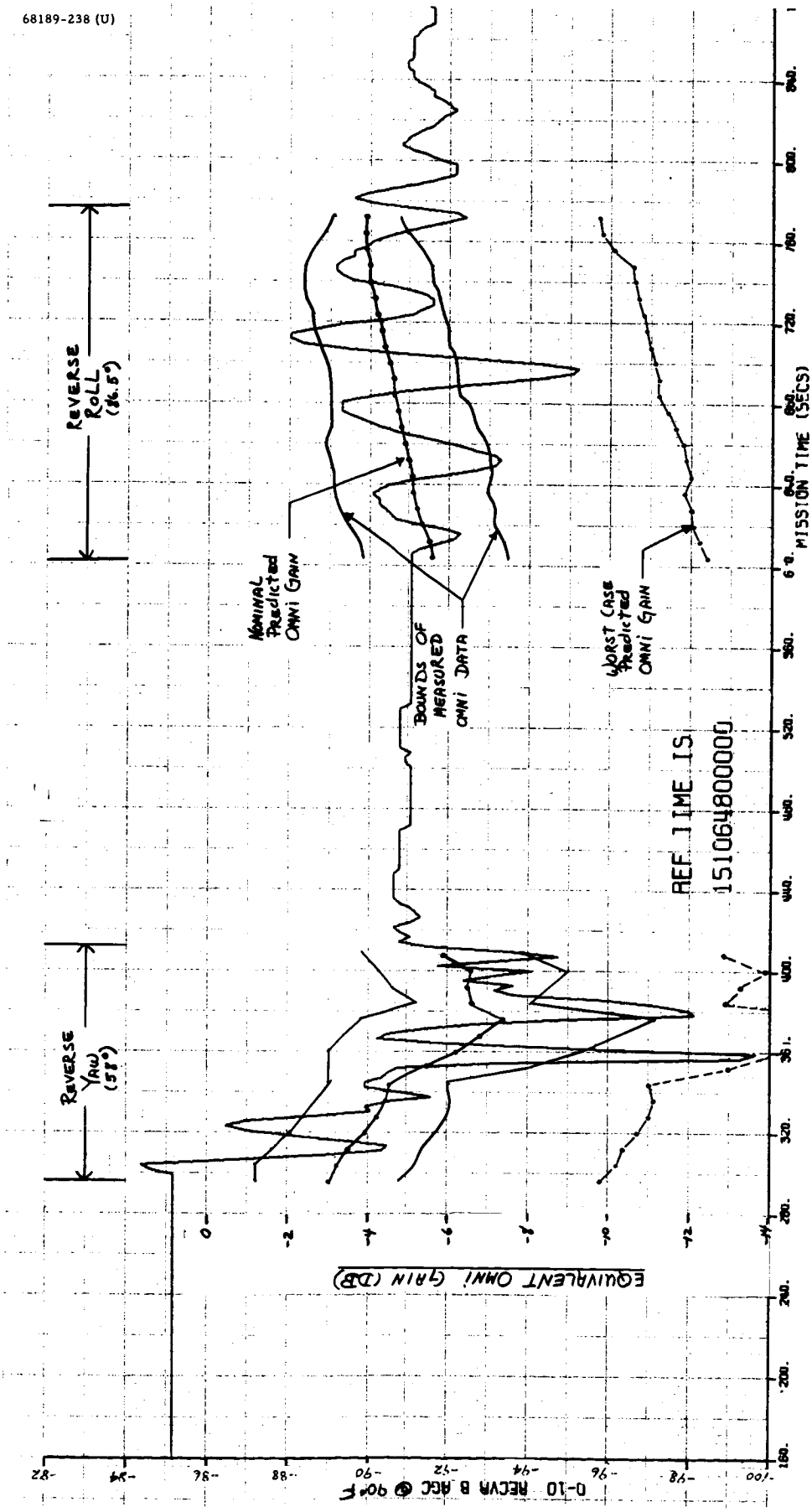
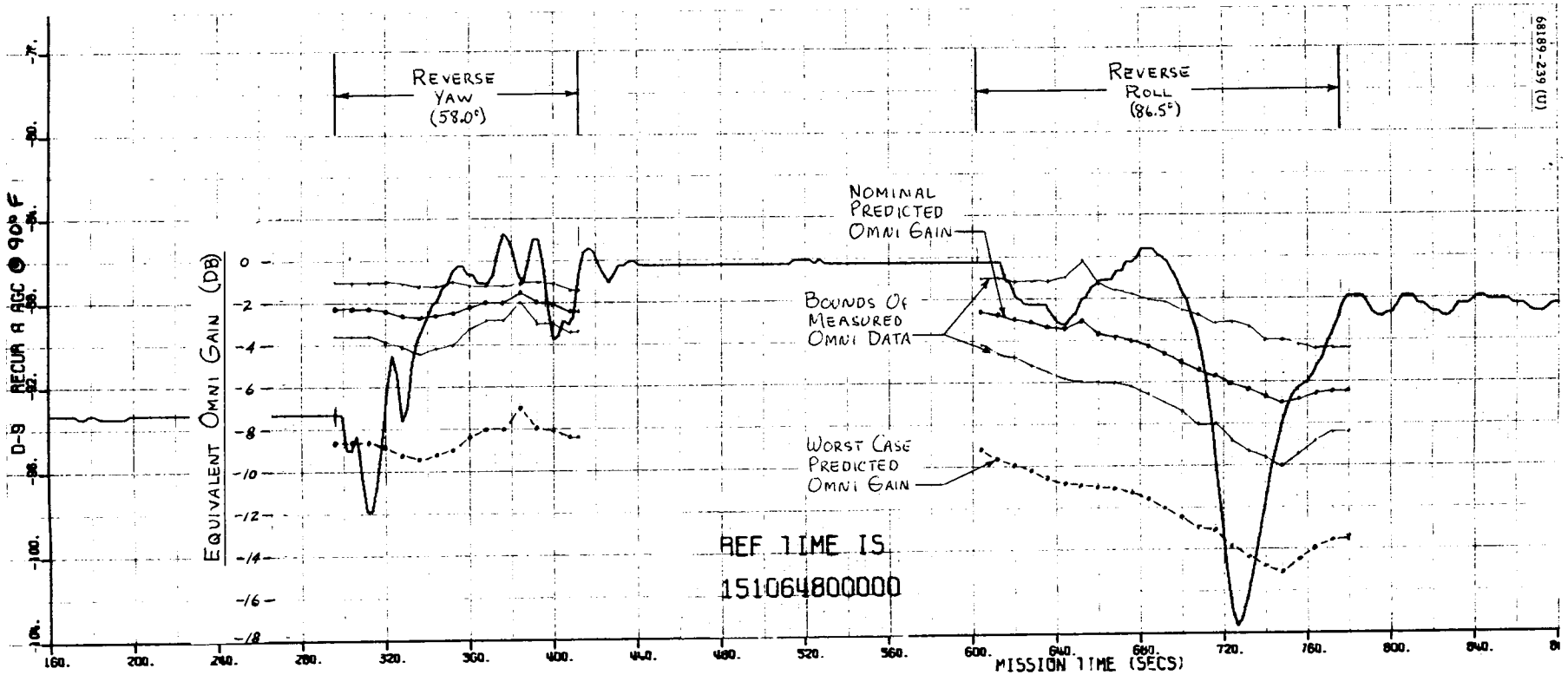


Figure 5.4-17. DSIF Received Signal Strength During Reverse Midcourse Maneuvers



a) Receiver B

Figure 5.4-18. Signal Strength During Reverse Midcourse Maneuvers



b) Receiver A

Figure 5.4-18 (continued). Signal Strength During Reverse Midcourse Maneuvers

TABLE 5.4-10. TERMINAL MANEUVER SUMMARY

Maneuvers Considered	Maneuver Duration		Spacecraft to Earth				Earth to Spacecraft			
	Angle, Degrees	Time, Seconds	Antenna A Gain,* db	Antenna B Gain,* db	Margin A	Margin B	Antenna A Gain,* db	Antenna B Gain,* db	Margin A	Margin B
1 Roll	179	258	-7	-5	-1	1	-10	-9	9	10
Pitch	60	120	-9	-5	-3	1	-10	-9	9	10
2 Roll**	89	178	-7	-5	-1	1	-10	-7	9	12
Yaw	60	120	-6	-6	0	0	-10	-12	9	7
Roll	116	232	-15	-6	-9	0	-20	-10	-1	9
3 Roll	89	178	-7	-5	-1	1	-10	-7	9	12
Yaw	60	120	-6	-6	0	0	-10	-12	9	7
4 Pitch	-60	120	-7	-15	-1	-9	-8	-15	11	4
Yaw	0	0	-1	-15	5	-9	-1	-15	18	4

*Antenna gains are minimum measured gains, not worst-case predicted gains.

**Selected maneuver.

A roll-yaw-roll maneuver was selected even though three maneuvers were required. This maneuver used the final roll to optimize the antenna gain on omnidirectional antenna B for subsequent terminal descent data. Zero margins were predicted for this maneuver with an uncertainty of ±3 db in the margin.

It was also recommended that the maneuver be made in one way even though adequate margins were available for transponder operation. This recommendation was made because one way was required for the terminal descent sequence and operationally it was safer to go to one way before the terminal maneuver.

The maneuver was executed using commutator mode 1, which does not contain receiver signals. Therefore, no data is available on the spacecraft receiver signal levels during the maneuver. DSIF AGC data was available, and the signal levels again followed the downlink predictions (see Figure 5.4-19). Data at 1100 bits/sec was maintained with no data dropouts as predicted.

During the first roll maneuver, a receiver index was noted indicating that one of the receivers experienced a severe drop in signal level. This posed no problem since all subsequent commands were accepted. The receiver index, however, is considered to be further evidence that omnidirectional antenna A had not deployed up to the time of this maneuver.

The transmitter output power after touchdown and just prior to the turning on of transmitter A for lunar TV was computed to be ≃39.9 dbm. This data indicates that the output power during the terminal maneuver phase was at least 39.9 dbm and probably somewhat higher.

5.4.7.6 Landing Phase Performance

The spacecraft made a successful touchdown at 06:18:20. Touchdown strain gage data was received at touchdown and DSIF receiver phase lock was maintained throughout the retro burn to touchdown phase. The touchdown strain gages were turned on at ≃06:16 right after the main retro eject signal.

Preterminal maneuver analysis indicated that during the descent phase the strain gages would be turned on with the 1100 bits/sec PCM data. It was also predicted that the PCM data would remain good through touchdown with a bit error rate $>3 \times 10^{-3}$. The analysis was based on a predicted carrier signal level of -123.3 ± 3.0 db at the end of the terminal maneuver.

As can be observed in Figure 5.4-19, the actual signal level at the end of the terminal maneuver was -122.5 dbm, again showing good agreement with predictions.

Figure 5.4-20 shows the DSIF signal level from the time of retro ignition through touchdown. The signal level remained relatively constant from the time of retro ignition through the time when the strain gages were commanded on. The drop in signal level at this time is due to additional modulation loss in the carrier. This data is consistent with the fact that the spacecraft attitude was relatively stable throughout the entire descent phase.

Although DSIF phase jitter data is not available at this time, reported data indicates that the phase jitter during the retro phase and at touchdown was very small and well below the maximum specified values. Solid DSIF receiver phase lock was observed during this phase.

The SNR in the predetection bandpass of each of the telemetry subcarriers at touchdown is as follows:

1100 bits/sec PCM channel ≃ 19 db

Strain gage 1 ≃ 21 db

Strain gage 2 ≃ 18 db

Strain gage 3 ≃ 18 db

The above SNR values are estimated to be accurate to $^{+1.5}_{-2.5}$ db.

5.4.7.7 Lunar Phase

The data relative to the lunar phase consists of many disjointed topics. The following discussion will thus deal with each topic in near chronological order.

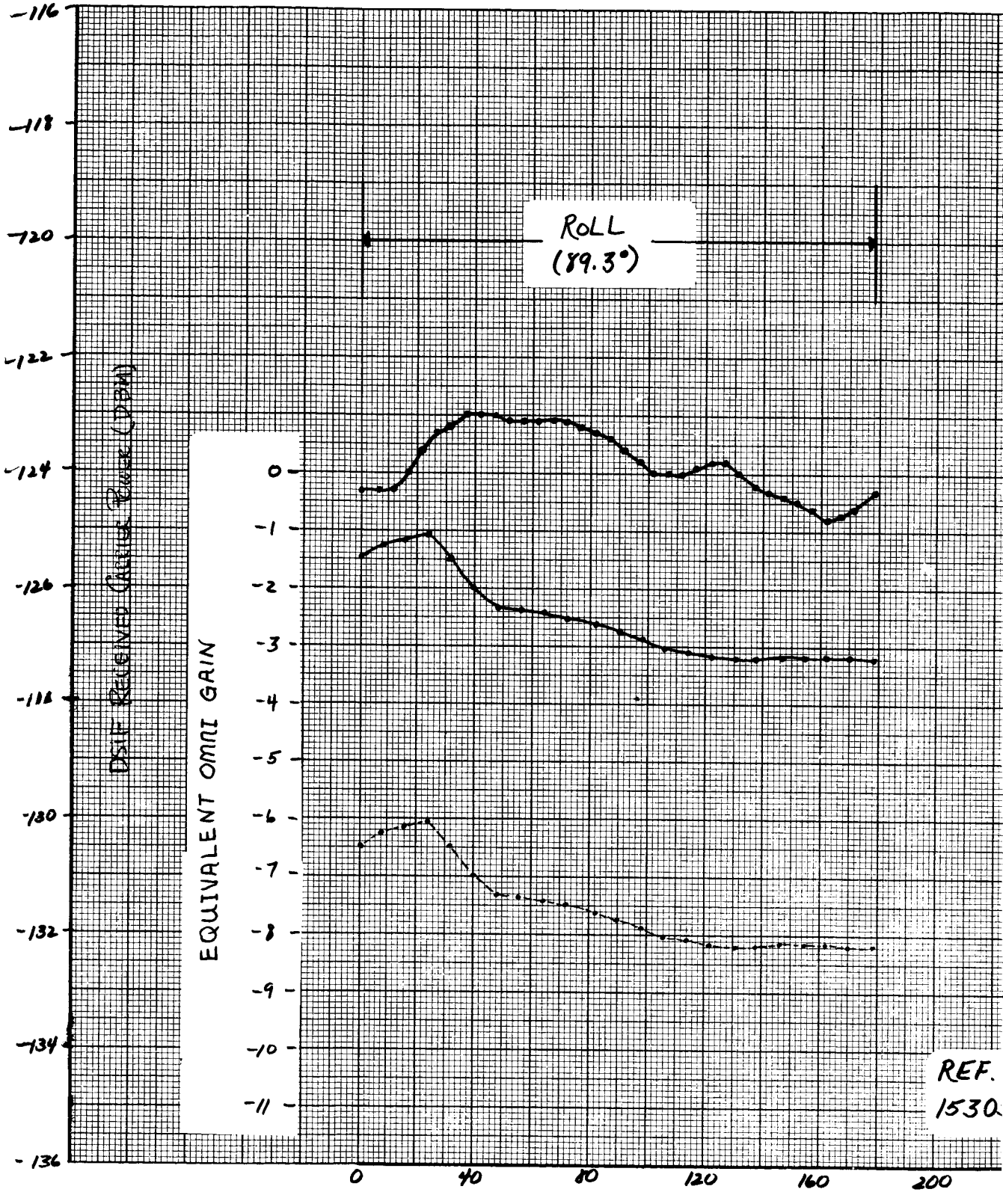
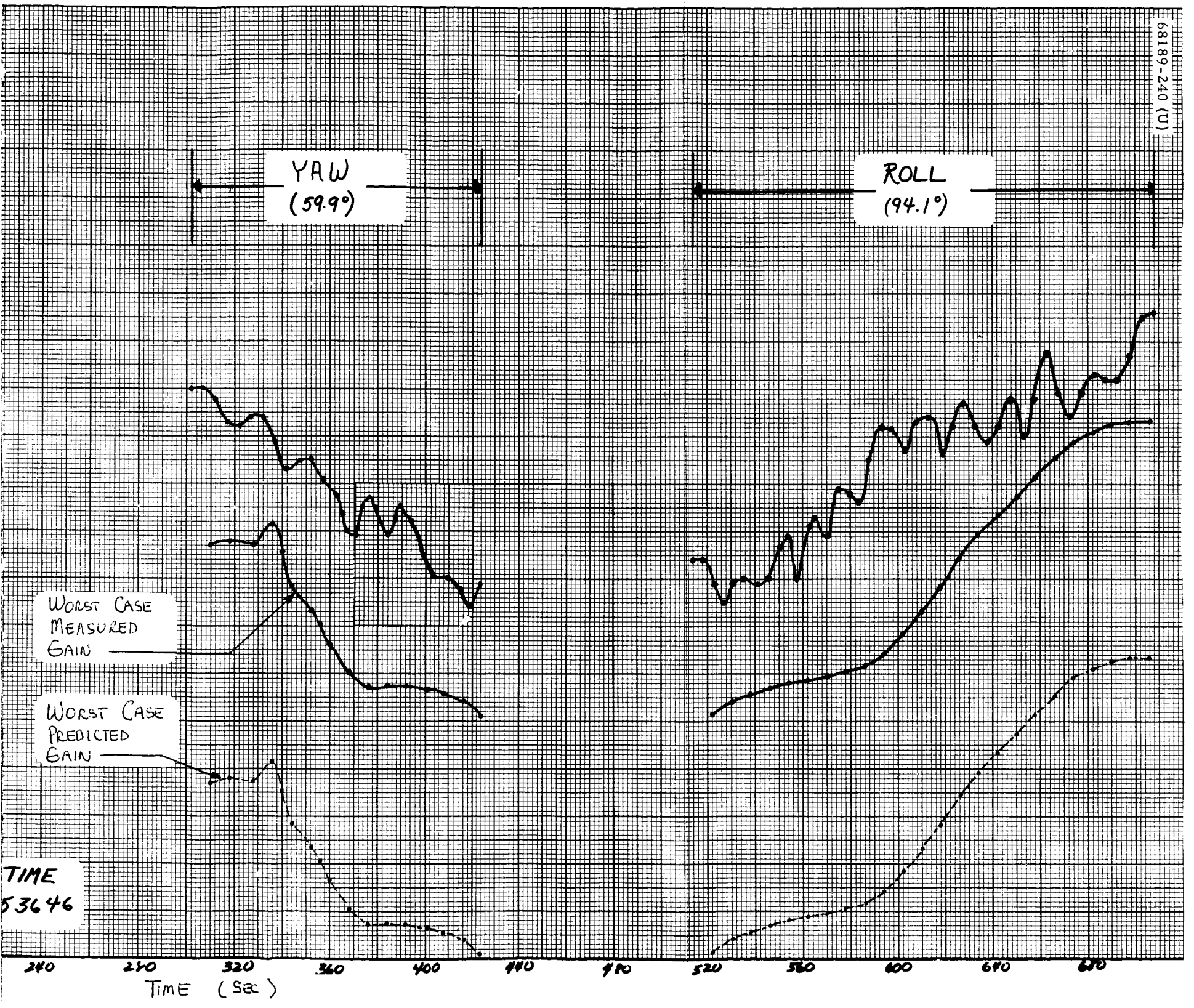


Figure 5.4-19. DSIF Received Signal Strength During Preterminal Maneuve

FOLDOUT FRAME



rs

FOLDOUT FRAME

FOLDOUT FRAME

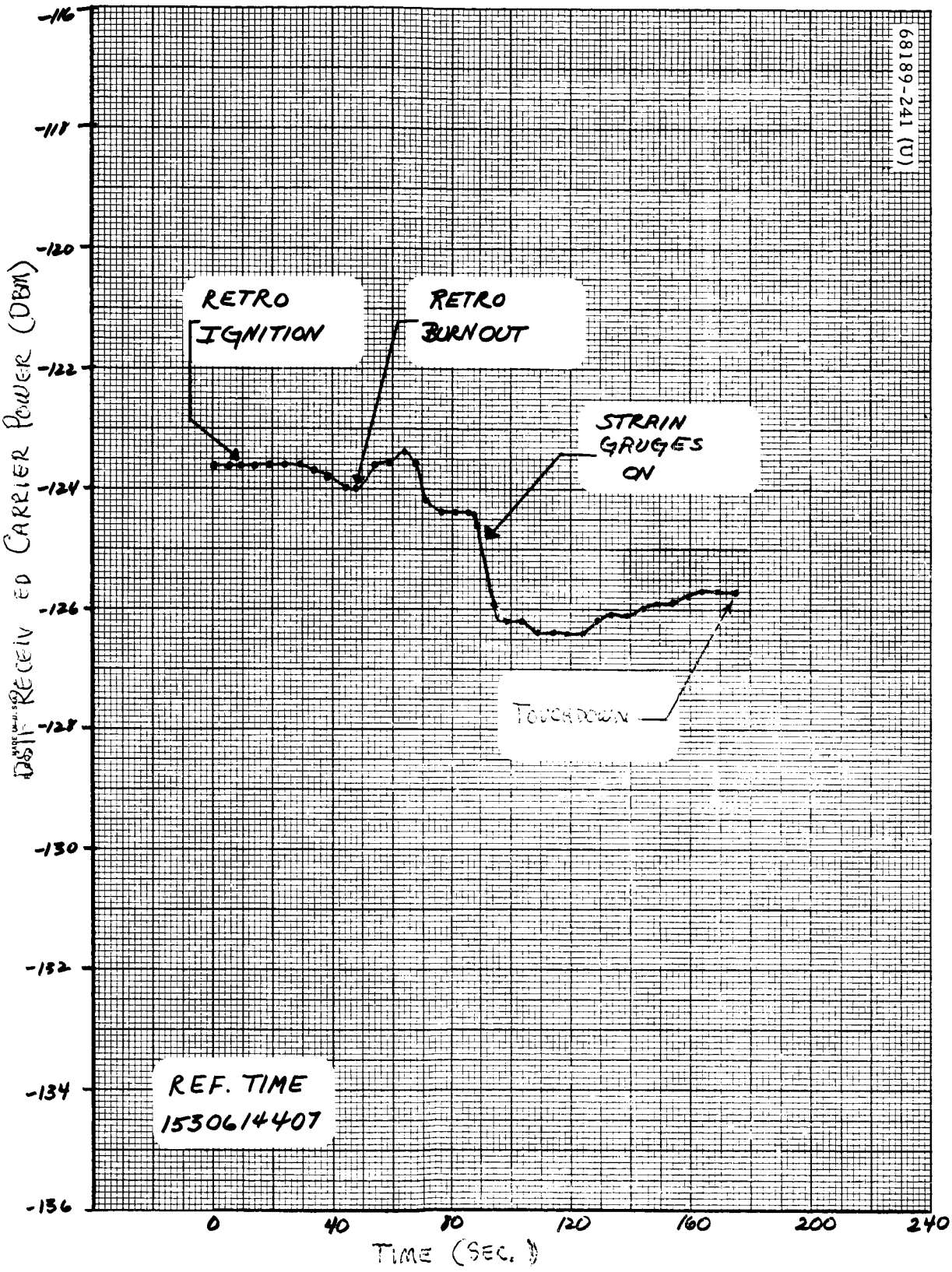


Figure 5.4-20. DSIF Received Signal Strength During Terminal Descent

Post-Touchdown RF Assessment

Shortly after touchdown, omnidirectional antenna A was selected for transmission for the first time since the prelaunch countdown. The signal level at the DSIF changed from -123.3 dbm to -133 db as was predicted from the omnidirectional antenna patterns.

The transmitter B output power after touchdown was ≃ 39.9 dbm. At approximately 1 hour after touchdown, transmitter A was turned on for the first time since the prelaunch countdown. The output power for transmitter A was computed to be 40.4 dbm at turnon and decreased to 39.7 dbm at turnoff, which was ≃ 1 hour and 45 minutes later. Figure 5.4-21 is a plot of transmitter A output power from turnon until ≃30 minutes before turnoff. The gradual power dropoff is apparent in this plot.

The traveling-wave tube temperature for transmitter A during the first 7 minutes after turnon is shown in Figure 5.4-22. STV 6 data adjusted to the same initial conditions at turnon is also plotted on this figure and shows good correlation between the thermal rise time for both sets of data. This data is included in this report because there was some indication that the transmitter A temperature rise at turnon increased during the prelaunch test phases. This rise does not seem to be the case, however, based on the data.

TV Performance

The first 200 line TV picture was transmitted at ≃49 minutes after touchdown. Based on reported DSIF signal levels, the computed SNR for the first picture was 15.5 db ± 2 db.

The first 600 line TV picture was transmitted at ≃ 4 hours after touchdown shortly after the planar array was aligned with the earth. Based on reported DSIF signal levels, the computed SNR for the first picture was 15.0 ± 2 db.

In both cases, the SNR was high enough to provide good quality detected video data as can be noted in the quality and resolution of the pictures.

Optimum positioning of the planar array and higher transmitter output power later on during the lunar day increased the 600 line SNR as much as ≃4 db above the SNR of the first 600 line TV picture. The SNR for the 600 line TV thus varied between 15 and 19 ± 2 db during the picture taking sequence.

Receiver Signal Level Variations Resulting from A/SPP Positioning

During the positioning of the solar panel and planar array after landing, large variations in receiver A signal levels were observed. This was not surprising since the position of omnidirectional antenna A (now extended) was such that the A/SPP could interfere with the line of sight between the

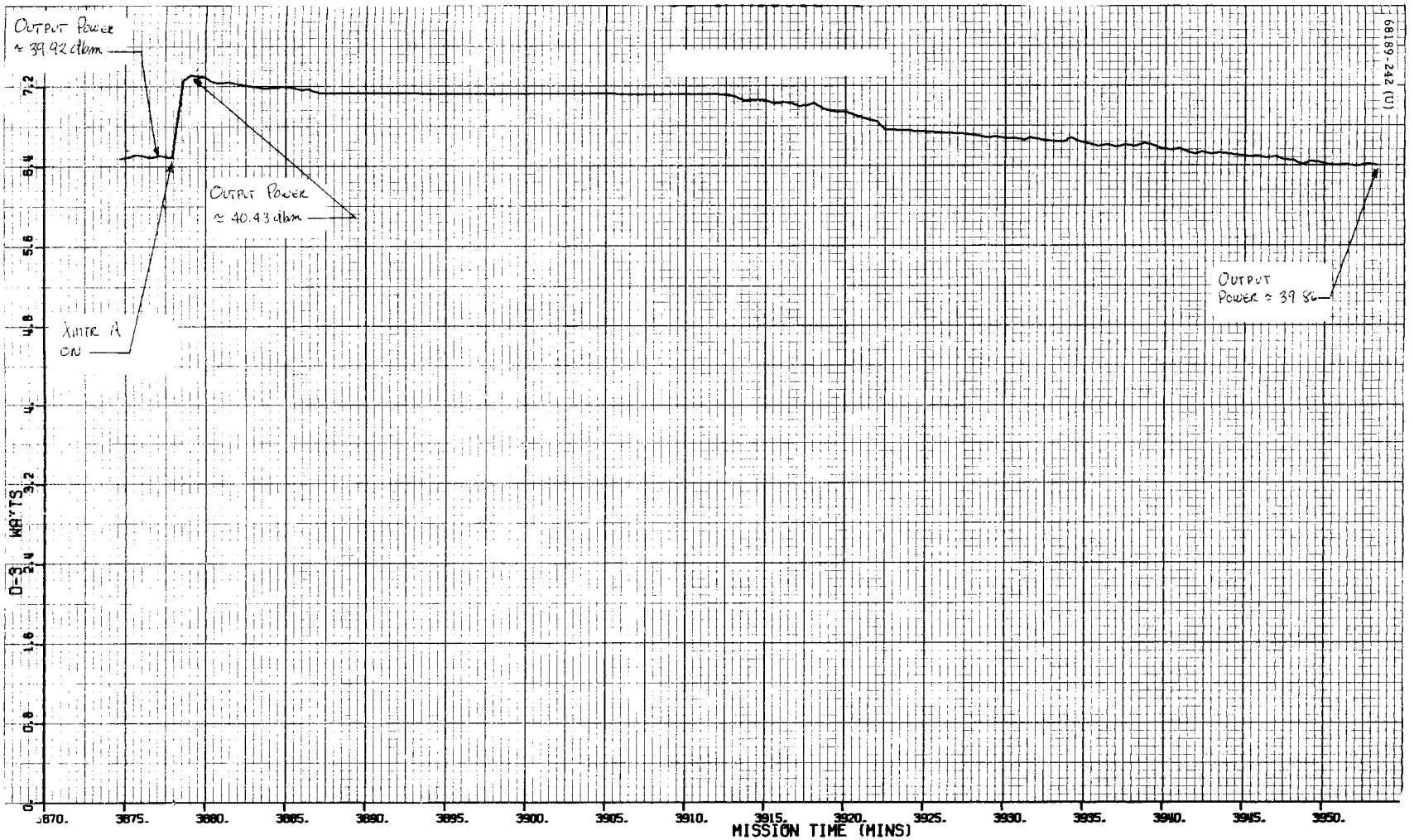


Figure 5.4-21. Omnidirectional Antenna B Transmitter Power

PRECEDING PAGE BLANK NOT FILMED.

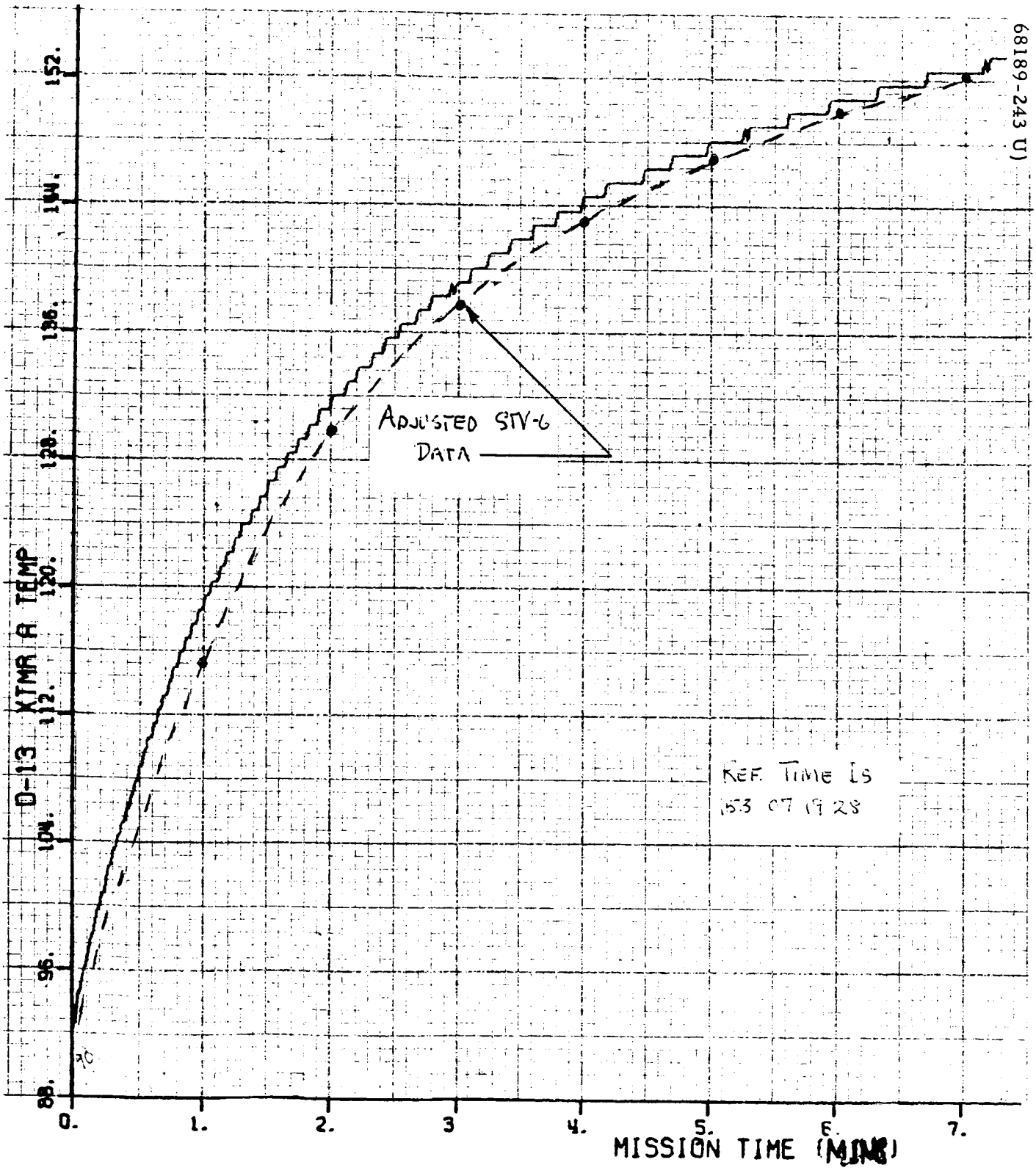


Figure 5.4-22. Transmitter A Traveling-Wave Tube Temperature Versus Time

omnidirectional antenna and the earth. The signal levels for both receivers during this period are shown in Figure 5.4-23.

This data is quite significant since it demonstrates that large variations in omnidirectional antenna gain patterns can result from movement of the A/SPP. Omnidirectional antenna patterns are consequently made invalid once the position of the A/SPP is moved significantly from the position the A/SPP was in during the omnidirectional antenna pattern measurements.

Special Receiver Threshold Test

On day 160 at ≃16:00 GMT, a special spacecraft command receiver threshold test was run. The DSIF transmitter output power was decreased from 70 to 46 dbm, at which time a spacecraft receiver/decoder index was observed. Receiver A and B AGC in raw counts was recorded during this test, and correlation to previous test data was attempted. As discussed in subsection 5.4.7, the previously assumed temperature-engineering data relationship was shown to be in error and, consequently, the data from this test was used to establish a new calibration curve for postmission analysis work. The test data is summarized in Table 5.4-11.

TABLE 5.4-11. TELETYPE DATA DURING RECEIVER THRESHOLD TEST

Time, GMT	Station 11 Transmitter Power, dbm	Spacecraft Receiver/ Decoder	D9-Receiver A AGC	D10-Receiver B AGC
16:28:00	P70	B A	239	177
16:35:30	P60	B A	338	262
16:36:35	P58	B A	356	280
16:39:15	P56	B A	369	295
16:43:50*				
16:51:00	P58	B A	357	281
16:52:15	P56	B A	369	279
16:53:15	P54	B A	380	311
16:54:10	P52	B A	388	325
16:56:00	P50	B A	393	335
16:56:45	P48	B A	396	343
16:57:15	P46	A B	398	349
16:59:10	P44	Oscillating	399	353
	P70	B B	246	182
	P70	A A	246	182
		Command mode off		
	P70	B A	244	180

*At this point it was found that receiver B was locked to a sideband. Transmitter power was returned to P58 dbm, and receiver B acquired. Receiver/decoder selector cycled to obtain original combination.

Note: Phase lock was held on both receivers A and B throughout.

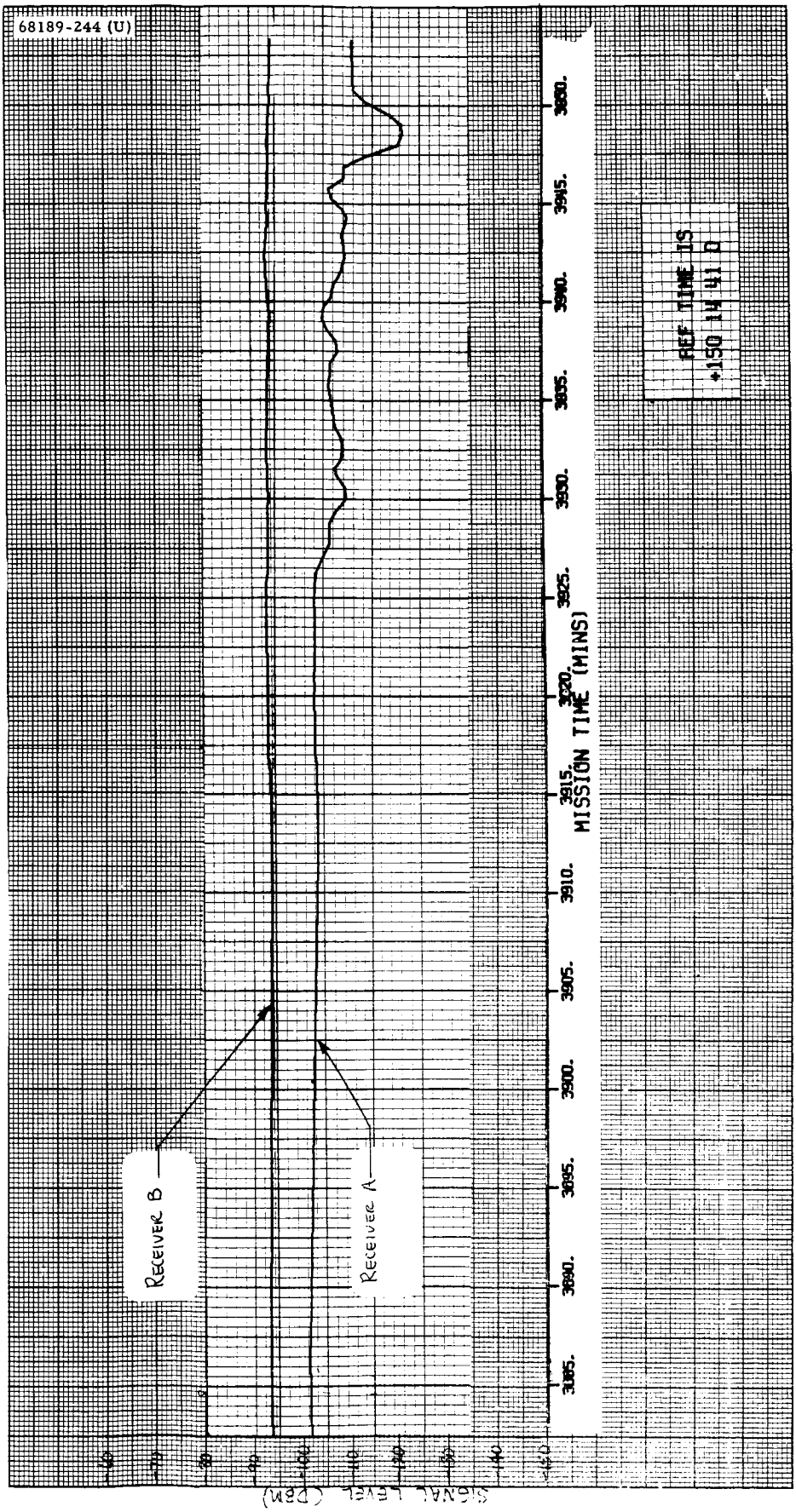


Figure 5.4-23. Receiver Signal Level Variations During A/SPP Positioning

Voice Transmission via the Transponder

On day 164 during the first lunar day (June 13), an experiment was run in which the uplink carrier was modulated by voice, tracked by the spacecraft transponder, and relayed back to the ground. The experiment was considered to be more or less an attempt to determine the feasibility of the voice transmission scheme. Consequently, no detailed analysis of the expected voice quality or bandwidth limitations was undertaken.

The basic scheme used was to phase modulate the uplink carrier, resulting in the voice data being tracked by the spacecraft transponder. The transponder tracking loop filter has a 3 db information bandwidth of $\simeq$100 cps and falls off at 12 db/octave. Due to the low frequency response of the loop filter, severe attenuation to the voice information occurred.

The ground detection was via a standard FM detector. By using FM discrimination, the amplitude falloff due to the phase lock loop filter response was partially compensated. The resulting detected voice information at the ground receiver was of poor quality, as expected, but was audible.

5.4.7.8 Subsystem Telemetry Data (Transit)

The pertinent subsystem telemetered data for the transit and early lunar phase are contained in Figures 5.4-24 through 5.4-33. Variations in the data are explained in each figure. In general, all data indicated nominal performance, and no variations were noted which were unexplainable or suspect of anomalous performance.

Due to postmission data processing problems, the subsystem data from L + 36 to L + 42 hours is missing (see Section 5.1). The plots are thus invalid during this period even though there appears to be data in the above mentioned period.

A brief summary of each figure and the more significant points relative to each figure follow:

Receiver A AGC (Figure 5.4-24) – In review, the data tends to confirm the fact that omnidirectional antenna A was not deployed. Step changes in signal level occurred whenever the pointing vector changed either due to DSIF station transfer or termination of gyro drift checks.

Receiver B AGC (Figure 5.4-25) – This data compared well with predictions and also exhibited sensitivity to small pointing vector changes.

Receiver A AFC (Figure 5.4-26) – Receiver A was in the AFC mode throughout transit. This data represents the DSIF transmitter frequency offset from the AFC center frequency during the transit phase. A large error due to doppler shift rate is noted at acquisition. Steps in the data occurred at station transfer because the stations retuned their transmitters to compensate for expected doppler shift due to the earth's rotation. The downward

shift between station transfers is caused by the earth's rotation. Signal processing induced "glitches" can also be observed in this data. Due to the high impedance of this signal, several predicted signal processing effects are apparent. Steps occurred in the data at high power turnon due to return line drop caused by the additional current in the ground return lines during high power operation. Spikes occurred during engineering interrogations of mode 4 due to step change in commutator unbalance current.

Receiver B Static Phase Error (SPE) (Figure 5.4-27) – Receiver B was used for transponding through most of the mission. This data thus represents the DSIF transmitter frequency offset from the receiver phase lock center frequency. Since this data is analogous to the AFC data discussed above, the comments apply equally well to this data. It should be noted, however, that this signal is not as sensitive to signal processing induced errors.

Receiver A SPE (Figure 5.4-28) – Since receiver A was in the AFC mode, the transponder and, hence, SPE telemetry was not actually used. However, the telemetered data does contain some interesting points. Signal processing induced steps occur during high power operation. The temperature sensitivity of the isolation amplifier is noticeable in the gradual variations in the telemetry output. These variations correlate exactly with variations in the compartment A bottom tray temperature (see Figure 5.4-31). The telemetry value of ≃ 600 kc offset corresponds to the 0 or near 0 volt telemetry output of the isolation amplifier.

Receiver B AFC (Figure 5.4-29) – Since the receiver was phase locked during the majority of the transit phase, this telemetry signal was not a valid signal. Unlike the SPE signal, which has a 0 volt output when not being selected, the AFC telemetry does vary with frequency changes even when the receiver is not in the AFC mode. However, the telemetry is not valid and is essentially meaningless. As in the AFC telemetry for receiver A, this signal also shows several signal processing induced "glitches."

Compartment A Tray Temperature (Figures 5.4-30 and 5.4-31) – This data represents the temperatures of the top (V-15) and bottom (V-16) of the compartment A thermal tray. The receivers and transmitters are attached to this tray and, consequently, this data is the only temperature data which even approximate subsystem unit temperatures. The tray bottom data tends to be less responsive to local heating at the transmitter traveling-wave tubes and is considered more indicative of unit temperatures.

Transmitter Traveling-Wave Tube Temperatures (Figures 5.4-32 and 5.4-33) – This data represents the temperature of the traveling-wave tubes used for high power transmitter operation.

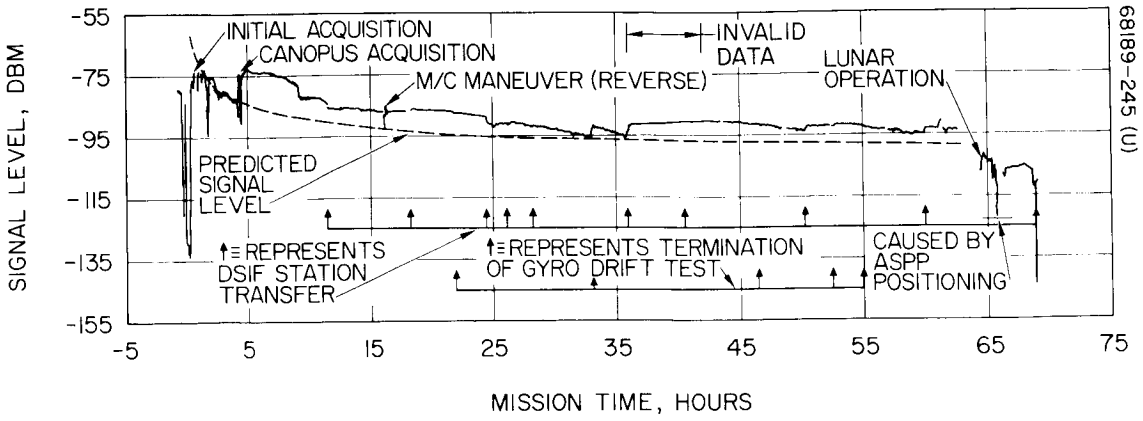


Figure 5.4-24. Receiver A Automatic Gain Control Versus Time

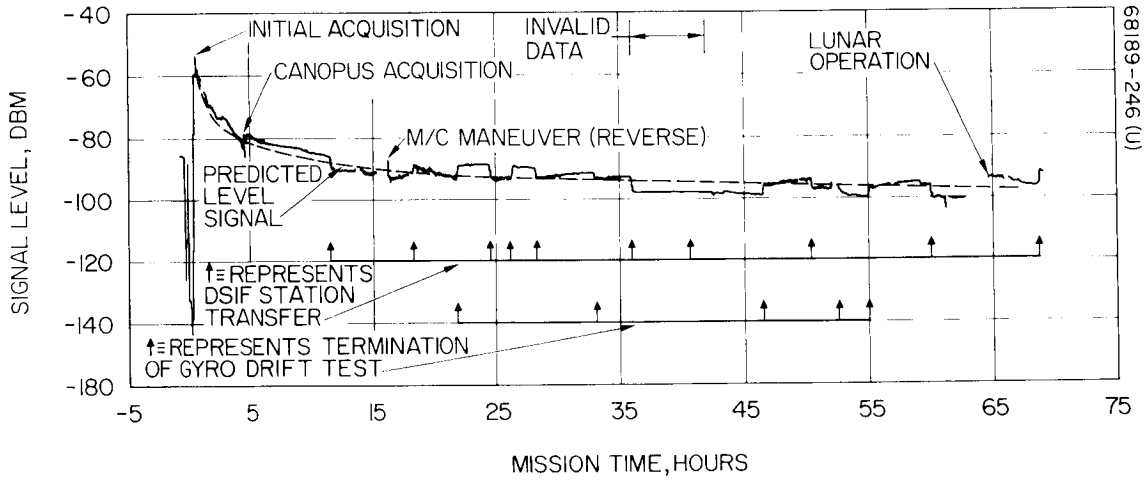


Figure 5.4-25. Receiver B Automatic Gain Control Versus Time

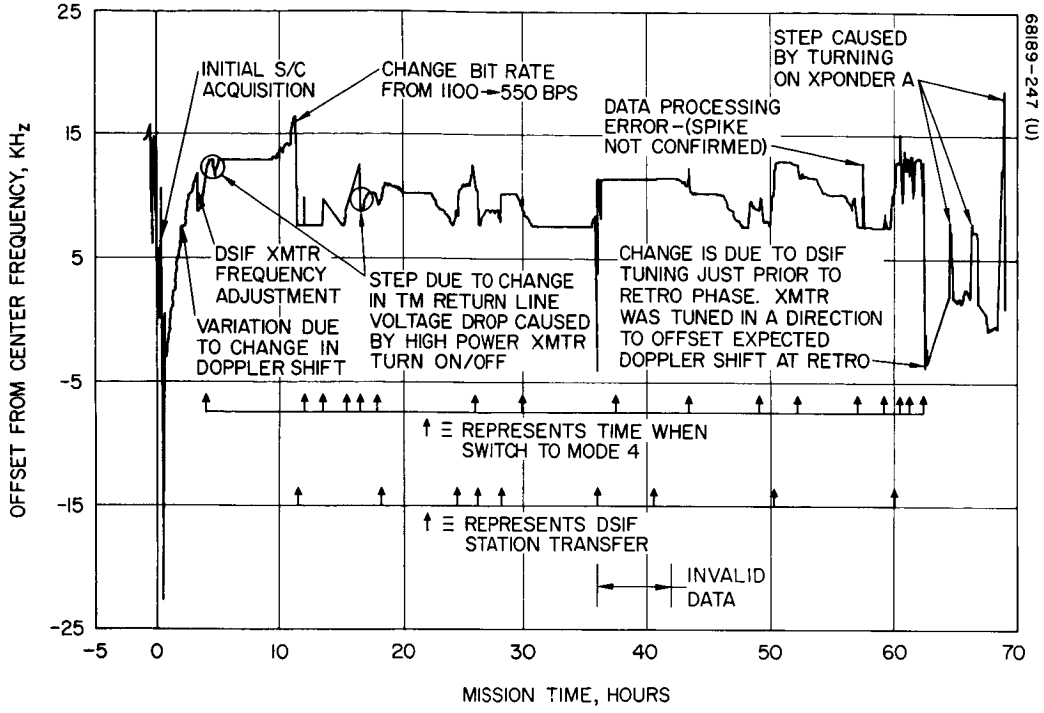


Figure 5.4-26. Receiver A Automatic Frequency Control Versus Time

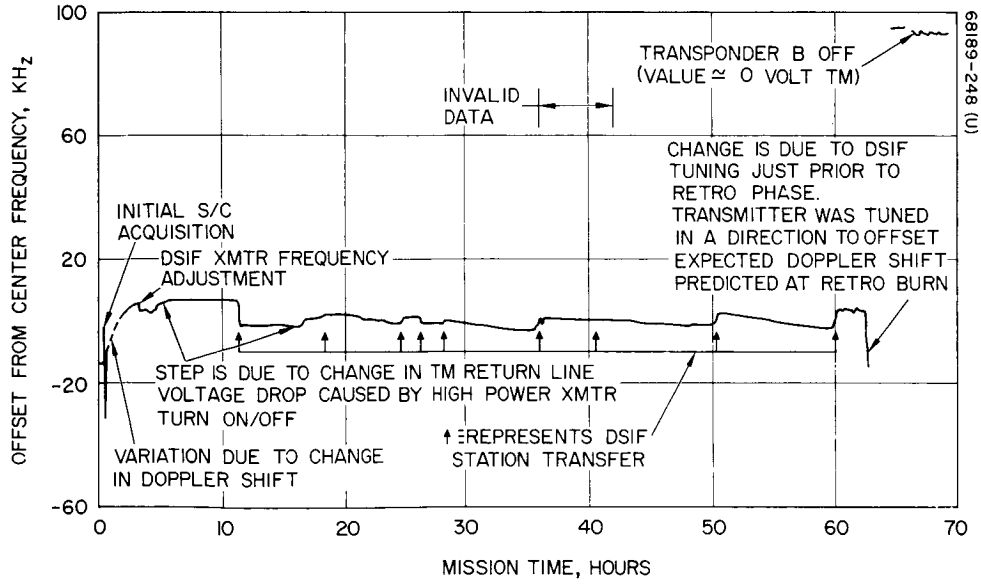


Figure 5.4-27. Static Phase Error B Versus Time

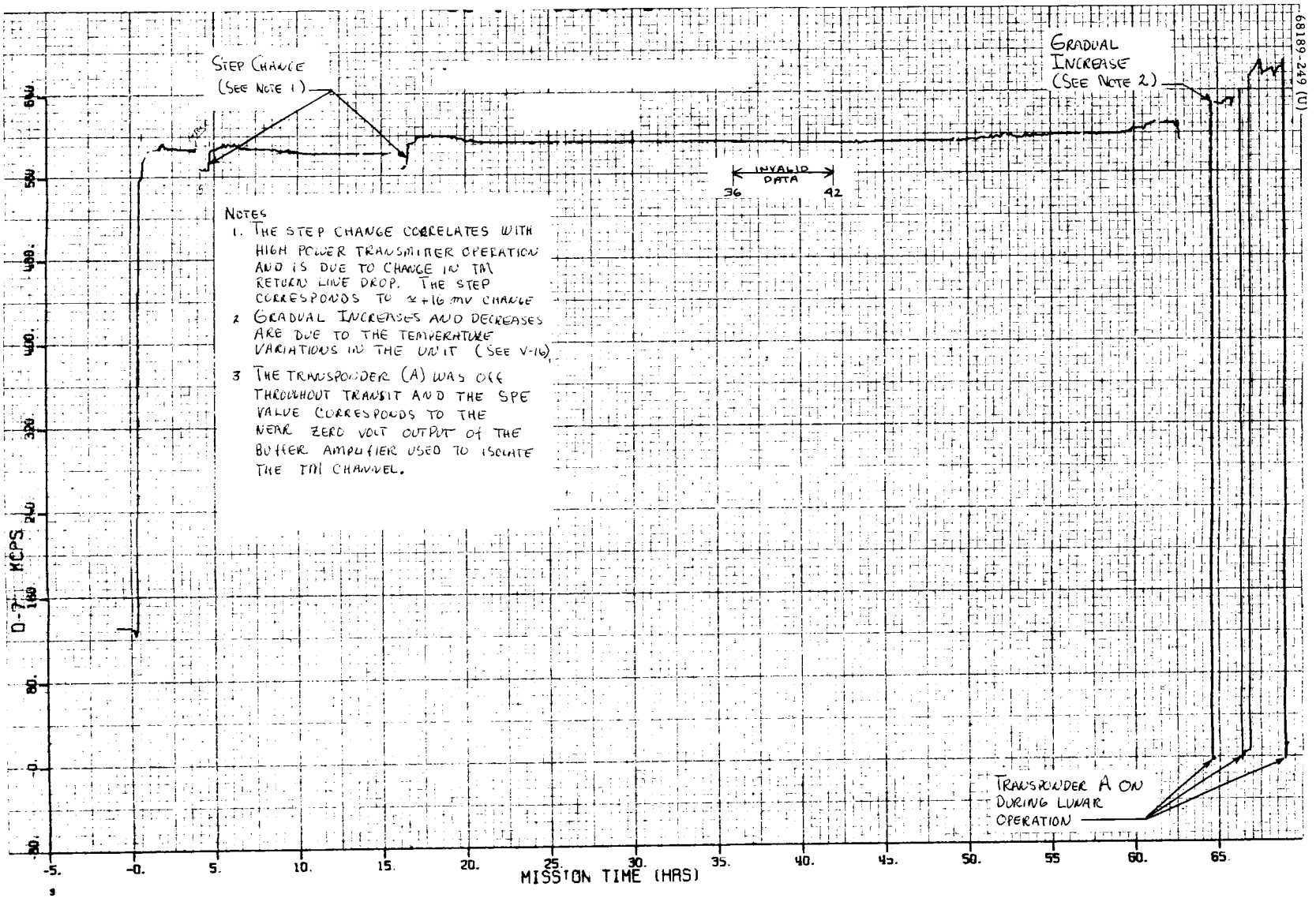


Figure 5.4-28. Static Phase Error A Versus Time

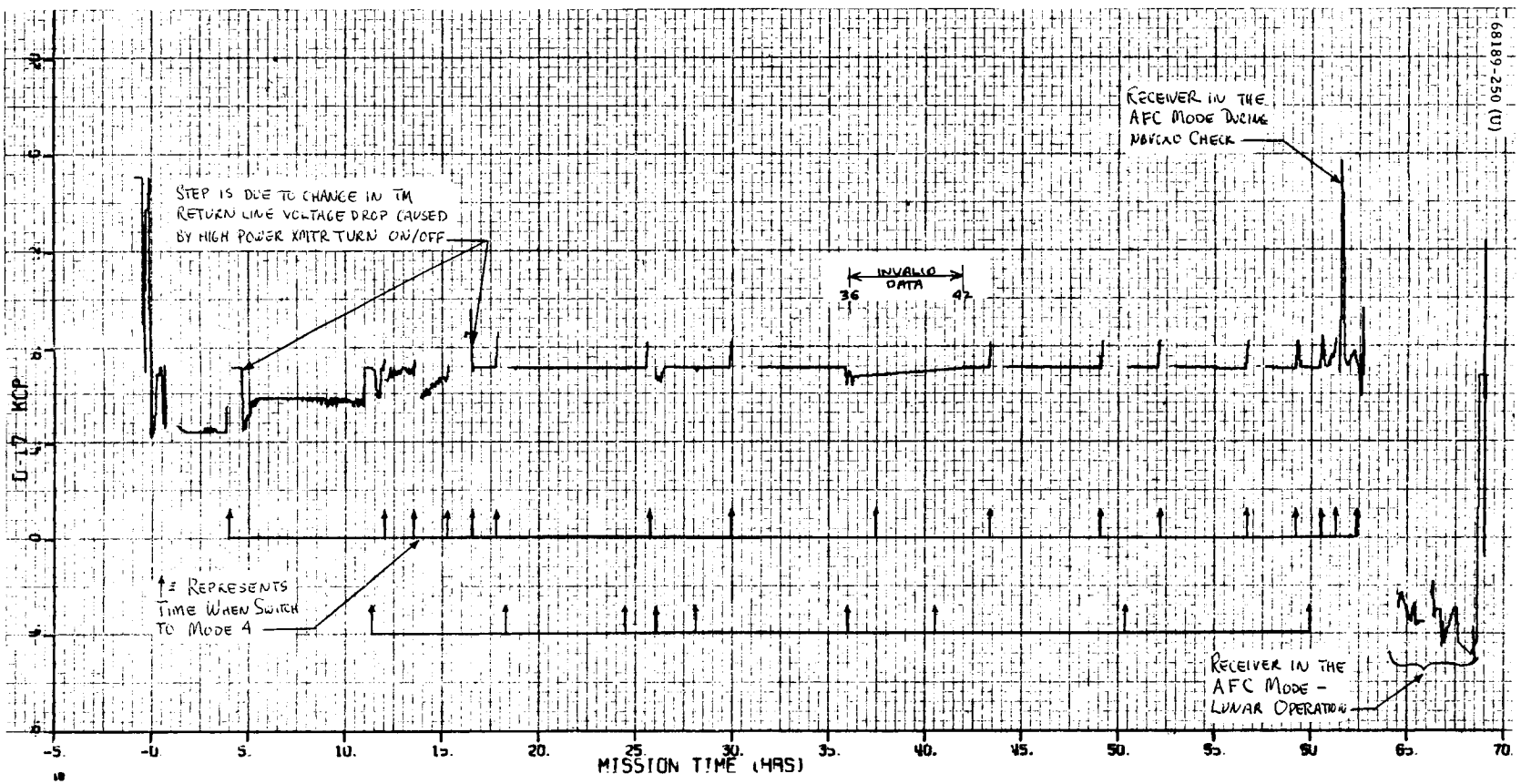


Figure 5.4-29. Receiver B Automatic Frequency Control Versus Time

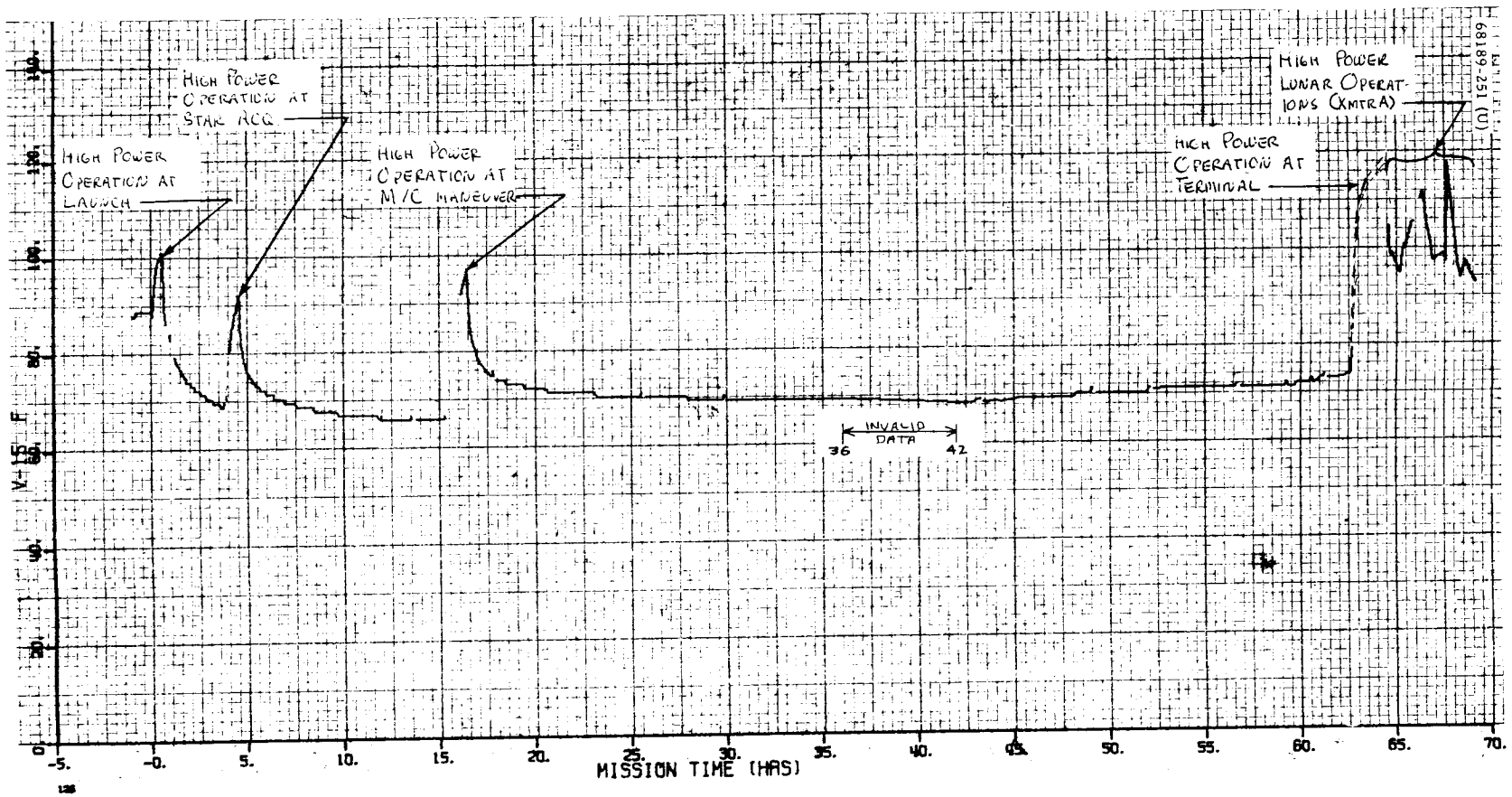


Figure 5.4-30. Compartment A Tray Top Temperature Versus Time

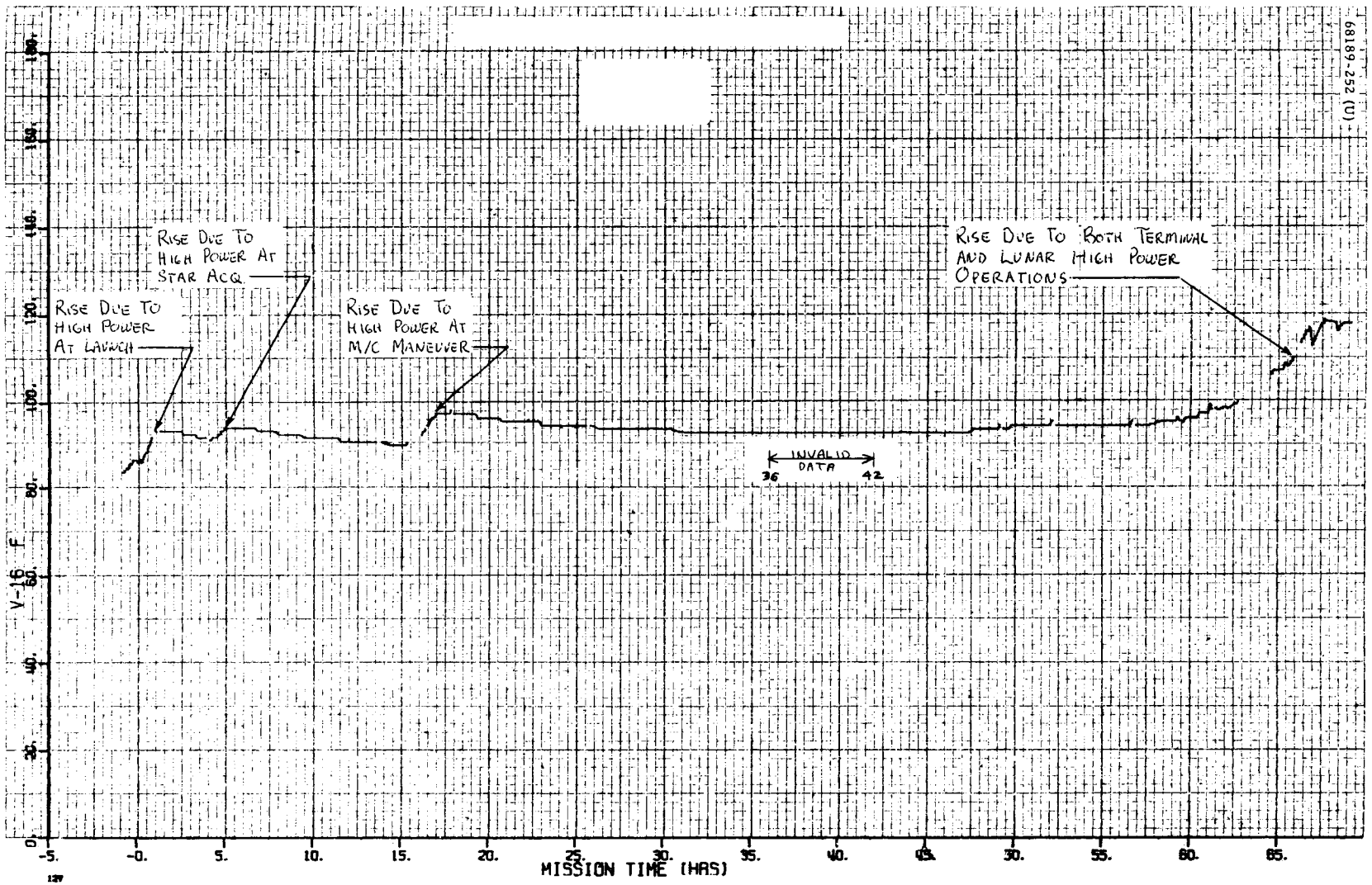


Figure 5.4-31. Compartment A Tray Bottom Temperature Versus Time

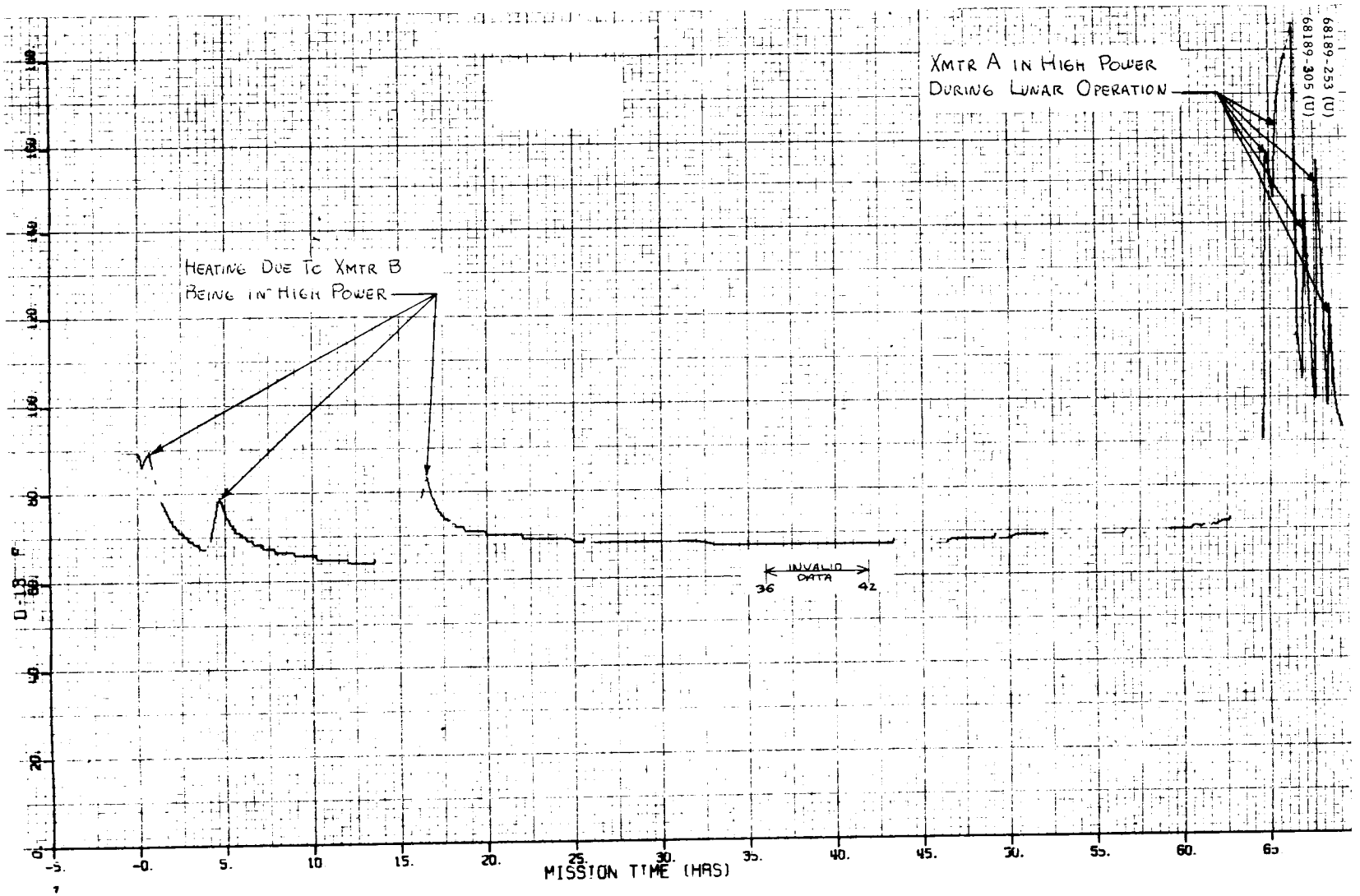


Figure 5.4-32. Transmitter A Temperature Versus Time

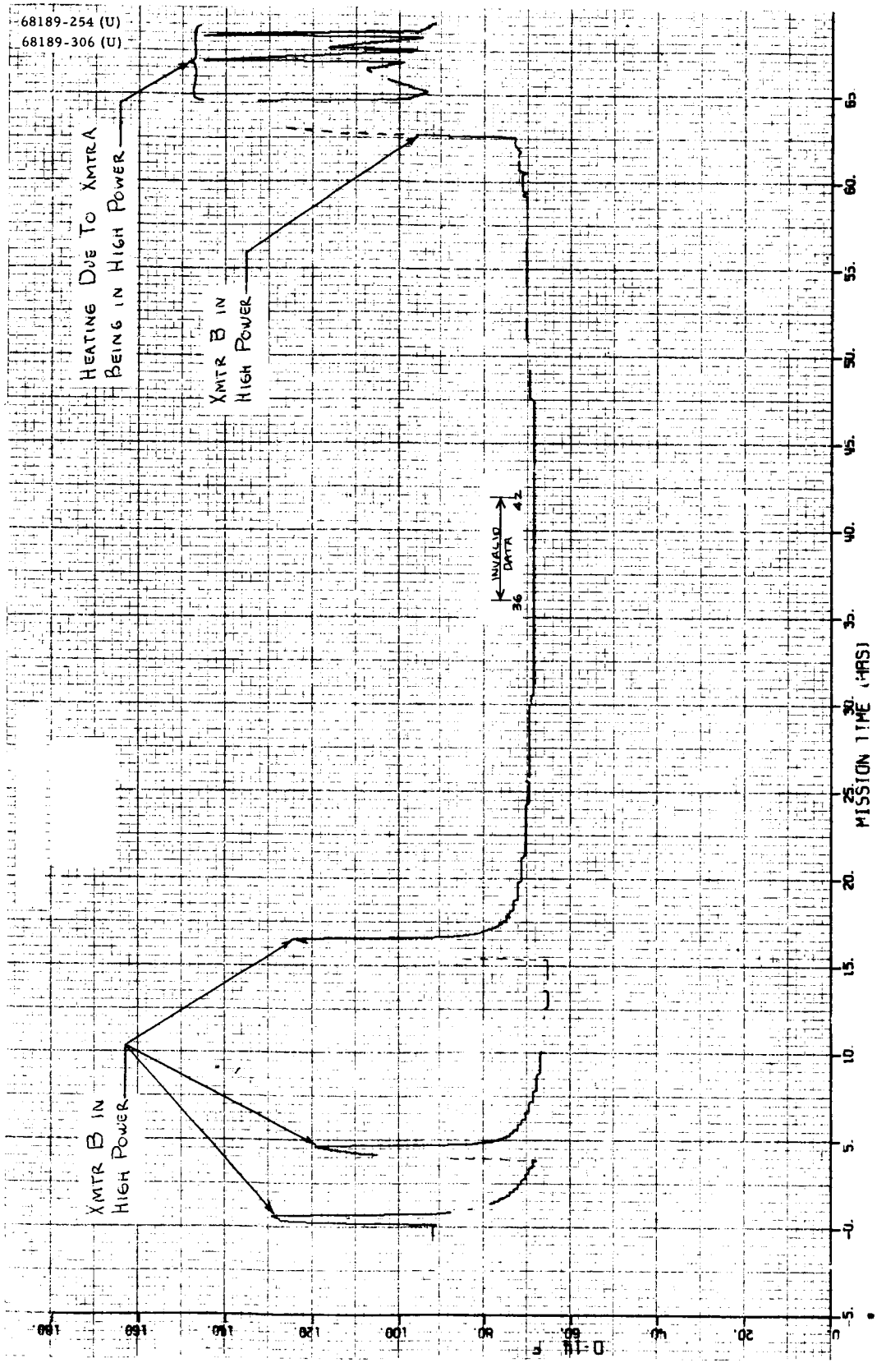


Figure 5.4-33. Transmitter B Temperature Versus Time

5.4.8 REFERENCES

1. M.R. Weiner, "Surveyor Mission A – Telecommunications Subsystem Prediction and Performance Summary Document," Hughes Aircraft Company, SSD 64181R.

2. J. Votaw, "Telecommunication Subsystem SPAC Detailed Operational Procedures (Telcom DOP)."

3. K.C. Beall and L.C. Gee, "Surveyor I Flight Performance Quick Look Report," 17 June 1966.

4. C.M. Meredith, "Surveyor I – Flight Path Analysis and Command Operations Report," Hughes Aircraft Company, SSD 68142R, 24 June 1966.

5. F.K. Rickman, "Data Link and Signal Processing Subsystem Final Report on the SC-1 STV Test," IDC No. 2253.3/451, 11 April 1966.

5.4.9 ACKNOWLEDGMENTS

Frank K. Rickman, coordinator of this section.

The following people also contributed to the preparation of this section of this report:

The SPAC Telecommunications Team consisting of John Steineck, Vern Story, Joe Votaw, and Mike Williams who managed to maintain an accurate set of records and note significant events on the data in real time so that the postmission analysis was much more easily accomplished.

The Post Flight Analysis section, headed by R. Leuschner, for their invaluable aid in processing and presenting the majority of the data contained in this section.

Jan Garrick for her assistance in the plotting of antenna pattern data on the receiver AGC data plots.

R. Leuschner for the investigation and analysis of the parity errors observed during the latter portion of the mission.

5.5 SIGNAL PROCESSING

5.5.1 INTRODUCTION

The signal processing subsystem is composed of the following units:

1) Engineering signal processor (ESP)

2) Auxiliary engineering signal processor (AESP)

3) Central signal processor (CSP)

4) Signal processing auxiliary (SPA)

5) Low data rate auxiliary (LDRA)

These units contain two electronic commutators with a total of six operational modes, two analog to digital converters that have available 5 digital bit rates, 17 subcarrier oscillators for transmission of pulse coded modulation data and continuous real-time data, 9 summing amplifiers, and signal conditioning circuits for the measurement of electrical currents and temperatures. The subsystem performed normally throughout the transit and lunar phase of the SC-1 mission.

5.5.2 MAJOR SIGNAL PROCESSING SUBSYSTEM EVENTS DURING TRANSIT

The commutator modes and bit rates used throughout the transit phase are listed in Table 5.4-2 in Section 5.4. The signal processing configuration (A/D converter used) is shown in Table 5.4-3 of Section 5.4.

5.5.3 PERFORMANCE SUMMARY

Listed in Table 5.5-1 are the significant performance parameters compared with the values measured during STV.

TABLE 5.5-1. SUMMARY OF SIGNAL PROCESSING PERFORMANCE PARAMETERS

Telemetry Signal	Average Value During Mission	Average Value During STV Test Phase
S-1 reference voltage	4.88 volts	4.90 volts
S-2 reference return	0.0024 to 0.0072 volt	0.005 volt
S-5 commutator unbalance current (ESP)	-3.1 microamperes (mode 4)	-3.3 microamperes (mode 4)
	-4.4 microamperes (mode 2)	-4.6 microamperes (mode 2)
S-7 commutator unbalance current (AESP)	-2.8 microamperes	-2.8 microamperes
Bit rate stability	0.002 percent	Specification = ±0.1 percent
A/D conversion stability	1.4 millivolts maximum	Specification = less than 10 millivolts

5.5.4 ANOMALY SUMMARY

No anomalies were detected during the SC-1 mission.

5.5.5 CONCLUSIONS AND RECOMMENDATIONS

The signal processing subsystem of the SC-1 spacecraft functioned normally throughout the transit phase and first lunar day of the mission. No anomalies were noted, and there was no evidence of degradation of any specified subsystem parameters. In addition, a special test was conducted on day 160 to exercise and assess the signal processing subsystem. During this test, the operation of all subcarrier oscillators, both analog to digital converters, all data rates and commutator modes, and the FM and PM modulation modes was verified. The time duration of this test was from 160:14:14:17 to 160:17:02:09 GMT. A modified version of this special test, optional sequence No. 17, has been incorporated in EPD-180 and is scheduled to be performed on all future spacecraft.

To provide the necessary data to more fully evaluate the subsystem, the following information is requested when the tapes from optional sequence No. 17 are processed in the future:

1) Six frames of raw data for all commutator modes with A/D converter 2 at the 550 bits/sec data rate

2) Six frames of raw data for coast mode commutator with A/D converter 1 at the 550 bits/sec data rate

3) Recorded data rate frequencies for all A/D converter 2 data rates, and for the 550 bits/sec rate for A/D converter 1

4) Recorded frequency of all accelerometer and touchdown strain gage subcarrier oscillators

5) Recorded frequency of the gyro speed subcarrier oscillator

6) Recorded maximum and minimum frequency of the enable/reject subcarrier oscillator

7) Recorded maximum and minimum frequency of all the PCM subcarrier oscillators

This information was not available for the evaluation of the SC-1 subsystem.

Changes to the engineering data reduction program for unbalance current correction (see subsection 5.5.6.1) and for current amplifier calibration (see subsection 5.5.6.3) are also recommended.

5.5.6 SUBSYSTEM PERFORMANCE ANALYSIS

5.5.6.1 Commutator Unbalance Current Correction

In the ESP and AESP commutators, transistor switches connect each analog output voltage, which represents either a spacecraft voltage, temperature, or current, with a common commutator line connected to the input of one of two analog to digital converters. A bootstrap unloader is connected to this common line to reduce the stray capacitance, equalize the load impedance, and provide bias current for the commutator and master switches. Since the bias current required for the commutator and master switches is not exactly equal, a difference or unbalance current exists, which is delivered to, or must be supplied by, the telemetry circuit being commutated. The magnitude of the error in each telemetry channel due to unbalance current is a function of the unbalance current at the time of commutation and the telemetry channel's output impedance.

The unbalance current for a specific telemetry channel in the ESP and in the AESP commutators is measured and commutated in modes 2, 4, and 5. The telemetry plots of the unbalance current indicated that the approximate

current in mode 2 (Figure 5.5-1) was -4.5 microamperes (μa), in mode 4 was -3.1 μa, and in mode 5 (Figure 5.5-2) was -2.8 μa during the transit phase of the mission. The change in current between modes 2 and 4 is caused by internal ESP load changes and is listed on the SC-1 signature list (Reference 1) as follows:

> S-5, Commutator Unbalance Current, Variations
>
> There is approximately a 1 to 1.5 microamp change in unbalance current in going from Mode 4 to Mode 2 (2 microamps versus 3.2 microamps), and a variation of approximately 0.5 microamps within the same mode.

The AESP mode 5 unbalance current initially read -2.0 μa at launch, but there was no good data from launch to L + 15 minutes. After that period, the current increased to -2.8 μa. It was noted that each time the unit was turned off, the magnitude of unbalance current at unit turnon was less than -2.8 μa. This is particularly evident at mission times 1 hour and 65 hours. This is attributed to unit warmup, and a similar condition existed during the STV test phases.

In order to fully correct the telemetry data for unbalance current effects, it is necessary to know the value of the unbalance current for each word in each commutator. This can be done by knowing the relationship of the unbalance current for each word to that commutated telemetered unbalance current. This can be shown as a correction to be applied to the telemetered unbalance current in Reference 2, determined from unit FAT data. The output impedance of each channel, used to determine the nominal unbalance current correction, is shown in Table 5.5-2.

Automatic Corrections Incorporated in EDRS Program

The engineering data reduction program utilizes the commutated value of unbalance current, multiplied by the appropriate output resistance, to correct for offset errors caused by unbalance current in the other telemetry channels. Several approximations, which affect the accuracy of these corrections, are made to simplify this program. The first approximation was that the commutated value of unbalance current was the same for each commutator switch. Unit test data for the SC-1 units indicates that the unbalance current for certain commutator switches may be as much as -3.9 to 4.5 μa offset from the commutated value. For telemetry channels with a high output impedance (50 K ohms), this approximation could result in a worst-case correction error of 46 decimal counts.

The second approximation was the assumption that the output impedance of each telemetry signal was a pure resistance. The majority of the flight control telemetry channels output circuits (see Table 5.5-2) are a parallel combination of a resistor and capacitor. A typical circuit, such as FC-16 (pitch gyro error), has a resistance of 27.5 K in parallel with a capacitance of 2.7 μf. At the high telemetry data rates of 4400, 1100, and 550 bits/sec, the output capacitor will tend to nullify the effects of the unbalance current.

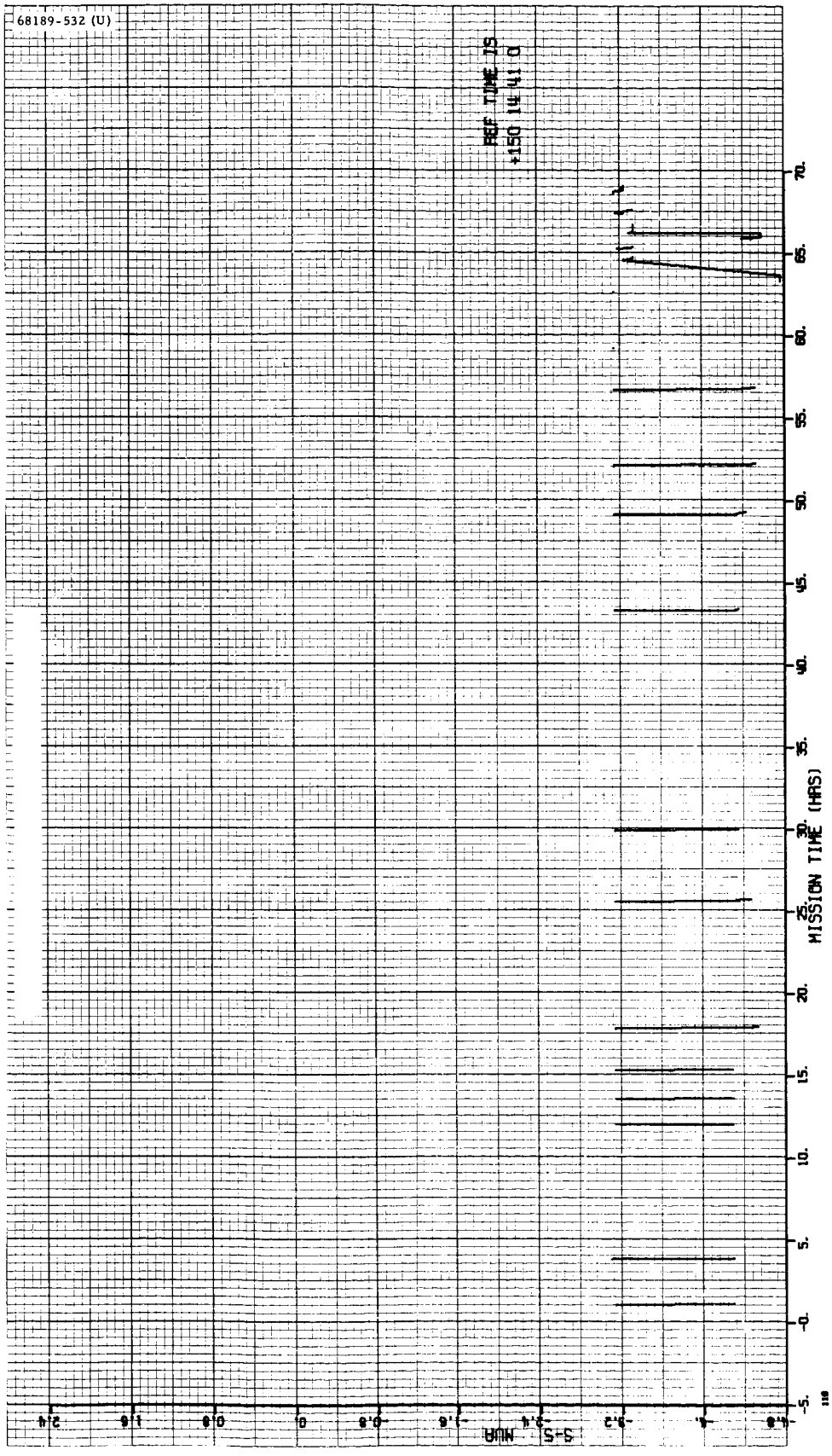


Figure 5.5-1. ESP Commutator Unbalance Current

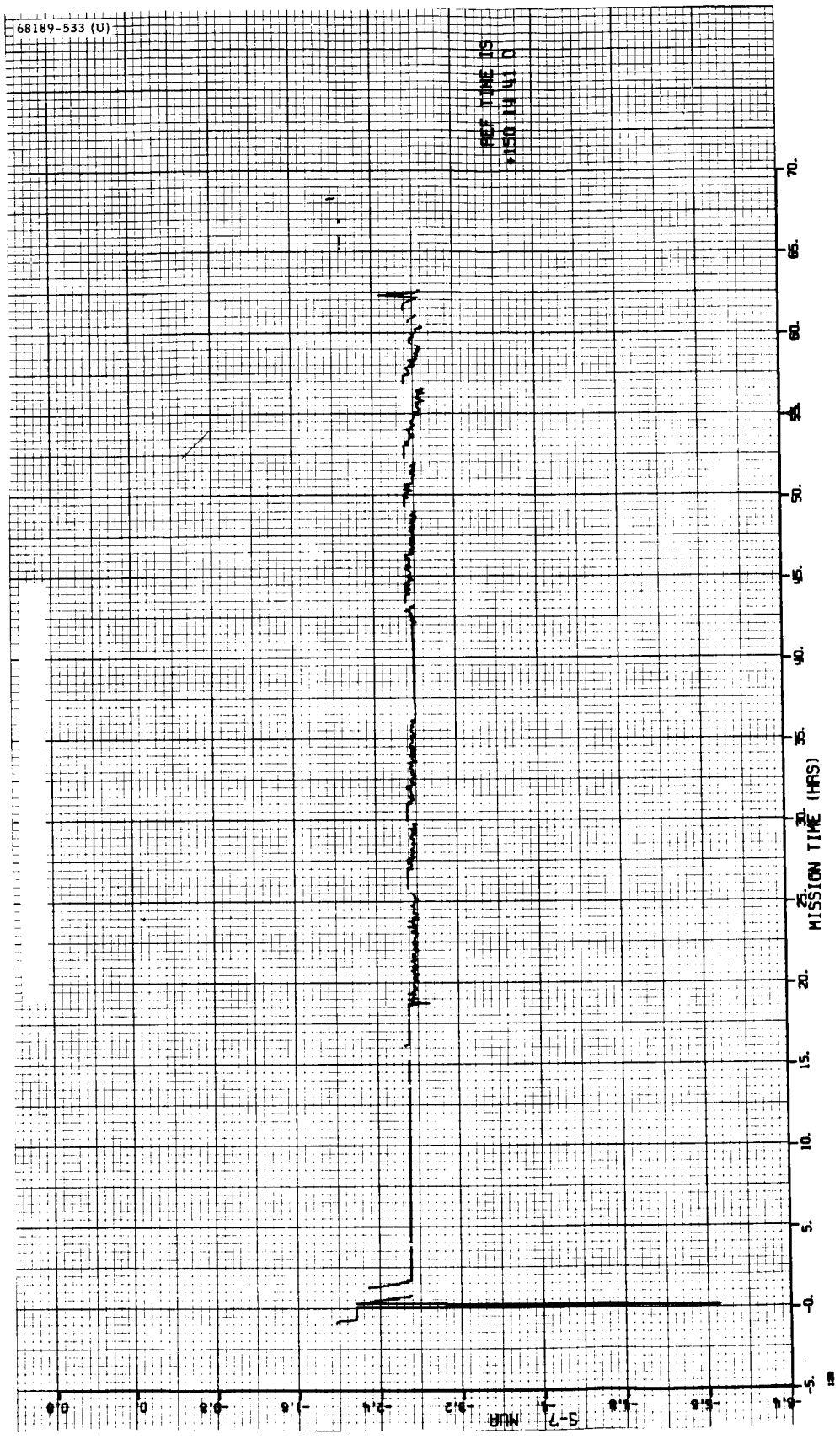


Figure 5.5-2. AESP Commutator Unbalance Current

Correcting for the offset error, without considering the output capacitor, will introduce an error of approximately 16 decimal counts for this telemetry channel.

TABLE 5.5-2. DATA CHANNEL OUTPUT IMPEDANCES

Subsystem	Output Impedance for Analog Telemetry Channels	
	Resistance, ohms	Capacitance, μf
Data Link (D)		
1. Omnidirectional antenna A transmitted power	50	–
3. Omnidirectional antenna B transmitted power	50	–
7. Static phase error A	800	–
8. Static phase error B	800	–
9. Receiver A AGC	11 K	4.7
10. Receiver B AGC	11 K	4.7
13. Transmitter A temperature	700 at 100°C	
14. Transmitter B temperature	1000 at 250°C	
16. Receiver A AFC	4.7 K	1
17. Receiver B AFC	4.7 K	1
Electrical Power (EP)		
1. 29 volt nonessential voltage	2.55 K	–
2. Unregulated bus voltage	4.125 K	–
3. Main battery manifold pressure	≥2 K	–
4. Unregulated output current	<40	
5. Main battery voltage	4.166 K	–
6. Battery charge current	<40	–

Table 5.5-2 (continued)

Subsystem	Output Impedance for Analog Telemetry Channels	
	Resistance, ohms	Capacitance, μf
Electrical Power (EP) (Cont)		
7. Boost regulator difference current	<40	–
8. Main battery temperature	700 at 100°C, 1000 at 250°C	
9. Battery discharge current	<40	–
10. Solar cell array voltage	2.37 K	–
11. Solar cell array current	<40	–
12. Solar cell array temperature	700 at 100°C, 1000 at 250°C	
13. Boost regulator temperature	700 at 100°C, 1000 at 250°C	
14. Regulated output current	<40	
16. Optimum charge regulator output current	<40	–
17. RADVS and squib current	<40	–
18. Full scale current calibration (ESP)	–	–
19. Midscale current calibration (ESP)	–	–
20. Zero scale current calibration (ESP)	–	
21. Compartment A heater current	<40	
22. Compartment B heater current	<40	

Table 5. 5-2 (continued)

Subsystem	Output Impedance for Analog Telemetry Channels	
	Resistance, ohms	Capacitance, μf
Electrical Power (EP) (Cont)		
23. Auxiliary battery voltage	4. 166 K	
24. Solar cell string No. 4 current	<40	
25. Solar cell string No. 6 current	<40	
26. Auxiliary battery temperature	<40	
27. Full scale current calibration (AESP)	<40	
28. Midscale current calibration (AESP)	<40	
29. Zero scale current calibration (AESP)	<40	
30. Boost regulator preregulated voltage	2. 55 K	
34. Battery charge regulator temperature	700 at 100°C, 1000 at 250°C	
Flight Control (FC)		
4. Nitrogen gas pressure	≤1. 65 K	–
5. Primary sun sensor pitch error	15. 2 K	10
6. Primary sun sensor yaw error	15. 2 K	10
7. Secondary sun sensor cell A		
8. Secondary sun sensor cell B		

Table 5.5-2 (continued)

Subsystem	Output Impedance for Analog Telemetry Channels	
	Resistance, ohms	Capacitance, μf
Flight Control (FC) (Cont)		
9. Secondary sun sensor cell C		
10. Secondary sun sensor cell D		
12. Canopus error	25.5 K	10
14. Star intensity signal	50 K	10
15. Acceleration error	21.6 K	0.68
16. Pitch gyro error	27.5 K	2.7
17. Yaw gyro error	27.5 K	2.7
25. Thrust command to vernier engine No. 1	42.5 K	0.68
26. Thrust command to vernier engine No. 2	42.5 K	0.68
27. Thrust command to vernier engine No. 3	42.5 K	0.68
32. Retro accelerometer	5 K	
35. Radar altimeter range signal	44.6 K	10
39. Doppler velocity V_x	31.2 K	10
40. Doppler velocity V_y	31.2 K	10
41. Doppler velocity V_z	44.6 K	10
43. Roll actuator signal	20 K	10
44. Flight control electronics unit temperature No. 1	700 at 100°C 1000 at 250°C	

Table 5.5-2 (continued)

Subsystem	Output Impedance for Analog Telemetry Channels	
	Resistance, ohms	Capacitance, μf
Flight Control (FC) (Cont)		
45. Flight control electronics unit temperature No. 2	700 at 100°C 1000 at 250°C	
46. Roll gyro temperature	No effect	
47. Canopus sensor temperature	700 at 100°C 1000 at 250°C	
48. Nitrogen gas tank temperature	700 at 100°C 1000 at 250°C	
49. Roll precession command	78 K	3.9
50. Pitch precession command	78 K	3.9
51. Yaw precession command	78 K	3.9
53. Secondary sun sensor centercell		
54. Pitch gyro temperature	51.1 K	
55. Yaw gyro temperature	No effect	
70. Attitude gas jet No. 2 temperature	700 at 100°C 1000 at 250°C	
71. Roll actuator temperature	700 at 100°C 1000 at 250°C	
Mechanisms (M)		
3. Solar panel position	≤525	
4. Polar axis position	<510	
6. Elevation axis position	<525	

Table 5.5-2 (continued)

Subsystem	Output Impedance for Analog Telemetry Channels	
	Resistance, ohms	Capacitance, uf
Mechanisms (M) (Cont)		
7. Roll axis position	<525	
8. Planar array temperature	700 at 100°C 1000 at 250°C	
10. Solar panel stepping motor temperature	700 at 100°C 1000 at 250°C	
12. Elevation axis stepping motor temperature	700 at 100°C 1000 at 250°C	
Propulsion (P)		
1. Helium pressure	< 1.65 K	–
2. Oxidizer pressure No. 3	<525	–
3. Upper retro case temperature	700 at 100°C 1000 at 250°C	
4. Vernier lines No. 2 temperature		
5. Vernier fuel tank No. 2 temperature		
6. Vernier oxidizer tank No. 3		
7. Vernier engine No. 1 temperature		
8. Vernier lines No. 1 temperature		
9. Vernier lines No. 3 temperature		
10. Vernier engine No. 2 temperature		

Table 5.5-2 (continued)

Subsystem	Output Impedance for Analog Telemetry Channels	
	Resistance, ohms	Capacitance, μf
Propulsion (P) (Cont)		
11. Vernier engine No. 3 temperature	700 at 100°C 1000 at 250°C	
12. Lower retro case temperature		
13. Vernier fuel tank No. 1 temperature		
14. Vernier fuel tank No. 3 temperature		
15. Vernier oxidizer tank No. 1 temperature		
16. Vernier oxidizer tank No. 2 temperature		
17. Helium tank temperature		
18. Vernier engine No. 1 strain gage	350	
19. Vernier engine No. 2 strain gage		
20. Vernier engine No. 3 strain gage		
22. Retro nozzle temperature	700 at 100°C 1000 at 250°C	
Radar (R)		
2. RADVS – R amplitude	11.7 K	10
3. RADVS – D_1 amplitude	11.7 K	10
4. RADVS – D_2 amplitude	11.7 K	10

Table 5.5-2 (continued)

Subsystem	Output Impedance for Analog Telemetry Channels	
	Resistance, ohms	Capacitance, μf
Radar (R) (Cont)		
5. RADVS – D_3 amplitude	11.7 K	10
6. Altitude marking radar antenna temperature No. 1 (back of dish)	700 at 100°C 1000 at 250°C	
7. Altitude marking radar electronics temperature		
8. Altimeter and doppler klystron unit temperature		
9. Radar signal data converter temperature		
10. Doppler radar sensor temperature		
12. Altitude marking radar power output (mag. current)	30 K	1
13. Altimeter radar sensor temperature	700 at 100°C 1000 at 250°C	
14. Altitude marking radar AGC	50	1
27. Altitude marking radar antenna temperature No. 2	700 at 100°C 1000 at 250°C	
29. AMR late gate signal	2.7 K	
Signal Processing (S)		
1. Reference voltage		
2. Reference voltage		
5. Commutator unbalance current (ESP)		
7. Commutator unbalance current (AESP)		

Table 5.5-2 (continued)

Subsystem	Output Impedance for Analog Telemetry Channels	
	Resistance, ohms	Capacitance, μf
Survey Television Camera (TV)		
16. Survey camera electronics temperature	700 at 100°C 1000 at 250°C	
17. Survey camera mirror assembly temperature		
Approach Television Camera (T)		
1. Approach camera vidicon faceplate temperature	700 at 100°C 1000 at 250°C	
3. Approach camera electronics temperature		
Vehicle (V)		
5. Landing gear No. 1 deflection	<656	
6. Landing gear No. 2 deflection		
7. Landing gear No. 3 deflection		
15. Compartment A temperature thermal tray top	700 at 100°C 1000 at 250°C	
16. Compartment A temperature lower support		
17. Compartment A temperature insulated retainer		
18. Compartment A temperature canister		
19. Compartment A temperature switch No. 5 in contact ring		
20. Compartment A temperature switch No. 5 in face radiator		

Table 5. 5-2 (continued)

Subsystem	Output Impedance for Analog Telemetry Channels	
	Resistance, ohms	Capacitance, μf
Vehicle (V) (Cont)		
21. Compartment B temperature tray top center	700 at 100° C 1000 at 250° C	
22. Compartment B temperature lower support		
23. Compartment B temperature canister		
24. Compartment B temperature switch No. 4 in face radiator		
25. Compartment A temperature switch No. 8 in face radiator		
26. Compartment B temperature switch No. 4 in contact ring		
27. Upper spaceframe temperature No. 1		
28. Lower spaceframe temperature under compartment B		
29. Wiring harness temperature thermal tunnel		
30. Shock absorber No. 1 temperature		
31. Leg No. 2 upper web temperature		
32. Shock absorber No. 2 temperature		
33. Shock absorber No. 3 temperature		

Table 5.5-2 (continued)

Subsystem	Output Impedance for Analog Telemetry Channels	
	Resistance, ohms	Capacitance, μf
Vehicle (V) (Cont)		
34. A/SP mast temperature	700 at 100° C 1000 at 250° C	
35. Upper spaceframe temperature No. 2		
36. Lower spaceframe temperature under compartment A		
37. Retro attach point No. 1 temperature		
38. Retro attach point No. 2 temperature		
39. Retro attach point No. 3 temperature		
44. Crushable block temperature		
45. Compartment B temperature switch No. 1 in face radiator		
46. Compartment B temperature switch No. 5 in face radiator		
47. Compartment A temperature switch No. 2 in face radiator		
48. Auxiliary battery compartment temperature bottom outside		

The third approximation was that all temperature channels had an average output impedance of 700 ohms, which corresponds to a temperature value of 217°F. Since 98 percent of the spacecraft temperatures are below 120°F, an approximation of 600 ohms or less is more accurate. The error here, however, is negligible.

The following changes to the engineering data reduction program for unbalance current corrections are recommended:

1) The temperature channels should not be corrected for unbalance current offsets. With a 6 μa unbalance current, the maximum uncorrected unbalance current error is 3.6 millivolts, or less than one decimal count.

2) Telemetry channels that have an output circuit of a parallel resistor and capacitor, with an RC time constant greater than 20 milliseconds, should not be corrected. The uncorrected unbalance current error is less than the present correction error when the capacitor is ignored at the three high data rates.

3) Some provision should be made in the program for specifying the unbalance current for each individual commutator switch as a function of the commutated value of unbalance current.

Procedure for Applying Unbalance Current Corrections

A method for more completely correcting for commutator unbalance current has been developed by M. R. Weiner (Reference 2). This method is intended for use where required for nonreal time, postflight data analysis. It includes the following.

1) A method for determining for each channel whether it is necessary to correct for unbalance current.

2) A method for hand calculating the correction for telemetry channels having an output impedance that is either all resistive or a parallel combination of a resistor and a capacitor.

3) A computer program for correcting those channels having an output impedance consisting of a parallel combination of a resistor and a capacitor.

The computer program has been used to correct data from SC-1 STV tests with very good results.

From the above procedures, Tables 5.5-3 and 5.5-4 have been prepared. These tables indicate the ratio of the correction factor (assuming 6 μa and 12 μa of unbalance current, respectively) to the total telemetry error for each voltage channel at each bit rate. The ratio shown is that obtained at full scale where the offset voltage is greatest and the total error percentage is minimum. Thus, those channels where the correction factor

TABLE 5.5-3. OFFSET VOLTAGE CORRECTIONS COMPARED TO TOTAL ERROR FOR 6 μa UNBALANCED CURRENT

Channels	Bit Rates, bits/sec									
	4400		1100		550		137.5		17.2	
	1:10	1:5	1:10	1:5	1:10	1:5	1:10	1:5	1:10	1:5
Gyro-pitch, yaw (FC-16, FC-17)	X	X	X	X	X	X				
Precession command (FC-49, FC-50, FC-51)		X		X		X				
Primary sun sensor (FC-5, FC-6)	X	X	X	X	X	X	X	X	X	X
Canopus error (FC-12)	X	X	X	X	X	X	X	X		
Star intensity (FC-14)	X	X	X	X	X	X	X	X		
Secondary sun sensor center cell (FC-53)										
Acceleration error (FC-15)	X	X		X						
Retro accelerometer (FC-32)	X	X	X	X	X	X	X	X	X	X
Roll actuator (FC-43)	X	X	X	X	X	X		X		
Radar altimeter (FC-35)										
Doppler– V_x, V_y (FC-39, FC-40)										
Doppler– V_z (FC-41)										
Vernier engine thrust command (FC-25, FC-26, FC-27)	X	X	X	X		X				
Vernier engine strain gages (P-18, P-19, P-20)	Negligible influence									
Regulated voltage (EP-1) at 29 volts										
Unregulated voltage (EP-2) at 22 volts										
Main battery voltage (EP-5) at 22 volts										
Solar cell array volt (EP-10) at 50 volts										
Auxiliary battery voltage (EP-23) at 22 volts										
Boost regulator preregulated voltage										
Voltage (EP-30) at 30 volts										
A/SPP readout potentiometer										
N_2 pressure (FC-4)	X	X	X	X	X	X	X	X	X	X
Helium pressure (P-1)	X	X	X	X	X	X	X	X	X	X
Manifold pressure (P-2)	X	X	X	X	X	X	X	X	X	X
Main battery pressure (EP-3)	X	X	X	X	X	X	X	X	X	X
Landing gear deflection (V-5, V-6, V-7)										
Receiver AFC (D-16, D-17)										
Repeatability										
Receiver AGC (D-9, D-10)										
Repeatability	X	X		X		X				

Note: Xs denote conditions where ratio of offset voltage correction to total channel error is $\leq$ 1:10 or $\leq$ 1:5 as indicated.

TABLE 5.5-4. OFFSET VOLTAGE CORRECTIONS COMPARED TO TOTAL ERROR FOR 12 μa UNBALANCED CURRENT

Channels	Bit Rates, bits/sec									
	4400		1100		550		137.5		17.2	
	1:10	1:5	1:10	1:5	1:10	1:5	1:10	1:5	1:10	1:5
Gyro-pitch, yaw (FC-16, FC-17)	X	X	X	X		X				
Precession command (FC-49, FC-50, FC-51)										
Primary sun sensor (FC-5, FC-6)	X	X	X	X	X	X	X	X		X
Canopus error (FC-12)	X	X	X	X	X	X		X		
Star intensity (FC-14)		X		X		X		X		
Secondary sun sensor center cell (FC-53)										
Acceleration error (FC-15)		X								
Retro accelerometer (FC-32)										
Roll actuator (FC-43)	X	X	X	X	X	X				
Radar altimeter (FC-35)										
Doppler – V_x, V_y (FC-39, 40)										
Doppler – V_z (FC-41)										
Vernier engine thrust command (FC-25, FC-26, FC-27)	X	X		X						
Vernier engine strain gages (P-18, P-19, P-20)				Negligible influence						
Regulated voltage (EP-1) at 29 volts										
Unregulated voltage (EP-2) at 22 volts										
Main battery voltage (EP-5) at 22 volts										
Solar cell array volt (EP-10) at 50 volts										
Auxiliary battery voltage (EP-23) at 22 volts										
Boost regulator preregulated voltage (EP-30) at 30 volts										
A/SPP readout potentiometer										
N_2 pressure (FC-4)		X		X		X		X		X
Helium pressure (P-1)	X	X	X	X	X	X	X	X	X	X
Manifold pressure (P-2)	X	X	X	X	X	X	X	X	X	X
Main battery pressure (EP-3)		X		X		X		X		X
Landing gear deflection (V-5, V-6, V-7)										
Receiver AFC (D-16, D-17)										
Repeatability										
Receiver AGC (D-9, D-10)										
Repeatability		X								

Note: Xs denote conditions where ratio of offset voltage correction to total channel error is $\leq$ 1:10 or $\leq$ 1:5 as indicated.

is less than 1/5 or 1/10 of the total error need not be corrected as the correction will not significantly improve the overall accuracy. In addition, to those indicated in these tables, none of the current channels need be corrected as their output impedances are very small (see Table 5.5-2).

5.5.6.2 Potentiometer Reference Voltage

The 4.85 volt reference voltage is supplied by either the ESP or AESP units to the landing gear and solar panel position potentiometers, to the helium and oxidizer pressure transducers, and to the secondary sun sensors. This reference voltage, which is derived from the 29 volt nonessential bus, varies due to load and input supply voltage changes. The values of the ESP reference voltage and return is telemetered in modes 2 and 4 to increase the accuracy of the channels using this voltage. Since the value of the AESP reference voltage is not telemetered, it is necessary to compute its value and apply the necessary corrections to the telemetry signals.

The method used to compute the difference between the ESP and AESP reference voltage was to record the raw count telemetry value for signals M-3 (solar panel position), M4 (polar axis position),and M7 (roll axis position) when commutated in mode 4 (ESP) and mode 5 (AESP). The data taken during an engineering interrogation prior to midcourse was used for this purpose. At that time, the antenna solar panel was in the transit pinned position and thus should be constant. Table 5.5-5 gives the data recorded and computations.

From the calculations, it can be concluded that the AESP reference voltage is approximately 10 decimal counts or 48.8 millivolts greater than the ESP reference voltage. This correction should be applied to all AESP telemetry channels that use the reference voltage.

Data plots of the ESP reference voltage (Figure 5.5-3) and return (Figure 5.5-4) indicate normal operation throughout the mission. An increase of approximately 15 millivolts in the ESP reference voltage was noted when switching from mode 2 to mode 4. The SC-1 signature list states, "S1 (Pot Ref. Volt) will change 20 to 35 mv in going from Mode 2 to Mode 4 due to internal ESP loading changes."

The ESP reference return voltage was less than 10 millivolts throughout the mission. Some variations due to load changes at terminal descent were noted, but these are considered normal when the AMR is commanded on.

5.5.6.3 Current Calibration Signals

Current measurements are accomplished by measuring the voltage drop across a low resistance shunt which is in series with the power line being monitored. This measurement is in the range of 0 to 100 millivolts. Since this voltage is not referenced to ground and is not scaled to the 0 to 5 volt telemetry input level range, it is necessary to amplify it with a differential amplifier. The nominal gain of this amplifier is 50, but its actual

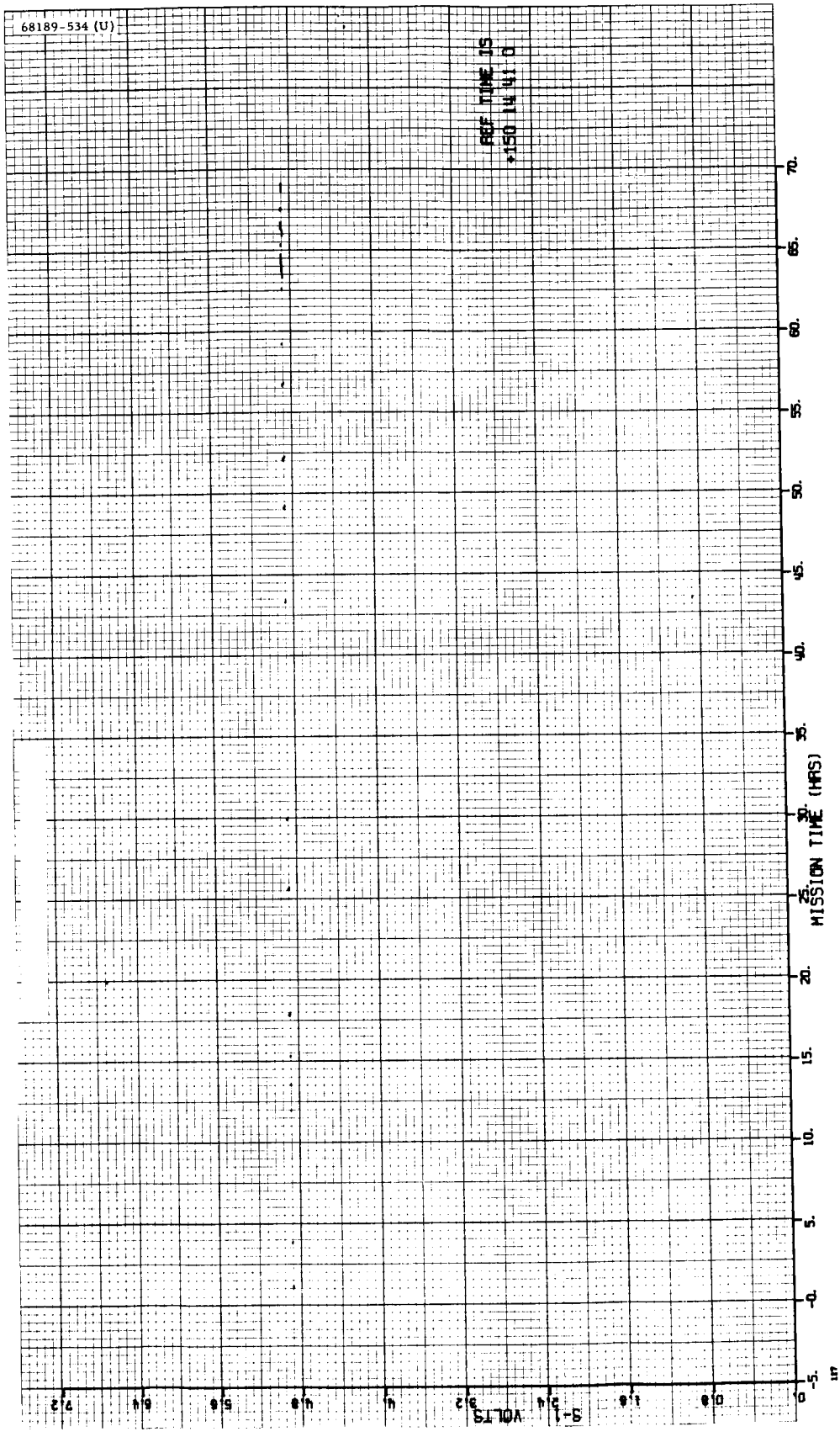


Figure 5.5-3. Reference Voltage

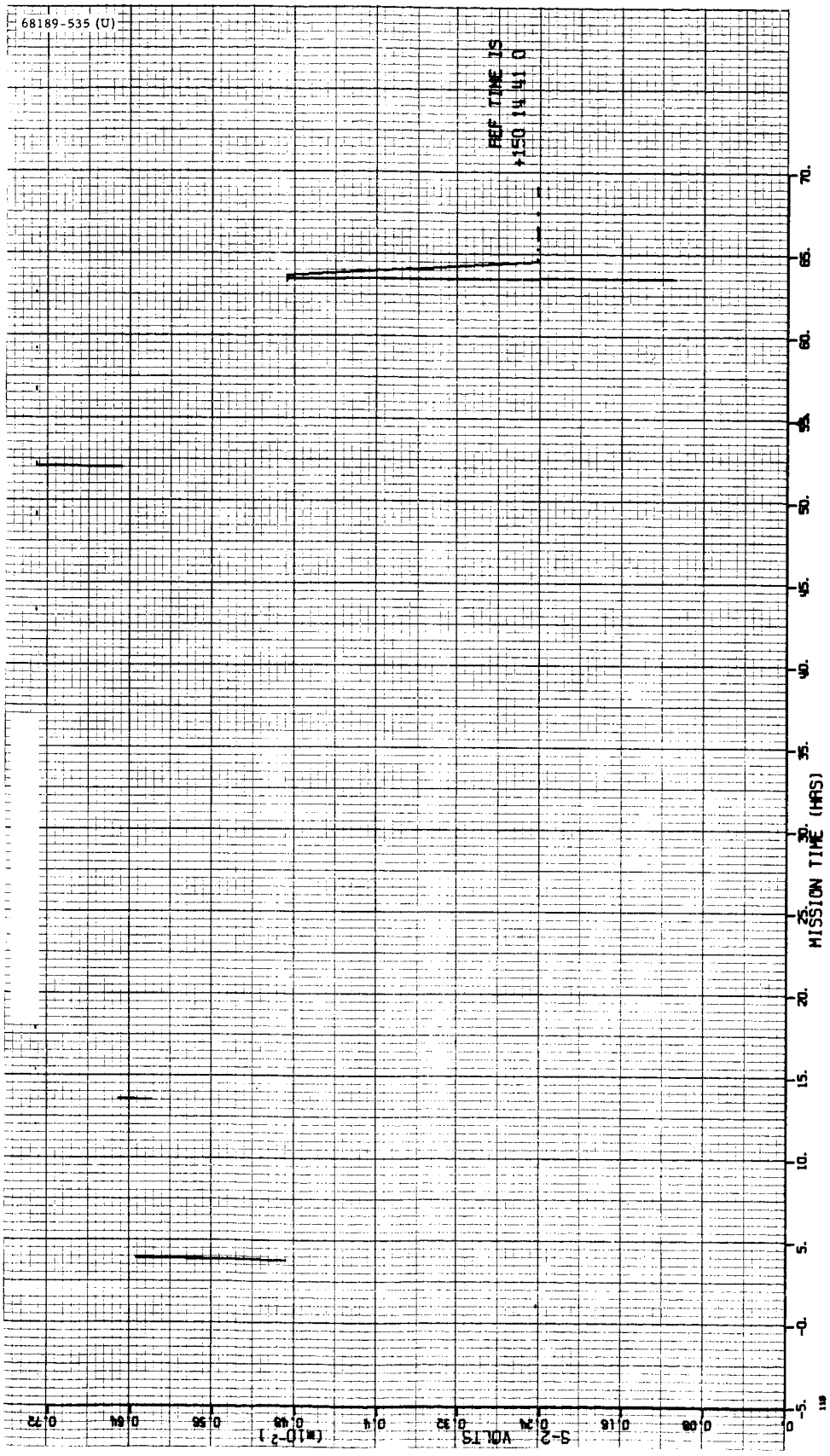


Figure 5.5-4. Potentiometer Reference Return

TABLE 5.5-5. COMPARISON OF MECHANISM SIGNALS IN ESP AND AESP COMMUTATORS

Time, GMT	Mode	Signal	Telemetry Value
151:6:1:25	4	M-3	760
		M-4	353
		M-7	491
		S-1 reference voltage	1001
151:6:1:6	5	M-3	768
		M-4	357
		M-7	496

Let X = AESP reference voltage

Then

$$\frac{760}{1001} = \frac{768}{X} \quad \text{and} \quad \frac{353}{1001} = \frac{357}{X} \quad \text{and} \quad \frac{491}{1001} = \frac{496}{X}$$

$$X = 1011.5 \qquad X = 1012.3 \qquad X = 1011.2$$

gain linearity and stability are not specified to a tight tolerance. To determine these parameters of the current amplifier and thus increase the accuracy of the current measurements, three calibration signals, which have a specified stability of 0.2 percent, are individually amplified and commutated by the telemetry system. The data reduction program uses these telemetered calibration values to define the computer coefficients for the current measurement channels for each frame of data.

Telemetry plots of these calibration values indicate that the gain of the current amplifiers in the ESP and AESP remained essentially constant throughout the transit phase of the SC-1 mission. The average telemetered ranges of values for these calibration signals are given in Table 5.5-6. Some noise was detected on these calibration signals, and an investigation of the extent of the variations was completed for the time period beginning on 151:14:41:02 GMT and ending on 151:14:56:00 GMT. The data indicated that EP-27 was constant at a decimal count of 920, EP-28 was constant at a count

TABLE 5.5-6. AVERAGE VALUE OF CURRENT CALIBRATION SIGNALS

Signal, millivolts	Telemetry Range, millivolts
EP-18 current calibration (90) ESP	90.9 ± 0.2
EP-19 current calibration (50) ESP	50.6 ± 0.2
EP-20 current calibration (10) ESP	10.3 ± 0.2
EP-27 current calibration (90) AESP	90.7 ± 0.2
EP-28 current calibration (50) AESP	50.7 ± 0.2
EP-29 current calibration (10) AESP	10.6 ± 0.2

of 513 with a jump to 515 every ten or twenty data points, and EP-29 was varying between a count of 105 and 108. These variations are attributed to system noise and are listed on the SC-1 Signature List (Reference 1) as follows:

> EP-18, 19, 20, 27, 28, 29, Current Calibration Signals, Variations
>
> Variations of 3 to 5 BCD have been noted on all of the current calibration signals (ESP as well as AESP) during the SC-1 STV test phases when the transmitter was operating in low power and thrust phase power was not on. Variations of up to 7 BCD have also been seen during transmitter high-power operation.

The variations in the output level of the current calibration during the transit phase indicate that, without any correction for the current amplifiers' gain, the error of the current readings would be ±0.2 percent of full scale. The present data reduction program updates the coefficients for the current measurement channels each data frame. Since the long-term gain of this amplifier is constant, it is recommended that the program be modified to update the current measurement coefficients once immediately after commutator turn on and once every hour following turn on.

5.5.6.4 Temperature Measurement Errors at 4400 Bits/Sec Data Rate

The errors in temperature signals at 4400 bits/sec data rate result from insufficient settling time for the constant current source used for these measurements. The output capacitor on the constant current source, when it is unloaded, charges to a value of approximately 6.8 volts. At the high data rate, this voltage does not reach the correct value by the time the particular temperature channel is sampled. These errors may be partially corrected in the manner described in the following paragraph.

The basic accuracy temperature channels can be grouped into two categories when considering measurement accuracies at 4400 bits/sec. The first group, listed in Table 5.5-7, contains those measurements which will have errors only if the preceding temperature measurement (as indicated in the table) is substantially different. These errors are roughly 10 percent of the difference in the two temperatures and in the direction of the earlier measurement; i.e., it can be a positive or negative error. The second group, listed in Table 5.5-8, contains those measurements which will always have significant positive errors at 4400 bits/sec. The amount of the error is a function of the transmitted digital value as well as various circuit parameters. Table 5.5-9 lists the range of the true value in BCD as a function of the transmitted value in BCD. Also, the approximate errors in degrees Fahrenheit have been computed (using a nominal scale factor of 0.9°F/bcd).

5.5.6.5 Telemetry Bit Stream Characteristics

To retrieve the maximum amount of reliable telemetry information from the spacecraft, it is necessary to understand the characteristics of the telemetry bit stream during periods when the commutator mode or the telemetry bit rate is changed. Erroneous telemetry data may be processed at these times, and it must be disregarded.

When the ESP or AESP commutator is turned off in order to switch to the other commutator, the power supply voltages will not settle to zero voltage until approximately 10 milliseconds after the acceptance of the off command. During this period, the commutator output will be unreliable. Therefore, the last word of data at 17.2, 137.5, or 550 bits/sec, the last two words of data at 1100 bits/sec, and the last five words at 4400 bits/sec should be rejected. When the commutator is completely off, the telemetry bit stream should contain data words that have a value of approximately zero counts.

If a different mode on the same commutator is selected, with the exception of mode 3, a maximum of two data words may be affected during the mode change. The exact transition point can be determined by comparing each word in the commutator frame during which the mode change took place with the corresponding word in the preceding and following commutator frames. Switching modes will not affect the commutator word counter.

Since mode 3 has a 50 word commutator frame and modes 1, 2, and 4 have 100 word frames, several abnormal conditions may exist when switching to mode 3. If the commutator word count is less than 48 at mode change, a maximum of two data words may be affected at transition, and then the commutator would process mode 3 data with no interruption of the word counter. If the commutator word count is greater than 48 and less than 89, the word counter will continue to count to word 88 and then jump to word 39. The information that will be commutated from word 49 to 88 is listed in Table 5.5-10. At word 39, normal mode 3 data will be commutated. If the commutator word count is greater than 89 and less than 98, the word counter will continue to count to word 98 and then return to word 00. The information

TABLE 5.5-7. TEMPERATURE MEASUREMENTS INFLUENCED BY PRECEDING TEMPERATURE MEASUREMENT AT 4400 BITS/SEC

Temperature Measurement Affected			Preceding Temperature Measurement	
	Signal	Word	Signal	Word
Mode 1				
	P-9	82	P-22	80
	R-27	26	FC-45	24
	V-44	46	FC-47	44
Mode 2				
	EP-26	78	P-14	76
	P-3	68	P-5	66
	P-5	66	R-7	64
	P-6	86	P-16	84
	P-12	88	P-6	86
	P-13	56	R-6	54
	R-13	96	R-10	94
	V-32	58	P-13	56
Mode 4				
	EP-8	4	D-13	2
	EP-13	10	EP-12	8
	M-8	14	D-14	12
	M-12	64	V-28	62
	P-17	20	FC-48	18
	TV-16	16	M-8	14
	V-16	26	V-15	24
	V-18	30	V-17	28
	V-20	36	V-19	34
	V-22	46	V-21	44
	V-26	54	V-24	52
	V-27	56	V-26	54
	V-29	66	M-12	64
	V-33	76	V-35	74
	V-36	96	FC-44	94
	V-37	84	V-34	82
	V-38	86	V-37	84
Mode C				
	D-13	10	V-32	8
	D-14	30	P-12	28
	EP-8	42	FC-45	40
	EP-12	36	V-24	34
	EP-13	20	R-8	18
	EP-26	96	V-25	94
	EP-34	46	M-10	44

Table 5.5-7 (continued)

Temperature Measurement Affected			Preceding Temperature Measurement	
	Signal	Word	Signal	Word
Mode C (cont)				
	FC-45	40	M-8	38
	FC-47	48	EP-34	46
	FC-48	82	R-27	80
	FC-70	102	P-22	100
	FC-71	104	FC-70	102
	M-8	38	EP-12	36
	M-10	44	EP-8	42
	P-4	6	P-13	4
	P-6	56	P-14	54
	P-8	88	P-17	86
	P-9	84	FC-48	82
	P-10	50	FC-47	48
	P-11	60	V-21	58
	P-12	28	R-7	26
	P-13	4	P-16	2
	P-14	54	V-31	52
	P-15	92	V-44	90
	P-17	86	P-9	84
	R-7	26	R-13	24
	R-8	18	T-3	16
	R-9	22	EP-13	20
	R-10	76	V-22	74
	R-13	24	R-9	22
	R-27	80	V-16	78
	T-3	16	V-28	14
	TV-17	116	V-47	114
	V-15	66	V-18	64
	V-16	78	R-10	76
	V-18	64	V-29	62
	V-20	32	D-14	30
	V-21	58	P-6	56
	V-22	74	V-38	72
	V-24	34	V-20	32
	V-25	94	P-15	92
	V-27	12	D-13	10
	V-28	14	V-27	12
	V-29	62	P-11	60
	V-31	52	P-10	50
	V-32	8	P-4	6
	V-38	72	P-7	70
	V-44	90	P-8	88

Table 5.5-7 (continued)

Temperature Measurement Affected			Preceding Temperature Measurement	
	Signal	Word	Signal	Word
Mode C (cont)				
	V-45	108	V-48	106
	V-47	114	V-46	112
	V-48	106	FC-71	104
Mode T				
	None			

that will be commutated from word 89 to 98 is listed in Table 5.5-10. During the terminal descent phase of the SC-1 mission when the commutator mode was switched from 2 to 3, the transition occurred at commutator word 64 at 06:15:59.506 GMT.

The normal sequence for changing the telemetry from a high to low data rate is: the low data rate is selected, the high data rate subcarrier oscillator is turned off, and the low data rate SCO is turned on. During the interval beginning at the execution of the first command and ending at the execution of the third command, a period of 1 second, all data will be lost. It will then be necessary to obtain decommutator lock before the data will be meaningful.

When the telemetry data rate is changed from a low to high data rate the command sequence is: the low data rate subcarrier oscillator is turned off, the high data rate subcarrier oscillator is turned on, and the high data rate is selected. For a period of 1 second, all data will be lost. Since only five data rate changes were commanded during the SC-1 mission, the telemetry data lost is negligible.

5.5.6.6 Analog to Digital Conversion Accuracy

Since it is impossible to quantitatively evaluate the accuracy of the analog to digital converters without making hardline measurements, a comparison was made of the telemetered value of three current amplifier calibration signals (EP-27, -28 and -29), using each of the two analog to digital converters. These three signals were selected because they were stable throughout the mission, and they range in value from 0.5 to 4.5 volts. The period chosen for the comparison was during the postlanding engineering

TABLE 5.5-8. TEMPERATURE MEASUREMENTS THAT WILL HAVE SIGNIFICANT POSITIVE ERRORS AT 4400 BITS/SEC

ESP					
Mode 1		Mode 2		Mode 4	
Signal	Word	Signal	Word	Signal	Word
FC-45	24	FC-46	60	D-13	2
FC-47	44	FC-54	20	D-14	12
P-4	2	FC-55	80	EP-12	8
P-8	52	P-7	24	EP-34	78
P-22	80	P-10	34	FC-44	94
		P-11	44	FC-48	18
		P-14	76	M-10	10
		P-15	82	V-15	24
		P-16	84	V-17	28
		R-6	54	V-19	34
		R-7	64	V-21	44
		R-8	38	V-23	48
		R-9	62	V-24	52
		R-10	94	V-25	38
		T-3	70	V-28	62
				V-30	68
				V-34	82
				V-35	74
				V-39	88

AESP		
Mode C		Mode T
Signal	Word	All temperatures in this mode
FC-46	68	
FC-54	110	
FC-55	98	
P-7	70	
P-16	2	
P-22	100	
V-46	112	

TABLE 5.5-9. LIMITS OF TRUE VALUES IN BCD AND APPROXIMATE TEMPERATURE ERROR FOR THOSE MEASUREMENTS LISTED IN TABLE 5.5-8

Transmitted Value, bcd	Range of True Value, bcd	Approximate Error, °F
1023	961-1023	0-56
1022	954-996	23-61
1020	944-991	26-68
1016	932-985	28-76
1008	914-976	29-85
1000	961-963	33-35
992	888-960	29-104
976	884-940	32-83
968	929-931	33-35
960	902-928	29-52
944	900-901	39-40
936	898-899	33-34
928	829-897	28-89
912	825-877	31-78
904	867-868	32-33
896	774-866	27-110
864	771-829	31-84
848	768-816	29-72
840	806-807	30-31
832	732-805	24-90
816	778-778	34-34
808	776-777	28-29
800	716-775	22-76
784	712-756	25-65
776	746-747	26-27
768	651-745	21-105
736	698-701	31-34
720	689-697	20-28
712	687-688	22-23
704	625-686	16-71
688	660-661	24-25
680	657-659	19-21
672	609-656	14-57
656	604-639	15-47
648	628-630	16-18
640	562-627	12-70
608	556-597	10-47
592	550-588	4-38
584	569-572	11-14
580	568-568	10-11
576	522-567	8-49
560	544-548	11-14
552	540-543	8-11

Table 5.5-9 (continued)

Transmitted Value, bcd	Range of True Value, bcd	Approximate Error, °F
548	538-539	8-9
544	504-537	6-36
532	523-524	7-8
528	497-522	5-28
520	495-514	5-23
516	508-509	6-7
512	442-507	4-63
480	468-473	6-11
472	465-467	4-6
468	463-464	3-5
466	462-462	3-4
464	456-461	3-7
460	455-455	4-5
457	454-454	2-3
456	440-453	2-14
452	439-449	2-12
450	447-447	2-3
448	419-446	2-26
440	435-435	4-5
436	432-434	2-4
434	431-431	2-3
432	415-430	2-15
428	425-425	2-3
Except for the following BCD values, all transmitted values less than 428 will have an error of no more than 2 bcd (2°F) at 4400 bits/sec.		
424	412-422	2-11
420	417-418	2-3
416	398-414	2-16
408	397-407	1-10
404	396-403	1-7
400	387-399	1-12
392	383-391	1-8
388	381-387	1-6
384	361-383	1-21
368	359-367	1-8
362	358-361	1-4
360	354-360	0-5
356	352-356	0-4
352	349-352	0-3
344	339-344	0-5
340	337-340	0-3
332	329-332	0-3
328	324-328	0-4
324	321-324	0-3
320	311-320	0-10
312	309-312	0-3
304	300-304	0-4
288	284-288	0-4
256	250-256	0-5

TABLE 5.5-10. COMMUTATOR TABLE FOR CHANGE FROM MODE 2 TO MODE 3

Commutator Word Number	Commutator Switch Number	Data Channel
49	—	(Full scale)
50	—	(Full scale)
51	4-13	FC-26
52	4-14	FC-27
53	4-15	FC-41
54	—	(Full scale)
55	—	(Full scale)
56	—	(Full scale)
57	4-12	FC-43
58	—	(Full scale)
59	4-16	FC-25
60	—	(Full scale)
61	4-13	FC-26
62	4-14	FC-27
63	4-15	FC-41
64	—	(Full scale)
65	—	DIG 4
66	—	(Full scale)
67	4-12	FC-43
68	—	(Full scale)
69	4-16	FC-25
70	—	DIG 4
71	4-13	FC-26
72	4-14	FC-27
73	4-15	FC-41
74	—	(Full scale)
75	—	DIG 4
76	—	(Full scale)
77	4-12	FC-43
78	—	(Full scale)
79	4-17	FC-25
80	—	DIG 4
81	4-13	FC-26
82	4-14	FC-27
83	4-15	FC-41
84	—	(Full scale)
85	—	DIG 4
86	—	(Full scale)
87	4-12	FC-43
88	—	(Full scale)
89	4-17	FC-25
90	—	DIG 4
91	4-13	FC-26

Table 5.5-10 (continued)

Commutator Word Number	Commutator Switch Number	Data Channel
92	4-14	FC-27
93	4-15	FC-41
94	—	(Full scale)
95	—	DIG 4
96	—	(Full scale)
97	4-12	FC-43
98	—	(Full scale)

evaluation. One 30 sample data point for each signal was taken prior to turning A/D 1 off, and one 30 sample data point was taken after turning A/D 2 on. The data is as follows:

Time of sample: 153:07:10:50 to 153:07:11:25

Commutator mode: 5

Data rate: 1100 bits/sec

Analog to digital converter No. 1:

EP-27: 4.4917 volts

EP-28: 2.4976 volts

EP-29: 0.5083 volts

Analog to digital converter No. 2 commanded On: 153:07:11:33

Time of sample: 153:07:12:2 to 153:07:12:37

Commutator mode: 5

Data rate: 1100 bits/sec

Analog to digital converter No. 2:

EP-27: 4.4906 volts

EP-28: 2.4990 volts

EP-29: 0.5083 volts

The maximum difference between the data digitized on A/D No. 1 and No. 2 is 1.4 millivolts. The accuracy of the A/D converters is specified at less than ±10 millivolts error.

Based on this comparison, there is no evidence of degradation of the accuracy of the analog of digital converters at this test time.

5.5.6.7 Commutator Data Rates

The data rate for analog to digital converter No. 1 was checked during the terminal descent phase of the mission for approximately 7 minutes or 420 commutator frames. At this time, commutator mode 2 was selected at the 1100 bits/sec data rate. The start time was 153:06:09:00.625, and the finish time was 153:06:15:59.616. The frame time for 100 words, containing 11 bits each at the 1100 bits/sec data rate, should be 1 second. The average time recorded for each frame during this interval was 0.99998 second. This verifies that the 1100 bits/sec data rate in A/D converter No. 1 was within the specified value of 1100 bits/sec ±0.1 percent.

The other A/D converter No. 1 data rates will also be within the specified value since they are all derived from one common frequency source.

A/D converter No. 2 was not used during the transit phase of the mission, and data is not available to accurately determine its data rate.

5.5.6.8 Subcarrier Oscillator Frequencies

Frequency data to determine subcarrier oscillator frequency stability was not available.

5.5.7 REFERENCES

1. SC-1 Signature List, IDC 2253.1/636.

2. M.R. Weiner, "Methods for Correcting Offset Voltage Due to Commutator Unbalance Current," IDC 2253.1/575 and IDC 2253.1/584.

3. Surveyor Spacecraft Functional Description, Volume II, Section V, Hughes Aircraft Company, SSD 239524E.

4. Surveyor I Flight Performance Quick Look Report, Hughes Aircraft Company, SSD 64136R.

5.5.8 ACKNOWLEDGMENTS

This section was coordinated by J.A. Steineck.

Assistance was received from M.R. Weiner on commutator unbalance current corrections, and J. Stivers on temperature measurement errors at 4400 bits/sec.

5.6 FLIGHT CONTROL

5.6.1 INTRODUCTION

The principal requirements of the Surveyor flight control system are attitude control, accurate angular maneuvers, precision velocity corrections, and soft lunar landing. In order to accomplish these functions, the control system utilizes such hardware as gyros, gas jets, solid fuel engine, liquid fuel engines, optical sensors, timing devices, radars, and acceleration sensing mechanisms.

5.6.1.1 Attitude Control

Attitude control is accomplished by two basic types of active control systems. During coast phase, a bang-bang type of attitude gas jet system is employed which utilizes a novel technique of artificial rate feedback for loop stabilization and, during periods of large moment disturbances such as the main retro phase, the throttle-controlled vernier engine system is used. The error signals required for controlling the propulsion systems are derived from optical sensors or rate integrating gyros which are mounted on the spacecraft in such a way as to provide a three-axis coordinate system. During coast phase, where the gas jet system is used, two modes of operation are available. One choice is celestial referencing, using the sun and Canopus, and the second is self-contained inertial referencing (gyros). The first mode is used to establish accurate attitude, and the second mode is generally used when momentary inertial reference is desired; such an instance occurs during an attitude maneuver.

5.6.1.2 Angular Maneuvers

The rate integrating gyros are also used for accurate angular maneuvers which are accomplished by precessing the gyros at precise rates for given time intervals and slaving the spacecraft to the gyros through the gas jet system.

5.6.1.3 Velocity Correction

Midcourse velocity correction capability of exact magnitudes is provided by a system consisting of three vernier engines, a precision timer, and an accurate acceleration sensing device. The difference between the commanded acceleration level and the output from the accelerometer provides

the error signal that commands the vernier engines to the required thrust levels. The constant acceleration and variable time concept used by the Surveyor flight control system provides the flexibility of choosing velocity corrections from 0 to 50 m/sec.

5.6.1.4 Soft Landing

Surveyor's soft landing capability is provided by a sophisticated technique utilizing radars for computing velocities and range. The range information is then used by an on-board computer to provide velocity commands to the vernier engine system according to an approximate, constant acceleration, V^2/R function. The velocity information is used by the vernier engine-attitude control loop to produce a near gravity turn descent by caging the spacecraft thrust axis to the true velocity vector. The velocity information is also used, along with velocity commands, to generate error signals for the velocity control loop.

In order to provide the required condition of low velocity for the soft landing phase, a large amount of approach velocity is removed by a solid fuel rocket engine during the initial portion of the terminal descent phase. The spacecraft attitude during this phase is inertially stabilized by the gyro-vernier engine control system.

5.6.1.5 Mission Performance

During the successful Surveyor SC-1 mission, each of the above mentioned tasks was requested of the spacecraft and, in each instance, without exception, the flight control system performed perfectly. This overwhelming success is evidence of and bears witness to the sound philosophy incorporated in the Surveyor control system design.

5.6.1.6 Analysis

In order to properly evaluate the spacecraft, a list of analysis items was prepared and can be found in subsection 5.6.2. The items are categorized under major mission phases (such as Centaur separation, coast phase, and midcourse correction) for easier identification and performance evaluation. A log of time and events is presented in Table 5.6-1, and a table of results (Table 5.6-2) is given in subsection 5.6.4. In subsection 5.6.5, a table of anomalies is presented along with a brief description of each anomaly. Subsection 5.6.6 contains the conclusions and recommendation of the investigation, and subsection 5.6.7 contains the analysis effort.

5.6.2 ANALYSIS ITEMS

The following list of items constitutes the postflight performance analysis effort for the flight control system. The degree to which the individual items were investigated depended on the impact of that parameter on the overall flight control performance assessment.

5.6.2.1 Flight Control System

1) Prelaunch

   a) Verify proper gyro temperature control including temperature, time to reach steady state, duty cycle, comparison with CST and J-FACT.

2) Centaur separation

   a) Verify proper nulling of separation rates.

   b) Determine the following:

      Time required to null rates to less than 0.1 deg/sec

      Total angular excursion

      Magnitude of angular rate at separation

      N_2 gas used (see item 12a)

3) Sun acquisition

   a) Verify proper acquisition of sun.

   b) Determine the following:

      Time required to acquire sun

      Angular motion required to find sun

      N_2 gas used (see item 12a)

4) Star acquisition

   a) Verify proper acquisition and verification of Canopus.

   b) Determine the following:

      Roll angle from beginning of maneuver to Canopus

      Other stars identified

      Mean roll rate when rolling from first Canopus to second Canopus

Effective gain (relative to nominal Canopus) of Canopus sensor

Margin between acquisition limits and Canopus intensity

Magnitude of window fogging over 63-hour mission

N_2 gas used (see item 12a)

5) Coast mode

a) Limit cycle frequency and amplitude.

b) Sun and star tracking errors and tracking noise.

c) N_2 gas used.

d) Give individual and averaged results of gyro drift measurements and compare with FAT results.

e) Gas jet thrust level

6) Premidcourse maneuver

a) From gyro error signals and precession logic signals, determine gyro precession time to best accuracy and compare to commanded times.

b) From the above, make best determination, with resultant tolerances noted, of the midcourse pointing accuracy.

c) Verify roll accuracy by analysis of star map (see item 3b).

7) Postmidcourse maneuver

a) From gyro error signals and precession logic signals, determine gyro precession time to best accuracy and compare to commanded times.

b) From the above, make best determination, with resultant tolerances noted, of the maneuver accuracy.

c) Verify total maneuver accuracy, pre- and postmidcourse, by evaluating sun and star pointing errors after maneuver completed but before initiating tracking modes.

8) Midcourse engine firing

a) Determine engine startup characteristics from initial attitude transients.

b) Determine engine shutoff dispersions from postshutoff attitude transients.

c) Determine thrust misalignment during burning.

d) Determine roll disturbance during burning and compare to predicted.

e) Determine actual burn time to best accuracy and compare to that commanded; estimate actual ΔV to best accuracy and compare to that indicated by postmidcourse orbit determination.

f) Prepare curves of corrected thrust and attitude parameters versus time, and determine the moment disturbances during burning.

g) Determine N_2 gas used during midcourse phase (including maneuvers) (see item 12a).

9) Preretro maneuvers

a) From gyro error signals and precession logic signals, determine gyro precession time to best accuracy and compare to commanded times.

b) From the above and the initial sun and Canopus error signals, make best determination, with resultant tolerances noted, of the terminal pointing accuracy.

c) Verify 8b by comparison with pointing error determined from main retro burnout conditions (see 10 below).

d) Gas used for maneuvers (see item 12a).

10) Main retro phase

a) Determine accurate time relationships and compare with expected.

b) Verify, from timing relationships, whether AMR or backup command initiated descent sequence.

c) Determine vernier engine startup characteristics from initial attitude transients and compare with first startup (midcourse burn).

d) Evaluate attitude transients during retro ignition.

e) From vernier engine thrust levels and roll actuator position, determine main retro thrust vector to center-of-gravity misalignment throughout burning. Compare with that expected from initial alignment and vernier fuel usage.

f) Plots of raw data.

11) Vernier descent phase

a) Determine accurate time relationships and compare with expected.

b) Reconstruct descent trajectory. Compare with predicted.

c) Evaluate attitude control loop performance.

d) Corrected telemetry plots.

12) Postlanding

a) Determine landed attitude from gyro error signals.

13) Miscellaneous

a) Determine total N_2 gas consumption, compare with predictions, and modify prediction model, if necessary.

b) Determine gyro nulls.

c) Determine the main retro thrust vector offset from spacecraft center of gravity using gyro angles.

d) Radar noise.

e) Analysis of gyro speed.

f) Vernier system pressurization/Canopus sensor phenomenon.

g) Roll control system performance.

h) Terminal precutoff glitch anomaly.

5.6.3 MAJOR EVENTS

A listing of major flight control events and the corresponding time of occurrence is given in Table 5.6-1.

5.6.4 FLIGHT CONTROL

Table 5.6-2 presents flight control results.

5.6.5 CONTROL SYSTEM ANOMALIES

A control system anomaly is any deviation of the flight control performance from that expected and/or specified by the unit, system, and functional specifications.

TABLE 5.6-1. TIME AND EVENTS LOG

Event	Command	GMT (at DSIF), day:hr:min:sec	Mission Time, hr:min:sec
Launch		150:14:41:01	00:00:00
Electrical separation		150:14:53:32	000:12:31
Start of sun acquisition		150:14:54:23	00:13:22
Sun acquisition completed		150:15:00:35	00:19:34
Start of Canopus acquisition	0714	150:18:53:39	04:12:38
Star acquisition complete	0716	150:19:13:20	04:32:19
First gyro drift check	0700	150:20:54:02 to 150:23:51:10	06:13:01 to 09:10:09
Premidcourse roll	0714	151:06:30:12.888	15:49:11.112
Premidcourse yaw	0713	151:06:34:48.861	15:53:47.861
Midcourse thrust	0721	151:06:45:03.801	16:04:02.801
Postmidcourse yaw	0713	151:06:52:55.754	16:11:54.754
Postmidcourse roll	0714	151:06:58:02.224	16:47:01.224
Second gyro drift check	0700	151:09:30:14 to 151:12:30:16	18:49:13 to 21:49:15
Third gyro drift check	0700	152:04:18:39 to 152:06:25:57	37:37:38 to 39:34:56
Fourth gyro drift check	0700	152:07:34:15 to 152:09:52:16	40:53:14 to 43:11:58
Fifth gyro drift check	0700	152:09:55:42 to 152:13:05:03	43:14:41 to 46:24:02
Sixth gyro drift check	0700	152:19:20:42 to 152:21:41:50	52:39:41 to 55:00:49
Preretro roll number 1	0714	153:05:36:46.295	62:55:45.295
Preretro yaw	0713	153:05:41:47.766	63:00:46.766
Preretro roll number 2	0711	153:05:45:17.745	63:04:16.745
AMR mark		153:06:14:39.708	63:33:38.958
Vernier ignition		153:06:14:47.558	63:33:46.518
Retro ignition		153:06:14:48.958	63:33:47.618
3.5 g switch		153:06:15:27.957	63:34:26.943
Retro eject		153:06:15:39.956	63:34:38.943
Start RADVS descent		153:06:15:42.093	63:34:41.093
Segment acquisition		153:06:16:05.893	63:35:04.893
1000-foot mark		153:06:17:10.494	63:36:09.494
10 ft/sec mark		153:06:17:28.719	63:36:27.719
13-foot mark		153:06:17:34.169	63:36:33.169
Touchdown (from telemetry)		153:06:17:35.700	63:36:34:700

TABLE 5.6-2. FLIGHT CONTROL RESULTS

	Controlling Specification	Specification Value	Results	Comments
Prelaunch				
Proper gyro temperature control			Roll 167.2°F Pitch 172°F Yaw 177.2°F	Time was 14:43:18. Roll gyro heater was cycling at time of flight control power on. Pitch gyro heater started cycling approximately 30 minutes later.
Verification of N_2 loading		4.5 pounds	4.55 pounds	1 percent difference between the two values is well within the accuracy of telemetry.
Centaur separation				
Verify proper nulling of separation rates	224510E (3.3.3)	Near zero	≈ 0 deg/sec	A large portion of telemetry data was missing during the separation phase.
Time required to null rates to less than 0.1 deg/sec	224510E (3.3.3.3)	< 0.1 deg/sec within 50 seconds	15 seconds	
Magnitude of angular rate at separation	224510E (3.3.2.1)	≤ 3.0 deg/sec	0.38 deg/sec (pitch)	
Sun acquisition	224510E (3.4.1)	Roll maneuver until activation of acquisition sun sensor and then a yaw maneuver until primary sun sensor illumination		Although much of the data during sun acquisition phase was lost, sufficient data is available for a complete analysis of system performance.
Proper sun acquisition				
Roll			-87 degrees of roll	
Yaw			99 degrees of yaw	
Total time			372 seconds	
Quality of sun sensor output				
N_2 gas used	Design	0.054 pound(average)	0.040 pound	Tank temperature may not have been at steady state.
Star acquisition	224510E (3.4.2)	Positive roll maneuver sufficient to produce an adequate star map for Canopus verification. Provide a lockon signal when Canopus appears in the sensor field of view		Intentional high gain setting of Canopus sensor to compensate for possible window fogging removed the capability of automatic star lockon.
Proper acquisition and verification of Canopus			Manual lock	
Roll angle from beginning of maneuver to Canopus			220.627 degrees	
Stars identified			Alpha Doradus, Phi Eridani, Markab, Pi Cygni, Alderamin, Merak, Algeiba, Regulus, Alpha Hydrae, Naos, Canopus	
Mean roll rate during star map phase	224510E (3.4.2.1.1)	0.5 deg/sec	+0.5004 deg/sec	
Effective gain (relative to nominal Canopus) of Canopus sensor			1.5 x Canopus	Normally the gain setting is 1 x Canopus
Margin between Canopus lockon and Canopus intensity			Indiscernible	

Table 5.6-2 (continued)

	Controlling Specification	Specification Value	Results	Comments
Magnitude of window fogging over 63-hour mission			None	
N_2 gas used	Design	0.048 pound (average)	0.030 pound	
Coast mode				
Sun and star tracking errors – tracking noise	224510E (4.3.1.1)	Roll axis shall be held to within 0.20 degree of sun-spacecraft line, plus a ±0.30 degree limit cycle		Sun and star error signal noise level were low enough to have no effect on the limit cycle performance.
Average error from sun line			-0.058 (pitch) -0.053 (yaw) -0.055 (roll)	
Average error from Canopus line of sight		Same magnitudes as above for Canopus-spacecraft line		
Limit cycle (gas jet system)				
Optical mode/inertial mode	224510E(4.3.1.1 and 4.3.1.2)	±0.30 degree		Values are that of the total deadband. Predicted values were:
Average amplitude – roll			0.441/0.415	0.44/0.44
Average amplitude – pitch			0.470/0.443	0.44/0.44
Average amplitude – yaw			0.457/0.417	0.44/0.44
Average period			65 (optical) and 50 sec/pulse (inertial)*	80 (optical) and 117 sec/pulse (inertial)
Average N_2 usage	Design	0.0012 lb/hr (average)	0.0022 lb/hr	Much of the difference was caused by a double pulsing action of the roll gas jet system which occurred periodically during the mission, giving rise to a higher limit cycle frequency.
Gyro drifts	224510E (4.3.1.5)	<1 deg/hr		Terminal maneuvers were compensated for the following drifts: Roll = +0.2 deg/hr Pitch = 0.0 deg/hr Yaw = +0.75 deg/hr

	No. 1	No. 2	No. 3	No. 4	No. 5	No. 6
Roll	0.084	0.204	0.25	–	–	0.295
Pitch	0	0.024	0.03	–	–	0.07
Yaw	0.64	0.660	0.90	0.85	0.85	0.84

Gas jet thrust level	224510E (4.3.3.2)	>0.052 pound	0.054 pound (roll)	Design value is 0.057 pound
Premidcourse maneuvers				
Maneuver angles	224510E (4.3.2.1)	Rates shall be controlled to be 0.5 ± 0.0011 deg/sec		Assuming a precession level of 0.5000 deg/sec
Roll			-86.585 degrees	
Yaw			-57.900 degrees	
Precession command times	224510E (3.6.4.8)	0.2 second plus 0.02 percent of command interval magnitude		These times were obtained from the gyro error signal response profile
Roll			173.17 seconds	
Yaw			115.80 seconds	
Pointing accuracy (includes drift, initial attitude errors, and limit cycle)	224510E (3.6.3.1)	±0.7 degree of computed direction	0.313 degree	Calculated using actual data of drift, attitude errors, and execution errors

*These are mean times between gas jet pulses.

Table 5.6-2 (continued)

	Controlling Specification	Specification Value	Results	Comments
Postmidcourse maneuvers				
Maneuver angles	224510E (4.3.2.1)	Rates shall be controlled to be 0.5 ± 0.0011 deg/sec		Telemetry rate of 550 bits/sec excluded any use of mission data for obtaining accurate information
Yaw			86.5 degrees (command)	
Roll			57.99 degrees (command)	
Precession command times	224510E (3.6.4.8)	0.2 second plus 0.02 percent of command interval magnitude		Telemetry rate of 550 bits/sec excluded any accuracy
Yaw			115.5 seconds	
Roll			173.0 seconds	
Total attitude accuracy from pre-maneuver to postmidcourse maneuver utilizing sun-star information			< 0.15 degree	
N_2 gas consumption for both pre- and postmidcourse maneuvers	Design	0.092 pound (average)	0.150 pound	
Midcourse thrust phase				
Ignition characteristics (time)			< 0.15 second	
Engine startup characteristics				
Peak engine thrust	224510E (4.2.2.12)	Maximum thrust capability > 104 pounds	Engine 1 = 80 pounds	
Peak attitude transients/ angular rate				
Roll			-0.429 degree	
Pitch			0 degree/0.25 deg/sec	
Yaw			-0.08 degree/-0.36 deg/sec	
Mean attitude error during burn	224510E (4.3.1.4)	Within 0.10 degree		These values are within 1 bcd of telemetry data
Roll			-0.326 degree	
Pitch			0.011 degree	
Yaw			-0.005 degree	
Thrust misalignment	224510E (3.6.3.1)	±0.7 degree of computed direction	0.313 degree	This value was calculated from actual mission data
Roll disturbance moment				
Peak magnitude of disturbance	224510E (4.3.3.1.2)	Capable of 90 lb-in.		
Average roll disturbance				
Roll actuator position				
Peak value			0.9 degree	
Mean value			0.65 degree	
Thrust command time	224510E (3.6.4.8)	0.025 second plus 0.02 percent of command interval	20.815 seconds	Desired burn time was 20.800 seconds

Table 5. 6-2 (continued)

	Controlling Specification	Specification Value	Results	Comments
Maximum acceleration error	224510E (3.6.3.2)	ΔV error < ±1.3 ft/sec		
Estimated ΔV/tracking ΔV			20.365 m/sec / 20.266 m/sec	Calculated value does not include scale factor errors
Startup/shutdown impulse	224510E (4.2.2.7)	< 5 lb-sec/engine Δ impulse < 0.66 lb-sec		Units are lb-sec
Engine 1			-0.08/0.27	
Engine 2			-0.23/-0.31	
Engine 3			0.312/0.10	
Preretro maneuvers				
Maneuver angles	224510E (4.3.2.1)	Rates shall be controlled to be 0.5 ± 0.0011 deg/sec		Values only include execution error. The desired values were:
Roll 1			89.27 degrees	Roll = 89.30 degrees
Yaw			59.975 degrees	Yaw = 59.90 degrees
Roll 2			94.415 degrees	Roll = 94.19 degrees
Precession command times	224510E (3.6.4.8)	0.2 second plus 0.02 percent of the command interval magnitude		The command values were:
Roll 1			178.60 seconds	178.66 seconds
Yaw			120.00 seconds	119.85 seconds
Roll 2			188.80 seconds	188.17 seconds
Pointing accuracy (includes drift, initial attitude errors, and limit cycle)	224510E (3.9.3.2)	Within ± 1 degree	-0.336 degree	In direction of minus yaw axis
Gyro drifts compensation values				
Roll			0.20 deg/hr	
Pitch			0	
Yaw			0.75 deg/hr	
N_2 gas used	Design	0.071 pound (average)	0.116 pound	Estimated value using midcourse information
Terminal descent				
Approach angle of velocity vector to lunar vertical			5.91 degrees	
AMR marking altitude	224510E (3.9.1.1)	Nominal slant range of 60 miles	59.2 miles	
Main retro				
Burn time (from ignition to 3.5 g switch)	224510E (3.9.2.4)	Approximately 42 seconds	39.325 seconds	
Maximum retro thrust	224510E (4.2.1.3)	< 10,000 pounds	9910 pounds	Computed using retro accelerometer data

Table 5.6-2 (continued)

	Controlling Specification	Specification Value	Results	Comments
Peak attitude transient at vernier ignite – retro ignite				
Roll			-0.41 degree	
Pitch			-1.03 degree	
Yaw			< 0.02 inch	Exact values were limited by telemetry accuracy of the parameters
Main retro thrust vector to spacecraft center of gravity offset	224510E (4.1.3.3)	< 0.18 inch	0.263 degree	
Thrust vector pointing accuracy during retro burn	224510E (3.9.3.2)	Within ±1 degree		
Mean attitude error during burn				
Roll			0 degree	Less than 1 bcd count
Pitch			0 degree	Less than 1 bcd count
Yaw				
Roll actuator position				
Peak at retro ignition				
Mean value during burn				
Time between major events	224510E (3.9.2)			
AMR and vernier ignite		0 to 20 seconds	7.825 seconds	
Vernier ignite and retro ignite		1.1 ± 0.1 seconds	1.100 seconds	
Retro ignite and retro burnout		Approximately 42 seconds	39.325 seconds	
Retro burnout to retro eject		12.0 ± 0.1 seconds	12.000 seconds	
Retro eject to RADVS descent on		First possible attitude reference change: 2.15 ± 0.1 seconds	2.150 seconds	
Vernier engine startup/shutdown characteristics		< 10 lb-sec		
Engine 1			-0.02/0.19	
Engine 2			0.22/-0.26	
Engine 3			-0.20/0.07	
Total change in velocity during retro phase				
Retro burnout condition				
Altitude/slant range	224510E (3.9.4)	Depends on midcourse	27,851 feet (SR)	
Velocity	224510E (3.9.4)	Depends on midcourse	V_z = 425.3 ft/sec	V_x = +70.4 ft/sec and V_y = -4.03 ft/sec
Angle between thrust vector and velocity vector				
Flight path angle (angle between velocity vector and local vertical)	224510E (3.9.4)	0 ± 16 degrees		

Table 5.6-2 (continued)

	Controlling Specification	Specification Value	Results	Comments
Time to cage the spacecraft Z axis to velocity vector from the start of velocity controlled descent	224510E (3.10.2.1)	9 seconds maximum	3.3 seconds	Obtained from Section 5.15.
Descent segment intercept conditions				
Altitude			18,000 feet (SR)	Obtained from Section 5.15.
Velocity			442 ft/sec (V_z)	Obtained from Section 5.15.
Flight path angle			1.34 degrees	Obtained from Section 5.15.
Vernier engine cutoff conditions				
Altitude	224510E (3.10.3.1)	14 ± 4.5 feet	13 feet	Obtained from Section 5.15.
Velocity (vertical)	224510E (3.10.3.2)	5 ft/sec ± 1.5 ft/sec	5 ft/sec	Obtained from Section 5.15.
Flight path angle	224510E (3.10.3.5)	0 ± 4.8 degrees	0.3 second	Obtained from Section 5.15.
Time before touchdown	224510E (3.11.1)	< 2 seconds	1.5 seconds	Obtained from Section 5.15.
Touchdown conditions				
Vertical velocity	224510E (3.11.2.1)	< 15 ft/sec	12 ft/sec	Obtained from Reference 18.
Lateral velocity	224510E (3.11.2.2)	< 5.0 ft/sec	≈ 0	
Approach angle	224510E (3.11.2.3)	< 7 degrees	≈ 0	
Additional information				
Total nitrogen gas used	Design	0.546 pound (average)	0.680	See coast mode gas consumption
Gyro speeds	235159	Telemetry value = 50 cps for all three gyros		These values are expected since similar values were obtained during STV.
Roll gyro			Roll = 63 cps (average)	
Pitch gyro			Pitch = 55 cps (average)	
Yaw gyro			Yaw = 51 cps (average)	
Gyro heater duty cycle				
Roll			Roll = 13 percent ON	These values are equivalent to those for a low to medium sun condition.
Pitch			Pitch = 29 percent ON	
Yaw				
Radar noise				These values are function of altitude. The largest values are presented.
V_z			2.1 ft/sec (3σ)	
V_x and V_y			5.0 ft/sec (3σ)	

For the SC-1 mission, only three anomalies, which were of minor significance, can be attributed to the flight control system. One anomaly is that Canopus lockon, which is an automatic feature of the optical system, was not achieved because the output of the sensor, while viewing Canopus, was greater than the upper threshold of the lockon range. Just prior to the flight, the Canopus sensor gain was intentionally increased by 50 percent to compensate for the possibility of sensor window fogging. This action was brought about by the window fogging that occurred on the SC-2 sensor which was at that time in the STV test phase.

Star acquisition was achieved by commanding cruise-mode on (0704) followed by a manual lockon command (0716).

The second flight control anomaly was the high indications of gyro speeds. This anomaly has always existed, was expected, and did occur during the mission. The third anomaly occurred just prior to touchdown at an approximate altitude of 14 feet. An instant before engine cutoff, it was noticed that all three engines were momentarily commanded to throttle up by about 15 pounds. This anomaly did not affect the soft landing performance.

A brief description of each anomaly is presented in Table 5.6-3. The Canopus lockon anomaly is analyzed in subsection 5.6.7.4, and the other two anomalies explained in subsection 5.6.7.13.

TABLE 5.6-3. CONTROL SYSTEM ANOMALIES

Anomaly	Brief Description of Anomaly	Phase of Mission
Canopus lockon	When Canopus sensor viewed a star of magnitude Canopus, Canopus lockon was not achieved	Throughout the mission
Gyro speeds	Gyro speed checks for FC-1, FC-2, and FC-3 read much higher than the required 50 cps	151:04:26:03
Vernier engine system – high thrust glitch	Just prior to vernier engine cut-off, a momentary high thrust command was observed	Landing

5.6.6 CONCLUSIONS AND RECOMMENDATIONS

From the tremendous amount of evidence compiled in this section, the following conclusions were obtained:

1) The nitrogen fuel supply is adequate.

2) Gyro drift measurements are feasible and required for accurate maneuvers.

3) The flight control system is capable of precise angular maneuvers.

4) The flight control system is capable of accurate velocity corrections.

5) The flight control inertial mode control system can maintain accurate inertial reference.

6) The flight control optical system can maintain accurate attitude reference.

7) The flight control attitude control system is stable under the influence of moment disturbances.

8) The magnitude register and programmer operates as designed.

9) The terminal guidance scheme, which incorporates the use of radars, performs well as expected.

Because of the near perfect performance by the flight control system, only a very few recommendations evolved from the analysis:

1) If Canopus sensor fogging is still anticipated for future flights, the sensor gain should be set to 1.25 times Canopus instead of 1.5.

2) Delete the gyro speed measurements.

5.6.7 FLIGHT CONTROL SYSTEM

5.6.7.1 Prelaunch

Flight control parameters of interest during the prelaunch phase are the gyro temperatures. (Comparisons between mission data and previous test data are presented in Table 5.6-4.)

In the final report of the J-FACT ETR test (Reference 1) a comment was made that the values obtained during the test were 10 to 15° F higher than those expected at launch because several sheets of mylar covering the

TABLE 5.6-4. GYRO TEMPERATURES, ° F

Gyro	FC No.	Mission 2 Hours Prior to Launch	Mission 2 Minutes After Launch	Prelaunch Countdown Dry Run Test on 26 May 1966	J-FACT (ETR) Test on 25 April 1966	J-FACT (ETR) Dry Run Test on 18 April 1966
Roll	46	165.4	167.2	168.1	178.6	178.6
Pitch	54	163	172.0	174.0	172.6	173.5
Yaw	55	168.1	177.2	177.1	175.4	175.4

inertial reference unit (IRU) were not removed prior to encapsulation. While this appears to be true for the roll gyro, it does not appear to fit the results obtained during the mission for the pitch or yaw gyro temperatures.

The average duty cycle of the pitch and roll gyro heaters for the mission were 29 and 13 percent, respectively. These values are similar to those seen during the STV test for a low to medium sun condition.

The events that occurred during the period between launch and Centaur separation are given in Table 5.6-5. Information in this table was obtained from the Quick Look Report (Reference 1) published on 17 June 1966.

5.6.7.2 Centaur Separation

After extending each of its landing legs, Surveyor is separated from the Centaur booster. When the three legs-down signals and the separation signal have been generated, the programmer removes the logic signal which has been inhibiting operation of the gas jet amplifiers. At this same instant, the magnitude register begins to count down a total of 1024 counts for a 51-second interval; register counting inhibits the start of sun acquisition for these 51 seconds to give the cold gas attitude control system opportunity to rate stabilize the spacecraft. Table 5.6-1 presents these events in time reference.

Rate stabilization is accomplished by using the three-axis attitude control system to torque the spacecraft to drive the error sensors (caged integrating rate gyros) to within the deadband of each of the gas jet amplifiers. Thus, at the end of a nominal rate stabilization maneuver, the spacecraft has achieved a low angular velocity with a random orientation in inertial space. The system response is dependent upon the magnitude and direction of the initial velocity vector and the gas jet thrust levels, and is essentially deadbeat in nature.

Flight control system performance just after booster separation was evaluated in terms of verification of the proper nulling of the separation

TABLE 5.6-5. EVENTS BETWEEN LAUNCH AND CENTAUR SEPARATION

Time				Event	Observation
GMT, hr:min:sec	From Launch				
	min:sec	sec	Expected		
14:41:01				Lift off	No noticeable effect on telemetry.
:06	00:05	5	3	Atlas roll started	Roll precession command, FC-49, indicates start of a roll. Expected time for start of roll was lift-off plus 3 seconds. (Note: The spacecraft was launched at 550 bits/sec. At this bit rate, it takes 2.4 seconds to sample a frame of data. The differences from the observed telemetry time and the actual event time is thus partially attributable to the data bit rate.)
:18	:17	17	16	Atlas pitch started	Pitch precession command, FC-50, and pitch gyro error, FC-16, indicate a pitch of about -0.7 deg/sec until L + 1M. At L + 1M, both FC-16 and FC-17, pitch and yaw gyro errors, become erratic for about 20 seconds until L + 1M 23S. The pitch precession is then -0.5 deg/sec until L + 2M 3S. At L + 2M 3S, the pitch rate changes to -0.23 deg/sec and remains at this rate until Atlas booster engine cutoff.
14:42:56	1:55	115	-	Inertia switch opens	Acceleration reaches about 3.7 g (FC-63).
14:43:22	2:21	141	-	Inertia switch closes	Acceleration decays to about 3.5 g (FC-63).
14:43:26	2:25	145	145.6	Booster engine package jettison (Mark 2)	Gyros indicate separation rates caused by booster engine separation. Pitch at separation rose to 1.72 deg/sec.
14:43:54	2:53	173	-	Atlas-Centaur attitude stabilized	Pitch rate goes to about -0.15 deg/sec
14:44:25	3:24	204	203.5	Jettison nose fairing (Mark 4)	The secondary sun sensors, FC-7, -8, -9, and -10 go to values between 2.5 and 3. The primary sun sensor apparently saw the nose fairings and indicated pitch and yaw sun sensor errors for about 60 seconds or until after Centaur ignition. Canopus intensity also rose to about 3.2.
14:45:02	4:01	241	241.7	Atlas SECO and VECO (Marks 5 and 6)	Indicated by pitch and yaw gyros.
14:45:06	4:05	245	243.6	Atlas Centaur separation (Mark 7)	Indicated by separation rates of gyros.
14:45:13	4:12	252	251.9	Start Centaur main engine (Mark 8)	Indicated by separation rates being eliminated. Pitch rate returns to -0.15 deg/sec.
14:47:56	6:55 to 6:60	415	-		Five-second loss of data.
14:49:46	8:45 9:00	525	-		Fifteen-second loss of data.

rates, time required to null rates to less than 0.1 deg/sec, total angular excursion, and magnitude of the angle rates at separation. In addition, the nitrogen gas expended during the maneuver was estimated.

Spacecraft telemetry data available for analysis of the tipoff transient is presented in Figures 5.6-1 and 5.6-2. Other pertinent data is found in Reference 2 as follows:

1) Time of separation command (commutated data) T + 756.57 ± 0.5 sec (or ~150-14-53-38 GMT)

2) Time of spring extension

Measurement No.	Spring No.	Time of First Motion, seconds	End of Motion, seconds	Spring Extension Time, seconds
CY2D	1	756.933	757.055	0.122
CY4D	2	756.933	757.054	0.121
CY5D	3	756.933	757.052	0.120

3) Preseparation Centaur plus SC-1 angle rates (deg/sec):

Pitch -0.05

Yaw +0.15

Roll +0.01

Table 5.6-6 presents the results of SC-1 data analysis in comparison with other sources as noted.

TABLE 5.6-6 CENTAUR SEPARATION PHASE

Parameter	FC Number	Null, bcd	Preseparation Rates			Peak Rates at Separation		Time to Reduce Separation Rates to <0.1 deg/sec, seconds
			Spacecraft		Centaur,* deg/sec	bcd	deg/sec	
			bcd	deg/sec				
Pitch gyro error	FC-16	522.2	535	-0.054	-0.05	606	-0.378	15
Yaw gyro error	FC-17	518.4	560	-0.170	0.15	560	-0.170	0
Roll precession command	FC-49	519.4	523	-0.014	0.01	524	-0.018	0

*Reference 2.

Note: See Table 5.6-8 for the calibration coefficients used in this analysis.

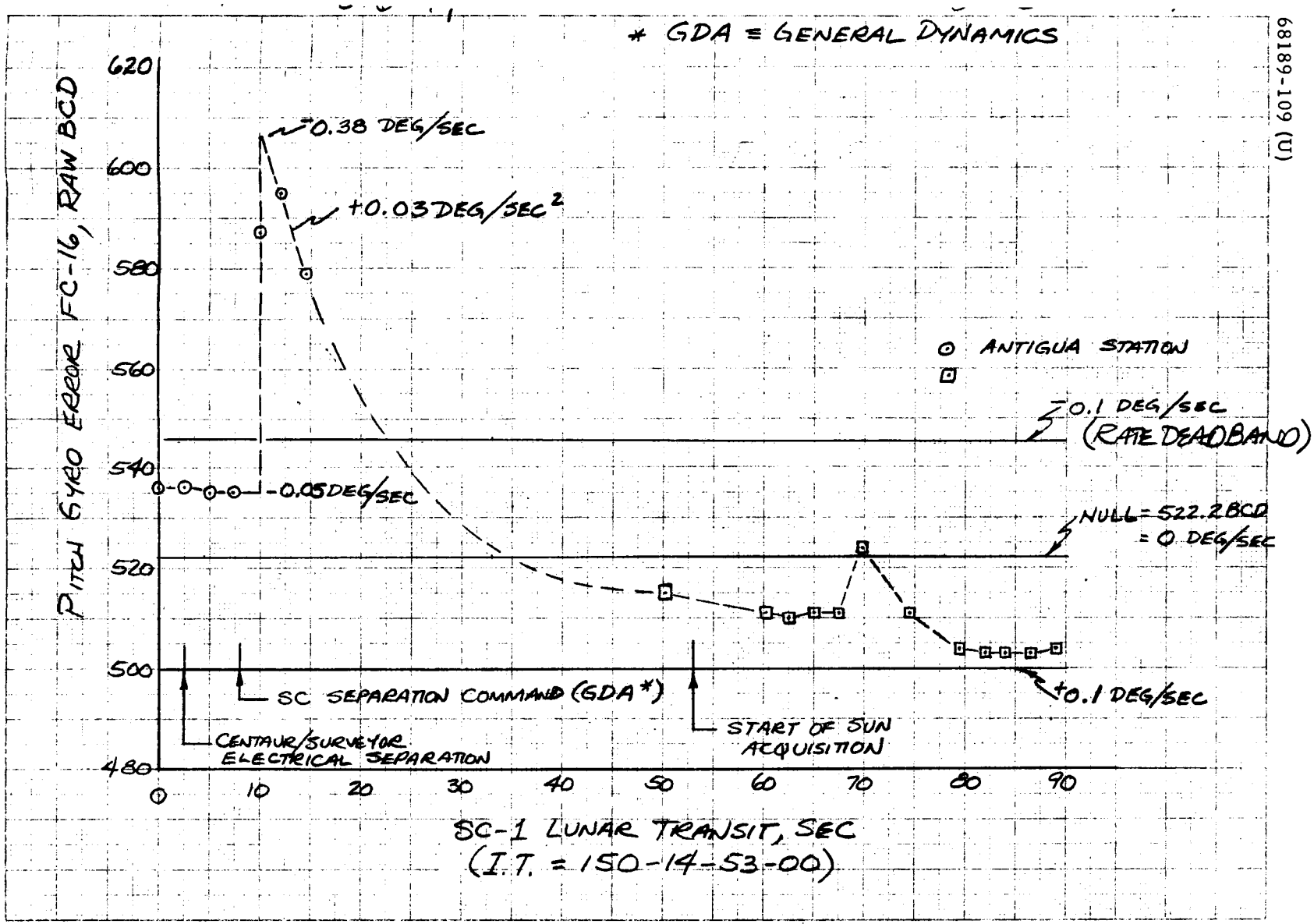


Figure 5.6-1. Pitch Gyro Error, FC-16
Centaur separation phase

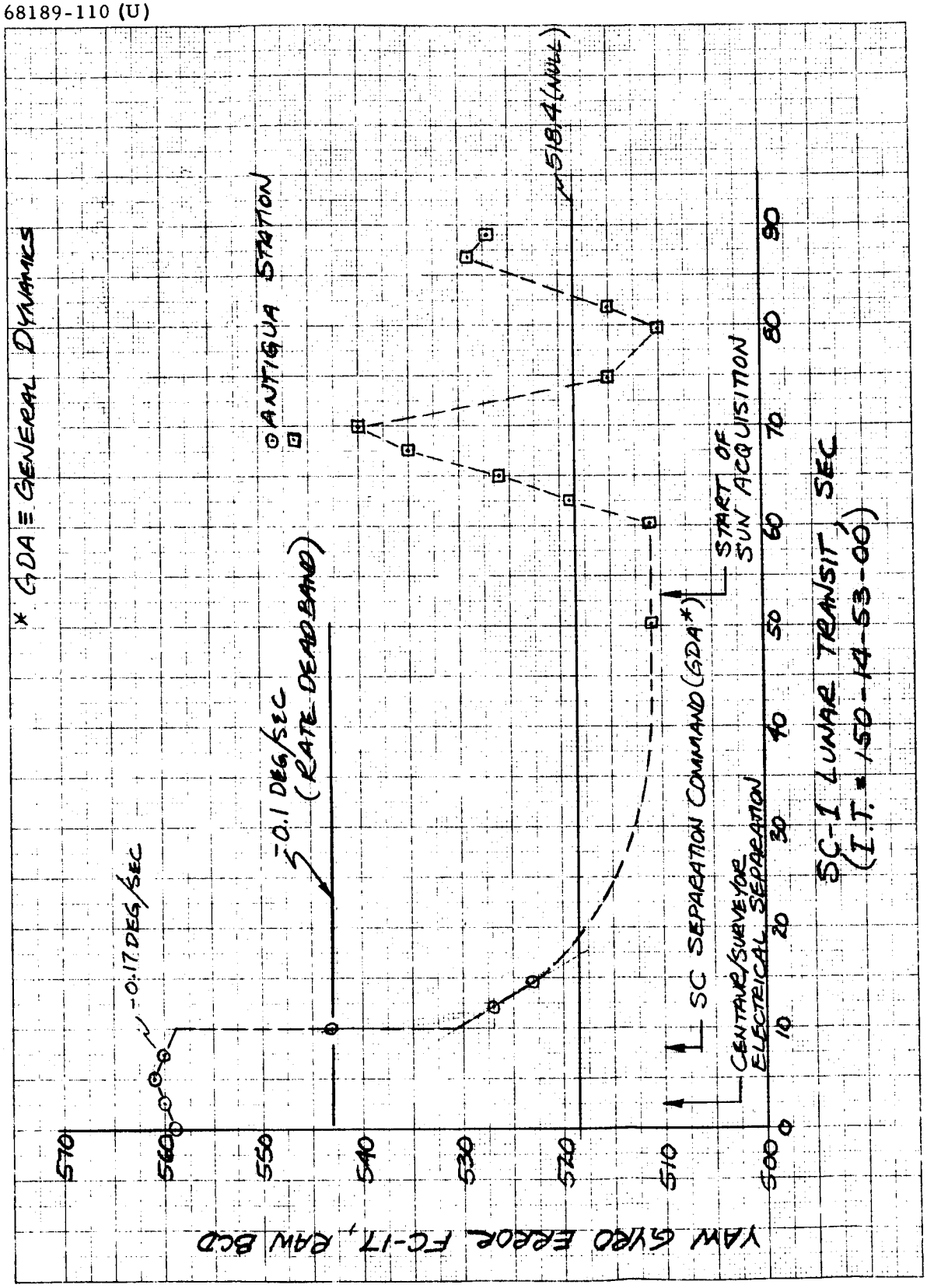


Figure 5.6-2. Low Gyro Error, FC-17
Centaur separation phase

General Dynamics (GDA) and Surveyor telemetry preseparation values agree well, lending confidence with regard to the validity of the post-separation data. The differences in sign are due to different coordinate references used by GDA and HAC (Reference 29). As expected, the major tipoff transients occurred in pitch and yaw, with little change in the roll rate. Although there was a 30-second loss of data beginning 15 seconds after separation, it is apparent that proper nulling of separation rates was achieved.

The assumed shape of the pitch and yaw transients at separation is based on the impulsive nature of the separation force, the Centaur-spacecraft springs extending in ~0.120 second. Correcting torques were applied by means of the gas jets beginning at electrical separation for rates >0.067 deg/sec (nominal).

The peak pitch angle rate was ~0.38 deg/sec, the highest rate experienced in any channel. The telemetry channel saturates at ~5.6 deg/sec (see Table 5.6-7 for rate mode coefficients used).

The initial return acceleration of the pitch gyro error signal was ~0.027 deg/sec^2, which is well within the gas jet torque capability of 0.1 deg/sec^2. If the remainder of the nulling transient is as shown in Figure 5.6-1, then the nulling time (time to <0.1 deg/sec) is ~15 seconds, and the angular excursion due to separation is 2.3 degrees.

The yaw separation torque tended to null the existing rate, so that the peak rate was the preseparation value. Further, the time required for nulling to <0.1 deg/sec was essentially the separation time.

The roll rate was changed only slightly due to the effect of separation, being very small at all times (~0.014 deg/sec) so that roll correction torques were not required.

Telemetered nitrogen usage (pressure and temperature corrected) indicated that the nitrogen expended during rate dissipation was as expected from a nominal stabilization maneuver. At 150:15:01:30 GMT, the cumulative nitrogen usage was determined to be (4.503 - 4.424) = 0.079 pound (see Table 5.6-8). It has been estimated that a minus roll of 86 degrees and a positive yaw rotation of 99 degrees were accomplished during sun acquisition (see Reference 3, Table 1). These rotations indicate a nominal sun acquisition fuel consumption of 0.054 pound (see Reference 4, Fuel Budget). The remaining 0.025 pound would have been used in rate stabilization.

5.6.7.3 Sun Acquisition Phase

Automatic sun acquisition as specified in "System Functional Requirements," Revision E, Paragraph 3.4.1, is as follows:

> "Fifty-one (51) seconds after separation, sun acquisition is initiated by a command from the flight control programmer, which causes a vehicle roll maneuver of -0.5 deg/sec and

TABLE 5.6-7. CALIBRATION COEFFICIENTS FOR RATE MODE CALCULATIONS

(SC-1 Telemetry Calibration Handbook 291031)

Coefficient	FC-16
A0	0.731710 E 01
A1	-0.192280 E -01
A2	0.229569 E -04
A3	-0.401800 E -07
A4	0.324409 E -10
A5	-0.101840 E -13
	FC-17
A0	0.708950 E 01
A1	-0.225860 E -01
A2	0.476819 E -04
A3	-0.101770 E -06
A4	0.102760 E -09
A5	-0.396360 E -13
	FC-49
A0	0.778800 E 01
A1	-0.358289 E -01
A2	0.117219 E -03
A3	-0.263310 E -06
A4	0.278600 E -09
A5	-0.111960 E -12

TABLE 5.6-8. NITROGEN GAS CONSUMPTION*

Day	Time	N_2 Pressure		N_2 Temperature		Bit Rate	N_2 (lbs) Remaining	Total N_2 Used	Event	N_2 Used	Expected Usage	Remarks
		FC-4	Corrected	FC-48	Corrected							
150	143001	4906	4650	86.0		550	4.49					
	144558	4906	4650	85.1			4.503					
	145632	4841	4580	82.5			4.476	0.027		0.027		After rate stabilization and start of minus roll.
	145937	4778	4515	82.5			4.445	0.058	Rate Stabilization and Sun Acq.	0.031		After end of minus roll and start of plus yaw.
	150130	4741	4490	81.6			4.424	0.079		0.021	0.100	
	192834	4418	4170	56.9			4.409	0.094	Star Acq.	0.015	0.159	Post Canopus Acquisition
151	055952	4225	4000	46.3			4.382	0.121	Coast			Pre MC
	071225	3957	3725	44.6			4.145	0.358	MC	0.237	0.403	Post MC
153	051252	3746	3525	47.2			3.94	0.563	Coast	0.205	0.511	Pre Terminal
												This value of gas consumption is high due to the many gyro drift checks. Post T.D.

*Data derived from Reference 3.

No N_2 pressure data available after T.D. and not available on SPAC format after completion of pre-terminal maneuvers.

See subsection 5.6.7.13 for a complete analysis of nitrogen consumption.

continues until the sun comes into the field-of-view of the secondary sun sensor* which is affixed approximately on the spacecraft roll-pitch plane. When this occurs, the roll command is removed and a yaw command is initiated to bring the primary sun sensor line of sight toward the sun. When the sun falls into the field-of-view of the primary sun sensor, a lock-on signal is generated. This signal switches vehicle attitude control to the primary sun sensor and also serves to indicate (via telemetry) the completion of sun acquisition."

Although much of the data was lost during the sun acquisition phase, sufficient data is available to verify proper spacecraft operation and to reconstruct, with some degree of accuracy, the sequence of events.

Following a successful Centaur separation and rate dissipation mode, the spacecraft initiated its first sun acquisition maneuver (minus roll) at 150:14:54:23.5 GMT. At 150:14:57:17.5 GMT (L + 16 M 16.5 S) of the same day, after rotating through an angle of -87 degrees, the acquisition sun sensor was illuminated, ending the roll maneuver and initiating the next programmed maneuver (plus yaw maneuver). Ninety-nine degrees later at 150:15:00:35.458 GMT, sun acquisition was completed and confirmed by the sun lockon signal (FC-69). The total sequence was completed in 372 seconds.

Analysis

Initiation Time of Sun Acquisition Mode. Although several seconds of data at the beginning of the first roll maneuver were lost, sufficient roll gyro response data is available to estimate the actual start time. This estimation is accomplished by comparing the roll gyro response with that of the roll gyro during premidcourse maneuver (Figures 5.6-3 and 5.6-4). The dotted points in the figures represent acquisition phase data, and the crossed marks represent data taken during midcourse maneuvers. From Figure 5.6-3, the start time was T_{SR} = 150:14:54:23.5 GMT.

Start of Plus Yaw Maneuver. Since data was also lost during the start of the yaw maneuver, the same method for determining the start time of the roll maneuver is used for determining yaw start time. In fact, the same parameter, roll gyro signal, is used since the end of the roll maneuver constitutes the beginning of the yaw maneuver.

The response of the roll gyro was compared with the response obtained during the beginning of star verification (plus roll) because the removal of a negative rate command and the application of a positive rate command of the same magnitude produces the same system response (Figure 5.6-5). From Figure 5.6-6, it can be seen that the start time of the yaw maneuver was T_{SY} = 150:14:57:17.5 GMT.

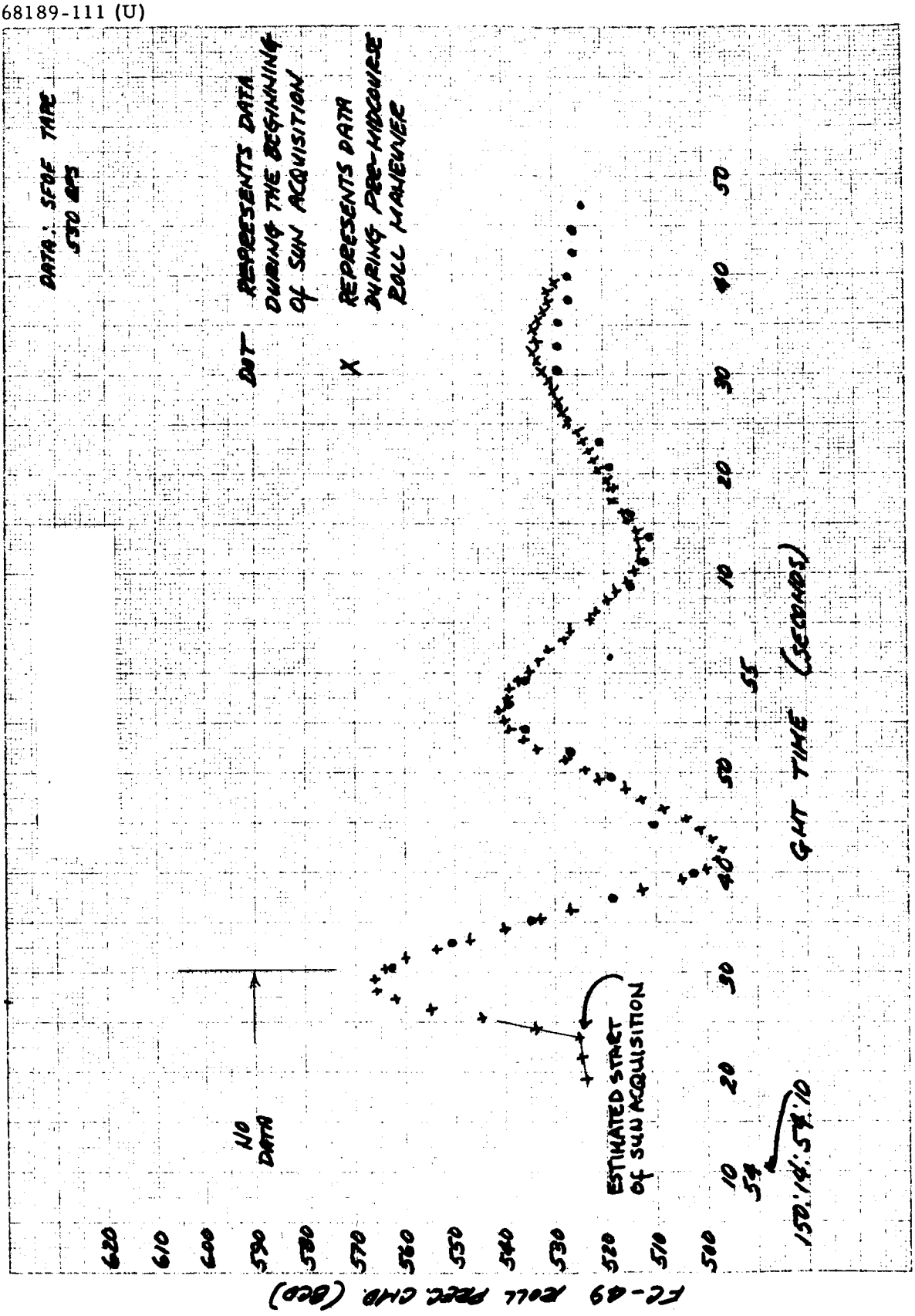


Figure 5.6-3. Roll Gyro Response at Beginning of Sun Acquisition Phase

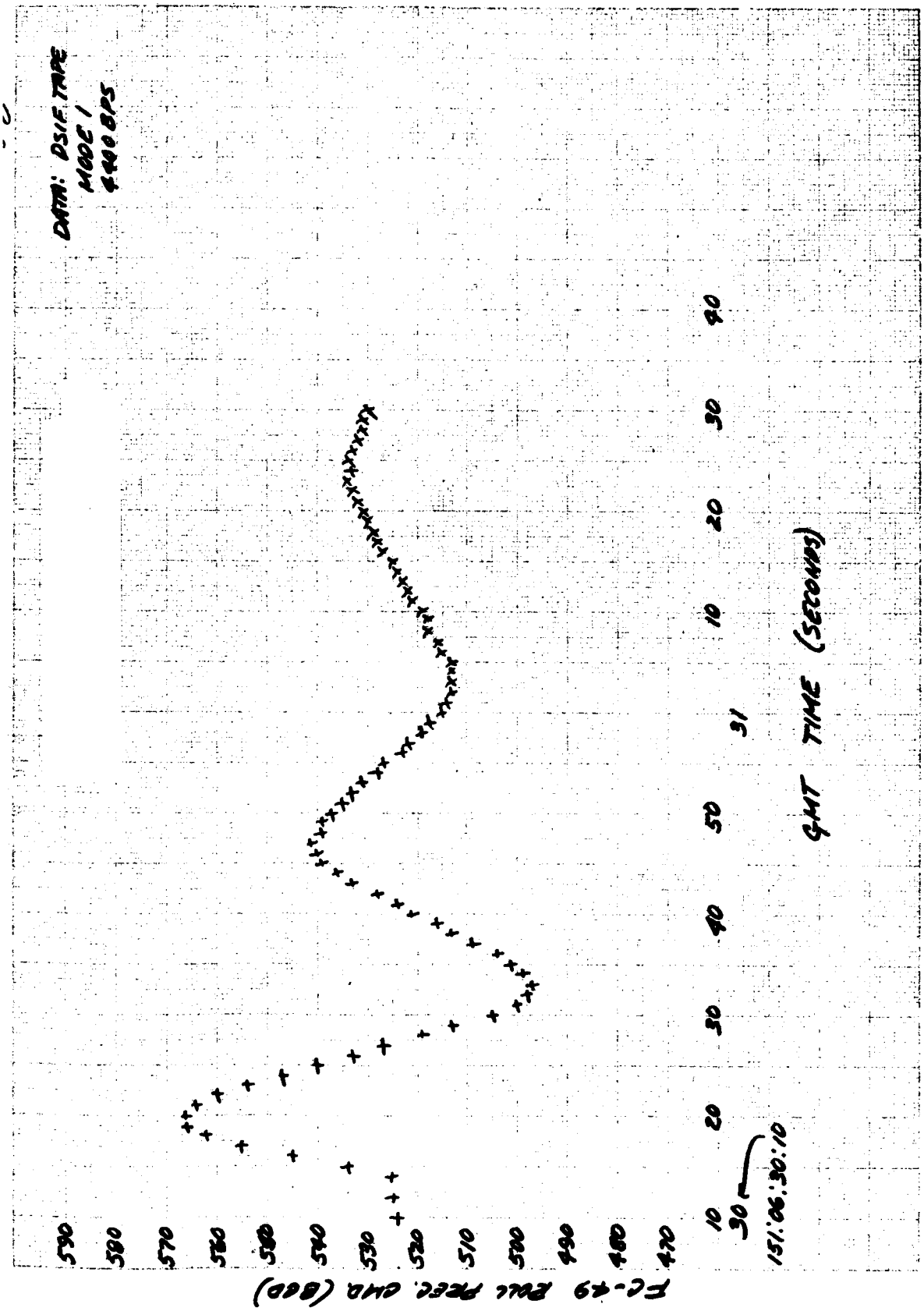


Figure 5.6-4. Roll Gyro Response to a Negative Rate Command at Midcourse

68189-113 (U)

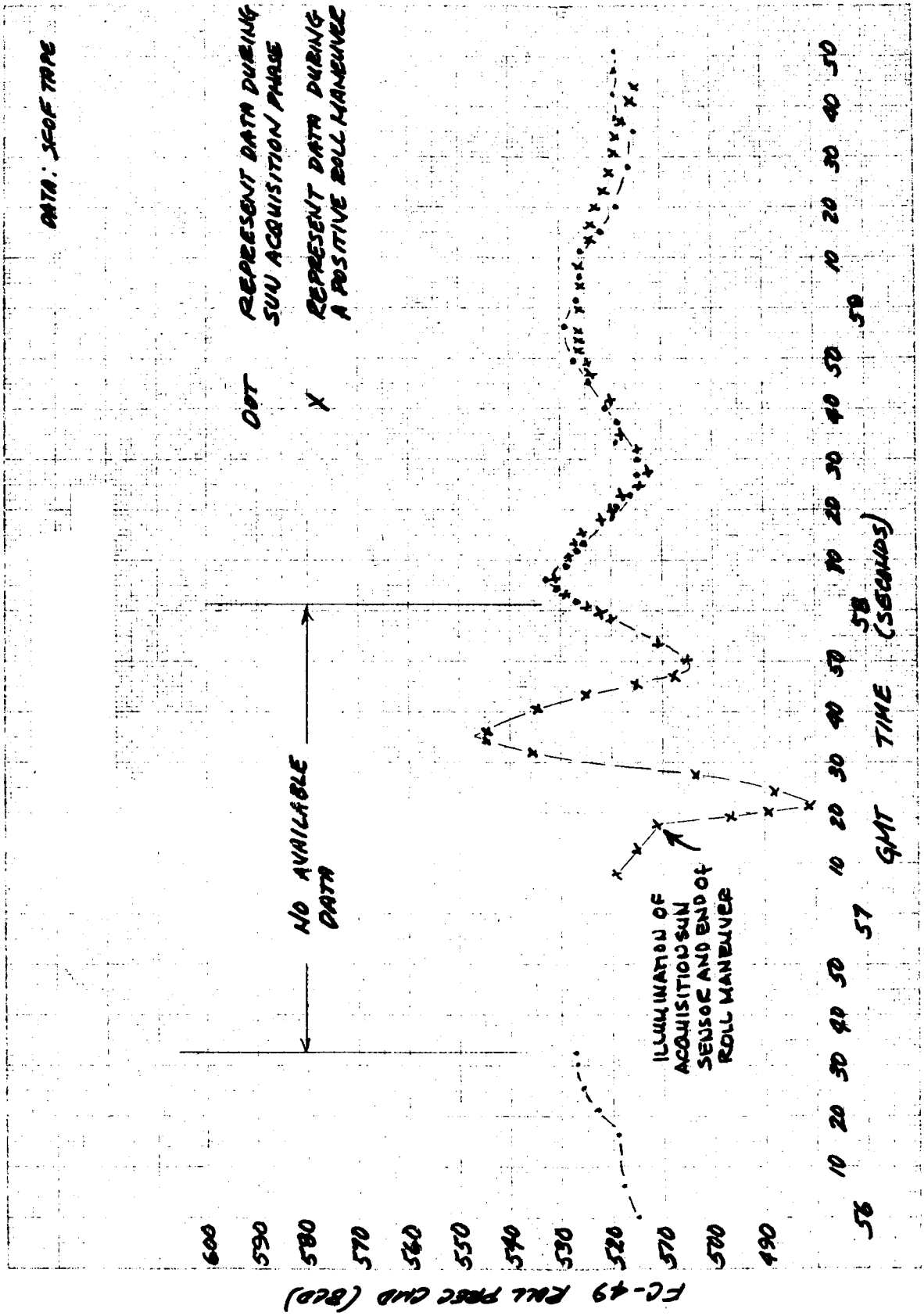


Figure 5.6-5. Roll Gyro Response During Sun Acquisition Phase

68189-114 (U)

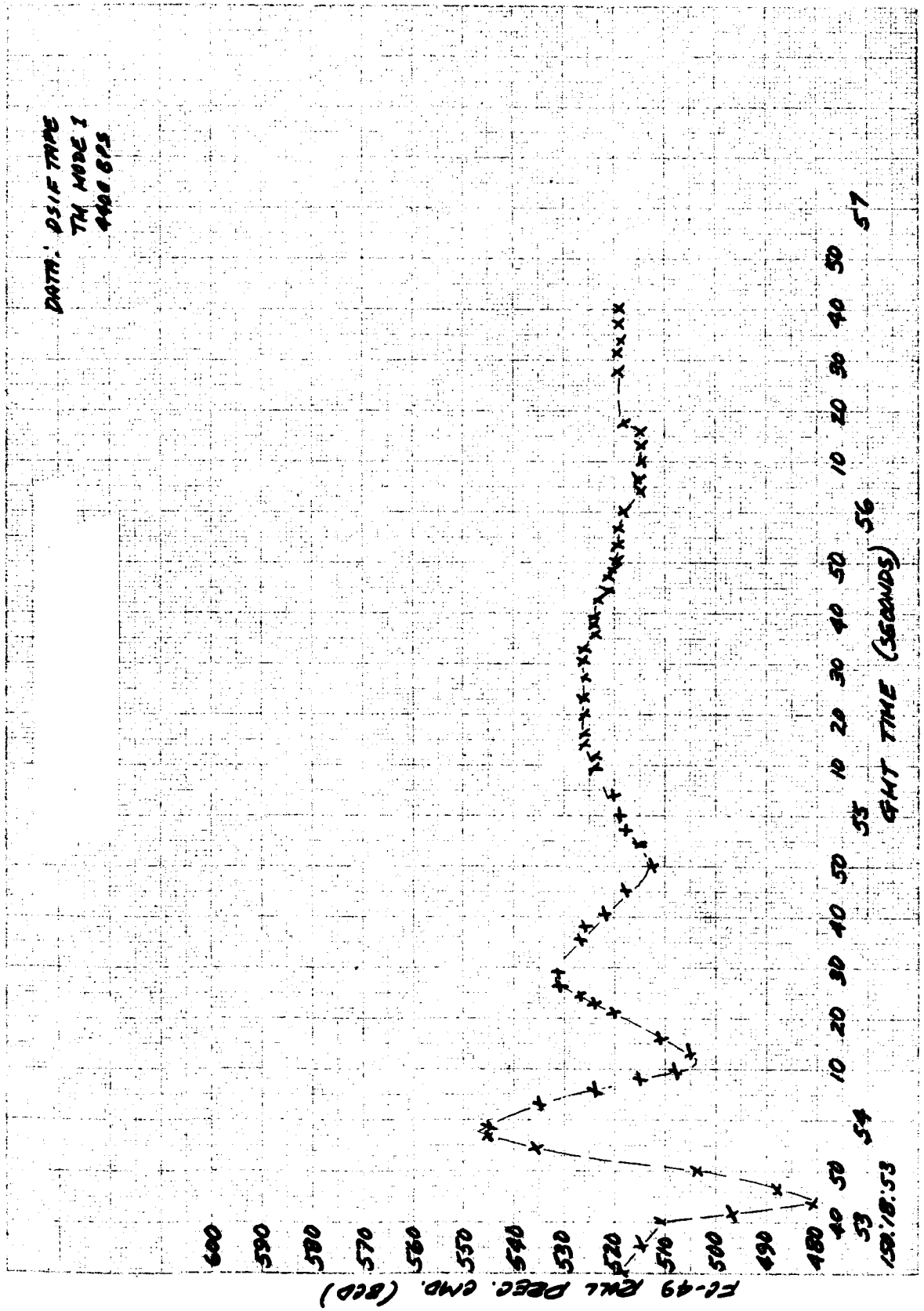


Figure 5.6-6. Roll Gyro Response to a Positive Rate Command

Determination of Maneuver Angles. The angles through which the spacecraft rotated during the sun acquisition phase were obtained by multiplying the maneuver time by 0.500 deg/sec. Thus the angles were:

$$\varphi_R = -0.5 \times 174 = -87 \text{ degrees}$$

$$\psi_Y = 0.5 \times 198 = 99 \text{ degrees}$$

5.6.7.4 Star Acquisition Phase

As defined by the "Surveyor System Functional Requirements Specification," 224510E, Paragraph 3.4.2, "A star acquisition command starts a vehicle position roll of 0.5 deg/sec until a star of the correct brightness falls into this sensor field-of-view. When this occurs, a lockon signal is generated which stops the 0.5 deg/sec roll rate and switches the vehicle roll control to the star sensor error signal."

Automatic lockon was not achieved because the output of the sensor was greater than the upper threshold of the lockon range. This was caused by an intentional increase in sensor gain to compensate for the possibility of window fogging. Star acquisition was achieved by commanding cruise-mode on (0704) followed by a manual lockon command (0716).

Analysis

Star acquisition began with command 0714 (sun and roll) at 150:18:53:39.290 GMT and ended at 19:13:20.723 with command 0716 (manual lockon).

Star Map – Verification of Canopus. The various stars and the number of stars that appear in a particular star map are very sensitive to the hour of the year and the angular position of the sensor axis relative to the spacecraft-sun line. During the May-June launch, the angle between the Canopus-spacecraft line of sight and spacecraft-sun line was approximately 78 degrees. With the aid of a computer program that produces a star map for any given angle and time, the actual Canopus sensor alignment was found to be -11.7 degrees. The star map that launch personnel used was for a -12.0 degree angle that did not indicate Regulus. This was one of the reasons why launch personnel were intrigued when the star Regulus was identified during the mission. At an angle of -11.3 degrees, the star Merak, which is located approximately 232 degrees from Canopus, disappears.

With the aid of a computer generated star map as reference, the other stars which can be identified are as follows:

Star	Angle from Canopus, degrees
Alpha Doradus	16.58
Phi Eridani	37.58
Markab	118.37
Pi Cygni	156.65
Alderamin	170.62
Merak	231.55
Algeiba	269.45
Regulus	277.95
Alpha Hydrae	301.29
Naos	338.44

A comparative plot between actual and computed is shown in Figure 5.6-7.

Mean Roll Rate. The mean roll rate equal to the positive roll precession rate can be determined as follows:

1) Angle between Markab and Naos is 220.073 degrees.

2) Time interval between the two stars is 439.792 seconds.

Thus

$$\dot{\varphi}_Z = 0.5004 \text{ deg/sec}$$

Effective Gain of Canopus Sensor. In general, the Canopus sensor gain is set such that a star of Canopus brightness will produce a signal of nominal Canopus lockon value. This value is approximately 5 volts.

For SC-1, the sensor gain was increased 50 percent by installing a sun filter on the sensor's sun input which is used as reference. This action was initiated to compensate for the possibility of excess fogging of the sensor's window.

From the investigation, the Canopus sensor gain appears to have been slightly greater than 1.5 times Canopus. This value was obtained by comparing the actual data to calibration curves of the particular sensor (Figure 5.6-8). The Canopus error signal was plotted along with star intensity to determine the zero angle position.

Since the upper acquisition limit is 1.5 times Canopus intensity and the intensity of Canopus with the high sensor gain setting was determined to be just slightly higher than 1.5 times Canopus, little margin existed between the two.

Window Fogging. From FC-14 data (star intensity signal), it appears that very little change occurred in the overall gain of the Canopus sensor during the 63-hour mission (Figures 5.6-8, 5.6-9, and 5.6-10). A slight change in gain appears to have occurred, as indicated in Figure 5.6-10, during the beginning of the preretro maneuver, but this is believed due to telemetry network lag effect. In the first two cases (Figures 5.6-8 and 5.6-9), the angular rates are at a steady-state value of 0.5 deg/sec; thus, the input to the telemetry conditioning network is essentially a ramp type function, whereas during the beginning of a maneuver the input is a parabolic function. From the three plots, it can be concluded that no fogging or very little fogging of the sensor window occurred during the mission.

Roll Angle from Beginning of Maneuver to Canopus. From the data of roll gyro angle, roll was initiated at 18:53:40.100 GMT. First Canopus peak occurred at 19:01:00.650 GMT, and the roll rate was 0.5008 deg/sec. Thus, the angle between the beginning of star mode and first Canopus appearance was φ = 220.627 degrees.

Additional Information

During the investigation of Canopus sensor gain, the null level of FC-12 (Canopus error signal) was much lower than expected. The expected null (zero angle) value is 520 bcd, and the data during the star mapping phase indicates an apparent null of 445 bcd, or a difference of approximately 0.3 degree.

Further investigation of this signal during other phases of the mission, such as midcourse maneuver, revealed that the null point of the sensor was indeed 520 bcd when looking at Canopus, but changed to approximately 450 bcd when observing less intense stars or relatively empty space (Figure 5.6-11).

A false star of considerable intensity is evident at approximately 5 degrees before the first observation of Canopus. This star did not appear on the second approach to Canopus or on any subsequent maneuver. It was first theorized that, since the star map is sensitive to the angle which the sensor makes with the spacecraft-sun line, the change in yaw angle caused by the optical mode limit cycle possibly was sufficient to introduce another star in the field of view. However, investigation of the sun sensor yaw and pitch error signals revealed that this was not the cause.

The results were as follows:

1) 5 degrees before first Canopus (19:00:47.450)

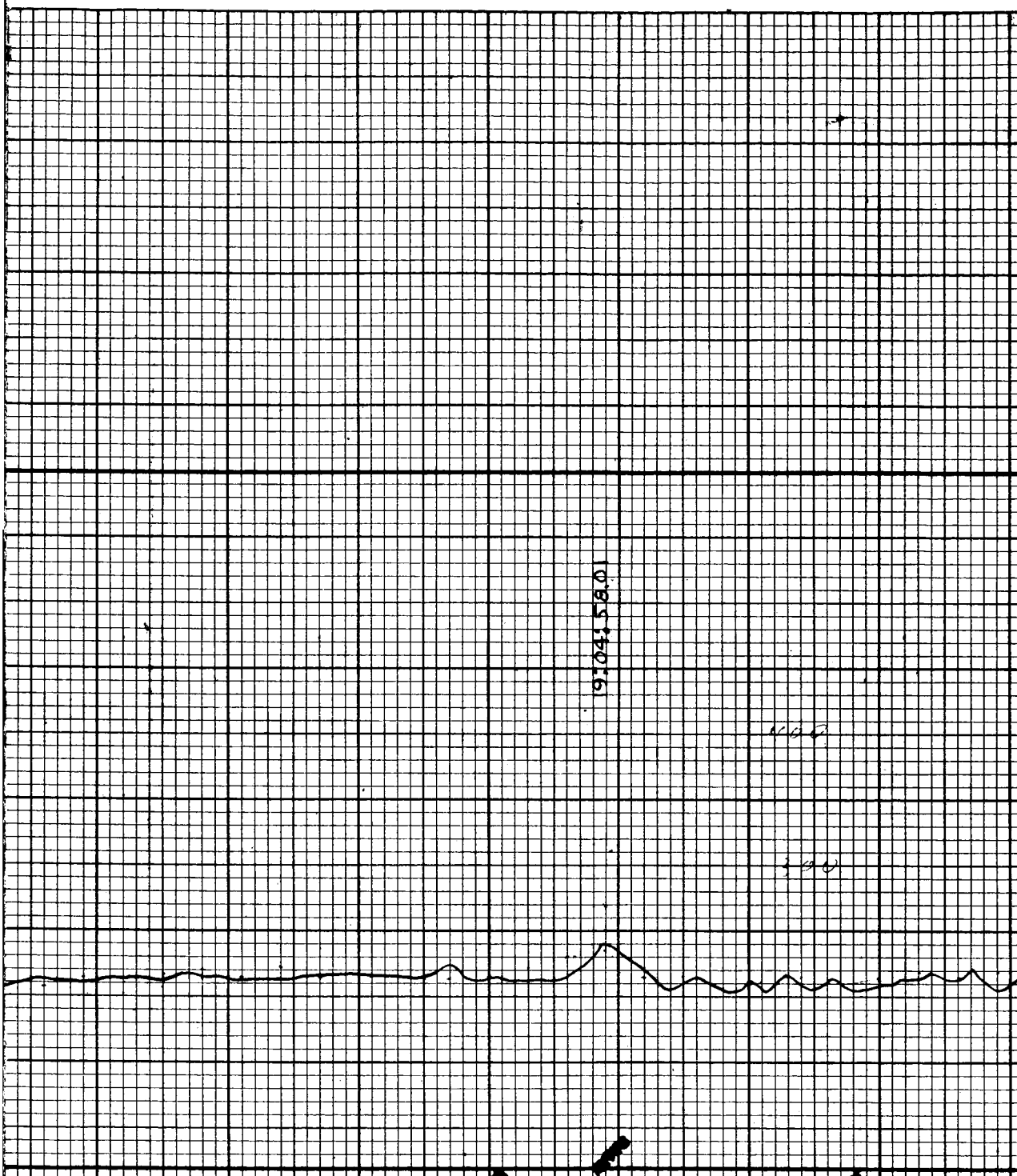
   FC-5 = -0.103 degree (489 bcd)

   FC-6 = -0.213 degree (505 bcd)



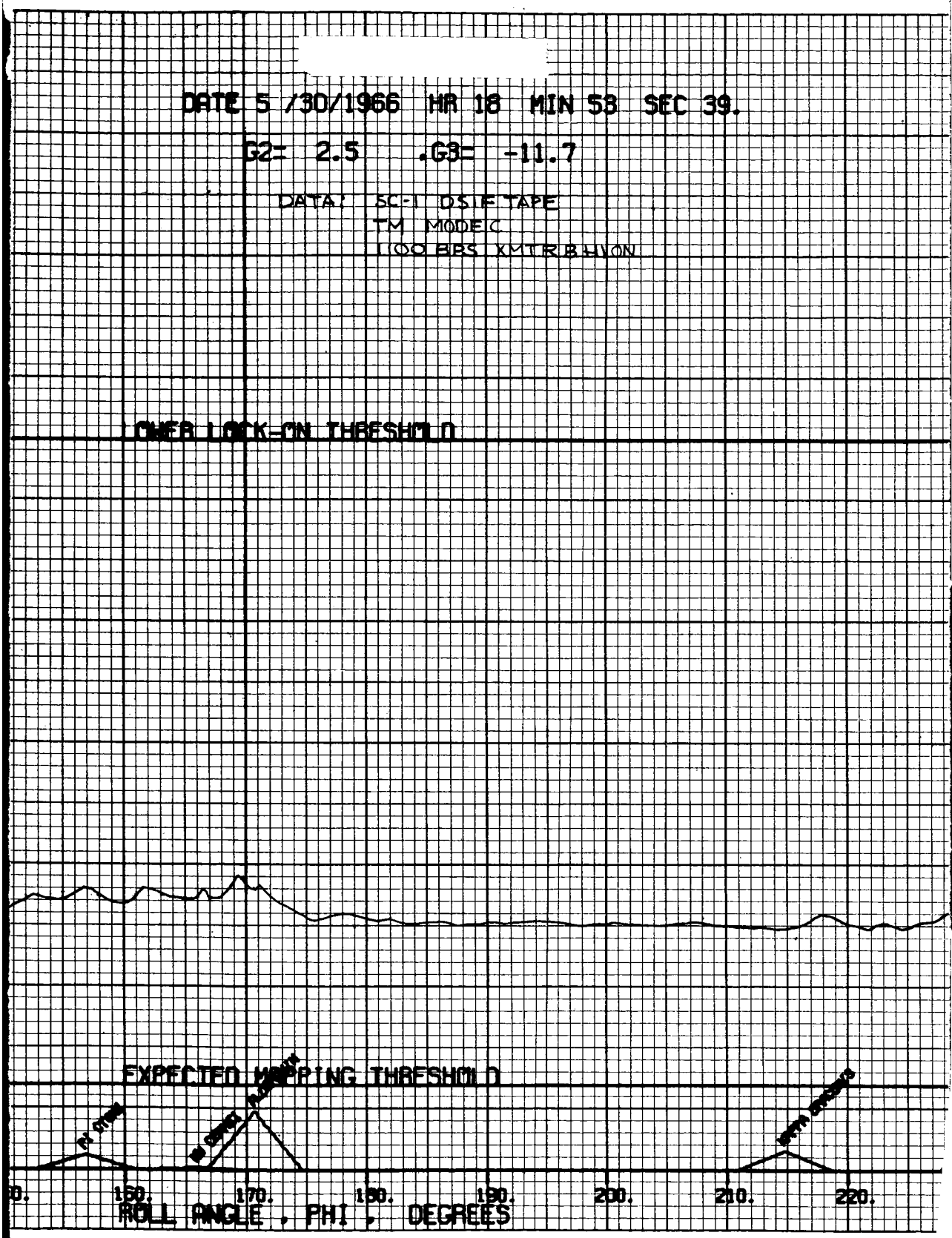
Figure 5.6-7. Star Map

FOLDOUT FRAME



FOLDOUT FRAME

5.6-31-2



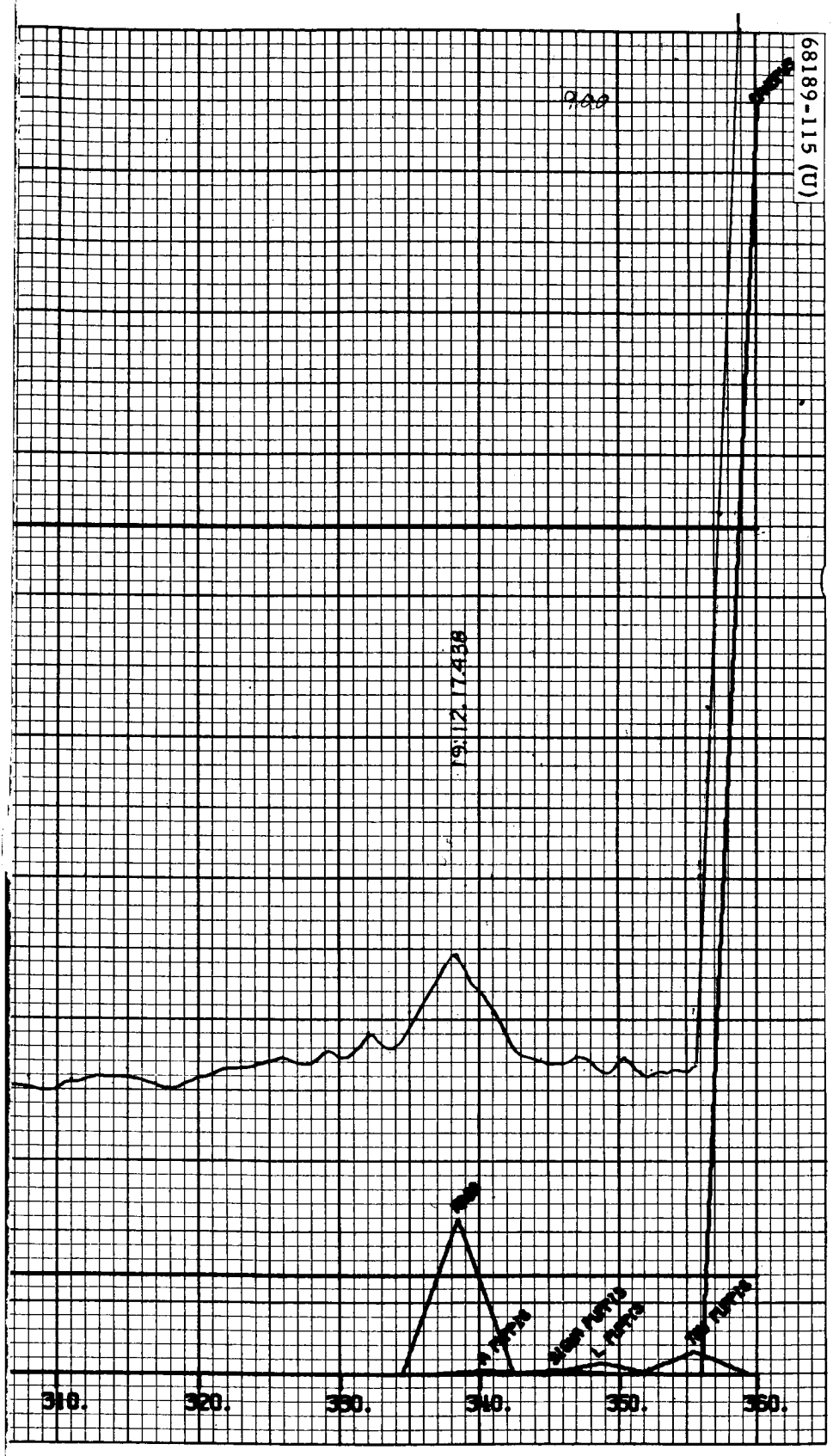
5.6-31-3

FOLDOUT FRAME



FOLDOUT FRAME

5.6-32-1



68189-115 (U)

5.6-3.0-2

FOLDOUT FRAME

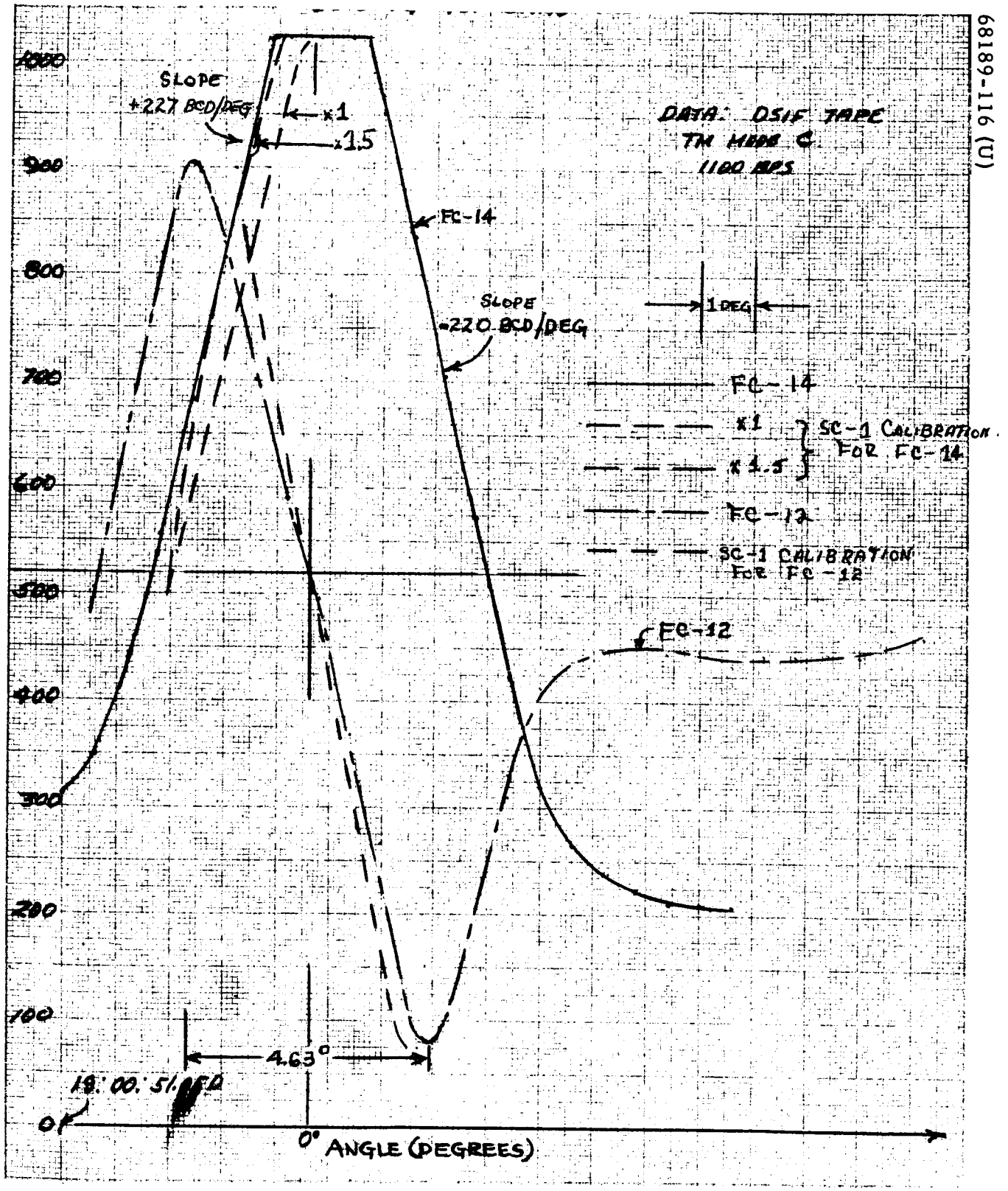
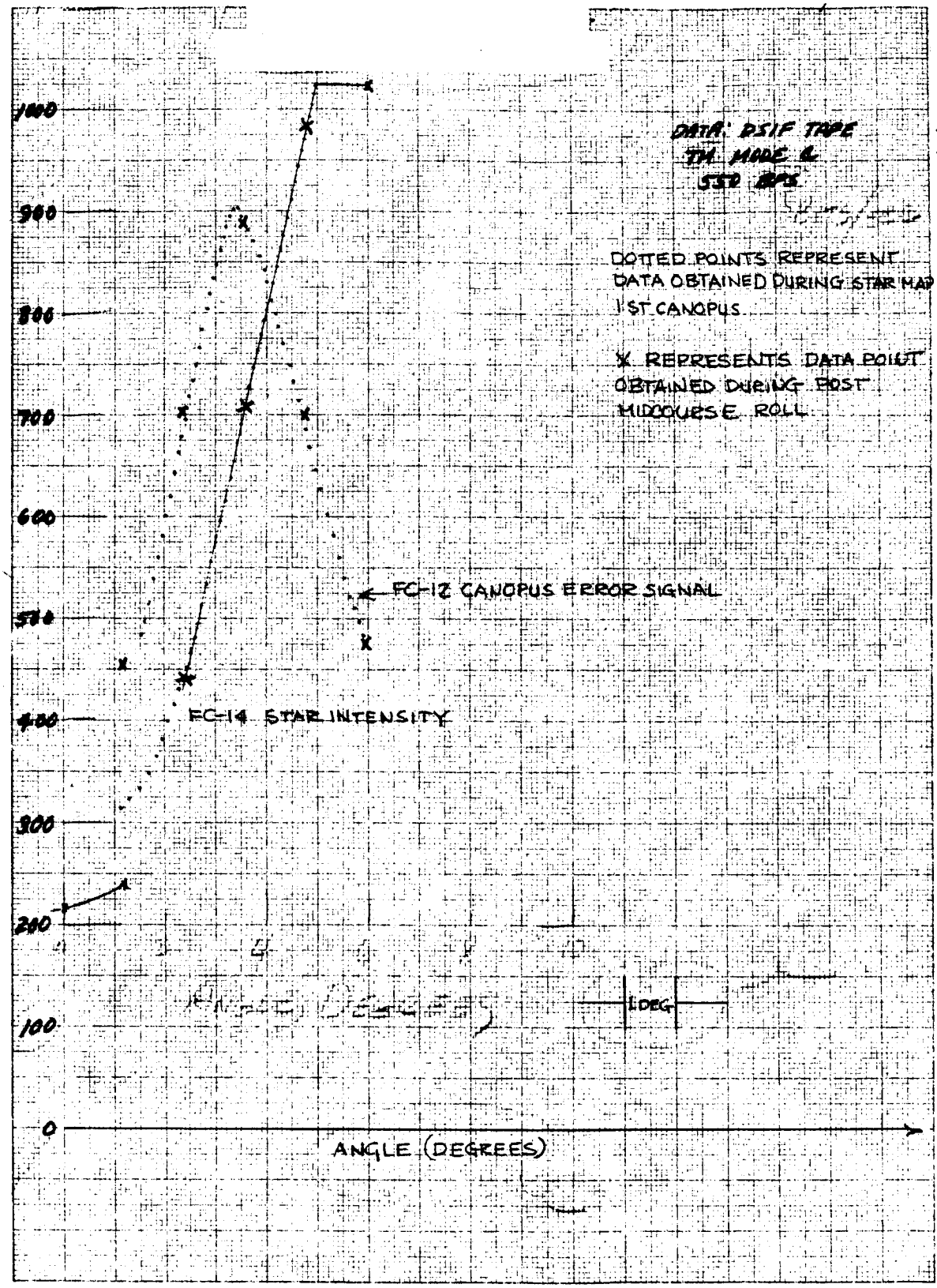


Figure 5.6-8. Star Intensity Profile During First Canopus



68189-117 (U)

Figure 5.6-9. Star Intensity Profile During Postmidcourse Roll

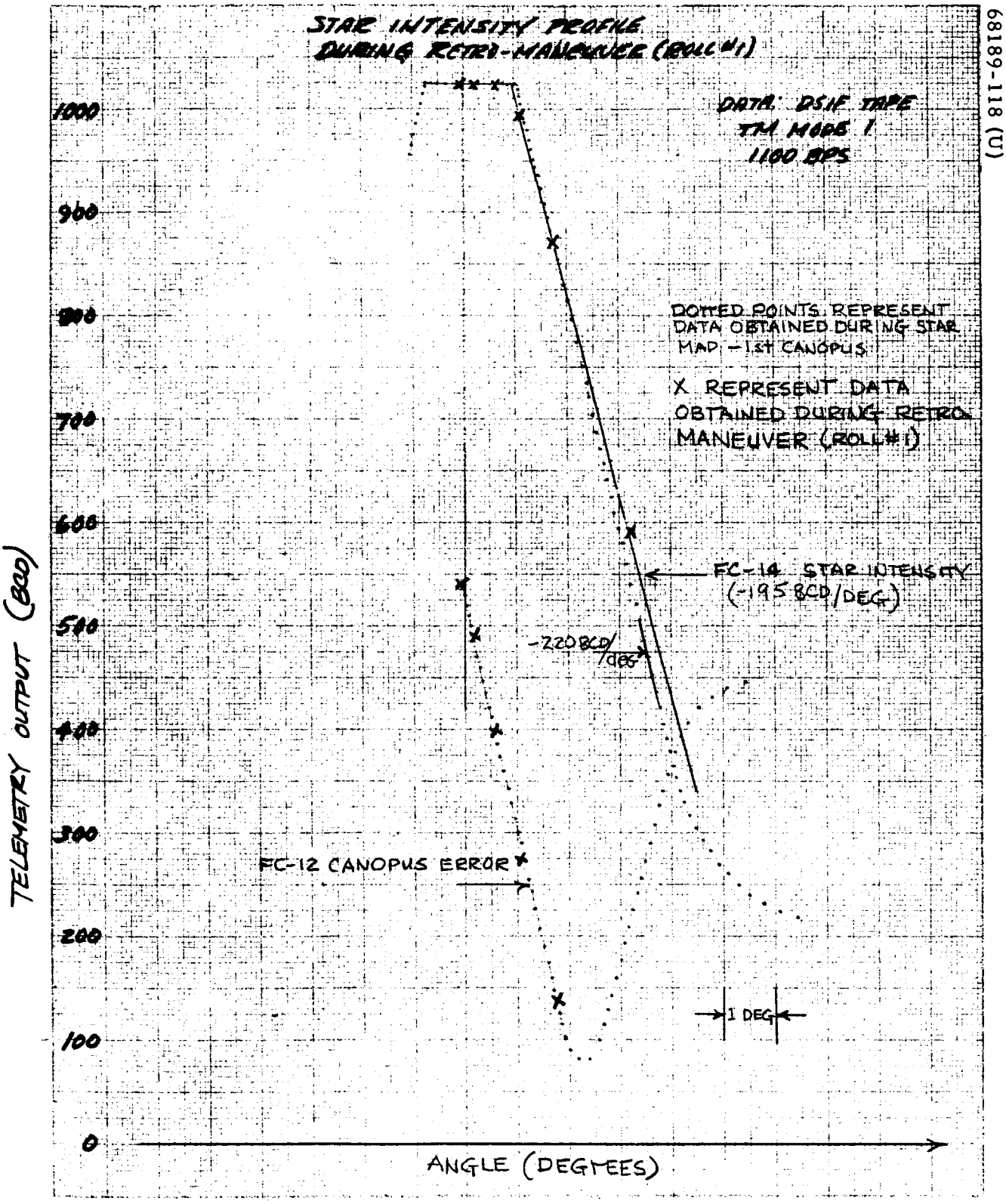


Figure 5.6-10. Star Intensity Profile During Ratio Maneuver (Roll

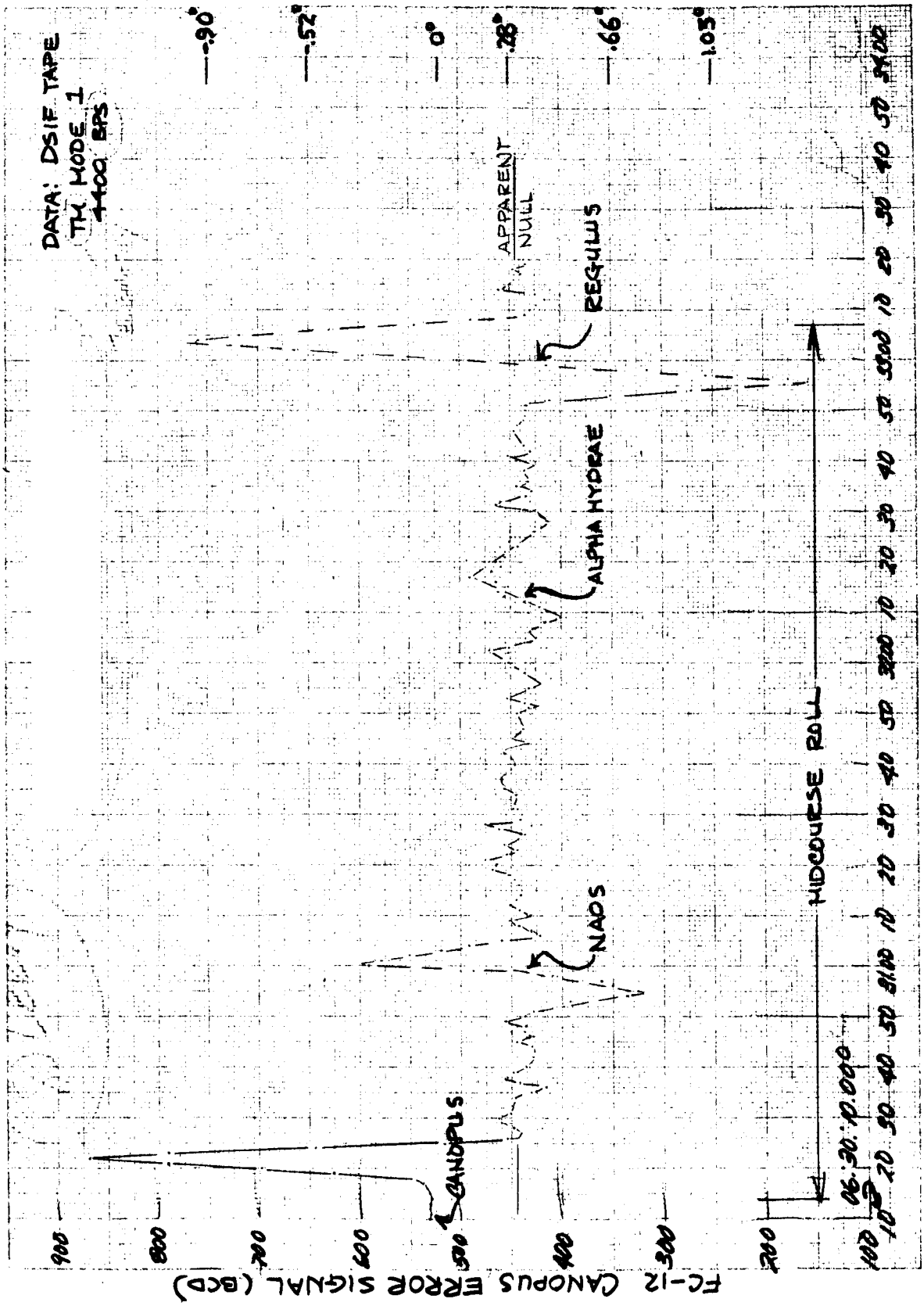


Figure 5.6-11. Canopus Error Signal Profile During First Midcourse Roll

2) 5 degrees before second Canopus (19:12:47.438)

FC-5 = -0.154 degree (496 bcd)

FC-6 = -0.152 degree (496 bcd)

Thus, the difference in yaw attitude at 5 degrees prior to first and second Canopus was -0.061 degree. The remaining conclusion is that a particle was momentarily in the field of view (Figures 5.6-12 and 5.6-13).

Intermittent lockon signals occurred throughout the star verification and acquisition phase. FC-13 data (Canopus lockon) indicates that the on-off periods are not random but periodic in nature (Table 5.6-9). It is believed that passage through the Van Allen belt with the high gain setting of the sensor was the cause of this minor anomaly. Figures 5.6-14 through 5.6-18 are included for additional information.

TABLE 5.6-9. CANOPUS LOCKON SIGNAL

Time, GMT	FC-13	ΔT	Time, GMT	FC-13	ΔT	Time, GMT	FC-13	ΔT
			150185510536	0		150185724934	1	
			150185518936	1	8.4	150185726134	0	1.2
			150185520136	0	1.2	150185729734	1	3.6
150185332000	0		150185521336	1	1.2	150185730934	0	1.2
150185340538	1		150185523736	0	2.4	150185732134	1	1.2
150185341738	0	1.2	150185523737	1		150185735734	0	3.6
150185344138	1	2.4	150185526136	0	2.4	150185744134	1	8.4
150185345338	0	1.2	150185534536	1	8.4	150185747734	0	3.6
150185346538	1	1.2	150185535736	0	1.2	150185753733	1	6.0
150185348938	0	2.4	150185554935	1	9.2	150185754933	0	1.2
150185350138	1	1.2	150185557335	0	2.4	150185757333	1	2.4
150185351338	0	1.2	1501856 6935	1	9.6	150185759733	0	2.4
150185402137	1	10.9	150185610535	0	3.6	1501858 0933	1	1.2
1501854 4537	0	2.3	150185615335	1	4.8	1501858 2133	0	1.2
1501854 5737	1	1.2	150185616535	0	1.2	1501858 3333	1	1.2
1501854 6937	0	1.2	150185618935	1	2.4	1501858 4533	0	1.2

Table 5.6-9 (continued)

Time, GMT	FC-13	ΔT	Time, GMT	FC-13	ΔT	Time, GMT	FC-13	ΔT
1501854 9337	1	2.4	150185620135	0	1.2	1501858 5733	1	1.2
150185410537	0	1.2	150185630935	1	10.8	1501858 9333	0	3.6
150185415337	1	4.8	150185633335	0	2.4	150185810533	1	1.2
150185416537	0	1.2	150185635735	1	2.4	150185812933	0	2.4
150185417737	1	1.2	150185638135	0	2.4	150185814133	1	1.2
150185420137	0	2.4	150185646535	1	8.4	150185818933	0	4.8
150185422537	1	2.4	150185647735	0	1.2	150185820133	1	1.2
150185426137	0	3.6	150185651335	1	3.6	150185826133	0	6.0
150185445337	1	1.2	150185652535	0	1.2	150185829733	1	3.6
150185446537	0	1.2	150185656135	1	3.6	150185830933	0	1.2
150185447737	1	1.2	150185658534	0	2.4	150185832133	1	1.2
150185454937	0	7.2	1501857 4534	1	6.0	150185833333	0	1.2
150185456137	1	1.2	1501857 5734	0	1.2	150185845333	1	12.0
150185457337	0	1.2	150185710534	1	4.8	150185846533	0	1.2
1501855 3336	1	6.0	150185714134	0	3.6	150185854932	1	8.4
1501855 4536	0	1.2	150185718934	1	4.8	150185856132	0	1.2
1501855 6936	1	2.4	150185720134	0	1.0	150185902132	1	6.0
1501859 4532	0		15019 208129	1		15019 4 3327	0	
150185923732	1		15019 211729	0	3.6	15019 4 6927	1	
150185924932	0		15019 224929	1	13.2	15019 4 9327	0	
150185926132	1		15019 232129	0	8.2	15019 410527	1	
150185928532	0	2.4	15019 233329	1	1.2	15019 411727	0	
150185936932	1	8.4	15019 239328	0	6.0	15019 414127	1	
150185938132	0	1.2	15019 241728	1	2.4	15019 415327	0	
150185940532	1	2.4	15019 244128	0	2.4	15019 432127	1	
150185941732	0	1.2	15019 246528	1	2.4	15019 438126	0	

Table 5.6-9 (continued)

Time, GMT	FC-13	ΔT	Time, GMT	FC-13	ΔT	Time, GMT	FC-13	ΔT
150185942932	1	1.2	15019 248928	0	2.4	15019 441726	1	
150185944133	0	1.2	15019 254928	1	6.0	15019 442926	0	
150185946532	1	2.4	15019 256128	0		15019 444126	1	
150185947732	0	1.2	15019 3 0929	1		15019 447726	0	
150185948931	1	1.2	15019 3 3328	0		15019 448926	1	
150185951331	0	2.4	15019 3 8128	1		15019 451326	0	
150190009331	1	8.0	15019 3 9328	0		15019 454926	1	
150190011731	0	2.4	15019 315328	1		15019 456126	0	
150190012931	1	1.2	15019 316528	0		15019 5 4526	1	
150190023731	0	10.8	15019 317728	1		15019 5 5726	0	
150190024931	1	1.2	15019 318928	0		15019 5 8126	1	
150190029731	0	4.8	15019 321328	1		15015 5 9326	0	
150190048930	1	19.2	15019 322528	0		15019 512926	1	
150190051330	0	2.4	15019 324928	1		15019 514126	0	
150190109330	1	8.0	15019 326128	0		15019 518926	1	
150190111730	0	2.4	15019 327328	1		15019 520126	0	
150190115330	1	3.6	15019 328528	0		15019 521326	1	
150190117730	0	2.4	15019 333328	1		15019 522526	0	
150190120130	1	2.4	15019 338127	0		15019 528526	1	
150190121330	0	1.2	15019 351327	1		15019 529726	0	
15019 130930	1	9.6	15019 352527	0		15019 535725	1	
150190133330	0	2.4	15019 354927	1		15019 536925	0	
150190153729	1	20.4	15019 356127	0		15019 539325	1	
15019 158529	0	4.8	15019 358527	1		15019 540525	0	

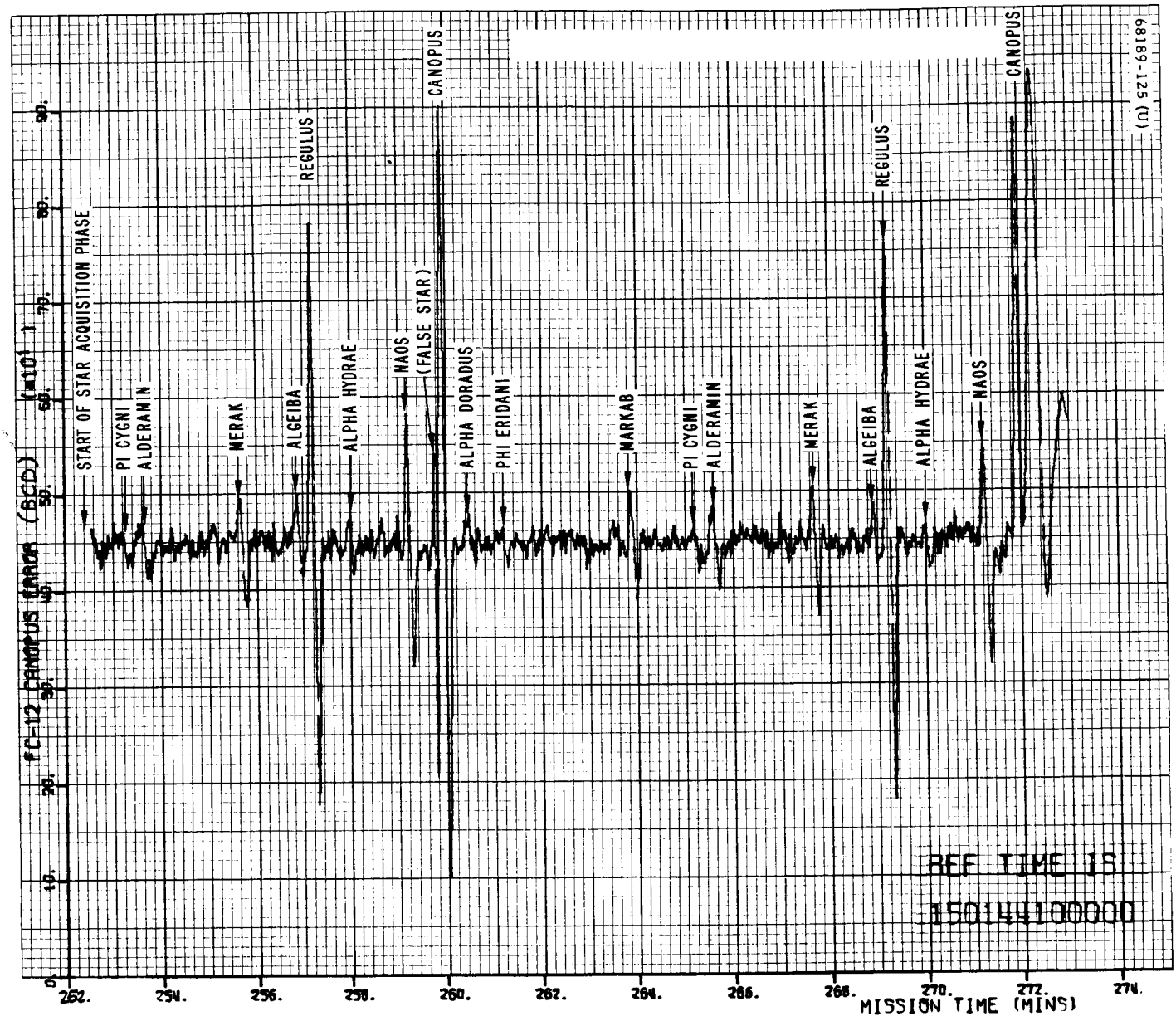


Figure 5.6-12. Canopus Error Signal (Star Map)

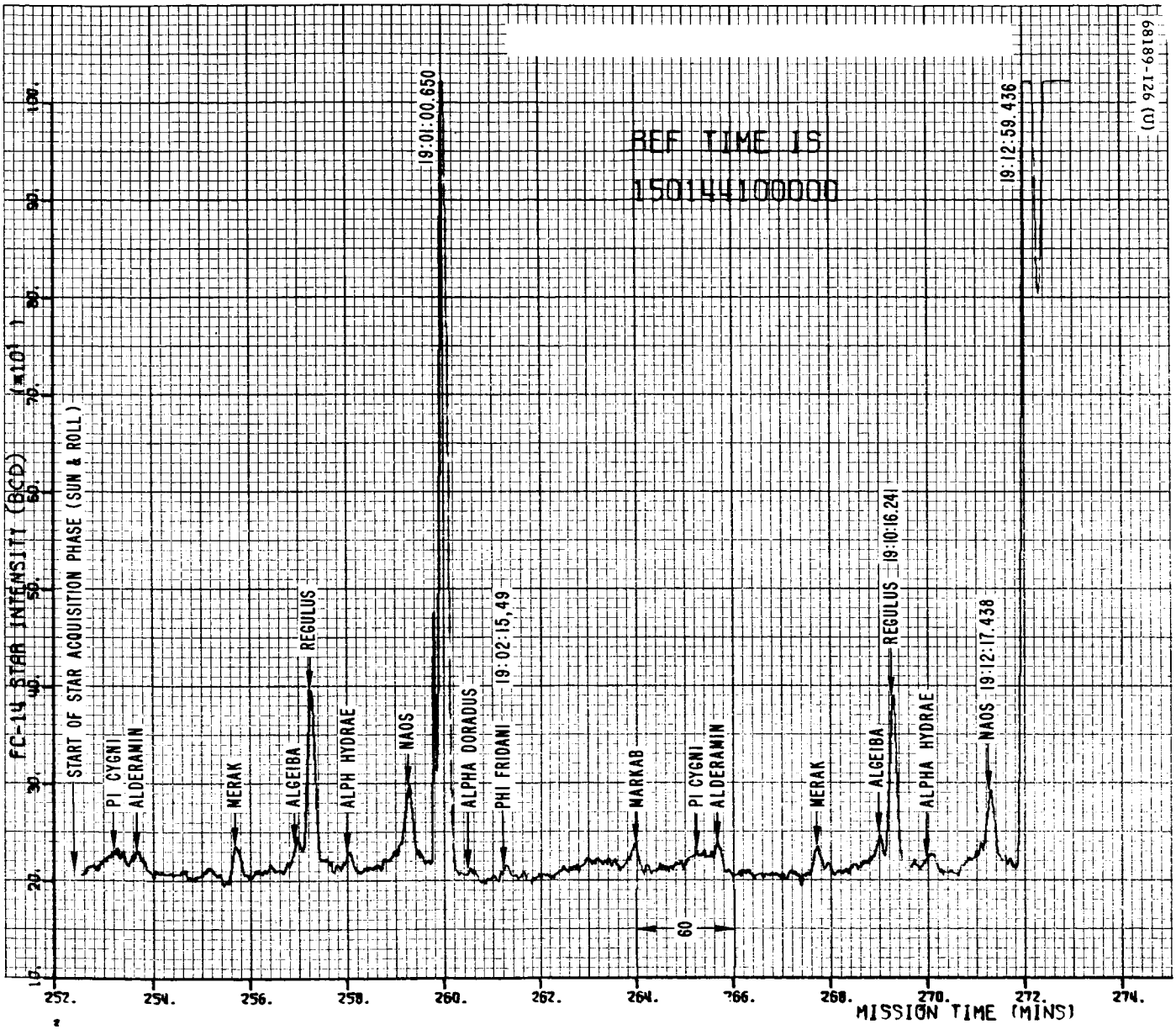


Figure 5.6-13. Star Intensity Signal (Star Map)

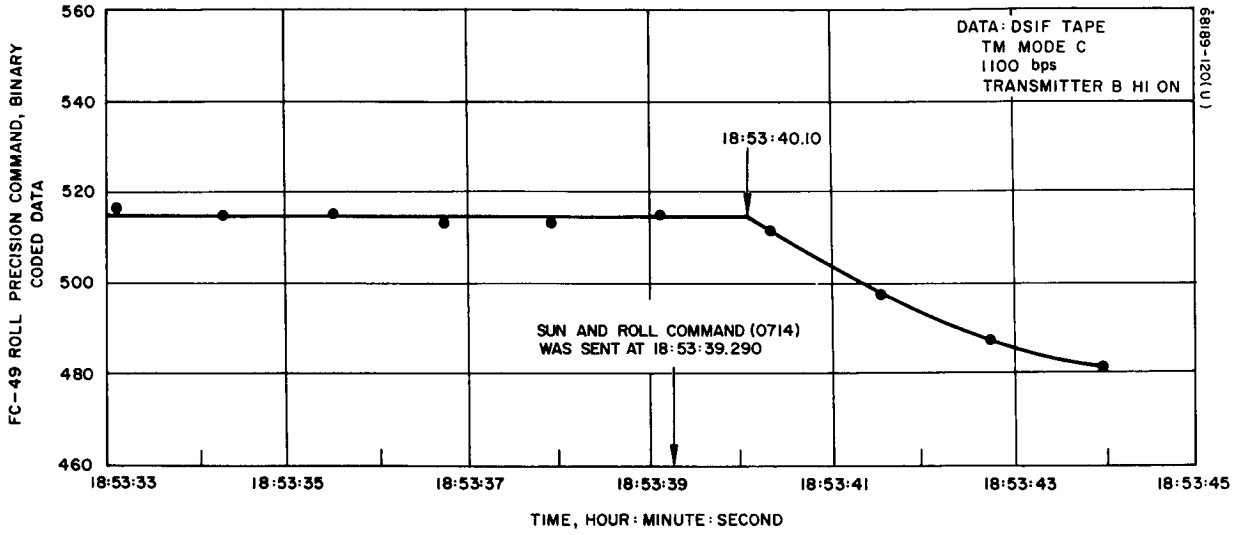


Figure 5.6-14. Roll Gyro Response at Beginning of Star Acquisition

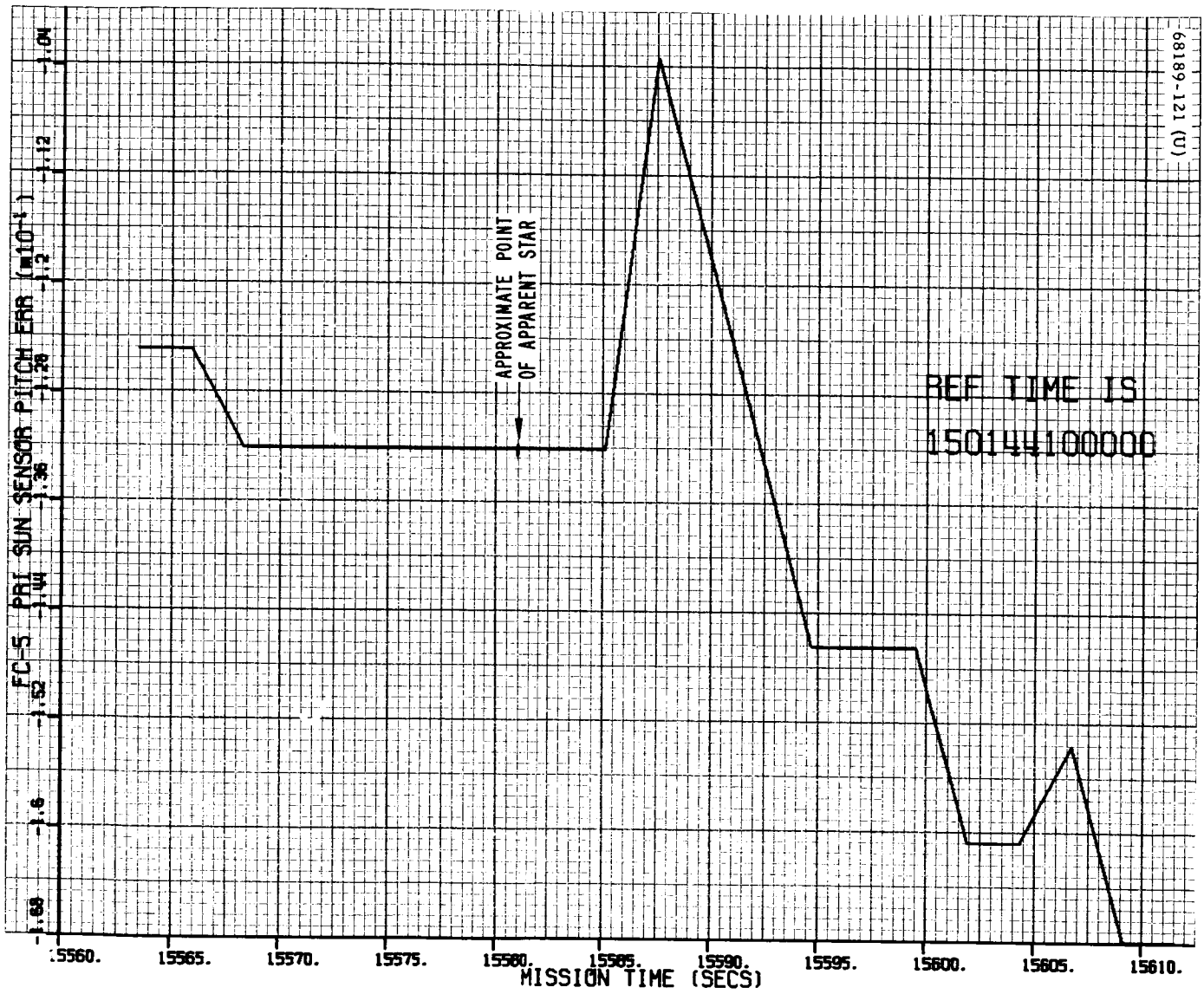


Figure 5.6-15. Primary Sun Sensor Pitch Error Approaching Canopus first time

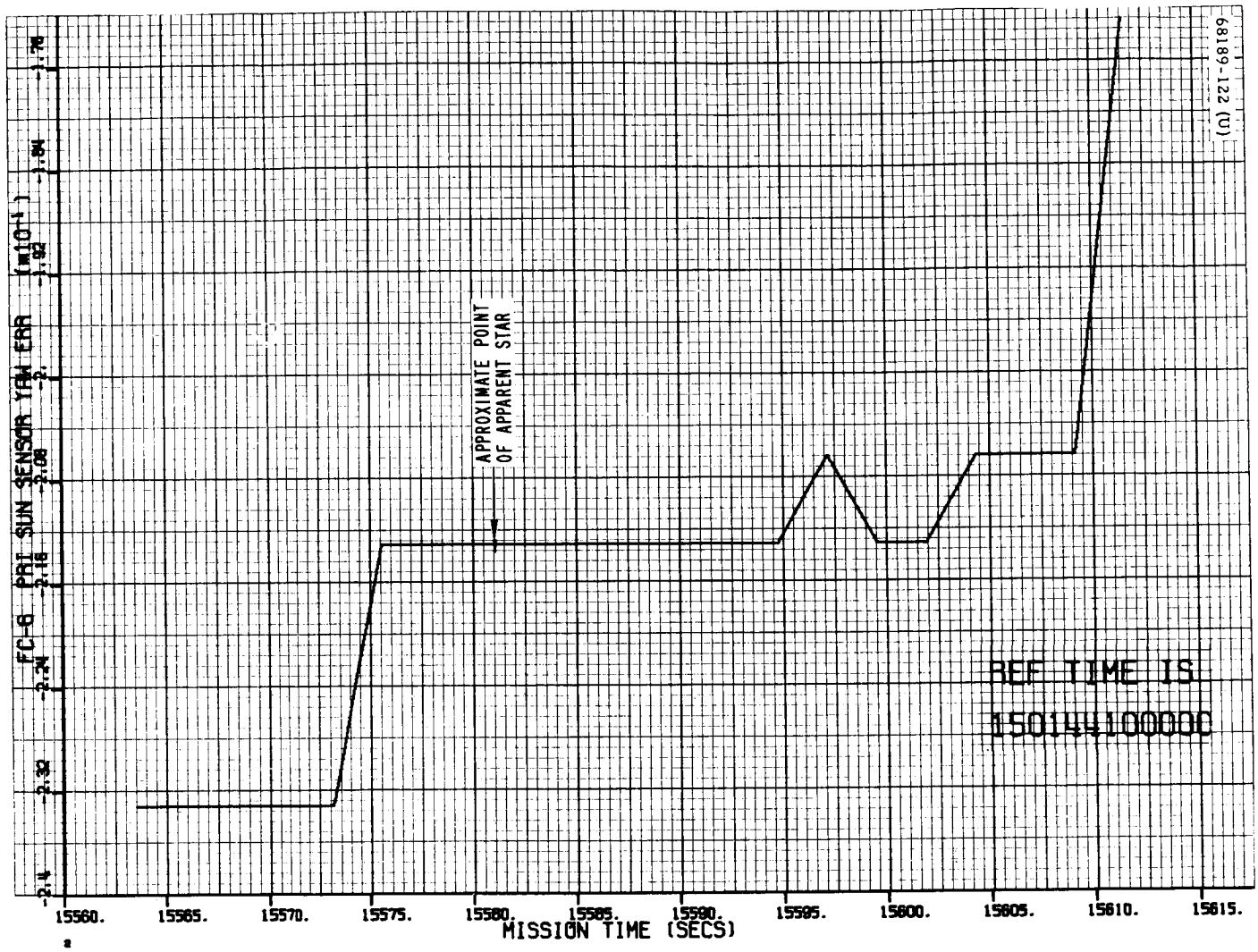


Figure 5.6-16. Primary Sun Sensor Yaw Error Approaching Canopus first time

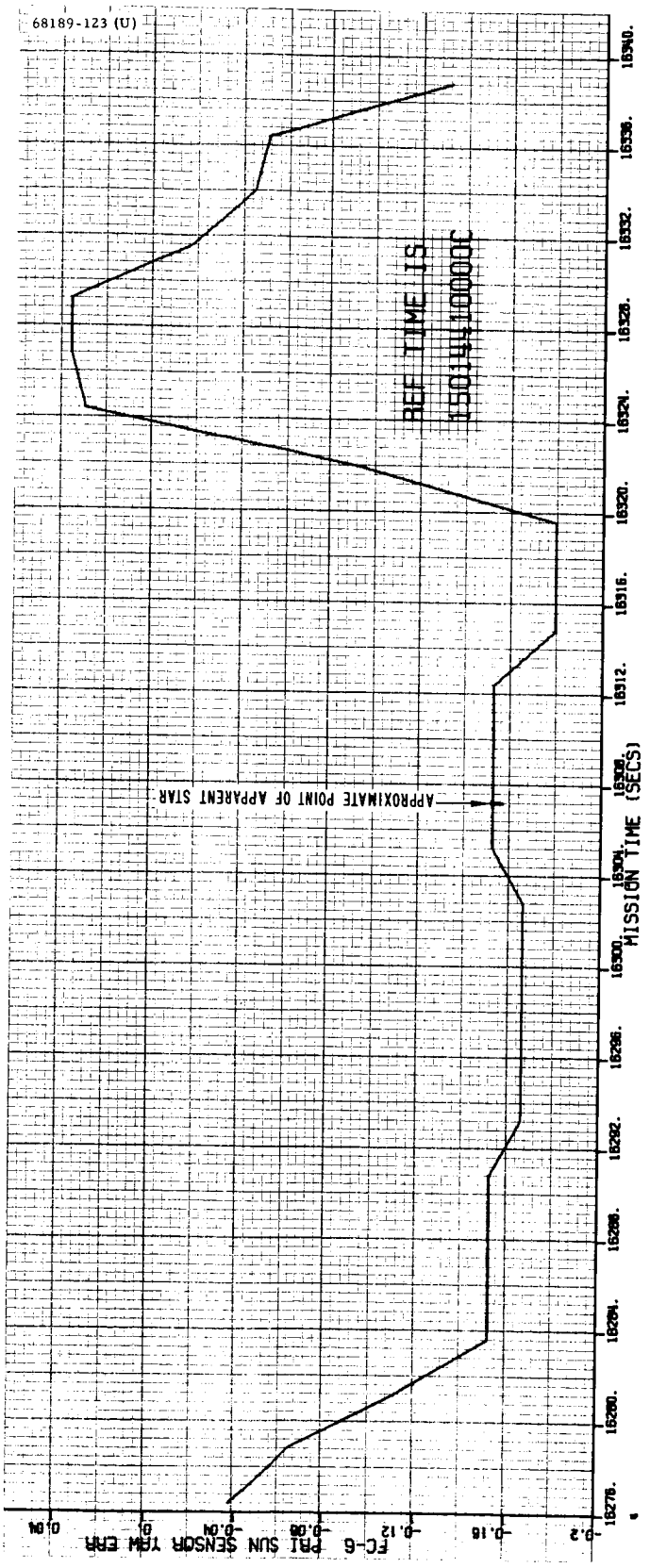


Figure 5.6-17. Primary Sun Sensor Yaw Error
Approaching Canopus second time

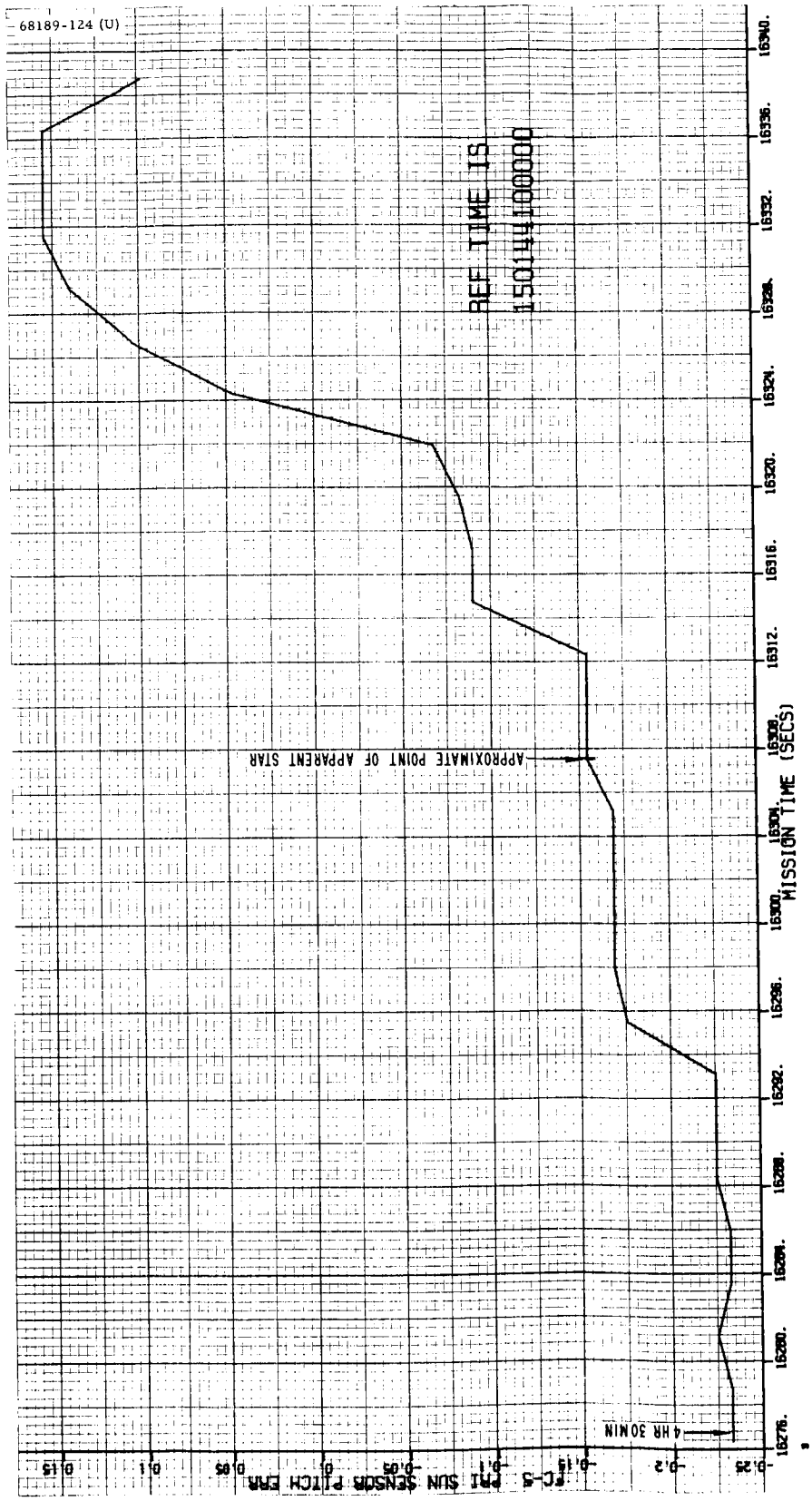


Figure 5.6-18. Primary Sun Sensor Pitch Error
Approaching Canopus second time

5.6.7.5 Coast Mode

The three-axis cold gas attitude control system is designed to maintain an optical or inertial reference during the nonthrusting portions of the Surveyor flight. The spacecraft pitch and yaw optical references are provided by a narrow field of view sun sensor; the roll optical reference is provided by a Canopus sensor whose field of view is 5 degrees latitude and 8 degrees longitude. The spacecraft inertial references are provided by three body-fixed rate integrating gyros.

The actuators used in the coast mode are the cold gas jets. The on-off operation of these jets plus the deadbands built into the system at the gas jet amplifiers cause the spacecraft to function in a three-axis limit cycle. In the steady state, the Surveyor attitude coasts along a straight line within the three-dimensional deadband of θ, φ, ψ space. Upon intercepting a bounding plane, a gas jet pulse is emitted, driving the system back within the deadband along a new straight line. These motions are entirely analogous to the motions of a ball bouncing internally within a closed three-dimensional planar-sided polygon of six sides wherein the law of reflection is that the velocity components of the ball change by discrete amounts (as caused by a jet pulse), the amounts being constant for any one plane. The motions are aperiodic and are a strong function of initial velocity conditions.

The non-g sensitive drift rates of the integrating rate gyros were measured six times during Mission A by slaving the spacecraft to the drifting inertial references and observing the drift rates by means of the telemetered optical references.

The principal items of analysis for the flight control system coast phase were as follows:

1) Limit cycle frequency and amplitude

2) Sun and star tracking errors and tracking noise

3) N_2 gas used

4) Individual and averaged results of gyro drift measurements compared with FAT results

The major events for the coast phase, together with their corresponding times, are presented for reference in Table 5.6-10. Table 5.6-11 is a summary of the analysis results for the coast phase.

Conclusions and Recommendations

1) Limit cycle behavior was as predicted except that the roll limit cycle occasionally exhibited the tendency to double-pulse at each side of the deadspace (ideally, it should always single-pulse). About 24 percent of the fuel consumed during the sampled limit cycle period was a result of double pulsing. However, since the fuel penalty was very low (about 0.04 pound) and the limit cycle width was unchanged, this additional pulsing was readily tolerated.

TABLE 5.6-10. MAJOR EVENTS AND TIMES

Event	Time, GMT	Command
Sun lockon	150:15:00:34	Automatic sequence
Star map (begin)	150:18:53:39	0714
Canopus acquire (manual lockon)	150:19:13:20	0716
Begin gyro drift check 1	150:20:54:02	0700
End gyro drift check 1	150:23:51:10	0704
Begin premidcourse maneuvers	151:06:30:12	0714
End postmidcourse maneuvers	151:07:00:55	0714
Begin gyro drift check 2	151:09:30:14	0700
End gyro drift check 2	151:12:30:16	0704
Begin gyro drift check 3	152:4:18:39	0700
End gyro drift check 3	152:6:25:57	0704
Begin gyro drift check 4	152:7:34:15	0700
End gyro drift check 4	152:9:52:16	0704
Begin gyro drift check 5	152:9:55:42	0700
End gyro drift check 5	152:13:05:03	0704
Begin gyro drift check 6	152:19:20:43	0700
End gyro drift check 6	152:21:41:51	0704
Begin preretro maneuvers	153:5:36:46	0714

Note: The above times were obtained from Reference 5, "Flight-Time Command Log," and from Reference 2, Table I and Section B.4.

TABLE 5.6-11. SUMMARY OF RESULTS

Limit Cycle Frequency

	Mission A	Predicted
Inertial:	50 sec/pulse	117 sec/pulse (Reference 6, page 3)
Optical:	65 sec/pulse	80 sec/pulse (For 1 σ Canopus sensor noise: Reference 6, Figure 1).

Limit Cycle Amplitude (Single Axis)

	Mission A		Predicted
Inertial, degrees:			
Roll	0.415	From DSIF data gyro drift test number 6	0.44
Pitch	0.443		0.44
Yaw	0.417		0.44
Optical, degrees:			
Roll	0.441	From DSIF data 153:01:51:23 to 153:05:36:23	0.44
Pitch	0.470		0.44
Yaw	0.457		0.44

Sun and Star Tracking Errors, degrees

	Mission A	Specification
Roll null:	-0.055	±0.10
Pitch null:	-0.058	±0.10
Yaw null:	-0.053	±0.10

Nulls obtained from DSIF data: 153:01:51:23 to 153:05:36:23

Table 5.6-11 (continued)

Sun and Star Tracking Noise

The sun and star error signal noise levels were low enough to have no effect upon limit cycle performance.

Fuel Consumption

Mission A

0.112 pound	(Extrapolated for entire mission using 365-minute sample and assuming I_{sp} = 60 seconds and minimum impulse = 0.0018 lb-sec.)

Predicted

0.070 pound	(nominal) – See Reference 3, "Fuel Budget."

Gyro Drift Measurements

The time history of gyro drift measurements is plotted in Figure 5.6-22. The roll and pitch gyros were relatively consistent from one drift check to the next. The yaw gyro inflight measurements differed appreciably from most earlier data.

Drift rates (deg/hr) measured in flight* are as follows:

Check	Roll	Pitch	Yaw
1	0.08	0	0.64
2	0.2	- 0.02	0.66
3	0.25	0.03	0.9
4	–	–	0.85
5	–	–	0.85
6	0.295	0.07	0.84 No. 1 0.81 No. 2

*Taken from Reference 2, Section B.4.

2) Sensor noise did not affect the coast mode control system performance.

3) Extrapolated fuel consumption was about what was predicted (after allowing for the additional double-pulsing of the roll jets).

4) The gyro drift measurements proved the following:

   a) The technique used is feasible.

   b) They are necessary, if changes between prelaunch gyro drift rates and postlaunch gyro drift rates are to be determined.

Analysis Details

Limit Cycle Frequency. The three-axis limit cycle is characterized by a crosscoupling of the torques resulting from a gas jet pulse. This coupling is shown by the following:

1) A pulse from the No. 1 gas jet pair causes a change in rotational velocity about the roll and yaw axes.

2) A pulse from the No. 2 or 3 gas jet pair causes a change in rotational velocity about the pitch and yaw axes.

Consequently, limit cycle frequency determination is simply a matter of simultaneously examining the pitch, yaw, and roll error signals and counting slope changes, making sure that a pulse is not counted twice because of the system crosscoupling.

A 215-minute sample of the optical limit cycle (Figure 5.6-19) had a mean time between gas jet pulses of 65 seconds. The data was taken from DSIF tapes of 153:01:51:23 to 153:05:36:23. A 140-minute sample of the inertial limit cycle (Figure 5.6-20) had a mean time between gas jet pulses of 50 seconds. The data was taken from DSIF tapes of 152:19:20:43 to 152:21:40:43.

Limit Cycle Amplitude. The roll optical and inertial deadspaces were determined from the roll error sensors during limit cycle operation. Both the roll optical and inertial deadspaces were consistent throughout the sampling period.

In pitch and yaw, there is an additional measurement consideration. A No. 2 or 3 gas jet will fire whenever the sum or difference of the pitch and yaw error signals exceeds either's single-axis deadspace voltage. Hence, a pure pitch or yaw deadspace measurement can only be made when one or the other is at null. This point will result in the maximum possible swing of the error signal which is met at null. The values recorded in Table 5.6-11 were the maximum total deadspaces observed during the indicated sample period.

Tracking Noise. Because the single-axis deadspaces are approximately equal for both inertial and optical modes and because the mean time between gas jet pulses was actually less for the optical sample than for the inertial sample, it is certain that optical sensor noise had no harmful effect upon limit cycle operation.

The difference in pulsing rates (23 percent) is probably a result of differential initial velocities and different durations for this aperiodic mode.

Tracking Errors. The tracking errors, recorded in Table 5.6-11, were taken to be the optical nulls during limit cycle operation.

Fuel Consumption. Both samples had double-pulsing at a deadband boundary which accounts for about 24 percent of the gas jet pulses. (Double-pulsing is detected from the telemetry signals by noting the magnitude of the error slope change at a boundary.) All double-pulsing seemed to be confined to the No. 1 gas jet pair, but doubtless this additional activity in roll also caused extra fuel consumption in yaw.

Now, what was the fuel penalty? If the two-limit cycle samples are weighted according to time, the average combined pulsing rate is 60 sec/pulse. The elapsed time in limit cycle operation is [time of sun lockon to beginning of preretro maneuvers] − [time of star map to Canopus acquisition] − [beginning of premidcourse maneuvers to end of postmidcourse maneuvers] ≅ 62.1 hours. So, limit cycle fuel consumption (W)

$$= (62.1\ \text{hr}) \left(\frac{1}{\text{average pulsing rate}} \right) \left(\frac{\text{gas jet impulse}}{\text{pulse}} \right) \left(\frac{1}{I_{sp}} \right)$$

Assuming I_{sp} = 60 seconds and gas jet impulse = 0.06 pound x 0.03 second = 0.0018 lb-sec,

$$W = (62.1\ \text{hours}) \left(\frac{1}{60\ \text{sec/pulse}} \right) \left(\frac{0.0018\ \text{lb-sec}}{\text{pulse}} \right) \left(\frac{1}{60\ \text{seconds}} \right)$$

$$= 0.112\ \text{pound}$$

The predicted nominal limit cycle fuel consumption (corrected for a 62.1-hour coast mode) is (0.075 pound) (62.1/66) = 0.070 pound (see Reference 4, "Fuel Budget"). The overage is thus (0.112 - 0.070 pound) = 0.042 pound, Reference 3, Table 6, notes that the mission nitrogen usage exceeded the predicted nominal by 0.052 pound; the bulk of that difference can be accounted for here.

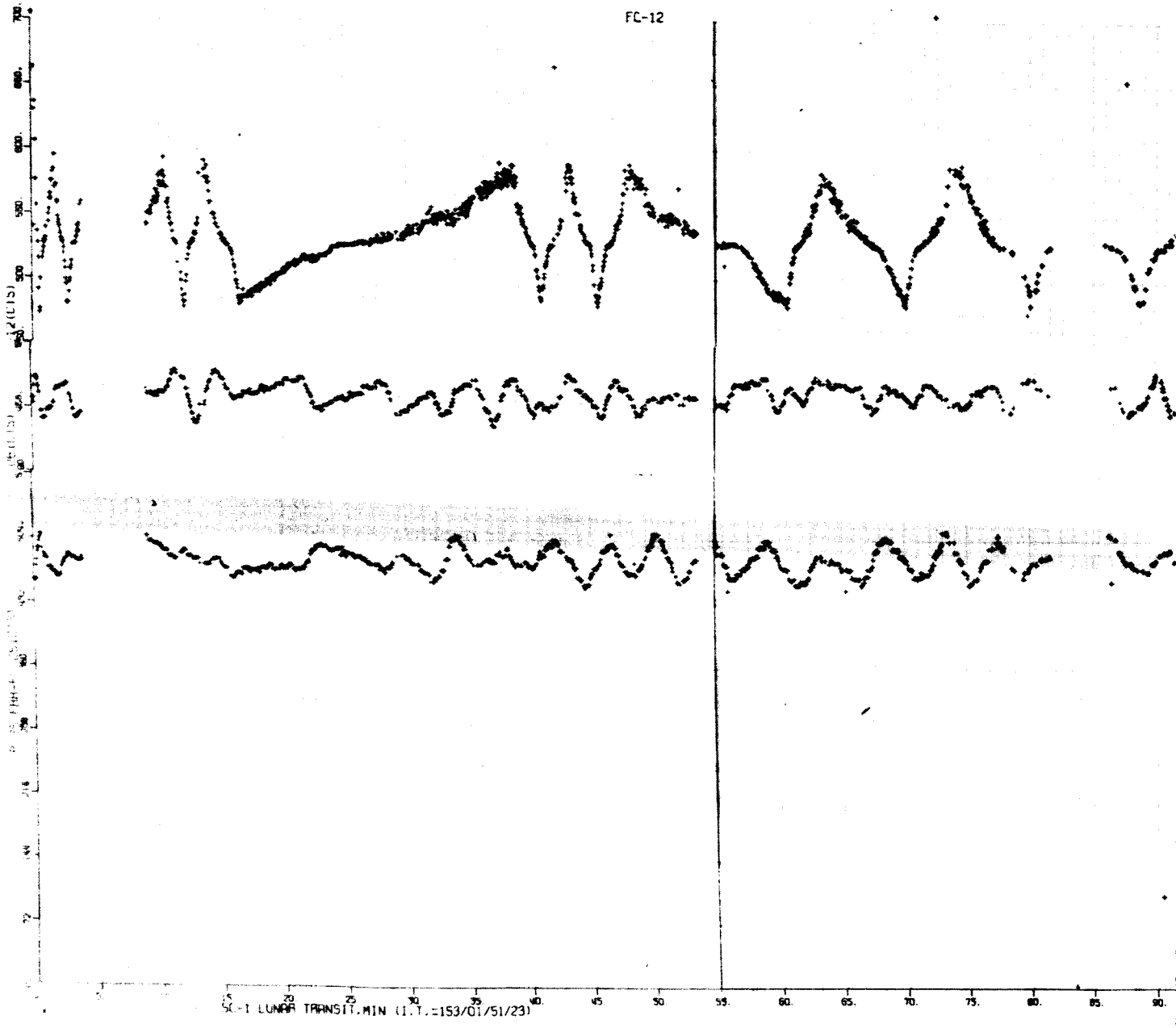
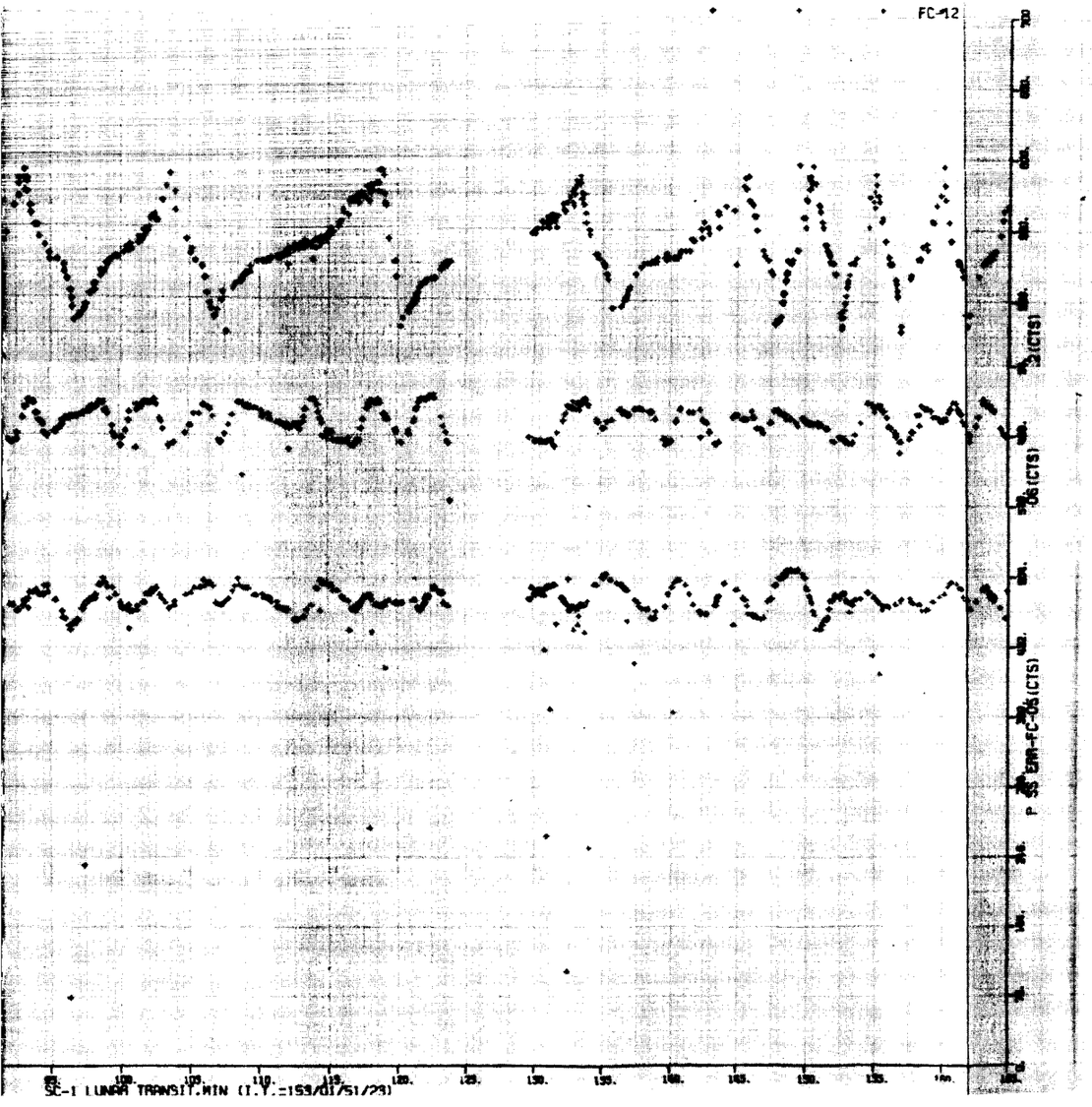
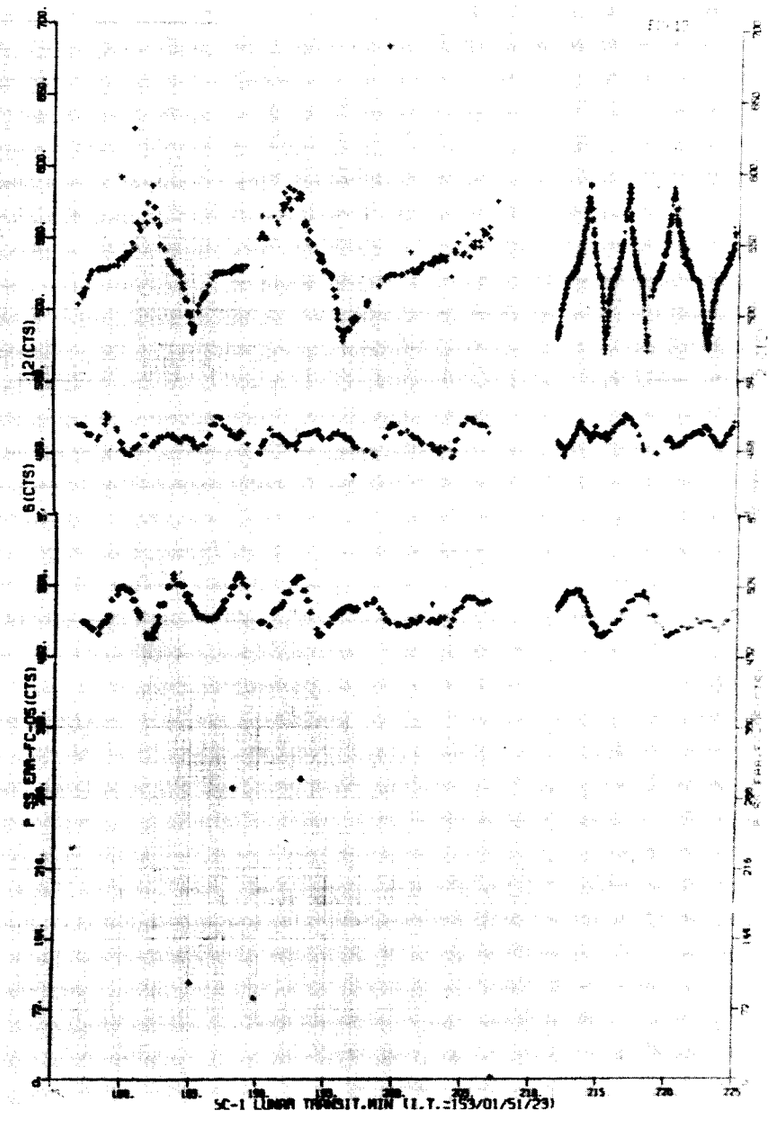


Figure 5.6-19. 215-Minute Sample of Opitcal Limit Cycle

 FOLDOUT FRAME





FOLDOUT FRAME

5.6-53-2

FOLDOUT FRAME

5.6-54

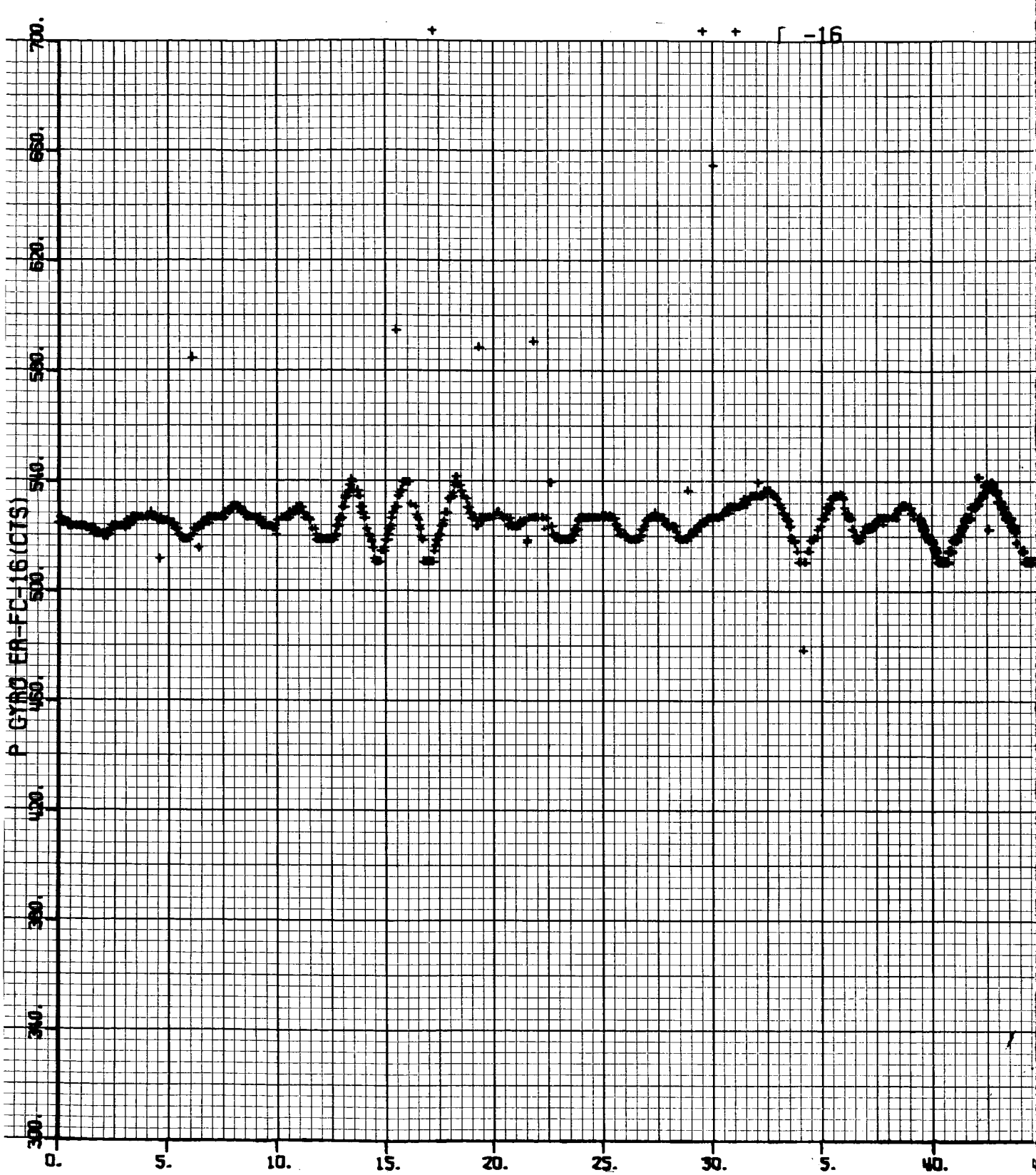
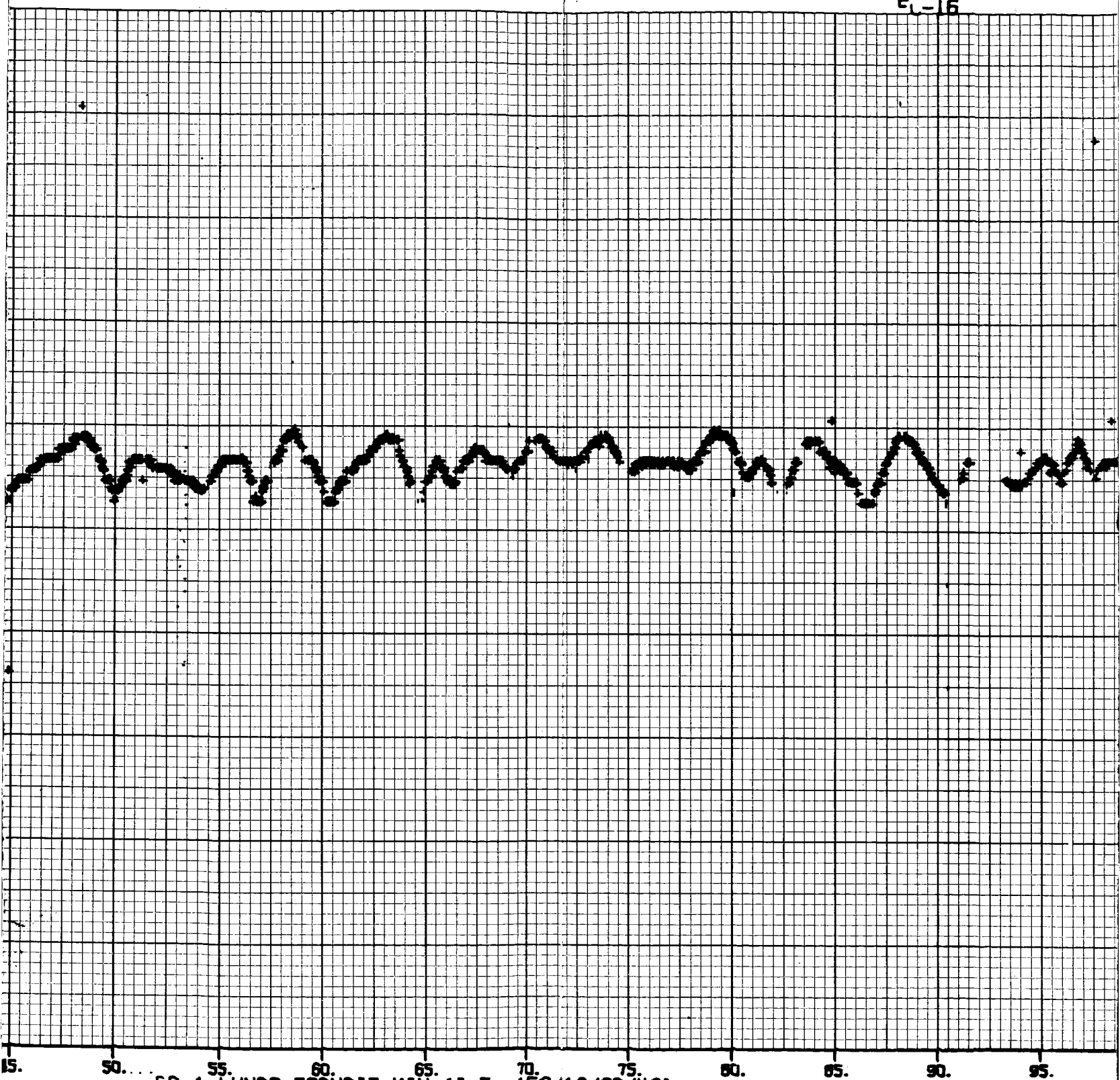


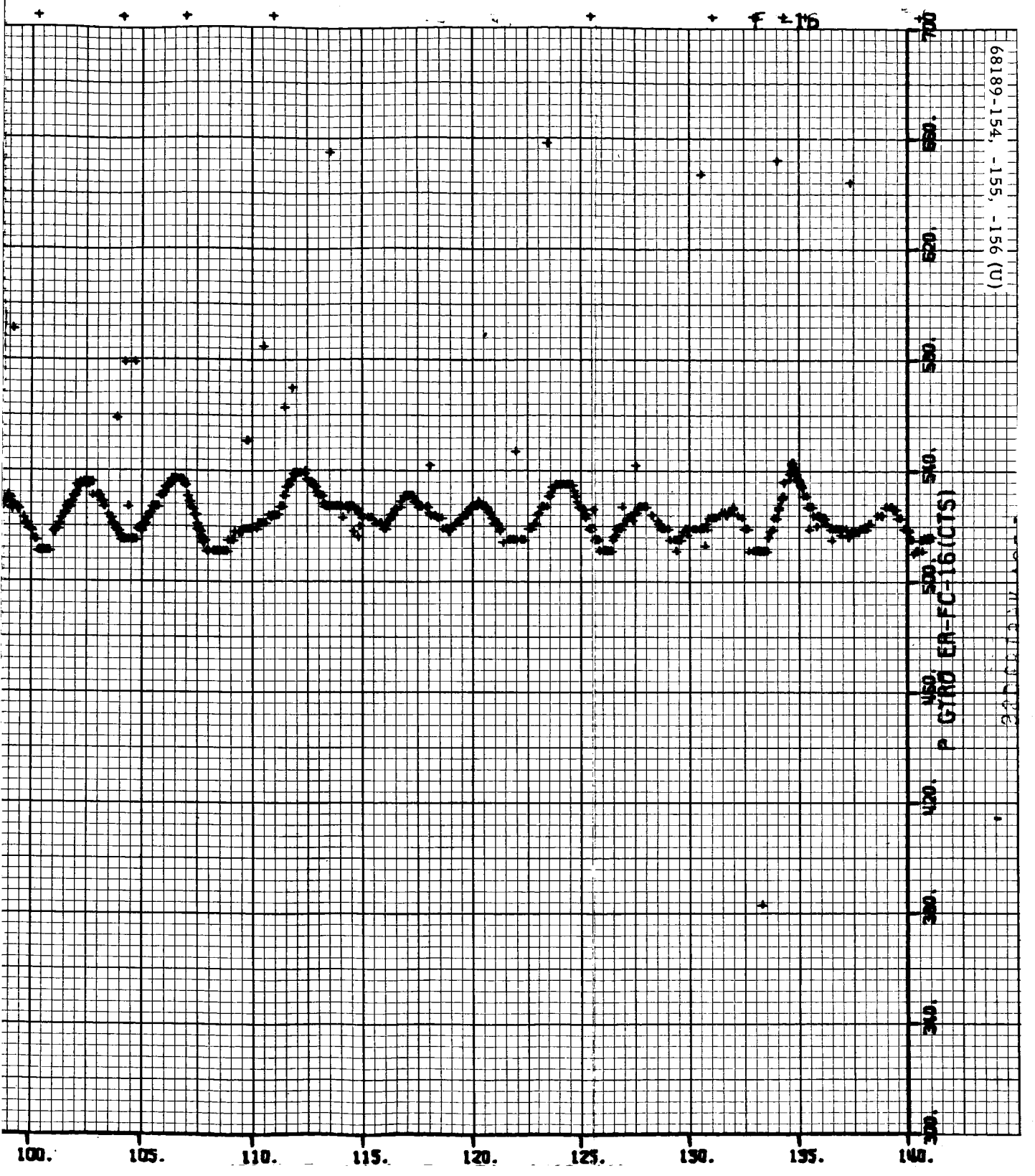
Figure 5.6-20. 140-Minute Sample of Intertial Limit Cycle

FOLDOUT FRAME



5.6-55-2

FOLDOUT FRAME



56-56 1

FOLDOUT FRAME

56-56-2

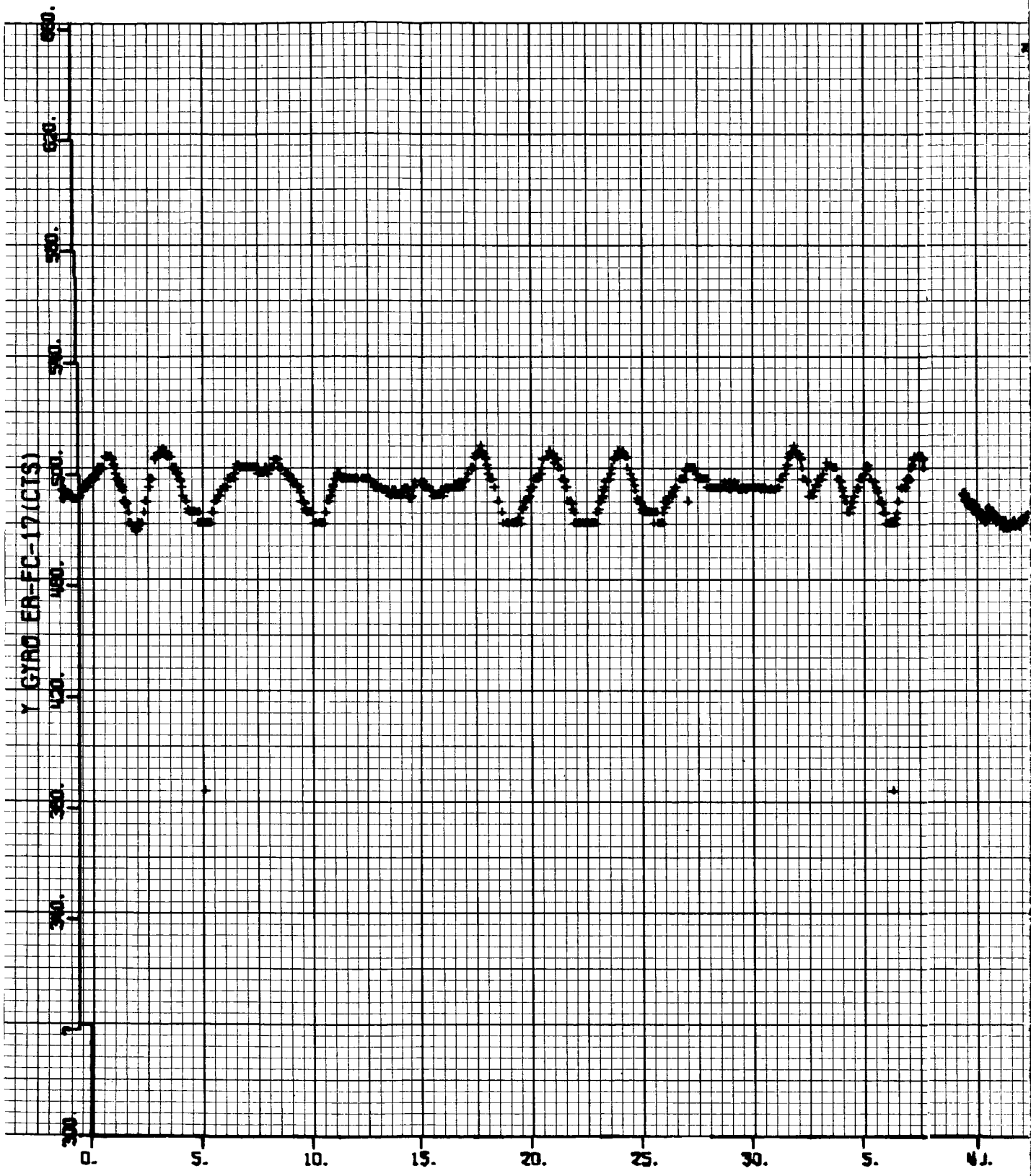


Figure 5.6-20 (continued). 140-Minute Sample of Inertial Limit Cycle

FOLDOUT FRAME



FOLDOUT FRAME

5-3-57-2



FOLDOUT FRAME

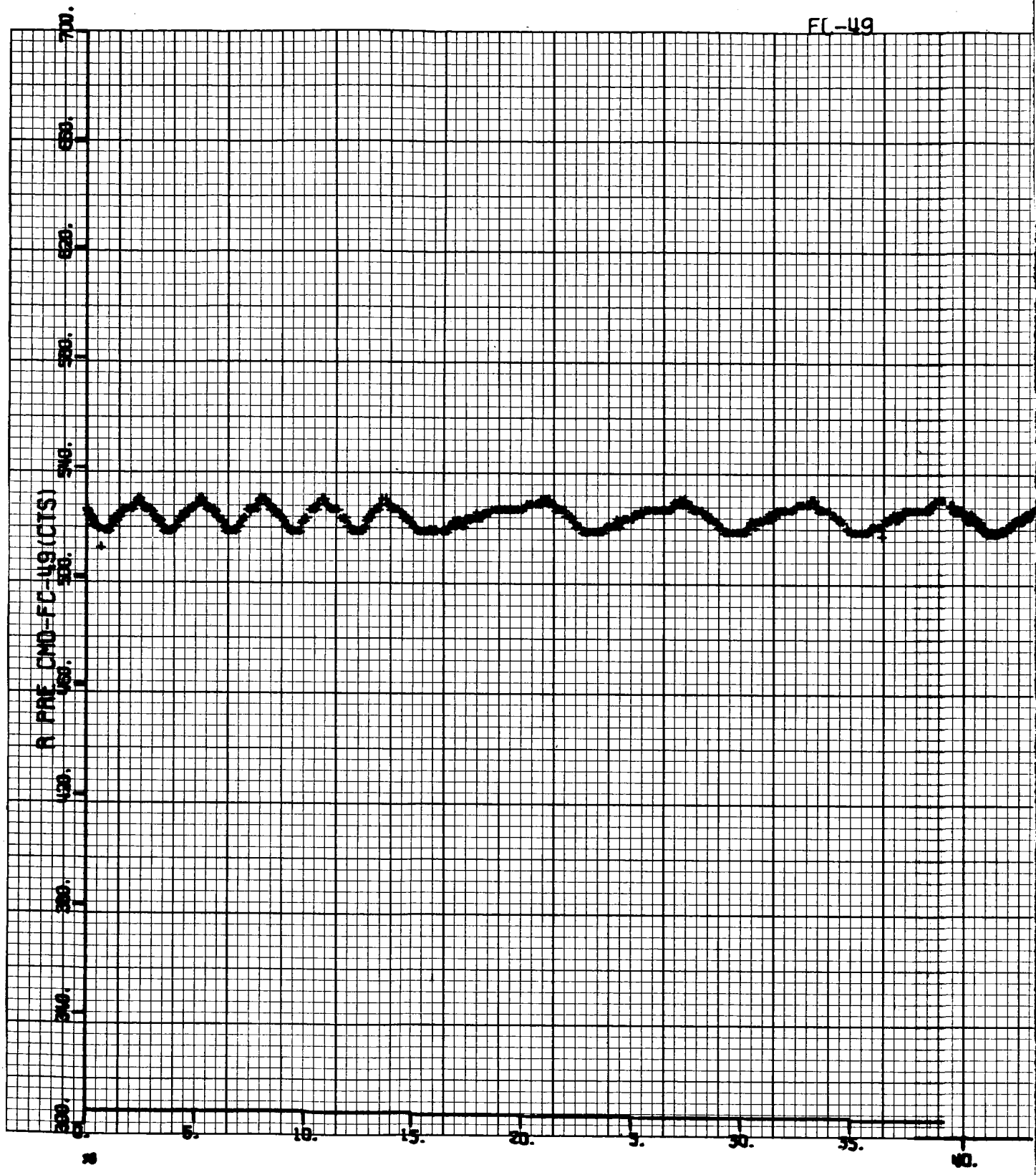


Figure 5.6-20 (continued). 140-Minute Sample of Inertial Limit Cycle

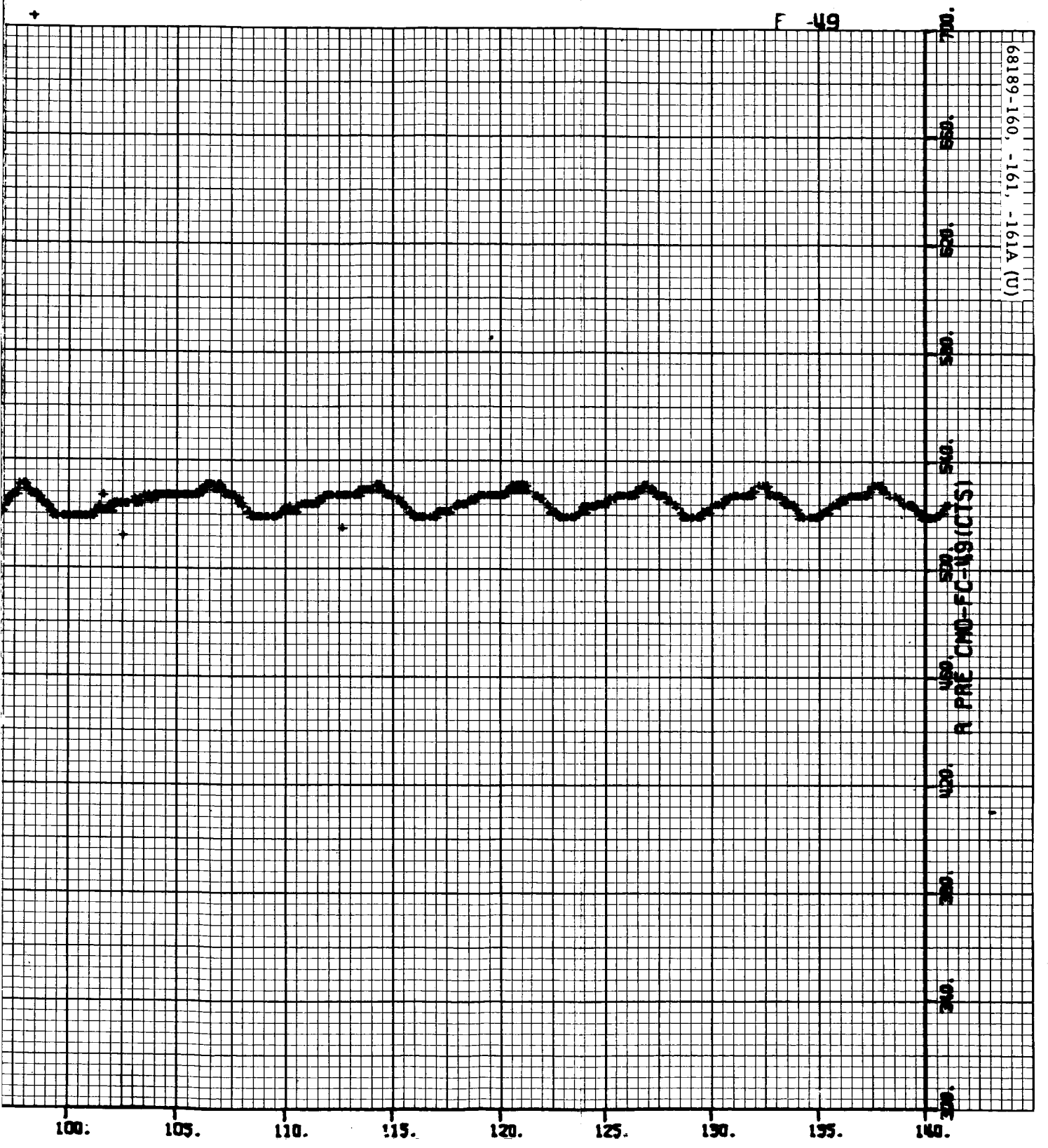
FC-49



SC-1 LUNAR TRANSIT.MIN (I.T.=152/19/20/42)

FOLDOUT FRAME

5.6-59-2



FOLDOUT FRAME

5.6-60

Gyro Drift Measurements. A procedural form for measuring gyro drift is included in Reference 7. An analysis of the accuracy of the measurement procedure is reported in Reference 8. The results are summarized in Table 5.6-11. See also Figures 5.6-21 and 5.6-22.

Gas Jet Thrust Level. Although the "Surveyor Functional Requirements Specification," 224510E, does not directly dictate the minimum allowable thrust level, it does infer these levels by specifying the minimum allowable gas jet torque values. These values are presented as follows:

Spacecraft Axis	Minimum Torque Requirement, in.-lb	Moment Arm, inch	Number of Gas Jets	Minimum Thrust Value, pounds
Roll	4.00	77	1	0.052
Pitch	4.25	45	2	0.047
Yaw	7.00	68	2	0.052

It is apparent from the above data that the minimum allowable gas jet thrust is 0.052 pound. The gas jet system was designed for a nominal thrust value of 0.057 pound.

In References 9 and 28, a method is proposed whereby the gas jet thrust level can be determined from the time response of the gyro error signal received during a roll maneuver. It also mentions that a weighting factor may be requred for the basic equation derived in the references. The equation is:

$$T = \frac{I_z \dot{\varphi}_c}{R t_p}$$

From an analog computer simulation program of the gas jet system, the average weighting value was determined to be 0.85. The values for the various parameters in the previous equation are as follows:

$I_z = 189$ slug-ft^2

$R = 6.4$ feet

$\dot{\varphi}_c = 0.500$ deg/sec

$t_p = 5.66$ seconds

t_p represents the time it takes the gyro output to reach its first maximum from the time the maneuver command is initiated (Figure 5.6-23). Multiplying the value of t_p with the weighting factor of 0.85, the corrected time is 4.81 seconds. Thus the gas jet thrust level for SC-1 roll was T = 0.054 pound.

5.6.7.6 Premidcourse Maneuvers

In order to accomplish the required velocity correction, it was necessary to perform a negative roll maneuver and a negative yaw maneuver of magnitude 86.50 degrees and 57.99 degrees, respectively. The analysis to follow is an attempt to accurately reconstruct the total premidcourse maneuver phase from the beginning of the first roll maneuver to vernier ignition and to compute the roll axis final pointing error exclusive of any tracking data.

Several variables affect the accuracy of an angular maneuver: precession rate accuracy, precession command time, gyro drift, and initial attitude errors due to biases and limit cycle. When several maneuvers are performed with large time intervals between them, attitude errors due to gyro drift must be included. A list of all parameters affecting the midcourse maneuver accuracy is presented in Table 5.6-12 along with their allowable 3σ values and actual performance values whenever possible.

Determination of Precession Times

The register was loaded with 433 bits for roll and 290 bits for yaw. With a clock rate of 2.5 cps, the respective times are 173.20 seconds and 116.00 seconds with a maximum error of 0.20 second.

The gyro error signal data was used in determining the actual precession time. The sampling rate during the maneuvers was 20 times/second, giving a resolution of 0.05 second. The results are as follows (Figures 5.6-24 and 5.6-25).

T = 173.17 seconds (roll)

T = 115.80 seconds (yaw)

Precession Rates. The accuracy of the precession rates imposed by the "Surveyor System Functional Requirements Specification" is 0.5000 ± 0.0011 deg/sec. The precession rate obtained during the star mapping phase indicates that the positive precession rate is 0.5004 deg/sec.

It is unfortunate that data is not available which can be used to determine the negative roll precession rate with the same degree of accuracy. A good indication of the negative precession rate value is that after performing the postmidcourse yaw and roll maneuvers with the same precession times as those for the premidcourse maneuvers, the Canopus error signal indicates that the previous attitude about roll was obtained to within 0.05 degree.

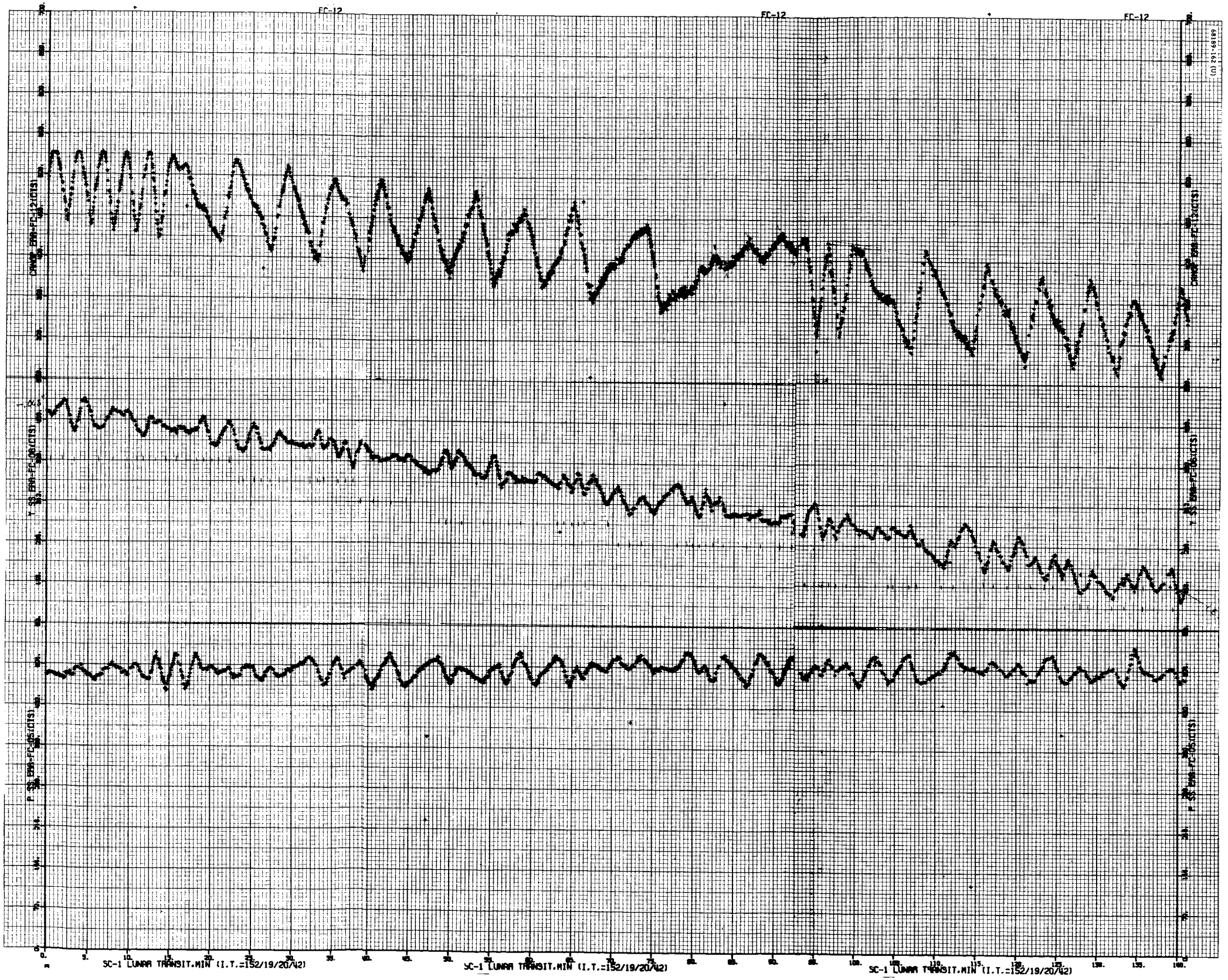


Figure 5.6-21. Gyro Drift Test

FOLDOUT FRAME

FOLDOUT FRAME

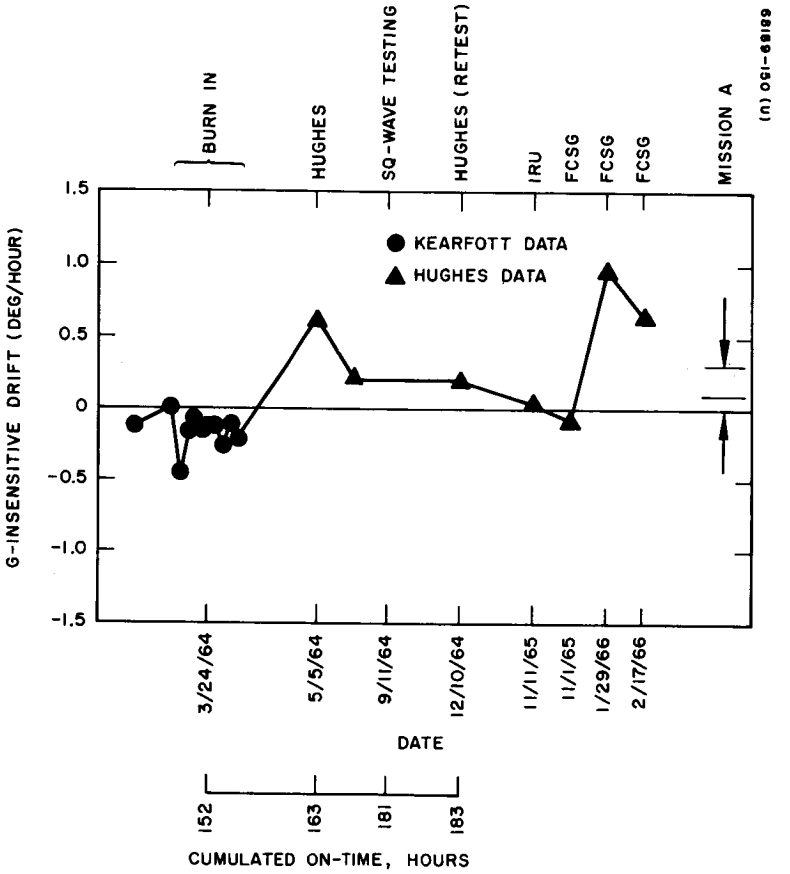


Figure 5.6-22. Time History of Gyro (Non-g) Drift

a) Roll (S/N 57)

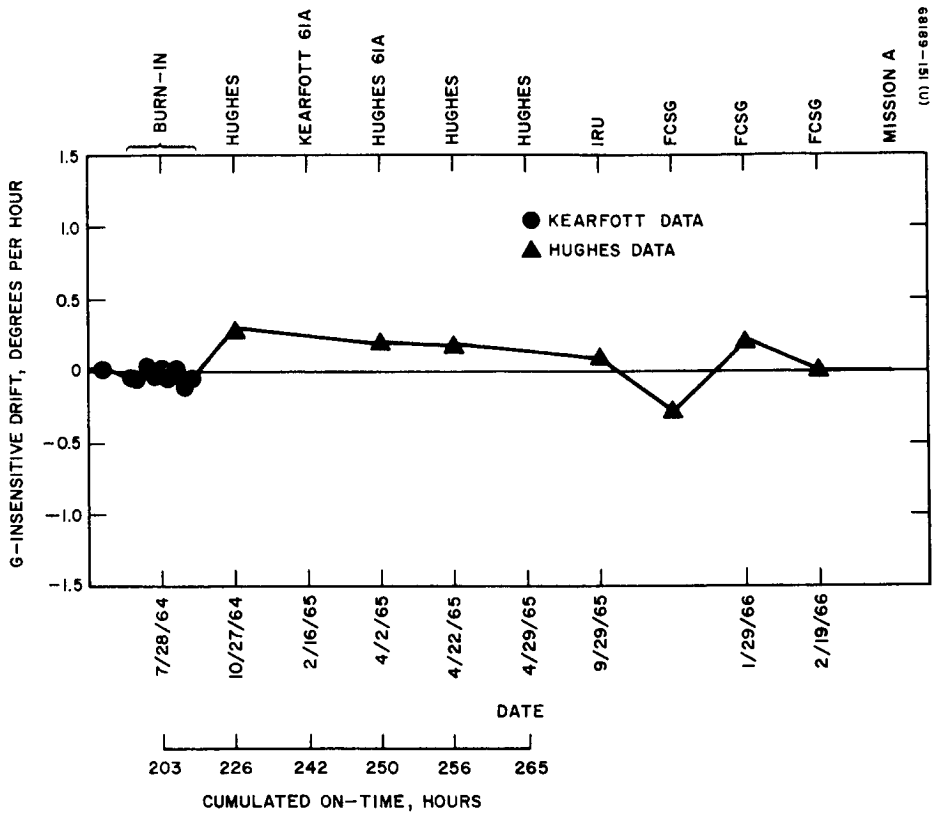


Figure 5.6-22 (continued). Time History of Gyro (Non-g) Drift

b) Pitch (S/N 61)

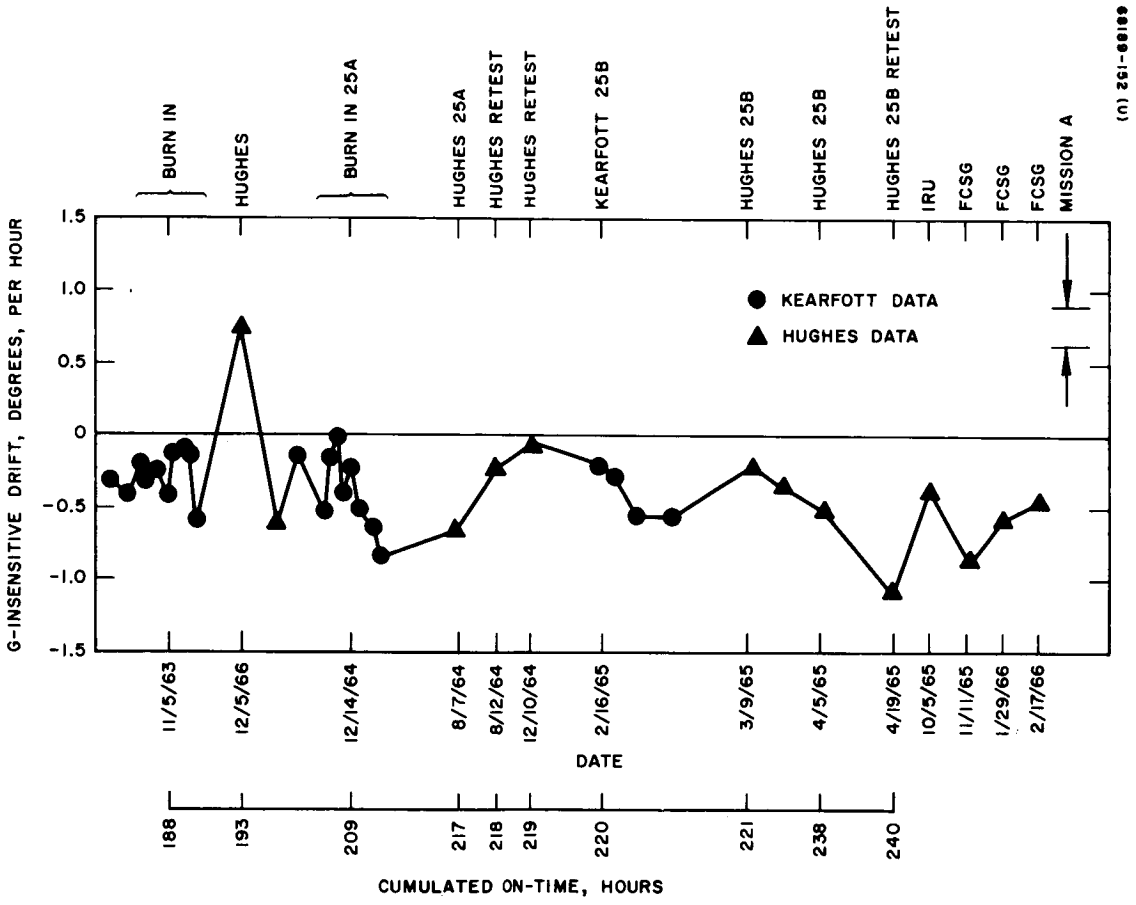


Figure 5.6-22 (continued). Time History of Gyro (Non-g) Drift

c) Yaw (S/N 25)

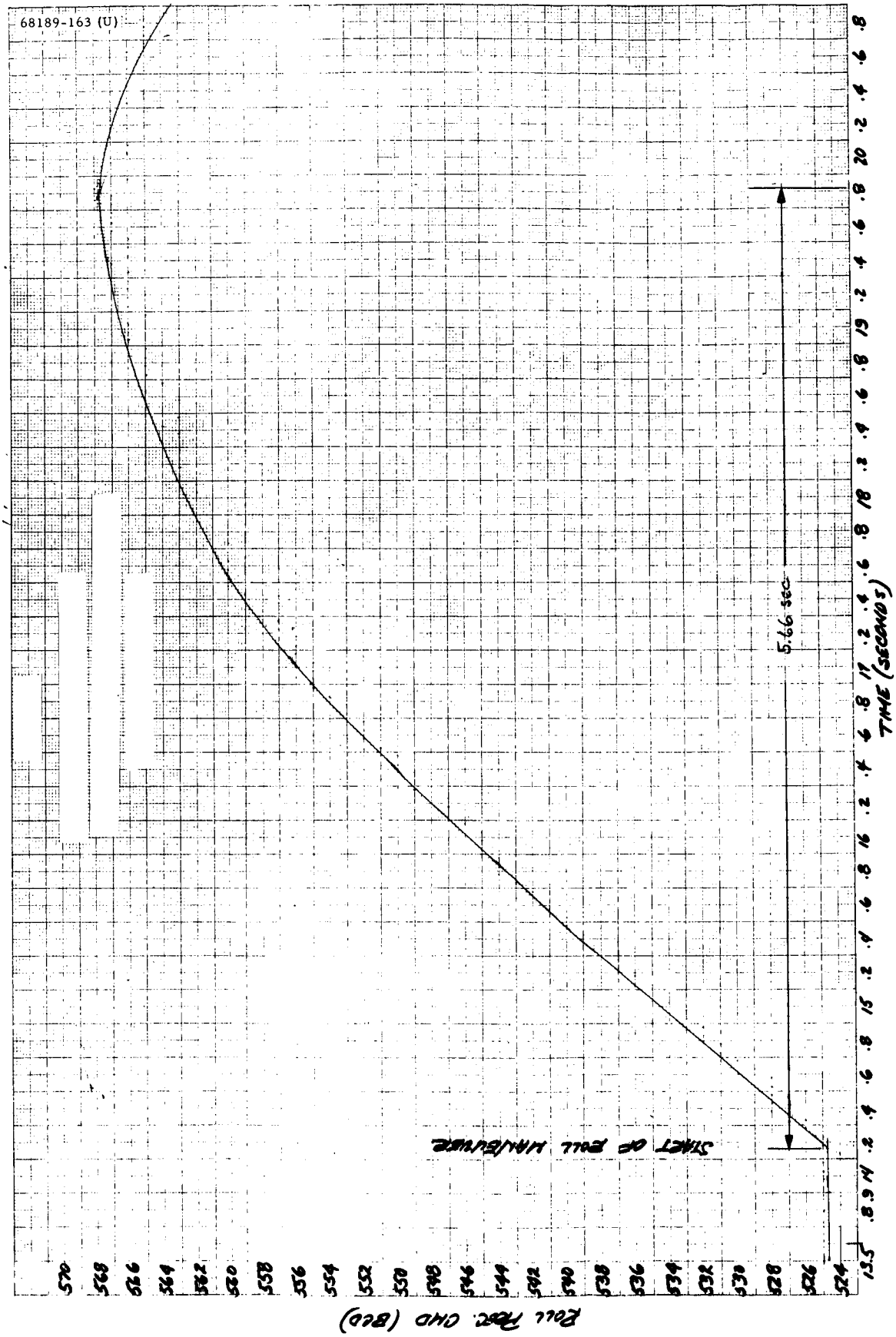


Figure 5.6-23. Roll Gyro Response for Premidcourse Roll Maneuver

DSIF tape data

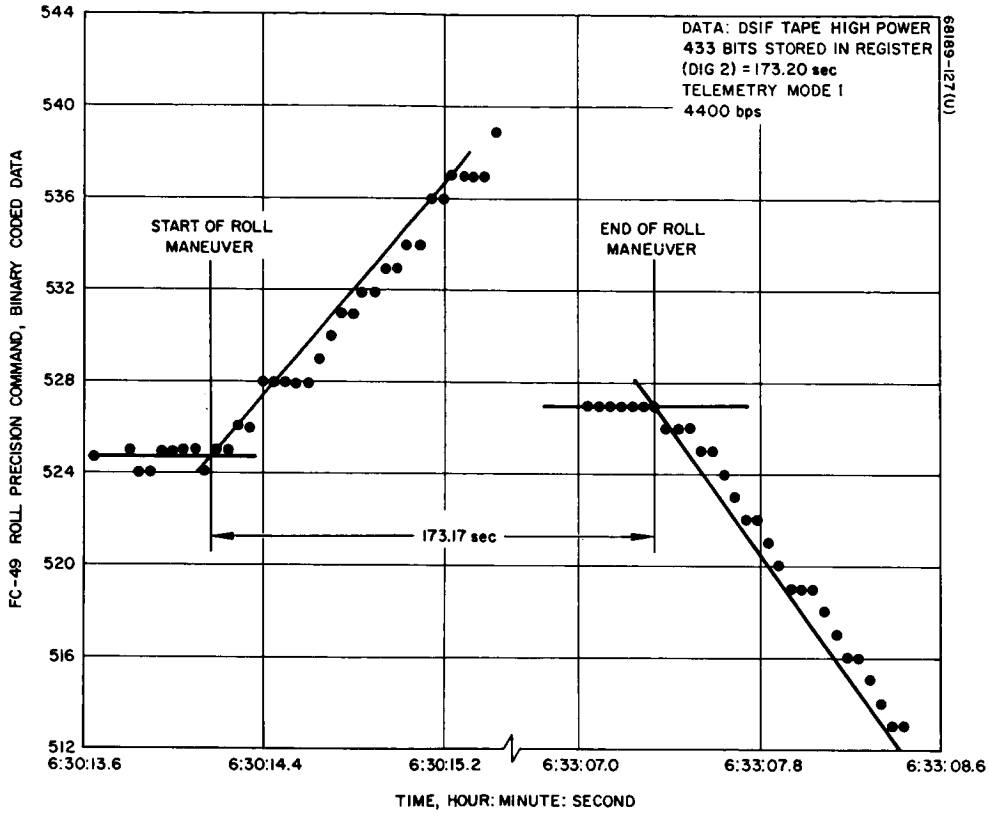


Figure 5.6-24. Roll Gyro Response Profile for Premidcourse Roll Maneuver

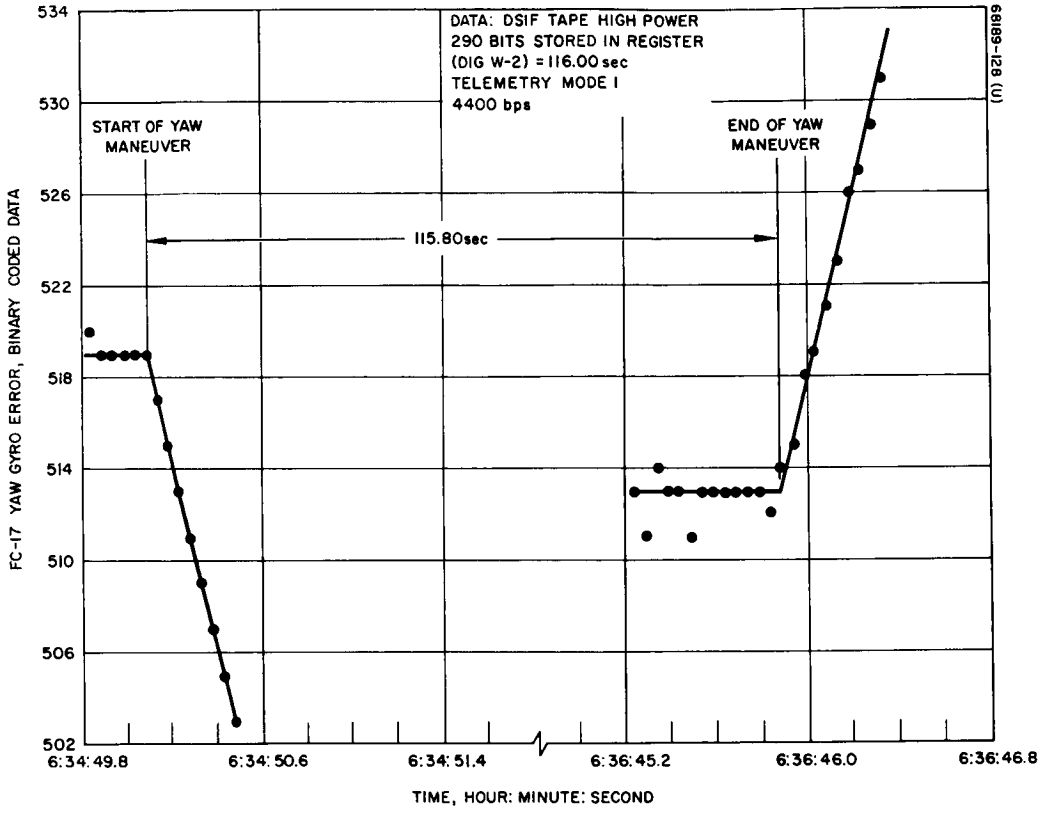


Figure 5.6-25. Yaw Gyro Response Profile for Premidcourse Yaw Maneuver

TABLE 5.6-12. SC-1 PERFORMANCE DETAIL

Characteristic: Midcourse Angular Error: Phase: Midcourse Correction

Item	Parameter	3σ Requirement	Specification	Performance Value	Comments
1	Initial position errors				
	Sensor group roll axis to sun spacecraft line	0.2 degree	224510D 4.3.1.1	0.005 degree	SSD 64102R, Table IV (weight, balance, and alignment report)
	Pitch/yaw limit cycle	0.3 degree	224510D 4.3.1.1	0.014 degree/ -0.232 degree	See "Initial Attitude Errors"
	Sensor group roll-pitch plane to Canopus-spacecraft line	0.2 degree	224510D 4.3.1.2	0.031 degree	SSD 64102R, Table IV.
	Roll limit cycle	0.3 degree		0.15 degree	See "Initial Attitude Errors"
2	Rotational magnitude errors	0.05 percent	234633		
	Gyro torquer scale factor 45-degree rotation 180-degree rotation	0.05 percent	234633 3.3.5.7	0.08 percent	From precession rate determination. Desired rate is 0.5000 deg/sec. The actual rate was 0.5004 deg/sec.
	Precision current accuracy (0.13) 45-degree rotation 180-degree rotation	0.13 percent	234610 4.4.2.2.1		
	Timing source accuracy 45-degree rotation 180-degree rotation	0.2 second		0.015 degree (roll) 0.1 degree (yaw)	These values correspond to a timing error of 0.03 second for the roll maneuver and 0.20 second for the yaw maneuver.
	Precession current circuit drift 45-degree rotation 180-degree rotation	0.1 percent			
3	Rotational axis error				
	Gyro alignment to IRU A, B, and C axis	0.1 degree	234630 4.2.4.3		
	IRU roll and pitch axis to sensor group roll and pitch axis	0.1 degree	234600 3.5.1		
4	Final position errors				
	Vernier engine thrust vector to nozzle centerline	0.33 degree	287015 3.5.4	0.280 degree	With respect to spacecraft coordinates, the vector representation is $\bar{I}_A = -0.00462\,\bar{I}_X - 0.00160\,\bar{I}_Y - \bar{I}_Z$
	Installation alignment and bracket bending compensation	0.1 degree			
	Spacecraft roll axis to sensor group roll axis	0.1 degree	224510D 4.1.3.7.1		
	Attitude control steady state error	0.1 degree	224510D 4.3.1.4 EO	0.005 degree	Based on a moment disturbance value of 74 in-lb. This value was obtained from "Midcourse-Vernier Engine System Parameters."
	Reference axis drift gyro non-g drift	1 degree/hr	224510D 4.3.1.5	0.121 degree	Calculated value of pointing error due to drift ("Analysis" subsection).
	Midcourse maneuver duration	15 minutes	224510D 3.6.4.2	4 minutes 36 seconds	From time and events log
5	Total attitude error	0.7 degree	3.6.3	0.313 degree	

Note: The performance values cannot be added algebraically to obtain the total error because the problem is three-dimensional.

This indicates that the negative precession rate must have been almost the same as the positive rate. Sun sensor error signals indicate that the previous attitude in pitch and yaw was obtained to within the limit cycle value of 0.2 degree.

For this analysis, a negative precession rate of 0.5000 deg/sec will be used for both yaw and roll commands.

Gyro Drifts. During a 3-hour period just following the midcourse phase, a gyro drift check was made. The drift rate values were obtained from the plots of FC-5, FC-6, and FC-12 which are the pitch sun sensor error signal, yaw sun sensor error signal, and Canopus error signal, respectively (Figures 5.6-26 through 5.6-28). The results are as follows:

Roll drift = 0.202 deg/hr

Yaw drift = 0.675 deg/hr

Pitch drift = -0.021 deg/hr

Normally, if the pitch gyro drift rate is much larger, a more sophisticated technique of determining roll gyro drift would be used to account for coupling between the pitch and Canopus sensor line-of-sight axes.

Initial Attitude Errors. The initial attitude errors prior to maneuvers were as follows:

Start of roll (151:06:30:14.16), degree

Pitch = 0
Yaw = 0
} caged to the sun during first roll maneuver

Roll = -0.015

Start of yaw (151:06:34:50.80), degree

Pitch = 0.014 (FC-5)

Yaw = 0.232 (FC-6)

Roll = -0.150 (FC-49)

Analysis

The initial attitude of the spacecraft to that assumed is

$$\begin{pmatrix} I_{xo} \\ I_{yo} \\ I_{zo} \end{pmatrix} = \begin{bmatrix} 1 & \varphi_z & -\varphi_y \\ -\varphi_z & 1 & \varphi_x \\ \varphi_y & -\varphi_x & 1 \end{bmatrix} \begin{pmatrix} I_{10} \\ I_{20} \\ I_{30} \end{pmatrix} \qquad (1)$$

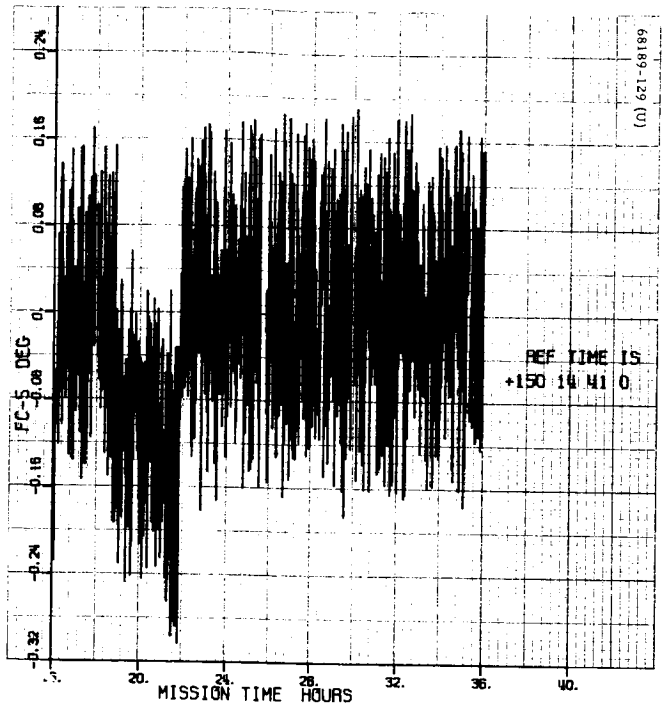


Figure 5.6-26. Pitch Sun Sensor Error Signal

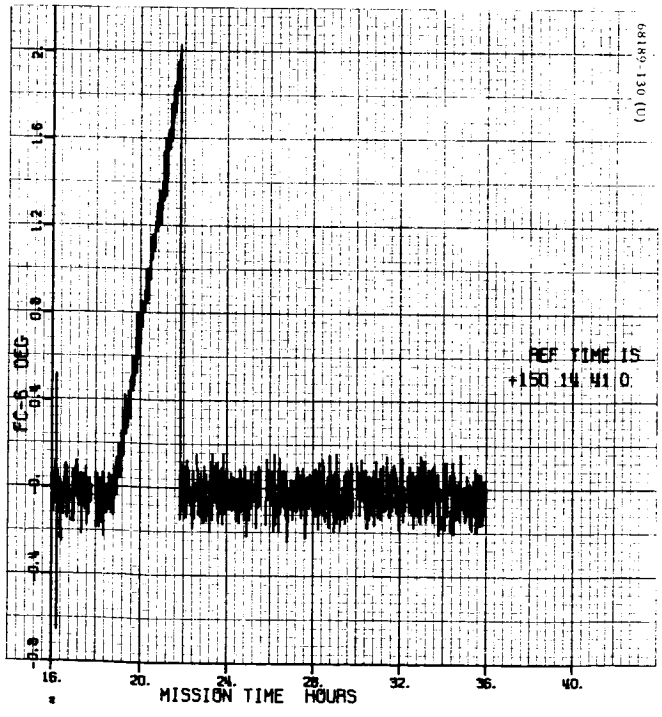


Figure 5.6-27. Yaw Sun Sensor Error Signal

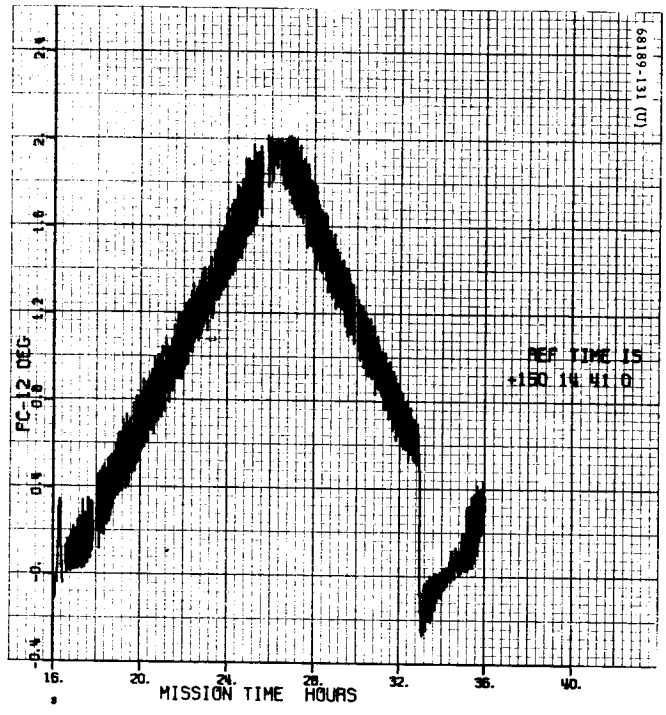


Figure 5.6-28. Canopus Error Signal

where I_{io}s are unit vectors of an inertial coordinate system established by perfect alignment to the sun and Canopus, and the φ matrix is derived from the small angle approximation of a three-sequential rotation matrix.

For the roll maneuver, φ_x and φ_y will be set to zero since the pitch and yaw axes are slaved to the sun line and are subject to the optical limit cycle which tends to average the error to zero.

Roll maneuver is represented by the following matrix representation:

$$\begin{pmatrix} I_{xR} \\ I_{yR} \\ I_{zR} \end{pmatrix} = \begin{bmatrix} \cos(\Psi + \epsilon_R) & S(\Psi + \epsilon_R) & 0 \\ -\sin(\Psi + \epsilon_R) & \cos(\Psi + \epsilon_R) & 0 \\ 0 & 0 & 1 \end{bmatrix} \begin{pmatrix} I_{xo} \\ I_{yo} \\ I_{zo} \end{pmatrix} \qquad (2)$$

where Ψ is the desired roll maneuver angle and ϵ_R is the error in rotation due to timing error and gyro drift. $\epsilon_R = -0.10$ degree.

Attitude change due to gyro drifts is determined from the following:

$$\begin{pmatrix} I_{x1} \\ I_{y1} \\ I_{z1} \end{pmatrix} = \begin{bmatrix} L_1 & L_2 & L_3 \\ M_1 & M_2 & M_3 \\ N_1 & N_2 & N_3 \end{bmatrix} \begin{pmatrix} I_{xR} \\ I_{yR} \\ I_{zR} \end{pmatrix} \qquad (3)$$

where

$$1) \quad L_i(t) = L_{io} \cos \Omega T + \frac{M_{io} W_z - N_{io} W_y}{\Omega} \sin \Omega t + \frac{L_{io} W_x^2 + M_{io} W_x W_y + N_{io} W_x W_z}{\Omega^2} (1 - \cos \Omega T)$$

$$2) \quad N_i(t) = N_{io} \cos \Omega t + \frac{L_{io} W_y - M_{io} W_x}{\Omega} \sin \Omega T + \frac{L_{io} W_x W_z + M_{io} W_y W_z + N_{io} W_z^2}{\Omega^2} (1 - \cos \Omega T)$$

3) $$M_i(t) = M_{io} \cos \Omega T + \frac{(N_{io} W_x - L_{io} W_z)}{\Omega} \sin \Omega T$$

$$+ \frac{L_{io} W_y W_y + M_{io} W_y^2 + N_{io} W_y W_z}{\Omega^2} (1 - \cos \Omega T)$$

4) L_{io}, N_{io}, and M_{io} are initial direction cosines

5) $i = 1, 2, 3$

6) $\Omega^2 = W_y^2 + W_y^2 + W_z^2$

7) W = spacecraft drift rates

8) t = time

Initial attitude error prior to the yaw maneuver is similar to Equation 2.

Yaw maneuver is represented by the following matrix equation:

$$\begin{pmatrix} I_{x3} \\ I_{y3} \\ I_{z3} \end{pmatrix} = \begin{bmatrix} \cos(\theta + \epsilon_y) & 0 & -\sin(\theta + \epsilon_y) \\ 0 & 1 & 0 \\ \sin(\theta + \epsilon_y) & 0 & \cos(\theta + \epsilon_y) \end{bmatrix} \begin{pmatrix} I_{x2} \\ I_{y2} \\ I_{z2} \end{pmatrix} \quad (4)$$

where θ is the desired yaw maneuver angle and ϵ_y is the error in rotation due to timing error and gyro drifts. $\epsilon_y = 0.01$ degree.

Equation 3 can be used to represent the attitude change from the end of the yaw maneuver to the point of vernier ignition.

A digital computer program was developed to facilitate the calculation of the pointing accuracy. The program output is represented in five different direction cosine matrices which illustrate the contribution of each error source to the final pointing accuracy. The various matrix outputs are as follows:

1) Perfect case (no errors)

2) Initial attitude errors only

3) With gyro drifts only

4) Angular maneuver execution errors only

5) Actual case (all error sources)

The matrices are presented in Table 5.6-13.

TABLE 5.6-13. DIRECTION COSINE MATRICES

Positive Unit Vectors

	Perfect Case	
3.23598 E-2	-0.529079	0.847956
0.998135	6.10485 E-2	0
-5.17664 E-2	0.846374	0.530067
	Attitude Error	
3.05669 E-2	-0.525742	0.850095
0.998291	5.84362 E-2	2.44344 E-4
-4.98048 E-2	0.848635	0.526629
	Drift Error	
3.57482 E-2	-0.530651	0.846836
0.997996	0.063228	-2.50886 E-3
-5.22124 E-2	0.845229	0.531848
	Maneuver Error	
3.14451 E-2	-0.529282	0.847863
0.99824	5.93064	0
-5.02837 E-2	0.846371	0.530215
	Total Error	
3.30384 E-2	-0.527534	0.848891
0.998263	5.88641 E-2	-2.27153 E-3
-4.87709 E-2	0.847492	0.528563

The results (Figure 5.6-29) of the investigation are as follows:

1) Gyro drift contribution = 0.121 degree

2) Maneuver execution contribution = 0.0855 degree

3) Initial attitude error contribution = 0.263 degree

4) Actual (all error sources) = 0.204 degree

Notice that the sum of the individual error source contribution does not equal the actual pointing error value. This is as expected since the problem is three-dimensional.

5.6.7.7 Postmidcourse Maneuver

The postmidcourse maneuver is generally used to realign the spacecraft to celestial reference after performing a midcourse velocity correction. To accomplish this, two reacquisition schemes are available. One method is to perform the premidcourse maneuvers in reverse and the other is to perform another automatic sun acquisition sequence. The first method is most desirable since real time monitoring of optical sensor signals will provide good indications of premidcourse maneuver accuracy and attitude control during the thrust period; that is, if reacquisition of the sun and Canopus is not achieved to within a fair degree of accuracy, one or more of the following conditions must have existed:

1) Nonsymmetrical precession commands.

2) Spacecraft attitude change occurred between maneuver periods.

3) Premidcourse maneuvers were not accurate.

4) Postmidcourse maneuvers were not accurate.

The first method was chosen for the SC-1 mission and, at approximately 151:07:00:56, the initial premidcourse attitude was successfully reacquired to within 0.15 degree.

Determination of Precession Times

For the premidcourse maneuvers, the magnitude register was loaded with 290 bits for yaw and 433 bits for roll. This corresponds to 116.00 and 173.20 seconds, respectively.

The precession time, using gyro error signal data, was found to be:

T = 115.5 seconds (yaw)

T = 173.0 seconds (roll)

The reason for the large difference between the commanded values and the values above is that for the postmidcourse maneuver phase the telemetry rate was reduced from 4400 to 550 bits/sec, increasing data granularity from 0.25 to 2.00 seconds (Figures 5.6-30 and 5.6-31).

Maneuver Accuracy

The total midcourse maneuver accuracy can be appreciated from the following optical sensor data. These values represent the final attitude orientation with respect to the sun and Canopus prior to optical control mode operation:

Pitch sun sensor error signal = -0.15 degree

Yaw sun sensor error signal = -0.04 degree

Canopus error signal = 0.00 degree

Plots of the star intensity signal during premidcourse and postmidcourse roll maneuvers are included to illustrate the identical nature of the maneuvers (Figures 5.6-32 through 5.6-35).

5.6.7.8 Midcourse Velocity Correction Phase

The Surveyor I midcourse correction was successfully executed at 06:45:24:651 GMT on 31 May 1966. From orbit determination, the actual magnitude of the velocity change was estimated to be 20.266 m/sec. Compared to the desired value of 20.347 m/sec and the commanded value of 20.396 m/sec, this constitutes an error of 0.081 m/sec in the desired value and a ΔV execution error of 0.130 m/sec. Also from orbit determination, the midcourse thrust vector pointing error was calculated to be 0.221 degree. Using prelaunch alignment information and in-flight data, the thrust vector pointing error was calculated to be 0.313 degree. The directions of the actual and calculated thrust vectors were in agreement.

Midcourse Engine Ignition Characteristics

The SC-1 midcourse maneuver was characterized by a smooth vernier ignition followed by a nominal, uneventful thrusting phase. Peak pitch and yaw gyro errors during thrusting were 0.15 degree or less during the ignition transient and virtually zero thereafter until engine cutoff. A summary of the midcourse pitch and yaw gyro errors is given in Table 5.6-14.

Prior to vernier ignition, pitch and yaw gyro errors were maintained within ±0.22 degree by the gas jet system. At the instant of ignition, these errors were -0.15 and 0.04 degree for pitch and yaw, respectively, and the subsequent transient was reduced to zero in approximately 4 seconds. The yaw error transient overshoot was -0.08 degree, while the pitch error exhibited no overshoot. The transient behavior of both errors was dominated by the 1.0-second time constant of the attitude control loops.

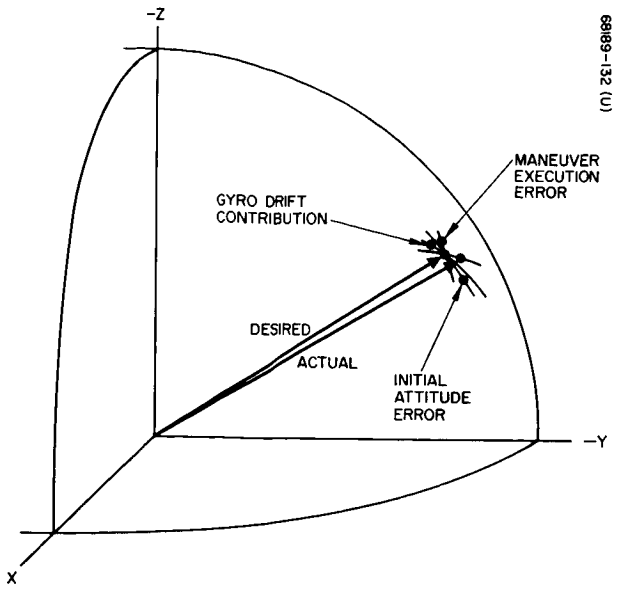


Figure 5.6-29. Premidcourse Maneuver Errors

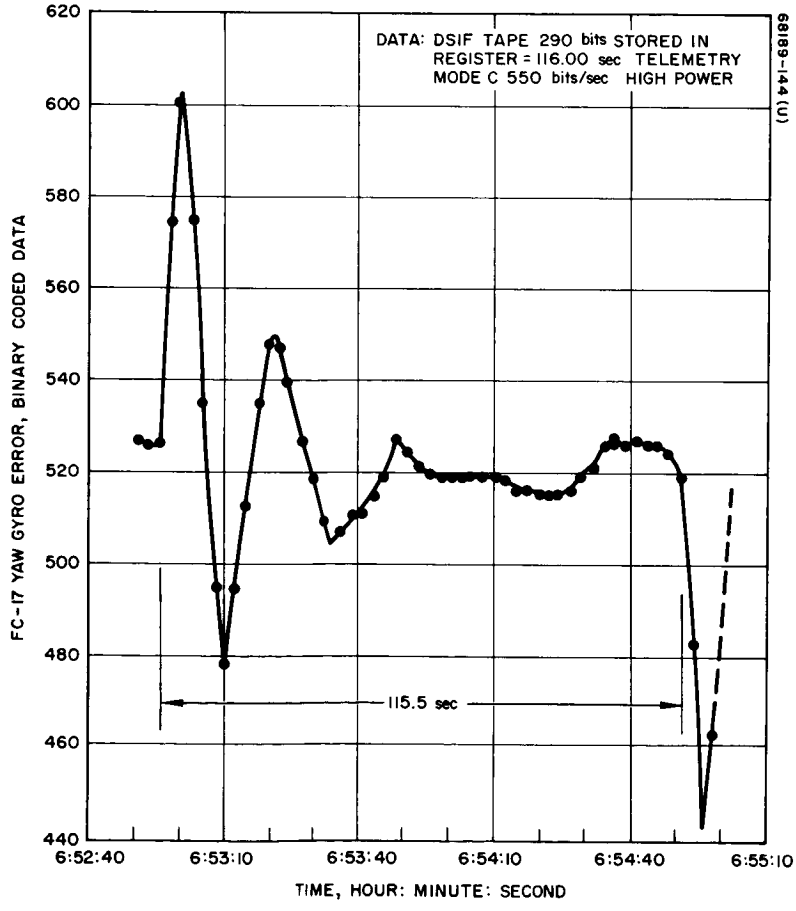


Figure 5.6-30. Yaw Gyro Response Profile for Postmidcourse Yaw Maneuver

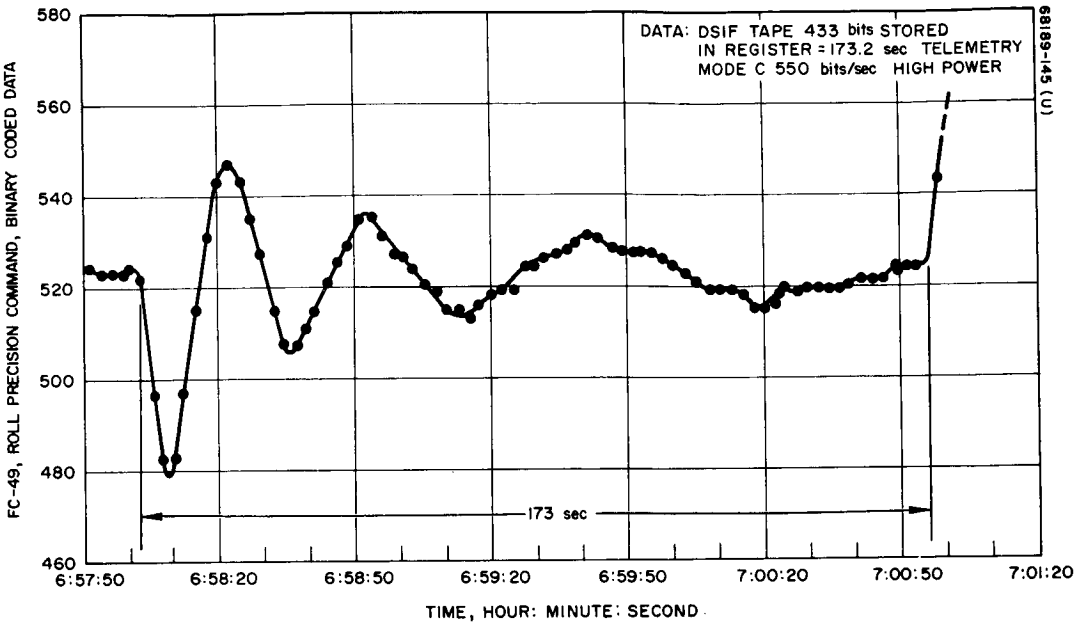


Figure 5.6-31. Roll Gyro Response Profile for Postmidcourse Roll Maneuver

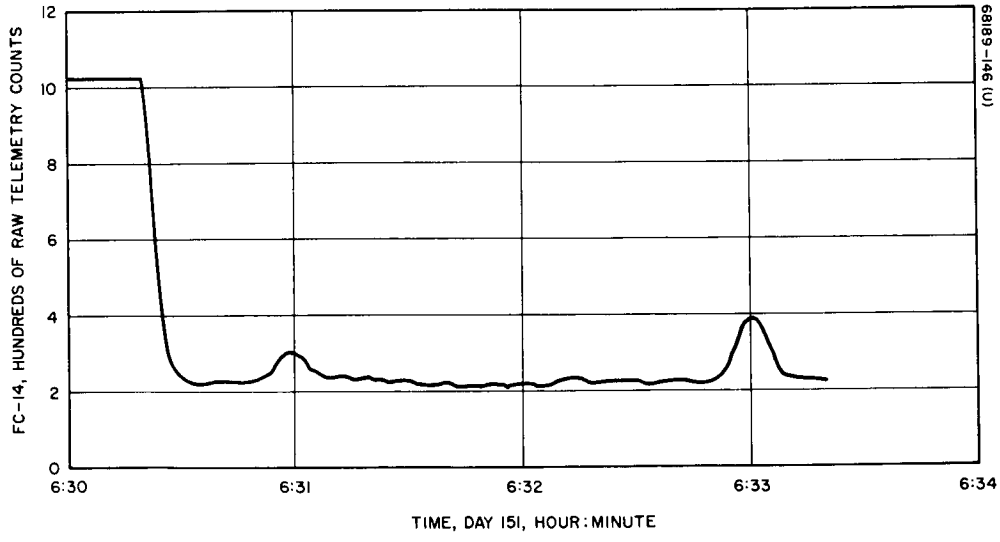


Figure 5.6-32. Star Intensity, FC-14, During Premidcourse Roll Maneuver

151:06:30:13 to 06:33:06 GMT

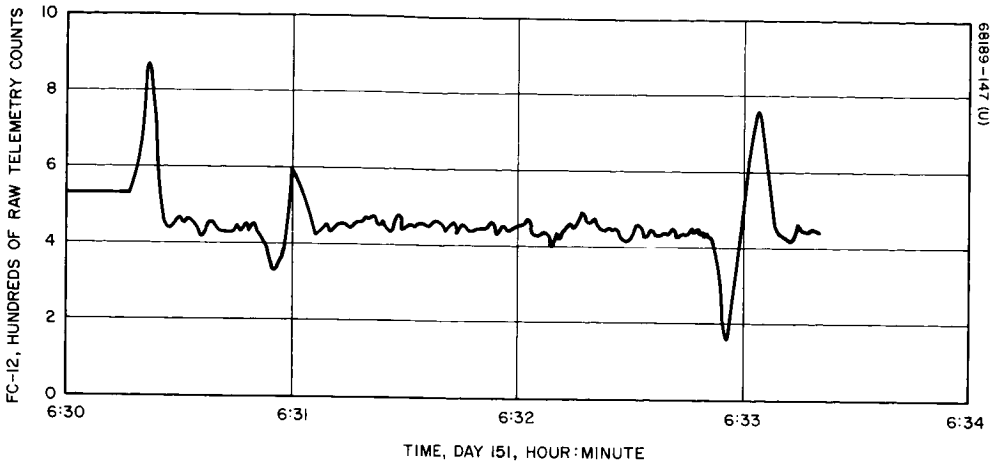


Figure 5.6-33. Canopus Error, FC-12, During Premidcourse Roll Maneuver

151:06:30:13 to 06:33:06 GMT

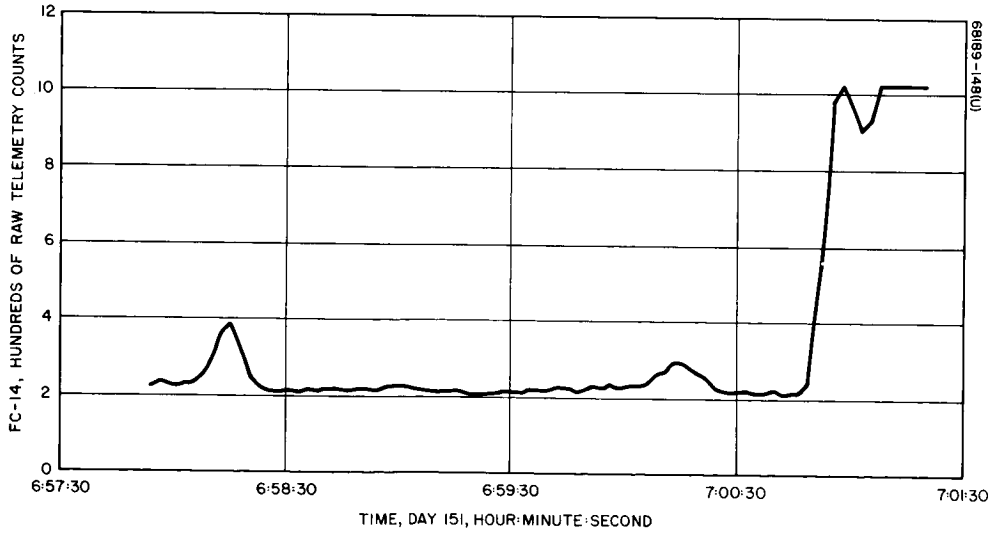


Figure 5.6-34. Star Intensity, FC-14, During Postmidcourse Roll Maneuver

151:06:58:02 to 07:00:56 GMT

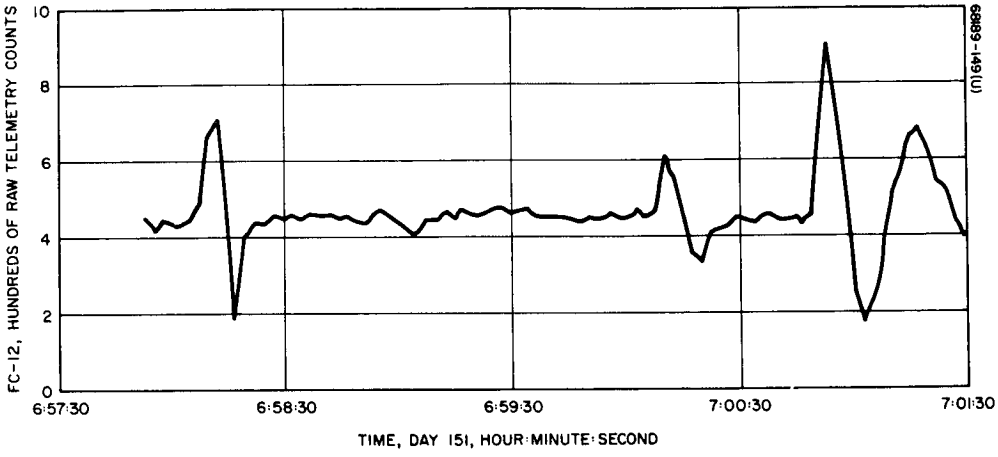


Figure 5.6-35. Canopus Error FC-12, During Postmidcourse Roll Maneuver

151:06:58:02 to 07:00:56 GMT

TABLE 5.6-14. MIDCOURSE IGNITION TRANSIENT CONTROL SUMMARY

Gyro Error Telemetry Resolution = 0.013 degree

Initial(pre-ignition)gyro errors, degrees:

Pitch = -0.15

Yaw = 0.04

Peak angular overshoot, degrees:

Pitch = 0

Yaw = -0.08

Peak angular rates, deg/sec:

Pitch = 0.25

Yaw = -0.36

Net 0.44

Vernier engine startup time = <0.15 second

Peak angular rates of (approximately) 0.25 deg/sec in pitch and -0.36 deg/sec in yaw occurred at vernier ignition. The startup impulse dispersions (deviations from average startup impulse) of the three engines are calculated by the procedure outlined to be approximately as follows:

Leg 1: -0.08 lb-sec

Leg 2: -0.232 lb-sec

Leg 3: 0.312 lb-sec

which implies a maximum startup impulse variation (between legs 2 and 3) of 0.544 lb-sec. This is an order of magnitude less than the allowable variation between engines specified in Reference 10.

Based on the startup impulse figures listed above, it is concluded that leg 3 produced thrust first, and leg 2 last. The behavior of vernier engine throttle-valve signals at ignition corroborate these conclusions. For example, leg 2 throttle-valve signal (FC-26) remains high longer than either of the other two in order to compensate for the relatively slow startup. Based on the acceleration error telemetry signal (FC-15), it is concluded that all three engines were producing controlled thrust within about 0.150 second of the ignition command signal. Therefore, acceleration signal amplifier saturation, which requires a startup delay of 0.26 second, did not occur, and no ΔV error information was lost.

Calculation of Engine Ignition and Shutdown Impulse Dispersions

Calculation of engine ignition or shutdown impulse dispersions follows the procedure outlined in Reference 11. Pitch and yaw angular rate increments following ignition or shutdown are related to engine impulses by

$$\Delta\omega_x = \frac{1}{I_x}(-2.94\, I_1 + 0.53\, I_2 + 2.43\, I_3)$$

$$\Delta\omega_y = \frac{1}{I_y}(-1.08\, I_1 + 3.10\, I_2 - 2.10\, I_3)$$

where

$\Delta\omega_x$, $\Delta\omega_y$ = pitch and yaw rate increments (rad/sec)

I_x, I_y = pitch and yaw moments of inertia (slug-ft^2)

I_1, I_2, I_3 = total ignition or shutdown impulse of engines 1, 2, and 3 (lb-sec)

These relations follow directly from vernier engine locations on the spacecraft.

Since the difference in impulse between engines is of concern here, the total impulse of each engine can be expressed as

$$I_i = I_o + \Delta I_i \qquad i = 1, 2, 3$$

where I_o represents average single engine impulse (i.e., one-third of total) and ΔI_i represents deviation from average. This means that

$$I_1 + I_2 + I_3 = 3 I_o$$

or

$$\Delta I_1 + \Delta I_2 + \Delta I_3 = 0$$

Combining this last equation with the first two given above yields the following matrix equation:

$$\begin{pmatrix} I_x\,\Delta\omega_x \\ I_y\,\Delta\omega_y \\ 0 \end{pmatrix} = \begin{pmatrix} -2.94 & 0.53 & 2.43 \\ -1.08 & 3.10 & -2.10 \\ 1 & 1 & 1 \end{pmatrix} \begin{pmatrix} \Delta I_1 \\ \Delta I_2 \\ \Delta I_3 \end{pmatrix}$$

which relates angular rate increment to impulse dispersions. Inversion of this equation yields

$$\begin{pmatrix} \Delta I_1 \\ \Delta I_2 \\ \Delta I_3 \end{pmatrix} = \begin{pmatrix} -0.200 & -0.073 \\ 0.0392 & 0.207 \\ 0.161 & -0.133 \end{pmatrix} \begin{pmatrix} I_x \Delta\omega_x \\ I_y \Delta\omega_y \end{pmatrix}$$

which was used to compute impulse dispersions from angular rate increments obtained from pitch and yaw gyro error telemetry data (FC-16 and -17).

Midcourse Engine Shutdown Dispersions

Shutdown of the vernier engines following midcourse correction resulted in attitude motion transients of the same magnitude predicted on the basis of FAT engine data and flight control system response characteristics (Reference 12). A summary of the peak spacecraft angles and angular rates and computed vernier engine shutdown impulse dispersions, with a comparison to preflight FAT measurements of impulse dispersion, are given in Table 5.6-15.

TABLE 5.6-15. MIDCOURSE SHUTDOWN SUMMARY

Peak angular errors, degrees:

Pitch = -0.6
Yaw = -1.9
Roll = 0.7

Peak angular rates, deg/sec:

Pitch = -0.21
Yaw = -0.47
Net = 0.51

Vernier shutdown impulse dispersions, lb-sec:

S/N	Leg	FAT Data	SC-1 (Computed)
545	1	-0.20	0.27
541	2	-0.22	-0.37
539	3	0.42	0.10

It may be noted that peak gyro angles were less than 2 degrees and well within the required travel range of ±10 degrees. Inertial reference was therefore retained, and reacquisition of the sun and Canopus were routinely accomplished via the reverse maneuver sequence.

Vernier engine shutdown impulse dispersions (relative to mean impulse of the three engines), calculated from pitch and yaw angular rate data as per the procedure outlined in the "Midcourse Engine Startup Characteristics," were well within the specification limit of ±0.63 lb-sec (Reference 8).

Determination of Thrust Vector Misalignment

The following error sources will be considered in the determination of the actual thrust vector position:

1) Premidcourse maneuver errors

2) Limit cycle error

3) Gyro drift errors

4) Vernier engine alignment offsets and support bracket bending

5) Attitude error during burn caused by moment disturbance.

The total error in the position of the spacecraft Z axis due to the first three items above is given in the "Premidcourse Maneuvers." The final orientation (just prior to vernier ignition) of the spacecraft with respect to the initial celestial reference in matrix notation is

$$\begin{pmatrix} \bar{1}_{xf} \\ \bar{1}_{yf} \\ \bar{1}_{zf} \end{pmatrix} = \begin{bmatrix} 3.30384\ E\text{-}2 & -0.527534 & 0.848891 \\ 0.998263 & 5.88641\ E\text{-}2 & -2.27153\ E\text{-}3 \\ -4.87709\ E\text{-}2 & 0.847492 & 0.528563 \end{bmatrix} \begin{pmatrix} \bar{1}_{xo} \\ \bar{1}_{yo} \\ \bar{1}_{zo} \end{pmatrix} \quad (1)$$

The error due to item 4 above is given in Reference 13. The acceleration vector presented in the reference is given in spacecraft coordinates as follows:

$$AMC = AMC\ (-0.00462\ \bar{1}_{xf} - 0.00160\ \bar{1}_{yf} - 0.999988\ \bar{1}_{zf}) \quad (2)$$

Using Equation 1, the acceleration vector can be referenced to the initial celestial reference. The result is

$$\bar{1}_{AMC} = 0.0470204\ \bar{1}_{xo} - 0.8451388\ \bar{1}_{yo} - 0.5324749\ \bar{1}_{zo} \quad (3)$$

The desired vector position with respect to the celestial reference (from "Premidcourse Maneuvers") is

$$\bar{1}_{o} = 0.0517664\ \bar{1}_{xo} - 0.8463740\ \bar{1}_{yo} - 0.5300670\ \bar{1}_{zo} \quad (4)$$

The pointing error can now be determined by performing a dot product of the two vectors (3 and 4). The result is a pointing error of $\varphi_{\epsilon} = 0.313$ degree.

Roll Control During Midcourse

The roll disturbance torques which were estimated using telemetry of the roll control nozzle actuator commands (FC-43), the roll precession commands (FC-49), and the preflight predicted vernier engine bracket bending were determined to be extremely small. The telemetry data for the roll actuator angular position during midcourse agreed quite closely with the values expected due to bracket bending. The predicted roll control nozzle angle to compensate for bracket bending was computed from the prelaunch alignment angles, a bracket spring constant of 0.045 deg/lb, and predicted thrust levels of the vernier engines. The roll disturbance torques due to vernier engine thrust vector misalignments other than bracket bending can be determined from the difference between the two curves of telemetered roll actuator position and predicted roll actuator position in Figure 5.6-36. It is seen that the difference between these curves is a maximum of 0.25 degree or a roll disturbance of less than 1.0 ft-lb.

The maximum commanded angle of the roll actuator was 0.9 degree, and the maximum roll actuator rate (slope) was 0.4 deg/sec. The commanded position of the roll control nozzle after initial transients is seen to jump between 0.6 and 0.75 degree from telemetry signal FC-43. This agrees quite well with the angle expected from the initial vernier engine alignment and the bracket bending of 0.75 degree.

To ensure that the commands to the roll actuator were actually due to roll gyro error signals (Figure 5.6-37), the roll precession command as determined from FC-49 and the commanded angle to the roll actuator as monitored with FC-43 are compared on the same graph (Figure 5.6-38). The two signals are seen to be closely correlated, in that when one signal changes significantly so does the other value.

Midcourse Velocity Determination

The general concept of midcourse correction capability employed by Surveyor is to apply a constant acceleration for a finite period of time. Thus, in theory, once the magnitude of the velocity correction is known, the exact duration of the constant acceleration phase can be determined. In practice, this approach is slightly altered to account for such error sources as engine ignition transients, shutdown impulse, and hysteresis. Thus, the actual command time ΔT is slightly higher.

The actual values used during flight were as follows:

1) Desired ΔV = 20.347 m/sec

2) Desired ΔT = 20.800 seconds

3) Register load = 417 bits = 20.850 seconds

Duration of Burn Time. The acceleration error signal data (FC-15) and thrust command data (FC-25, -26, and -27) were used in an attempt to determine the actual burn time (Figure 5.6-39). Since each parameter was monitored at different times, all four parameters were used whenever possible to reduce the region of uncertainty (Figure 5.6-39).

The result of the above effort indicates that the burn time was $T_B = 20.815$ seconds $^{+0.035}_{-0.029}$. The error in timing is 0.035 second.

Estimate of ΔV. Assuming that acceleration command remained at the design value of 3.226 ft/sec^2, the actual acceleration level was determined by subtracting the acceleration error value from the above value. From the plot of the acceleration error signal, the magnitude appears to decrease almost linearly with time (Figure 5.6-40).

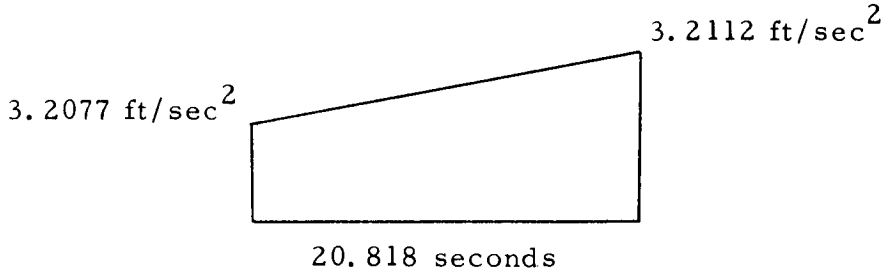
ϵ_A (start of midcourse) = 0.0183 ft/sec^2

ϵ_A (end of midcourse) = 0.0148 ft/sec^2

Thus, the actual acceleration levels for the corresponding periods were

A_s = 3.2077 ft/sec^2 (start of midcourse)

A_f = 3.2112 ft/sec^2 (end of midcourse)



From the acceleration profile above, the midcourse ΔV was ΔV = 66.8143 fps = 20.365 m/sec. From orbit determination, it was determined that the actual midcourse ΔV was 20.266 m/sec. This ΔV value obtained from data is within 0.49 percent of the actual.

A list of parameters which affects the accuracy of the velocity correction is presented in Table 5.6-16 along with the values of maximum allowable errors. Actual performance values were given wherever possible.

Midcourse – Vernier Engine System Parameters

From the telemetry of the differential current which actuates the throttle valve of the vernier propulsion system thrust chamber assembly (TCA), the specific thrust commanded to a given vernier engine can be

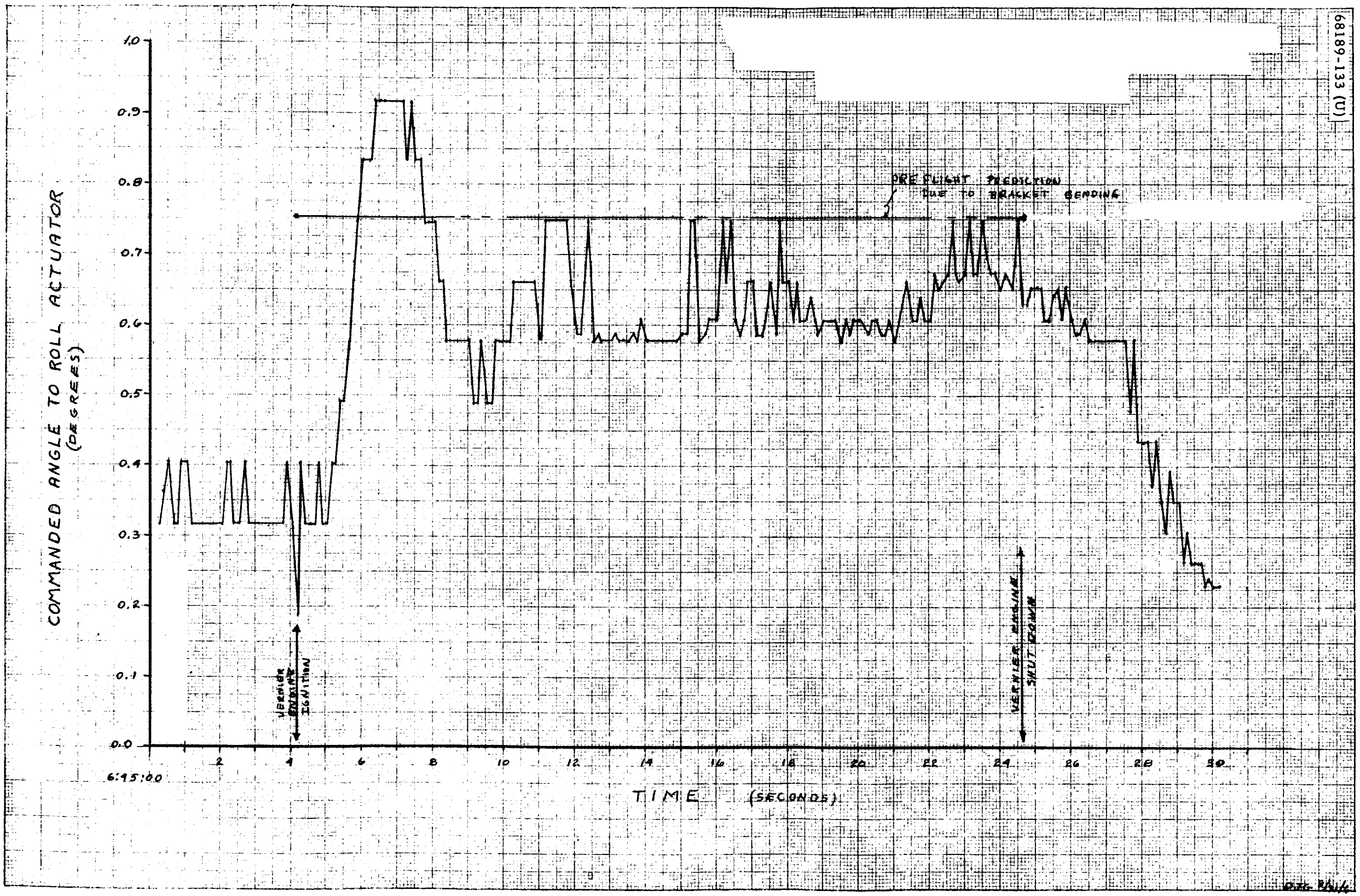


Figure 5.6-36. Commanded Angle to Roll Actuator From SC-1 Telemetry of FC-43 at Midcourse

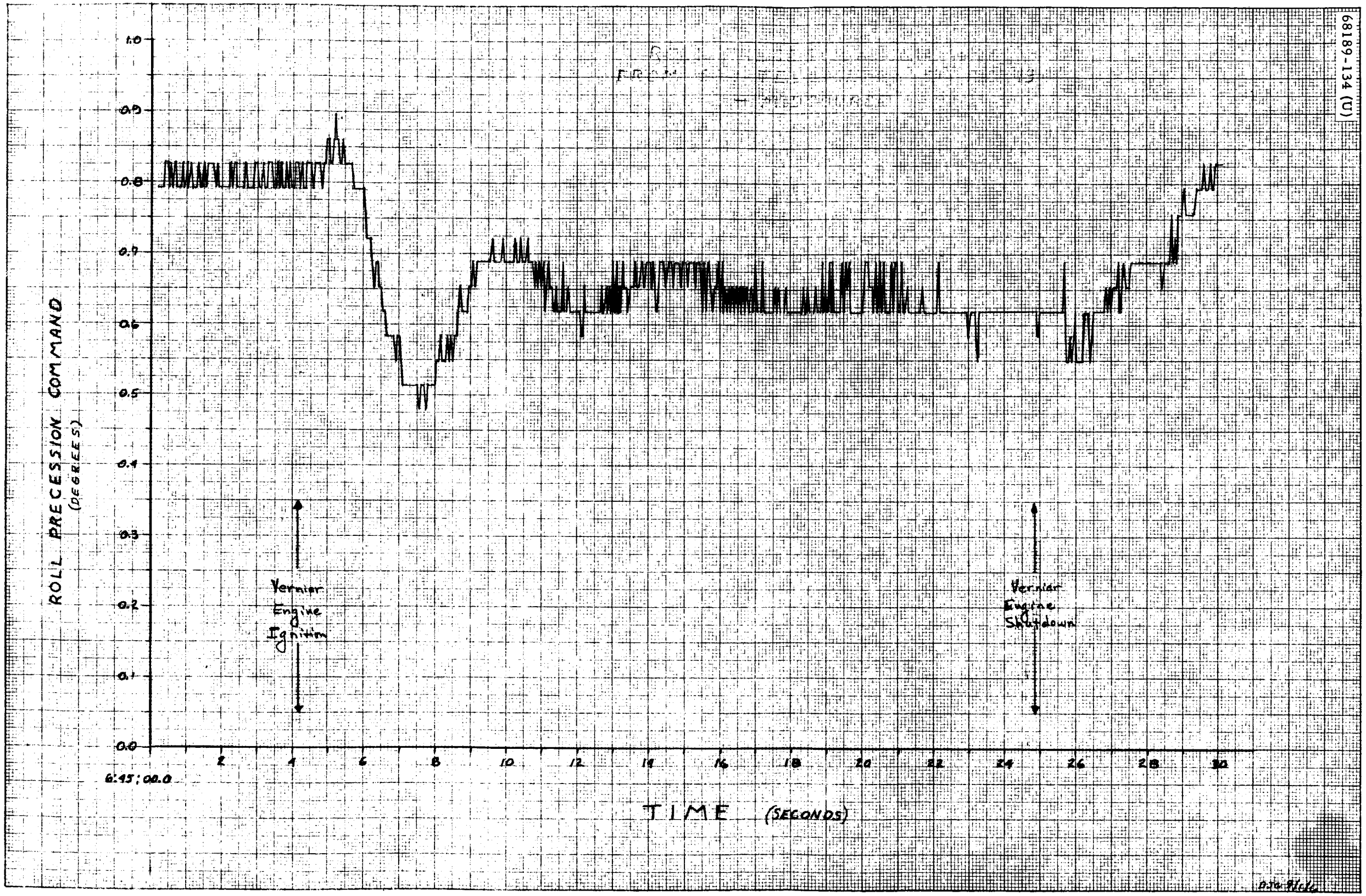


Figure 5.6-37. Roll Precession Command From SC-1 Telemetry of FC-49 at Midcourse

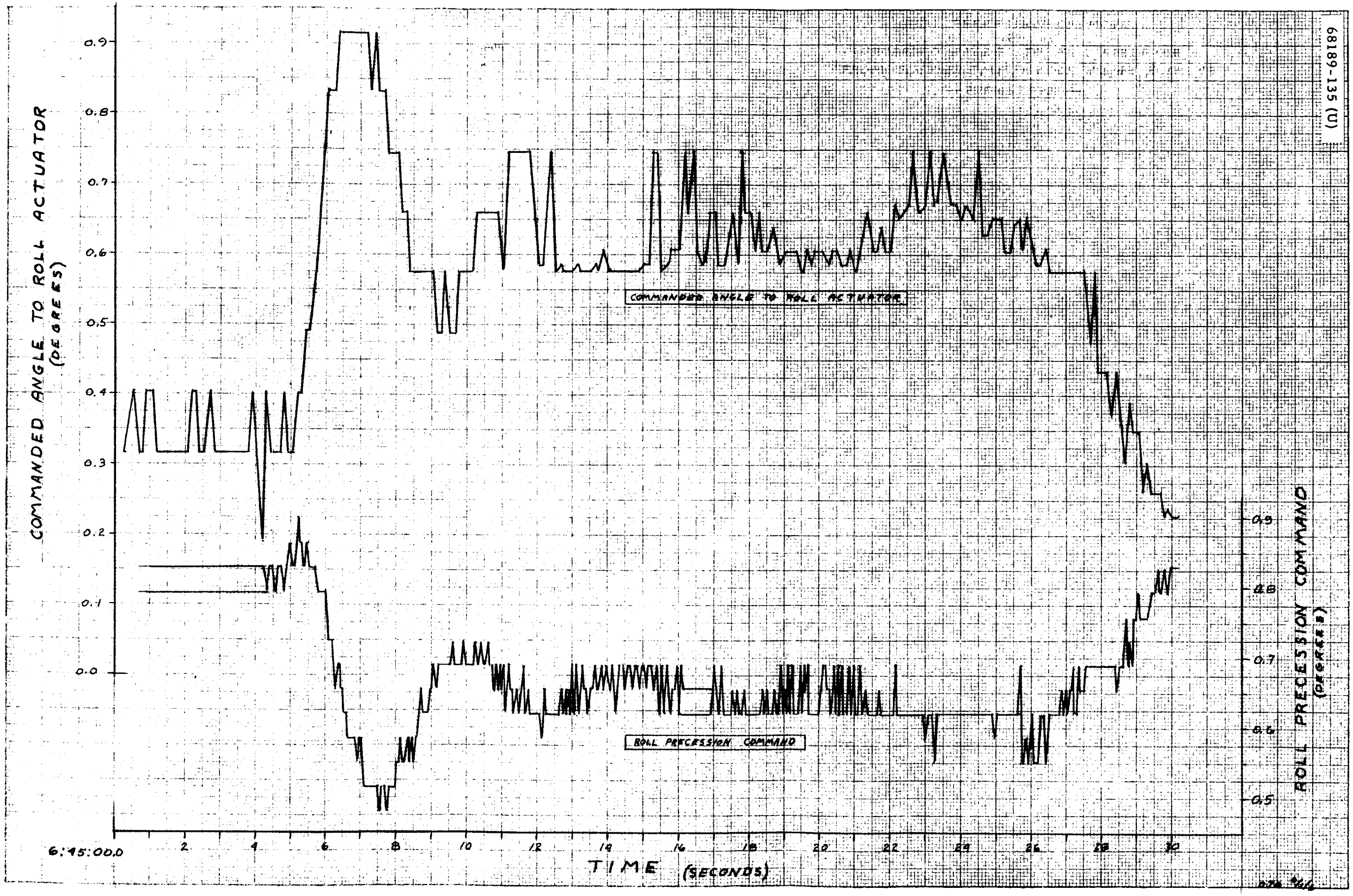


Figure 5.6-38. Roll Precession Command and Commanded Angle to Roll Actuator From SC-1 Telemetry of FC-49 and FC-43 at Midcourse

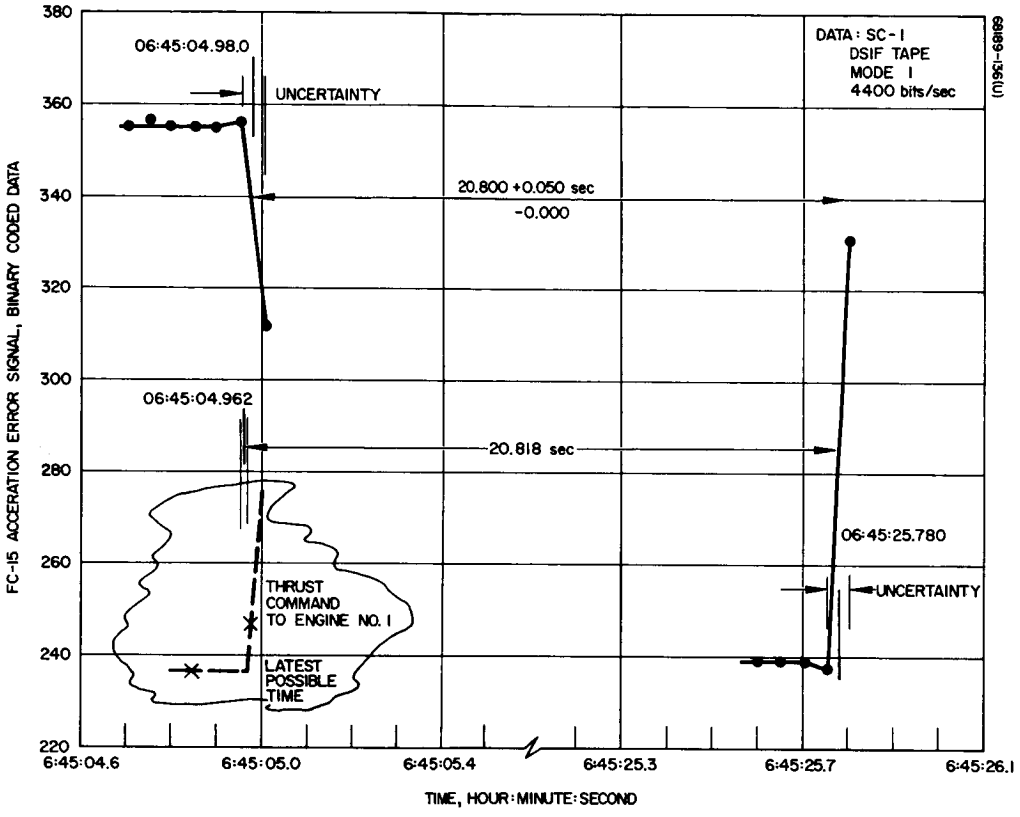


Figure 5.6-39. Acceleration Error Signal Profile at Midcourse

TABLE 5.6-16. SC-1 PERFORMANCE DETAIL

Characteristic: Midcourse Magnitude Error (20.35 mps correction);
Phase: Midcourse Correction

Item	Parameter	Requirement 3σ or Limit	Ft/sec	Specification	Performance Value, ft/sec	Comments
1	Errors proportional to maneuver magnitude					Much of the error was anticipated and was included in the calculation of the desired burn time. The difference between the actual value of ΔV and the desired value is -0.266 ft/sec. This value is more meaningful than the -0.725 ft/sec given as performance value.
	Accelerometer accuracy	1.1 percent	0.732	234632C		
	Reference signal	0.5 percent	0.334	234600E		
	FCE null	0.15 percent	0.098	234600E		
	Thrust bias variation	0.09 percent	0.061	287105		
	Control channel gain variation	0.07 percent	0.045	234600E		
	Accelerometer misalignment	0.06 percent	0.406	234600E		
	Total proportional errors (RSS)	1.22 percent	0.816		0.615	
2	Errors independent of maneuver magnitude					
	Shutdown impulse dispersion	±0.63 lb-sec	0.016	287015		
	Hysteresis limit cycle	3 milliampere	0.035	287105		
	Ignition transient	–	0.30	–		
	Timing granularity		0.16	224510D 3.6.3.2	-0.11	
	Total independent errors (RSS)		0.335			
3	Total magnitude errors (RSS)		0.865		-0.725	

determined. The telemetry output of the throttle valve commands (FC-25, FC-26, and FC-27) can thus be employed to determine the thrust level of each vernier engine during midcourse, and the sum of these thrust levels gives the total thrust acting on the spacecraft. As each engine is throttleable to produce pitch-yaw moment control, the individual thrust level and measured location of each TCA provides a means to determine the pitch and yaw moment disturbances during the maneuver. From these moment disturbances, the offset between the spacecraft center of gravity and the combined vernier engine thrust vector could be found. These vernier engine parameters have been analyzed using the telemetry of the commanded differential current.

Thrust Levels. The accuracy of telemetered values of differential current is affected by many variables. The telemetry output of the throttle valve commands may vary due to manufacturing differences in throttle valve torque motor coil resistance from nominal, owing to the change of coil resistance with operating time caused by heating effects through the coil,

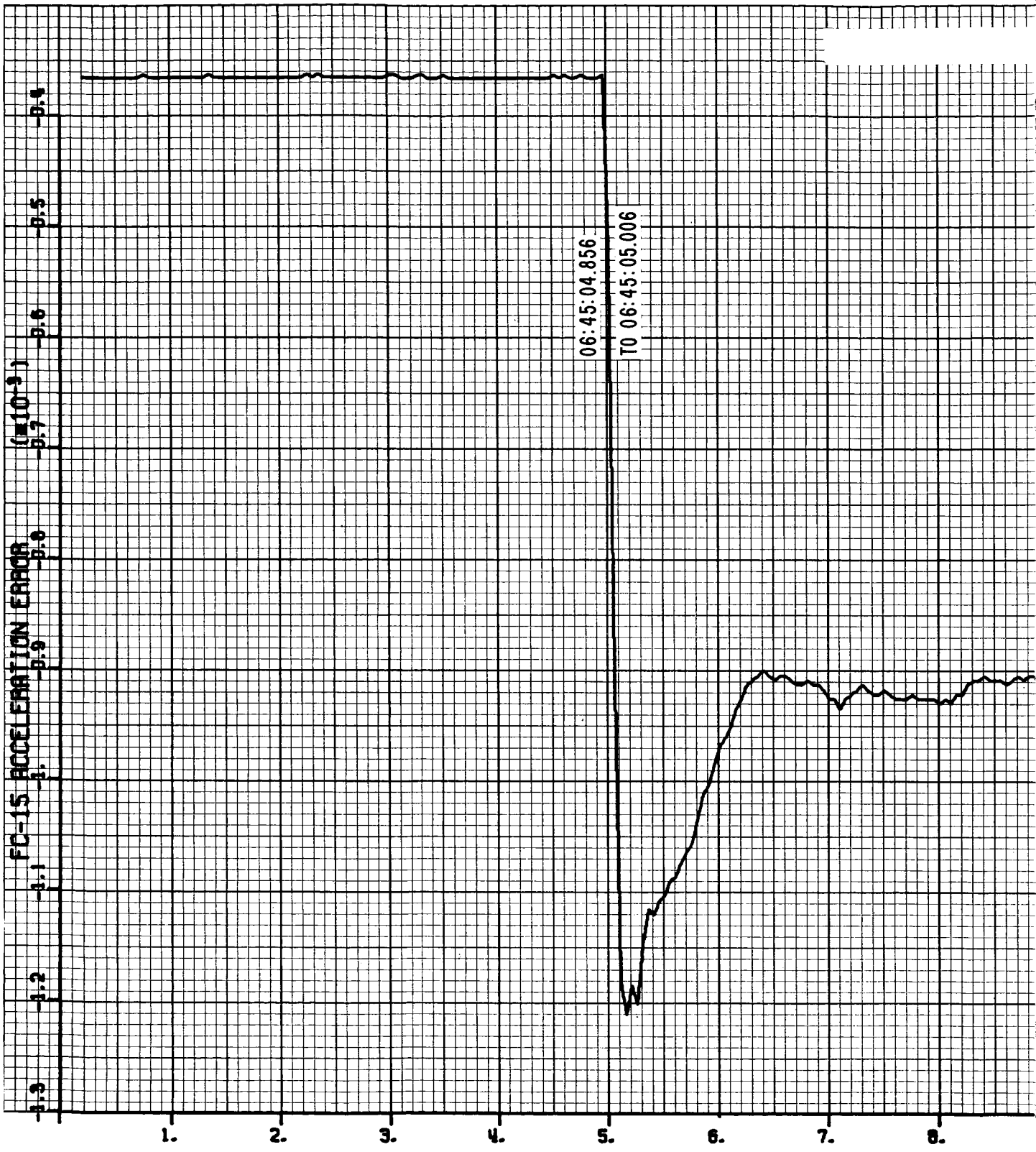
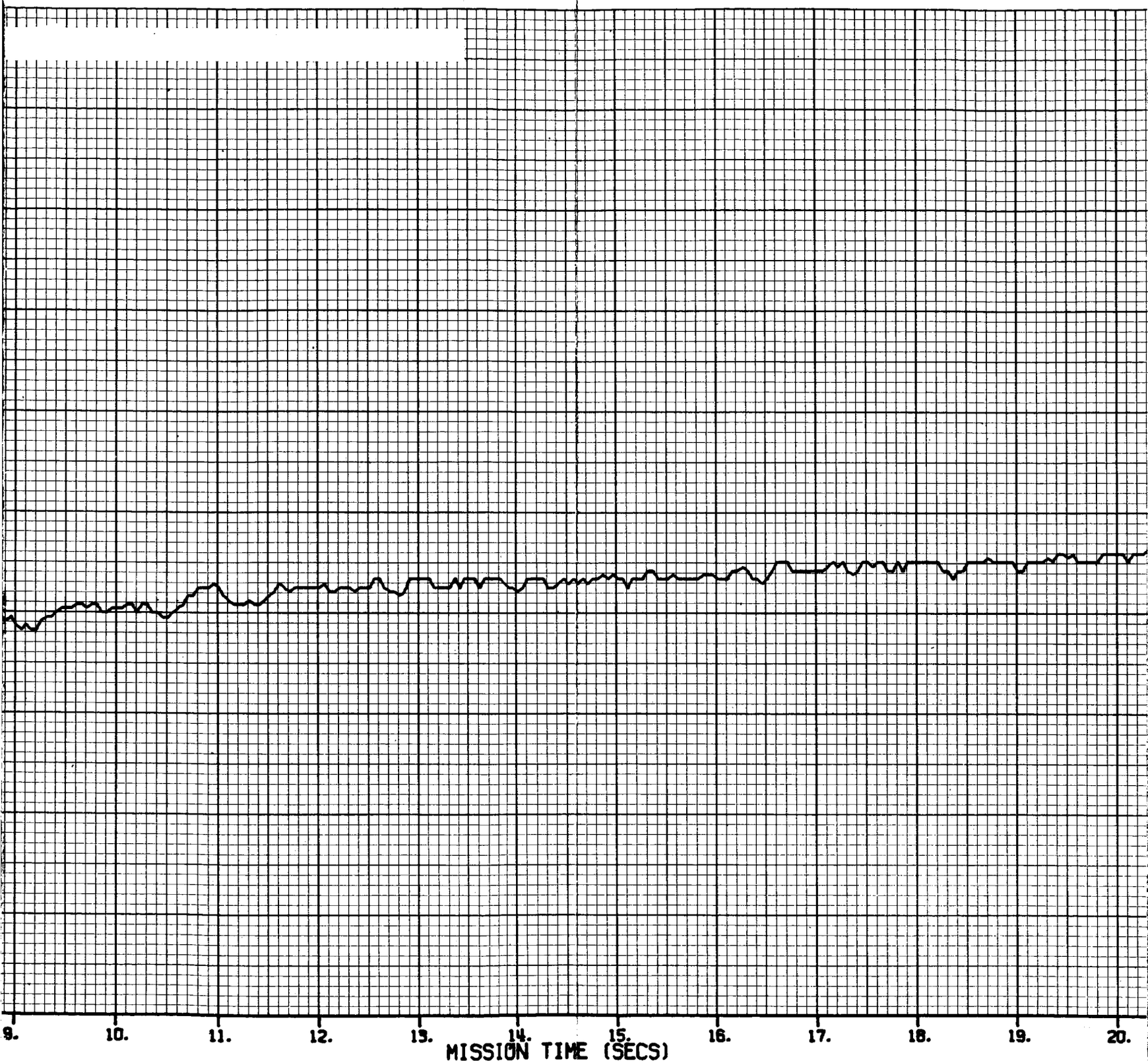


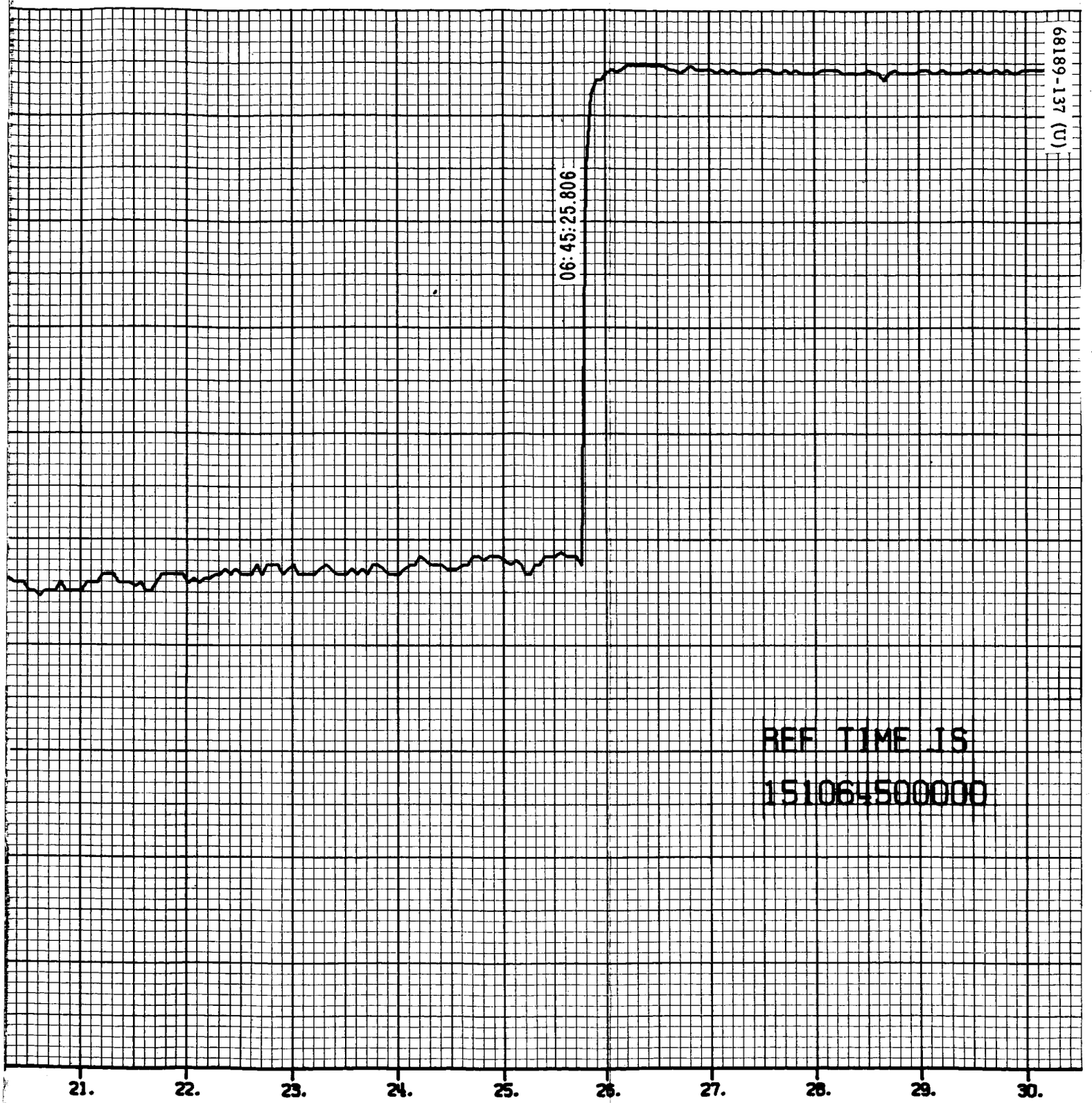
Figure 5.6-40. Acceleration Error Signal

FOLDOUT FRAME



FOLDOUT FRAME

5.6-97-2



FOLDOUT FRAME

5.6-98-1

5.6-98-2

and owing to inaccuracy of the telemetry link, including variables such as commutator unbalance current. To improve the telemetry data, a theoretical method suggested in Reference 14 was used to convert the telemetry data from BCD counts to milliamperes of differential current. This conversion method attempts to compensate for the inaccuracy in the telemetry signal caused by the varying resistance of the torque motor coil due to operational heating and by the difference in the actual torque motor coil from the nominal value. The signal error due to commutator unbalance current was less than 1 bcd so that the telemetry data could not be adjusted to eliminate this variable. Nevertheless, careful inspection of the data indicates that these corrected values of commanded differential current, ΔI, are accurate to within ±2 milliamperes.

To establish a specific magnitude of thrust from the corrected values of ΔI for each TCA, approximate slopes of differential current versus pounds of thrust were determined from flight acceptance test (FAT) data. The calibration curves were generated from FAT data points taken at approximately -40 and 0 milliamperes. The slope was taken to be linear and extended up to the appropriate region for midcourse of between 10 and 20 milliamperes. It is unfortunate that FAT data points were not taken in this region as this approximation introduced error in the absolute magnitudes of the thrust levels of the order of ±0.5 pound.

The midcourse thrust versus time profile, determined in the above manner, for each vernier engine is shown in Figure 5.6-41. The accuracy of any specific value of thrust is no less than ±1.0 pound. From the thrust-time plot, the initial transients at ignition are seen to peak out within 2 seconds, and the thrust levels settle into steady-state values. The maximum and minimum values for each vernier engine are as follows:

During initial transients:

Maximum thrust on engine 1 = 80.0 pounds

Maximum thrust on engine 2 = 77.9 pounds

Maximum thrust on engine 3 = 75.1 pounds

After initial transients:

Maximum thrust on engine 1 = 74.3 pounds

Maximum thrust on engine 2 = 74.1 pounds

Maximum thrust on engine 3 = 73.4 pounds

Minimum thrust on engine 1 = 72.6 pounds

Minimum thrust on engine 2 = 71.2 pounds

Minimum thrust on engine 3 = 72.4 pounds

It was expected that engine 1 (the roll control gimbaled engine) would have a little higher thrust level than the other two engines, and this is verified by the data. Due to the location of the combined spacecraft center of gravity being closer to leg 3, the thrust on engine 3 would have to be somewhat higher than the vernier engine located near leg 2. This expectation is also verified by the reduced telemetry data. The thrust-time profile for vernier engine 2 has a greater slope than the other two engines. No explanation of this observation has been determined. A slight decline in thrust levels is expected for all three vernier engines since control loop is in a constant acceleration mode and the engines are expending propellant. Movement of the spacecraft center of gravity due to propellant consumption was predicted to be toward the spacecraft coordinate origin which would cause the thrust on vernier engine 3 to be lowered and engine 2 to slightly increase; however, the data shows the opposite trend. One explanation could be that combined vernier engine thrust vector was moving away from TCA 2 such that the resultant moment disturbances required these lower thrust levels. Another reason could be that the telemetry signal for engine 2 (FC-26) was not completely corrected for the error due to torque motor coil resistance (which causes the signal and, thus, the indicated thrust level, to drop). However, this type of signal change was not evident for FC-26 from the terminal descent data.

The total thrust of the vernier propulsion system during midcourse for any given time was calculated from the sum of the individual vernier engine thrust levels that were sampled at that time. Of course, all three channels were not sampled at the exact same time, but at the high bit rate during midcourse of 4400 bits/sec, all three channels were sampled within a time interval of 0.1 second. Summation of these closely grouped samples should be a good approximation of the total thrust for that time interval. The total midcourse thrust versus time plot is given in Figure 5.6-42. For comparison purposes, the required average thrust level to maintain the telemetered value of ΔV for the midcourse time interval of 20.85 seconds is shown on the graph. Also, the required total thrust to maintain the expected constant acceleration of 0.1 g is included in this plot. These curves were obtained by connecting initial and final points, which were found in the following manner:

SC-1 weight at injection = 2192.71 pounds

Nitrogen gas used (see Figure 5.6-81) = 0.23 pound

ω_o = weight at start of midcourse = 2192.48 pounds

ΔV_{actual} = 20.266 m/sec (Reference 15) 3.280833 feet = 1 meter

$$I_{SP} = \frac{\Delta V}{g \ell n \frac{\omega_o}{\omega_f}}$$

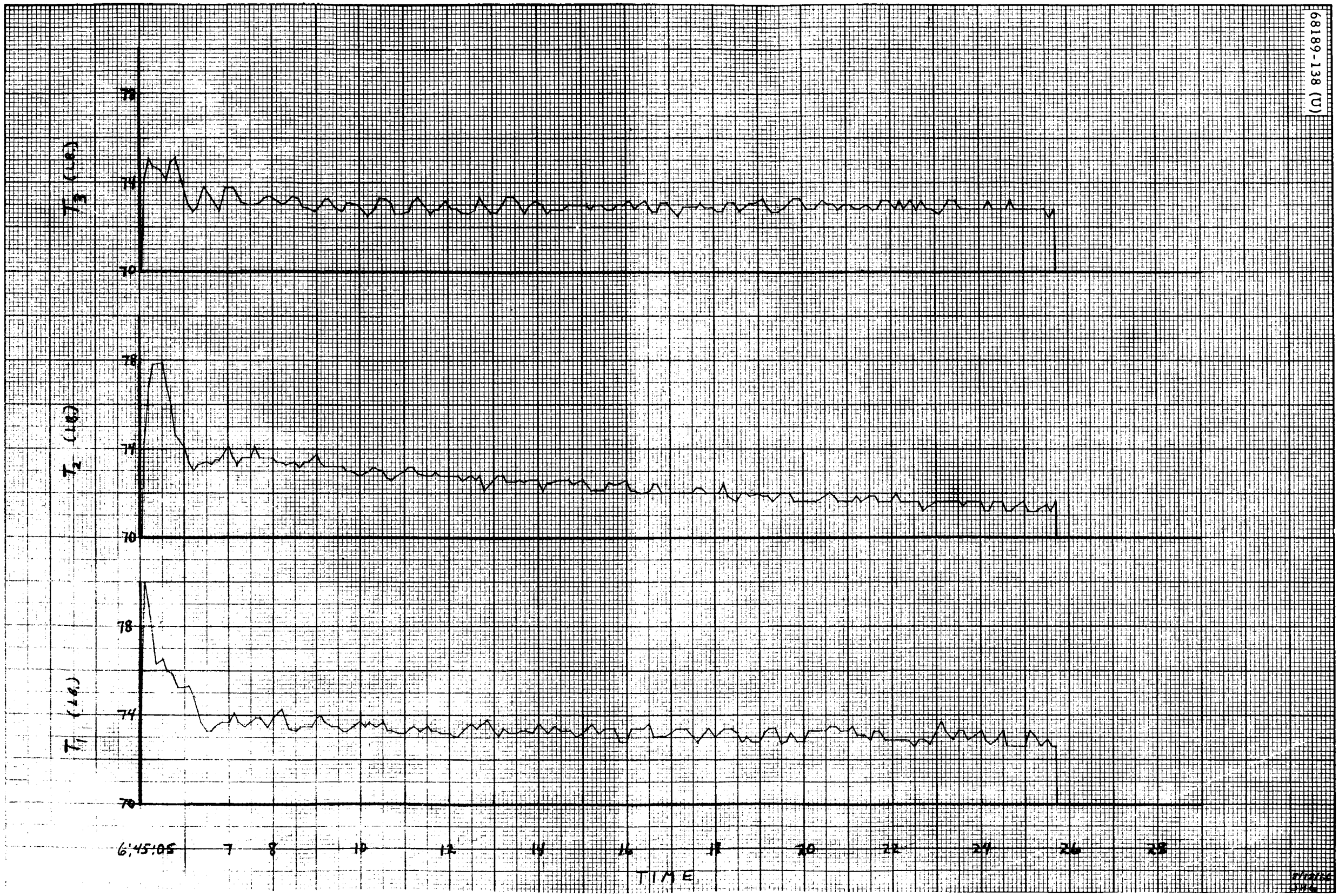


Figure 5.6-41. Midcourse Thrust-Time Profile From Flight Control Telemetry

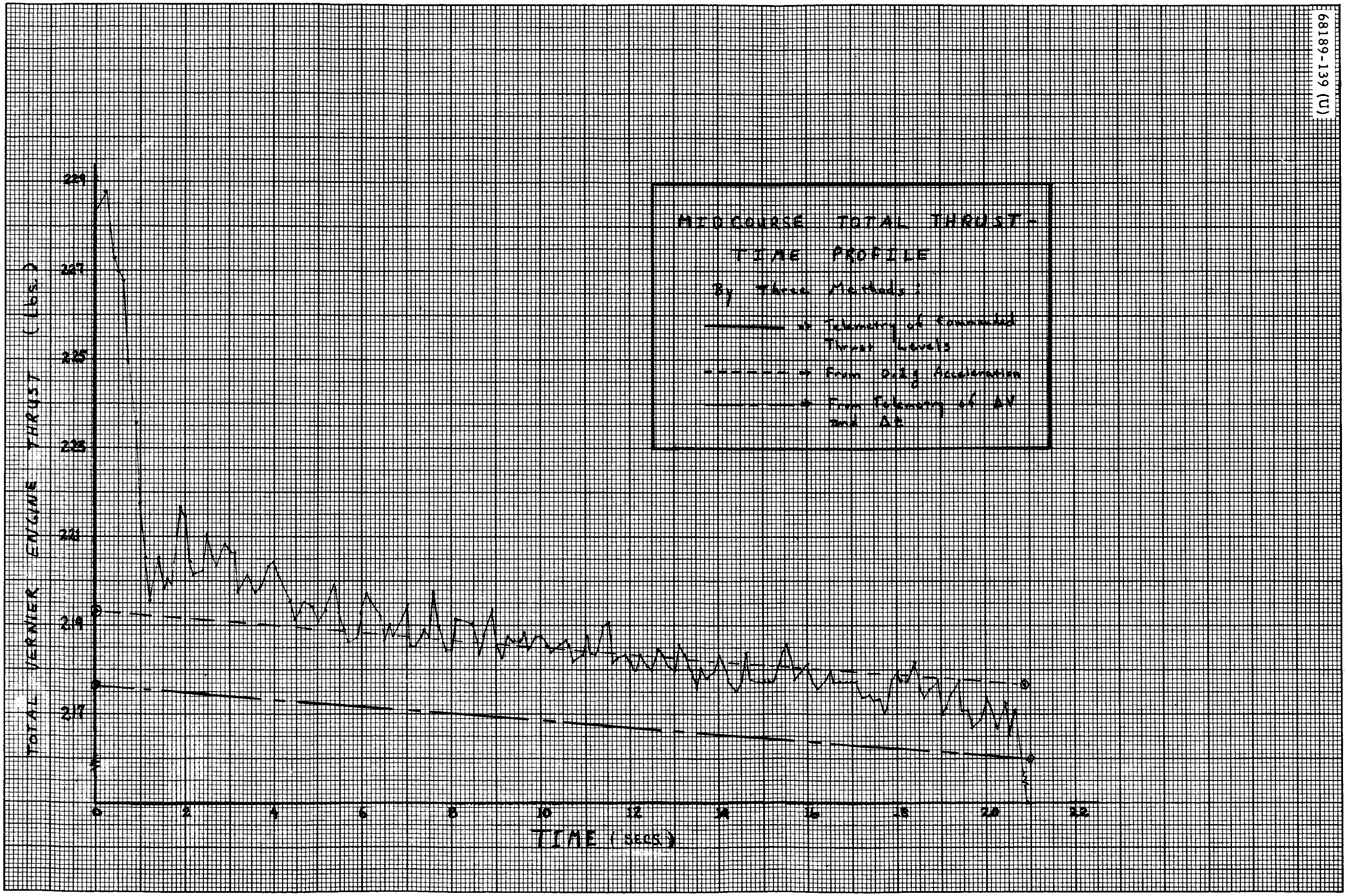


Figure 5.6-42. Midcourse Total Thrust-Time Profile

$$\Delta w = w_f - w_o$$

$\Delta w = 16.81$ (Reference 13)

$w_f = 2175.67$ pounds

Postflight analysis of the time interval of midcourse (see "Midcourse Velocity Determination") shows that $\Delta t = 20.818$ seconds.

From the telemetered average acceleration level:

$$\text{Average acceleration from telemetry} = \hat{a}_{TM} = \frac{\Delta V}{\Delta t}$$

$$\hat{a}_{TM} = 3.19384 \text{ ft/sec}^2 = 0.09927 \text{ g}$$

$$\text{Average total thrust} = \hat{T} = m\hat{a}$$

At start of midcourse:

$$(\hat{T})_i = \frac{w_o}{g} \hat{a}_{TM} = 217.65 \text{ pounds}$$

At end of midcourse:

$$(\hat{T})_f = \frac{w_f}{g} \hat{a}_{TM} = 215.98 \text{ pounds}$$

From expected acceleration of $\hat{a}_o = 0.1$ g:

$$(\hat{T})_i = \frac{w_o}{g} (0.1 \text{ g}) = 219.248 \text{ pounds}$$

$$(\hat{T})_f = \frac{w_f}{g} (0.1 \text{ g}) = 217.567 \text{ pounds}$$

The total thrust levels as determined from the commanded differential current compare very favorably with the values as determined above. The accuracy of these values from the sum of the individual vernier engine thrust levels is roughly ±3 pounds. After the initial transients, the thrust values from telemetry are about 2 pounds higher than the level predicted from ΔV and are very close to that predicted for 0.1 g of acceleration. The slope of the telemetry thrust versus time profile is again somewhat more than predicted by the constant accelerations. This is due to the steeper decline of the thrust on vernier engine 2 discussed previously.

Moment Disturbances: The orientation of the vernier engines in spacecraft coordinates is shown in Figure 5.6-43. The pitch and yaw moments, taken about any point in the spacecraft center of gravity plane (X_o, Y_o), given by the individual thrust levels of the three vernier engines (T_1, T_2, and T_3), are:

$$\Sigma M_x = -(R_{1y} - Y_o) T_1 + (R_{2y} + Y_o) T_2 + (R_{3y} + Y_o) T_3$$

$$\Sigma M_y = -(R_{1x} - X_o) T_1 + (R_{2x} + X_o) T_2 - (R_{3x} - X_o) T_3$$

The SC-1 measured values of the vernier engine radial arms ("SC-1 Mass Properties Handbook") are as follows:

$R_1 = 37.734$ inches

$R_2 = 37.744$ inches

$R_3 = 37.829$ inches

Using the orientation of the vernier engines in the X-Y plane shown in Figure 5.6-43, the SC-1 vernier engine moments about the pitch and yaw axes taken at (X_o, Y_o) are found to be as follows:

$$\Sigma M_x = -0.9424 (R_1 - Y_o) T_1 + 0.1816 (R_2 + Y_o) T_2 + 0.7608 (R_3 + Y_o) T_3$$

$$\Sigma M_y = -0.3345 (R_1 - X_o) T_1 + 0.9834 (R_2 + X_o) T_2 - 0.6489 (R_3 - X_o) T_3$$

The moment disturbance curves of Figure 5.6-44 were generated from the previously presented SC-1 corrected thrust command data versus time plots and the above equations. In this plot, the moments were taken about the spacecraft coordinate origin such that $X_o = 0$ and $Y_o = 0$. The commanded thrust levels for a given time interval were all sampled within 0.05 second, and the moments were computed using these closely grouped telemetry values as was done to obtain the total thrust-time profile.

The moment disturbances at any given time, as shown, are only accurate to within ±40 in-lb since the values of T_i in the above equations are only known to within ±1 pound. As most of the moments found were of this order, very little can be determined from these plots. On the graph, the predicted moments due to the spacecraft center of gravity offset from the spacecraft origin is shown for the two cases of omnidirectional antenna A stowed and omnidirectional antenna A extended. Because of the relatively large inaccuracy of the data points, nothing could be concluded from a comparison of these two cases and the telemetered data. Therefore, no attempt to predict the spacecraft center of gravity to combined thrust vector offset was made.

The computed moments about the X axis (pitch) are seen to be fairly constant (between -30 and 10 in-lb) during most of the 20-second time period of the midcourse maneuver. Moments taken about the Y axis (yaw) tend to increase in magnitude, after the initial transients, from approximately zero to around -60 in-lb during the time of commanded thrust. This is attributable to the unexplained decrease in the telemetered thrust command of vernier engine 2 (T_2) previously discussed. TCA 2 is located out along the positive X axis and the decrease in T_2 produced negative moments about the Y coordinate axis.

The maximum pitch (M_x), yaw (M_y) and total (M_{TOTAL}) moments as determined by using the above equations and the telemetry corrected values of commanded thrust on the vernier engines are as follows:

During initial transients:

Maximum magnitudes $M_x = -203$ in-lb

$M_y = 122$ in-lb

$M_{TOTAL} = 215$ in-lb

After initial transients:

Maximum magnitudes $M_x = -40$ in-lb

$M_y = -74$ in-lb

$M_{TOTAL} = 74$ in-lb

Corrected plots of the pitch and yaw gyro error signals are included to illustrate the response of the attitude loop and to confirm the low moment values calculated above (Figures 5.6-45 and 5.6-46).

5.6.7.9 Preretro Maneuvers

Before retro ignition, it is required that the spacecraft thrust axis (positive roll axis) be aligned to the translation velocity vector of the spacecraft. This is an integral part of the gravity turn design for the terminal descent phase guidance.

This alignment is to be performed by means of two or three sequential rotations about the spacecraft body axes. The first two rotations are to provide the actual alignment of the roll axis; the third rotation (if required) is a roll rotation to align the high-gain planar array with the spacecraft-earth line. On SC-1 the final roll was performed to secure a favorable omnidirectional antenna pattern.

These maneuvers are accomplished by using the cold gas attitude control system, with the body-fixed integrating rate gyros as inertial references. To accomplish a rotation, the appropriate gyro torquer winding is

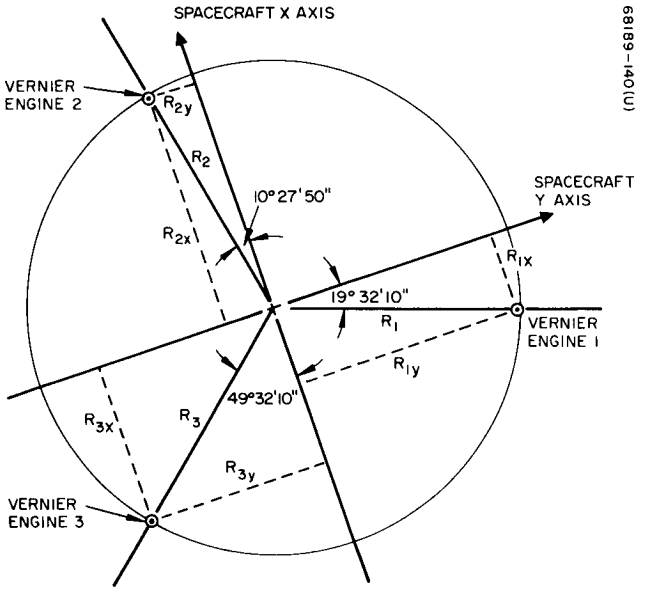


Figure 5.6-43. Orientation of Vernier Engines in Spacecraft Coordinates

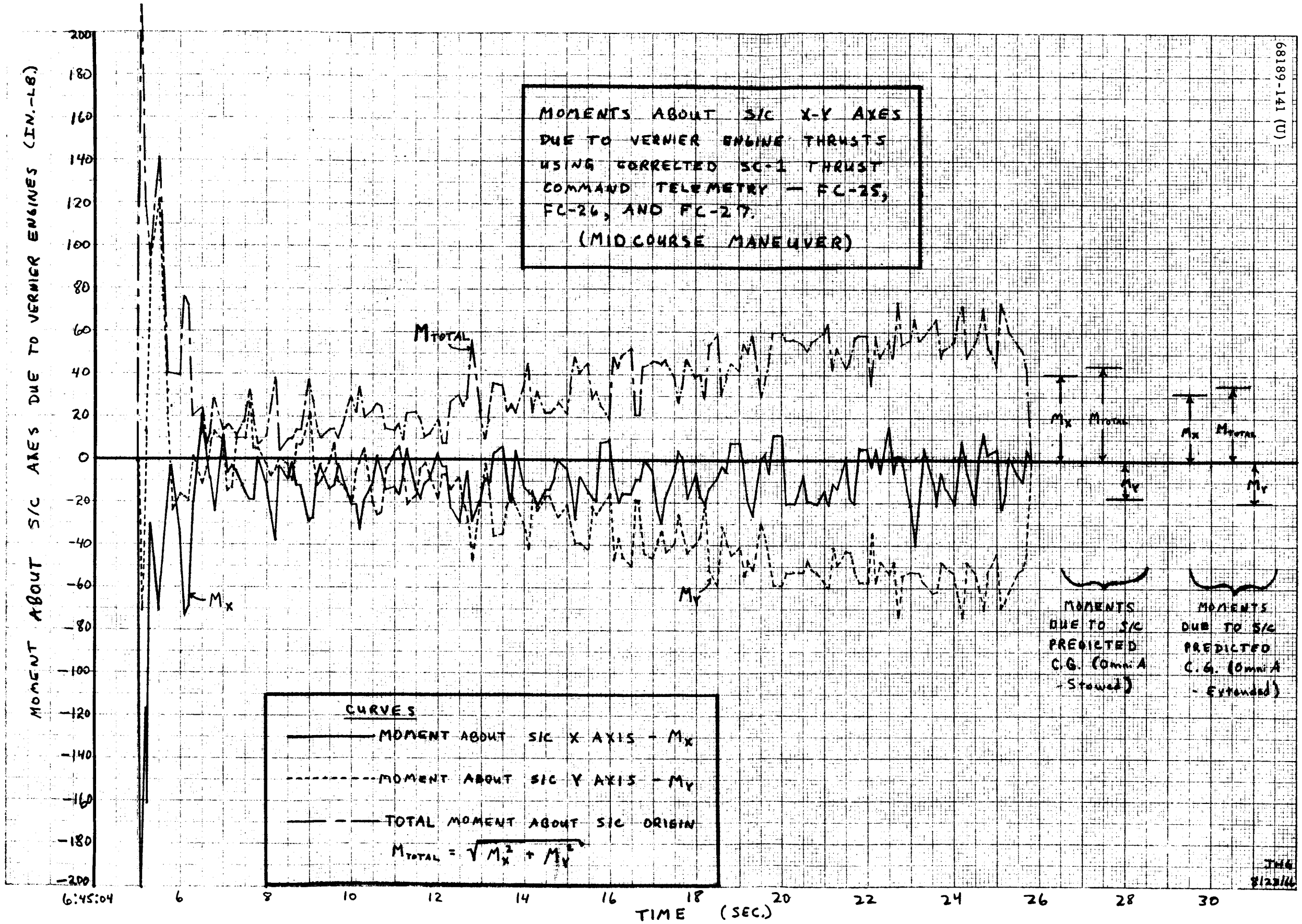


Figure 5.6-44. Moments About Spacecraft X-Y Axes Due to Vernier Engine Thrusts Using Corrected SC-1 Thrust Command Telemetry for FC-25, FC-26, and FC-27

Midcourse maneuver

5.6-109

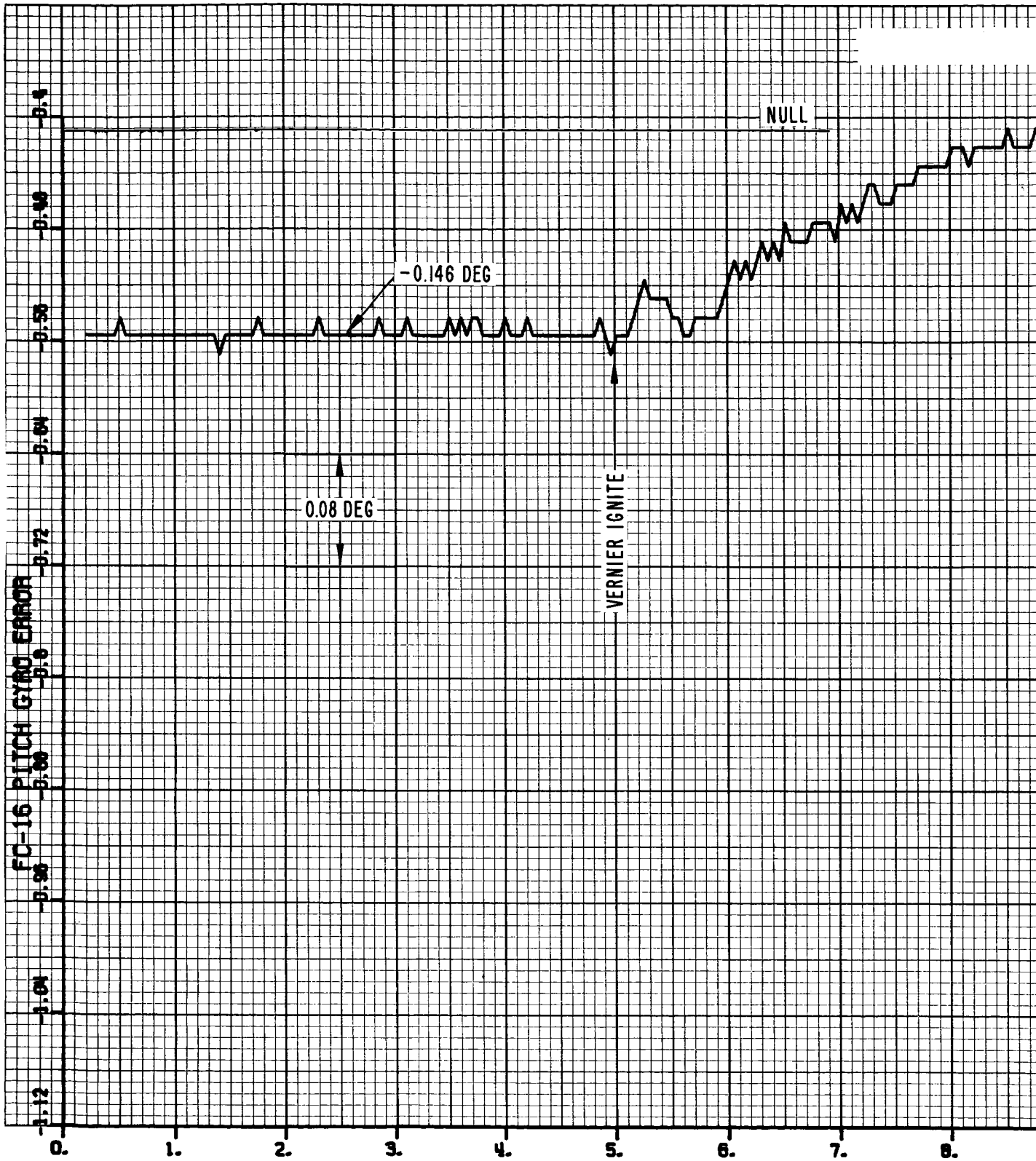
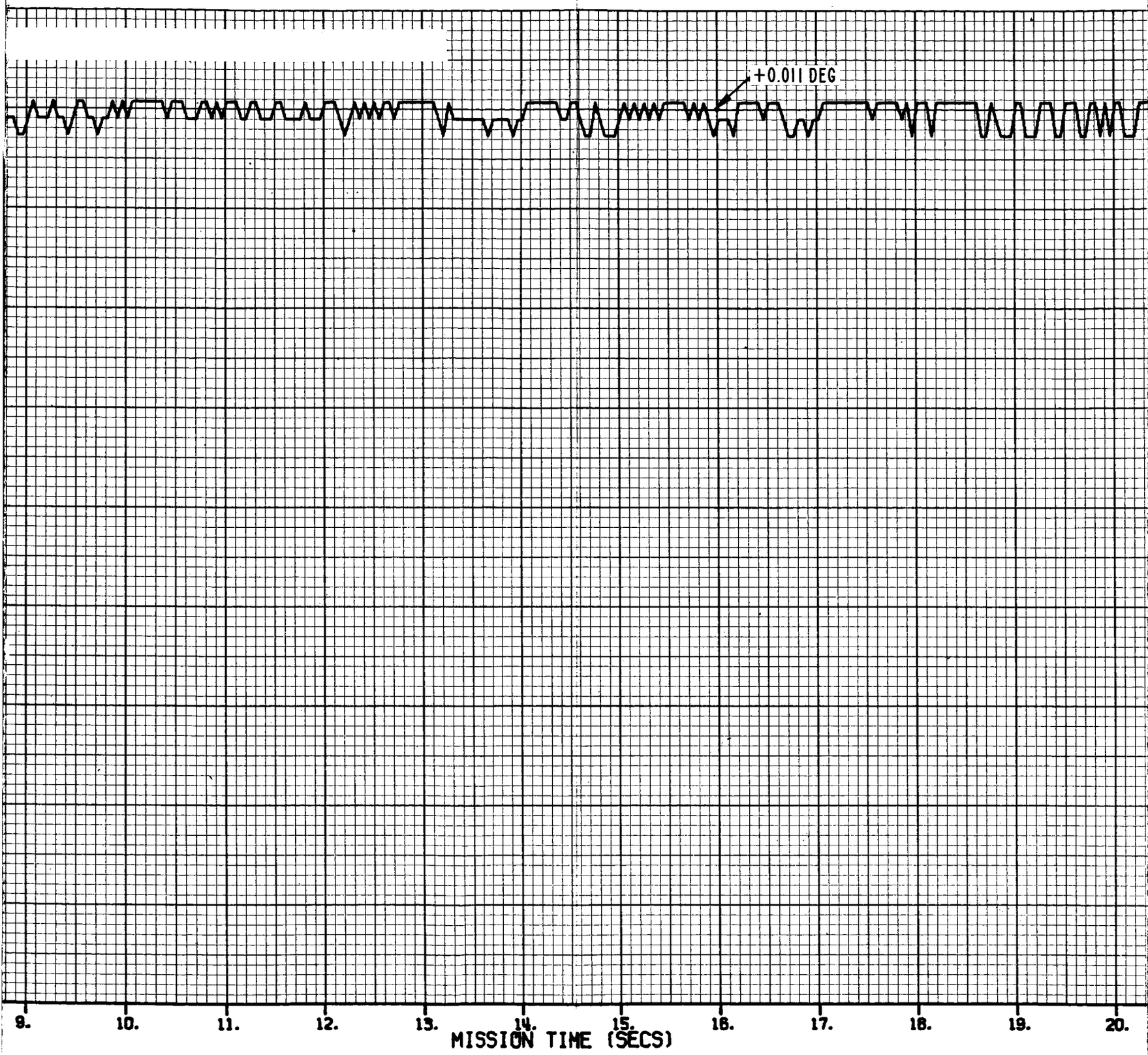


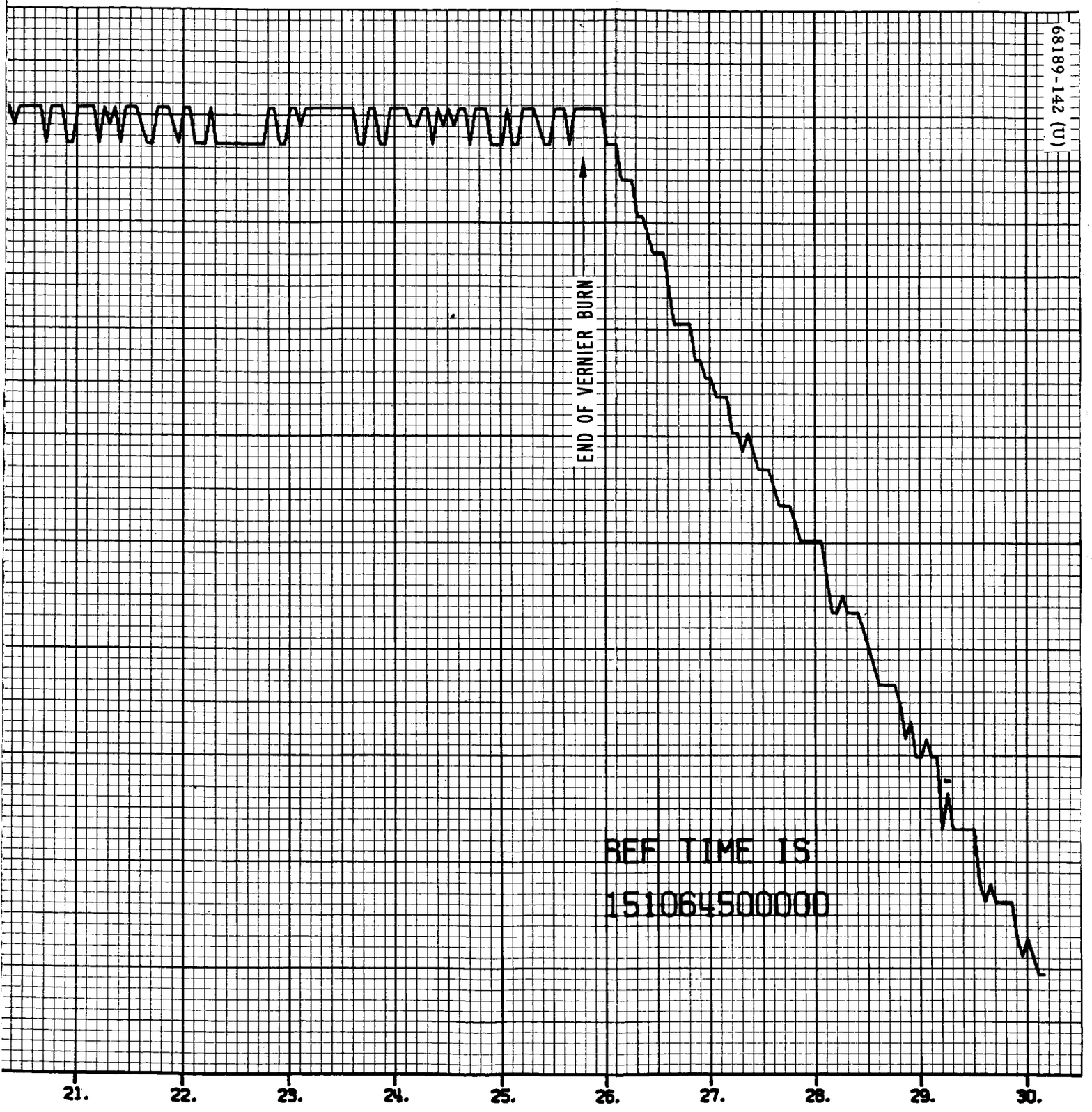
Figure 5.6-45. Pitch Gyro Error Signal at Midcourse

FOLDOUT FRAME



FOLDOUT FRAME

5-6-111-3



FOLDOUT FRAME

5-6-112

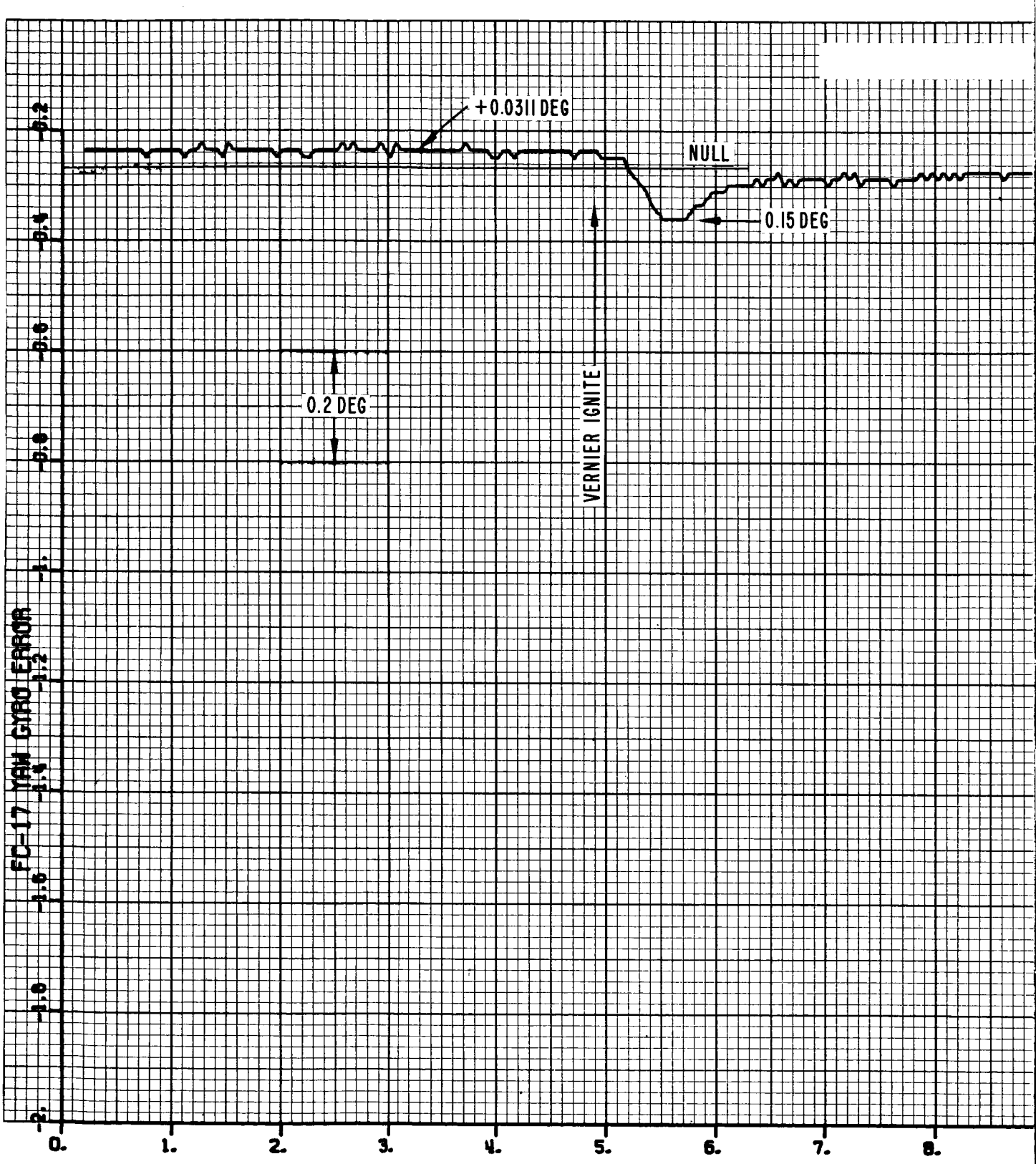
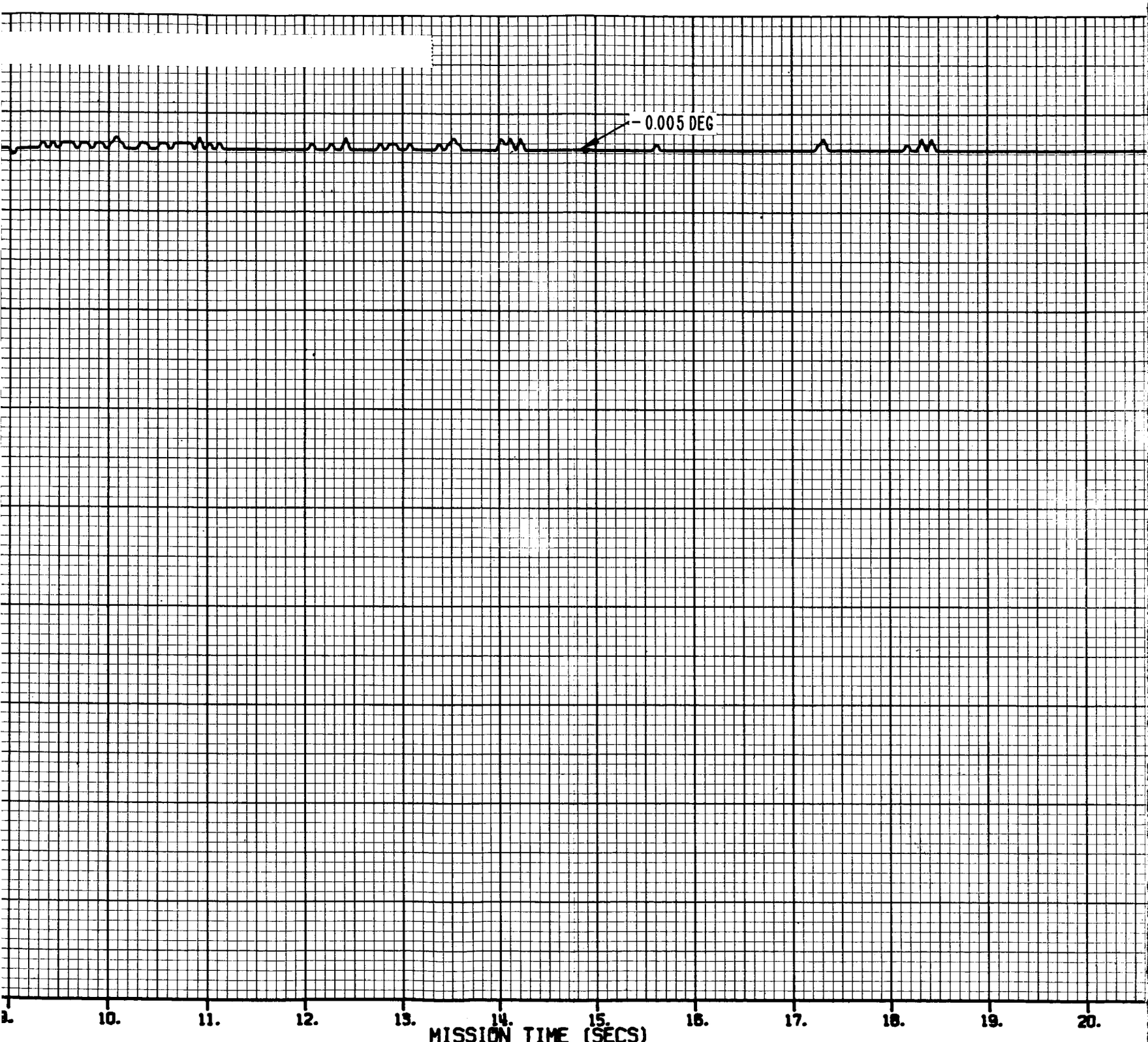


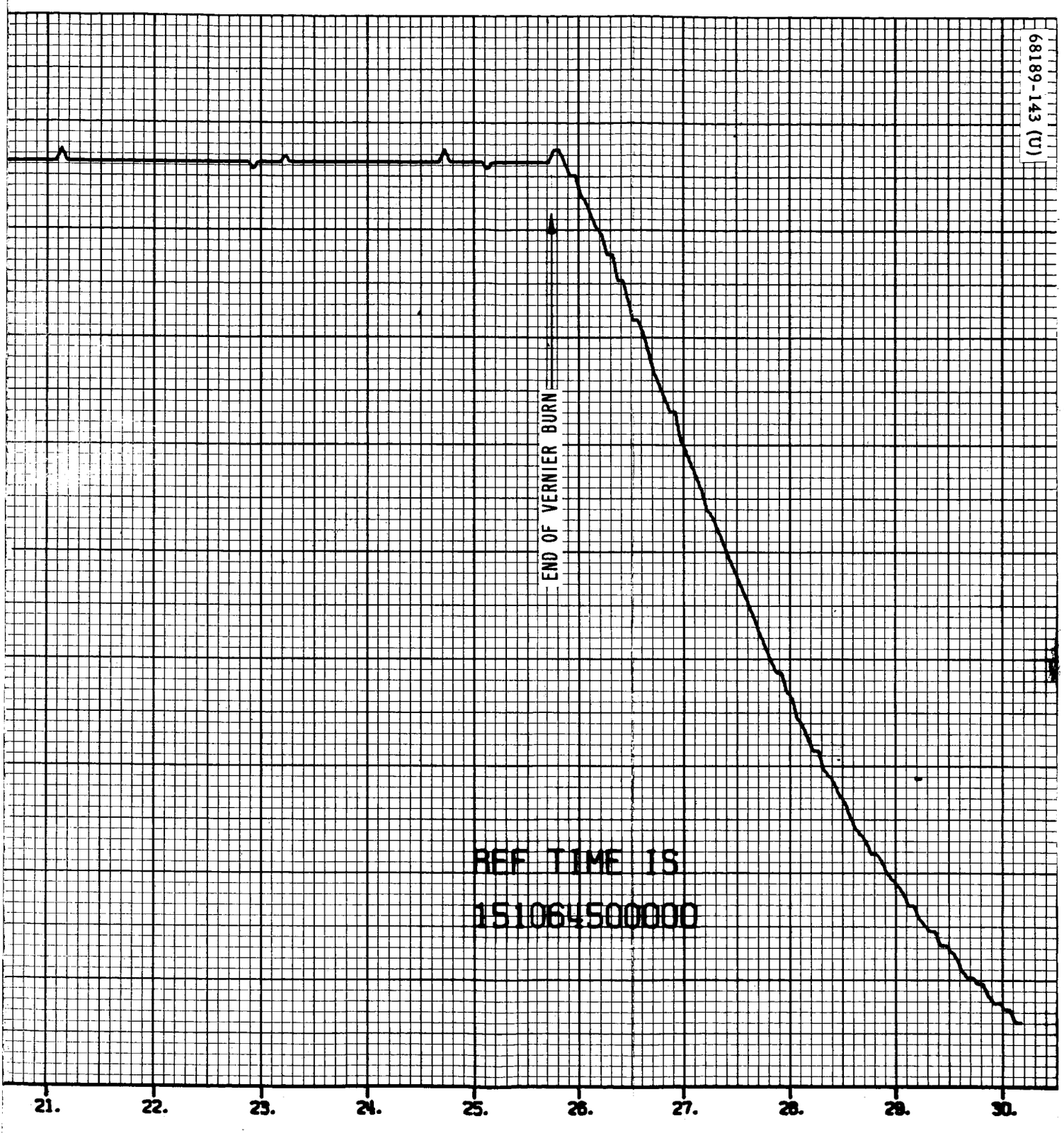
Figure 5.6-46. Yaw Gyro Error Signal at Midcourse

FOLDOUT FRAME



FOLDOUT FRAME

5.3-113-2



FOLDOUT FRAME

driven by a constant current source for a precise length of time; the spacecraft is slaved to this changing reference.

The major events and times associated with the preretro maneuvers are given in Table 5.6-17.

The preretro maneuvers were analyzed in terms of the following:

1) From gyro error signals and precession logic signals, determine gyro precession time to best accuracy and compare to commanded times.

2) From the above and the initial sun and Canopus error signals, make best determination, with resultant tolerances noted, of the terminal pointing accuracy.

3) Verify item 2 above by comparison with pointing error determined from main retro burnout conditions.

TABLE 5.6-17. MAJOR EVENTS AND TIMES (DAY 153), PRERETRO MANEUVERS

Event	Command	GMT Time
Begin roll 1	0714	5:36:49.097
End roll 1		5:39:47.693
Begin yaw	0713	5:41:50.320
End yaw		5:43:50.318
Begin roll 2	0711	5:45:20.285
End roll 2	5:48:29.081	
Retro ignition		6:14:49.65 (Reference 18, Table II)

Determined from DSIF tabulated data

Analysis Details

Gyro Transients. One of the primary requirements of the preretro maneuver is that the inertial reference of the spacecraft never be inadvertently changed; that is, no gyro must be permitted to saturate at any point in the three rotation sequence. The minimum linear range of each of the gyros is ±10 degrees.

Recall that Mission A preretro rotations were as follows:

Roll 1 89.3 degrees

Yaw 59.9 degrees

Roll 2 94.1 degrees

Typical roll and yaw inertial maneuvers (for rotations ≥ 40 degrees) are shown in Figures 5.6-47 and 5.6-48 as simulated on the analog computer. For comparison purposes, Mission A first roll preretro is recorded in Figures 5.6-49 through 5.6-51; the yaw maneuver is recorded in Figures 5.6-52 and 5.6-53; the second roll maneuver is recorded in Figures 5.6-54 through 5.6-56.

The following is noted:

1) All gyro overshoots are << 10 degrees. Hence, the spacecraft inertial reference was maintained.

2) The transient waveforms from the mission agree closely with the traces (from the analog computer mechanization).

Gyro Precession Times. The following table gives the gyro precession times.

Maneuver	Commanded Time, seconds*	Observed Time, seconds**	ΔT, seconds	Rotation Error, degrees
Roll 1	178.66	178.60	-0.06	$\Delta\varphi_1 = -0.030$
Yaw	119.85	120.00	0.15	$\Delta\psi = 0.075$
Roll 2	188.17	188.80	0.63	$\Delta\varphi_2 = 0.315$

*Reference 3, Table 5.

**DSIF tabulated data.

Optical Error Signals. The following optical error signals were read from DSIF tabulated data at the instant the preretro maneuvers began (153:5:36:49):

Roll: $\delta\hat{i}$ = -0.268 degree

Pitch: $\delta\hat{j}$ = 0.027 degree

Yaw: $\delta\hat{k}$ = -0.167 degree

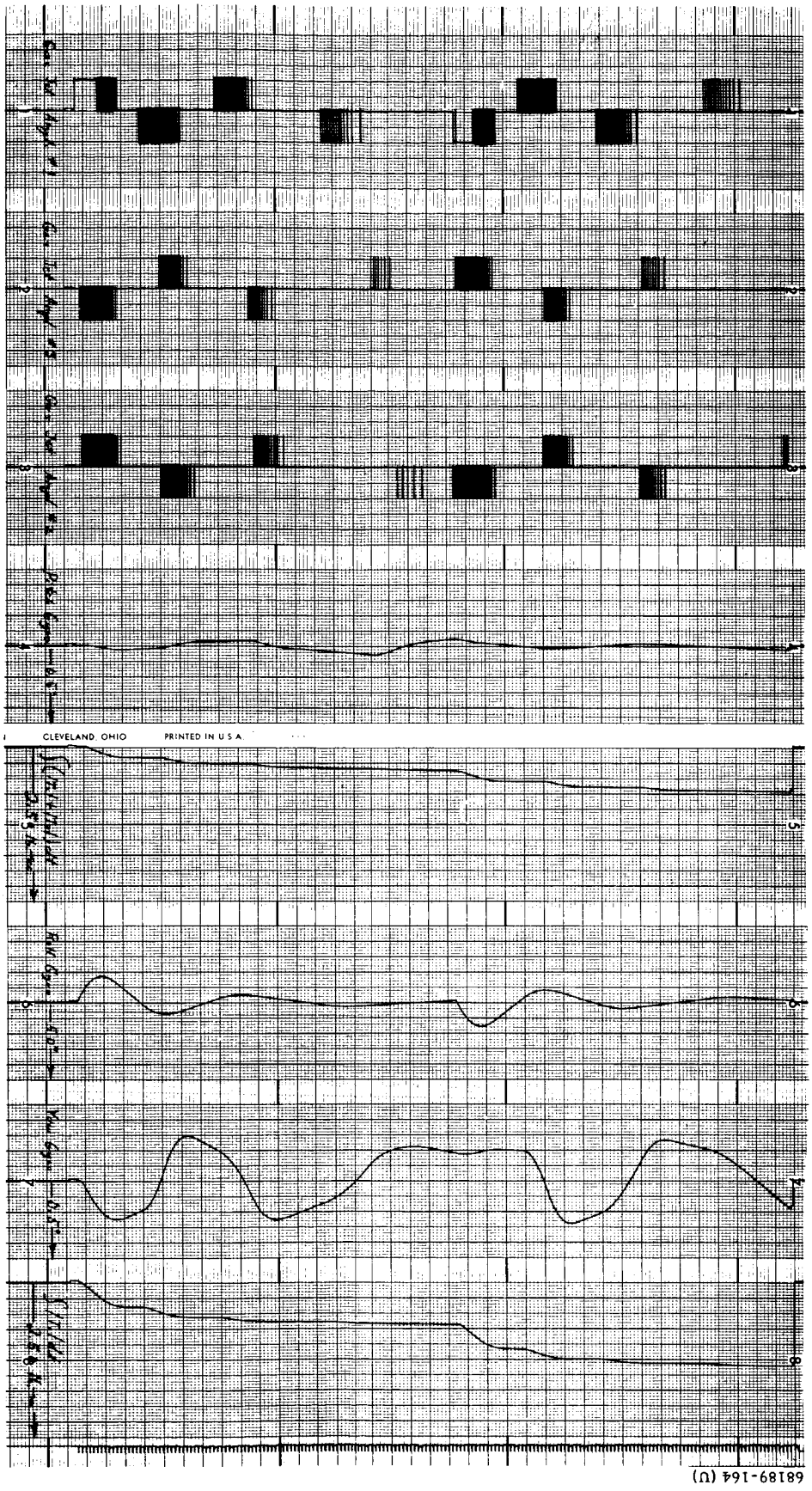


Figure 5.6-47. Roll Inertial, Long Duration Attitude Maneuver

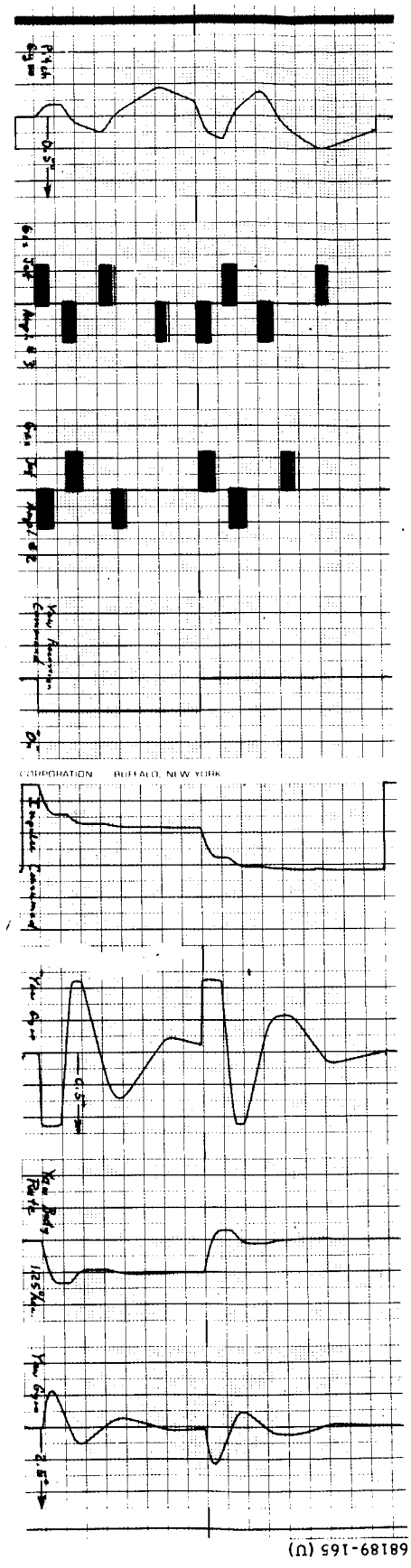


Figure 5.6-48. Yaw Inertial, Long Duration Attitude Maneuver

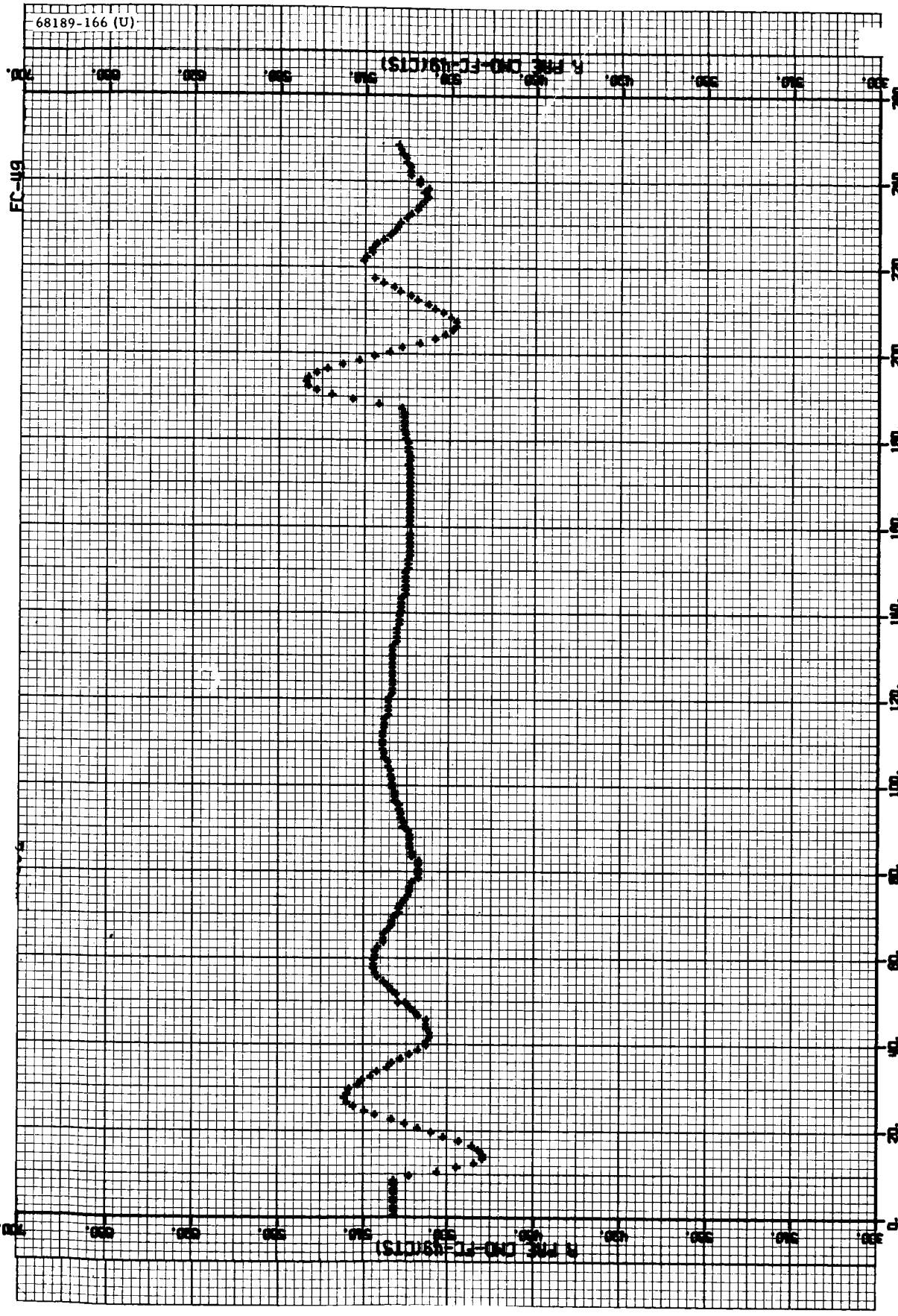


Figure 5.6-49. Roll Precession Command (First Roll)

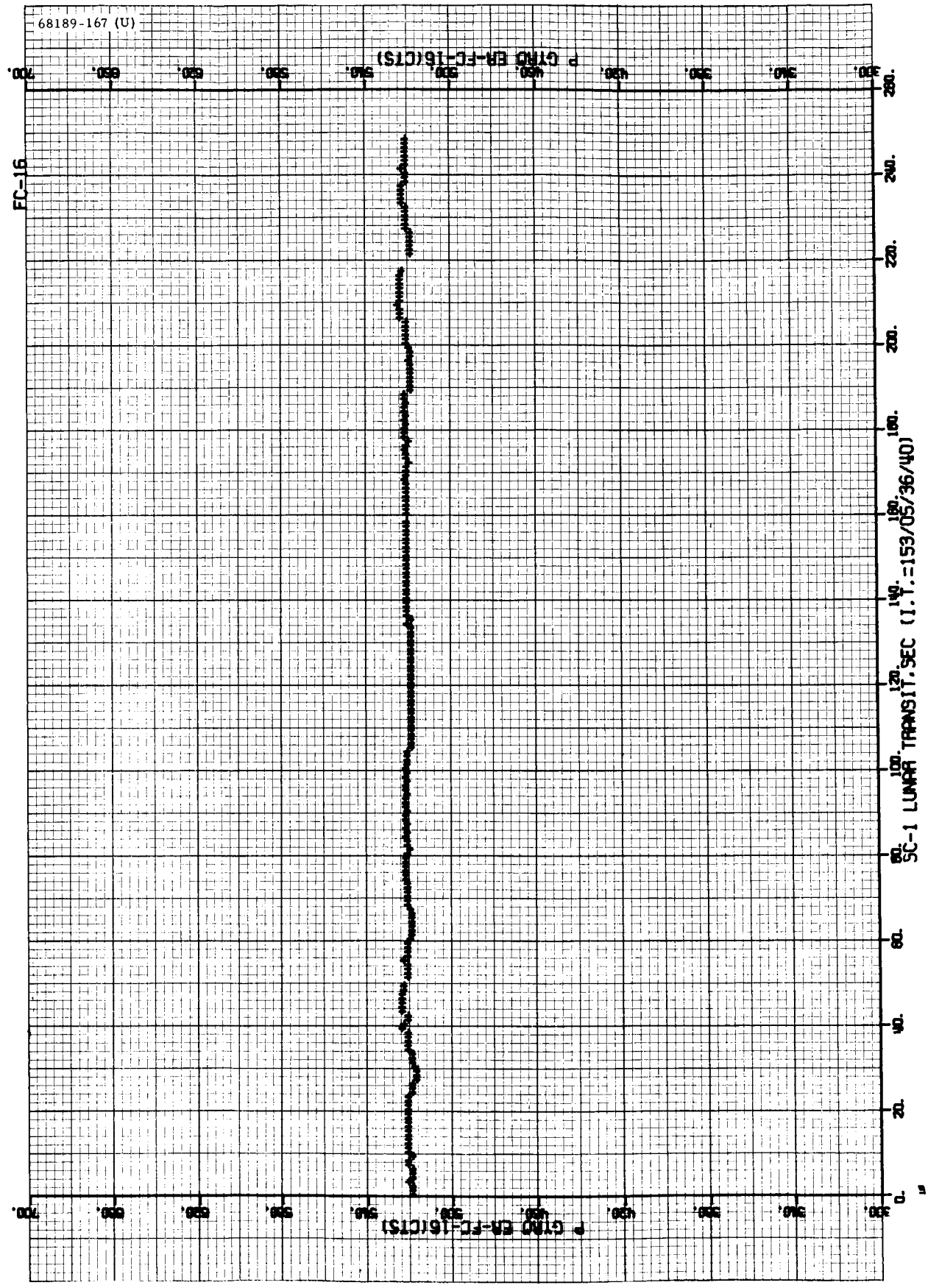


Figure 5.6-50. Pitch Gyro Error (First Roll)

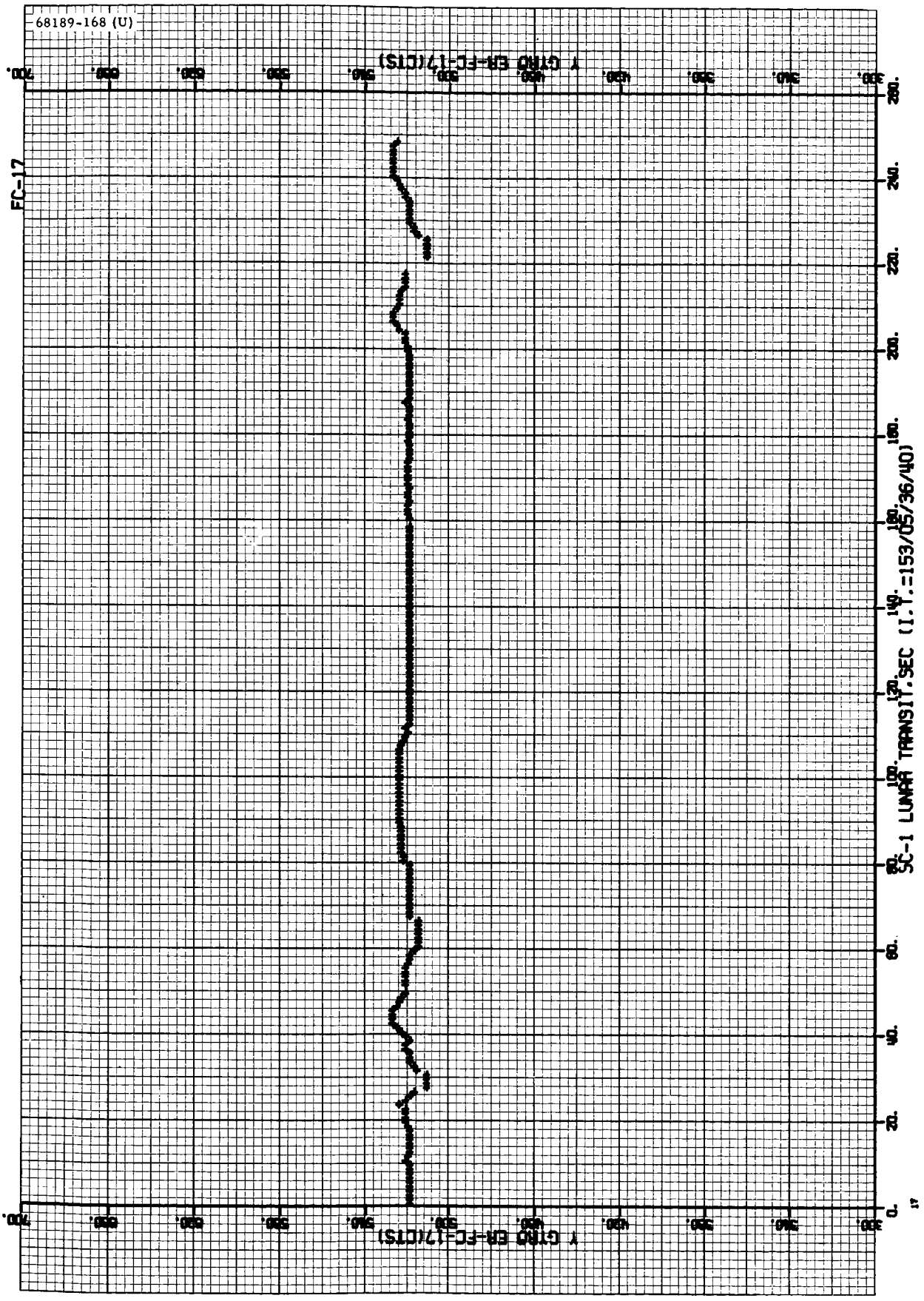


Figure 5.6-51. Yaw Gyro Error (First Roll)

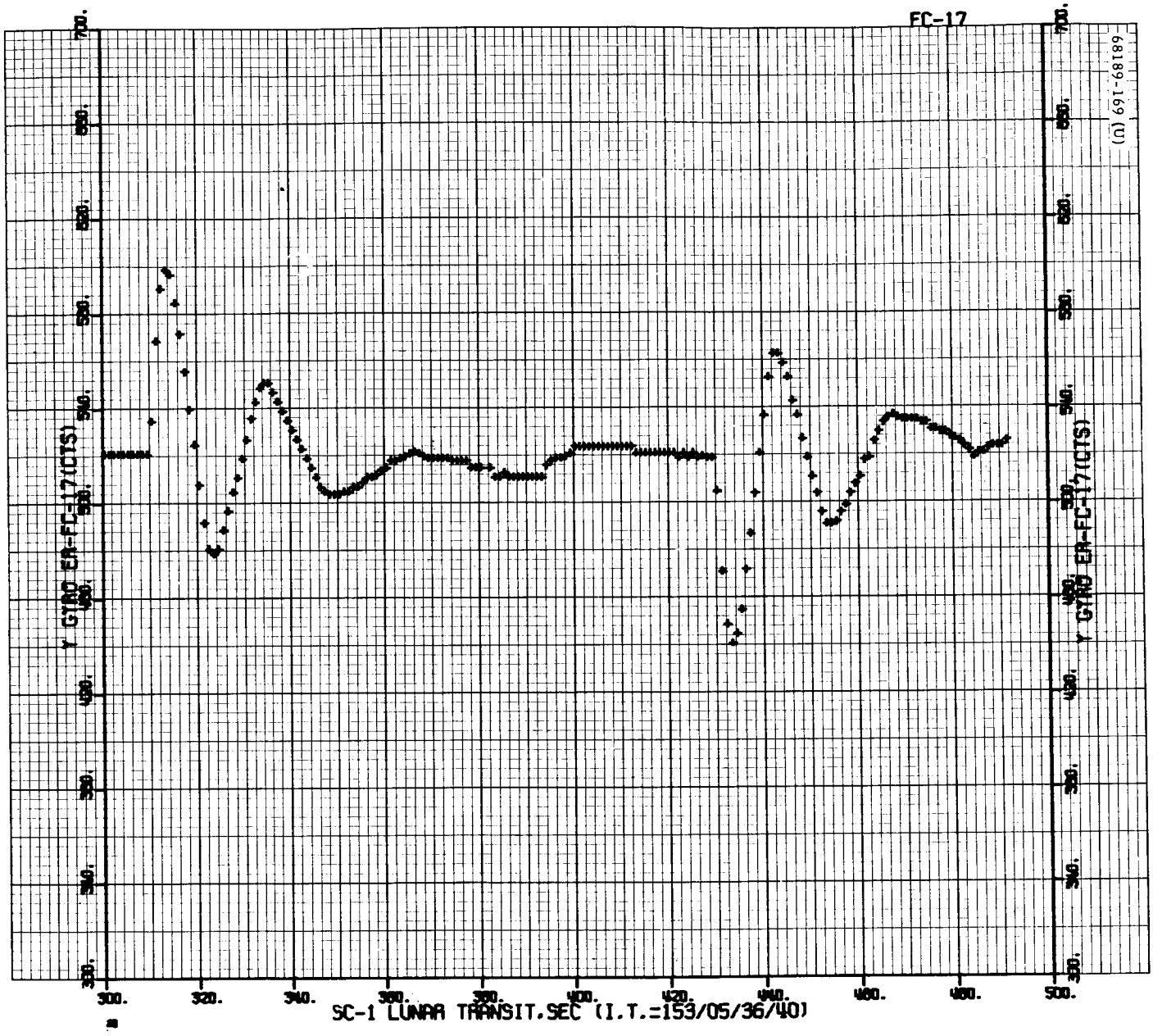


Figure 5.6-52. Yaw Gyro Error (Yaw Maneuver)

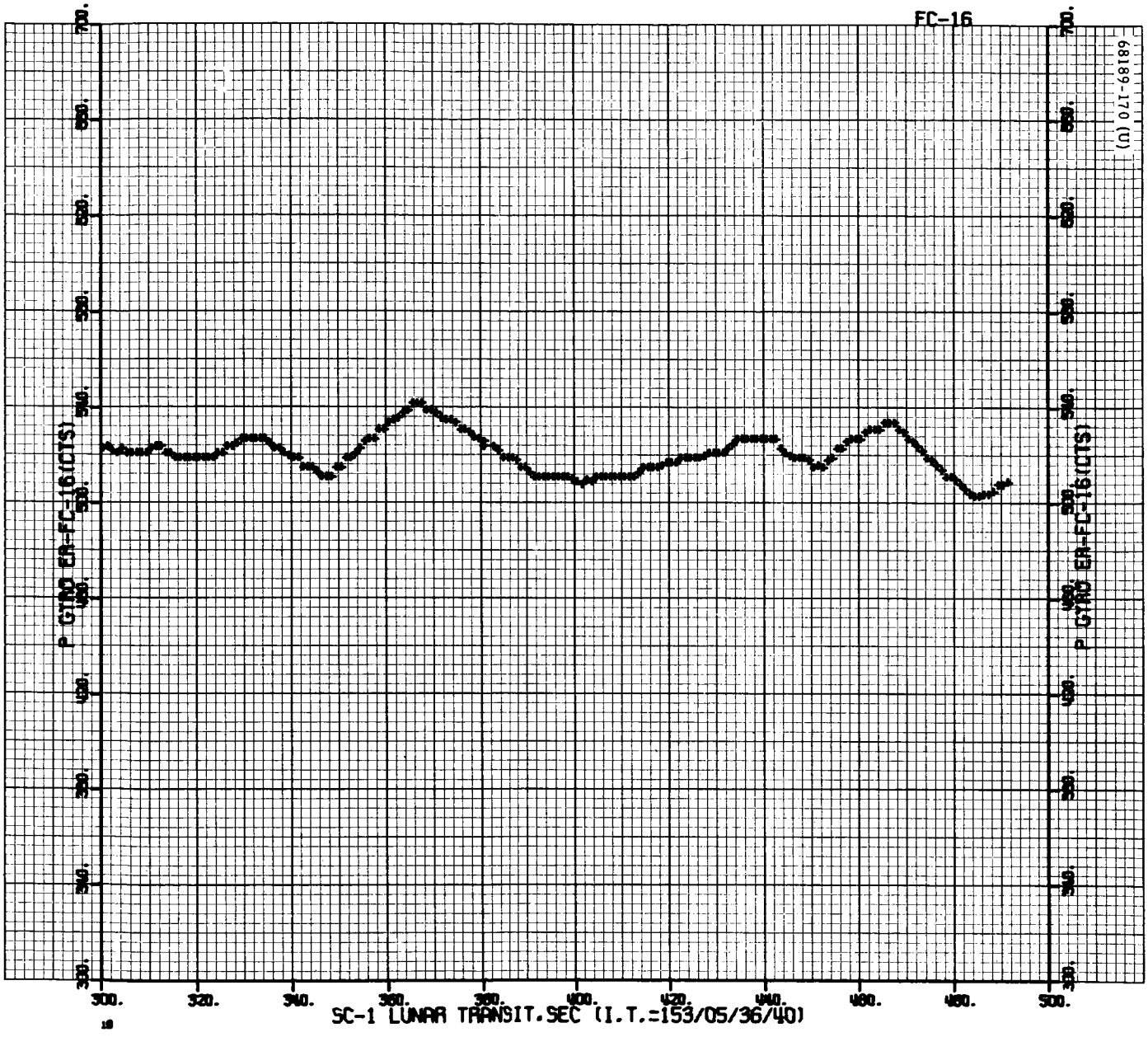


Figure 5.6-53. Pitch Gryo Error (Yaw Maneuver)

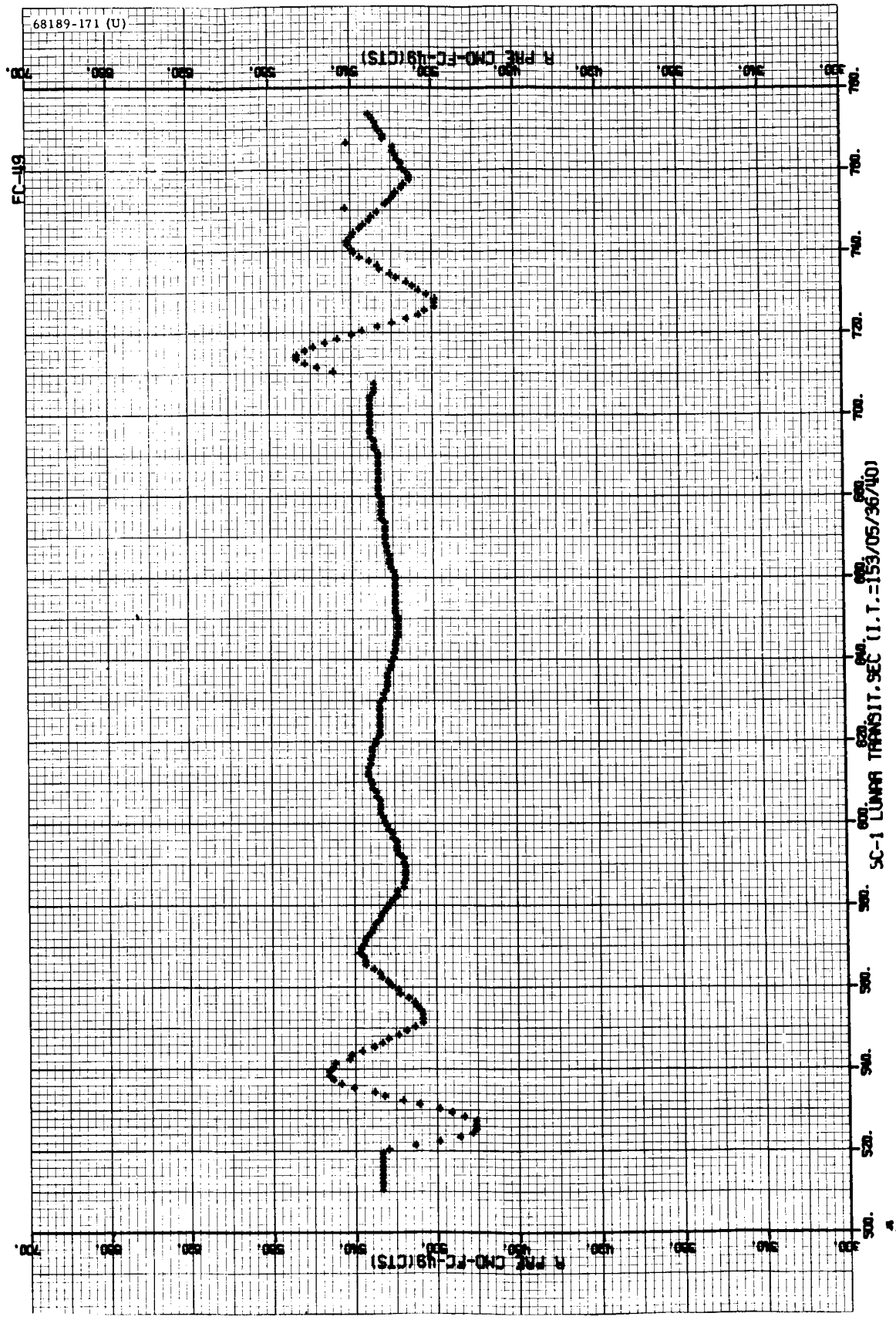


Figure 5.6-54. Roll Precession Command (Second Roll)

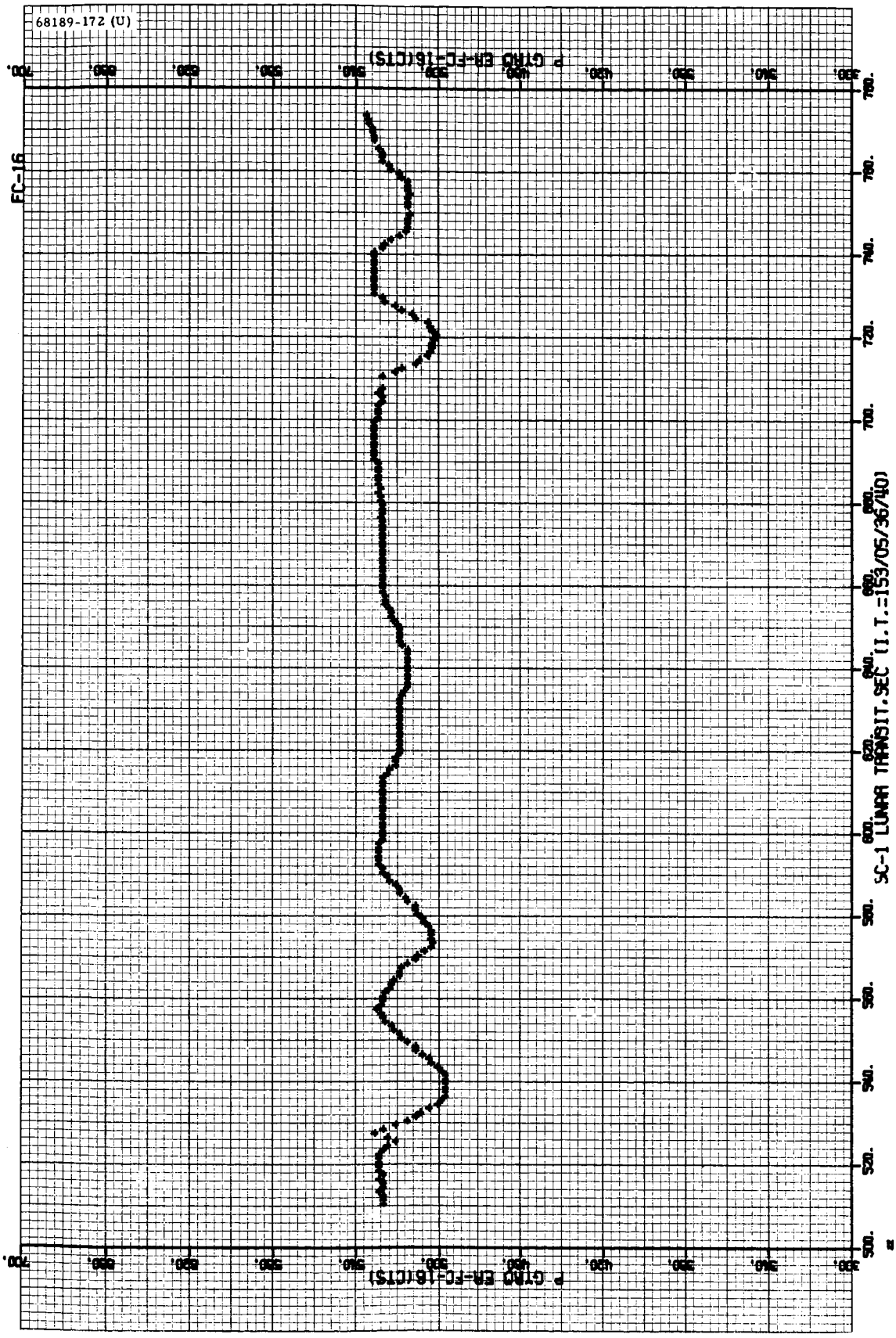


Figure 5.6-55. Pitch Gyro Error (Second Roll)

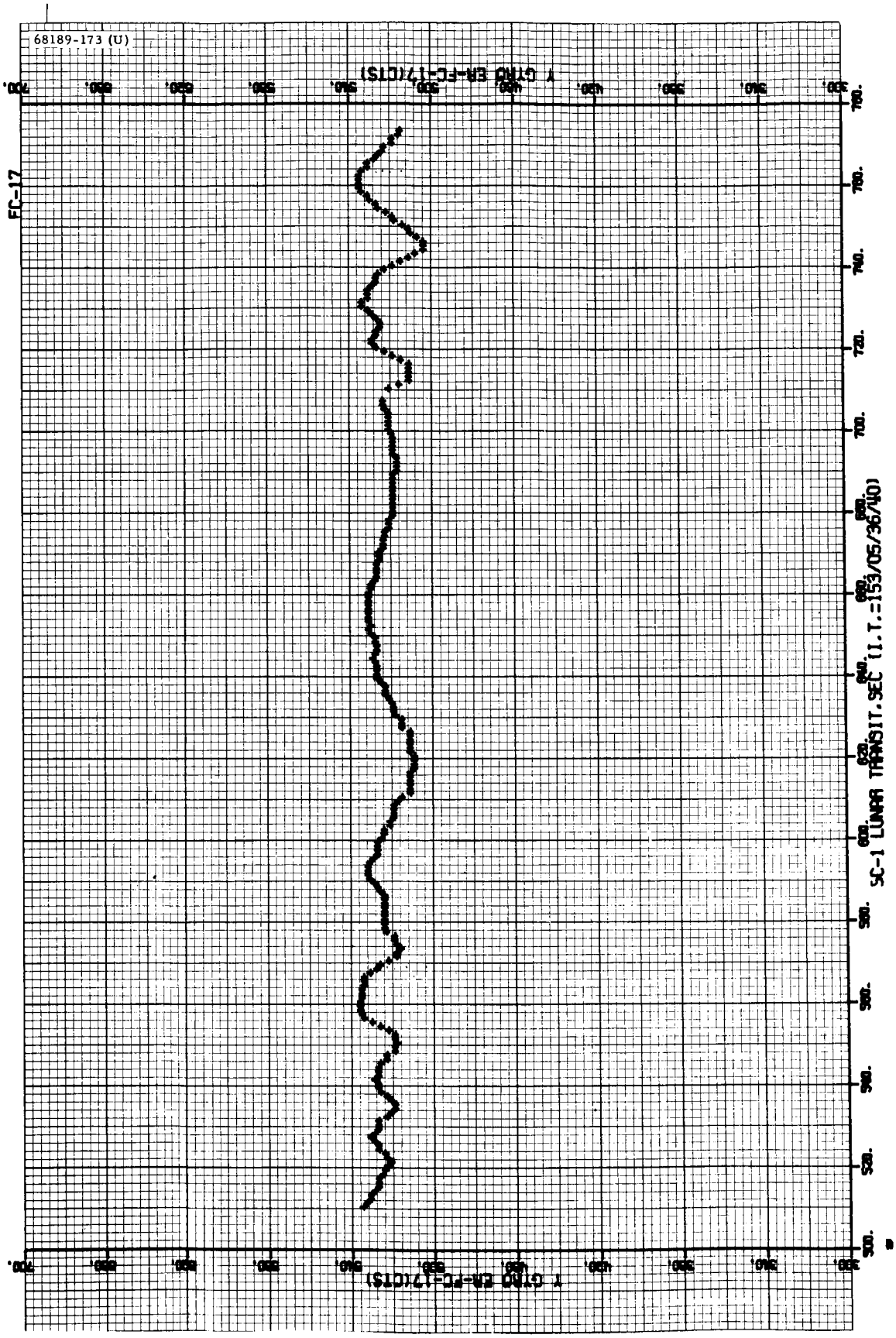


Figure 5.6-56. Yaw Gyro Error (Second Roll)

Preretro Pointing Error Determination. The method used for preretro pointing error determination is that developed in Reference 16.

1) An initial coordinate system is defined with unit vectors, $\hat{i}$, $\hat{j}$, and $\hat{k}$ being along the vehicle's roll, pitch, and yaw axes, respectively.

2) Assuming that the position of $\hat{i}$, $\hat{j}$, and $\hat{k}$ is known exactly (initially) and that the rotations φ_1, ψ, and φ_2 are performed without error, a matrix $[(A)]$ is developed which defines the relation between $(\hat{i}\ \hat{j}\ \hat{k})$ and the final coordinate system $(\hat{i}'\ \hat{j}'\ \hat{k}')$.

3) Initial position errors are represented by $\delta_{\hat{i}}$, $\delta_{\hat{j}}$, and $\delta_{\hat{k}}$ about the roll, pitch, and yaw axes. The effect of each one of these errors upon the final orientation of $\hat{i}'$ is determined from

$$\begin{bmatrix} \bar{\ell}'_{1,2,3} \\ \bar{m}'_{1,2,3} \\ \bar{n}'_{1,2,3} \end{bmatrix} = [A] \begin{bmatrix} \bar{\ell}_{1,2,3} \\ \bar{m}_{1,2,3} \\ \bar{n}_{1,2,3} \end{bmatrix} = [A]\,[B_{1,2,3}] \begin{bmatrix} \hat{i} \\ \hat{j} \\ \hat{k} \end{bmatrix}$$

where $[A]$ represents the ideal transformation and $[B_{1,2,3}]$ is the applicable small angle approximation to the matrix which represents the disturbing of

$$\begin{bmatrix} \hat{i} \\ \hat{j} \\ \hat{k} \end{bmatrix}$$

with an initial position error.

4) Now the actual errors are obtained by comparing $\bar{\ell}'_1$, $\bar{\ell}'_2$, and $\bar{\ell}'_3$ with $\hat{i}'$. The components of each error source are resolved into components along the $\hat{j}'$ and $\hat{k}'$ axes by taking the dot products of $\bar{\ell}'_1$, $\bar{\ell}'_2$, and $\bar{\ell}'_3$ with $\hat{j}'$ and $\hat{k}'$.

5) Errors in making rotations are represented by $\Delta\varphi_1$, $\Delta\psi$, and $\Delta\varphi_2$ for the three maneuvers of Mission A. The effect of each one of these errors upon the final orientation of $\hat{i}'$ is determined from

$$\bar{\ell}'_4 = \hat{i}' + \frac{\partial \hat{i}}{\partial \varphi_1}\,\Delta\varphi_1$$

and

$$\bar{\ell}_5 = \hat{i}' + \frac{\partial \hat{i}}{\partial \psi} \Delta\psi$$

Again, $\bar{\ell}_4'$ and $\bar{\ell}_5'$ are resolved into components along the $\hat{j}'$ and $\hat{k}'$ by taking the dot products $\bar{\ell}_4' \cdot \hat{j}'$, $\bar{\ell}_4' \cdot \hat{k}'$, $\bar{\ell}_5 \cdot \hat{j}'$, and $\bar{\ell}_5' \cdot \hat{k}$.

6) Now it is a matter of bookkeeping. All errors along the $\hat{j}'$ and $\hat{k}'$ are added and a resultant computed:

$$\begin{Bmatrix} \hat{i}' \\ \hat{j}' \\ \hat{k}' \end{Bmatrix} = [A] \begin{Bmatrix} \hat{i} \\ \hat{j} \\ \hat{k} \end{Bmatrix}$$

where

$$[A] = \begin{bmatrix} C\varphi_2 & S\varphi_2 & 0 \\ -S\varphi_2 & C\varphi_2 & 0 \\ 0 & 0 & 1 \end{bmatrix} \begin{bmatrix} C\psi & 0 & -S\psi \\ 0 & 1 & 0 \\ S\psi & 0 & C\psi \end{bmatrix} \begin{bmatrix} C\varphi_1 & C\varphi_1 & 0 \\ -S\varphi_1 & C\varphi_1 & 0 \\ 0 & 0 & 0 \end{bmatrix}$$

$$\begin{bmatrix} (C\varphi_2\, C\psi\, C\varphi_1 - S\varphi_1\, S\varphi_1) & (C\varphi_2\, C\psi S\varphi_1 + S\varphi_2\, C\varphi_1) & (-C\varphi_2\, S\psi) \\ (-S\varphi_2\, C\psi\, C\varphi_1 - C\varphi_2\, S\varphi_1) & (-S\varphi_2\, C\psi\, S\varphi_1 + C\varphi_2\, C\varphi_1) & (S\varphi_2\, S\psi) \\ (S\psi\, C\varphi_1) & (S\psi\, S\varphi_1) & (C\psi) \end{bmatrix}$$

$$\begin{Bmatrix} \bar{\ell}_i' \\ \bar{m}_i' \\ \bar{n}_i' \end{Bmatrix} = [A][B_1] \begin{Bmatrix} \hat{i} \\ \hat{j} \\ \hat{k} \end{Bmatrix} = [A] \begin{bmatrix} 1 & 0 & -\delta_{\hat{k}} \\ 0 & 1 & 0 \\ \delta_{\hat{k}} & 0 & 1 \end{bmatrix} \begin{Bmatrix} \hat{i} \\ \hat{j} \\ \hat{k} \end{Bmatrix}$$

where the small angle approximations $\sin \delta_{\hat{k}} \cong \delta_k$ and $\cos \delta_{\hat{k}} \cong 1$ have been made.

$$\bar{\ell}'_1 = \hat{i}[(c\varphi_2\ c\psi\ c\varphi_1 - s\varphi_2\ s\varphi_1) + (-c\varphi_2\ s\psi)\ (\delta_{\hat{k}})]$$
$$+ \hat{j}\ [(c\varphi_2\ c\psi\ s\varphi_1 + s\varphi_2\ c\varphi_1)]$$
$$+ \hat{k}\ [(c\varphi_2\ c\psi\ c\varphi_1 - s\varphi_2\ s\varphi_1)\ (-\delta_{\hat{k}}) - c\varphi_2\ s\psi]$$

$$\begin{Bmatrix} \bar{\ell}'_2 \\ \bar{m}'_2 \\ \bar{n}'_2 \end{Bmatrix} = [A] \begin{bmatrix} 1 & 0 & 0 \\ 0 & 1 & \delta_j \\ 0 & -\delta_j & 1 \end{bmatrix} \begin{Bmatrix} \hat{i} \\ \hat{j} \\ \hat{k} \end{Bmatrix}$$

$$\bar{\ell}'_2 = \hat{i}\ [(c\varphi_2\ c\psi\ c\varphi_1 - s\varphi_2\ s\varphi_1)]$$
$$+\hat{j}\ [(c\varphi_2\ c\psi\ s\varphi_1 + s\varphi_2\ c\varphi_1) + \delta_{\hat{j}}\ (c\varphi_2\ s\psi)]$$
$$+ \hat{k}\ [(c\varphi_2\ c\psi\ s\varphi_1 + s\varphi_2\ c\varphi_1)\ (\delta_{\hat{j}}) + (-c\varphi_2\ s\psi)]$$

$$\begin{Bmatrix} \bar{\ell}'_3 \\ \bar{m}'_3 \\ \bar{n}'_3 \end{Bmatrix} = [A] \begin{bmatrix} 1 & \delta_{\hat{i}} & 0 \\ -\delta_{\hat{i}} & 1 & 0 \\ 0 & 0 & 1 \end{bmatrix} \begin{Bmatrix} \hat{i} \\ \hat{j} \\ \hat{k} \end{Bmatrix}$$

$$\bar{\ell}'_3 = \hat{i}\ [(c\varphi_2\ c\psi\ c\varphi_1 - s\varphi_2\ s\varphi_1) + \delta_{\hat{i}}\ (-c\varphi_2\ c\psi\ s\varphi_1 - s\varphi_2\ c\varphi_1)]$$
$$+ \hat{j}\ [(c\varphi_2\ c\psi\ c\varphi_1 - s\varphi_2\ s\varphi_1)\ (\delta_{\hat{i}}) + (c\varphi_2\ c\psi\ s\varphi_1 + s\varphi_2\ c\varphi_1)]$$
$$+ \hat{k}\ [-c\varphi_2\ s\psi]$$

Recall from $[A]\,\hat{j}' = (-s\varphi_2\, c\psi\, c\varphi_1 - c\varphi_2\, s\varphi_1)(\hat{i})$

$$+ (-s\varphi_2\, c\psi\, s\varphi_1 + c\varphi_2\, c\varphi_1)(\hat{j})$$

$$+ (s\varphi_2\, s\psi)(\hat{k})$$

and

$$k' = (s\psi\, c\varphi_1)(\hat{i})$$

$$+ (s\psi\, s\varphi_1)(\hat{j})$$

$$+ (c\psi)(\hat{k})$$

Now, taking the dot products:

$$\bar{\iota}_1' \cdot \hat{j}' = [(c\varphi_2\, c\psi\, c\varphi_1 - s\varphi_2\, s\varphi_1) + (-c\varphi_2\, s\psi)(\delta_{\hat{k}})]\,[-s\varphi_2\, c\psi\, c\varphi_1 - c\varphi_2\, s\varphi_1]$$

$$+ [(c\varphi_2\, c\psi\, s\varphi_1 + s\varphi_2\, c\varphi_1)]\,[-s\varphi_2\, c\psi\, s\varphi_1 + c\varphi_2\, c\varphi_1]$$

$$+ [(-c\varphi_2\, c\psi\, c\varphi_1 + s\varphi_2\, s\varphi_1)(+\delta_{\hat{k}}) - c\varphi_2\, s\psi]\,[s\varphi_2\, s\psi]\,[s\varphi_2\, s\psi]$$

$$= s\psi\, s\varphi_1\, \hat{\delta}_k$$

$$\bar{\iota}_1' \cdot \hat{k}' = [(c\varphi_2\, c\psi\, c\varphi_1 - s\varphi_2\, s\varphi_1) + (-c\varphi_2\, s\psi)(\delta_{\hat{k}})]\,(s\psi\, c\varphi_1)$$

$$+ [c\varphi_2\, c\psi\, s\varphi_1 + s\varphi_2\, c\varphi_1]\,[s\psi\, s\varphi_1]$$

$$+ [(-c\varphi_2\, c\psi\, c\varphi_1 + s\varphi_2\, s\varphi_1)(\delta_{\hat{k}}) - c\varphi_2\, s\psi]\,[c\psi]$$

$$= \delta_{\hat{k}}\,[s\varphi_2\, s\varphi_1\, c\psi - c\varphi_2\, c\varphi_1]$$

$$\bar{\ell}_2' \cdot \hat{j} = [(c\varphi_2\, c\psi\, c\varphi_1 - s\varphi_2\, s\varphi_1)]\,[-s\varphi_2\, c\psi\, c\varphi_1 - c\varphi_2\, s\varphi_1]$$

$$+ [(c\varphi_2\, c\psi\, s\varphi_1 + s\varphi_2\, c\varphi_1) + \delta_{\hat{j}}\,(c\varphi_2\, s\psi)]\,[-s\varphi_2\, c\psi\, s\varphi_1 + c\varphi_2\, c\varphi_1]$$

$$+ [(c\varphi_2\, c\psi\, s\varphi_1 + s\varphi_2\, c\varphi_1)(\delta_{\hat{j}}) + (-c\varphi_2\, s\psi)]\,[(s\varphi_2\, s\psi)]\,[s\varphi_2\, s\psi]$$

$$= \delta_{\hat{j}}\,[s\psi\, c\varphi_1]$$

$$\bar{\ell}_2' \cdot \hat{k} = [(c\varphi_2\, c\psi c\varphi_1 - s\varphi_2\, s\varphi_1)]\,[s\psi\, c\varphi_1]$$

$$+ [(c\varphi_2\, c\psi\, s\varphi_1 + s\varphi_2\, c\varphi_1) + \delta_{\hat{j}}\,(c\varphi_2\, s\psi)]\,[s\psi\, s\varphi_1]$$

$$+ [(c\varphi_2\, c\psi\, s\varphi_1 + s\varphi_2\, c\varphi_1)\,(\delta_{\hat{j}}) + (-c\varphi_2\, s\psi)]\,[c\psi]$$

$$= \delta_{\hat{j}}\,[c\varphi_2\, s\varphi_1 + s\varphi_2\, c\varphi_1\, c\psi]$$

$$\bar{\ell}_3' \cdot \hat{j}' = [(c\varphi_2 c\psi\, c\varphi_1 - s\varphi_2\, s\varphi_1) + \delta_{\hat{i}}(-c\varphi_2\, c\psi\, s\psi_1 - s\varphi_2\, c\varphi_1)]\,[-s\varphi_2 c\psi c\varphi_1 - c\varphi_2 s\varphi_1]$$

$$+ [(c\varphi_2 c\psi\, c\varphi_1 - s\varphi_2\, s\varphi_1)(\delta_{\hat{i}}) + (c\varphi_2\, c\psi\, s\varphi_1 + s\varphi_2 c\varphi_1)]\,[-s\varphi_2 c\psi s\varphi_1 + c\varphi_2 d\varphi_1]$$

$$+ [-c\varphi_2\, s\psi]\,[s\varphi_2\, s\psi]$$

$$= \delta_{\hat{i}}\,(c\psi)$$

$$\bar{\ell}_3' \cdot \hat{k}' = [(c\varphi_2\, c\psi\, c\varphi_1 - s\varphi_2\, s\varphi) + \delta_{\hat{i}}\,(-c\varphi_2\, c\psi\, s\varphi_1 - s\varphi_2\, c\varphi_1)]\,[s\psi\, c\varphi_1]$$

$$+ [(c\varphi_2\, c\psi\, c\varphi_1 - s\varphi_2\, s\varphi_1)\,(\delta_{\hat{i}}) + (c\varphi_2\, c\psi\, s\varphi_1 + s\varphi_2\, c\varphi_1)]\,[s\psi\, s\varphi_1]$$

$$+ [\,c\varphi_2\, s\psi]\,[c\psi]$$

$$= \delta_{\hat{i}}\,[-s\varphi_2\, s\psi]$$

Considering the errors from incorrect rotations:

$$\bar{\ell}_4' = \hat{i}' + \frac{\partial \hat{i}}{\partial \varphi_1} \Delta\varphi_1$$

$$= \hat{i}' + \hat{i}\,[-c\varphi_2\, d\psi\, s\varphi_1 - s\varphi_2\, c\varphi_1]\,\Delta\varphi_1$$

$$+ \hat{j}\,[c\varphi_2\, c\psi\, c\varphi_1 - s\varphi_2\, s\varphi_1]\,\Delta\varphi_1$$

$$\bar{\ell}_5' = \hat{i}' + \frac{\partial \hat{i}}{\partial \psi}\Delta\psi$$

$$= \hat{i}' + \hat{i}\,[-c\varphi_2\, s\psi\, c\varphi]\,\Delta\psi$$

$$+ \hat{j}\,[-c\varphi_2\, s\psi\, s\varphi_1]\,\Delta\psi$$

$$+ \hat{k}\,[-c\varphi_2\, c\psi]\,\Delta\psi$$

$$\bar{\ell}_4' \cdot \bar{j}' = (c\varphi_2\, c\psi\, c\varphi_1 - s\varphi_2\, s\varphi_1)(-s\varphi_2\, c\psi\, c\varphi_1 - c\varphi_2\, s\varphi_1)$$

$$+ (c\varphi_2\, c\psi\, s\varphi_1 + s\varphi_2\, c\varphi_1)(-s\varphi_2\, c\psi\, s\varphi_1 + c\varphi_2\, c\varphi_1)$$

$$+ (-c\varphi_2\, s\psi)(s\varphi_2\, s\psi)$$

$$+ (-c\varphi_2\, c\psi\, s\varphi_1 - s\varphi_2\, c\varphi_1)(-s\varphi_2\, c\psi\, c\varphi_1 - c\varphi_2\, s\varphi_1)\,\Delta\varphi_1$$

$$+ (c\varphi_2\, c\psi\, c\varphi_1 - s\varphi_2\, s\varphi_1)(-s\varphi_2\, c\psi\, s\varphi_1 + c\varphi_2\, c\varphi_1)\,\Delta\varphi_1$$

$$= c\psi\,\Delta\varphi_1$$

$$\underline{\underline{\bar{\ell}_4' \cdot \bar{k}'}} = (c\varphi_2\ c\psi\ c\varphi_1 - s\varphi_2\ s\varphi_1\ (s\psi\ c\varphi_1)$$

$$+ (c\varphi_2\ c\psi\ s\varphi_1 + s\varphi_2\ c\varphi_1)\ (s\psi\ s\varphi_1)$$

$$+ (-c\varphi_2\ s\psi)\ (c\psi)$$

$$+ (-c\varphi_2\ c\psi\ s\varphi_1 - s\varphi_2\ c\varphi_1)\ (s\psi\ c\varphi_1)\ \Delta\varphi_1$$

$$+ (c\varphi_2\ c\psi\ c\varphi_1 - s\varphi_2\ s\varphi_1)\ (s\psi\ s\varphi_1)\ \Delta\varphi_1$$

$$= \Delta\varphi_1\ (s\varphi_2\ s\psi)$$

$$\underline{\underline{\bar{\ell}_5' \cdot \bar{j}'}} = (-c\varphi_2\ s\psi\ c\varphi_1)\ (-s\varphi_2\ c\psi\ c\varphi_1 - c\varphi_2\ s\varphi_1)\ \Delta\psi$$

$$+ (-c\varphi_2\ s\psi\ s\varphi_1)\ (-s\varphi_2\ c\psi\ s\varphi_1 + c\varphi_2\ c\varphi_1)\ \Delta\psi$$

$$+ (-c\varphi_2\ c\psi)\ (s\varphi_2\ s\psi)\ \Delta\psi$$

$$= 0$$

$$\underline{\underline{\bar{\ell}_5' \cdot k'}} = (-c\varphi_2\ s\psi\ c\varphi_1)\ (s\psi\ c\varphi_1)\ \Delta\psi$$

$$+ (-c\varphi_2\ s\psi\ s\varphi_1)\ (s\psi\ s\varphi_1)\ \Delta\psi$$

$$+ (-c\varphi_2\ s\psi)\ (c\psi)\ \Delta\psi$$

$$= \Delta\psi\ (-c\varphi_2)$$

So the error tabulation is:

Error Source	Error Component Along $\hat{j}'$	Error Component Along $\hat{k}'$
$\delta_{\hat{k}}$	$s\psi\ s\varphi_1\ \delta_{\hat{k}}$	$(s\varphi_2\ s\varphi_1\ c\psi - c\varphi_2\ c\varphi_1)\ \delta_{\hat{k}}$
$\delta_{\hat{j}}$	$s\psi\ c\varphi_1\ \delta_{\hat{j}}$	$(c\varphi_2\ s\varphi_1 + s\varphi_2\ c\varphi_1\ c\psi)\ \delta_{\hat{j}}$
$\delta_{\hat{i}}$	$c\psi\ \delta_{\hat{i}}$	$-s\varphi_2\ s\psi\ \delta_{\hat{i}}$
$\Delta\varphi_1$	$c\psi\ \Delta\varphi_1$	$-s\varphi_2\ s\psi\ \Delta\varphi_1$
$\Delta\psi$	0	$-c\varphi_2\ \Delta\psi$

For $\varphi_1 = 89.3$ degrees, $\psi = 59.9$ degrees, and $\varphi_2 = 94.1$ degrees, the above table reduces to the following:

Error Source	Error Component Along j'	Error Component Along k'
$\delta_{\hat{k}}$	$0.866\ \delta_{\hat{k}}$	$0.502\ \delta_{\hat{k}}$
$\delta_{\hat{j}}$	$0.010\ \delta_{\hat{j}}$	$0.429\ \delta_{\hat{j}}$
$\delta_{\hat{i}}$	$0.500\ \delta_{\hat{i}}$	$-0.865\ \delta_{\hat{i}}$
$\Delta\varphi_1$	$0.500\ \Delta\varphi_1$	$-0.865\ \Delta\varphi_1$
$\Delta\psi$	0	$0.070\ \Delta\psi$

Using the measured values for $\delta_{\hat{k}}$, $\delta_{\hat{j}}$, $\delta_{\hat{i}}$, $\Delta\varphi$, and $\Delta\psi$ results in the following:

1) The net error along $\hat{j}'$ = 0.026 degree

2) The net error along $\hat{k}'$ = -0.336 degree

The resultant pointing error is $\cong$0.34 degree in the direction of the minus yaw axis.

The pointing error as determined from main retro burnout conditions was 0.26 degree in the direction of the plus pitch axis.

The above two calculations do not corroborate each other. However, it is noted that some large error contributors not included in the calculation must indeed affect the resultant pointing error. These error sources are as follows:

1) Alignment of main retro thrust axis with respect to sensor group roll axis: 0.40 degree

2) Tracking error: 0.30 degree

3) Control system stiffness: 0.20 degree

It is felt that the combination of the above three errors could well have dominated the final pointing error at burnout.

Note that at the time of main retro ignition and throughout main retro burning, the actual main retro thrust axis is required to be aligned to the actual initial velocity vector plus offset (if applicable) within ±1 degree (Reference 17, Paragraph 3.9.3.2).

The preretro maneuvers were nominal.

5.6.7.10 Main Retro Phase

Main retro phase began at 153:06:14:39.958 GMT with the indication of AMR mark and successfully ended at 06:15:39.943 of the same day with the acknowledgement of retro eject. The approach velocity at the time of ignition was approximately 8565 ft/sec, and the altitude was 246,636 feet. At main retro burnout, the velocity was reduced to approximately 431 ft/sec with a slant range of 27,851 feet. The predicted values for burnout conditions were 393 ft/sec at an altitude of 28,571 feet.

During this phase, the functions of the flight control system were to maintain the attitude of the spacecraft inertially fixed and to provide and execute a fixed sequence of commands to accomplish vernier descent phase conditions. The following analysis reveals that these two functions were performed to the utmost expectations.

A list of retro phase events and their corresponding time of occurrence is given in Table 5.6-18 along with expected time intervals. These results confirm the performance of the magnitude register and programmer.

The following data confirms that AMR mark occurred prior to emergency AMR:

	Spacecraft Time
AMR mark (FC-64)	06:14:38.513
Emergency AMR	06:14:39.420

The data for emergency AMR was obtained from Reference 5.

TABLE 5.6-18. TIME AND EVENTS LOG

Retro Phase

Main Retro Phase Event	Time of Occurrence, GMT, Day 153	Time Between Events, seconds	Expected Time Intervals, seconds
Altitude marking radar signal (FC-64)	06:14:39.958		
Vernier ignition (FC-28)	06:14:47.518	7.560	0 to 20
Retro ignition (FC-29)	06:14:48.618	1.100	1.1
Retro burnout (FC-30)	06:15:27.943	39.325	≈40
Retro eject (FC-31)	06:15:39.943	12.000	12.0
Start RADVS controlled descent (FC-42)	06:15:42.093	2.150	2.15

Terminal Descent Phase Ignition and Shutdown Characteristics

Both ignition and shutdown of the vernier engines during the terminal landing phase were executed smoothly, with impulse dispersions between engines well within the respective specification values. The startup and shutdown impulse dispersions (measured from average impulse of the three engines) of each engine are listed in Table 5.6-19. These values were computed from pitch and yaw gyro error telemetry data according to the procedure outlined in "Engine Ignition Characteristics." Specification requirements from Reference 8 are also listed for comparison.

TABLE 5.6-19. TERMINAL DESCENT PHASE IMPULSE DISPERSIONS

Impulse Dispersions in lb-sec

Leg	Startup		Shutdown	
	SC-1	Requirement*	SC-1	Requirement
1	-0.02		·0.19	
2	0.22	< ±10	-0.26	<±0.32
3	-0.02		0.07	

*Assuming a startup time of < 150 m/sec.

Owing to the low telemetry sampling rate (2 samples/sec) of gyro error signals and the low absolute magnitudes of the errors encountered on SC-1, accuracy of the impulse dispersion figures listed in Table 5.6-19 is of the order of 50 percent. Therefore, the results are valid only insofar as giving gross indication that impulse dispersions were small and within requirements.

Retro Phase Attitude Control

During the main retro phase, extending from vernier ignition through case separation, spacecraft attitude motion was small in all three axes. Peak pitch and yaw inertial attitude motion, as read directly from gyro error telemetry data (FC-16 and FC-17), occurred at vernier ignition and amounted to -0.89 degree in yaw and -0.13 degree in pitch. (See figures in "Raw Plots.") Following ignition, static attitude error was virtually zero in both pitch and yaw axes. Roll inertial attitude error was maintained less than 0.50 degree throughout the main retro phase (less than 1.0 degree is required).

Since all gyro error signals were maintained within ±1.0 degree (during retro burn), each gyro was exercised less than 10 percent of the available travel range of more than ±10 degrees. A summary of pitch and yaw inertial attitude angles produced at various points in the retro phase is given in Table 5.6-20. No attitude disturbance was noted at retro eject, indicating a perfectly clean case separation.

Pitch and yaw control moments generated by the vernier engines were estimated by means of the following equations:

$$L_x = -2.969\ T_1 + 0.5723\ T_2 + 2.397\ T_3$$

$$L_y = -1.053\ T_1 + 3.098\ T_2 - 2.045\ T_3$$

TABLE 5.6-20. RETRO PHASE ATTITUDE CONTROL SUMMARY

Peak Attitude Motion, degrees

Event	Pitch	Yaw
Vernier ignition	-0.13	-0.89
Retro ignition	0.08	0.03
Retro burnout	0.05	0.09
Retro eject	0	0

where L_x and L_y are pitch and yaw control torques (ft-lb), respectively, and T_1, T_2, and T_3 are thrusts (pounds) generated by engines 1, 2, and 3, respectively. Values for T_1, T_2, and T_3 were estimated from the thrust command telemetry signals (FC-25, FC-26, and FC-27) (Figure 5.6-57). As indicated by the telemetry data, e.g., Figure 5.6-87, very little throttling of the engines occurred during the retro period. Shortly after retro ignition, differential throttling equivalent to approximately 14 ft-lb of control torque was produced. And, at about 8 seconds prior to 3.5 g burnout occurrence, approximately 10 ft-lb of torque was produced. At all other times during the retro burn period, there was essentially no differential engine throttling.

The maximum thrust-vector to center of gravity offset can be estimated from the maximum control torque magnitude of 14 ft-lb. Assuming a 9000-pound retro thrust, the offset is estimated as

$$\text{Maximum center of gravity offset} = \frac{14 \text{ ft-lb}}{9000 \text{ pounds}} \times \frac{12 \text{ inch}}{\text{feet}}$$

$$= 0.019 \text{ inch}$$

This is an order of magnitude less than the required value of 0.18 inch (Reference 17).

The maximum attitude error produced by the retro disturbance torques is also determined from the maximum torque magnitude of 14 ft-lb. Since the static gain (stiffness) of the pitch and yaw attitude control loops is

$$\text{static gain} = 1200 \text{ ft-lb/deg}$$

the maximum static attitude error is estimated to be

$$\text{maximum static error} = \frac{14}{1200} = 0.012 \text{ degree}$$

which is an order of magnitude less than the allowable value of 0.12 degree.

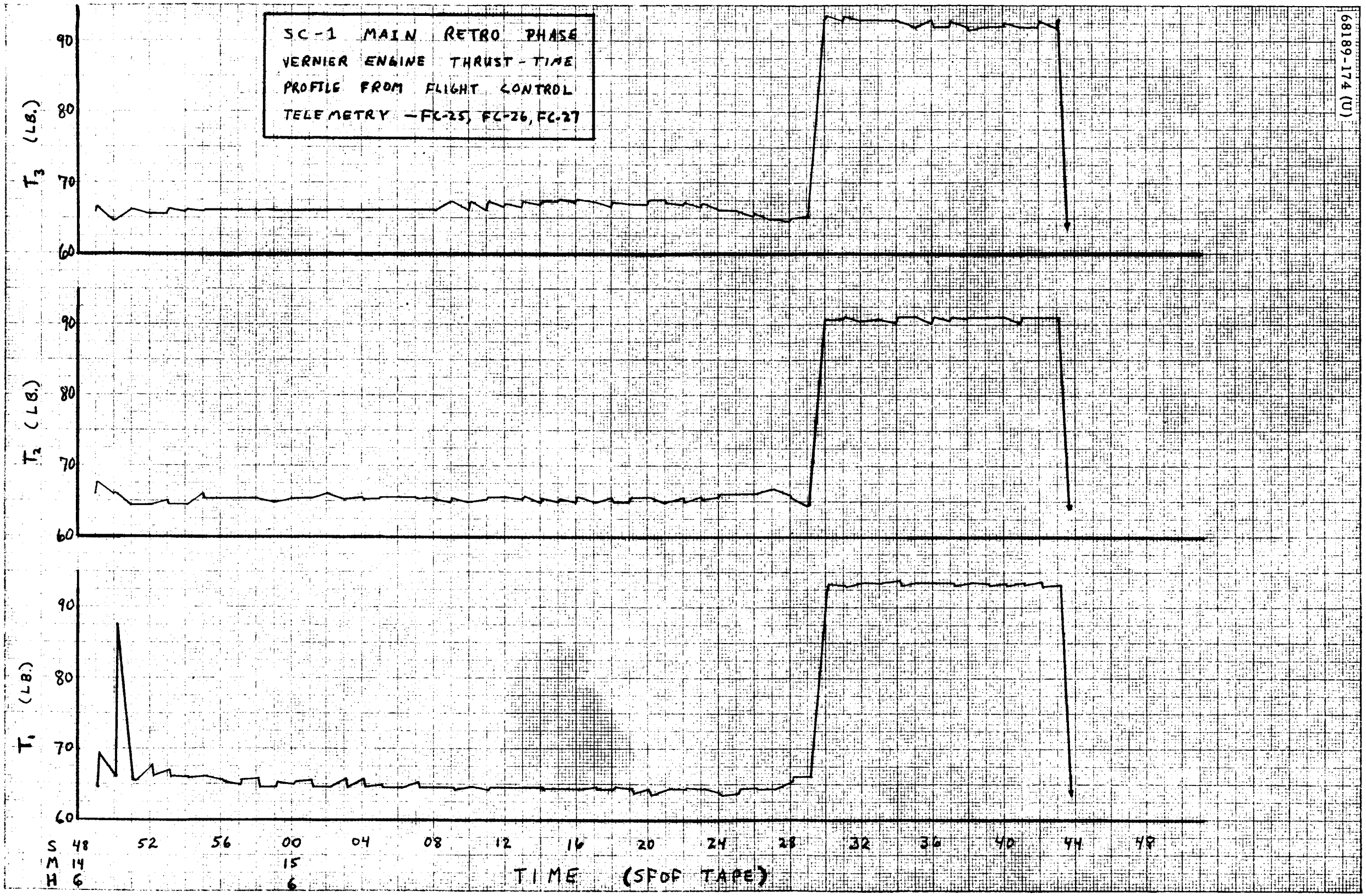


Figure 5.6-57. Main Retro Phase Vernier Engine Thrust-Time Profile From Flight Control Telemetry for FC-25, FC-26, and FC-27

FOLDOUT FRAME

FOLDOUT FRAME

Main Retro Phase Vernier Engine Parameters

Using the telemetry of the differential current that actuates the throttle valve of the vernier propulsion system TCA, the commanded thrust to each vernier engine was determined for the main retro phase. As was done for the midcourse phase, the telemetered throttle valve commands (FC-25, FC-26, and FC-27) were corrected and converted to thrust levels on each engine for the period of main retro burn and the time from retro burnout (3.5 g) to retro separation. From these thrust levels, the pitch and yaw moment disturbances that the vernier propulsion system was controlling were computed.

Thrust Levels. The same correction procedure for converting the telemetry data from BCD counts to milliamperes of commanded differential current employed for midcourse was used for the main retro phase. This conversion method (Reference 14) requires a time period when a known value of differential current, ΔI, is being commanded such as "thrust phase power on" immediately before and after the time interval of concern. For midcourse, this known commanded level both before and after the thrust period is available. However, for the main retro phase, there is only the period prior to vernier engine ignition which can be used for calibration. This phase is broken into a nominal thrust level period and a high thrust interval which presents further difficulties. The known commanded current level before ignition can be used to correct the nominal current commands to within ±2 milliamperes, as was done for midcourse. However, telemetered high thrust throttle valve commands will not be as accurate since there is no recalibration period available. Using the same initial calibration of a known value of ΔI for the high thrust portion of this phase reduces the accuracy at any specific magnitude of command current to approximately ±3 milliamperes.

FAT data was used to establish the expected resultant thrust level for a given value of ΔI. For the nominal thrust period (during main retro burn), calibration curves generated from FAT data points were taken at around -40 and 0 milliamperes. The slope of the thrust versus ΔI curve for the region of nominal thrust or zero differential current was taken as that between these two points. The errors in the absolute magnitudes of the thrust levels due to this ΔI-to-pounds of thrust conversion for the nominal thrust period are ±0.5 pound. However, conversion of the high thrust commands (between 45 and 55 milliamperes) was not so accurate. There were no data points taken in the FAT for this region, and hysteresis ramps had to be employed to estimate the slope of the ΔI versus thrust curves. The slope, thus determined, was assumed to be linear from the known data point at around 0 milliampere. This was a very weak approximation, and the conversion of high thrust telemetered commands is accurate to only ±2 pounds.

The retro phase thrust versus time profiles for each vernier engine, determined as described above, are shown in Figure 5.6-57. In the nominal thrust period (from ignition to retro burnout), the accuracy of any thrust magnitude is of the order of ±1 pound. For the high thrust period (from retro burnout to 2 seconds after retro separation), the specific values of

thrust shown are only accurate to roughly ±2.5 pounds. From these individual thrust profiles, the initial transients from engine startup settle to steady state values within 4 seconds after vernier ignition.

During initial transients (nominal commanded thrust):

Maximum thrust on engine 1 = 87.5 pounds

Maximum thrust on engine 2 = 67.5 pounds

Maximum thrust on engine 3 = 66.6 pounds

After initial transients (nominal commanded thrust):

Maximum thrust on engine 1 = 66.1 pounds

Maximum thrust on engine 2 = 66.7 pounds

Maximum thrust on engine 3 = 67.6 pounds

Minimum thrust on engine 1 = 63.5 pounds

Minimum thrust on engine 2 = 64.4 pounds

Minimum thrust on engine 3 = 64.6 pounds

During high commanded thrust:

Maximum thrust on engine 1 = 93.6 pounds

Maximum thrust on engine 2 = 91.1 pounds

Maximum thrust on engine 3 = 93.5 pounds

Minimum thrust on engine 1 = 93.0 pounds

Minimum thrust on engine 2 = 90.3 pounds

Minimum thrust on engine 3 = 91.8 pounds

During the period of nominal commanded thrust on the vernier engines or while the retro is firing, the commanded thrust on engine 3 is expected to be higher than that on the other engines due to predicted spacecraft center of gravity and measured retro nozzle centerline (assumed to coincide with the retro thrust vector) locations. Also, the thrust commands to TCA 2 are expected to be somewhat higher than those to vernier engine 1 due to the predicted center of gravity to centerline offset. From the telemetry data, these expectations are confirmed as, in general, during the period of retro burning: $T_3 > T_2 > T_1$.

After retro burnout and before retro separation, the vernier propulsion system is commanded to high thrust, and the retro thrust is comparably small. During this time, the thrust on TCA 1 is expected to be higher than T_2 or T_3 as it is the roll control gimbaled engine. Also, due to the expected location of the center of gravity, the commanded thrust on engine 3 is expected to be higher than on TCA 2. For the time interval between the retro burnout signal and retro separation, these predictions from preflight measurements are in agreement with the thrust command data as: $T_1 > T_3 > T_2$.

The total commanded thrust of the vernier propulsion system during the main retro phase was computed from the sum of the telemetered individual thrust levels when each was sampled during a time interval of less than 0.05 second. The word placement of these telemetry channels in mode 2 was again a problem as only one data point per second of total thrust was usable. The individual channels were all interrogated within a 0.05-second interval at 0.1 second from the start of the frame (FC-25 — word 9, FC-26 — word 12, and FC-27 — word 8), and it was these signals that were used to determine the total commanded thrust versus time profile. It was felt that comparison of thrust commands over a larger time interval than 0.05 second would not be valid. Therefore, for this determination the other telemetry words could not be employed with any confidence. This method omitted the sudden jump of T_1 discussed above. The total thrust profile, as determined in this manner, is shown in Figure 5.6-58. For the main retro phase, the total commanded thrust is expected to be constant (for each level). The telemetry data indicates a total thrust that is constant with a band of 3.2 pounds for the nominal thrust region and of 1.3 pounds for the high thrust period. As the worst case accuracies of these total commanded thrust values are of the order of ±3 pounds for the nominal thrust commands and ±7.5 pounds for the high commanded level, it is seen that the telemetry does reflect constant total commanded thrust.

Moment Disturbances. The pitch and yaw moment disturbances for which the vernier propulsion system was correcting were determined from the geometry of the system and the individual commanded thrust levels — T_1, T_2, and T_3 — of the vernier engines. The equations for the moments

about any point in the spacecraft center of gravity plane (X_o, Y_o) were previously developed in the analysis of midcourse vernier engine parameters, using the measured radial moment arms of the SC-1 engines. From these equations and the telemetered values of commanded thrust for a specific time, the pitch, yaw, and total X-Y plane moments were computed about the spacecraft coordinate axes and about the predicted spacecraft center of gravity at retro ignition. The same sets of telemetry data for T_1, T_2, and T_3 were used for determining the moment disturbances for a given time as was employed for finding the total commanded thrust.

The moment disturbances taken about the spacecraft pitch-yaw axes are shown in Figure 5.6-59. For the period of time between the retro burnout signal and retro separation when the vernier engines are commanded to high thrust levels, this plot could be used for determination of the center of gravity offset from the coordinate origin, assuming the retro thrust is negligible compared to the combined vernier engine thrust. However, the inaccuracy of the corrected values of commanded thrust preclude such a determination. The accuracy of the computed moments during this period of high commanded thrust is no better than ±100 in.-lb. Since the observed values of moment disturbance are less than the inaccuracy (which was expected from preflight prediction of the center of gravity location), no further analysis of this time period was attempted.

For the period from retro ignition to the 3.5 g burnout signal, the moment disturbances computed from the telemetered thrust commands are considered to be accurate to within ±40 in.-lb. Examination of the moments about the spacecraft origin for this nominal commanded thrust period is quite difficult as they are due to the center of gravity offset from the coordinate origin, the excursions of the center of gravity from the predicted location, and the offset of the retro thrust vector from the combined center of gravity. In an attempt to separate these effects, the moments were taken about the predicted spacecraft center of gravity at retro ignition. The values computed for the center of gravity location using telemetry values of vernier propellant and nitrogen expended, the measured spacecraft center of gravity at injection, and the two cases of omnidirectional antenna A stowed or extended are shown in Table 5.6-21.

The moment disturbances which the vernier engines are balancing, when taken about the predicted spacecraft center of gravity locations at retro ignition, are shown, for the omnidirectional antenna A stowed case and for the omnidirectional antenna A extended case, in Figure 5.6-60. These plots are most meaningful for the period from retro ignition to retro burnout. The contributors to moment unbalance are the thrust vector to center of gravity offset and the movement of the center of gravity due to vernier and retro propellant usage. As stated above, for this time interval of nominal vernier engine thrusts, the moments computed from the telemetry of differential commanded current are accurate to within ±40 in.-lb.

Comparison of the two cases of moments about the center of gravity locations for omnidirectional antenna A stowed or extended shows them to be very similar. The measured retro nozzle centerline location for SC-1

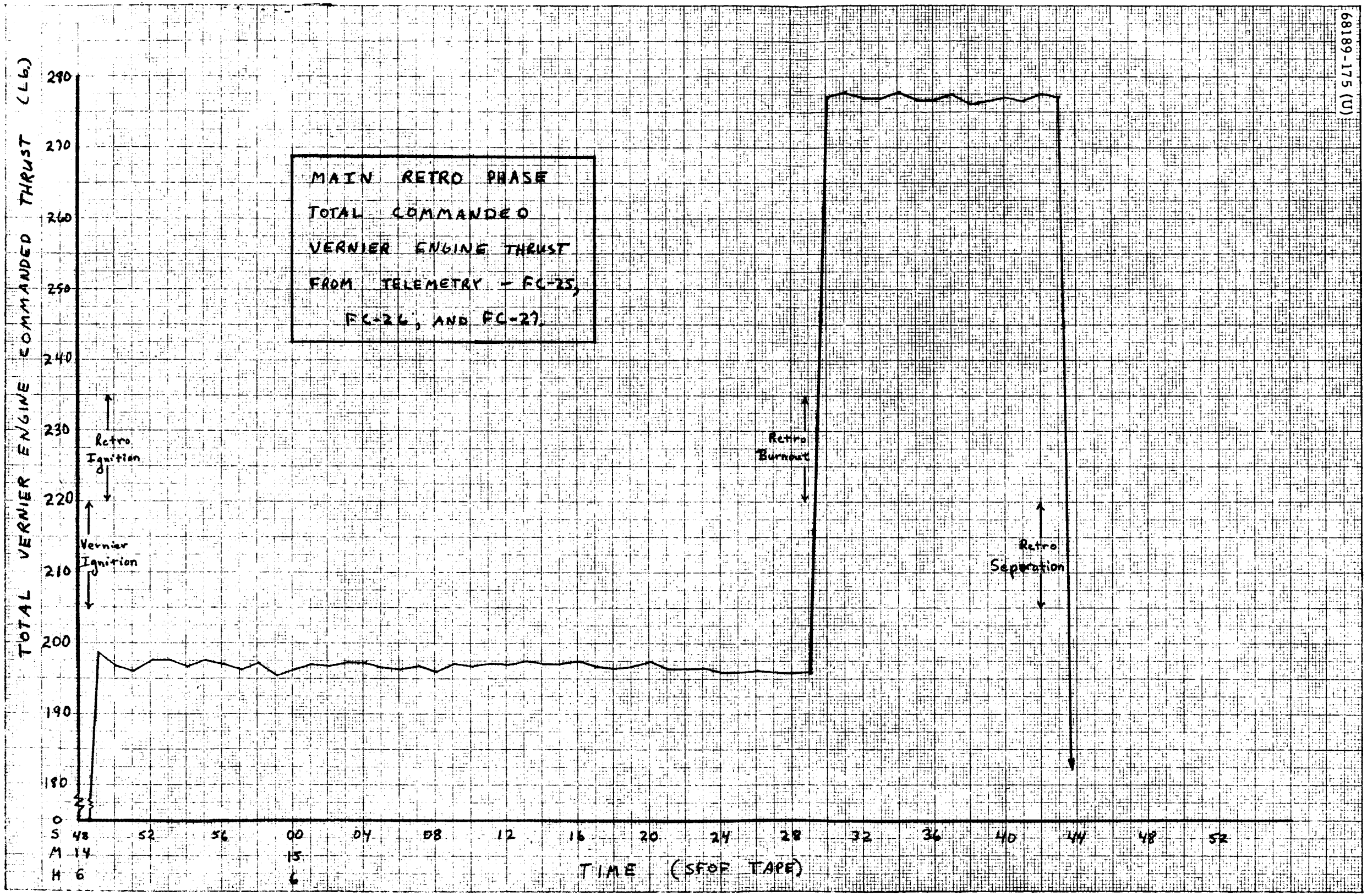


Figure 5.6-58. Main Retro Phase Total Commanded Vernier Engine Thrust From Telemetry for FC-25, FC-26, and FC-27

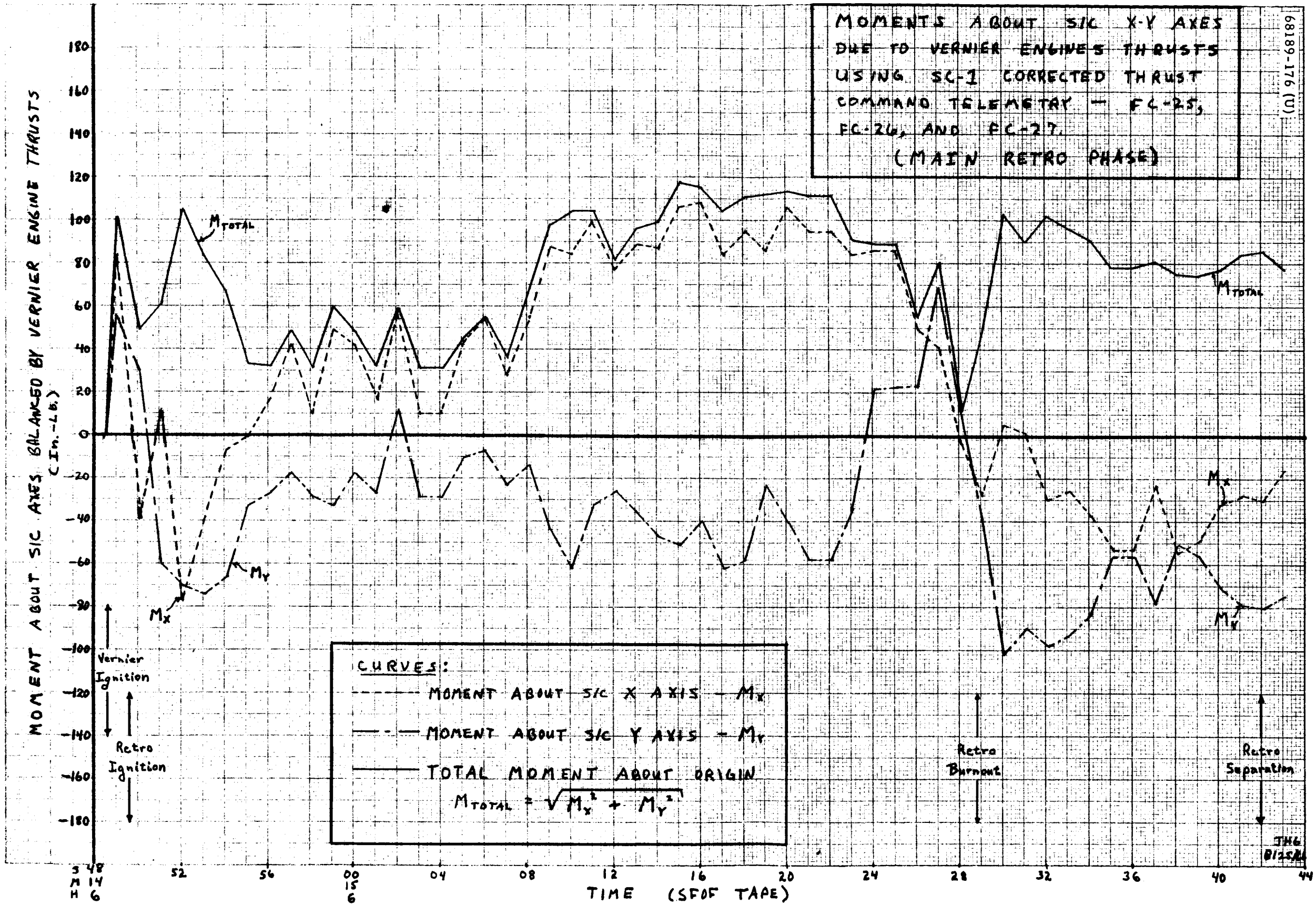


Figure 5.6-59. Moments About Spacecraft X-Y Axes Due to Vernier Engine Thrusts Using SC-1 Corrected Thrust Command Telemetry for FC-25, FC-26, and FC-27

Main retro phase

FOLDOUT FRAME

FOLDOUT FRAME

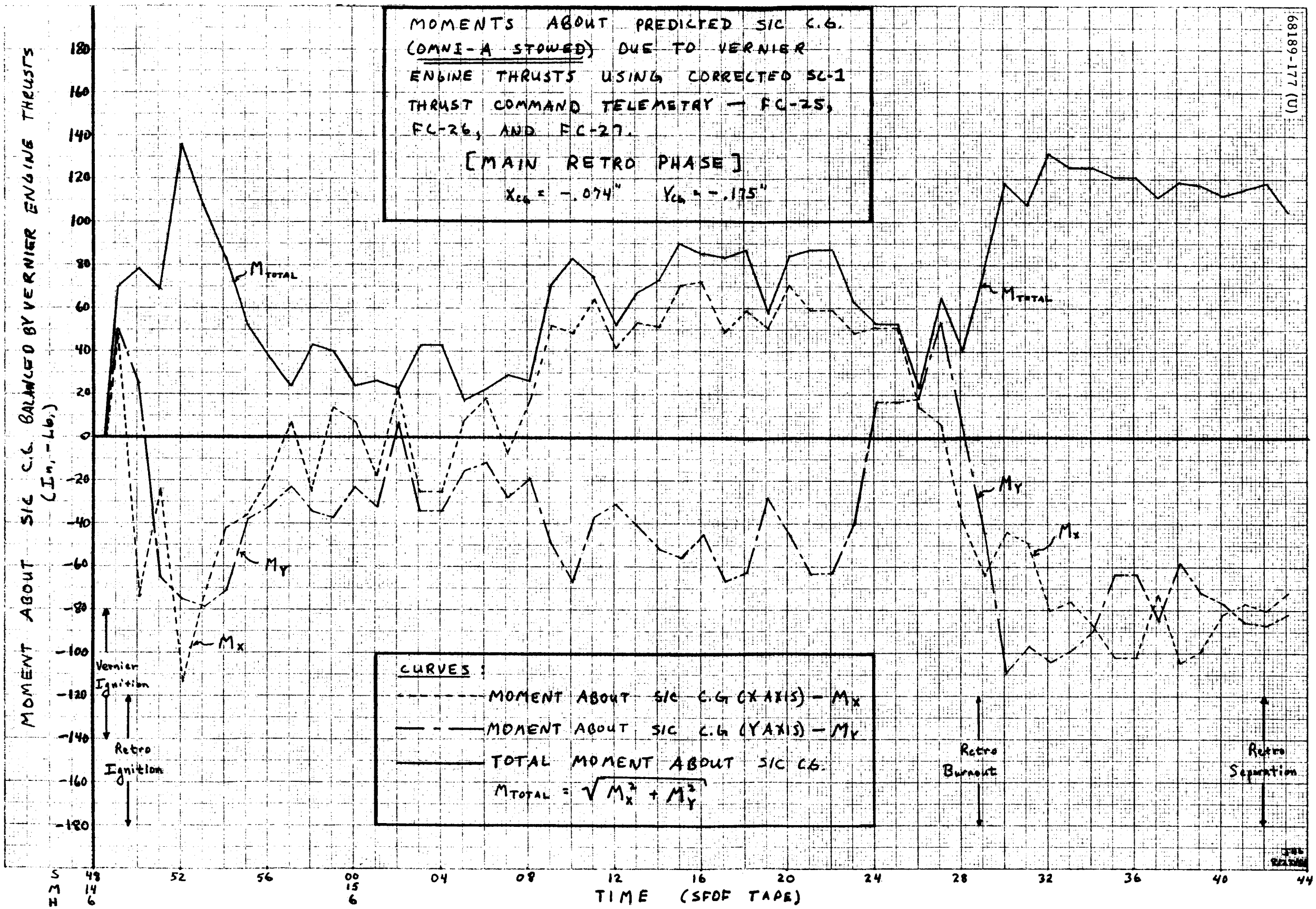


Figure 5.6-60. Moments About Predicted Spacecraft Center of Gravity Due to Vernier Engine Thrusts Using Corrected SC-1 Thrust Command Telemetry for FC-25, FC-26, and FC-27

Main retro phase

a) Omnidirectional Antenna A Stowed

FOLDOUT FRAME

FOLDOUT FRAME

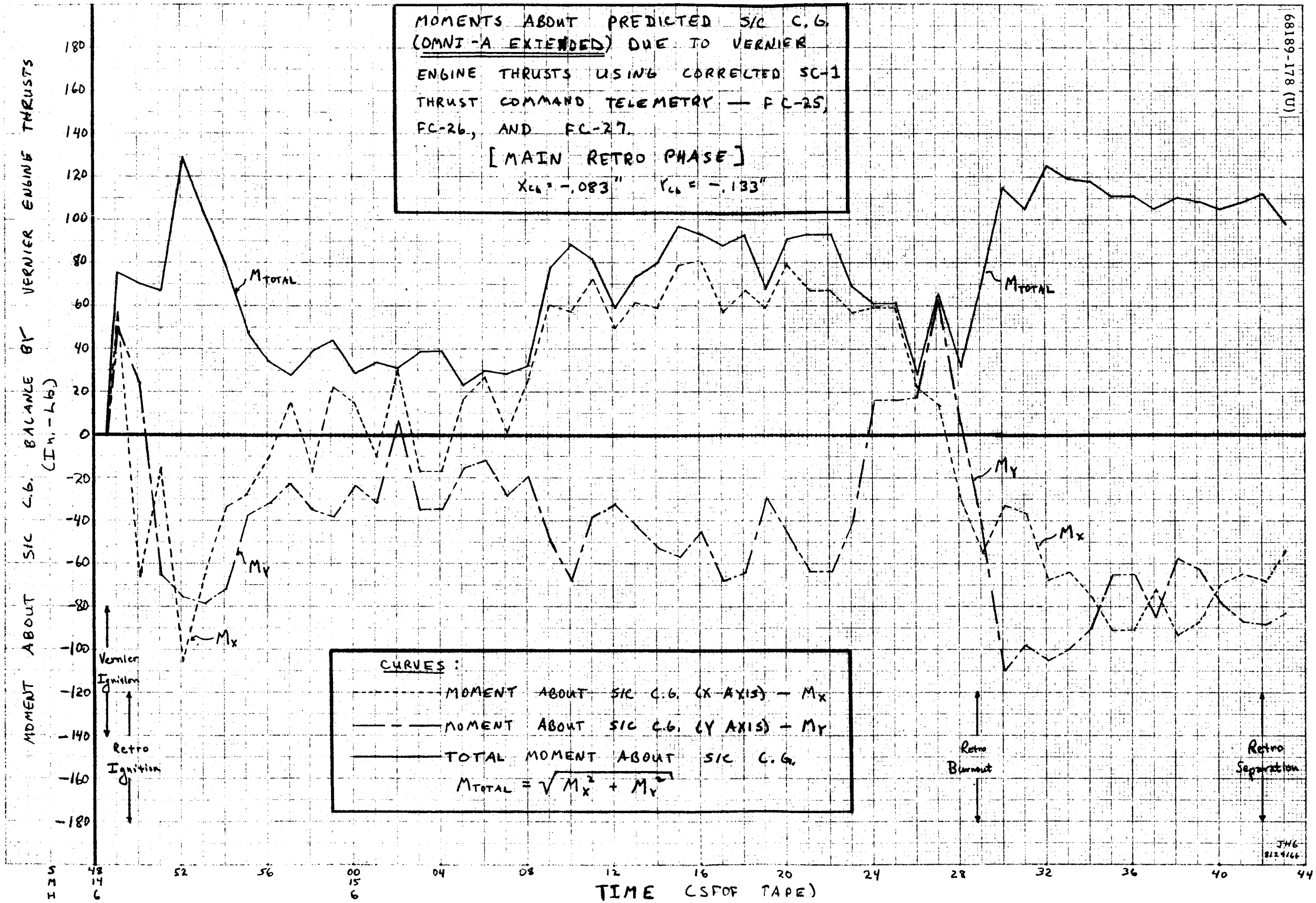


Figure 5.6-60 (continued). Moments About Predicted Spacecraft Center of Gravity Due to Vernier Engine Thrusts Using Corrected SC-1 Thrust Command Telemetry for FC-25, FC-26, and FC-27

Main retro phase

b) Omnidirectional Antenna A Extended

FOLDOUT FRAME

FOLDOUT FRAME

TABLE 5.6-21. CALCULATION OF SC-1 CENTER OF GRAVITY AT RETRO IGNITION

Condition	Weight, pounds	X_{cg}, inch	Y_{cg}, inch	W·X, in.-lb	W·Y, in.-lb
Spacecraft at injection preflight measure	2192.71	-0.092	-0.145	-201.729	-317.943
N_2 expended from telemetry	-0.70	0	-25.5	0	17.850
Vernier propellant used at midcourse	-16.10	0	0	0	0
Vernier propellant (1.1 seconds)	-0.80	0	0	0	0
Helium redistribution	—	—	—	3.915	10.005
Omnidirectional antenna A "stowed to extended" moments	—	—	—	19.2	-90.8
AMR expended —	-11.50	-1.585	-0.163	18.228	1.875
AMR attachments —	-0.18	-6.0	1.0	1.080	0.180
Pyrogen used	-1.33	-0.083	-0.125	0.110	0.166
Spacecraft at retro ignition (omnidirectional antenna A stowed)	2162.10	-0.074	-0.175	-159.196	-378.667
Spacecraft at retro ignition (omnidirectional antenna A extended)	2162.10	-0.083	-0.133	-178.396	-287.867

was at X = -0.088 inch and Y = -0.137 inch. From this centerline location, moments about the center of gravity due to approximate retro thrust vector offset can be predicted for these two cases. For 10,000 pounds of retro thrust, the case of omnidirectional antenna A stowed could have moments due to center of gravity-to-centerline offset of M_x = -380 in.-lb, M_y = -140 in.-lb, and M_{TOTAL} = 405 in.-lb. No disturbance moments of this size are observed for the main retro phase. The case of omnidirectional antenna A

extended could have moments to this offset of M_x = 40 in.-lb, M_y = -50 in.-lb, and M_{TOTAL} = 64 in.-lb, which are closer to the values determined by the above method. However, neither condition can be taken as correct from this analysis as the nozzle centerline is only an approximation to the true retro thrust vector, and the unequal vernier propellant consumption during midcourse was not considered in predicting the center of gravity locations. However, in each of these cases, the following occurrences can be noted: 1) for the first 4 seconds after retro ignition, moment disturbances about the center of gravity are as large as -100 in.-lb about the pitch axis and -80 in.-lb about the yaw axis; 2) during the next 12 seconds, the moments are less than the ±40 in.-lb accuracy and are considered negligible; and 3) during the remaining time before retro burnout, total moments of between 60 and 100 in.-lb about the spacecraft predicted center of gravity location have been determined.

Although determination of the retro thrust vector to combined spacecraft center of gravity offset by this method is not highly accurate, an upper bound may be set on the offset from this analysis. The largest total pitch-yaw moment about the predicted spacecraft center of gravity for either position of omnidirectional antenna A during the period from retro ignition to retro burnout is less than 140 in-lb. This value has an inaccuracy of the order of ±40 in.-lb. Thus, assuming a maximum retro thrust of 10,000 pounds, it would not be outside the limits of this analysis to state that the maximum observed center of gravity-to-retro thrust vector was less than 0.02 inch.

Raw Plots

Figures 5.6-61 through 5.6-67 are raw plots for the Surveyor I mission.

5.6.7.11 Vernier Descent

The vernier descent phase began at 153:06:15:42.093 GMT with initial conditions of V_z = 431 ft/sec and slant range of 27,851 feet and soft landed on the moon's surface at 06:17:35.700. The performance of the flight control system during this phase has been summed up on the comparative plot between the actual and expected range-velocity trajectory (Figures 5.6-68 and 5.6-69).

During the vernier descent phase, certain values of range and velocity were widely accepted as events. These events and their corresponding time of occurrence are given in Table 5.6-22. Also presented in the table are predicted times of occurrence.

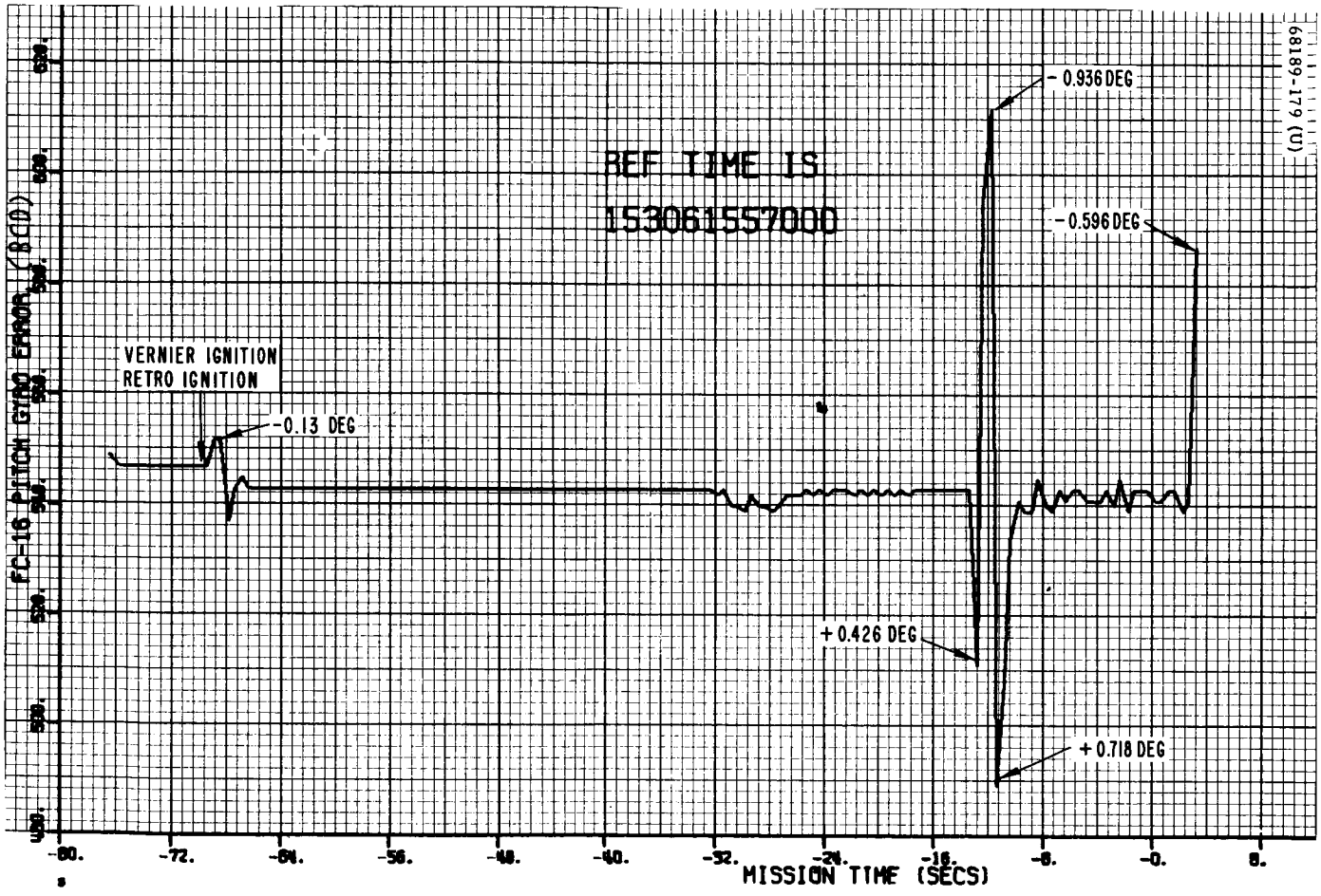


Figure 5.6-61. Pitch Gyro Error, FC-16

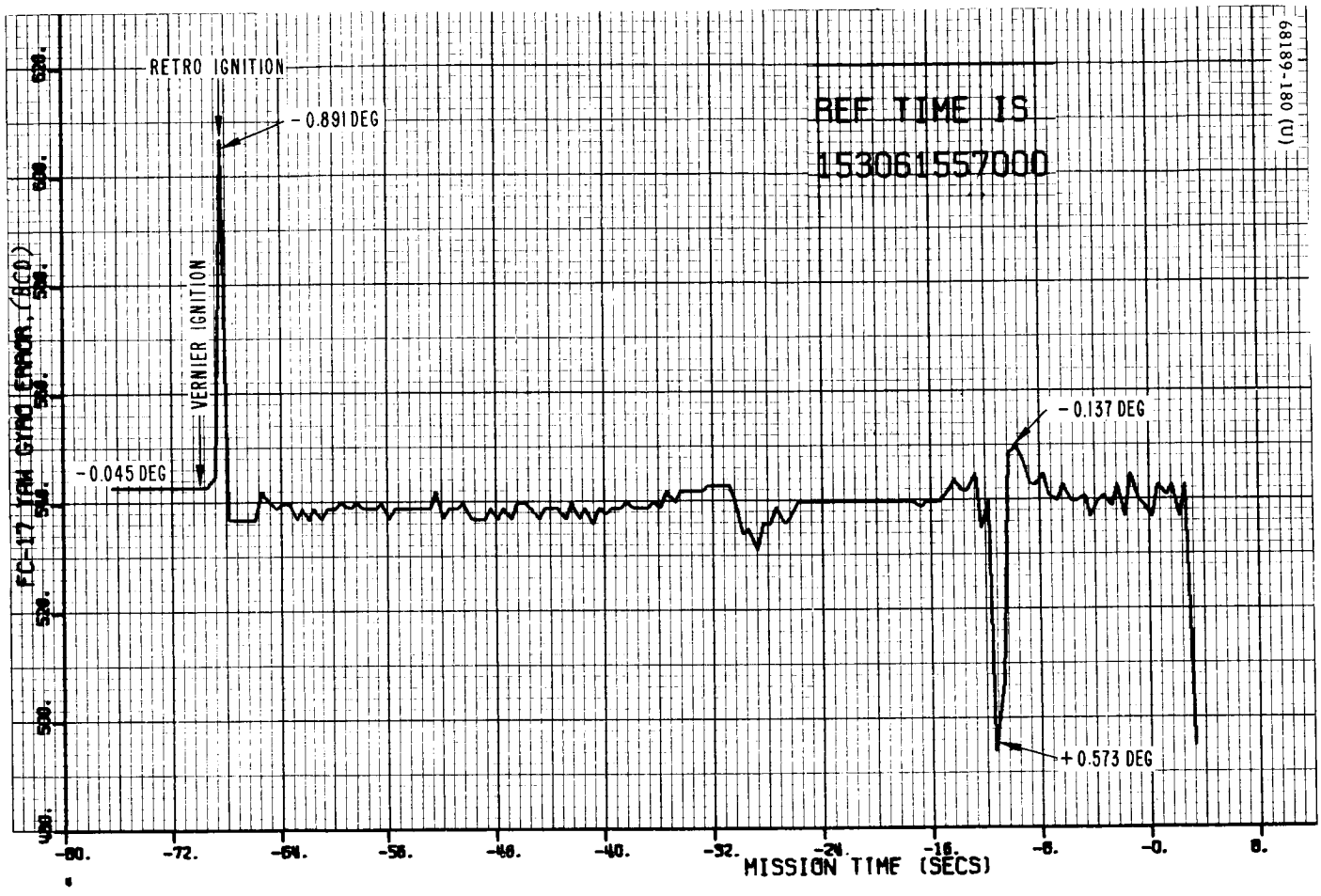


Figure 5.6-62. Yaw Gyro Error, FC-17

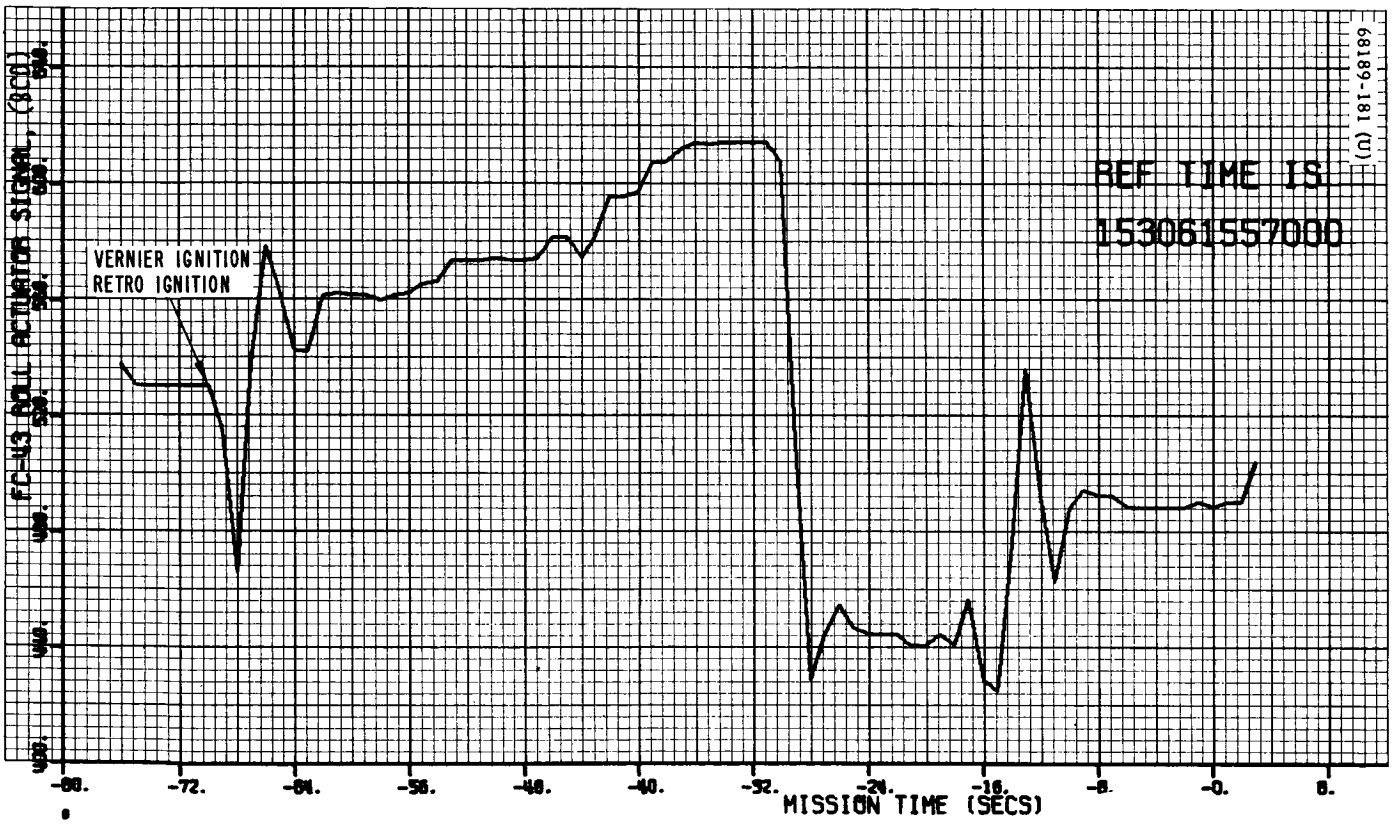


Figure 5.6-63. Roll Actuator Signal, FC-43

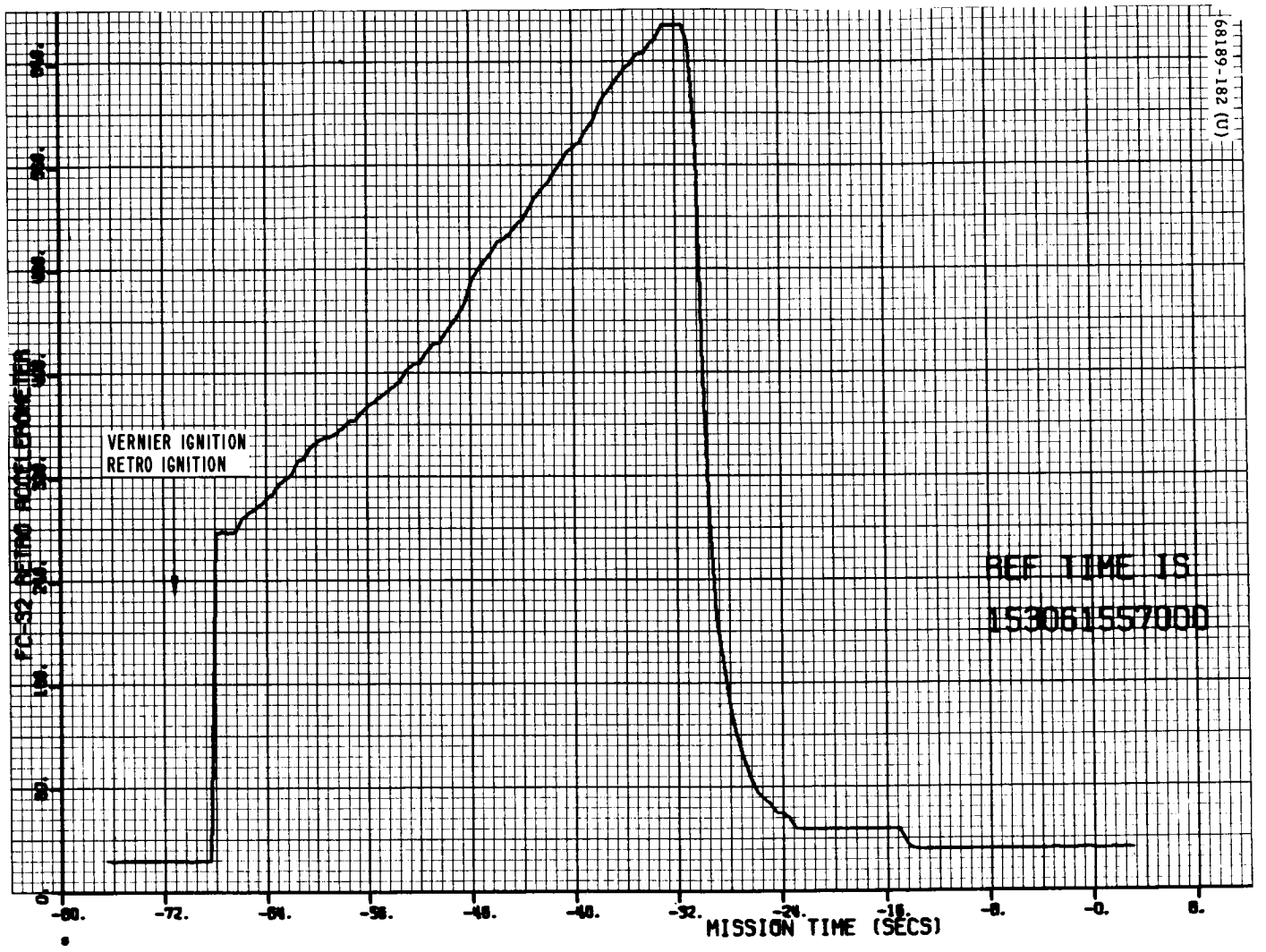


Figure 5.6-64. Retro Accelerometer, FC-32

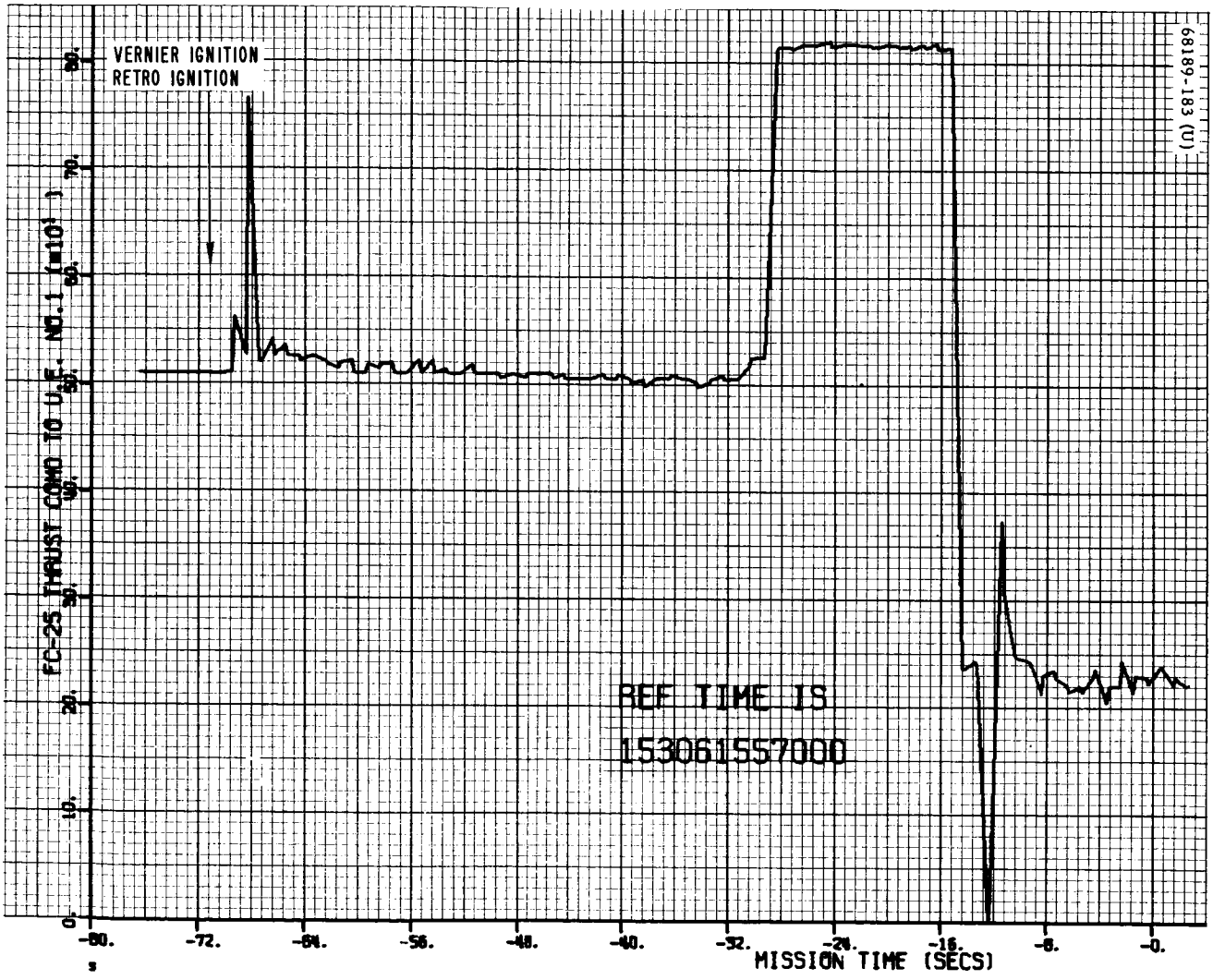


Figure 5.6-65. Thrust Command to Engine 1

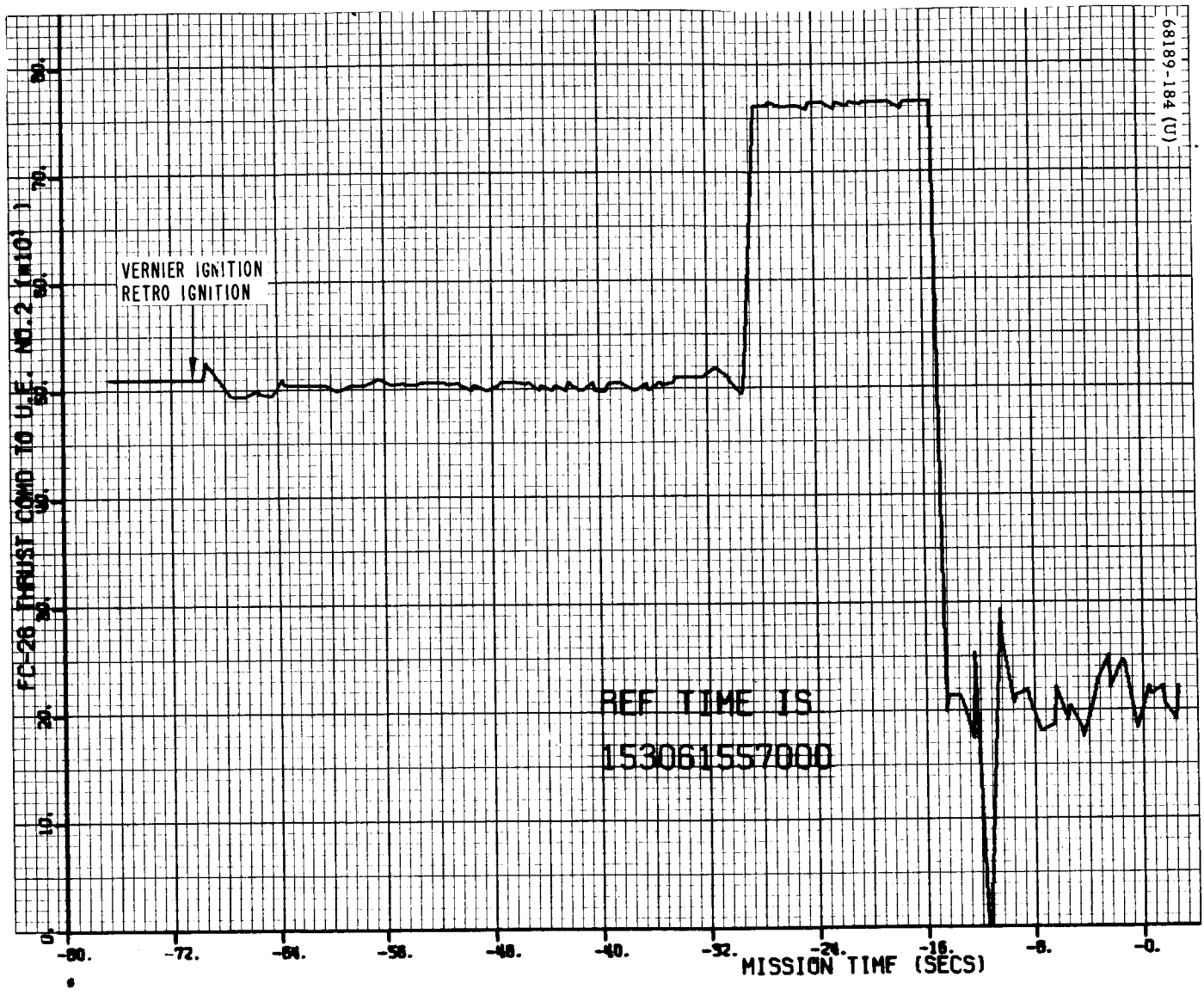


Figure 5.6-66. Thrust Command to Engine 2

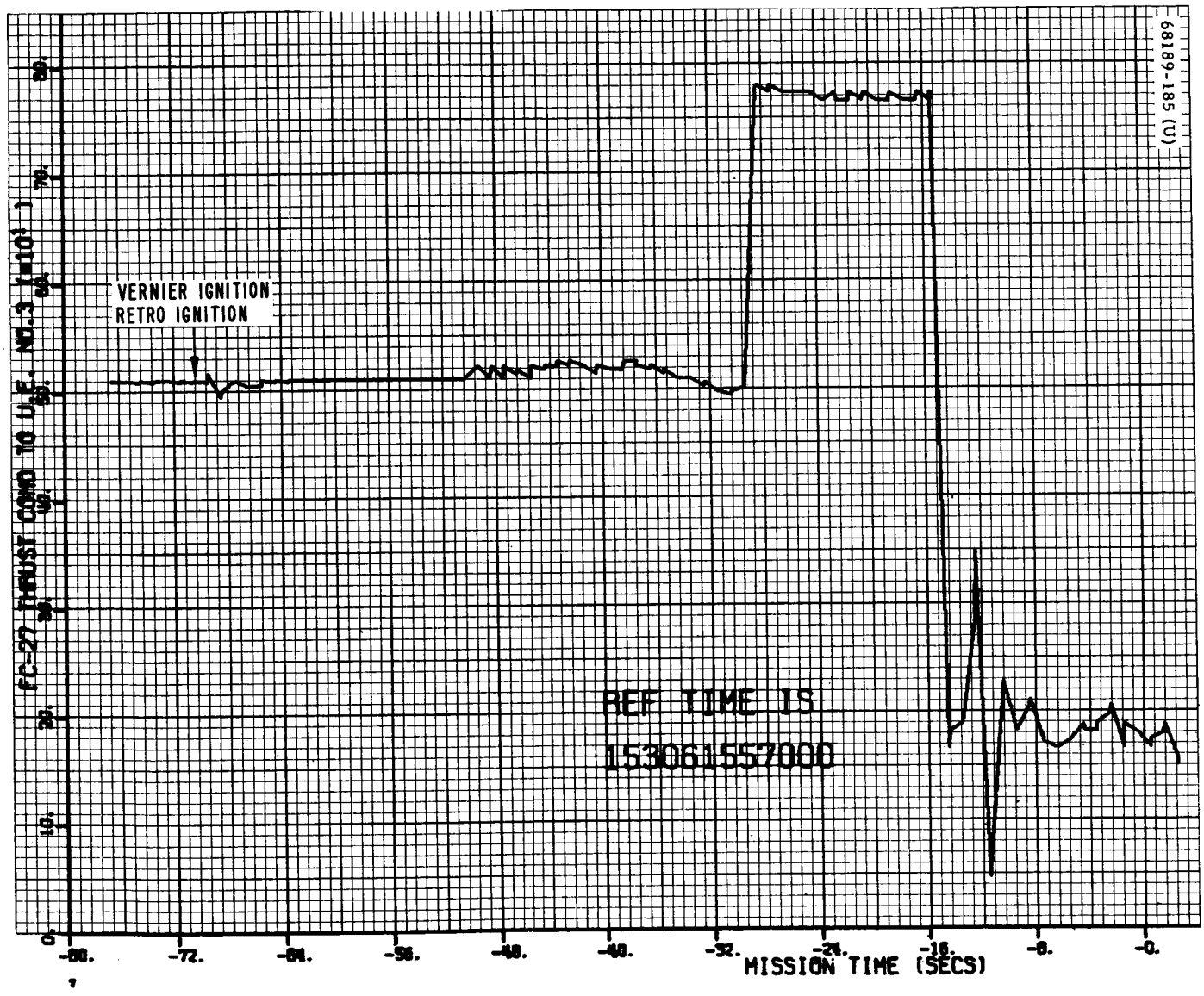


Figure 5.6-67. Thrust Command to Engine 3

68189-186 (U)

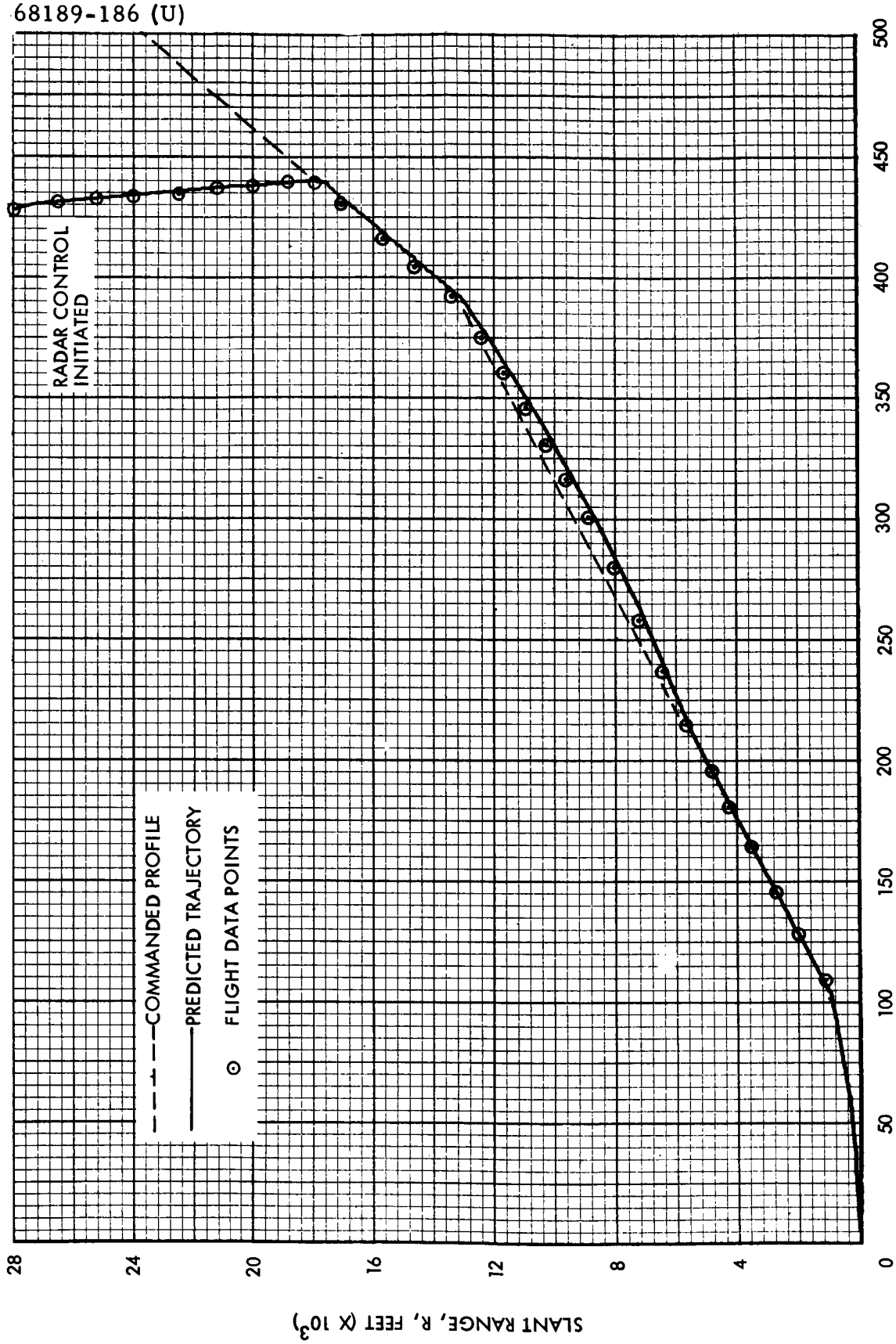


Figure 5.6-68. Vernier Descent Trajectory

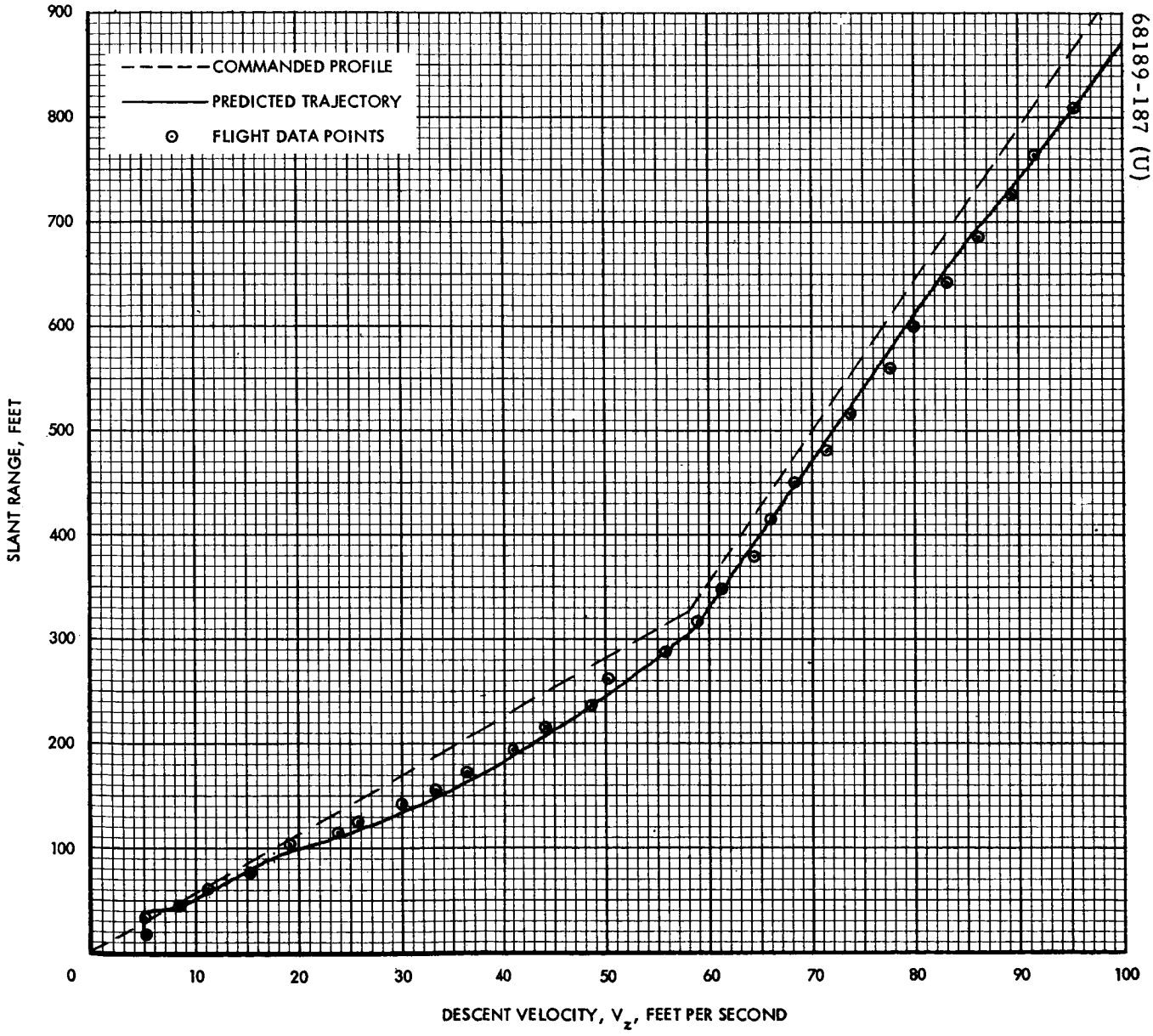


Figure 5.6-69. Vernier Descent Trajectory, Range > 1000 Feet

TABLE 5.6-22. TIME AND EVENTS LOG

Vernier Phase

Vernier Descent Phase Events	Time of Event, GMT	Predicted Time
Start RADVS controlled descent	06:15:42.093	06:15:40
Segment acquisition	06:16:05.893	06:16:15
End of segment 1	06:16:17.225	
End of segment 2	06:17:10.494	
1000 feet	06:17:10.494	06:17:12
End of segment 3	06:17:19.281	
10 ft/sec	06:17:28.719	06:17:30 (8.6 ft/sec)
13 feet	06:17:34.169	06:17:35
Touchdown	06:17:35.600	06:17:37

Note: Time of events was obtained from Reference 19; predicted times were obtained from Reference 15.

Range-Velocity Trajectory

The actual range-velocity trajectory is presented in Figure 5.6-68 along with the commanded profile. The nominal or expected descent trajectory is also provided to illustrate the fine performance of the flight control system.

Vernier Descent Attitude Control

Pitch and yaw attitude motions determined from pitch and yaw gyro error telemetry signals (FC-16 and FC-17) were maintained less than ±1.0 degree in each axis during the vernier descent phase. Required gimbal freedom of each gyro is ±10 degrees. (See Figures 5.6-70 and 5.6-71 in "Corrected Telemetry Plots.")

Measurable gyro gimbal errors (equivalent to spacecraft attitude error relative to the reference established by RADVS signals) occurred only during certain portions of the vernier descent phase, according to the following summary:

Peak Gyro Gimbal Errors, degrees

Phase of Descent	Pitch	Yaw
RODVS (start of alignment to velocity vector)	0.9	0.65
R < 1000 feet (due to RADVS noise)	<0.2	<0.2
Following engine cutoff	1.0	-0.9
Following touchdown	-0.65	0.58

Following generation of the RODVS signal by the RADVS, the spacecraft initiated an attitude maneuver to align the thrust axis with the total velocity vector. Initial velocity conditions preceding the maneuver were as follows (taken from RADVS telemetry data, FC-39, FC-40, and FC-41). (See Figures 5.6-72, 5.6-73, and 5.6-74 in "Corrected Telemetry Plots.")

Premaneuver velocity conditions (06:15:44.5 GMT) are as follows:

V_x = 32.1 fps

V_y = -25.2 fps

V_z = 430 fps

The alignment maneuver was completed in less than 2 seconds (9 seconds allowed), at which time V_x and V_y were held at zero and V_z became equal to the total velocity of 432 fps. The attitude maneuver magnitudes were computed as follows:

Pitch maneuver: $\Delta\theta_x = -\tan^{-1}\frac{V_y}{V_z} = 3.4$ degrees

Yaw maneuver: $\Delta\theta_y = \tan^{-1}\frac{V_x}{V_z} = 4.3$ degrees

The spacecraft Z axis was therefore maneuvered through a total of 5.5 degrees.

Gyro gimbal angle errors were maintained virtually at null during the descent above the 1000-foot range. Following generation of the RADVS 1000-foot mark, which increases the lateral velocity control channel gains by a factor of approximately six and thereby increases system sensitivity to noise on the V_x and V_y radar indications, increased gyro gimbal errors were developed but did not exceed 0.2 degree in either axis.

Following vernier engine cutoff, gyro gimbal errors (equivalent to inertial attitude motion) increased to approximately 1.0 degree in pitch and -0.9 degree in yaw during free-fall to the lunar surface. Following touchdown, these gimbal angles were -0.65 degree in pitch and 0.58 degree in yaw. The vector sum of these two quantities yields a net attitude error of 0.87 degree. Thus, if it is assumed that the gyro reference was aligned to vertical by the RADVS guidance signals, this would imply a lunar surface slope of 0.87 degree. Since the most accurate estimate of surface slope is 0.27 degree, it must be concluded that the gyro reference was misaligned to vertical by approximately 0.6 degree. This is well within the 4.8-degree allowance (Reference 17).

Corrected Telemetry Plots

The corrected telemetry plots are given in Figures 5.6-70 through 5.6-78.

5.6.7.12 Spacecraft Attitude Determination – Postlanding

The following analysis was obtained in its entirety from Reference 20:

1. The spacecraft attitude matrix is defined as the matrix by which vectors are multiplied to transform them from the selenographic coordinate system into the spacecraft coordinate system. Three independent data sources were used to generate attitude matrices. These sources were the ASPP, the TV camera, and the inertial reference unit. The ASPP and TV camera matrices were generated using the least-squared error method described in Reference [21]. This method, rather than the PLAS program, was used to permit generation of a single matrix for all vectors from a given data source. The PLAS program is only capable of accepting two vectors at a time. The gyro matrix was obtained by assuming x and y axis slopes to be exactly represented by the difference in

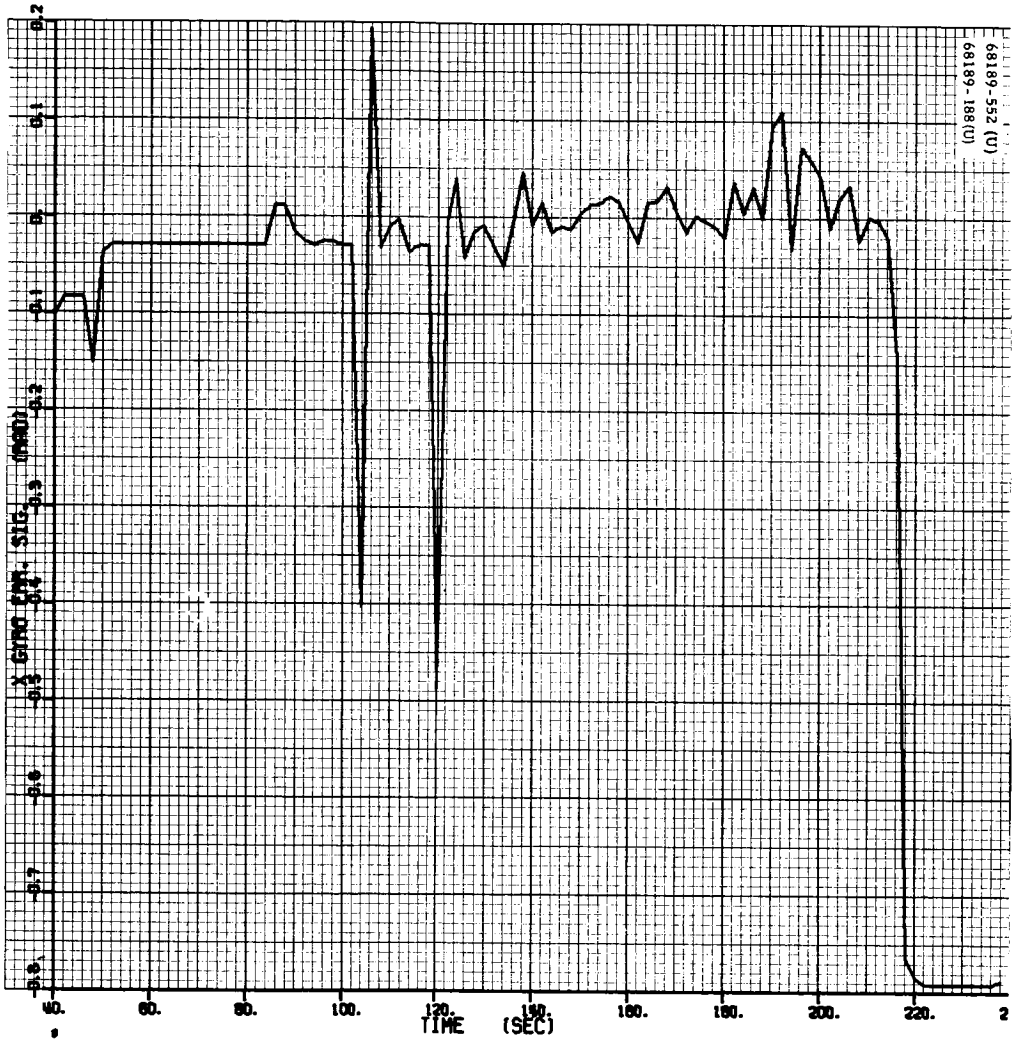


Figure 5.6-70. Pitch Gyro Error Signal

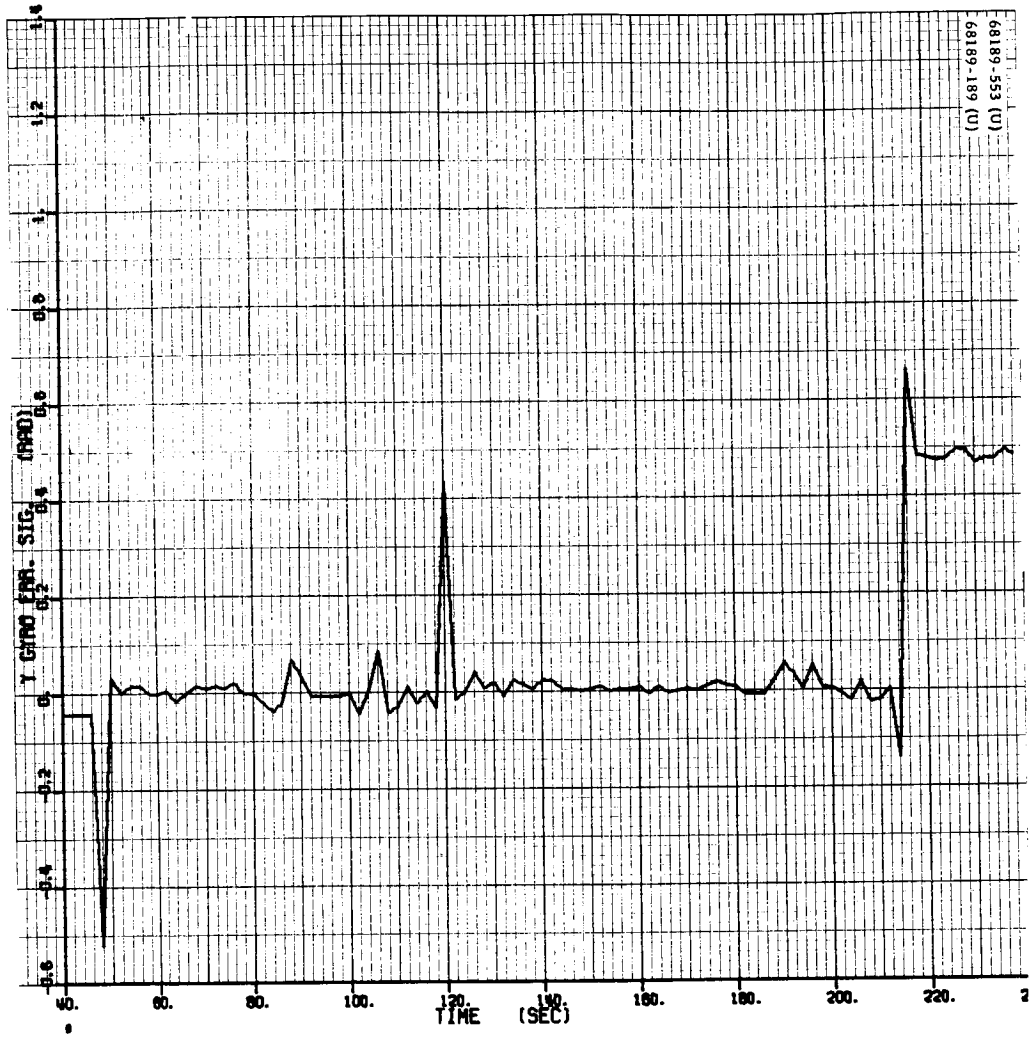


Figure 5.6-71. Yaw Gyro Error Signal

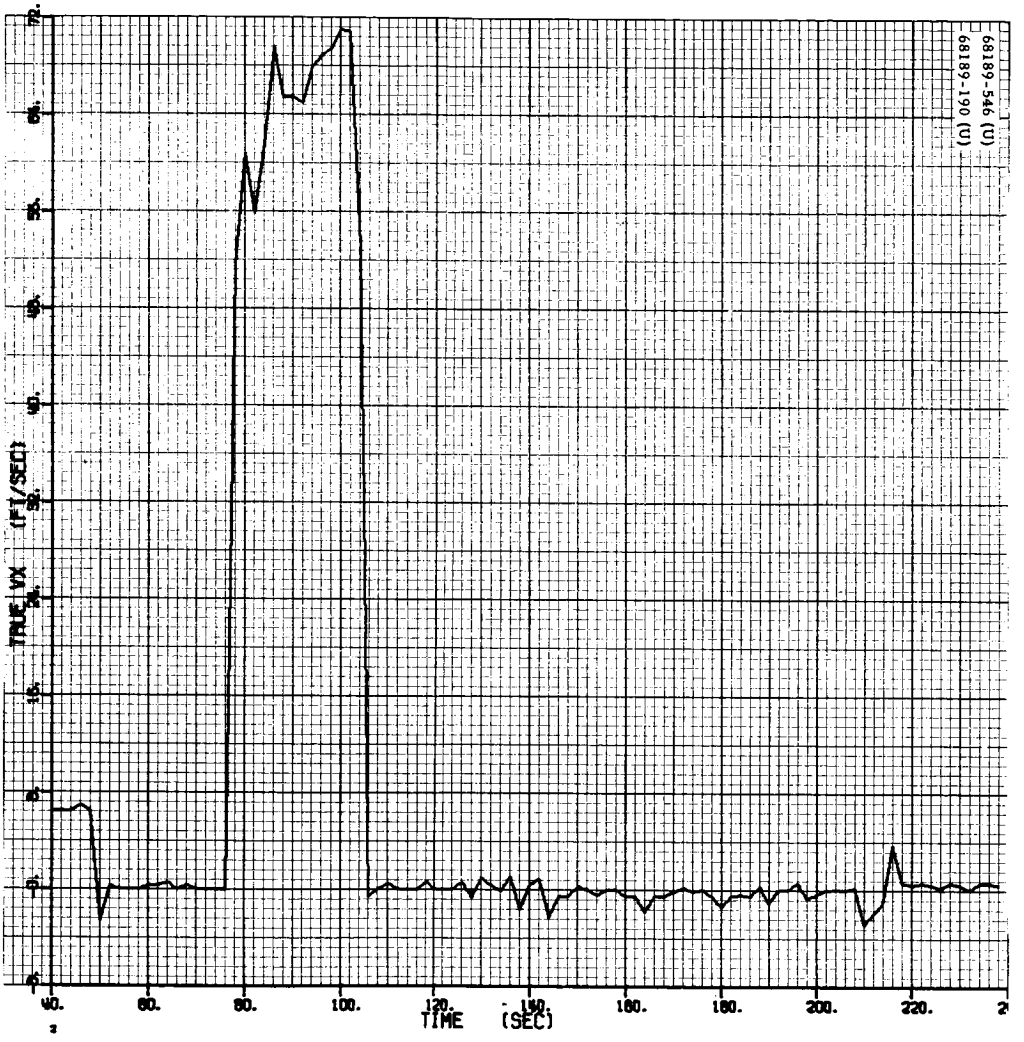


Figure 5.6-72. True V_x

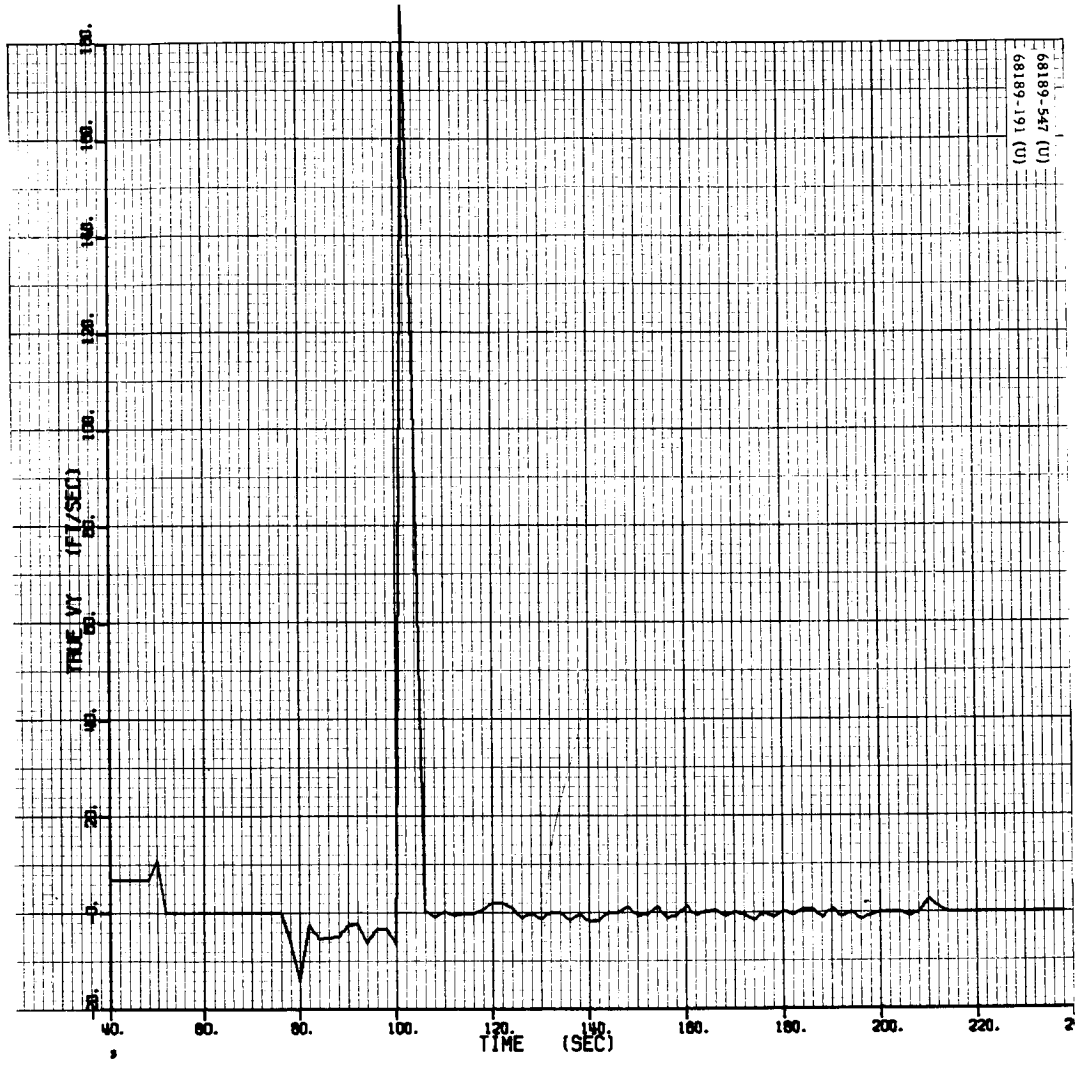


Figure 5.6-73. True V_y

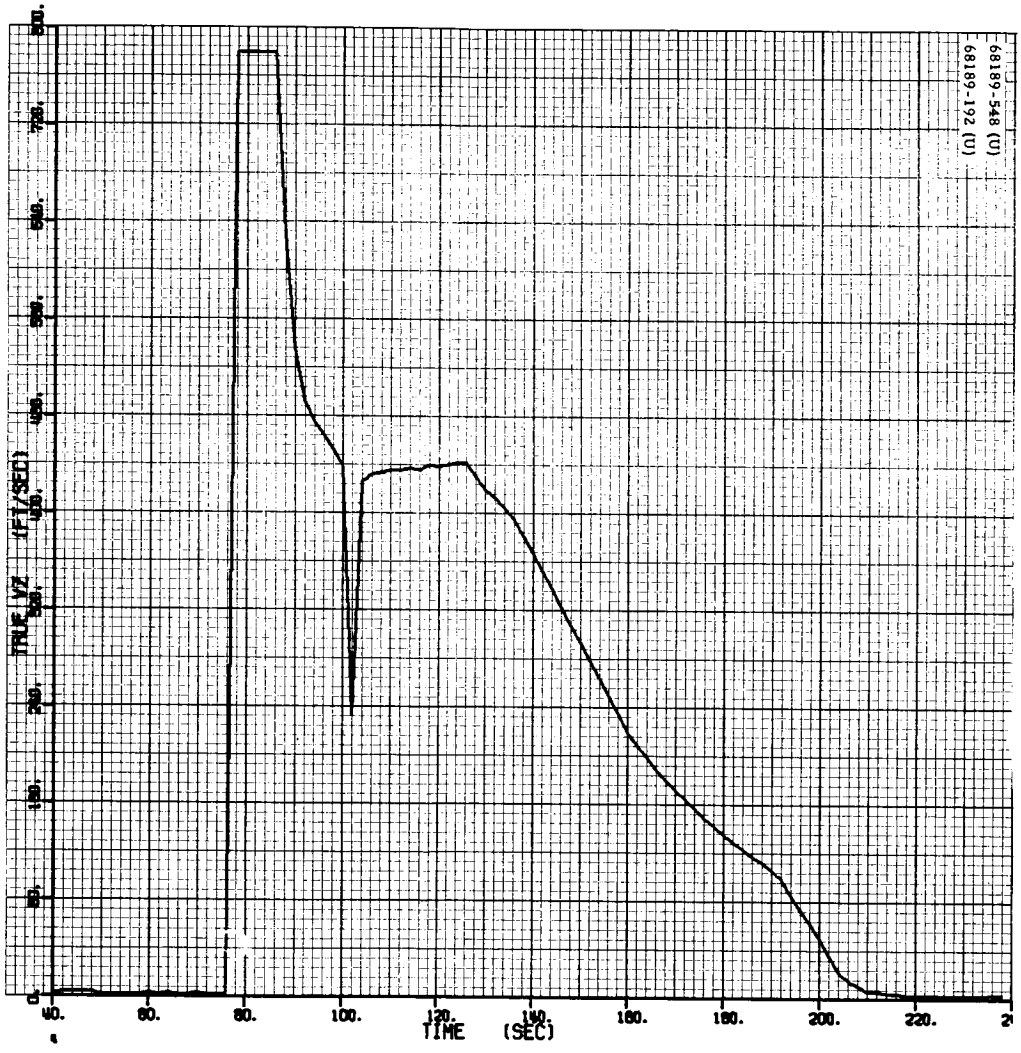


Figure 5.6-74. Ture V_Z

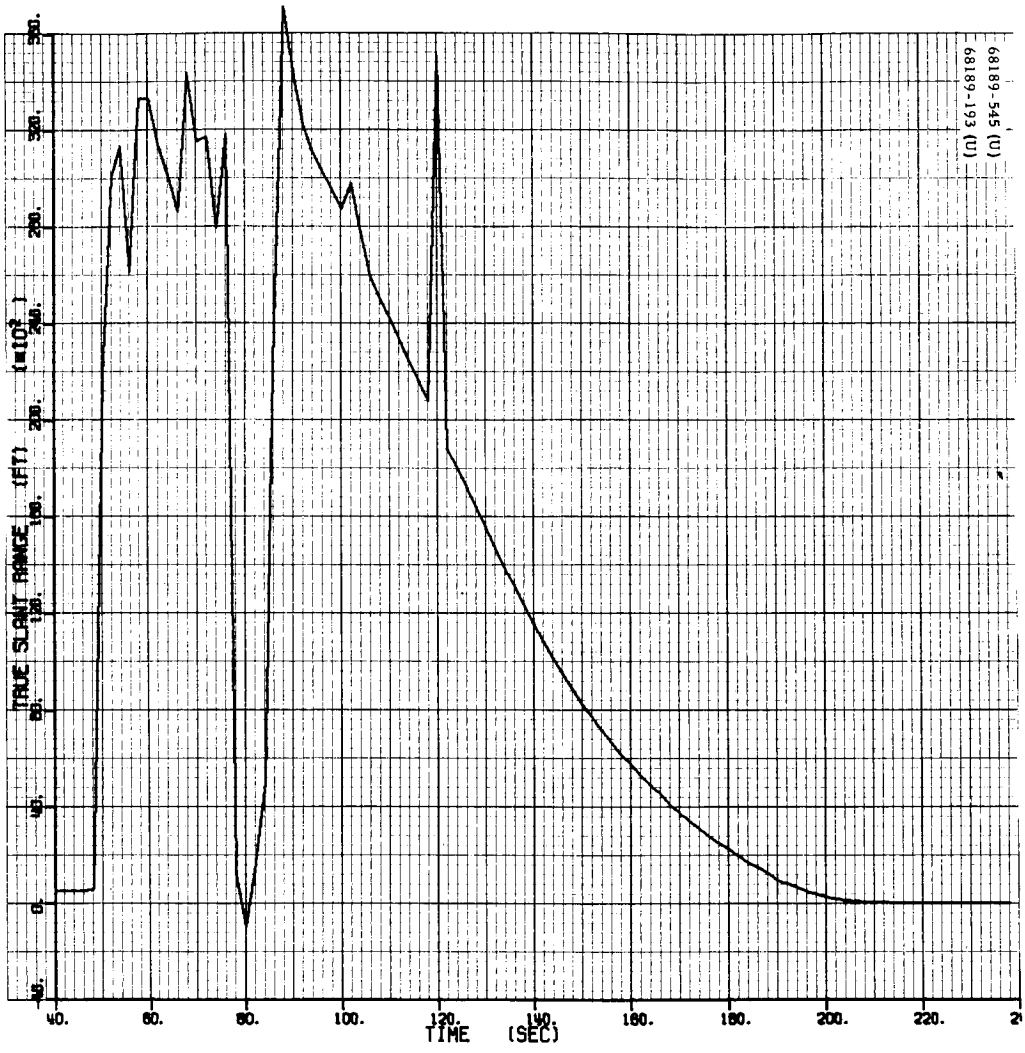


Figure 5.6-75. True Slant Range

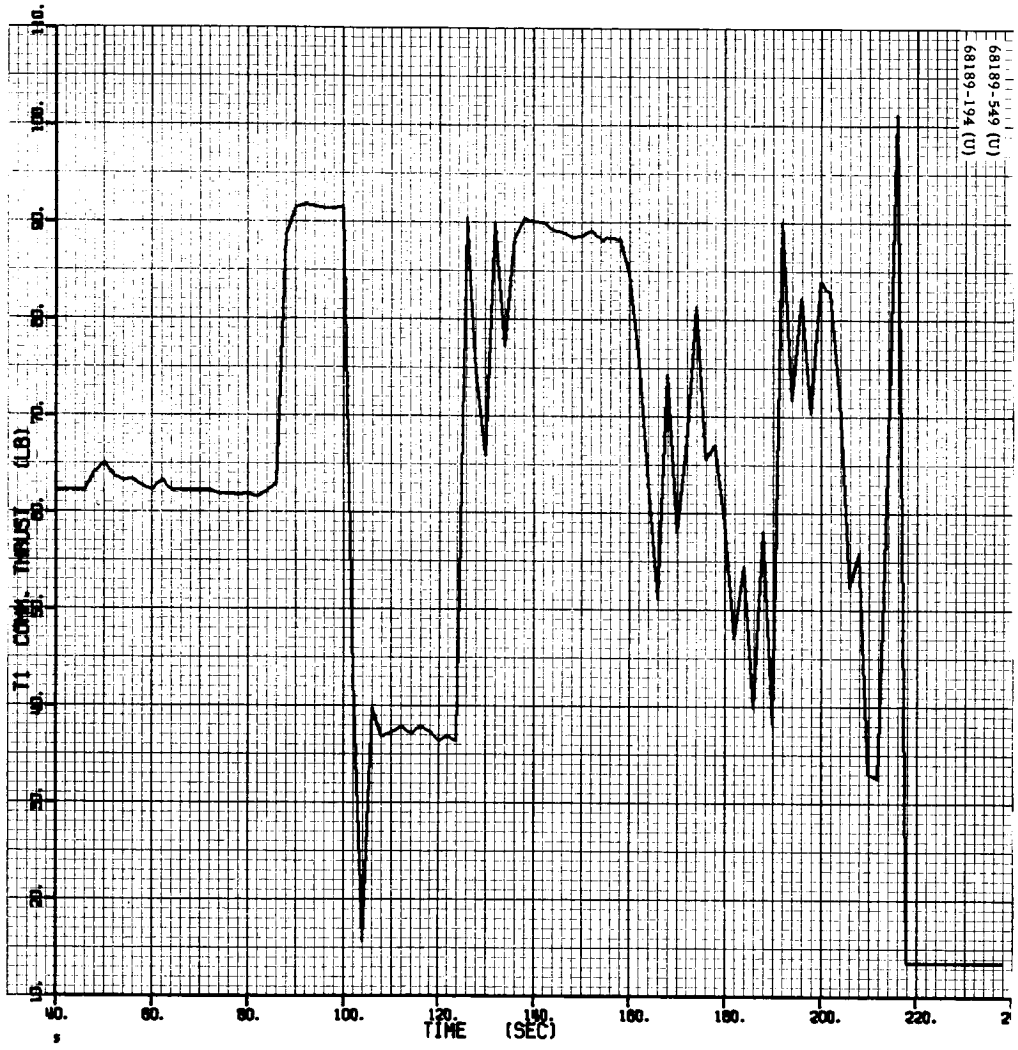


Figure 5.6-76. Thrust Command, Engine 1

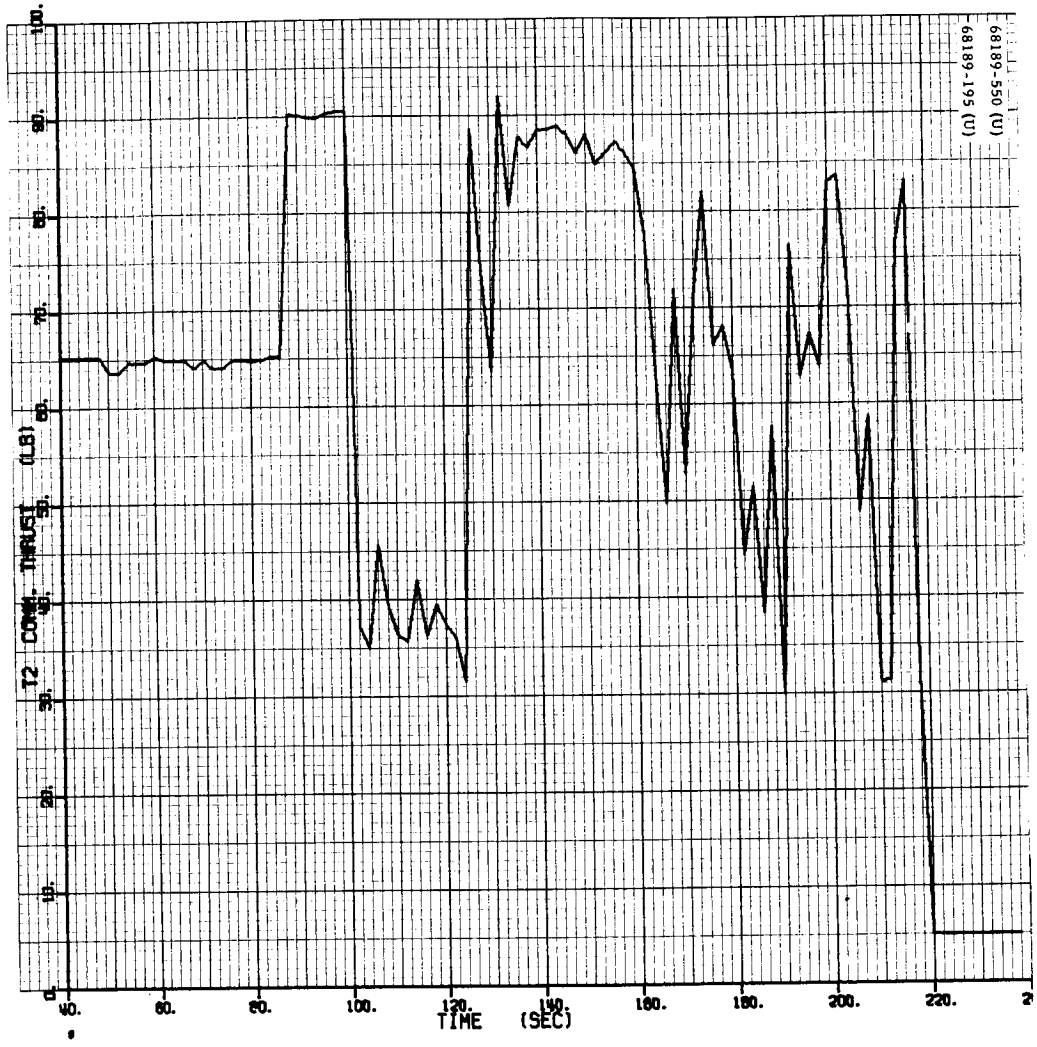


Figure 5.6-77. Thrust Command, Engine 2

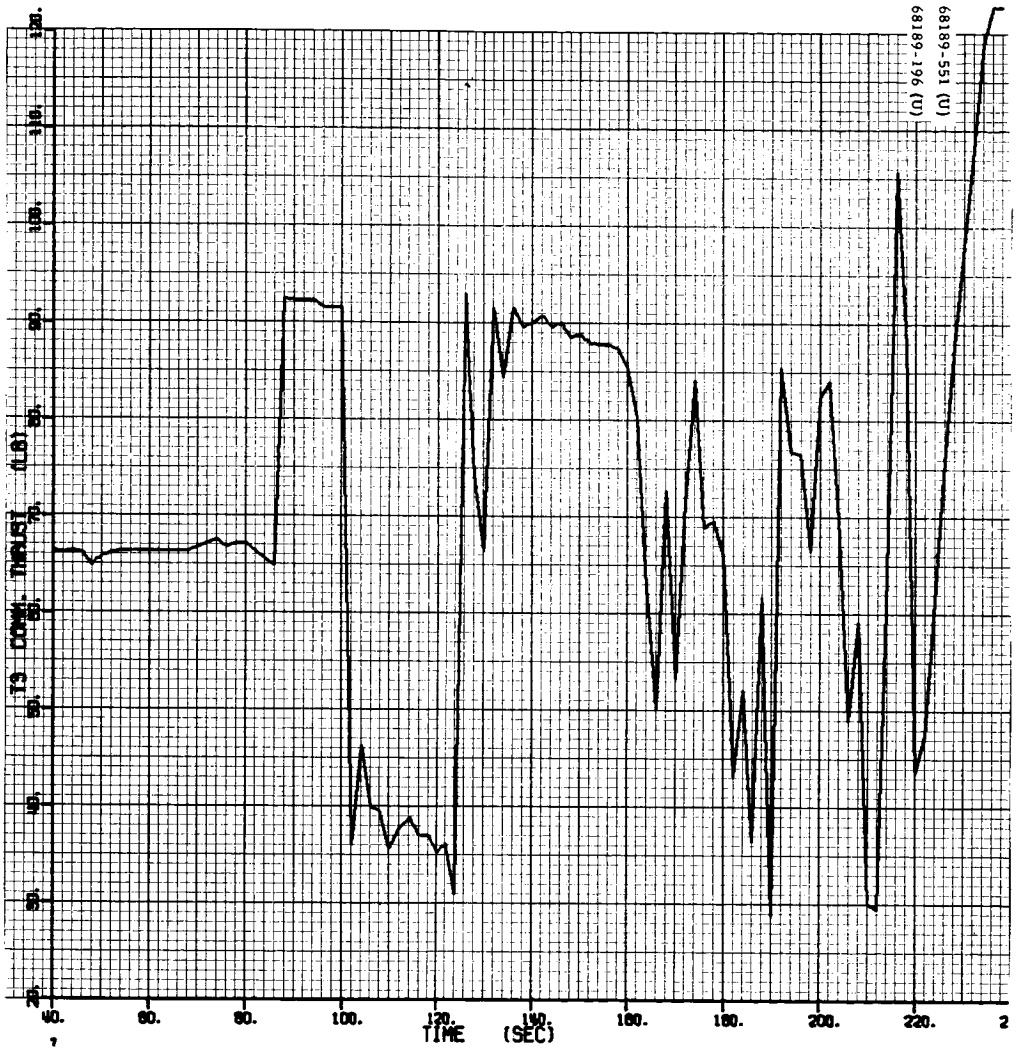


Figure 5.6-78. Thrust Command, Engine 3

gyro error signals before and after touchdown, assuming the spacecraft to be aligned along the gravity vector just prior to touchdown. The final SC-1 attitude was in turn obtained by combining the three individual matrices by the method described in Reference [22]. All three matrices were weighted equally in this final combination. Calculations were performed for a landing site of 43.345° W longitude and 2.411° S latitude. The various matrices and their data sources are as follows:

A. ASPP Matrix

The ASPP matrix was derived from 5 sun vectors and 5 earth vectors obtained during the first lunar day.

$$M_{ASPP} = \begin{bmatrix} -.01914 & +.03088 & -.99934 \\ -.69270 & -.72116 & -.00901 \\ -.72096 & +.69207 & +.03520 \end{bmatrix}$$

B. TV Camera Matrix

The TV camera matrix was derived from one sighting of Canopus and two sightings of Sirius during the first lunar day. A sighting of Jupiter was also obtained, but data was not available for inclusion in these calculations. Data from the three star sightings were corrected for lens and electronic distortions.

$$M_{TV} = \begin{bmatrix} -.02980 & +.04129 & -.99870 \\ -.67838 & -.73464 & -.01013 \\ -.73410 & +.67720 & +.04991 \end{bmatrix}$$

C. Gyro Matrix (Inertial Reference Unit)

The gyro matrix was derived from differences in telemetry signals FC-16, FC-77, and FC-49 before and after touchdown.

$$M_G = \begin{bmatrix} -.01844 & +.05338 & -.99840 \\ -.69692 & -.71669 & -.01828 \\ -.71691 & +.69534 & +.05041 \end{bmatrix}$$

D. Combined Matrix

SC-1 final attitude matrix was obtained by combining M_{ASPP} M_{TV}, and M_G using the method outlined in Reference [22].

$$M_{SC-1} = \begin{bmatrix} -.02413 & .04018 & -.99890 \\ -.68942 & -.72425 & -.01248 \\ -.72396 & .68836 & .04518 \end{bmatrix}$$

Using the above final matrix, the computed lunar slope downhill direction is 239.8° (WSW) with a magnitude of 0.27°.

The spacecraft is aligned in the selenographic coordinate system such that the angle from selenographic north to spacecraft -y axis is 89° as shown in Figure [5. 6-79].

2. Sun/Earth Positions

The sun earth positions in the tables below are specified in azimuths and elevations. Azimuth is defined as the angle from the spacecraft -x axis to the xy projection of the vector to the body of interest measured in a clockwise direction. Elevation is defined as the angle between the vector to the body of interest and the vectors projection in the spacecraft xy plane. (See Figure [5. 6-80].)

Positions are calculated at zero hours GMT for the day specified. Sunrise is defined as the time at which the leading rim of the sun would rise above a plane tangent to a spherical moon at the spacecraft landing site. Sunset is defined as the time at which the trailing rim of the sun drops below the tangent plane. Lunar noon is defined as the time at which the angle between the spacecraft sun vector and its projection in the tangent plane reaches a maximum. These times are determined solely from landing site and are not affected by the spacecraft attitude.

A. First Lunar Day

	Day	Hr/Min
Sunrise	150	2048
Lunar Noon	158	0629
Sunset	165	1541

DAY	SUN AZ	SUN EL	EARTH AZ	EARTH EL
153	88. 9	25. 4	88. 4	41. 8
154	88. 0	37. 6	86. 3	41. 5
155	86. 8	49. 7	84. 3	41. 3
156	84. 6	61. 9	82. 6	41. 4
157	79. 4	73. 9	81. 1	41. 7
158	48. 4	85. 2	79. 9	42. 3
159	291. 0	80. 7	78. 6	43. 1
160	279. 3	68. 8	78. 5	44. 2
161	275. 9	56. 7	78. 4	45. 4
162	274. 3	44. 5	78. 6	46. 7
163	273. 2	32. 3	79. 3	48. 1
164	272. 5	20. 1	80. 3	49. 4
165	271. 9	7. 9	81. 9	50. 5

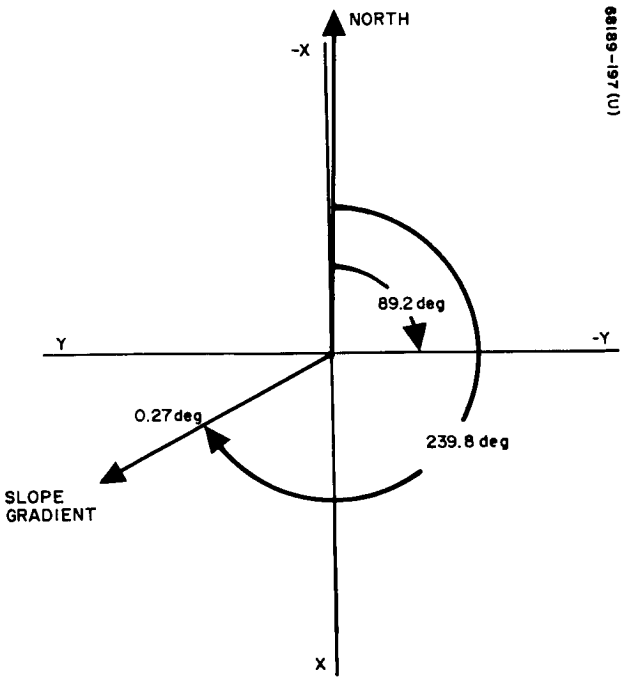


Figure 5.6-79. Spacecraft Attitude With Respect to Selenographic Coordinate System

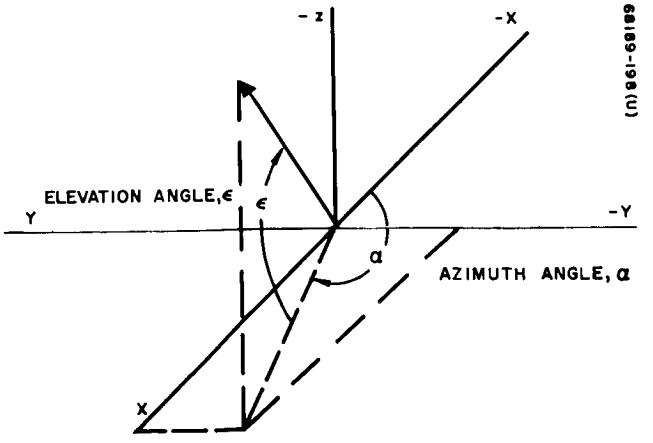


Figure 5.6-80. Geometry

B. Second Lunar Day

	Day	Hr/Min
Sunrise	180	0748
Lunar Noon	187	1725
Sunset	195	0241

DAY	SUN AZ	SUN EL	EARTH AZ	EARTH EL
181	89.2	7.69	86.8	41.2
182	88.5	19.8	84.9	41.1
183	87.7	32.0	83.1	41.3
184	86.5	44.1	81.6	41.7
185	84.6	56.3	80.3	42.2
186	80.7	68.3	79.4	43.0
187	67.9	80.1	78.8	43.9
188	321.6	85.0	78.6	45.0
189	284.7	74.1	78.8	46.3
190	278.4	62.1	79.3	47.7
191	275.8	50.0	80.2	49.1
192	274.4	37.8	81.5	50.4
193	273.4	25.6	83.3	51.6
194	272.7	13.4	85.4	52.5
195	272.1	1.2	87.8	53.0

5.6.7.13 Miscellaneous

Nitrogen Gas Consumption

The expected nominal value of nitrogen fuel consumption as per Reference 4 (revised to fit the actual mission), is 0.546 pound. The actual amount of nitrogen consumed during the SC-1 mission was determined to be 0.680 pound. Of this value 0.099 pound of nitrogen can be attributed to drift checks that were not included in the initial estimate of fuel budget. Thus, the true difference between the actual and expected value is 0.134 pound. Much of this difference was caused by a double pulsing action of the roll gas jet system which occurred periodically during the coast mode operation, giving rise to a higher limit cycle frequency.

Nitrogen Weight History. A graphical representation of nitrogen weight history is presented in Figure 5.6-81. The nitrogen weight values were determined from the N_2 weight curve * (Figure 5.6-82), using corrected

*The N_2 weight curve was derived from data obtained from "Thermodynamics Function of Gases," Din, Volume 3, Butterworth and Company, 1961.

telemetered nitrogen tank temperature and pressure information. The telemetry data of pressure was corrected using the latest available telemetry calibration information (Reference 23). (See Figure 5. 6-83.) A summary of the nitrogen gas consumption is presented in Table 5. 6-23.

Nitrogen Gas Consumption/Mission Phase.

Rate dissipation phase: The gas consumed during separation phase appears negligible.

Sun acquisition phase: From Figure 5. 6-81, it appears that approximately 0. 040 pound of nitrogen was used during sun acquisition. This value may be affected by the fact that the gas temperature had not reach steady state.

Star acquisition and verification phase: From Figure 5. 6-81, it appears that approximately 0. 030 pound of nitrogen was used during this phase of the mission.

Midcourse maneuvers: From Figure 5. 6-81, the total gas weight change during midcourse was 0. 200 pound. Extracting the expected values for vernier phase and postrate dissipation, the gas consumption for the maneuvers is estimated to be 0. 150 pound.

Coast phase: The average gas consumption rate during the period between the twenty-fourth and fortieth hour of the mission was used for computing coast phase gas consumption. This mission period was chosen because of the relative freeness of drift checks which were frequently made. The average rate was 0. 00219 lb/hr. Thus, the total amount of gas consumed during the coast mode was 0. 138 pound.

Preretro maneuvers: Temperature data was not available immediately after the preretro maneuvers because the telemetry was in a monitoring mode that did not include nitrogen temperature. It was thus necessary to estimate the gas used for the preretro maneuvers.

From Reference 24, it was noted that the ratio of gas consumed for a roll maneuver versus a yaw maneuver is 1. 2. With this knowledge and the amount of gas used during midcourse maneuvers, it was determined that the actual consumption per maneuver was 0. 0341 pound for yaw and 0. 041 pound for roll. Since SC-1 required three maneuvers consisting of two rolls and a yaw, the total gas consumed was as follows:

Two roll maneuvers	=	0. 082 pound
One yaw maneuver	=	0. 034 pound
Total gas consumption	=	0. 116 pound

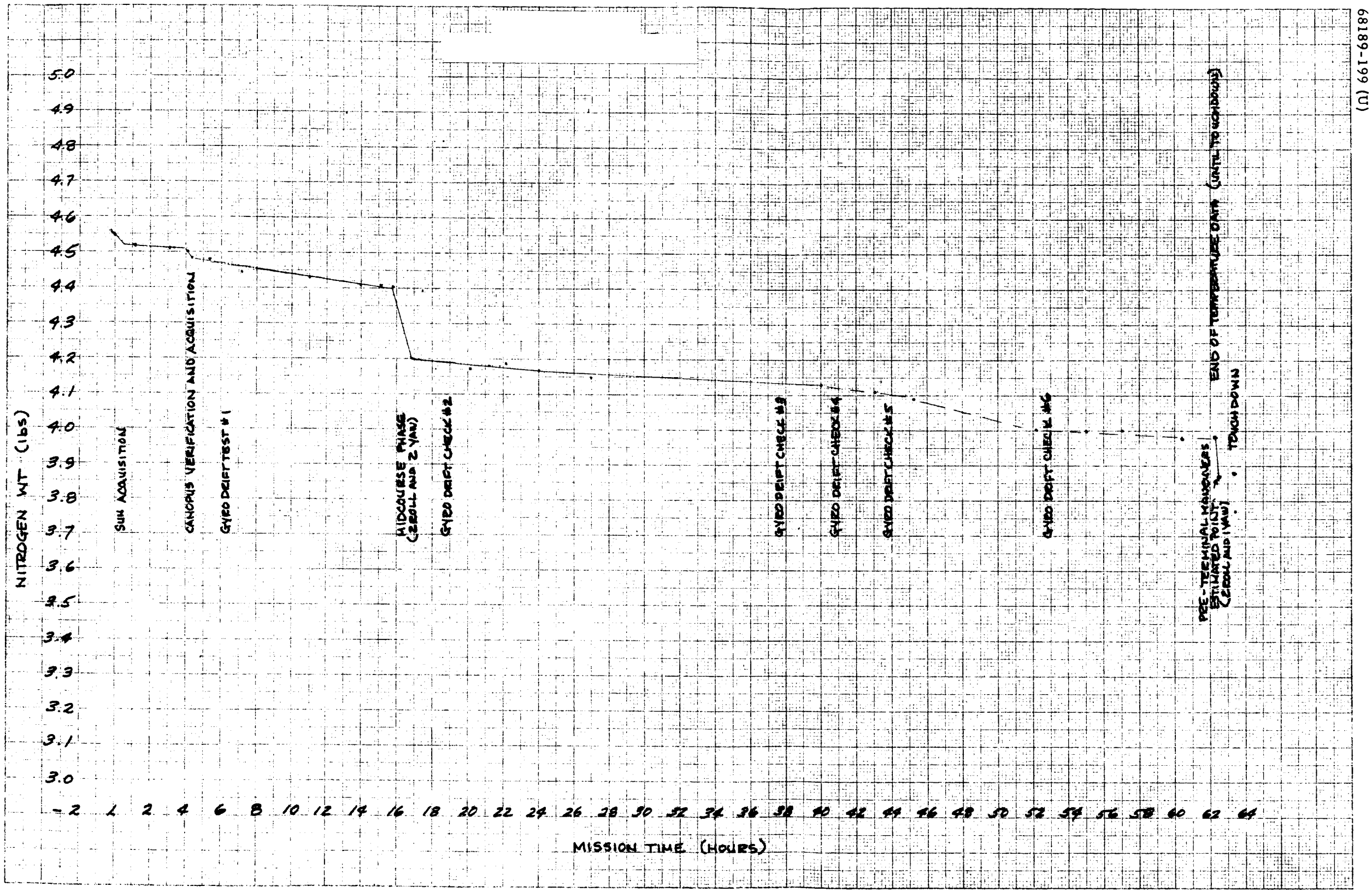


Figure 5.6-81. Nitrogen Weight History

FOLDOUT FRAME

FOLDOUT FRAME

68189-200 (U)

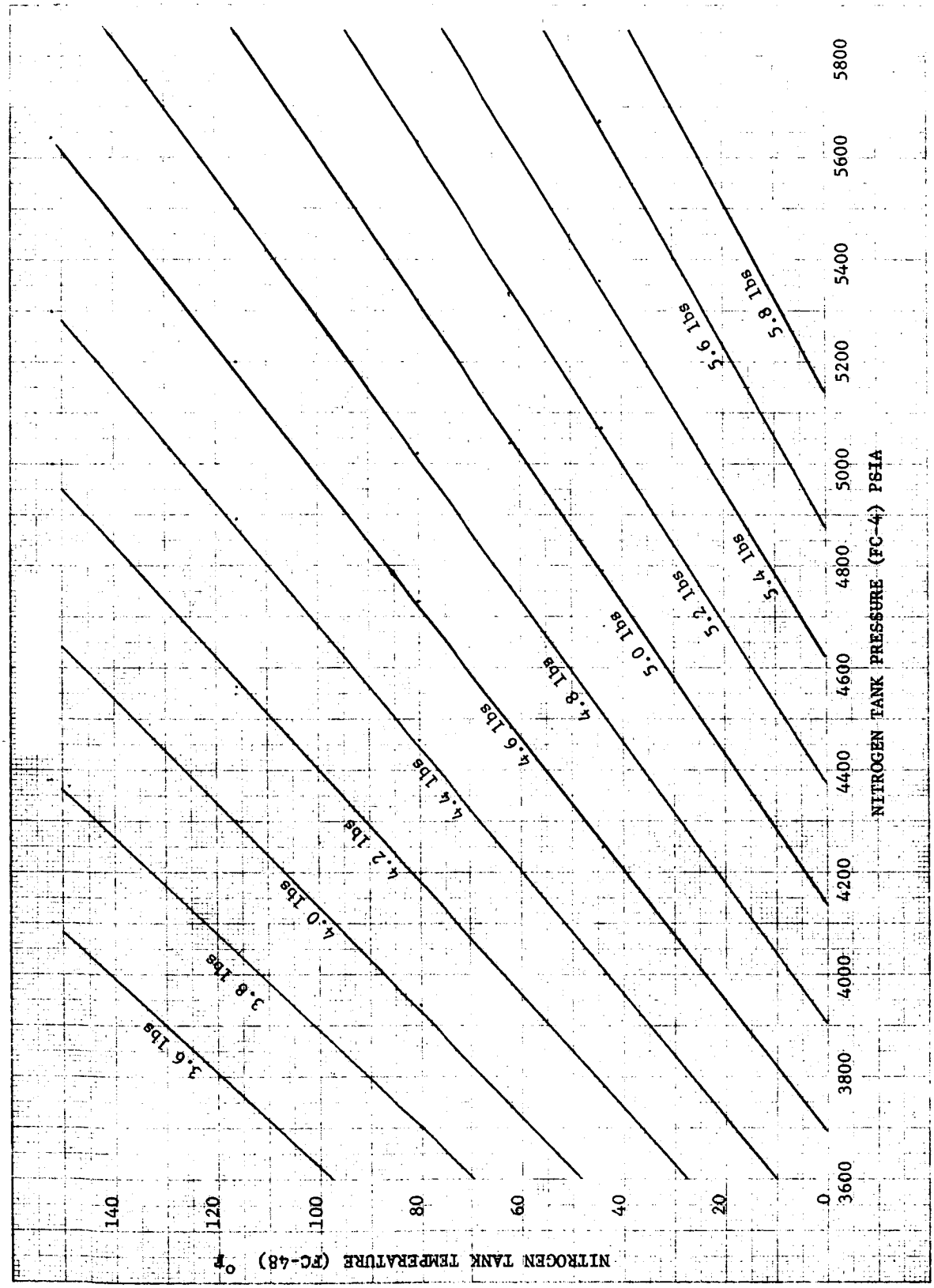


Figure 5.6-82. Nitrogen Weight Curve

68189-201 (U)

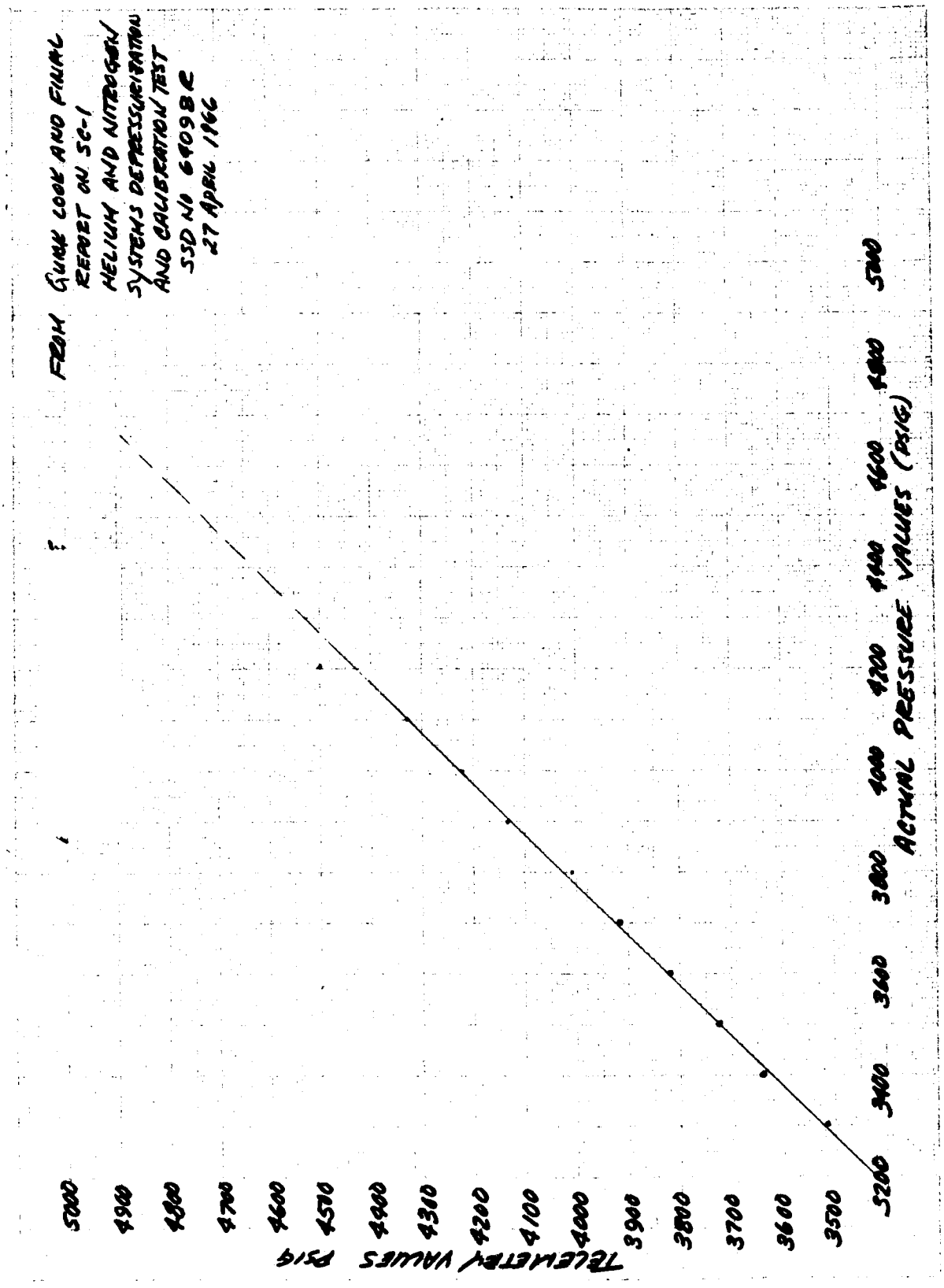


Figure 5.6-83. Nitrogen Pressure Telemetry Calibration Curve

TABLE 5.6-23. NITROGEN GAS CONSUMPTION

Mission Phase	Nitrogen Used During Mission, pounds	Expected Usage (Average), pounds	Comments
Rate dissipation		0 to 0.046	Not observable
Sun acquisition	0.040	0.054	Tank temperature may not have been at steady state
Star acquisition and verification	0.030	0.048	
Midcourse maneuvers	0.150	0.092	Values of vernier phase of midcourse and postmidcourse rate dissipation subtracted from 0.200 pound
Vernier phase of midcourse	0.033*	0.033	
Postmidcourse rate dissipation	0.017*	0.017	
Coast mode	0.138	0.075	
Drift checks	0.099		Calculated value
Preretro maneuvers	0.116**	0.071	
Leakage	0.057*	0.057	
Total N_2	0.680	0.493	
Equivalent total	0.680	0.546	Drift N_2 usage is added to expected value and rate dissipation is subtracted from expected value

*Expected values were used.

**Estimated value using data from midcourse maneuver.

An I_{SP} of 60 seconds is used for expected values. These values were obtained from R. H. Bernard, "Revised Gas Jet Consumption for 66 Hour Surveyor Flight," IDC 2223/843, 19 February 1965.

Leakage: Since leakage information was not available, the expected value of 0.057 pound is used.

Drift checks: During the mission, six separate drift checks were performed. The various times are shown in Figure 5.6-81. Notice that during the latter period of the mission where three successive drift checks were made, the gas consumption rate is high. The value for drift check gas consumption was indirectly obtained by subtracting all accountable gas usage from the total. Drift check gas consumption = 0.099 pound.

Determination of Gyro Nulls

Preflight calibration of the three gyro error signal channels indicates that the nulls are as follows:

Pitch (FC-16) = 503 bcd

Yaw (FC-17) = 508 bcd

In the SC-1 calibration handbook the gyro null values are as follows:

Pitch (FC-16) = 509.6 bcd

Yaw (FC-17) = 514.5 bcd

The reason for the difference in the above two sets of figures is that the calibration handbook compensates for a known error source of magnitude 6.6 bcd. This error is the line drop caused by the difference that exists between the flight control and telemetry grounds. During thrust phase power-on periods, an additional line drop of 17.4 bcd is known to exist. This is not accounted for in the calibration handbook.

The apparent null values during inertial mode phases were obtained and all known errors were removed. The results of the investigation are presented in Table 5.6-24.

Determination of the Main Retro Thrust Vector Offset From the Spacecraft Center of Gravity

Spacecraft moment control during large disturbances is provided by the vernier engine system. The three engines that are capable of being differentially throttled obtain their commands from the output of three rate integrating gyros which establish an inertial reference frame. A block diagram representation of the attitude control loop is given below.

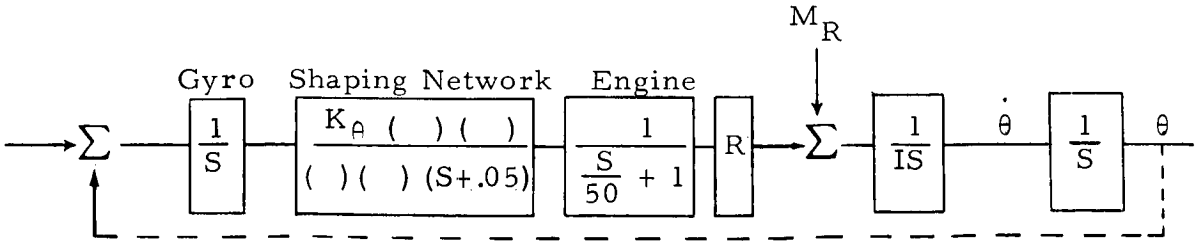


TABLE 5.6-24. GYRO NULLS

Mission Phase	Telemetry Condition	FC Number	Raw Data, bcd	Line Drop Correction	Unbalance Commutator Current	Corrected Value, bcd
Coast Mode 1	Low power, mode C, 550 bits/sec	FC-16	526.5	- 6.6	-3.7	516.2
		FC-17	525.0	- 6.6	-6.0	512.4
		FC-49	521.5	- 6.6	-1.90	513.5
Midcourse ΔV	High power, thrust phase power on, mode 1, 4400 bits/sec	FC-16	540	-24	-0.7	515.3
		FC-17	537	-24	-0.8	512.2
During gyro drift Test No. 6 (Coast Phase 2)	Low power, mode C, 550 bits/sec	FC-16	525	- 6.6	-3.7	514.7
		FC-17	525	- 6.6	-6.0	512.4
Prior to retro phase (thrust phase power on)	High power, thrust phase power on, mode 2, 1100 bits/sec	FC-16	543	-24	-2.0	517.0
		FC-17	537	-24	-2.6	510.4
		FC-49	539	-24	-1.77	513.2
Prior to retro (prior to the above period)	High power, mode 2, 1100 bits/sec	FC-16	524	- 6.6	-2.5	514.9
		FC-17	521	- 6.6	-2.6	511.8
		FC-49	520	- 6.6	-1.65	511.8
Average null value		FC-16				515.6
		FC-17				511.8
		FC-49				512.8
Average value using calibration handbook		FC-16				522.2
		FC-17				518.4
		FC-49				519.4

The steady-state relationship between moment disturbance M_R and attitude angle θ is as follows:

$$\theta = \frac{M_R \times 0.05}{K_\theta} \qquad (1)$$

where

$$\frac{K_\theta}{0.05} = \text{shaping network dc gain.}$$

Replacing $T_R \times d$ for M_R, the following relationship is obtained

$$d = \frac{K_\theta \times \theta}{0.05\ T_R} \qquad (2)$$

where

T_R = main retro thrust

d = distance of offset

K_θ = 3465

Retro Thrust Determination. The procedure in determining thrust is to utilize the acceleration data (FC-32) along with spacecraft mass at the instant of retro ignition.

1) Corrected acceleration value = 4.0923 g (see Figure 5.6-84)

2) Spacecraft mass at ignition is given in pounds as follows:

Injected weight	=	2192.71
Midcourse fuel	=	-16.81
Nitrogen	=	-0.68
AMR	=	-11.68
One second vernier	=	-0.80
Spacecraft weight at ignition	=	2162.74

Thus the thrust level at (near) retro ignite was

$$T_R = \frac{2162.74}{g} \times 4.0923\ g = 8850.58 \text{ pounds}$$

Gyro Angle Determination. During retro burn, the following gyro signals were obtained:

Pitch (FC-16) = 543 bcd
Yaw (FC-17) = 539 bcd
} raw data

After applying known corrections, the corrected values are (see Figures 5.6-85 and 5.6-86):

FC-16 (pitch) = 522.6 bcd

FC-17 (yaw) = 518.6 bcd

From the investigation of gyro nulls, the actual null values of the gyros were as follows:

FC-16 (pitch) = 522.2 bcd

FC-17 (yaw) = 578.4 bcd

Δ pitch = 0.4 bcd

Δ yaw = 0.2 bcd

Using Equation 1, the above values represent a moment disturbance value of less than 0.35 ft-lb or a θ/T_R ratio of 0.08×10^{-5} deg/lb.

Reference 28 mentions that the above technique is only good for offsets greater than 0.03 inch or θ/T ratio of 0.2×10^{-5} deg/lb or greater. Thus, it is concluded that the main retro thrust vector misalignment was less than 0.03 inch.

SC-1 Radar Noise Levels

Radar noise levels actually experienced in flight were estimated by visually comparing SC-1 telemetered data (Figure 5.6-87) with similar data generated by the six degree-of-freedom analog computer simulation of the radar controlled descent phase using various combinations of simulated V_x, V_y, V_z, and R noise inputs. Because the comparisons were qualitative and because the telemetry data is sampled rather than continuous, the accuracy is about ±20 percent on any estimate. Three data sources were used in the estimates: radar outputs, gyro outputs, and differential thrust commands. The most reliable of these were the differential thrust commands because of higher sampling rate and resolution. However, all three sources of data indicated approximately the same radar noise levels at any particular portion of the descent.

The analog computer runs were made from the six degree-of-freedom terminal descent simulation described in Reference 25. These results were supplemented by the S6-C closed-loop test data described in Reference 26.

V_Z Error Noise. V_Z error noise is due to noise on both the range and V_Z radar output signals. This noise caused large thrust command transients, giving a good data source for extracting the V_Z error noise level. The estimated levels for different mission times are given in Table 5.6-25.

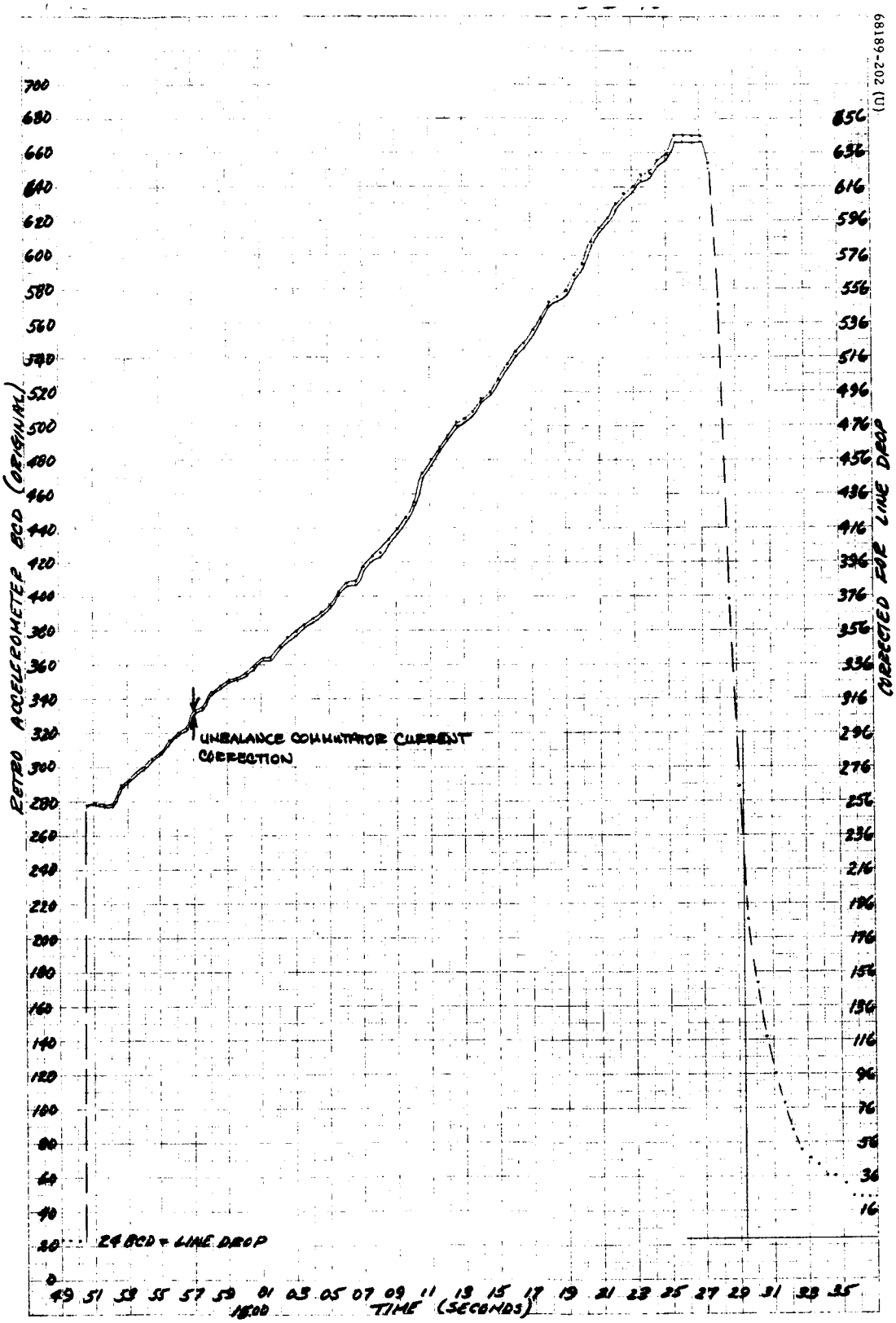


Figure 5.6-84. Acceleration Time History

Spaceflight Operations Facility
retro phase data

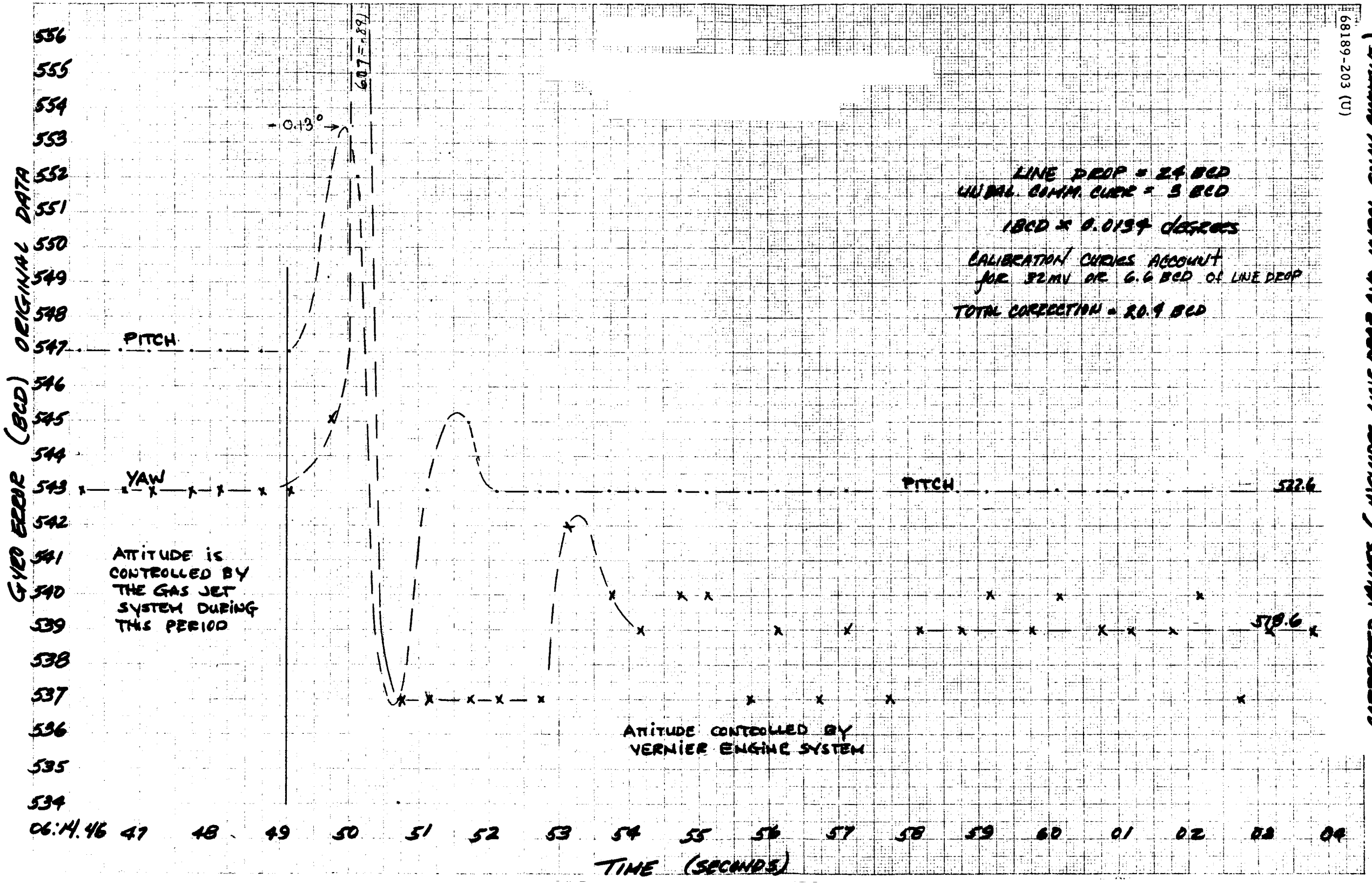


Figure 5.6-85. Pitch and Yaw Gyro Signals During Retro Phase
Spaceflight Operations Facility data tape

5.6-192

68189-203A (U)

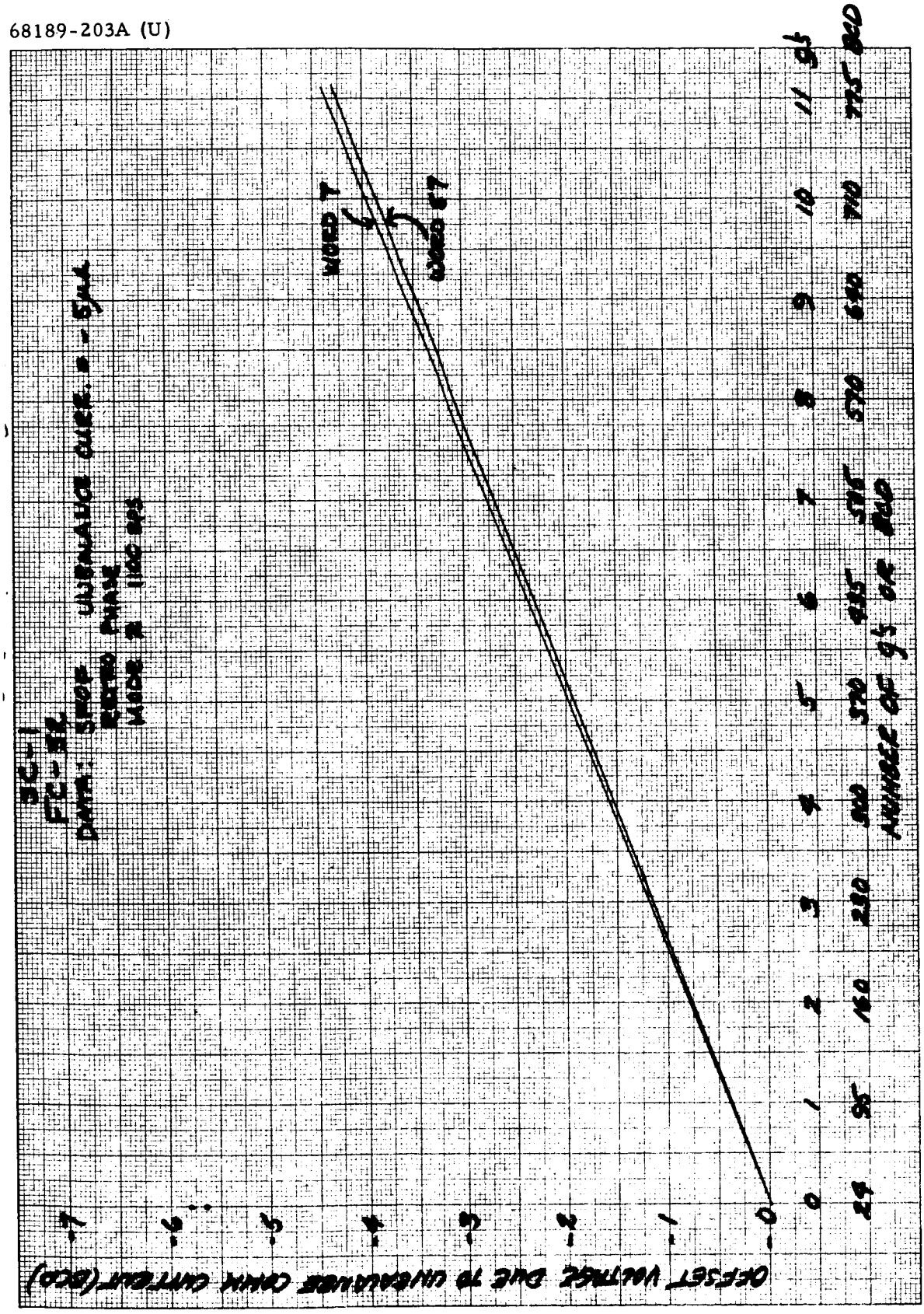


Figure 5.6-86. Offset Voltage Due to Unbalanced Commutator Current

TABLE 5.6-25. ESTIMATED LEVELS FOR DIFFERENT MISSION TIMES

Flight Condition		Time to Touch-down, seconds	3σ V_z Error Noise, ft/sec
Range, feet	V_z, ft/sec		
17,800 to 12,900	440 to 390	90 to 80	2.1
5500 to 980	215 to 105	55 to 25	1.5
980 to 300	105 to 57	25 to 17	1.0
100 to 25	20 to 8	11 to 8	1.0

V_x and V_y Noise. During maximum and minimum acceleration command periods, only V_x and V_y noise generates a differential thrust command. This command level is significantly lower than that generated by V_z error noise. The (approximately equal) estimated V_x and V_y noise levels for different mission times obtained from thrust command telemetry signals are as follows:

For R > 1000 feet (based on data from minimum and maximum acceleration command periods):

$$3\sigma\ V_x \text{ noise} = 3\sigma\ V_y \text{ noise} = 5.0 \text{ ft/sec}$$

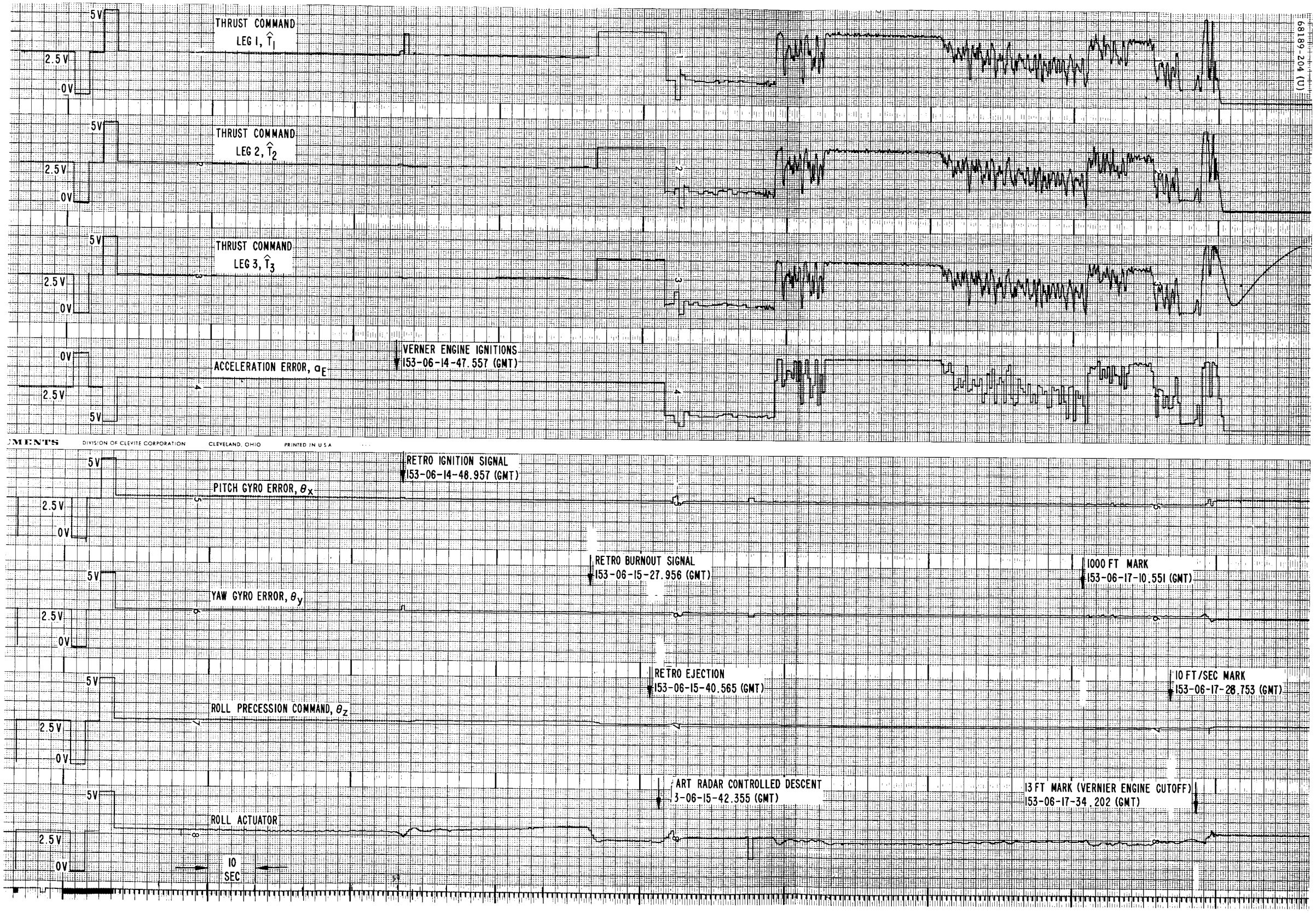
For R < 1000 feet (based on data from maximum acceleration command period):

$$3\sigma\ V_x \text{ noise} = 3\sigma\ V_y \text{ noise} = 2.5 \text{ ft/sec}$$

Comparison to Noise Specifications. The estimated SC-1 V_x, V_y, and V_z error noise levels are plotted in Figures 5.6-88, 5.6-89, and 5.6-90 in comparison to noise levels specified in the spacecraft functional requirements document (Reference 17). In Figure 5.6-88, V_z error noise is allotted entirely to the V_z radar signal, and in Figure 5.6-89, it is allotted entirely to the range radar signal. It is noted that SC-1 noise levels were generally within specification.

Analysis of Gyro Speed

The value of the gyro speed indications as to the assessment of the flight control system's condition has always been questionable. A thorough analysis on this subject has been performed and the text of the original memorandum is presented here as it appeared in Reference 27.



MENTS DIVISION OF CLEVITE CORPORATION CLEVELAND, OHIO PRINTED IN U.S.A.

68189-204 (U)

Figure 5.6-87. Flight Control Variables for Terminal Descent

5.6-195

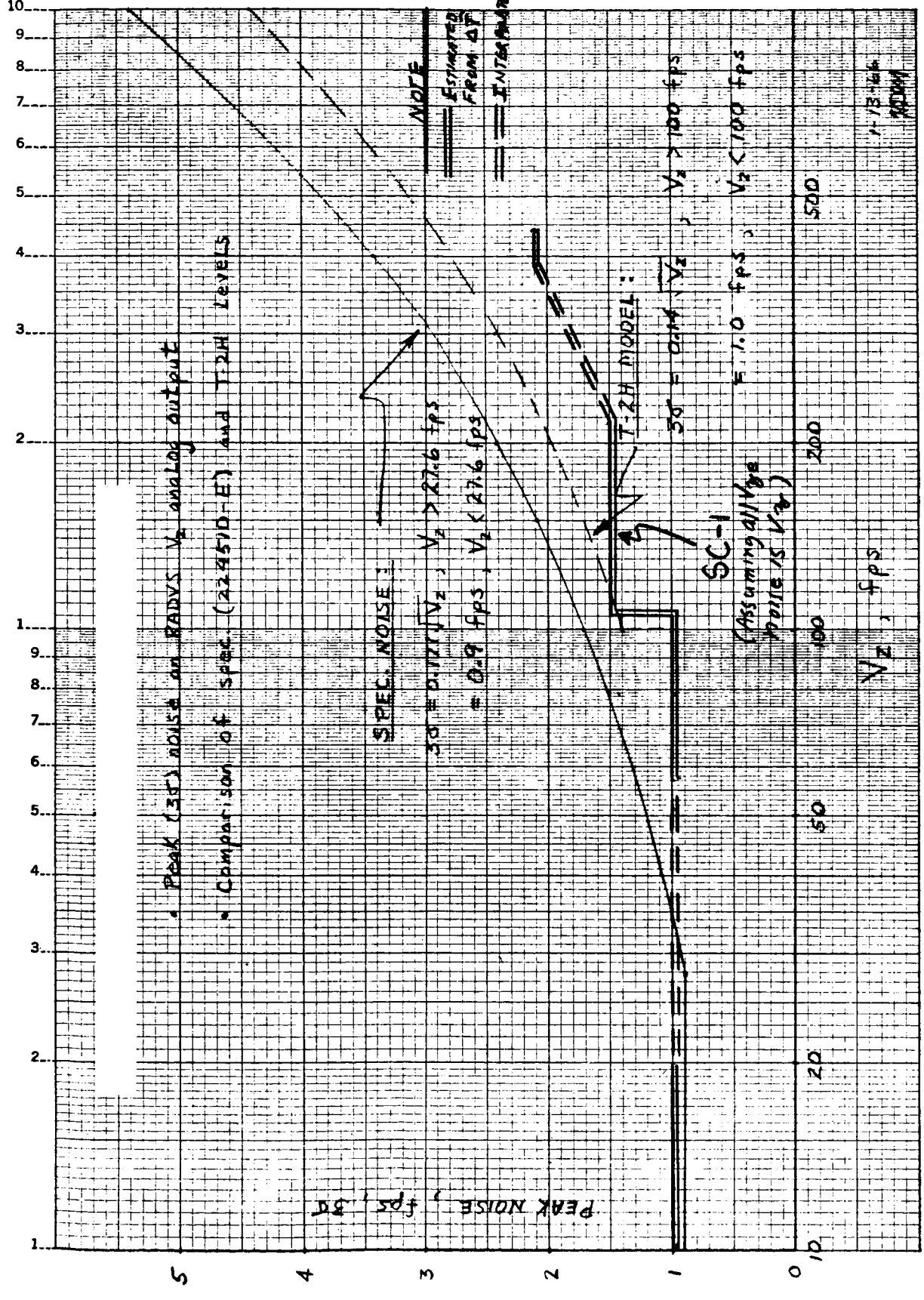


Figure 5.6-88. V_z Noise Amplitude

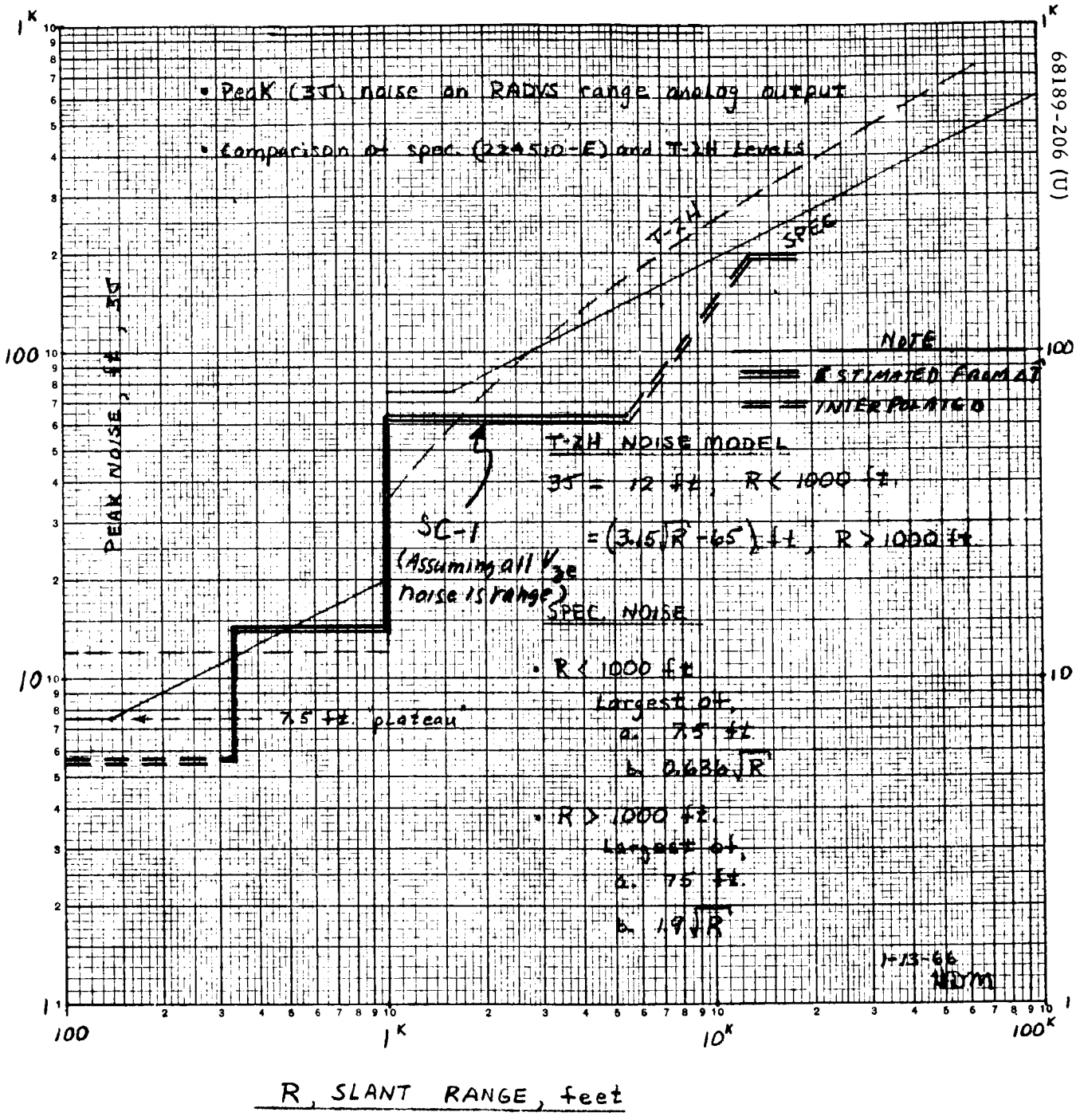


Figure 5.6-89. Slant Range Noise Amplitude

68189-207 (U)

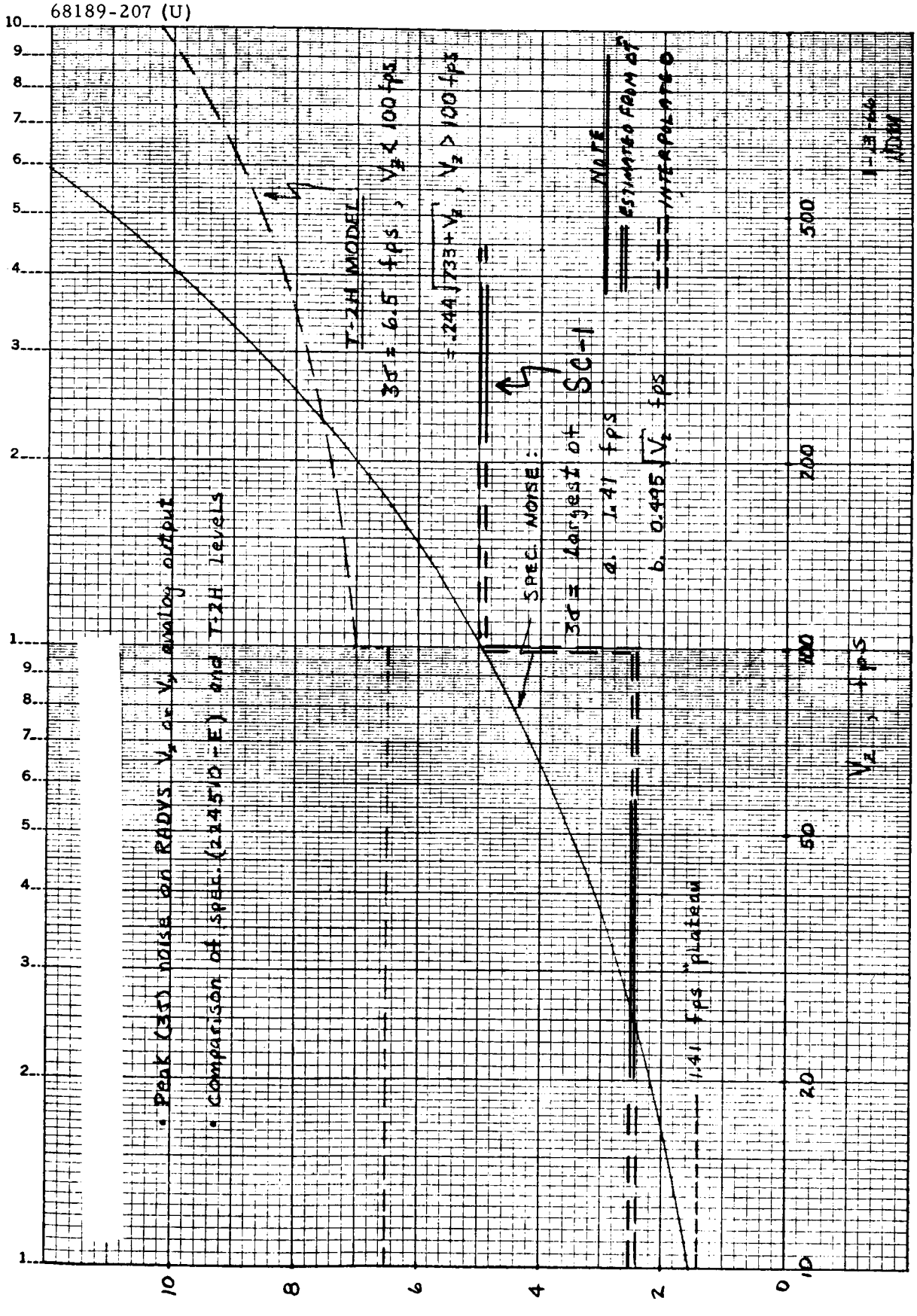


Figure 5.6-90. V_x or V_y Noise Amplitude

Introduction

The gyro speed signal processing was turned on once in flight during Surveyor Mission A and one cycle recorded by Goldstone (DSIF-11) about two hours before the midcourse maneuver. An analog strip chart of the 5.4 KC gyro speed subcarrier signal for its four minutes of operation was prepared by R. Lum of JPL's Data Analysis Lab from the on-site magnetic tape recording. The results of an examination of this analog record are presented here along with a general assessment of the gyro speed telemetry.

Summary

The history of the SC-1 gyro speed telemetry has been characterized by anomalous behavior which appears to have reached a climax in flight. The observed "gyro speeds" in flight were approximately 8% (yaw), 16% (pitch) and 26% (roll) higher than the corresponding values reported for the launch countdown. On the basis of test history one would expect the change, if any, from pre-launch to post-launch to be in the direction of a decrease for the roll and pitch gyros since both were out of tolerance on the high side before launch. At present the best explanation for this apparent anomaly lies in the different methods used to count the "gyro speed." In view of the problems associated with "gyro speed checks," it is recommended that they be deleted from system test and flight sequences.

Evaluation of Data

When first turned on in flight, the gyro speed processing stepping switch was set to sample the pitch gyro spin motor speed monitor. Since this switch was set to the null reference position at the conclusion of the pre-launch check, this might be considered a minor anomaly. A discussion of this with D. Hersey of the JPL Surveyor Telemetry Group revealed that the stepping switch assumes an arbitrary position when the gyro speed telemetry ECU is turned on by command 0221. Test data indicates that the Pitch Gyro selection is the "preferred" initial condition.

The data sequence and sample readouts are given in the following table (all times given are on 31 May, day 151):

Surveyor I Flight Gyro Speed Summary

GM Time	Event	Gyro Speed Count **
04 26 05 *	Command 0221 Initiated	
26 06.17	5.4 KC SCO on Select Pitch Gyro Speed	
26 08	Count Pitch Gyro Speed	68
27 00	Count Pitch Gyro Speed	67

GM Time	Event	Gyro Speed Count **
27 47	Count Pitch Gyro Speed	66
27 48 *	Command 0222 Initiated	
27 49. 66	Select Yaw Gyro Speed	
27 50	Count Yaw Gyro Speed	54
28 10	Count Yaw Gyro Speed	54
28 31	Count Yaw Gyro Speed	54
28 31 *	Command 0222 Initiated	
28 32. 15	Select Null Reference	
29 05 *	Command 0222 Initiated	
29 06. 15	Select Roll Gyro Speed	
29 07	Count Roll Gyro Speed	76
29 36	Count Roll Gyro Speed	75
30 04	Count Roll Gyro Speed	74
30 04 *	Command 0223 Initiated	
30 05. 18	Gyro Speed SCO off	

* Command times are taken from CDC Command Printer tape.

** Gyro speed count is the number of full cycles during a one-second interval at the beginning, middle and end of each readout period.

There was a very noticable variation in amplitude in the pitch and roll gyro speeds which appears to result from phase shifts. Large phase shifts on the order of 180° occurred frequently on the pitch gyro speed signal (over 25 times in 100 seconds), rarely on the yaw gyro speed, and never on the roll gyro speed. The amplitude of the yaw signal on the analog record (approximately 3V peak-to-peak) was significantly greater than for pitch and roll, but this may very well result from discriminator and/or oscillograph recorder response characteristics, since the yaw gyro signal frequency was lower.

Discussion

The telemetered gyro speed signals are derived by dividing down by 32 the 1600 cps (nominal) signal picked off from the gyro spin motors. The nominal count should thus be exactly 50 cps. It has been known for some time that noise on the signal lines upstream from the ÷ 32 circuit produces variable counts well above the spec tolerance.

A comparison of some SC-1 test data readings with the launch countdown and flight readings is given below. No actual readings were given, but

no gyro speed anomalies were reported in the Quick Look Reports for Combined System Tests at San Diego or Performance Verification Tests at ETR, leading to the conclusion that test GSE was a major contribution to the anomalous readings obtained during earlier tests. The STV Mission Sequence readings in the following table were taken from Quick Look Reports. The Launch Countdown values are average readings reported by R. Crabtree.

SC-1 Gyro Speed Test and Flight Comparison

Gyro	MS Test A 12/28/65	MS Test C 1/21/66	Launch Countdown	Flight
Roll	67-73	65-67	59	74-76
Pitch	58-66	66-70	58	66-68
Yaw	51-56	54-56	50	54

It is significant that the Mission Sequence Test C (plugs out) readings showed no improvement over Test A (or B), indicating that the variation in readings during the test history may be more dependent on the method of counting the output signal frequency than on the test configuration. The normal method used to obtain gyro speed count is to average the output of an "events-per-unit-time" (EPUT) meter using a Schmitt trigger to detect an "event" each time the signal voltage passes a certain level in one direction. Thus the setting of the trigger threshold is critical to insure a correct frequency count. The observed amplitude variation in the flight data signal indicates that it would be very difficult to adjust the trigger threshold to obtain a complete cycle count using this type of frequency counter.

The flight gyro speed counts are based on cycle peaks without regard to amplitude and therefore represent a true count, but even this count shows significant short-term variations, due obviously to noise on the signal line. Thus, the fact that the flight values given are higher than the pre-launch values which were obtained by a digital counter, does not necessarily mean that there were any significant changes in the SCO output signal. About the only valid conclusion that can be drawn from the data table is that the noise on the yaw gyro signal line was always considerably less than that on the roll and pitch gyro signal lines.

Value of the Gyro Speed Telemetry

The gyro speed telemetry is intended to provide an output signal pulse train whose frequency is proportional to the gyro spin motor speed. Its primary purpose is to verify that the gyros have reached synchronous operation after flight control power is turned on. This function on Ranger and Mariner was achieved by means of a hard-line monitor but was incorporated into the

Surveyor Spacecraft telemetry system because of a severe limitation on the number of signal leads available through the umbilical cable early in the Program.

The 1600 pps signal from the gyro Spin Motor Running Detector is fed through a frequency dividing network and should appear as a 50 cps oscillation on the subcarrier. Noise spikes of sufficient amplitude and duration to trigger the divider flip-flops are known to be present on the input signal line. This accounts for the observed readouts in excess of 50 counts. Since the noise is a generic design deficiency, the telemetry is virtually worthless for determining the true gyro spin motor speed.

How useful would the telemetry signal be if the noise problem were eliminated? Changes from the nominal 1600 of a few cps in the spin motor speed should not affect the gyro performance. Deviations on the order of 1-2%, the minimum detectable via telemetry using a digital frequency counter over reasonable sampling periods, indicate a failed gyro. There are more reliable telemetry signals available to detect such a failure.

Conclusion and Recommendations

The gyro speed telemetry is worthless as an indication of precession or commanded turning rates and unreliable as a failure indicator. In recognition of this fact the SPAC long ago abandoned any requirement for real-time reduction of this telemetry signal.

The basic design concept of the gyro speed telemetry is poor and redesigning the circuitry just to eliminate the noise problem would be a waste of time and money. In view of the large number of TFR's that have been and are still being written on this subject which is of such minor consequence to successful spacecraft operation, and because its testing and evaluation requires time consuming procedures and special equipment, logic would dictate that gyro speed checks be eliminated from system tests and flight conditions.

The recommended long-term solution is to remove the circuitry entirely from the ESP and replace it by a hard line monitor to verify gyro sync at turn-on and a sensor to monitor the 3-phase 400 cps gyro input signal from the Programmer with a readout on a PCM commutator.

Vernier System Pressurization/Canopus Sensor Anomaly

The following analysis was obtained from Reference 2 and is presented here in its entirety.

At the time of pressurization of the helium system just prior to midcourse, a rather interesting anomaly occurred affecting the output of the Canopus sensor. Figure [5. 6-91] shows a plot of the roll gyro error and the Canopus sensor signals during the period of interest. It is seen that, within 5 seconds after activation of the helium squib, the star intensity signal drops considerably and, in fact, a lock-on signal was generated for approximately two seconds.

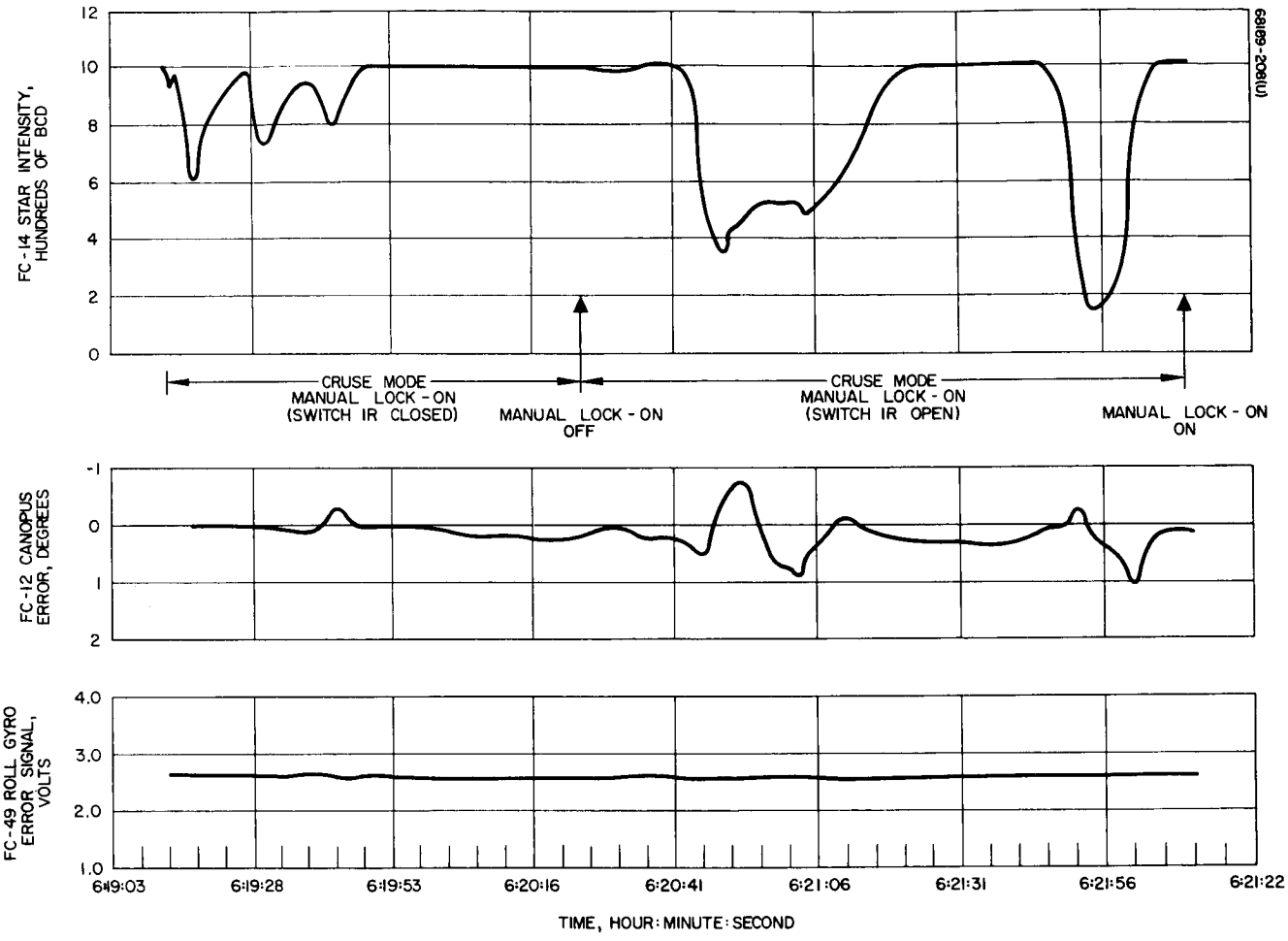


Figure 5. 6-91. Roll Gyro Error and Canopus Sensor Signals

Remembering that with the sensor calibrated high, it was necessary to attenuate the star light to produce this lock-on signal. The roll error signal was virtually unaffected suggesting that the cause of this behavior may have been a cloud of particles probably originating at the helium release squib. Figure [5. 6-92] shows that the squib valve and Canopus sensor are at the same station along the spacecraft Z axis and that there is a clear path from this valve assembly to the Canopus sensor field of view. It seems quite likely that the detonation of the squib could have liberated many small particles of white paint or vapor-deposited aluminum (VDA). Some of our astronauts have in the past reported a "shower of small particles" freed just by hitting the inside of their capsule with a hand, a fact which tends to lend some credence to this theory.

The next two "glitches" appear to be of a slightly different character but still caused by particles. Since a roll error curve is generated in each case that has the typical shape but of reduced amplitude, it appears that the cause of these is a single particle (or small group) and not a cloud of small particles. In addition, from the polarity of the curve it appears that if truly caused by particles, they are coming from the other direction. Figures [5. 6-92 and 5. 6-93] show how the coiled line assemblies on leg 1, which are coated with VDA, could liberate particles that could enter the field of view of the sensor. If one determines the trajectory that a particle must take if it comes directly off from this coiled line assembly and passes in front of the sensor (continuing in a plane containing this line assembly) the particle velocity computed checks out exactly (Figure [5. 6-94]) with the length of time that a particle was in the field of view for the first of these two "glitches." The second glitch appears to have been caused by a particle glancing off some other item on the spacecraft such as the RADVS antenna, thus taking longer to get into the field of view and also traveling up through the field just barely intersecting the negative side. It is only necessary to postulate a change in the approach angle from 21° (coplanar with coiled tubing) to 28° to come up with a particle velocity and trajectory consistent with the second glitch characteristic. The reduced amplitude error signal is probably caused by the size and range of the particles and the resultant defocusing effect.

The roll gyro error signal through all this remains essentially at null, indicating at least during the two large glitches (gyro in inertial) that no spacecraft movement took place.

In summary it can be said that the anomaly described here caused absolutely no difficulty; and although impossible to prove, was probably caused by particles liberated during helium system pressurization. The fact that all of this activity was confined to a single 3-minute interval beginning 3 seconds after squib activation out of a 63-hour mission in which these outputs were monitored continuously, should leave little doubt as to the correlation of the events. It is concluded that this operation should be considered quite understandable and that it will probably reoccur in subsequent flights.

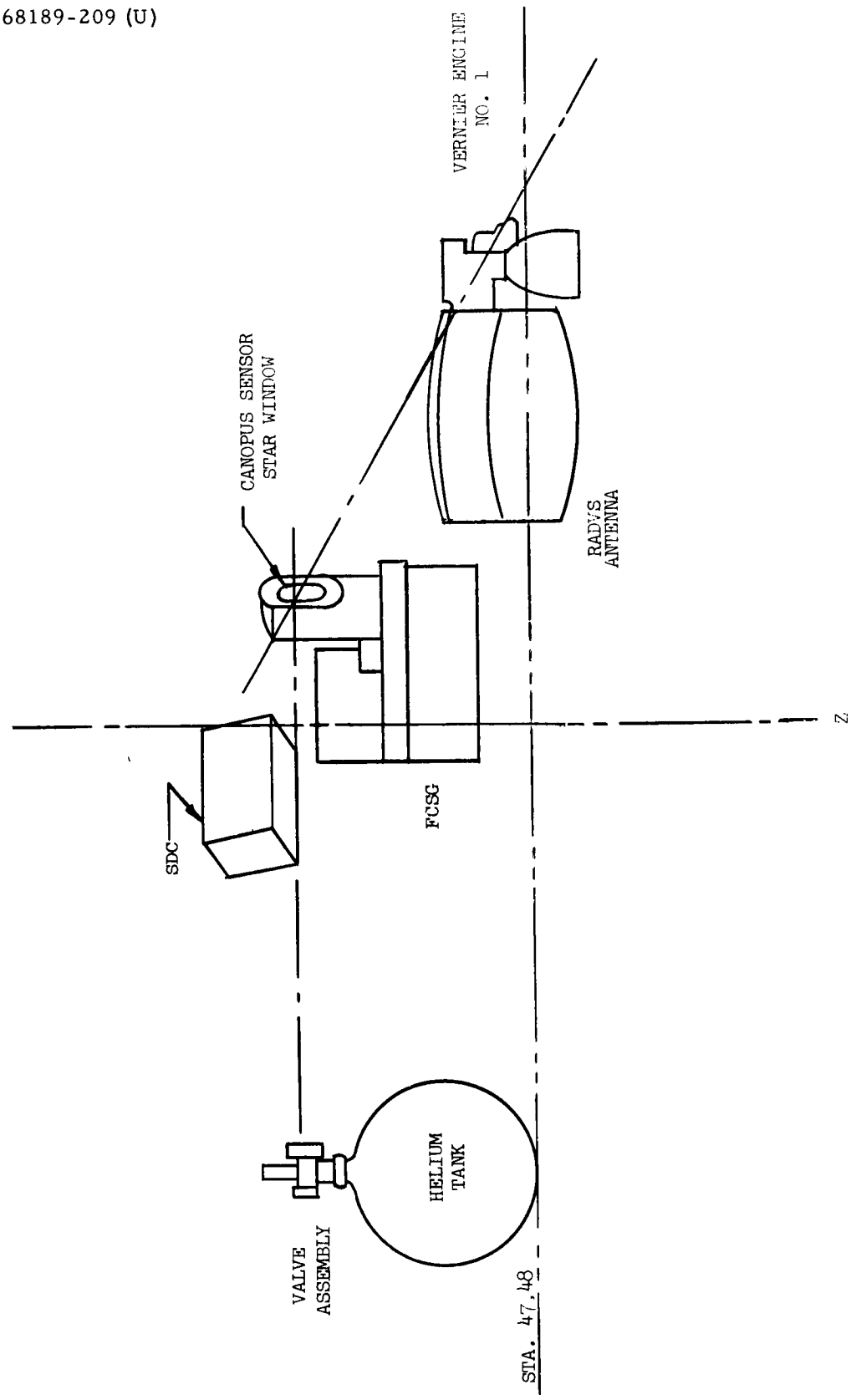


Figure 5.6-92. Spacecraft Seen Along Pitch Axis in Positive Direction

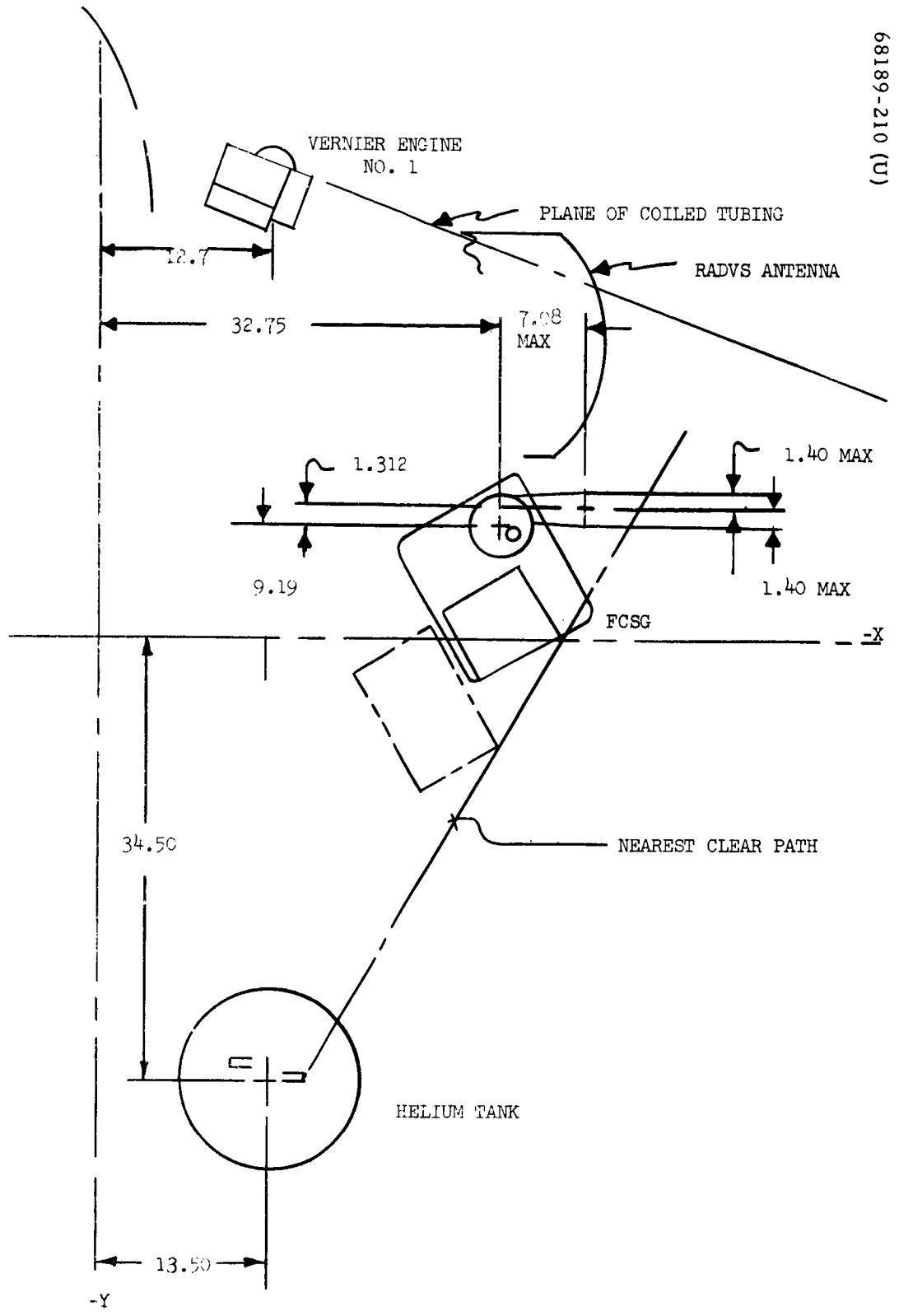
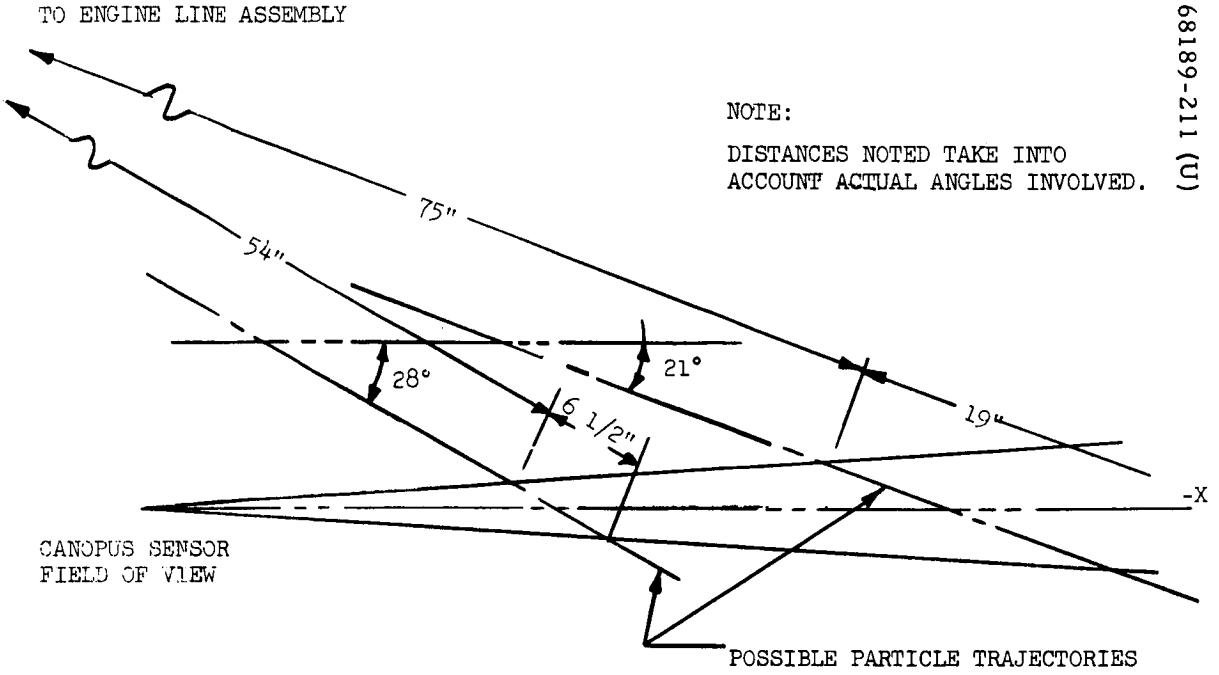


Figure 5. 6-93. Spacecraft Seen Along Roll Axis In Positive Direction



68189-211 (U)

FOR GLITCH #1

$V_1 = \frac{75 \text{ in}}{98 \text{ sec}} = 0.765 \text{ in/sec}$

$\Delta t_{F.A.V.} = \frac{19 \text{ in}}{0.765 \text{ in/sec.}} = 24.8 \text{ sec,}$ PARTICLE WAS IN FIELD OF VIEW FOR $\approx$ 24 SEC.

FOR GLITCH #2

Assume 28° approach -

$V_2 = \frac{54 \text{ in}}{158 \text{ sec}} = 0.34 \text{ in/sec.}$

$\Delta t = \frac{6.5 \text{ in}}{0.34 \text{ in/sec}} = 18.9 \text{ sec;}$ AND PARTICLE WAS IN FIELD OF VIEW FOR $\approx$ 18 SEC.

THEREFORE, IT'S POSSIBLE ---

Figure 5.6-94. Particle Trajectory

Roll Control System Performance

The estimated roll disturbance torque on SC-1 was extremely small during both midcourse and terminal maneuvers. The principal causes of vehicle roll disturbances were thrust vector excursions of the three vernier engines induced by bracket bending. Based on telemetry data, the maximum values of system parameters at any time in the mission were as follows:

Maximum roll actuator angle = 1.3 degrees

Maximum roll inertial error angle = 0.7 degree

Maximum roll actuator rate = 1.5 degrees

Maximum roll rate (estimated) = 0.5 deg/sec

It should be noted that the actuator angle was less than 1.1 degrees for all but 2 seconds of the mission based on the telemetry. The significant roll system parameters at different mission times are summarized in Table 5.6-26. These values were read directly from roll actuator (FC-43) and roll precession command (FC-49) telemetry signals.

The close agreement between predicted actuator angle from bracket bending and time actuator angle indicates that the roll disturbance due to retro and vernier propulsion systems was small (1 to 2 ft-lb) at all times.

TABLE 5.6-26. SUMMARY OF SIGNIFICANT ROLL SYSTEM PARAMETERS AT DIFFERENT MISSION TIMES

Time	Maximum Roll Actuator Angle, degrees (from pickoff, 0 volt reference)	Magnitude of Maximum Roll Actuator Rate, deg/sec	Steady-State Actuator Angle, degrees	Predicted** Steady-State Actuator Angle from Bracket Bending, degrees	Maximum Roll Angle, degrees‡	Steady-State Roll Angle, degrees‡‡
Midcourse	0.9*	0.4	0.6	0.75	-0.3	-0.2
Start of retro	-0.4	0.7	-0.2	0.2	0.2	0.1
End of retro	-0.9	0	-0.8	-0.3	0.4	0.4
Retro burnout through retro case ejection	1.2	1.0	1.0	1.0	-0.7	-0.6
Minimum acceleration	1.2	1.5	0.5	0.3	-0.6	-0.2
Segment control	1.3	1.0	1.1	0.8	-0.7	-0.6

*A plus actuator angle gimbals the No. 1 vernier engine to produce a plus vehicle roll control torque. See Figure 5.6-95.

**Based on a bracket spring constant of 0.0045 deg/lb and SC-1 initial alignment angles. See Figure 5.6-95.

‡Based on nominal roll gyro to roll actuator gain of 1.85 percent.

‡‡Figure 5.6-96 contains plots of both roll precession command and roll actuator signal during retro phase.

Terminal Precutoff Glitch Anomaly

Toward the end of the constant 5 ft/sec descent phase and during a 0.9-second period beginning at about 1.3 seconds prior to the 14-foot mark, all three vernier engines were commanded to throttle up by about 15 pounds from their normal quiescent level. This behavior may be observed on the three thrust command telemetry signals (FC-25, FC-26, and FC-27) as shown in Figure 5.6-97. It is also observed that all three thrust command signals behaved in unison and responded normally to the acceleration error signal (FC-15) which exhibited similar behavior, as indicated in Figure 5.6-97. This rules out the attitude control system as a possible cause for the anomaly and directs attention to the velocity control system in general and to the V_Z radar signal in particular.

Figure 5.6-98 shows a point-by-point, common-time-scale plot of vernier engine 1 thrust command (FC-25), RADVS V_Z analog output (FC-41), RADVS D1 gain number 2 (R-20), and RADVS D3 gain number 2 (R-24). From this data, it is possible to make the following observations:

1) The thrust command glitch was preceded by a shift in the V_Z analog indication of approximately 1.0 ft/sec. The normal system response to such a shift would be an up-throttle of the engines to reduce the V_Z indication to the 5 ft/sec level. The actual thrust command response was therefore normal.

2) Integration of the thrust command signals over the anomaly period indicates that approximately 20 lb-sec of thrust impulse were generated by the engines over and above that required to maintain constant descent velocity. Since spacecraft mass at this point was 20 slugs, the thrust anomaly resulted in a velocity decrease of 1.0 ft/sec. This is corroborated by the fact that the V_Z indication did decrease again by about 1.0 ft/sec following the up-throttle. This also indicates normal response of the velocity control loop, which continually acts to maintain the V_Z indication at 5 ft/sec.

3) The 1.0 ft/sec shift in V_Z analog indication was preceded by several switchings of the RADVS D1 and D3 No. 2 gain states. Since telemetry sampling period for these signals (R-20 and R-24) was 0.5 second, it is not possible to establish if more gain state changes than indicated in Figure 5.6-98 actually occurred. However, since it is known that rapid gain state switching caused DVS analog output glitches during the two final T-2N descent tests (although this was greatly magnified by the specific telemetry circuitry used on the T-2N vehicle), it seems reasonable to suspect that the SC-1 precutoff glitch may have ultimately been due to switching of D1 and D3 No. 2 gain states.

The following conclusions have been reached:

1) The precutoff glitch was caused by a 1.0 ft/sec shift in the RADVS V_Z analog output signal.

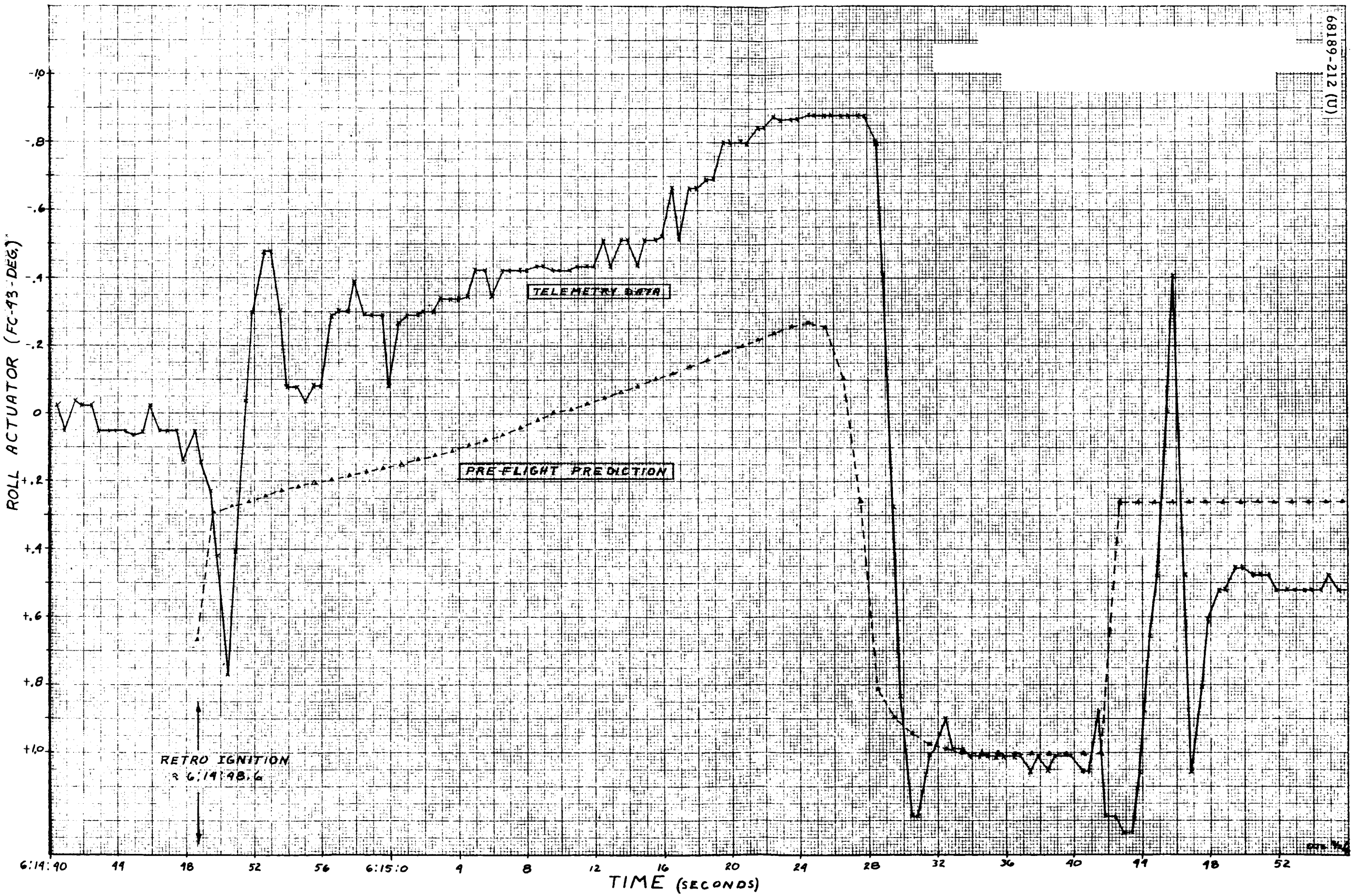


Figure 5. 6-95. Roll Actuator (FC-43) SC-1 Telemetry and Preflight Prediction

Retro phase

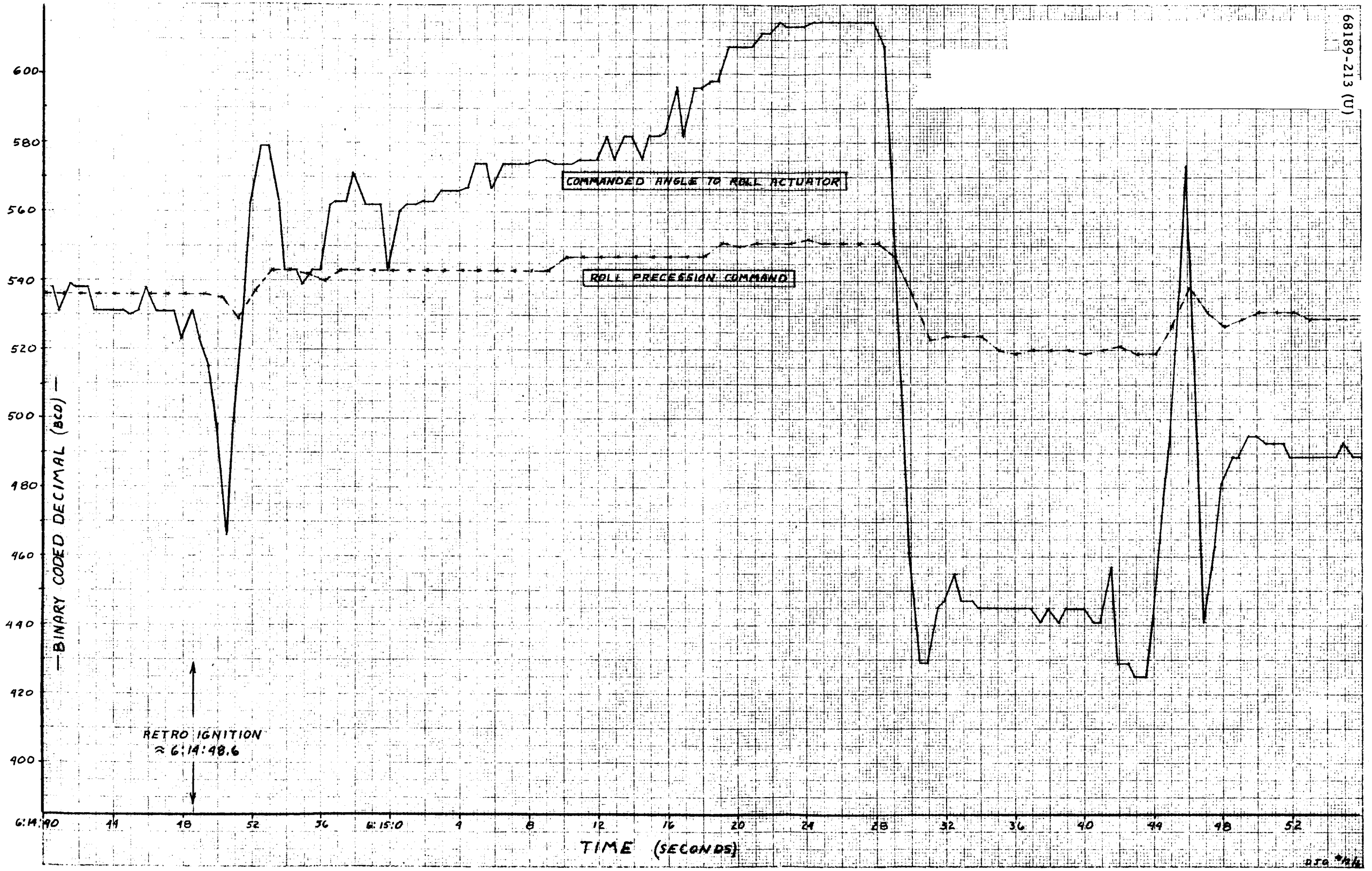


Figure 5.6-96. Roll Precession Command and Commanded Angle to Roll Actuator from SC-1 Telemetry of FC-49 and FC-43

Retro phase

FOLDOUT FRAME

FOLDOUT FRAME

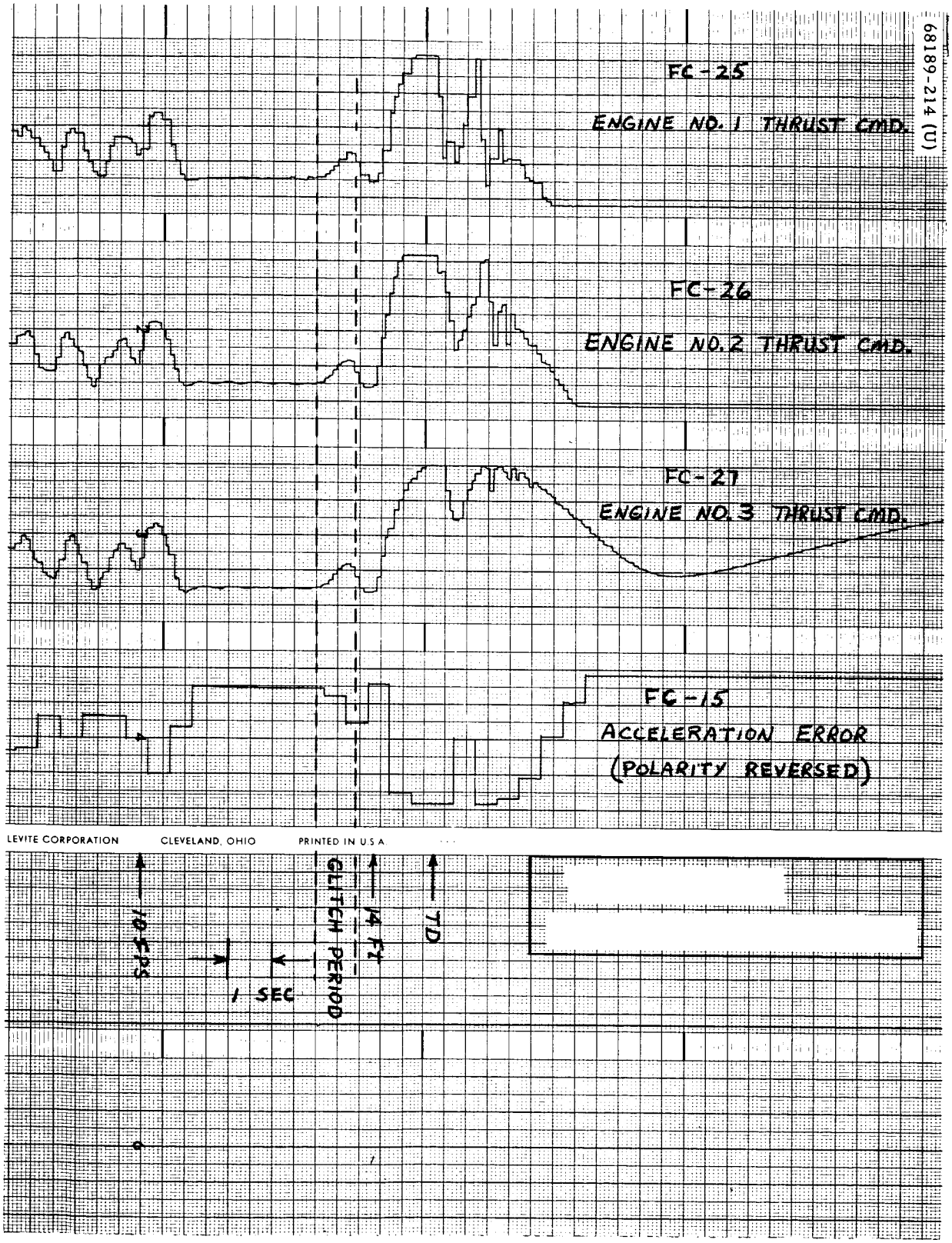


Figure 5. 6-97. Acceleration Loop Parameters (Near Cutoff)

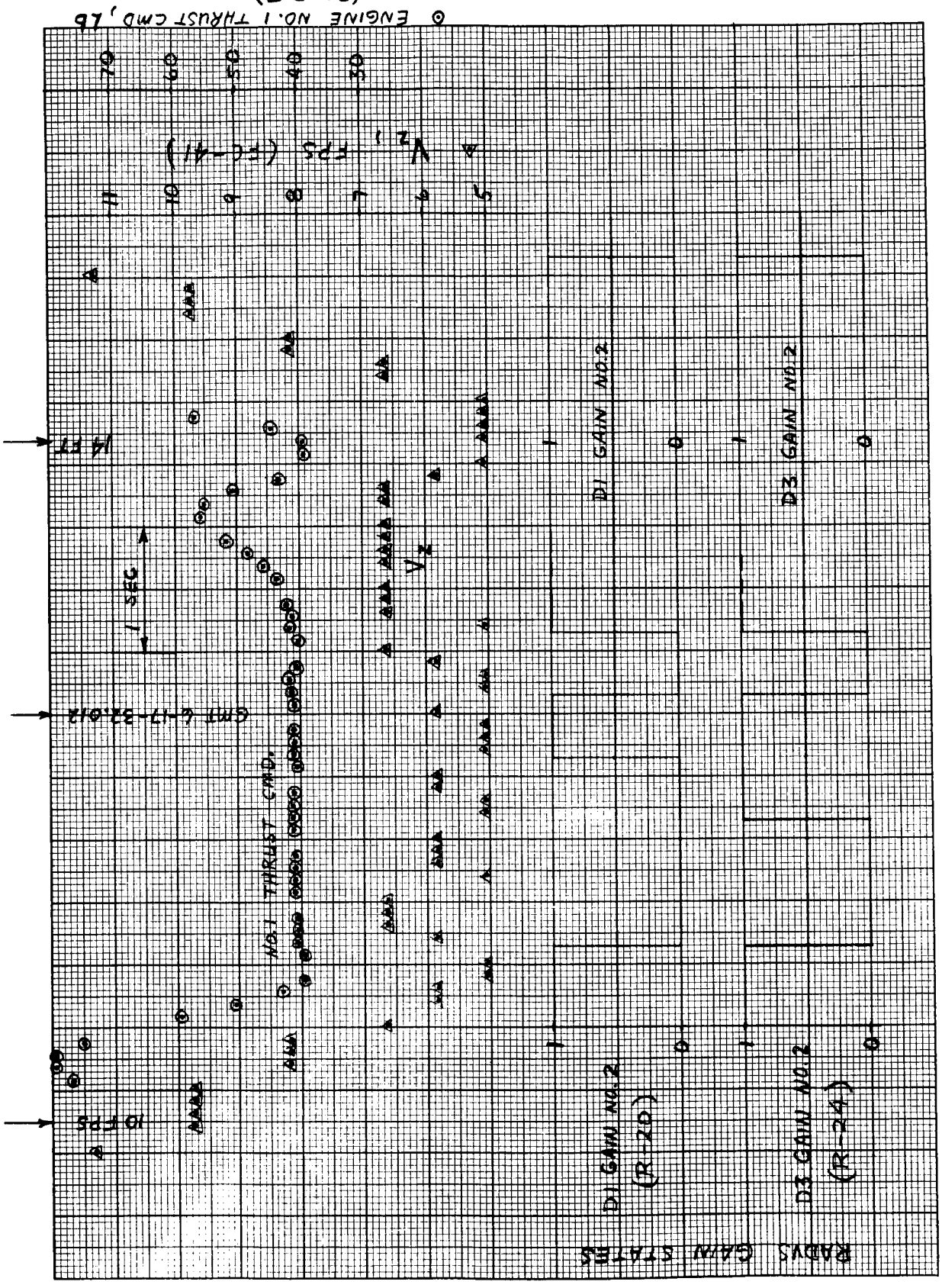


Figure 5.6-98. Analyses of Precutoff Glitch Anomaly

2) The cause of the V_Z shift is not definitely known at present, but it is suspected to be due to switching of RADVS D1 and D2 No. 2 gain states.

3) Since the V_Z analog accuracy specification allowance is $\pm \sqrt{1 + (0.02\, V_Z)^2}$, or $\pm$ 1.0 ft/sec for V_Z = 5 ft/sec (Reference 17), the V_Z indication apparently did not violate its accuracy requirement, at least not to any great extent, during the glitch.

4) Spacecraft soft landing performance was in no way compromised by the glitch.

5.6.8 REFERENCES

1. "Quick-Look Report," Hughes Aircraft Company, SSD 64110.
2. "General Dynamics Report," GD/C-BNZ66-036, page 7.
3. O. N. Hertzmann, "SC-1 Mission Performance – Flight Control Report," IDC 2223/2341, 23 June 1966.
4. R. H. Bernard, "Revised Gas Jet Consumption for 66 Hour Surveyor Flight," IDC 2223/843, 19 February 1965.
5. S. McCormick and D. R. Partridge, "Time Log of Command Sequences," IDC 2253.1/692, 7 July 1966.
6. R. H. Bernard, "Limit Cycle Behavior of the Surveyor Gas Jet Attitude Control System with Simulated Canopus Sensor Noise Included in the Analog Mechanization," IDC 2223/772, 15 February 1965.
7. Surveyor Flight Control SPAC Handbook, SC-1.
8. R. H. Bernard, "Flight Measurement of Gyro Random Drift for Surveyor," IDC 2223/1509, 20 September 1965.
9. K. Kobayashi, "A Method of Determining Gas Jet Thrust Level -- Post Mission Analysis," IDC 2253.4/25, 1 March 1966.
10. "Interface Document, Surveyor Vernier Propulsion Thrust Chamber Assembly," Hughes Specification 287015, Rev. 6, Model SC.
11. H. D. Marbach, "Angular Rates at Midcourse Shutdown," IDC 2223/731, 3 February 1965.
12. H. D. Marbach, "Probability of Maintaining Inertial Reference Following Midcourse Shutdown," IDC 2223/2339, 11 May 1966.

13. T. Zajicek, "Midcourse Acceleration Vector and Thrust Axis Alignment Error," IDC 2253.1/707, 18 July 1966.

14. P. Massie, "Telemetry of Thrust Chamber Throttle Valve Current," IDC 2258.8/75, 11 March 1966.

15. "Flight Path Analysis and Command Operations Report," Hughes Aircraft Company, SSD 68142R, 24 June 1966.

16. D. N. Gerding, "The Effect of Erroneous Rotations and Initial Position Errors in Determining the Final Location of a Vector," IDC 2253.3/167, 15 July 1964.

17. "Surveyor System Functional Requirements Specification, 224510," Revision E, 6 January 1966.

18. K. C. Beall and L. C. Gee, "Surveyor I Flight Performance Quick Look Report," Hughes Aircraft Company, SSD 64136R, 17 June 1966.

19. D. Bender, "SC-1 Event Times from Teltab," IDC 2253.2/616, 11 July 1966.

20. W. R. Heathcote, R. L. Lackman, and P. A. Stephens, "SC-1 Attitude Matrix and Sun/Earth Positions," IDC 2292/20, 19 August 1966.

21. P. A. Stephens, "Determination of S/C Attitude Matrix by Method of Least-Squared Error," IDC 2292/8, 11 August 1966.

22. J. Pachares, "Procedure for Combining Independent Estimates of a Transformation Matrix," IDC 2253.4/24, 29 February 1966.

23. "Quick Look and Final Report on SC-1 Helium and Nitrogen Systems Depressurization and Calibration Test," Hughes Aircraft Company, SSD 64098R, 27 April 1966.

24. R. H. Bernard, "Restoration and Updating of Surveyor Coast Phase Analog Computer Mechanization," IDC 2223/77, 29 July 1964.

25. R. R. Fagerlund, "Surveyor 6-Degree-of-Freedom Analog Computer Simulation," IDC 2223/1122, 29 April 1965.

26. "Surveyor S-6C Flight Control System Verification Test," Hughes Aircraft Company, SSD 56037R, February 1966.

27. A. E. Dickinson, "Analysis of Surveyor I Flight Gyro Speed Data," JPL IM 292-66-148, 15 July 1966.

28. "Surveyor Spacecraft Post Mission Analysis Handbook – Flight Control," Hughes Aircraft Company, SSD 68117R, 5 May 1966.

29. "Surveyor Spacecraft Model A-21 Equipment Specification, 224832," 15 June 1965.

5.6.9 ACKNOWLEDGMENTS

Although the SC-1 mission was almost perfect, several hundred analysis hours were required to properly evaluate the spacecraft performance. Varied talents were called upon to complete this effort. Those directly responsible for the contents of this section of the report are as follows:

K. K. Kobayashi, coordinator
R. H. Bernard
J. H. Green
H. D. Marbach
B. N. Smith